Novel ruthenium(II) and -(III) complexes encompassing biologically relevant multidentate chelates: synthesis, structural elucidation, electrochemistry and biological studies

by

Sanam Maikoo

Submitted in the fulfilment of the requirements for the degree of

Doctor of philosophy

In the School of Chemistry and Physics at the

University of KwaZulu-Natal

November 2019

Supervisor: Prof. Irvin N. Booysen

As the candidate's supervisor I have approved this dissertation for submission:

Signed: _____ Date: _____

Table of contents

Chapter 1

Introduction

Chapter 2

Materials and methods

Chapter 3

Structure-activity correlations of ruthenium compounds with mono- or bis-heterocyclic chelates

Chapter 4

Synthesis, characterization and cytotoxic studies of ruthenium complexes with Schiff bases encompassing biologically relevant moieties

Chapter 5

Formation, characterization and biomolecular interactions of new ruthenium compounds with thiosemicarbazone or benzothiazole Schiff base chelates

Chapter 6

Stabilization of the ruthenium(II) and -(III) centres by chelating *N*-donor ligands: Synthesis, Characterization, Biomolecular affinities and Computational studies

Chapter 7

Conclusion and future work

Preface

The experimental work described in this dissertation was conducted within the School of Chemistry and Physics at the University of KwaZulu-Natal, Pietermaritzburg, from July 2014 to August 2019, under the supervision of Professor Irvin Noel Booysen.

These studies represent original work by the author and have not otherwise been submitted in any form for any degree or diploma to tertiary institutions. Where use has been made of the work of others, it is duly acknowledged in the text.

Declaration 1 – Plagiarism

I, Sanam Maikoo, declare that:

1. The research reported in this thesis, except where otherwise indicated, is my original research.

2. This thesis has not been submitted for any degree or examination at any other university.

3. This thesis does not contain other persons data, pictures, graphs or other information, unless specifically acknowledged as being sourced from other persons.

4. This thesis does not contain other persons writing, unless specifically acknowledged as being sourced from other researchers. Where other written sources have been quoted, then:
   (a) Their words have been re-written, but the general information attributed to them has been referenced
   (b) Where their exact words have been used, then their writing has been placed in italics and inside quotation marks, and referenced.

5. This thesis does not contain text, graphics or tables copied and pasted from the Internet, unless specifically acknowledged, and the source being detailed in the thesis and in the References sections.

Signed: _____

Declaration 2 – Publications

Manuscript submitted and comments being attended to:

1. Maikoo, S.; Chakraborty, A.; Vukea, N.; Dingle, L.M.K.; Samson, W.J.; de la Mare, J.; Edkins, A.L.; Booysen, I.N. "Structure-activity correlations of ruthenium compounds with *mono*- or *bis*-heterocyclic chelates". *POLYH-D-19-00756*, 2019.

Manuscripts to be submitted:

2. Maikoo, S.; Dingle, L.M.K.; Chakraborty, A.; Xulu, B.; Edkins, A.L.; Booysen, I.N. "Synthetic, characterization and cytotoxic studies of ruthenium complexes with Schiff bases encompassing biologically relevant moieties, 2019.
3. Maikoo, S.; Booysen, I.N.; Xulu, B. "Formation, characterization and biomolecular interactions of new ruthenium compounds with thiosemicarbazone or benzothiazole Schiff base chelates". 2019.
4. Maikoo, S.; Booysen, I.N.; Xulu, B. "Stabilization of the ruthenium(II) and -(III) centres by chelating *N*-donor ligands: Synthesis, Characterization, Biomolecular affinities and Computational studies". 2019.

The free-ligands and their respective metal compounds reported in the aforementioned manuscripts have been synthesized, characterized and analysed by myself. In addition, I conducted the biomolecular electronic and emission spectrophotometric measurements as well as electrochemical, radical scavenging and computational studies. The majority of the single crystal X-ray diffraction analyses were run and solved by the technicians, Mr Sizwe Zamisa or Mr Leigh A. Hunter while Dr Eric Hosten from the Nelson Mandela University attained the low resolution structure of **1** and Prof Matthew Akerman from the University of KwaZulu-Natal attempting to fully refine it. In manuscripts 1 and 2, agarose gel electrophoresis studies, Hoechst DNA

competitive binding assays, *in vitro* anticancer cell line studies and cytotoxicity assays were conducted by the research groups of our collaborators at Rhodes University, Dr J. de la Mare and Professor A.L. Edkins. ESR spectra were acquired by Dr B. Xulu based at UKZN. I prepared the initial drafts of the manuscripts which was proof-read by my supervisor, Professor I.N. Booysen, and our collaborators.

Acknowledgements

I would like to express my gratitude to my supervisor, Prof Irvin N. Booysen, for his patience, guidance, encouragement and advice he has imparted to me throughout my time as his student.

To my colleagues, Sandipa, Leigh, Lesley and Dr M.B. Ismail, thank you for the support and guidance you guys have given me through these years.

Furthermore, I would like to thank Prof M.P. Akerman, Leigh Hunter, Sizwe Zamisa and Dr A. Xulu for running and solving my single crystal X-ray diffraction samples and for obtaining our raw data for Electron Spin Resonance. Notable thanks goes out to the School of Chemistry and physics for providing me with a laboratory space and equipment required during his study, as well as to the National Research Foundation and the *Deutscher Akademischer Austauschdienst* (DAAD *i.e.* German Academic Exchange Programme) for providing me with much needed funding.

My studies would not have been possible without the constant sacrifices of my mum, I am forever indebted to her for her love, support and financial contributions in my life. I would also like to thank my dad for the support and for making things a little easier for me in terms of finances and transport during this study.

To the love of my life, my dear husband Avinash, I was continuously amazed by your love and patience during all the ups and downs of my research. Thank you for all your sacrifices and for taking care of me so meticulously during this journey, I would not have been able to get this far without you.

Finally, I would like to thank God for the strength to continuously move forward and progress despite the storms I have faced.

Crystallographic data

Supplementary data for the crystal structures attained during this research are deposited on a compact disk that is attached to the inside back cover of this thesis.

This data includes the following:

- Final coordinates and equivalent isotropic displacement parameters of the nonhydrogen atoms
- Final crystal data and details of the structure determinations
- Isotropic displacement parameters
- Hydrogen atom positions
- Contact distances
- Torsion angles
- Hydrogen-bonds

List of tables and schemes

List of figures

Common abbreviations and acronyms

ALA	Alanine
ARG	Arginine
A-T	Adenine-Thymine
BAM	Biologically Active Moiety
bbb	4,4’-Bis(1H-benzimidazol-2-yl)-2,2’-bipyridine
BSA	Bovine Serum Albumin
btm	2-((5-hydroxypentylimino)methyl)benzothiazole
C-G	Cytosine-Guanine
cinap	1,5-dimethyl-2-phenyl-4-10-1,2-dihydro-3H-pyrazol-3-one
CT	Calf Thymus
cumap	1,5-dimethyl-2-phenyl-4-10-1,2-dihydro-3H-pyrazol-3-one
cumbh	N'-(4-isopropylbenzylidene)benzohydrazide

CV	Cyclic Voltammetry
DCM	Dichloromethane
DFT	Density Functional Theory
DMF	Dimethylformamide
DMSO	Dimethylsulfoxide
DNA	Deoxyribonucleic Acid
DPPH	2,2-di(4-tert-octylphenyl)-1-picrylhydrazyl
EPR	Electron Paramagnetic Resonance
ESR	Electron Spin Resonance
EtBr	Ethidium Bromide
FDA	U.S. Food and Drug Administration
FTIR	Fourier-Transform Infrared
G-C	Guanine-Cytosine
*g*DNA	Human genomic DNA
GLN	Glutamine
Hbpc	N-[1,3-benzothiazole-2-ylmethylidene]pyridine-2-carbohydrazide

HOMO	Highest Occupied Molecular Orbital
Hpmt	1-((pyridin-2-yl)methylene)thiosemicarbazide
HSA	Human Serum Albumin
Htmc	1-((thiophen-2-yl)methylene)thiosemicarbazide
Htpc	N-[(uracil-5-yl)methylidene]pyridine-2-carbohydrazide
Httc	N-(uracil-5-yl)methylene)thiophene-2-carbohydrazide
IR	Infrared
LMCT	Ligand-to-metal Charge Transfer
LUMO	Lowest unoccupied Molecular Orbital
LYS	Lysine
MeOH	Methanol
MLCT	Metal-to-Ligand Charge Transfer
NMR	Nuclear Magnetic Resonance
NO	Nitric Oxide
ombb	2,2’-[oxybis(methylene)]-bis-(1H-benzimidazole)
ORTEP	Oak Ridge Thermal Ellipsoid Plot

PBS	Phosphate Buffered Saline
PRO	Proline
RMSD	Root-Mean-Square-Deviation
SWV	Square Wave Voltammetry
T-A	Thymine-Adenine
TAE	Tris-Acetic Acid EDTA
TRP	Tryptophan
UV-Vis	Ultraviolet-Visible
VAL	Valine
VdW	Van der Waals
XRD	X-Ray Diffraction

Abstract

Chapter 1 reviews the coordination chemistry of ruthenium and rationalizes the design, synthesis and characterization of novel ruthenium compounds with multidentate chelators encompassing various bio-active moieties. Another core focal point of the research study is to generate structure-activity relationships between our new ruthenium-based drug candidate and closely-related metal compounds that we have previously reported. The relevance of this design approach is also motivated through describing the evolution of ruthenium anticancer drugs. Furthermore, cohesive and succinct descriptions of the general chemistry and the coordination behaviours of N, X (X = O, N or S) multidentate chelators towards ruthenium in its +II and +III oxidation states are discussed.

Chapter 3 details the formation and characterization of new ruthenium(II) compounds with *bis*-benzimidazole chelates: *cis*-[$Ru^{II}Cl(PPh_3)_2$(ombb)](PF_6) (**1**) (ombb = 2,2'-[oxy*bis*(methylene)]*bis*(1*H*-benzimidazole)) and *trans*-[$Ru^{II}Cl_2(PPh_3)_2$(bbb)] (**2**) (bbb = 4,4'-*bis*(1*H*-benzimidazol-2-yl)-2,2'-bipyridine). These metal compounds were characterized by numerous physicochemical techniques and their solid-state structures were attained using single crystal X-ray analysis. Voltammetry experiments were conducted to investigate the redox properties of the respective metal complexes. Radical scavenging studies revealed that **1** and **2** as well as the previously reported ruthenium compounds: [$RuCl(Hobz)_2(PPh_3)$]Cl (**3**) (Hobz = 2-hydroxyphenylbenzimidazole) and [$Ru^{III}Cl(obs)_2(PPh_3)$] (**4**) (Hobs = 2-hydroxyphenylbenzothiazole); showed high activities towards the neutralization of nitric oxide and 2,2-diphenyl-1-picrylhydrazyl radicals. Investigations of the Deoxyribonucleic Acid (DNA) interactions for **1** – **4** indicated that these metal compounds are groove-binders with intrinsic binding constants in the order of 10^4 – 10^7 M^{-1}. Optimal uptake of the ruthenium compounds by Bovine Serum Albumin (BSA) was observed based on their optimal apparent association and static quenching binding constants (K_{app} and $K_{SV} > 10^4$ M^{-1}). With the exception of compound **2** which was non-toxic, the other ruthenium compounds showed moderate cytotoxicity against a triple-negative breast cancer cell line that was greater than that of 5-fluorouracil, but lower than that of paclitaxel.

Chapter 4 describes the formation and characterization of novel paramagnetic ruthenium complexes, *cis-Cl*, *trans-P*-[$Ru^{III}Cl_2$(carboim)$(PPh_3)_2$] with bidentate chelating carbohydrazide Schiff bases (carboim = bpc for **1**, ttc for **2** and tpc for **3**). These metal complexes were synthesized by the equimolar coordination reactions of *trans*-[$RuCl_2(PPh_3)_2$] with *N*-[1,3-benzothiazole-2-ylmethylidene]pyridine-2-carbohydrazide (Hbpc), *N*-((uracil-5-yl)methylene)thiophene-2-carbohydrazide (Httc) and *N*-[(uracil-5-yl)methylidene]pyridine-2-carbohydrazide (Htpc), respectively. Physicochemical techniques including nuclear magnetic resonance-, electron-spin resonance- and infrared spectroscopy, UV-Vis spectrophotometry, voltammetry as well as molar conductivity measurements provided definitive determinations of the respective ruthenium compounds' structures. Numerous parallels were drawn with the optimized data of **1** – **3** and their experimental spectroscopic data as well as their solid-state structural features. The DPPH and NO radical scavenging capabilities of **1** – **3** and two previously reported ruthenium(II) complexes, *trans*-[$RuCl(PPh_3)_2$(Htdp)] (H_2tdp = 5-((thiophen-3-yl)methyleneamino)-6-amino-1,3-dimethyluracil) (**4**) and [$RuCl(PPh_3)(H_3$ucp)] (H_4ucp = 2,6-*bis*-((6-amino-1,3-dimethyluracilimino)methylene)pyridine) (**5**), were investigated. The calf-thymus DNA and BSA binding capabilities of **1** – **5** were explored using UV-visible spectroscopic techniques and gel electrophoresis which were supported by molecular docking simulations. *In vitro* anticancer studies showed that, while **1** and **2** were not active in the range tested, **3** – **5** were toxic to HCC70 breast carcinoma cells, with **4** showing promising EC_{50} at 3.9 µM.

Chapter 5 illustrates the formation of unique paramagnetic ruthenium compounds, *trans-P*-[$RuCl(PPh_3)_2$(pmt)]Cl (**1**) (Hpmt = 1-((pyridin-2-yl)methylene)thiosemicarbazide), *trans-P*-[$RuCl(PPh_3)_2$(tmc)]Cl (**2**) (Htmc = 1-((thiophen-2-yl)methylene)thiosemicarbazide) and a diamagnetic ruthenium complex, *cis-Cl, trans-P*-[$RuCl_2(PPh_3)_2$(btm)] (**3**) (btm = 2-((5-hydroxypentylimino)methyl)benzothiazole). Spectroscopic data supported by single crystal X-ray analysis affirmed the structures of the respective monomeric compounds. Their redox properties were metal-induced transformations which occurred within characteristic potential windows while the neutralizing capabilities towards the DPPH and NO radicals of **1** and **2** were more potent. UV-Vis DNA binding titrations revealed that **1** – **3** exhibits intrinsic binding constants in the order of 10^5 M^{-1} and as per the spectral alterations, the common interactive mode was ascribed to groove-binding. Molecular docking studies suggested that the preferential B-DNA binding modes of the optimized conformers are predominately dictated by nature of the intermolecular interactions oppose to only steric factors. Experimental BSA

interactions of the respective metal compounds monitored by UV-visible and fluorescence spectrophotometry, revealed that they are static quenchers where the molecules interact with hydrophophic sites. *In silico* studies corroborate that their optimized structures interact with BSA crystal structure's subdomains **IB** and **IIA**.

Chapter 6 demonstrated the formation of novel mononuclear ruthenium(III) compounds with chelating *N*-donor ligands: *fac*-[$RuCl_3(PPh_3)$(ap)] (**1**) {ap = 4-aminoantipyrine}, *trans*-P-[$Ru(PPh_3)_2$(cinap)$_2$](PF_6) (**2**) {cinap = 1, 5-dimethyl-2-phenyl-4-10-1,2-dihydro-3*H*-pyrazol-3-one} and *cis*-Cl, *trans*-P-[$RuCl_2(PPh_3)_2$(cumbh)] (**3**) {cumbh = 1,5-dimethyl-2-phenyl-4-10-1,2-dihydro-3*H*-pyrazol-3-one}. Structural confirmations were conducted primarily by spectroscopic techniques while the single crystal X-ray analysis revealed the distorted octahedrons of the respective metal compounds. Voltammetry experiments of **1** – **3** illustrated one-electron quasi-reversible redox waves which are attributed to metal oxidation state interconversions. The radical scavenging abilities and binding studies with DNA and BSA were conducted for these compounds and two previously reported compounds containing the chromone and 4-aminoantipyrine moieties, (*trans*-P, *cis*-Cl-[Ru(pch)$Cl_2(PPh_3)_2$] (**4**) (pch = 4-((pyridine-2ylimino)methylene)-chromone) and *cis*-[$RuCl_2$(bpap)(PPh_3)] (**5**) (bpap = 2,6-*bis*-((antipyrine-imino)methylene)pyridine)). CT-DNA binding affinities and modes were experimentally and computationally investigated while the paramagnetism of **1** – **4** encourages significantly higher NO and DPPH radical scavenging activities than the natural antioxidant, vitamin C. Experimental UV-visible BSA titrations revealed that the metal compounds are ideal binders which preferentially binds to site **IIA**.

Keywords: Ruthenium, crystal structures, spectral characterization, biomolecular interaction studies, cytotoxicity, benzimidazole, benzothiazole, uracil, Schiff base, carbohydrazide, heterocyclic, thiosemicarbazide, radical scavenging activities, cuminaldehyde, cinnamaldehyde, chromone, antipyrine.

Chapter 1

Introduction

1.1 General background

Ruthenium is a group 8 transition metal which is positioned in the *d*-block of the periodic table. The occurrence of this transition metal in the earth's crust is relatively rare and it is typically extracted from naturally occurring platinum ores. Thus, ruthenium is usually found along with other platinum group metals (*viz.* Os, Rh, Pd, Ir and Pt) [**1, 2**]. Due to its unique physical characteristics and diverse chemical properties, ruthenium has been utilized in various materials and coordination compounds, which portrays a multitude of different applications [**2-4**]. An extensive variation of ruthenium isotopes exist, though only seven of them are stable, while thirty-four are radionuclides. Amongst these are ^{106}Ru, ^{103}Ru and ^{97}Ru which possesses the half-lives of 376, 39 and 3 days, respectively [**5, 6**].

Ruthenium is one of the most adaptable metal centres as its organometallic complexes have been used for important chemical conversions such as C-H activation, oxidation and hydrogenation [**7-9**]. This is largely owing to the following attributes: it has a noble gas electronic configuration of [Kr]4$d^7$5s^1 which allows it a wide range of accessible oxidation states fluctuating from –**II** (*e.g.* [Ru(CO)$_4^{2-}$] corresponding to d^{10}) to +**VIII** (*e.g.* RuO_4 corresponding to d^0). In addition, its capability to exhibit the properties of both early- and late-transition metals (due to its location on the periodic table) leads to a combination of desirable properties optimal for catalysis. Ruthenium oxide (RuO_2) is considered as a highly active electro- and chemical catalyst for the oxygen evolution reaction (OER) and the chlorine evolution reaction (CER) [**10, 11**]. These types of reactions are important in industrial processes as the OER is an essential reaction for electrochemical conversion systems, such as fuel cells, whilst the CER reaction is a vital step in chloro-alkali reactions in industries where chlorine is used as a fuel source [**12**].

Besides these profound catalytic capabilities, the rich coordination chemistry of ruthenium accompanied with its optimal redox and luminescent properties, have led to structurally diverse metal complexes which exhibit diagnostic and/ or chemotherapeutic applications [**13**]. The majority of these ruthenium-based anticancer agents contains +**II** and +**III** centres which can be readily stabilized by triphenylphosphines (*e.g. trans*-[$Ru(PPh_3)_2$]), chloride (*e.g. fac*-[$RuCl_3$]$^{3+}$), bipyridine (*e.g. fac*-[$Ru(bipy)_2$]) and cymene (*e.g.* [$Ru(\eta^1\text{-}C_{10}H_{14})$] co-ligands [**14-18**]. The relative chemical "softness" of ruthenium gives the metal centre an avid affinity for nitrogen and sulphur donors, which are commonly present in major biomolecules. Consequently, numerous ruthenium complexes with N, X- (X = N or S) multidentate chelators have been isolated and studied as potential metallopharmaceuticals. In particular, the ruthenium "orphan" status drug NKP-1339 (sodium *trans*-[tetrachlorido*bis*(1*H*-indazole)ruthenate(III)]) has shown high tumour targeting capability and is currently undergoing FDA clinical trials [**19, 20**]. Ruthenium complexes encompassing the ^{106}Ru radionuclide have also been proven useful in the radiotherapy of tumours and are being extensively investigated due to its long half-life and β-emitting proficiency [**21, 22**].

1.2 Aim and motivation

1.2.1 Aims of research study

A fascinating avenue in metal-based drug discovery involves the design, synthesis and characterization of novel ruthenium-based complexes as potential metallopharmaceuticals [**23**]. Moreover, the next-generation of ruthenium medicinal agents should address the poor target-specificity of current chemotherapeutic drugs, by improving water solubility, cell-permeability and tumour affinity. Ultimately, successful implementation of the foreseen design features should culminate into less or no harmful side effects, improved bio-availability and anticancer activities [**24**]. Among the recent design strategies is the "directed therapy" drug design approach which places special emphasis on the enhancement of selectivity and efficacy of a candidate ruthenium drug [**25**]. This approach involves the chemical attachment of ruthenium to different biologically active organic groups with known biological targets, which directs the drugs to the cancerous cells which then leads to an increased cytotoxicity and physiological compatibility [**26**]. Another core prerequisite of these anticancer coordination compounds is the fine-tuning of their lipophilicity and hydrophobicity for improved solubility

in the blood-stream and *facile* transport across cell-membranes [**27**]. Subsequently, this class of anticancer agents should exhibit strong interaction of cancerous DNA [**28, 29**]. Moreover, the metallo-drugs must be able to kill the rapidly growing malicious tumours *via* various mechanism of activities to deter the development of drug resistant cancers [**30**]. The wide-spread interest in the bio-inorganic chemistry of ruthenium as well as the aforementioned challenging demands for drug discovery of new ruthenium-based anticancer agents, has emanated into the current research study where the main objectives include:

- To design, synthesize and study the structural diversity of the biologically active compounds of ruthenium.
- To investigate the biological properties of these and other ruthenium compounds *via* DNA and BSA interaction studies, antioxidant activities and cell line testing.

1.2.2 Rationale and motivation

As mentioned, the "directed therapy" design approach was employed where BAMs were incorporated within multidentate ligands that effectively stabilized ruthenium in its oxidation states +**II** and +**III**, respectively. It is hypothesized that the inherent complementary anti-microbial and anticancer activities of the following BAMs (*viz.* benz-(imidazole/ othiazole), uracil, thiosemicarbazide, chromone, antipyrine, cuminaldehyde and cinnamaldehyde, see **Figure 1.1**) can elevate or negate common harmful consequences associated with chemotherapy and promote defined biodistribution patterns of the respective ruthenium compounds. It was also foreseen that the structural features of the resultant metal compounds would be of pivotal importance in their biomolecular interactions, radical scavenging capabilities and *in vitro* anticancer studies.

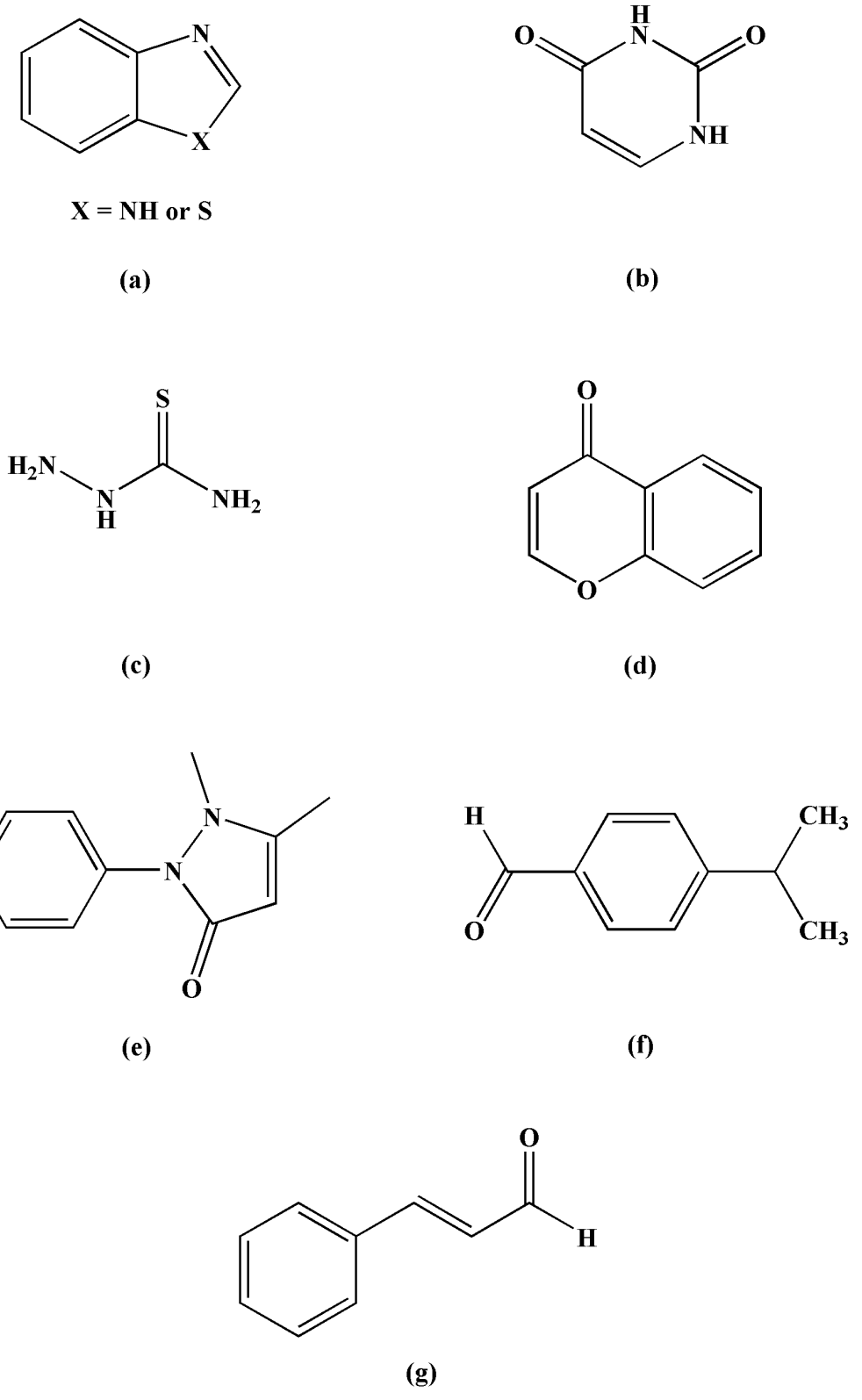

Figure 1.1: *Skeletal structures of the BAMs: (**a**) benz-(imidazole/othiazole), (**b**) uracil, (**c**) thiosemicarbazide, (**d**) chromone, (**e**) antipyrine, (**f**) cuminaldehyde and (**g**) cinnamaldehyde.*

Aromaticity is a particularly important structural feature in medicinal chemistry as delocalized *pi*-conjugated ring systems are common components to various medicines [**31**]. In fact, the pharmacokinetics of drugs are typically dependant on the stereoelectronic properties of its aromatic moieties [**32**]. More specifically, the substitution kinetics of labile co-ligands of ruthenium pyridyl compounds have been closely correlated to the nature of pyridyl *N*-donor ligands [**33**]. Also, the steric demands, scaffold rigidity and lipophilicity of the organic aromatic chelators often dictates the types of DNA binding modes afforded by anticancer metal-based drugs [**34**]. Therefore, it was envisaged to extrapolate interesting structure-activity relationship studies among the ligand series meticulously chosen for this research project.

Furthermore, the considered BAMs serves as pharmacophores in various organic compounds that have illustrated high *in vitro* anticancer activities. Like in the case of benzimidazoles and benzothiazoles which were found to have boundless value in drug synthesis since their derivatives possess interesting pharmacological profiles [**35**]. Evidently, literature discloses that derivatives of benzimidazoles and benzothiazoles, particularly 2-isopropyl-3-(2-phenyl-1*H*-benzoimidazol-6-yl)quinazolin-4(3*H*)-one and (*E*)-2-((1-(6-(benzyloxy)benzo[*d*]thiazol-2-yl)-3-phenyl-1H-pyrazol-4-yl)methylene)hydrazinecarboximidamide are considered hopeful anticancer candidates due to their remarkable potencies against the MCF-7 breast cancer cell line [**36, 37**]. Furthermore, two ruthenium(II) complexes containing benz-(imidazole/ othiazole)-containing ligands [**Figure 1.2**] have shown the ability to bind to and induce damage to DNA whilst also exhibiting cytotoxic activities against a leukemic cell line (HL60). The cytotoxic evaluation showed that the metal complexes were up 20 to 300-fold more potent than their free ligands [**38**]. Another prominent example is bendamustine, a benzimidazole-derived alkylating agent [**Figure 1.3**], that encourages inter-strand DNA cross-linking and is used in the treatment of chronic lymphocytic leukaemia [**39**]**.**

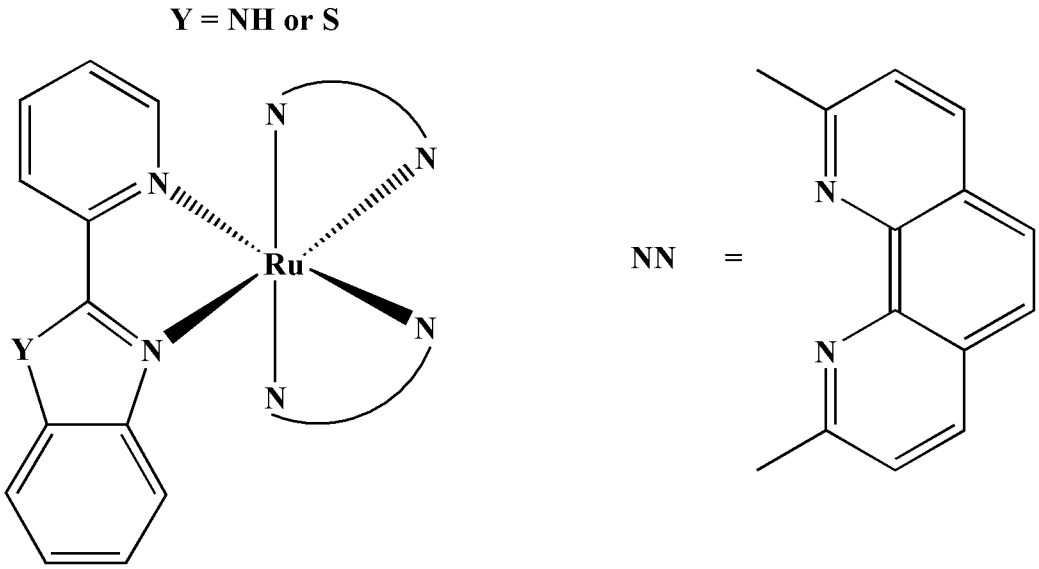

Figure 1.2: *Generic structure of DNA cleaver, ruthenium(II) complexes containing benz-(imidazole/ othiazole)-derived ligands.*

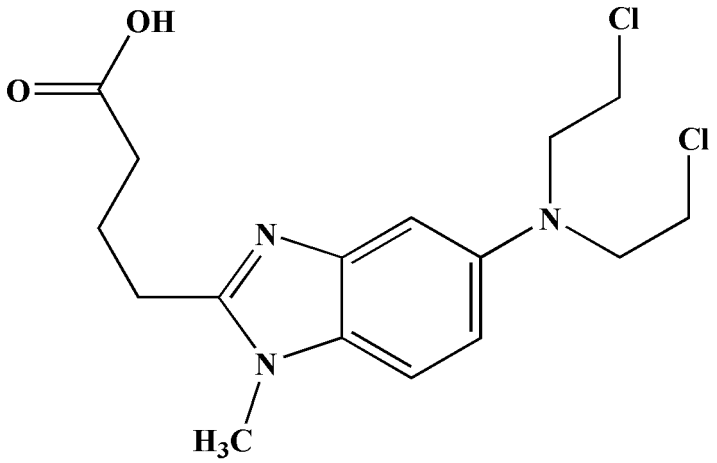

Figure 1.3: *Structure of the chemotherapeutic agent, bendamustine.*

Uracil is a nucleobase that is present in the nucleic acids of RNA and DNA. Derivatives of this natural occurring elementary unit, have been used as building blocks in the synthesis of nucleoside analogues that displays antiviral and antitumor potencies [**40, 41**]. 5-Fluorouracil is a popular antitumor agent which is used in the treatment of solid tumours occurring within breast and colon tumours [**40**]. In an effort to enhance the efficacy of 5-fluorouracil, Tegafur-uracil (a pro-drug of 5-fluorouracil) was developed. The *in vivo* metabolism of this pro-drug

maintains higher serum concentrations of the active-drug 5-fluorouracil in tumours and has been effective in the treatment of breast, gastric, lung and rectal cancers [**42, 43**]. The mechanism of action of these uracil-derived drugs are thought to occur by the inhibition of the enzyme, thymidylate synthase, which induces DNA damage of the tumour cells [**43**].

The medicinal relevance of thiosemicarbazones are well established and alteration of its core structure have brought about intriguing structure-activity relationships [**44**]. These biological activities are often mimicked or enhanced upon coordination of these potentially polydentate chelators to transition metals [**45**]. Their accessible coordination sites and various combinations of donor atoms, have afforded metal complexes with diverse geometries [**46**]. Literature trends have showed that bio-efficacies of thiosemicarbazones are improved by extending their *pi*-conjugated arrangements [**47-49**]. The most widely studied thiosemicarbazone drug candidate is Triapine (3-aminopyridine-2-carboxaldehyde-thiosemicarbazone) [**Figure 1.4**], which has presented promising results during phase I and II clinical trials, against haematological cancers. Other leading thiosemicarbazone drug candidates are COTI-2 (4-(2-pyridinyl)-2-(6,7-dihydro-8(5*H*)-quinolinylidene)hydrazide-1-piperazinecarbothioic acid) and DPC (*di*-2-pyridylketone-4-cyclohexyl-4-methyl-3-thiosemicarbazone) [**Figure 1.4**] that have promoted superior tumour mass reductions than Triapine, during clinical trials [**50**]. Unique inhibitory mechanisms of cancer cell replication by thiosemicarbazones can be controlled by multiple factors such as reticence of regulatory cell cycle and ribonucleotide reductase enzyme, minimizing ROS generation and restoration of P53 protein functionalities [**49**].

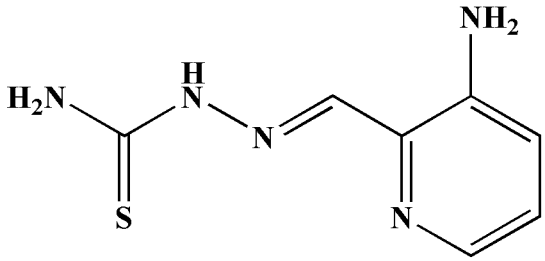

(a)

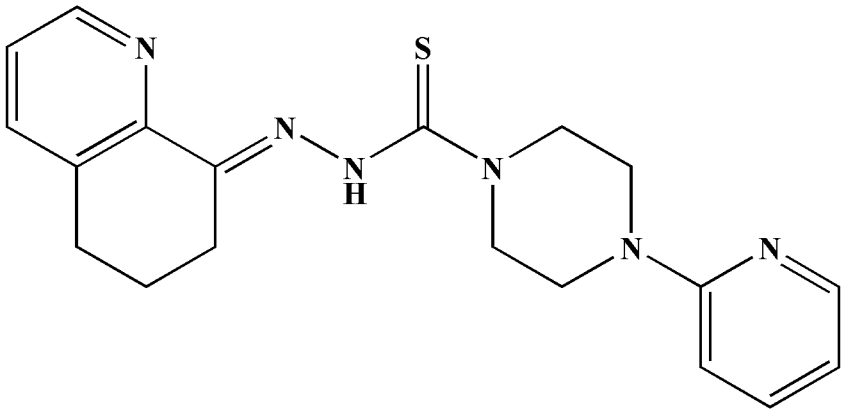

(b)

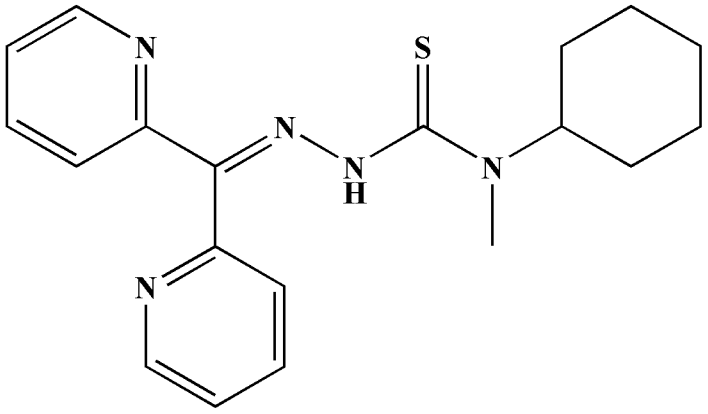

(c)

Figure 1.4: *Leading thiosemicarbazone drug candidates :(**a**) Triapine, (**b**) COTI-2 and (**c**) DPC.*

Cuminaldehyde and cinnamaldehyde are natural-occurring bioactive components extracted from plant-derived essential oils which display various health-endorsing benefits. In fact, cumin and cinnamon are commonly used household drugs due their anti-inflammatory, anti-oxidant and anti-microbial properties, and these essential oils have been used as supplemental therapeutics to treat cardiovascular diseases and neurodegenerative disorders [**51-53**]. Both compounds have displayed promising anti-tumour effects and are considered "safe" drug candidates. For example, studies have shown that cuminaldehyde triggers pro-apoptic proteins, changing the integrity of the mitochondria and inhibits the DNA integrity-conserving enzymes topoisomerase I and II, ultimately inducing apoptosis (cell death) of human colorectal adenocarcinoma cells [**54**]. Similarly, derivatives of cinnamaldehyde have been reported as effective candidates in the treatment of many malignant tumours [**55**].

Chromone-based compounds are natural-occurring metabolites that have illustrated various biological functions. Functionalization of the chromone scaffold renders constituents that promote DNA binding and interactions with key enzymes and proteins [**56**]. In the past decade, over one hundred derivatives of chromone with anticancer properties have been reported which largely focus on kinase inhibitors [**57, 58**], *e.g.* a chromone component found in the fungus Trichocomaceae [**Figure 1.5**] has shown cytotoxic behaviour against HepG-2 liver cancer cell lines [**56**]. Metal complexes containing the chromone moiety have also shown pronounced *in vitro* anticancer activities, $[CuL]_2(NO_3)_2$ (HL = a Schiff base ligand derived from 3-formylchromone and *S*-benzyldithiocarbazate) [**Figure 1.5**] has similarly displayed low IC_{50} values against HepG-2 cancer cell lines [**59**].

Substantial attention has also been focused on the isolation of antipyrine derivatives in an effort to discover novel non-toxic and more potent organopharmaceuticals [**60**]. Among these include the compound 3,3'-(4, 4'-sulfonyl-*bis*-(4,1-phenylene))-*bis*-(1-(1,5-dimethyl-3-oxo-2-phenyl-2,3-dihydro-1*H*-pyrazol-4-yl)-4-oxo-2-thioxo-1,2,3,4-tetrahydropyrimidine-5-carbonitrile). This compound has shown higher anticancer activity than the well-known chemotherapeutic doxorubicin against breast cancer carcinoma [**61**].

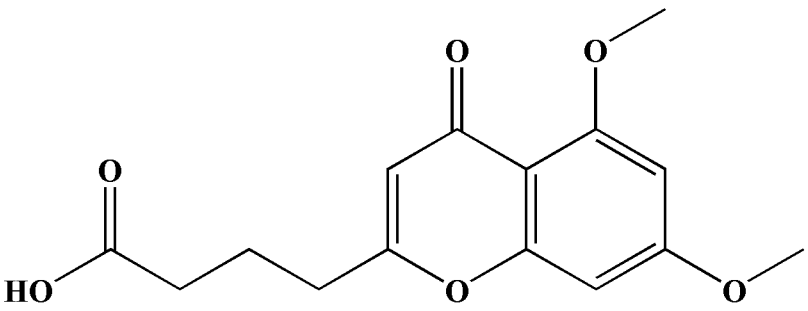

(a)

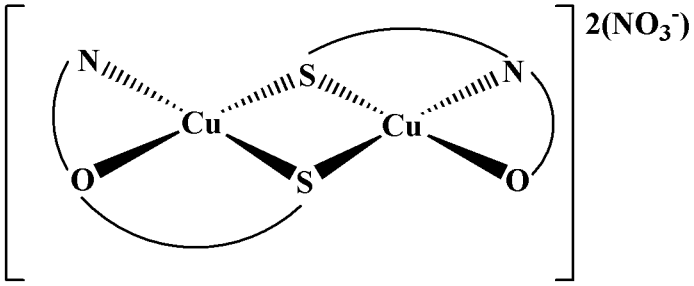

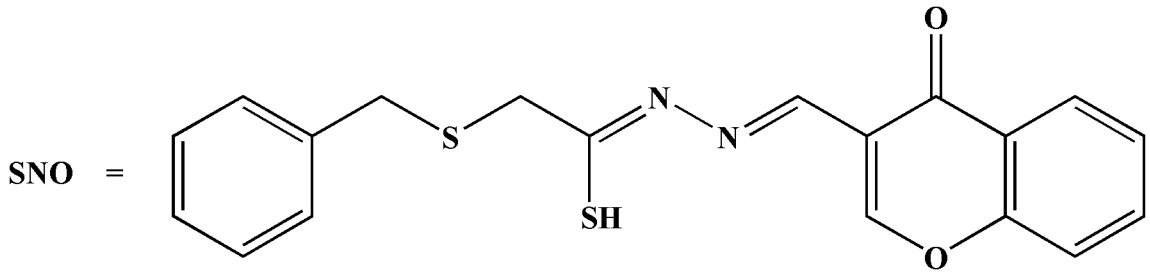

(b)

Figure 1.5: *Structures of (**a**) the chromone derivative found in the Trichocomaceae fungus and (**b**) a copper(II) complex containing a chromone derivatized Schiff base.*

1.2.3 The use of Schiff bases to incorporate BAMs

Schiff bases are structurally diverse and synthetically accessible compounds, classically synthesized by simplistic condensation between an aldehyde, or ketone with a primary amine. These compounds contain an imine functional group that can "stitch" together two or more biologically active moieties to form various compounds with synergistic properties [**62**].

Furthermore, studies have demonstrated that the lone pair of the sp^2-hybridized orbital located on the imino nitrogen is of considerable biological importance as they obstruct cellular processes by forming intermolecular hydrogen bonding between biological constituents and the imino nitrogen [**63**]. The electrophilic carbon and nucleophilic nitrogen of the imine group also has excellent binding affinities with various biological electrophiles and nucleophiles, thereby inhibiting targeted enzymes, diseases and DNA replications [**62**]. Schiff bases are prominent moieties in some drugs on the market [**Figure 1.6**], *e.g.* dantrolene and nifuroxazide which are used in a muscle relaxant and antibiotics, respectively [**64**].

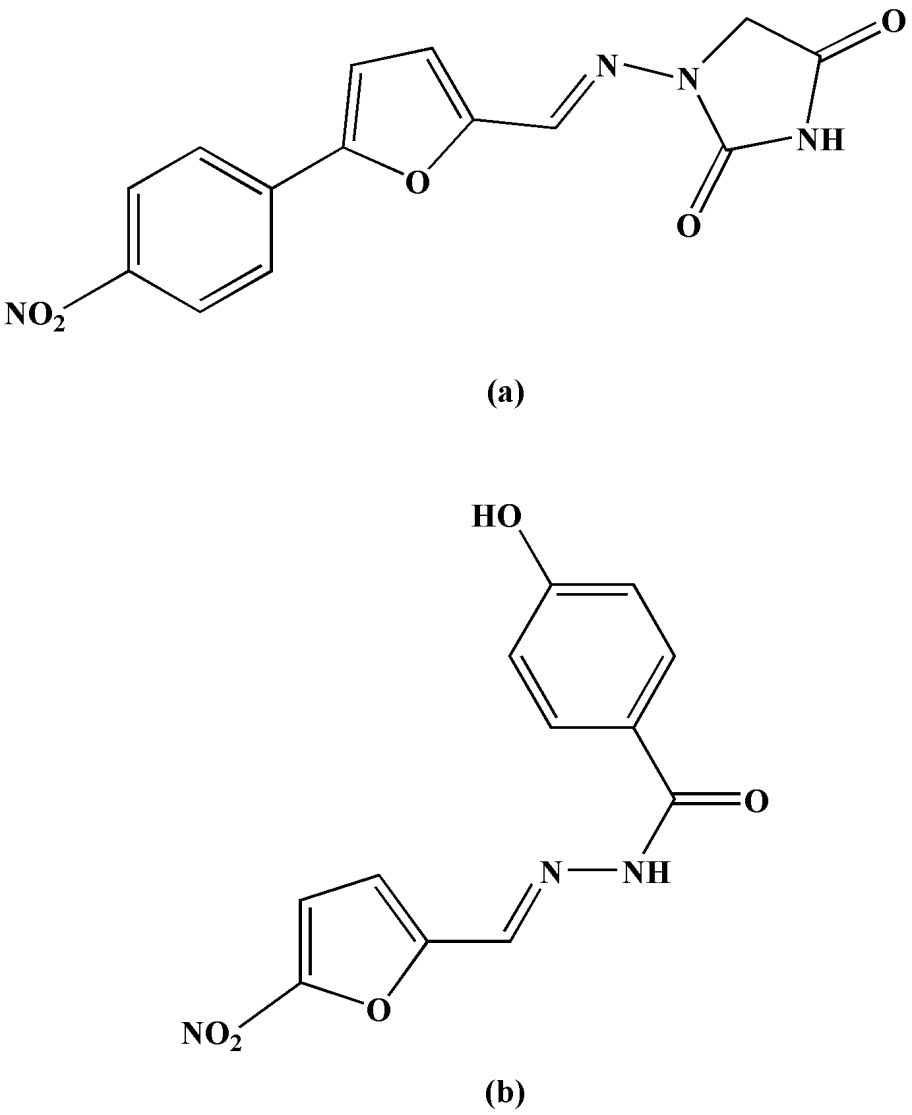

Figure 1.6: *Structures of the biologically active Schiff bases: (**a**) dantrolene and (**b**) nifuroxazide.*

It is well known that Schiff bases are stabilizers of metal centres in the low and high oxidation states [**65**]. The redox, photochemical and electronic properties of the metal centres are typically influenced by the nature of functional groups and the *pi*-conjugation adjoining the imine groups, while the Lewis acid character of the metal atom often has an impact on the stereoelectronic properties. Therefore, the coordination behaviours of metal centres have shown to have a significant influence on the bio-inorganic chemistry of Schiff base metal complexes. In fact, metal-ligand synergistic effects are often critical in diagnostic and therapeutic applications of metal-based drugs. Classical examples include theranostic ruthenium(II) polypyridyl compounds which have shown the delocalization of electron density of the *N*-donor ligand which promotes the photophysical properties (*e.g.* triplet quantum yield and lifetimes) to maximise the generation of ROS (*e.g.* singlet oxygen), while the planarity of the ligands has encouraged DNA intercalation or groove-binding [**66, 67**]. *In vitro* and *in vivo* imaging of this class of metal complexes are rendered from the capability to emit in the near infrared region.

1.3 The growth of ruthenium metallopharmaceuticals

Platinum-based drugs including cisplatin, oxaliplatin and carboplatin [**Figure 1.7**], have become the first line of chemotherapeutics that are regularly prescribed worldwide. Whilst their effectiveness is undeniable, their use is restricted by intrinsic drug resistance and severe side effects due to their poor target specificity of cancerous cells over healthy cells [**68, 69**]. Hence, design strategies are continuously evolving towards developing organometal complexes that exhibit defined biodistribution patterns and to combat the major concerns of drug resistant cancer strains.

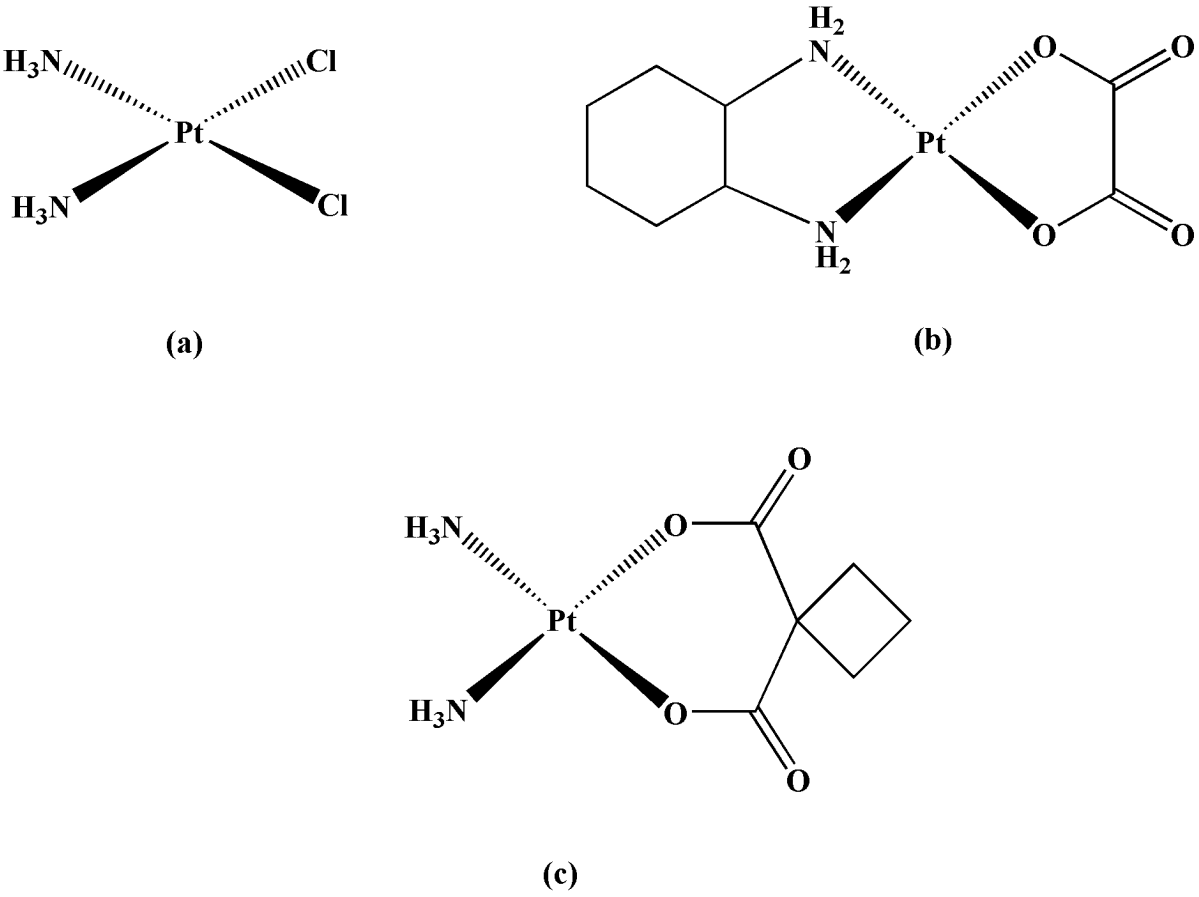

Figure 1.7: *Structures of (**a**) cisplatin (**b**) oxaliplatin and (**c**) carboplatin.*

Researchers have diverted their attention to ruthenium-based drugs as their metal complexes have displayed notable cytotoxic activities amidst the numerous metals studied; they offer many advantages over platinum drugs, such as high selectivity, potent efficacy, reduced drug resistance and a low toxicity profile [**70**]. Ruthenium complexes have also proven to be plausible alternatives to platinum drugs due to its comparable ligand exchange kinetics and its octahedral complexes have more available coordination sites as compared to the square planar platinum complexes [**24, 71**]. The uniqueness of ruthenium as one of the least toxic metals in bioinorganic chemistry is mainly attributed to: (*i*) the ability of ruthenium to utilize certain plasma proteins as a drug delivery system, (*ii*) the fact that ruthenium(III) complexes can function as pro-drugs under hypoxic conditions and (*iii*) the fact that ruthenium share similar chemistry to the essential metal, iron.

A crucial success in anticancer drug development is to accomplish selective drug delivery of the drug to the tumour site. Several studies have shown a strong affinity of ruthenium towards the plasma proteins transferrin and albumin, which are considered essential for tumour targeting and drug delivery [**19**]. As mentioned, ruthenium can mimic iron and can thus exploit its transport mechanism to sequester into tumour cells due to its higher demand for iron. This is mediated by the iron transport protein, transferrin. More notably, albumin-bound ruthenium achieves its selectivity for tumour cells as a result of the accumulation of albumin in tumour cells because of its poor lymphatic drainage and leaky blood capillaries [**72**]. Additionally, ruthenium(III) complexes may serve as prodrugs ("activation-by-reduction" hypothesis) which are reduced to the active ruthenium(II) form preferentially by the hypoxic environment of tumour cells, while sparing normal cells from toxic effects. These selective transport mechanisms, in combination with the redox activation, may be responsible for the general low toxicity and fewer side effects of ruthenium anticancer agents [**73**].

Widespread research in the last decade has led to the progression of two ruthenium(III) complexes into FDA clinical trials, *viz.* NAMI-A (imidazolium *trans*-[tetrachlorido(DMSO)(1*H*-imidazole)-ruthenate(III)]) and KP1019 (imidazolium *trans*-[tetrachlorido*bis*(1*H*-indazole)ruthenate(III)]). To improve the low solubility issues of KP1019, a modified version was formed and named NKP-1339 (sodium *trans*-[tetrachlorido*bis*(1*H*-indazole)ruthenate(III)]) [**Figure 1.8**]. These active species strongly associate to plasma proteins (transferrin and albumin) and function as pro-drugs under the physiological conditions of tumour cells. The compounds manifest a relatively low degree of toxicity but have distinct pharmacological profiles. NAMI-A mainly induces an antimetastatic effect by binding to extracellular collagen of tumour cells and thus reducing their invasiveness, while KP1019 and NKP-1339 produces cytotoxic effects by directly interfering with the cell signalling and metabolic pathways of tumour cells [**74, 75**].

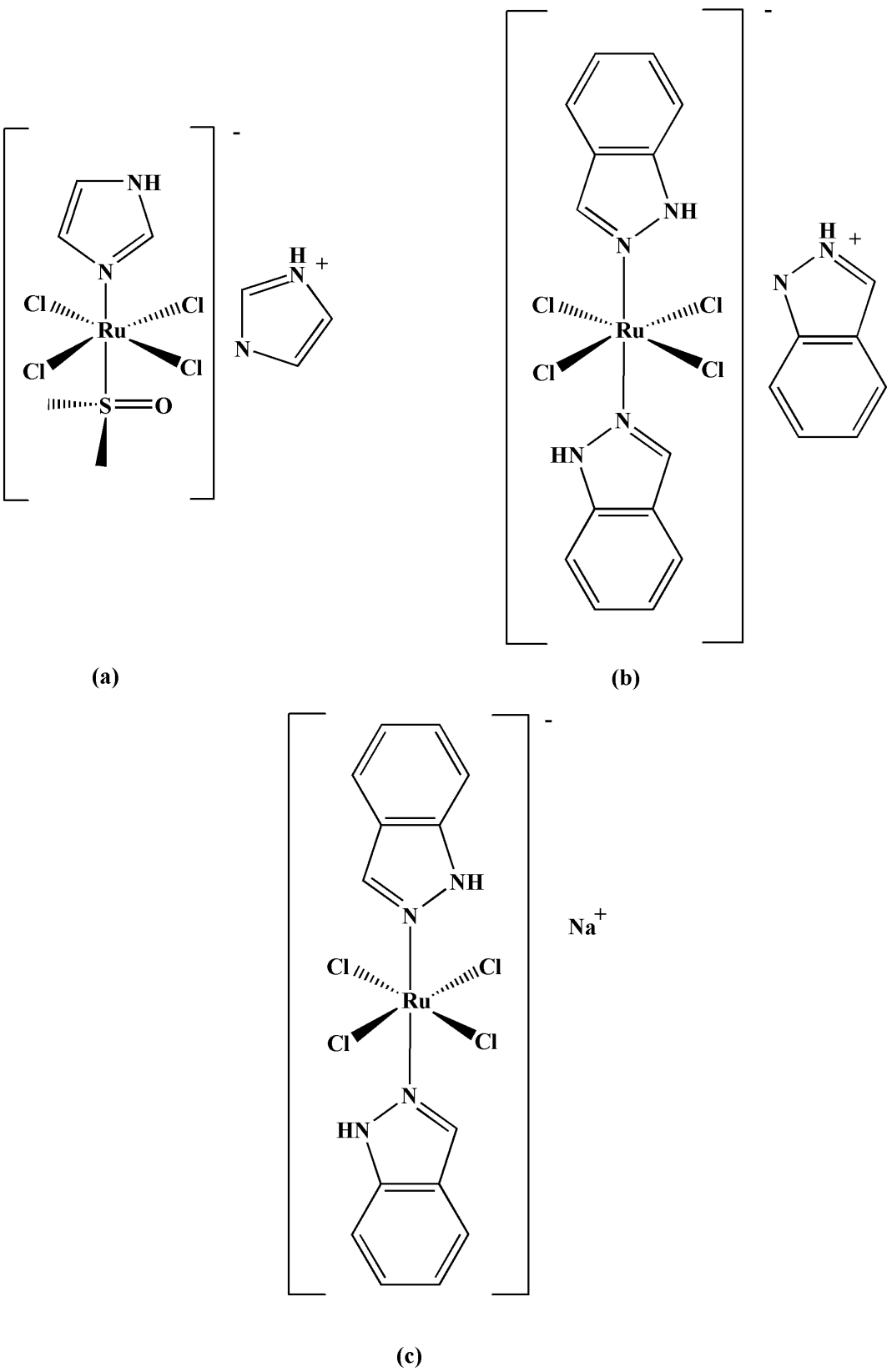

Figure 1.8: *Evolution of the leading ruthenium(III) anticancer drug candidates. (**a**) NAMI-A, (**b**) KP1019 and (**c**) NKP-1399.*

A number of promising ruthenium(II) compounds have also been evaluated against various cancer cell lines, a prominent organometallic compound RAPTA-C ([Ru(η^6-*p*-cymene)Cl_2(pta)]) (where pta = 1,3,5-triaza-7-phosphaadamantane) was initially shown to induce antimetastatic activity and anticancer effects by promoting apoptosis of Ehrlich ascites carcinoma cells. It has been demonstrated that RAPTA-C [**Figure 1.9**] interacts directly with chromatin histone proteins of tumour cells and indirectly causes antiangiogenic effects (suppression of growth of blood vessels in tumour cells), thereby supressing tumour growth [**76**].

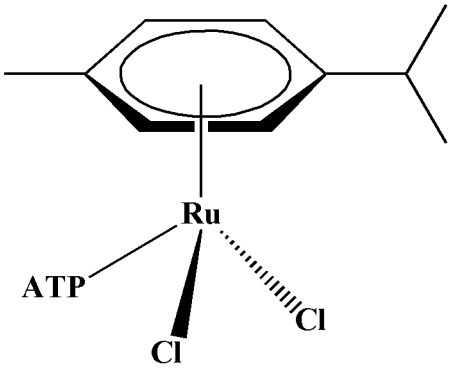

Figure 1.9: *Structure of the organometallic complex, RAPTA-C.*

1.4 General chemistry of ruthenium(II) and -(III)

1.4.1 Ligand substitution

Ligand substitution mechanisms of ruthenium(II) and -(III) complexes are largely dependent on the nature of the co-ligands, as well as that of the incoming ligand [**77, 78**]. Co-ligands containing electron withdrawing groups tend to decrease the electron density on the metal which enhances the π-back bonding capabilities of the ruthenium atom. Consequently, this makes the metal center more electrophilic, thereby enhancing the metal complex's propensity to undergo ligand substitution [**77**]. This trend can be seen from the substitution kinetic studies [**Equations 1 – 3**] of the three ruthenium(II) complexes, [Ru(Cl-Ph-tpy)(en)Cl]Cl, [Ru(Cl-Ph-tpy)(dach)Cl]Cl and [Ru(Cl-Ph-tpy)(bpy)Cl]Cl (where Cl-Ph-tpy = 4'-(4-chlorophenyl)-2,2':6',2''-terpyridine, en = 1,2-diaminoethane, dach = 1,2-diaminocyclohexane, bpy = 2,2'-bipyridine), with the organic nucleotide, 5'-GMP (guanosine-5'-monophosphate). In

particular, [Ru(Cl-Ph-tpy)(en)Cl]Cl and [Ru(Cl-Ph-tpy)(dach)Cl]Cl react twice as fast as [Ru(Cl-Ph-tpy)(bpy)Cl]Cl, which is triggered by the π-back bonding effect that the extra bpy chelator exerts on the metal centre. This increases the electron density at the ruthenium centre, rendering it less reactive [**79**].

$$[Ru(Cl\text{-}Ph\text{-}tpy)(en)Cl]^{+} + 5'\text{-}GMP \longrightarrow [Ru(Cl\text{-}Ph\text{-}tpy)(en)(5'\text{-}GMP)] + Cl^{-} \quad (\mathbf{1})$$

$$[Ru(Cl\text{-}Ph\text{-}tpy)(dach)Cl]^{+} + 5'\text{-}GMP \longrightarrow [Ru(Cl\text{-}Ph\text{-}tpy)(dach)(5'\text{-}GMP)] + Cl^{-} \quad (\mathbf{2})$$

$$[Ru(Cl\text{-}Ph\text{-}tpy)(bpy)Cl]^{+} + 5'\text{-}GMP \longrightarrow [Ru(Cl\text{-}Ph\text{-}tpy)(bpy)(5'\text{-}GMP)] + Cl^{-} \quad (\mathbf{3})$$

Another example can be seen from the ruthenium(III) complexes $[RuCl_3(L^1)]$ (L^1 = 2-bromo-6-(3,5-dimethyl-1*H*-pyrazol-1-yl)pyridine) and $[RuCl_3(L^3)]$ (L^3 = 2,6-*bis*(3,5-dimethyl-1H-pyrazol-1-yl)pyridine), where the substitution of the chloro co-ligands by thiourea molecules (TU) in $[RuCl_3(L^1)]$ occurs faster than that of $[RuCl_3(L^3)]$ [**Equations 4 – 5**]. This trend in reactivity was ascribed to the pyridine ring of L^1 that readily accepts *pi*-electron density from the metal, while the electron-rich pyrazole ring of L^3 is a better *σ*-donor towards the metal. This means that L^3 causes a net increase in electron-density around the metal center, thus decreasing its reactivity towards ligand substitution [**80**].

$$[RuCl_3(L^1)] + 3TU \longrightarrow [Ru(TU)_3(L^1)] + 3Cl^{-} \quad (\mathbf{4})$$

$$[RuCl_3(L^3)] + 3TU \longrightarrow [Ru(TU)_3(L^3)] + 3Cl^{-} \quad (\mathbf{5})$$

1.4.2 Redox reactions

Ruthenium complexes in their +**II** and +**III** oxidation states are known to be highly redox active species and are susceptible to ligand-induced oxidations and reductions. This may be observed in **Equation 6** for the formation of the ruthenium(III) compound, $[Ru^{III}(pym)]$, from the

reaction between the diamagnetic *trans*-$[Ru^{II}Cl_2(PPh_3)_3]$ and triamine chelator *tris*-((1*H*-pyrrol-2-ylmethylene)ethane)amine (H_3pym) [**81**].

$$trans\text{-}[Ru^{II}Cl_2(PPh_3)_3] + H_3pym \longrightarrow [Ru^{III}(pym)]^{-1} + 2Cl^- + 3H^+ + 3PPh_3 \quad (\mathbf{6})$$

Some ruthenium(III) complexes have indicated the tendency to access higher oxidations states, such as Ru^{+IV} or Ru^{+V}, by forming Ru-oxo species *via* a proton couple electron transfer (PCET) pathway. An example of this is seen in **Equations 7 – 11** during the catalytic cycle of an artificial photosynthesis process (*i.e.* splitting of water into dioxygen and dihydrogen), which is driven by $[Ru^{III}L(pic)_3]$ (H_3L = 3,6-di-tert-butyl-9*H*-carbazole-1,8-dicarboxylic acid and pic = 4-picoline) [**82**].

$$[RuL(pic)_3]^{3+} + H_2O \longrightarrow [RuL(pic)_2(H_2O)]^{3+} + pic \quad (\mathbf{7})$$

$$[RuL(pic)_3(H_2O)]^{3+} \longrightarrow [RuL(pic)_2(OH)]^{4+} + H^+ + e^- \quad (\mathbf{8})$$

$$[RuL(pic)_2(OH)]^{4+} \longrightarrow [RuL(pic)_2(O)]^{5+} + H^+ + e^- \quad (\mathbf{9})$$

$$[RuL(pic)_2(O)]^{5+} + H_2O \longrightarrow [RuL(pic)_2(HO_2)]^{4+} + H^+ + e^- \quad (\mathbf{10})$$

$$[RuL(pic)_2(HO_2)]^{4+} + H_2O \longrightarrow [RuL(pic)_3(H_2O)]^{3+} + H^+ + O_2 + e^- \quad (\mathbf{11})$$

Other ruthenium(II) complexes demonstrate the ability to act as green photocatalysts, which are typically activated by visible light. The photochemistry of $[Ru(bpy)_3]^{2+}$ (bpy = bipyridine) species has been extensively studied for these types of applications. The photocatalytic activity of these metal compounds can be characterized by its capability to promote electron transfer between the ground or excited state metal cores with closed-shell electron donors (D) and electron acceptors (A), respectively, as seen in **Equations 12 – 16** [**83**].

$[Ru(bpy)_3]^{2+} + h\nu \longrightarrow [Ru^*(bpy)_3]^{2+}$ **(12)**

$[Ru^*(bpy)_3]^{2+} + A \longrightarrow [Ru(bpy)_3]^{3+} + A^{\cdot -}$ (**13**)

$[Ru^*(bpy)_3]^{2+} + D \longrightarrow [Ru^*(bpy)_3]^{+} + D^{\cdot +}$ (**14**)

$[Ru^*(bpy)_3]^{+} + A \longrightarrow [Ru(bpy)_3]^{2+} + A^{\cdot -}$ (**15**)

$[Ru(bpy)_3]^{3+} + D \longrightarrow [Ru^*(bpy)_3]^{2+} + D^{\cdot +}$ **(16)**

1.4.3 Disproportionation

The disproportionation reactions of ruthenium (II) and -(III) compounds are important owing to their relevance in redox-mediated biological activities, such as DNA denaturation whereby deactivation of the active Ru(II) species typically occurs upon coordination to nucleic acids [**6, 84**] . Subsequently, the ruthenium(II) or –(III) adducts have a tendency to disproportionate to $Ru^{II/\ III}$ and Ru^{IV}. For instance, mononuclear metal compounds of the type *trans*-$[L(py)(NH_3)_4Ru^{III}]$ (L =guanosine or 2'-deoxyguanosine) disproportionate to form Ru^{II} and Ru^{IV} products, of which the Ru^{IV} product is thought to be responsible for the oxidative damage of DNA during cytotoxic activity, see **Equation 17** [**6, 85**].

$[LRu^{III}(NH_3)_4py] + OH^- \longrightarrow [LRu^{IV}(NH_2)(NH_3)_3py] + [LRu^{II}(NH_3)_4py] + H_2O$ (**17**)

1.5 The coordination chemistry of ruthenium(II) and –(III)

1.5.1 Ruthenium compounds with N, N-donor ligands

Ruthenium demonstrates a general affinity towards nitrogen-donor atoms [**86**]. Neutral aromatic N-donors, such as pyridine or imidazole, contain lone pairs in their sp^2 orbital which

function as σ-donors and overlap with the *d* orbitals of ruthenium to form stable metal-to-ligand bonds. The stability of Ru-$N_{pyridyl}$ bonds are further boosted by π-back donation from the d_π orbitals of ruthenium to the unoccupied π^* orbitals of their nitrogen donor atoms [**87, 88**]. Characteristic *sigma*-donor and *pi*-acceptor capabilities of pyridyl nitrogen donors are exemplified in the ruthenium(II) polypyridine complex cation, $[Ru(tbbpy)_2(L^x)]^{2+}$ (L^x = dipyrido[3,2-*a*:2',3'-*c*]phenazine-10,11-imidazole) [**Figure 1.10**] [**89**]. The σ-donating properties of anionic nitrogen-donors are also capable of stabilizing ruthenium in its +**II** and +**III** oxidation states [**90**]. For instance, the *di*-anionic coordination of the daba moiety through its amido donor atoms occurs in $[Ru^{II}(bipy)(daba)(NCS)_2]$ (H_2daba = 3, 4-diaminobenzoic acid, bpy = bipyridine and NCS = thiocyanate) [**Figure 1.11**] [**91**].

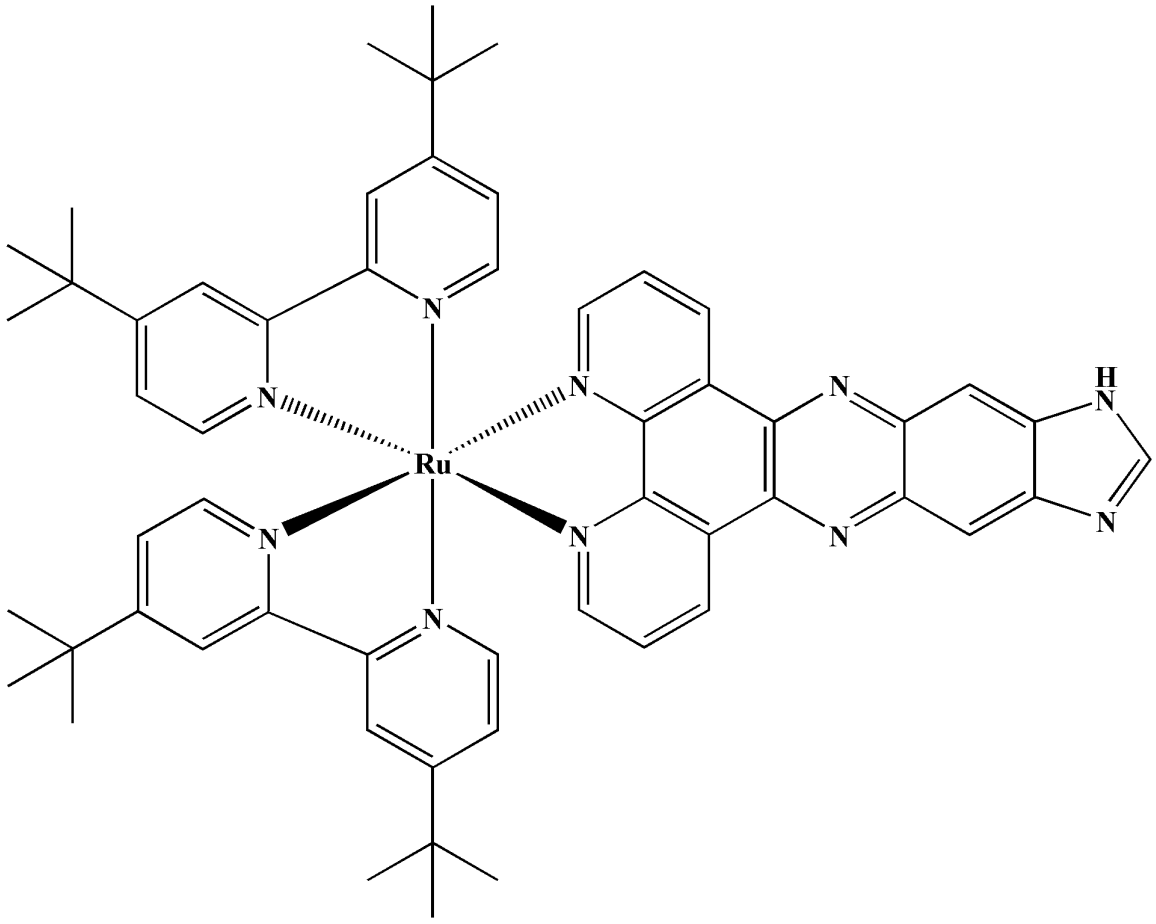

Figure 1.10: *A ruthenium(II) complex cation, $[Ru(tbbpy)_2(L^x)]^{2+}$ with three bidentate polypyridyl chelators.*

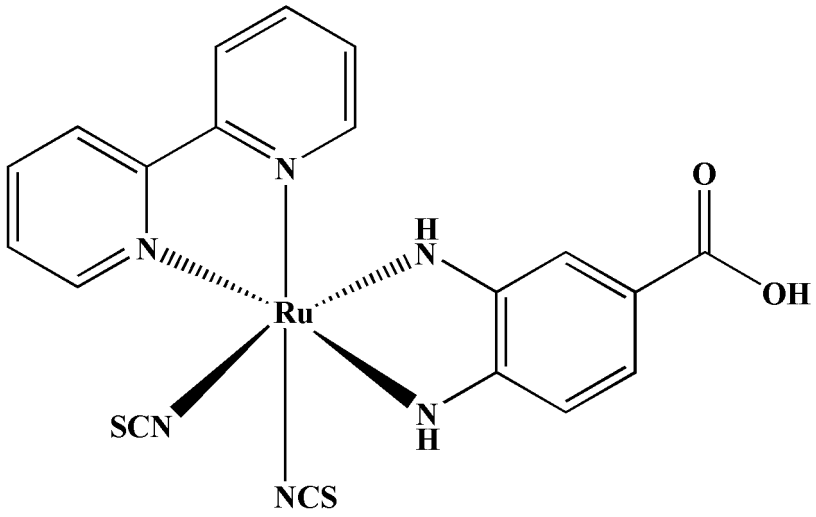

Figure 1.11: *Structural features of the monomeric ruthenium complex [Ru(II)(bipy)(daba)(NCS)$_2$].*

1.5.2 Ruthenium compounds with N, S-donor ligands

Chelating ligands with a combination of hard- and soft donors have shown various coordination modes towards ruthenium(II) and -(III) centres [**92-94**]. Structural diversity of the resultant metal compounds are brought about by the steric considerations of the ligands as well as the variable donor forms of the nitrogen and sulphur. More especially, the sulphur atom can exhibit multiple valencies (*e.g.* thiolate, thioether, sulfenato, sulfinato) and are considered useful nucleophiles since they can display different bonding stabilizations with metals, *i.e.* as a σ-donor or dually as a σ-donor and π-acceptor [**95**]. These coordination bonding trends are illustrated in the diamagnetic ruthenium compound, [Ru(dpphen)$_2$(dpte)](PF$_6$)$_2$] (dpphen = 4, 7-diphenyl-1,10-phenanthroline and dpte = 1,2-*bis*(phenylthio)ethane) where the thioether ligand acts as a sigma-donor and *pi*-acceptor ligand [**96**], see **Figure 1.12**.

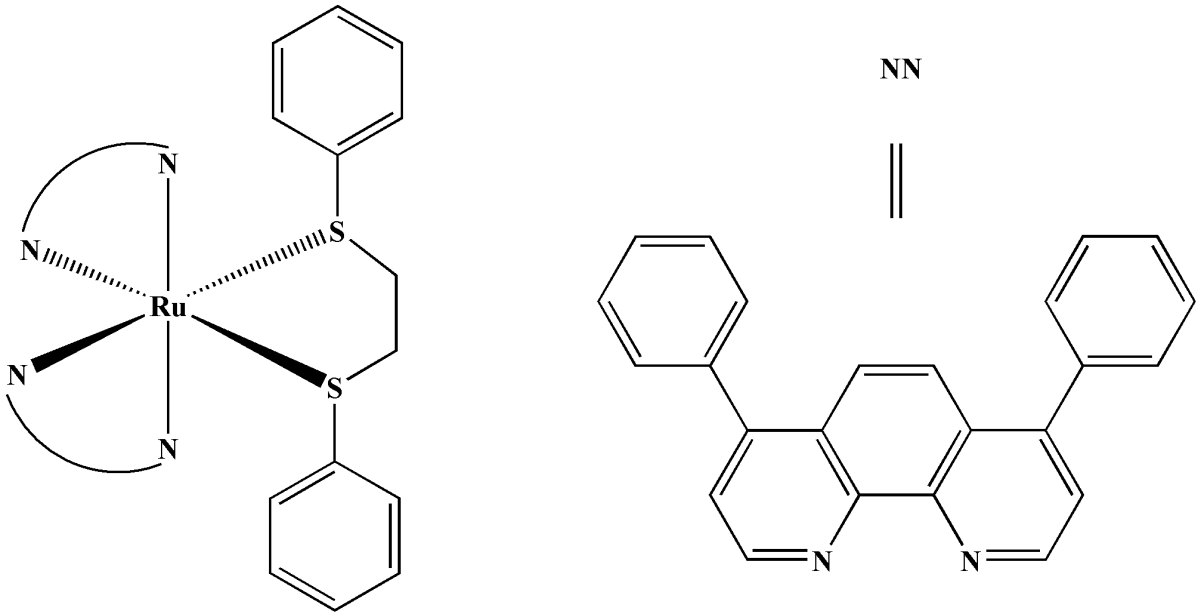

Figure 1.12: *Octahedral geometry of the ruthenium(II) complex salt, [Ru(dpphen)$_2$(dpte)](PF$_6$)$_2$.*

1.5.3 Ruthenium compounds with N, O-donor ligands

Numerous Schiff base ruthenium complexes are found in literature where the majority of these metal complexes contain the $N_{imino}O_{phenolate}$ coordination mode [**97, 98**]. Keto-enol tautomerization which is also a common phenomenon within the coordination chemistry of ruthenium, *e.g.* [Ru^{II}(bipy)(anth)$_2$] (bipy = bipyridine and anth = anthranilic acid), see **Figure 1.13** [**91**]. Selected *mono*-, *di*-oxo and oxo-bridged ruthenium species with neutral pyridyl ligands have been isolated [**99-102**]. In addition cyclic rings systems have shown to be effective reinforcing ligands of the [$Ru^{IV}O]^{2+}$ and *cis*-[$Ru^{V}O_2]^{+}$ in [RuO(phab)] (H_4phab = 1, 2-*bis*(hydroxydiphenylacetamide)phenylene) and *cis*-[RuO_2(Me_3tacn)(CF_3CO_2)](ClO_4) (Me_3tacn = *N, N′, N″*-trimethyl-1,4,7-triazacyclononane), respectively [**103, 104**].

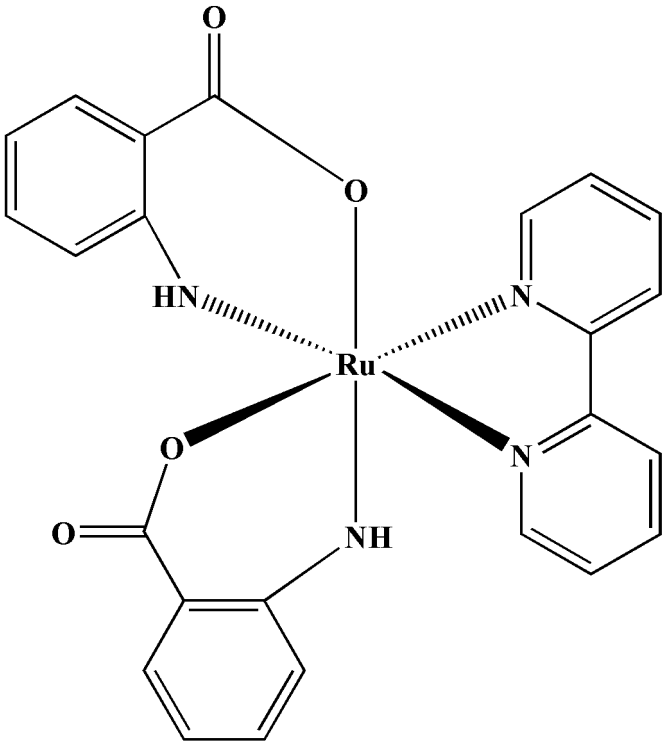

Figure 1.13: *The '2+2+2' octahedral structure of [Ru^{II}(bipy)(anth)$_2$]*.

1.6 DNA interaction studies of ruthenium compounds

It is well recognized that most cancers are mutated cells that grow and can spread exponentially throughout the body. Aggressive cancers typically impede normal organ functions faster which have been directly correlated with tumour mass. To cease the rapid mutation of normal cells, ruthenium-based drugs must penetrate the cellular membranes of cancerous cells and interact well with mitochondrial DNA to signal apoptosis. Thus, the structural features of these metal-based drugs must be conducive for these biological active functions. As reiterated, lipophilicity is essential for cell permeability while the presence of labile co-ligands (*e.g.* chloro) can facilitate hydrolysis or ligand substitution with biological nucleophiles, to promote water solubility. Alternatively, the presence of a water-soluble BAM within the coordination sphere may inherently induce solubility within the blood-stream.

In fact, DNA is the biomolecular target for many established metal-containing anticancer drugs [**105**]. Although many organic compounds display anticancer activities and cell apoptosis *via*

weak interactions with DNA (*viz*. van der Waals contacts or hydrogen bonding), inorganic compounds are able to additionally form stronger interactions *via* ionic or covalent bonding which may be reinforced by the stereo-electronic properties of the organic chelating ligand *via* DNA groove-binding or intercalation [**106**]. The DNA interaction studies of organometallic compounds, in amalgamation with computational modelling, can provide vital information with respect to the affinity of the compound to DNA, the mechanism of action with DNA and the ability of the compound to induce programmed cell death [**107, 108**].

It has been shown that the anticancer activities of functional compounds will be governed by the nature of the metal centre present, *i.e.*, its electron configuration, oxidation state and hard/ soft nature. Therefore, the selectivity of isostructural compounds can be fine-tuned towards specific DNA sequences by varying the metal centre. This is evident with the series of d^6 metal complexes containing different metal ions [Ru(II), Rh(II) and Ir(II)] all containing the ligand 2,2′-biimidazole [**Figure 1.14**]. In spite of their structural similarities, these metal complexes are found to have different affinities for DNA [**109**]. Similarly, copper(II) and Ni(II) complexes of the ligand 1,3-*bis*(4-((1*E*)-1-((2*E*)-(pyridine–2-ylmethylidene)hydrazonylidene)-ethyl}-phenoxy}propane [**Figure 1.14**] show distinct modes of binding towards DNA. The Cu(II) complex showed classical intercalative behaviour whilst the Ni(II) complex preferred to interact with DNA *via* weaker, external contacts [**106**].

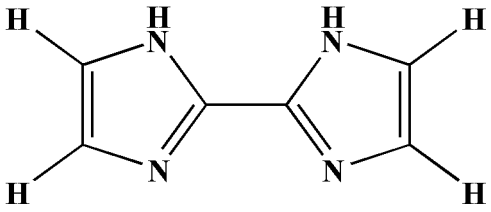

(a)

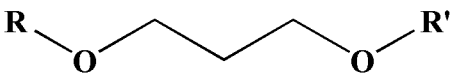

(b)

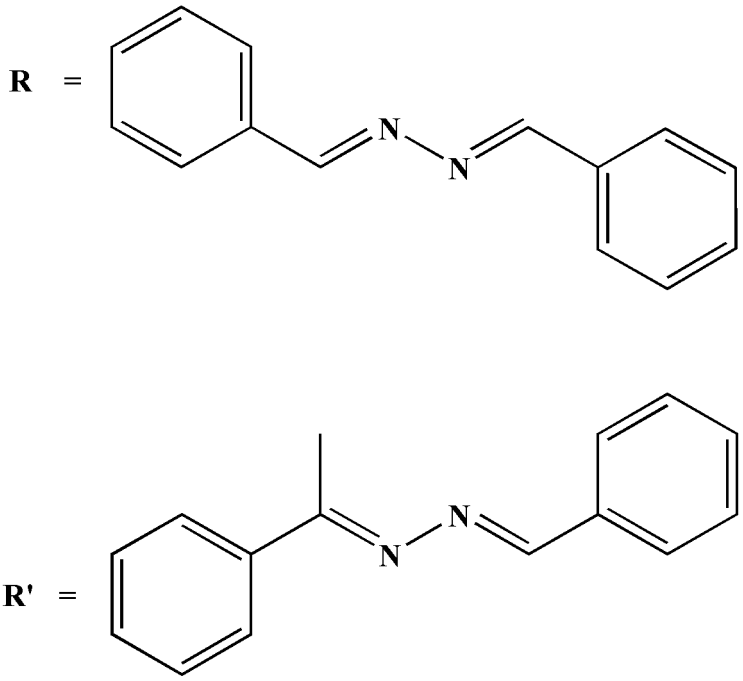

Figure 1.14: *Structures of the ligands: (**a**) 2,2'-biimidazole and (**b**) 1,3-bis(4-((1E)-1-((2E)-(pyridine-2-ylmethylidene)hydrazonylidene)-ethyl}-phenoxy}propane.*

The DNA interaction studies of the ruthenium-arene complexes have reported their tendencies to selectively metallate DNA, causing cell death. RAPTA-CF3 [**Figure 1.15**], [Ru(η^6-$C_6H_5CF_3$)(pta)Cl_2] (pta=1,3,5-triaza-7-phosphatricyclo[3.3.1.1]decane) shows a loss of the arene ring during its interaction with DNA, this is followed by the formation of multiple coordinative Ru-DNA adducts which subsequently causes cell death by averting enzymatic

DNA repair, whereas [Ru(η^6-tha)(en)Cl]$^+$ (tha = 5,8,9,10-tetrahydroanthracene and en = ethane-1,2-diamine [**Figure 1.15**] has also been reported to distort DNA *via* covalent metallation [**110**]. A combination of DNA binding modes can be seen with the dinuclear complexes of the type [Ru_2(N-N)$_4$(BPIMBp)]$^{4+}$ [*N-N* = 1,4,8,9-tetraazatriphenylene (dpq) or dipyrido[3,2-a:2′,3′-c] phenazine (dppz) and BPIMBp = 1,40-*bis*[(2-pyridine-2-yl)-(1H-imidazole-1-yl)methyl]-1,10-biphenyl] [**Figure 1.16**], which biophysical studies have shown to possess intercalative abilities through the bridging BPIMBp and groove-binding modes through the dpq or dppz co-ligands [**111**]**.**

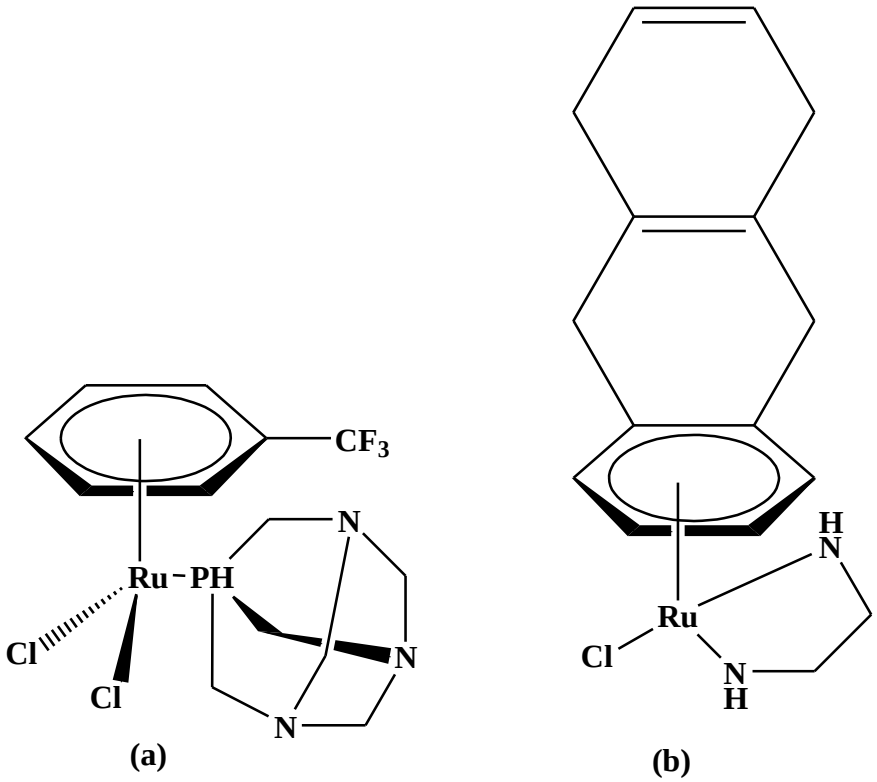

Figure 1.15: *Structures of arene ruthenium-based drugs (**a**) [Ru(η^6-$C_6H_5CF_3$)(pta)Cl_2] and (**b**) [Ru(η^6-tha)(en)Cl]$^+$.*

.

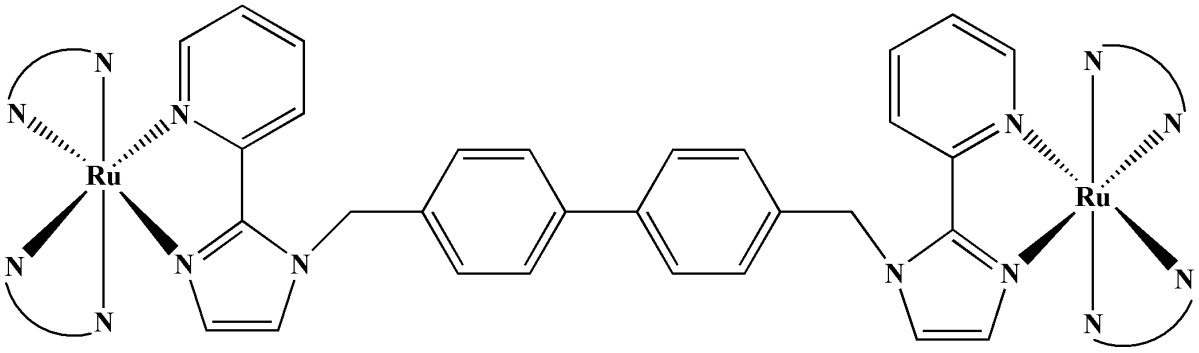

Figure 1.16: *Dinuclear ruthenium compound $[Ru_2(N\text{-}N)_4(BPIMBp)]^{4+}$ which exhibits a dual binding mode.*

1.7 Serum albumin interaction studies of ruthenium compounds

Albumin is the most prominent plasma protein in most organisms, constituting around 60% of the total protein content in plasma. Human serum albumin (HSA) fosters significant roles in the binding, storing and transportation of many exogenous ligands such as pharmacological drugs and several essential metals. Therefore, the investigation of the interactions between serum albumin and potential drug candidates is critical for the understanding of drug pharmacokinetics and -dynamics, as the nature and strength of these interactions will influence the mode of drug absorption and distribution pathways, metabolism and excretion [**112, 113**].

The ability of HSA to interact with transition metals has been used in clinical biochemistry for the design of metallodrugs [**113**]. It has been shown that both orally and intravenously administered drugs utilize HSA as a means of distribution, metabolism and excretion. This interaction can be advantageous due to the enhanced solubility and retention effect in tumour tissues which results in an accumulation of protein-bound drugs within cancer cells. On the contrary, irreversible protein binding could hinder effective drug distribution and cause toxicity. The interaction of the monomeric complex cations $[Ru(\eta^6\text{-}p\text{-cymene})(H_2O)(dhp)]^{2+}$ and $[Rh(\eta^5\text{-}C_5Me_5)(H_2O)(dhp)]^{2+}$ (dhp = 1,2-dimethyl-3-hydroxy-pyridin-4(1*H*)-one) [**Figure 1.17**] with HSA showed that the formation of the coordinate metal-HSA bonds kinetically hindered the release of these bound metallodrugs [**114**]. Thus, understanding how potential metallodrugs interact with HSA is of utmost importance.

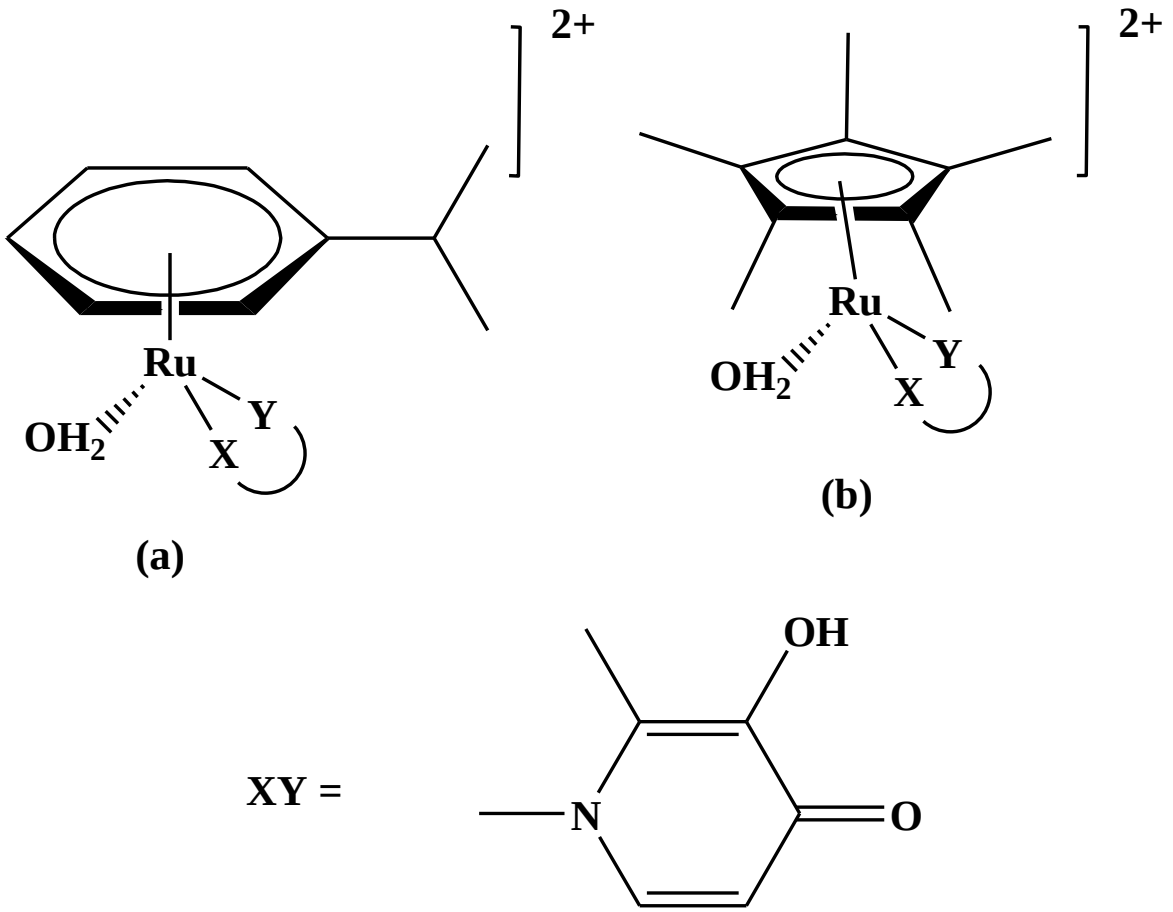

Figure 1.17: *Structures of the BSA binders: (**a**) [Ru(η^6-p-cymene)(H_2O)(dhp)]$^{2+}$ and (**b**) [Rh(η^5-C_5Me_5 (H_2O)(dhp)]$^{2+}$.*

Serum protein binding is particularly important for ruthenium-based agents, since albumin and transferrin are directly involved in their mechanisms of action. Recently, the serum albumin interaction of the ruthenium compound RuNTF ([Ru^{II}(dmso)$_2$(5-nitro-2-furaldehyde semicarbazone)]) [**Figure 1.18**] was accessed *via* various spectroscopic techniques and circular dichroism. This study discovered evidence of the formation of a RuNTF-HSA adduct and a conditional stability constant which reveals a moderate to strong interaction that was efficient enough to afford a strong adduct but still satisfactory for reversible binding, and therefore its distribution and delivery through the blood plasma was considered possible [**115**].

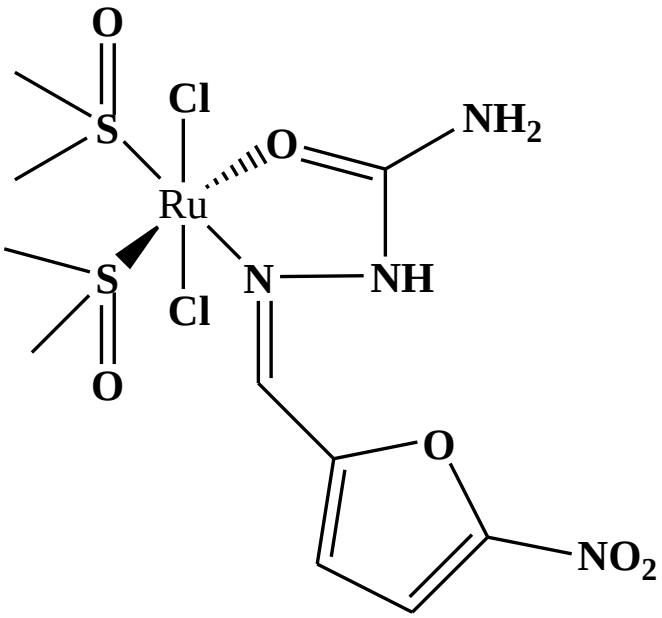

Figure 1.18: *Structure of RuNTF.*

1.8 References

1. A. K. Sahu, D. Dash, K. Mishra, S. P. Mishra, R. Yadav and P. Kashyap, *Properties and Applications of Ruthenium, Noble and Precious Metals - Properties, Nanoscale Effects and Applications (Chpt. 17)*, IntechOpen, 2018, 377-378.

2. S. Czerczak, J. Gromiec, A. pałaszewska-tkacz and A. Świdwińska-Gajewska, *Nickel, Ruthenium, Rhodium, Palladium, Osmium, and Platinum (Chpt. 19)*, John Wiley & Sons, 2012, 653-768.

3. A. K. Mishra and L. Mishra, *Ruthenium Chemistry*, Jenny Stanford Publishing, 2018.

4. L. Leckie and S. Mapolie, *Catal. Commun.*, 2019, **131**, 105803.

5. P. Bossew, F. Gering, E. Petermann, T. Hamburger, C. Katzlberger, M. A. Hernandez-Ceballos, M. De Cort, K. Gorzkiewicz, R. Kierepko and J. W. Mietelski, *J. Environ. Radioact.*, 2019, **205-206**, 79-92.

6. M. J. Clarke, *Coord. Chem. Rev.*, 2002, **232**, 69-93.

7. K. S. Singh, *Catalysts*, 2019, **9**, 173.

8. J. M. Kamdar and D. B. Grotjahn, *Molecules*, 2019, **24**, 494.

9. D. A. Hey, R. M. Reich, W. Baratta and F. E. Kuehn, *Coord. Chem. Rev.*, 2018, **374**, 114-132.

10. Z. Ma, Y. Zhang, S. Liu, W. Xu, L. Wu, Y.-C. Hsieh, P. Liu, Y. Zhu, K. Sasaki and J. N. Renner, *J. Electroanal. Chem.*, 2018, **819**, 296-305.

11. F. Zhang, X. Gu, S. Zheng, H. Yuan, J. Li and X. Wang, *Electrochim. Acta.*, 2019, **307**, 385-392.

12. J. Han, H. J. An, T.-W. Kim, K.-Y. Lee, H. J. Kim, Y. Kim and H.-J. Chae, *Catalysts*, 2019, **9**, 549-554.

13. J. Liu, H. Lai, Z. Xiong, B. Chen and T. Chen, *ChemComm.*, 2019, **55**, 9904-9914.

14. I. N. Booysen, A. Adebisi and M. P. Akerman, *Inorg. Chim. Acta.*, 2015, **433**, 13-20.

15. L. Gramni, N. Vukea, A. Chakraborty, W. J. Samson, L. M. K. Dingle, B. Xulu, J.-A. de la Mare, A. L. Edkins and I. N. Booysen, *Inorg. Chim. Acta.*, 2019, **492**, 98-107.

16. S. Mandal, V. Kundi, D. K. Seth, K. Srikanth and P. Gupta, *Polyhedron*, 2014, **80**, 290-297.

17. M. Premkumar, P. Vijayan and G. Venkatachalam, *J. Organomet. Chem.*, 2019, **902**, 120964.

18. G. S. Biggs, M. J. O'Neill, P. C. Mendez, T. G. Scrase, Y. Lin, A. M. Bin-Maarof, A. D. Bond, S. R. Boss and P. D. Barker, *Dalton Trans.*, 2019, **48**, 6910-6920.

19. R. Trondl, P. Heffeter, C. R. Kowol, M. A. Jakupec, W. Berger and B. K. Keppler, *Chem. Sci.*, 2014, **5**, 2925-2932.

20. M. Muralisankar, R. Dheepika, J. Haribabu, C. Balachandran, S. Aoki, N. S. P. Bhuvanesh and S. Nagarajan, *ACS Omega*, 2019, **4**, 11712-11723.

21. J. W. Arblaster, *Platin. Met. Rev.*, 2011, **55**, 251-262.

22. T. AlMahmoud, S. Quinlan-Davidson, G. R. Pond and J. Deschênes, *Middle East Afr. J. Ophthalmol.*, 2018, **25**, 103-107.

23. L. Zeng, P. Gupta, Y. Chen, E. Wang, L. Ji, H. Chao and Z.-S. Chen, *Chem. Soc. Rev.*, 2017, **46**, 5771-5804.

24. J. P. Coverdale, T. Laroiya-McCarron and I. Romero-Canelón, *Inorganics*, 2019, **7**, 31-45.

25. S. Vasaikar, P. Bhatia, P. G. Bhatia and K. Chu Yaiw, *Biomedicines*, 2016, **4**, 27.

26. W. M. Motswainyana and P. A. Ajibade, *Advances in Chemistry*, 2015, **2015**, 859730.

27. M. Nišavić, M. Stoiljković, I. Crnolatac, M. Milošević, A. Rilak and R. Masnikosa, *Arab. J. Chem.*, 2018, **11**, 291-304.

28. B. J. Pages, D. L. Ang, E. P. Wright and J. R. Aldrich-Wright, *Dalton Trans.*, 2015, **44**, 3505-3526.

29. N. C. de Carvalho, S. P. Neves, R. B. Dias, L. d. F. Valverde, C. B. Sales, C. A. Rocha, M. B. Soares, E. R. dos Santos, R. M. Oliveira and R. M. Carlos, *Cell Death Dis.*, 2018, **9**, 79.

30. S. Thota, D. A. Rodrigues, D. C. Crans and E. J. Barreiro, *J. Med. Chem.*, 2018, **61**, 5805-5821.

31. R. D. Taylor, M. MacCoss and A. D. Lawson, *J. Med. Chem.*, 2014, **57**, 5845-5859.

32. M. Montani, G. V. B. Pazmay, A. Hysi, G. Lupidi, R. Pettinari, V. Gambini, M. Tilio, F. Marchetti, C. Pettinari and S. Ferraro, *Pharmacol. Res.*, 2016, **107**, 282-290.

33. G. K. Mutua, R. Bellam, D. Jaganyi and A. Mambanda, *J. Coord. Chem.*, 2019, **72**, 2931-2956.

34. A. R. Simović, R. Masnikosa, I. Bratsos and E. Alessio, *Coord. Chem. Rev.*, 2019, **398**, 113011-113036.

35. M. A. Abdelgawad, K. R. Abdellatif and O. M. Ahmed, *Med. Chem. S.*, 2014, **S1**, 2161-0444.

36. D. C. Liu, M. J. Gao, Q. Huo, T. Ma, Y. Wang and C. Z. Wu, *J. Enzyme Inhib. Med. Chem.*, 2019, **34**, 829-837.

37. E. Taherian, G. Khodarahmi, M. R. Khajouei, F. Hassanzadeh and N. Dana, *Res. Pharm. Sci.*, 2019, **14**, 247-254.

38. D. Havrylyuk, D. K. Heidary, L. Nease, S. Parkin and E. C. Glazer, *Eur. J. Inorg. Chem.*, 2017, **2017**, 1687-1694.

39. K. Anand and S. Wakode, *Int. J. Chem. Stud.*, 2017, **5**, 350-362.

40. A. Pałasz and D. Cież, *Eur. J. Med. Chem.*, 2015, **97**, 582-611.

41. O. Michalak, P. Cmoch, P. Krzeczyński, M. Cybulski and A. Leś, *Org. Biomol. Chem.*, 2019, **17**, 354-362.

42. H. Kamio, T. Uchiyama, H. Kanno, Y. Onoe, K. Saito, S. Kameoka, T. Kamio and T. Okamoto, *Pharmacogenomics*, 2019, **20**, 353-365.

43. T. Ishikawa, *World J. Gastroenterol.*, 2008, **14**, 2797-2801.

44. A. Y. Lukmantara, D. S. Kalinowski, N. Kumar and D. R. Richardson, *Org. Biomol. Chem.*, 2013, **11**, 6414-6425.

45. B.-Q. Zou, X. Lu, Q.-P. Qin, Y.-X. Bai, Y. Zhang, M. Wang, Y.-C. Liu, Z.-F. Chen and H. Liang, *RSC Adv.*, 2017, **7**, 17923-17933.

46. A. Santoro, B. Vileno, Ò. Palacios, M. D. Peris-Diaz, G. Riegel, C. Gaiddon, A. Krężel and P. Faller, *Metallomics*, 2019, **11**, 994-1004.

47. S. Arora, S. Agarwal, S. Singhal, *Int. J. Pharm. Pharmaceut. Sci.*, 2014, **6**, 34-41.

48. P. Heffeter, V. F. Pape, E. A. Enyedy, B. K. Keppler, G. Szakacs and C. R. Kowol, *Antioxid. Redox Signaling.*, 2019, **30**, 1062-1082.

49. A. Mrozek-Wilczkiewicz, K. Malarz, M. Rejmund, J. Polanski and R. Musiol, *Eur. J. Med. Chem.*, 2019, **171**, 180-194.

50. S. Hager, K. Korbula, B. Bielec, M. Grusch, C. Pirker, M. Schosserer, L. Liendl, M. Lang, J. Grillari, K. Nowikovsky, V. F. S. Pape, T. Mohr, G. Szakács, B. K. Keppler, W. Berger, C. R. Kowol and P. Heffeter, *Cell Death Dis.*, 2018, **9**, 1052-1068.

51. R. Naveed, I. Hussain, A. Tawab, M. Tariq, M. Rahman, S. Hameed, M. S. Mahmood, A. B. Siddique and M. Iqbal, *BMC Complem. Altern. M.*, 2013, **13**, 265-274.

52. M. Imran, M. Nadeem, F. Saeed, A. Imran, M. R. Khan, M. A. Khan, S. Ahmed and A. Rauf, *Food Arg. Immunol.*, 2017, **28**, 543-572.

53. S. V. Rao, G. M. Muralidhara and P. S. Rajini, *Int. J. Neurology Res.*, 2016, **2**, 297-307.

54. M. E. Ebada, *J. Pharmacol. Clin. Res.*, 2017, **2**, 555-585.

55. Y. A. Larasati and E. Meiyanto, *Indonesian Journal of Cancer Chemoprevention*, 2018, **9**, 47-62.

56. J. Reis, A. Gaspar, N. Milhazes and F. Borges, *J. Med. Chem.*, 2017, **60**, 7941-7957.

57. C. F. M. Silva, V. F. Batista, D. C. G. A. Pinto and A. M. S. Silva, *Expert Opin. Drug Discov.*, 2018, **13**, 795-798.

58. Y.-d. Duan, Y.-y. Jiang, F.-x. Guo, L.-x. Chen, L.-l. Xu, W. Zhang and B. Liu, *Fitoterapia*, 2019, **135**, 114-129.

59. O. M. Adly and H. F. El-Shafiy, *J. Coord. Chem.*, 2019, **72**, 218-238.

60. K. M. Elattar and A. A. Fadda, *Synth. Commun.*, 2016, **46**, 1567-1594.

61. M. Ghorab, M. El-Gazzar and M. Alsaid, *Int. J. Mol. Sci.*, 2014, **15**, 7539-7553.

62. A. Hameed, M. al-Rashida, M. Uroos, S. Abid Ali and K. M. Khan, *Expert Opin. Ther. Pat.*, 2017, **27**, 63-79.

63. D. Chaturvedi, *Chem. Sci. J.*, 2016, **7**, 1000e1114.

64. A. S. Hassan, T. S. Hafez, S. A. M. Osman and M. M. Ali, *Turk. J. Chem.*, 2015, **39**, 1102-1113.

65. V. B. Arion, *Coord. Chem. Rev.*, 2019, **387**, 348-397.

66. F. E. Poynton, S. A. Bright, S. Blasco, D. C. Williams, J. M. Kelly and T. Gunnlaugsson, *Chem. Soc. Rev.*, 2017, **46**, 7706-7756.

67. H. Ke, W. Ma, H. Wang, G. Cheng, H. Yuan, W.-K. Wong, D. W. Kwong, H.-L. Tam, K.-W. Cheah and C.-F. Chan, *J. Lumin.*, 2014, **154**, 356-361.

68. A. De Luca, L. J. Parker, W. H. Ang, C. Rodolfo, V. Gabbarini, N. C. Hancock, F. Palone, A. P. Mazzetti, L. Menin and C. J. Morton, *Proc. Natl. Acad. Sci. U. S. A.*, 2019, **116**, 13943-13951.

69. R. Oun, Y. E. Moussa and N. J. Wheate, *Dalton Trans.*, 2018, **47**, 6645-6653.

70. T. Lazarević, A. Rilak and Ž. D. Bugarčić, *Eur. J. Med. Chem.*, 2017, **142**, 8-31.

71. U. Ndagi, N. Mhlongo and M. E. Soliman, *Drug. Des. Devel. Ther.*, 2017, **11**, 599-616.

72. A. A. Holder, L. Lilge, W. R. Browne, M. A. W. Lawrence and J. L. Bullock, *Ruthenium Complexes Photochemical and Biomedical Applications,* Wiley, VCH, 2018.

73. R. G. Kenny and C. J. Marmion, *Chem. Rev.*, 2019, **119**, 1058-1137.

74. L. S. Flocke, R. Trondl, M. A. Jakupec and B. K. Keppler, *Invest. New Drug.*, 2016, **34**, 261-268.

75. E. Alessio and L. Messori, *Molecules*, 2019, **24**, 1995-2014.

76. R. H. Berndsen, A. Weiss, U. K. Abdul, T. J. Wong, P. Meraldi, A. W. Griffioen, P. J. Dyson and P. Nowak-Sliwinska, *Sci. Rep.*, 2017, **7**, 43005-43020.

77. R. O. Omondi, D. Jaganyi, S. O. Ojwach and A. A. Fatokun, *Inorg. Chim. Acta.*, 2018, **482**, 213-220.

78. A. Chattopadhyay, A. Dey, P. Karmakar, S. Ray, D. Nandi, R. Sarkar and A. K. Ghosh, *Prog. React. Kinet. Mech.*, 2018, **43**, 274-285.

79. M. M. Milutinović, S. K. Elmroth, G. Davidović, A. Rilak, O. R. Klisurić, I. Bratsos and Ž. D. Bugarčić, *Dalton Trans.*, 2017, **46**, 2360-2369.

80. R. O. Omondi, S. O. Ojwach, D. Jaganyi and A. A. Fatokun, *Inorg. Chem. Commun.*, 2018, **94**, 98-103.

81. I. N. Booysen, A. Adebisi, M. P. Akerman, O. Q. Munro and B. Xulu, *J. Coord. Chem.*, 2016, **69**, 1641-1652.

82. Z. Lu, Y. Gao, H. Chen, Z. Liu and L. Sun, *Dalton Trans.*, 2017, **46**, 1304-1310.

83. T. P. Yoon, M. A. Ischay and J. Du, *Nat. Chem.*, 2010, **2**, 527-532.

84. O. Impert, A. Katafias, J. Fenska and P. Kita, *Trans. Met. Chem.*, 2012, **37**, 7-16.

85. K. J. LaChance-Galang, M. Zhao and M. J. Clarke, *Inorg. Chem.* , 1996, **35**, 6021-6026.

86. N. Ljubijankić, A. Zahirović, E. Turkušić and E. Kahrović, *Croat. Chem. Acta.*, 2013, **86**, 215-222.

87. S. Pal, *Pyridine: A Useful Ligand in Transition Metal Complexes* IntechOpen, 2018,

88. J. G. Małecki and A. Maroń, *Trans. Met. Chem.*, 2013, **38**, 133-142.

89. D. Isakov, R. Giereth, D. Nauroozi, S. Tschierlei and S. Rau, *Inorg. Chem.*, 2019, **58**, 12646 -12653.

90. J. Aguiló, A. Naeimi, R. Bofill, H. Mueller-Bunz, A. Llobet, L. Escriche, X. Sala and M. Albrecht, *New J. Chem.*, 2014, **38**, 1980-1987.

91. A. A. Soliman, M. A. Amin, A. A. El-Sherif, C. Sahin and C. Varlikli, *Arab. J. Chem.*, 2017, **10**, 389-397.

92. U. R. Gandra, S. K. Podiyanachari, A. R. Hlil, I. Kulai, S. Al- Meer, M. Al- Hashimi and H. S. Bazzi, *J. Polym. Sci., Part A: Polym. Chem.*, 2019, **57**, 1741-1747.

93. M. I. Gruia, V. Negoita, M. Vasilescu, M. Panait, I. Gruia, B. S. Velescu and V. Uivarosi, *Anticancer Res.*, 2015, **35**, 3371-3378.

94. J. H. Wallenstein, J. Sundberg, C. J. McKenzie and M. Abrahamsson, *Eur. J. Inorg. Chem.*, 2016, **2016**, 897-906.

95. B. Adhikari, S. Pramanik, T. Ghorui, S. Roy, U. Das and K. Pramanik, *J. Indian Chem. Soc*, 2015, **92**, 1903-1912.

96. N. A. Al-Rawashdeh, S. Chatterjee, J. A. Krause and W. B. Connick, *Inorg. Chem.*, 2013, **53**, 294-307.

97. M. M. Haghdoost, J. Guard, G. Golbaghi and A. Castonguay, *Inorg. Chem.*, 2018, **57**, 7558-7567.

98. N. Sathya, G. Raja and C. Jayabalakrishnan, *Synth. React. Inorg. M.*, 2011, **41**, 81-90.

99. I. López, S. Maji, J. Benet-Buchholz and A. Llobet, *Inorg. Chem.*, 2014, **54**, 658-666.

100. A. C. Dengel, A. M. El-Hendawy, W. P. Griffith, C. A. O'mahoney and D. J. Williams, *J. Chem. Soc., Dalton Trans.*, 1990, 737-742.

101. W.-L. Man, W. W. Lam, W.-Y. Wong and T.-C. Lau, *J. Am. Chem. Soc.* , 2006, **128**, 14669-14675.

102. C. M. Che, W. T. Tang, W. T. Wong and T. F. Lai, *J. Am. Chem. Soc.* , 1989, **111**, 9048-9056.

103. W.-C. Cheng, W.-Y. Yu, K.-K. Cheung and C.-M. Che, *J. Chem. Soc., Chem. Commun.*, 1994, 1063-1064.

104. N. L. Fackler, S. Zhang and T. V. O'Halloran, *J. Am. Chem. Soc.* , 1996, **118**, 481-482.

105. L. H. Hurley, *Nat. Rev. Cancer.*, 2002, **2**, 188-200.

106. V. Brabec and J. Kasparkova, *Coord. Chem. Rev.*, 2018, **376**, 75-94.

107. L. J. Boerner and J. M. Zaleski, *Curr. Opin. Chem. Biol.*, 2005, **9**, 135-144.

108. O. Surova and B. Zhivotovsky, *Oncogene*, 2013, **32**, 3789-3797.

109. A. Gilewska, B. Barszcz, J. Masternak, K. Kazimierczuk, J. Sitkowski, J. Wietrzyk and E. Turlej, *J. Biol. Inorg. Chem.*, 2019, **24**, 339-358.

110. K. Suntharalingam and R. Vilar, *Annu. Rep. Prog. Chem., Sect. A*, 2011, **107**, 339-358.

111. S. B. Singh, A. S. Kumbhar and A. Khan, *Chemistry*, 2016, **22**, 15760-15771.

112. T. Topală, A. Bodoki, L. Oprean and R. Oprean, *Clujul Med*, 2014, **87**, 215-219.

113. S. Al-Harthi, J. I. Lachowicz, M. E. Nowakowski, M. Jaremko and Ł. Jaremko, *J. Inorg. Biochem.*, 2019, **198**, 110716-110730.

114. O. Dömötör and É. A. Enyedy, *J. Biol. Inorg. Chem.*, 2019, **24**, 703-719.

115. B. Demoro, A. Bento-Oliveira, F. Marques, J. Costa Pessoa, L. Otero, D. Gambino, R. FM de Almeida and A. I. Tomaz, *Molecules*, 2019, **24**, 2861-2879.

Chapter 2

Materials and methods

2.1 The handling of ruthenium

Compounds of ruthenium are treated as environmentally unfriendly and hazardous substances as they display high toxicity and carcinogenic effects. When heated in the presence of air, these compounds form an extremely toxic and volatile substance called ruthenium tetroxide which can cause damage to the upper respiratory system and the eyes [**1**]. Due to these exposures, several safety measures were practiced during the handling all ruthenium compounds, this included the use of gloves, dust masks and fume cupboards in which all coordination reactions were performed.

2.2 Materials

2.2.1 Metal precursor

The metal precursor, *trans*-[$RuCl_2(PPh_3)_2$] was purchased at 97% purity from Sigma-Aldrich and no additional purification was carried out before use.

2.2.2 Commercially obtained chemicals

All common laboratory chemicals and solvents were of analytical grade and used as is. All chemicals listed below [**Table 2.1**] were also purchased from Sigma-Aldrich and used without additional purification.

Table 2.1: *Chemicals purchased from Sigma-Aldrich.*

Name	Purity
o-Phenylenediamine	98%
2,2'-Bipyridine-4,4'-dicarboxylic acid	98%
Diglycolic acid	98%
Ammonium hexafluorophosphate	95%
Pyridine-2-carbohydrazide	97%
Benzothiazole-2-carboxaldehyde	97%
Thiophene-2-carbohydrazide	98%
5-Formyluracil	98%
Thiosemicarbazide	99%
5-Aminopentanol	95%
2-Thiophenecarboxaldehyde	98%
2-Pyridinecarboxaldehyde	99%
Cuminaldehyde	98%
Cinnamaldehyde	95%
4-Aminoantipyrine	98%
Benzhydrazide	98%
Tetrabutylammonium hexafluorophosphate	98%
Phosphate buffered saline (PBS) tablets	-
Calf thymus (CT) DNA	-
Bovine serum albumin	-
2,2-di(4-*tert*-octylphenyl)-1-picrylhydrazyl (DPPH)	98%
Griess reagent	98%
Sodium nitroprusside	98%
L-Ascorbic acid	99%
Warfarin	98%
Ibuprofen	98%

2.3 Synthetic procedures for ligands

2.3.1 *Syntheses of 2,2'-[oxybis(methylene)]-bis-(1H-benzimidazole) (ombb) and 4,4'-bis(1H-benzimidazol-2-yl)-2,2'-bipyridine (bbb)*

The *bis*-benzimidazole ligands (**Chapter 3**), ombb and bbb, were synthesized according to formerly reported literature procedures [**2, 3**].

2.3.2 *Synthesis of N-[1,3-benzothiazole-2-ylmethylidene]pyridine-2-carbohydrazide (Hbpc)*

The Schiff base Hbpc (**Chapter 4**) was synthesized from a previously reported condensation method in literature [**4**].

2.3.3 *Synthesis of N*-((uracil-5-yl)methylene)thiophene-2-carbohydrazide *(Httc)*

Ligand Httc (**Chapter 4**) was synthesized by the condensation reaction between thiophene-2-carbohydrazide (0.500 g, 3.52 mmol) and 5-formyluracil (0.493 g, 3.52 mmol) was conducted by heating until reflux in methanol (30 cm^3) for 3 hours. The resulting light-yellow solution was allowed to cool to room temperature and then filtered. The pale-yellow precipitate obtained was washed with petroleum ether and then cold methanol. Yield: 72 %; m.p: 294.9 – 302.8 ˚C. IR (ν_{max}/cm^{-1}): ν(N-H)$_{uracil}$ 3465, 3416 (br, m); ν(N-H)$_{amide}$ 2963 (sh, m); ν(C=O)$_{uracil}$ 1718 (s), 1686 (vs); ν(C=O)$_{amide}$ 1625 (vs); ν(C=N)$_{imino}$ 1567 (br, s); ν(thiophene) 1415, 1228, 1151 (s); ν(C-N) 1064 (m). ^{1}H NMR (295K/ d^6 - CD_6SO/ ppm, enol = *, see **Figure 2.2**): 11.86 – 11.58 (m, 2H, *N4H*, *N3H*); 11.50 – 11.27 (m, 3H, *H8*, *H8'*, *N1H*); 8.33 (br, s, 1H, *H6*); 8.12 – 7.78 (m, 6H, *H1, H1', H2, H2*, H3, H3**). UV-Vis (DCM, ε, M^{-1} cm^{-1}): 267 nm (sh, 3660); 337 nm (6430).

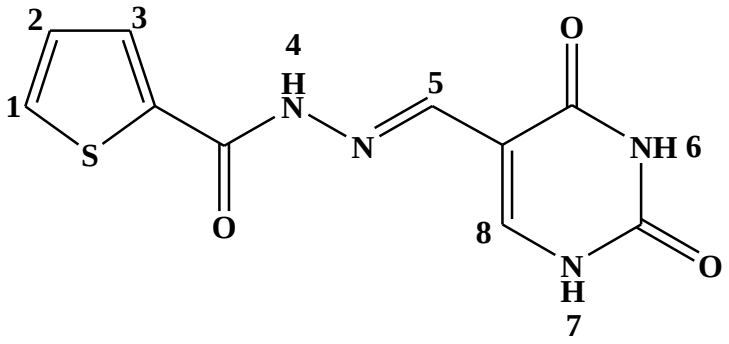

Figure 2.1: *Numbering scheme for Httc.*

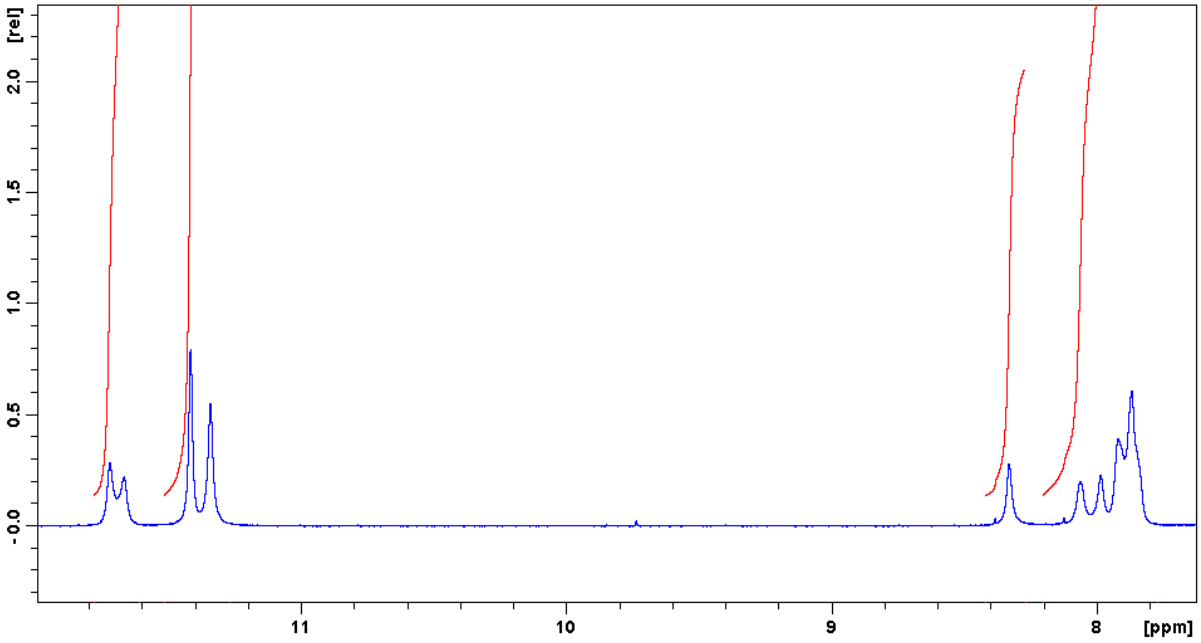

Figure 2.2: *^{1}H NMR spectrum of Httc.*

2.3.4 Synthesis of Htpc

Htpc (**Chapter 4**) was formed by a 1:1 molar ration of pyridine-2-carbohydrazide (0.500 g, 3.65 mmol) and 5-formyluracil (0.511 g, 3.65 mmol) were heated until reflux temperature in methanol (30 cm^{3}). After 3 hours, the yellow solution was cooled to room temperature and the yellow precipitate collected by filtration, followed by washing with petroleum ether and cold methanol. Yield: 66 %; m.p. 312.9 – 314.2 ˚C. IR (ν_{max}/cm^{-1}): υ(N-H)$_{uracil}$ 3224 (br, m); υ(N-H)$_{amide}$ 2900 (sh, w); υ(C=O)$_{uracil}$ 1769 (m), 1724 (s); υ(C=O)$_{amide}$ 1666 (vs); υ(C=N)$_{imino}$ 1543

(vs); ν(C=N)$_{benzothiazole}$ 1431 (m); ν(C-N) 1053 (m). ^{1}H NMR (295 K/ d^{6}-CD_6SO/ppm, see **Figure 2.4**): 12.11 (s, 1H, *N5H*); 11.46 – 11.29 (m, 2H, *N4H*, *N2H*); 8.68 (s, 1H, *H7*); 8.50 (s, 1H, *H11*); 8.13 – 7.90 (m, 2H, *H1*, *H4*); 7.88 (d, 1H, *H3*); 7.68 – 7.61 (m, 1H, *H2*). UV-Vis (DCM, ε, M^{-1} cm^{-1}): 275 nm (3840); 335 nm (5170).

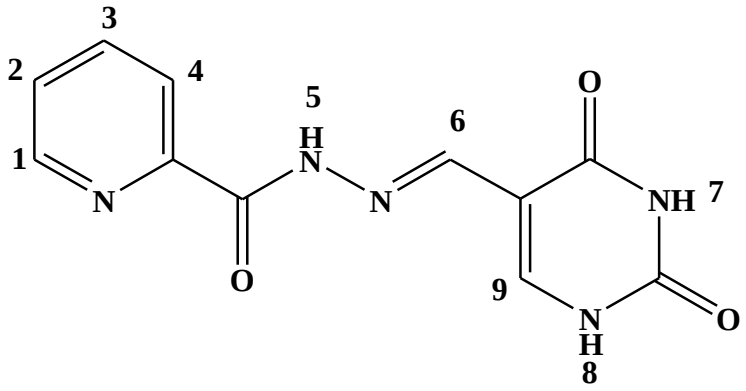

Figure 2.3: *Numbering scheme for Htpc.*

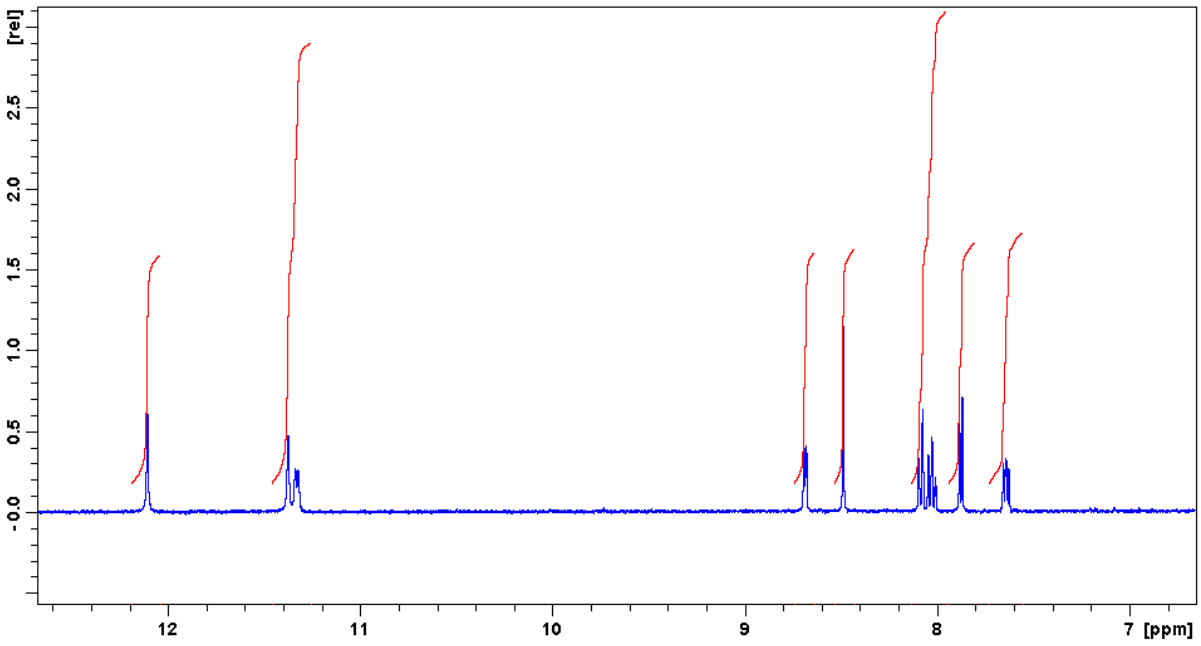

Figure 2.4: *^{1}H NMR spectrum of Htpc.*

2.3.5 Syntheses of 1-((pyridin-2-yl)methylene)thiosemicarbazide (Hpmt), 1-((thiophen-2-yl)methylene)thiosemicarbazide (Htmc) and 2-((5-hydroxypentylimino)methyl)benzothiazole (btm)

The Schiff bases: Hpmt, Htmc and btm (**Chapter 5**) were synthesized according to literature methods [**5-7**].

2.3.6 Synthesis of N'-(4-isopropylbenzylidene)benzohydrazide (cumbh)

The titled compound (**Chapter 6**) was formed from the condensation reaction between benzohydrazide (0.250 g, 1.84 mmol) and cuminaldehyde (0.272 g, 1.84 mmol) in the presence of three drops of glacial acetic acid. The reaction mixture was heated until reflux in ethanol (30 cm^3) for 5 hours. A light-yellow solution was attained which was cooled to room temperature and then filtered. Excess cuminaldehyde was removed by washing with petroleum ether to afford a cream precipitate. Yield: 61 %; m.p: 192.1 – 196.0 ˚C. IR (ν_{max}/cm^{-1}): ν(N-H)$_{amide}$ 3236; ν(C=O)$_{ketonic}$ 1647; ν(C=N)$_{imine}$ 1551. ^{1}H NMR (295 K/ d^6 - CD_6SO/ ppm, see **Figure 2.6**): 8.45 (s, 1H, *H10*); 7.92 (d, 2H, *H6*, *H8*); 7.69 – 7.51 (m, 6H, *N2H*, *H13*, *H14*, *H15*, *H16*, *H17*); 7.36 (d, 2H, *H5*, *H9*); 2.95 (*p*, 1H, *H2*); 1.244 (d, 6H, *H1*, *H1'*, *H1''*, *H3*, *H3'*, *H3''*). UV-Vis (DCM, ε, M^{-1} cm^{-1}): 229 nm (10100); 306 nm (17540).

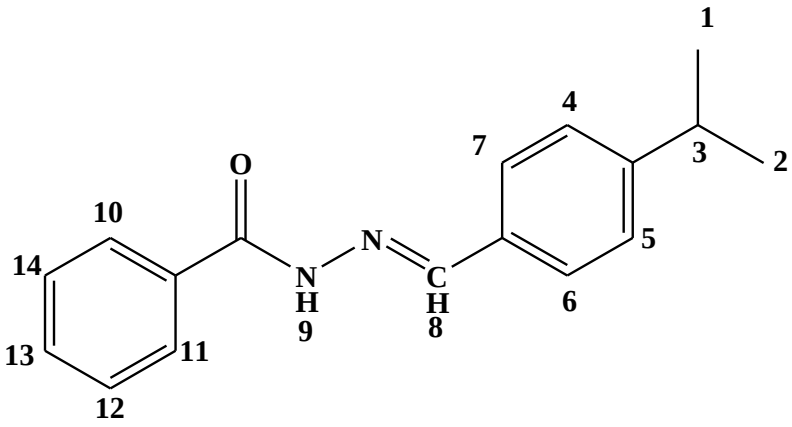

Figure 2.5: *Numbering scheme for cumbh.*

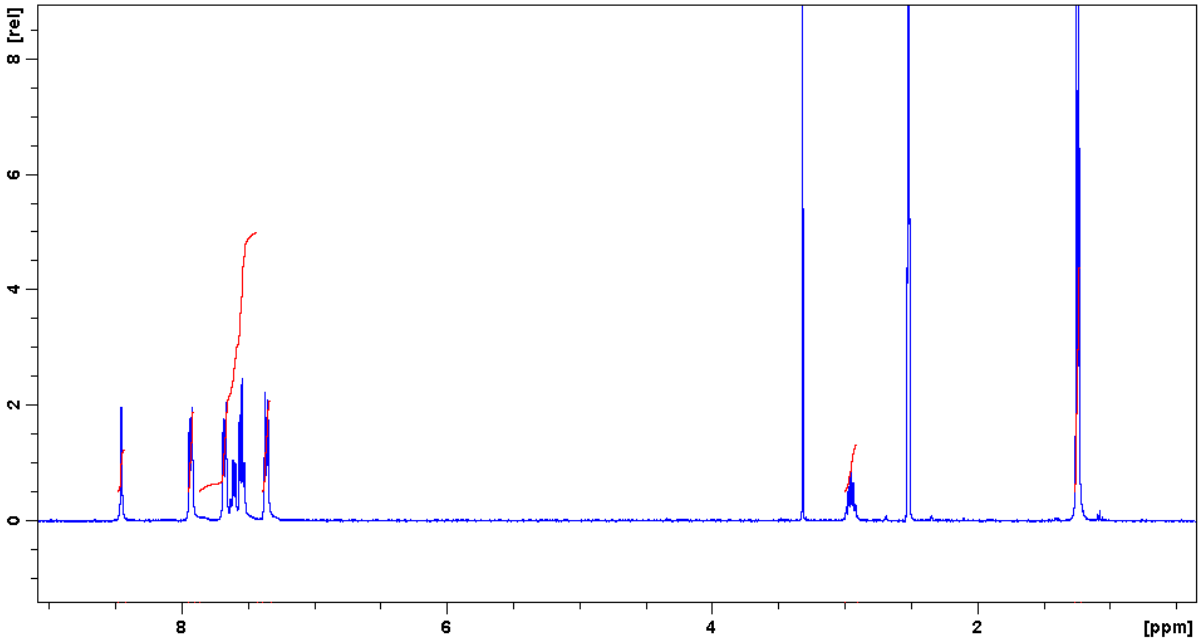

Figure 2.6: *^{1}H NMR spectrum of cumbh.*

2.3.7 Syntheses of 1,5-dimethyl-2-phenyl-4-10-1,2-dihydro-3H-pyrazol-3-one (cumap) and 1,5-dimethyl-2-phenyl-4-10-1,2-dihydro-3H-pyrazol-3-one)cinap)

The Schiff bases, cumap and cinap (**Chapter 6**), were prepared according to literature methods [**8**].

2.4 Instrumentation

2.4.1 Spectroscopic techniques

- ^{31}P and ^{1}H NMR spectra were obtained in DMSO-d_6 using a Bruker Advance 400 MHz spectrometer equipped with an autosampler.

- Solid-state infrared spectra were recorded using a Perkin-Elmer Spectrum 100 in the range 650 – 4000 cm^{-1}.

- Electronic spectra were collected using a Perkin-Elmer Lambda 25.

- Fluorescence measurements were carried out using a 1 cm quartz emission cell and a Perkin Elmer LS-45 fluorescence spectrometer equipped with a xenon lamp source.

2.4.2 *Conductivity and melting point measurements*

- Conductivity measurements for selected metal complexes were obtained using a Radiometer Analytical standard conductivity electrode on a MeterLab ION450 Ion Analyzer. The standard solution used was 0.745 g KCl in 1 L of H2O and all measurements were conducted at 295 K.

- Melting point ranges were determined with the aid of a Stuart SMP3 melting point apparatus.

2.4.3 *Single X-ray crystallography*

- Single crystal X-ray diffraction (XRD) was run using a Bruker Apex Duo diffractometer with a Inocoatec Mo ($K\alpha = 0.71073$ Å) microsource X-ray tube operating at 30 W. 10 – 20 second exposure times were used during data collection at mostly 100 or 200 K by ω and φ scans at stable angles of θ. Direct methods, SHELX-2016 [**9**] and WinGX [**10**] were used in the solving of the structures and the data was reduced using the SAINT software package [**11**]. All non-hydrogen atoms were refined anisotropically and hydrogen atoms were calculated in idealized geometric positions.

2.4.4 *Cyclic and squarewave voltammetry*

- Redox properties of the ruthenium compounds were probed by cyclic and squarewave voltammetry using a Metrohm Autolab potentiostat in conjunction with a three electrode system: a glassy carbon working electrode (GCWE), a pseudo Ag|AgCl reference electrode

and an auxiliary Pt counter electrode. Electrochemical grade tetrabutylammonium hexafluorophosphate (0.1 M) was added to the 2 mM dichloromethane solutions of the metal complexes as a supporting electrolyte. Amid each run, the GCWE surface was cleaned and polished with a mixture of ultrapure water and alumina on a Buehler felt pad and rinsed with more ultrapure water and absolute ethanol. Ultrapure water was attained from an ElgaPurelab Ultra system.

2.4.5 *Computational modelling*

- The Gaussian 09W software package was used to conduct *ab initio* calculations [**12**]. The B3LYP functional as well as the LANL2DZ basis sets were used during the geometry optimization of the metal complexes at the Density Functional Theory (DFT) level [**13**].

2.4.6 *Antioxidant studies*

- Experimental methodologies for the radical scavenging measurements were adapted from those in the literature [**14, 15**]. Data reproducibility was confirmed by conducting each experiment in triplicate and the standard equation shown below was used to determine the experimental percentage radical scavenging activities:

$$\%\ Radical\ scavenging\ activity = \left(\frac{A_c - A_f}{A_c}\right) x\ 100$$

Where the absorbance of the control is A_c (NO or DPPH radicals) and A_f is the absorbance upon addition of the individual metal compounds to the control. The metal compound concentrations that induce 50% radical scavenging activity (IC_{50} values) could be readily calculated from their distinctive experimental percentage radical scavenging activities. An experiment was initiated by collecting the UV-Vis spectrum of the control [DPPH (0.2 mM in MeOH)] followed by the addition of 0.1 cm^3 of a metal compound (30 μM in DMSO for complexes in chapter 3 or MeOH for complexes in chapters 4 – 6) and then the sample solution was mixed to ensure homogeneity.

Thereafter, the sample solution was incubated in the dark for 20 minutes and its UV-Vis spectrum was run.

The following experimental method was applied for the NO radical assay: firstly, a 10 mM solution of sodium nitroprusside was prepared in PBS buffer and incubated for a 3 hour period at room temperature. Afterwards, Griess reagent (1 cm^3) was added to 0.5 cm^3 of the nitroprusside solution and the resultant solution functioned as the control. Then the UV-Vis spectrum of the control was collected. The sample solutions were prepared by the addition of solution of a metal compound (30 μM in DMSO for complexes in chapter 3 or MeOH for complexes in chapters 4 – 6) to a 0.5 cm^3 aliquot of the sodium nitroprusside solution. After an incubation period of 3 hours, 1 cm^3 of Griess reagent was added to a sample solution and its UV-Vis spectrum was run.

2.4.7 *UV-Vis spectrophotometric DNA titrations*

- The ct-DNA interactive profiles of the ruthenium compounds were collected at a pH of 7.2 in phosphate-buffered saline (PBS). The ct-DNA solution in PBS yielded a ratio of 1.9:1 at 260 nm and 280 nm, which suggests that the ct-DNA was adequately free of protein. The CT-DNA concentration per nucleotide was calculated using the molar absorption coefficient (ε_{260} = 6600 $M^{-1}cm^{-1}$) [**16**]. The final ct-DNA stock solution was stored at 4 ºC and used within 48 hours. Methanolic solutions of the metal compounds (at 1 mM) and ct-DNA were incubated at 25 ºC for 24 hours prior to any UV-Vis measurements [**17**]. Thereafter, UV-Vis spectra of standard solutions for the respective metal compounds were collected in methanol and continuously monitored during the sequential additions of the standardized ct-DNA in PBS buffer. The intrinsic binding constant (K_b) was found by fitting the data from the titration into the following equation:

$$\frac{[DNA]}{(\varepsilon_a - \varepsilon_b)} = \frac{[DNA]}{(\varepsilon_b - \varepsilon_f)} + \frac{1}{K_b(\varepsilon_b - \varepsilon_f)}$$

In the above equation, [DNA] is the concentration of DNA in base pairs, ε_a corresponds to the extinction coefficient of the marked absorption band at the given DNA concentration (corresponding to A_{obs}/(complex), ε_f is the extinction coefficient of the free compound in solution, and ε_b is the extinction coefficient of the fully bound compound to DNA. The plot of [DNA]/[$\varepsilon_a - \varepsilon_b$] versus [DNA], yields a slope of $1/(\varepsilon_b - \varepsilon_f)$ and a Y intercept of $1/K_b(\varepsilon_b - \varepsilon_f)$. The ratio of the slope to the intercept is projected to be the intrinsic binding constant (K_b) [**17**].

2.4.8 *Agarose gel electrophoresis assessment of DNA binding*

- The ability of the metal compounds in chapter 3 to interact with human genomic DNA (gDNA) isolated from cancer cell lines was assessed by agarose gel electrophoresis. Compounds at two different concentrations (50 µM and 200 µM, selected in relation to the IC_{50} values) or the vehicle control (DMSO) were incubated with 100 ng of gDNA in a total reaction volume of 20 µl. Reaction mixtures were incubated at 37°C for 2-4 hours, followed by electrophoresis for 1 hour at 90 V in 1x *Tris*-acetic acid EDTA (TAE) buffer using 0.8% (w/v) agarose containing 0.5 ug/ml EtBr. The DNA was visualized under UV light. The assay was conducted as independent triplicates and the average fluorescence intensity of DNA treated with compounds was determined by ImageJ relative to the DMSO control.

- The DNA binding abilities of the metal complexes in chapter 4 were investigated by UV Agarose gel electrophoresis. Three variable dosages (3, 30 and 300 µM, selected to correspond to the range of EC_{50} values) of each metal complex and vehicle control (DMSO) were incubated with 500 ng of CT-DNA in a total reaction volume of 30 µl. Respective reaction mixtures were incubated at 37°C for 4 hours before being electrophoresed for 1 hour at 90 V in 1x TAE buffer using 0.8% agarose gel containing 0.5 µg/ml ethidium bromide. DNA visualization was conducted under UV light. The intensity of the DNA signal was quantified in ImageJ and the value calculated relative to the untreated DMSO control.

2.4.9 Hoechst DNA binding competition assay

- The abilities of certain metal compounds to compete with Hoechst for binding to DNA were assessed. Three concentrations of the metal compounds (5 µM, 50 µM and 100 µM) were incubated with a final concentration of 1 ug/ml of Hoechst-33342 in the presence or absence of DNA in a 100 µl reaction volume in a black-walled clear bottom 96 well plate at 25 °C. The fluorescence emission over the range of 400-600 nm was collected after excitation at 350 nm.

2.4.10 Molecular docking

- Molecular docking simulations for chapter 3 were carried out using the AutoDock 4 and AutoGrid 4 as well as the Graphical User Interface (GUI), AutoDock Tools 1.5.6 [**18**]. As per literature trends, the ligand molecules were edited by replacing their Ru atoms with Zn atoms as the AutoDock GUI and its accompanying execution files are not parameterized for ruthenium [**19**]. Input and output files were converted using Open Babel 2.4.1 GUI. In addition, amended versions of the B-DNA (PDB ID: 1F8N) or the BSA (PDB ID: 3VO3) crystal structures were the individual receptor molecules. The receptor molecules were altered by omitting the water molecules of crystallization, while additional alterations were implemented on the BSA structure with exclusion of its calcium ions and second co-crystallized BSA molecule. These versions of the B-DNA and BSA receptor molecules were edited by adding all hydrogens followed by the merging of non-polar hydrogens and computations of the Gasteiger chargers. A generic algorithm was applied as the search parameter, while the output files were expressed in a Lamarckian GA (4.2) format. The average grid box dimensions were 64 x 72 x 98 with spacing of 0.375 Å (*w.r.t* B-DNA) and 126 x 126 x 126 with spacing of 0.700 Å (*w.r.t.* BSA). From the AutoDock calculations, only the adducts with the lowest global energies were considered and processed using YASARA View [**20**].

- Molecular docking for chapters 4 – 6 was conducted using the online servers: PatchDock and FireDock where the optimized conformers were used as the ligands during each calculation [**21, 22**]. Receptor molecules were prepared by amending the crystal structures

of B-DNA (PDB ID: 1F8N) or the BSA (PDB ID: 3VO3) whereby water molecules of crystallization were omitted, while the BSA structure was further altered by eliminating its calcium ions and second co-crystallized BSA molecule. Afterwards, the preliminary structures of the B-DNA and BSA receptor molecules were edited by adding all hydrogens followed by the merging of non-polar hydrogens and computations of the Gasteiger chargers. During the computations, the complex-type and clustering RMSD were defined as protein-small ligand and a value of 4.0, respectively. After each simulation, the data was refined using FireDock and amongst 10 solutions, only the lowest energy biomolecule-optimized conformer hybrid was considered. YASARA view was used to compute short contact interactions between each metal compound and the respective biomolecular targets [**20**]. This software package also aided in generating perspective views of the individual biomolecule-metal compound adducts.

2.4.11 *BSA binding interaction studies*

- The BSA stock solution was prepared in PBS buffer at a pH of 7.2 and its concentration was determined spectrophotometrically using an extinction coefficient of 43824 M^{-1} cm^{-1} at 280 nm [**23**]. The stock solutions of the metal complexes were prepared in acetonitrile in chapter 3 and in MeOH in chapters 4 – 6.

- *Electronic spectrophotometric titrations*

  The BSA interaction experiments were conducted by sustaining the BSA concentration (~20 µM) whilst changing the concentrations of the respective metal compounds (0 – ~320 µM). A 2-minute incubation time was used for each sample mixture. Equal volumes of metal compound were added to both the sample and reference cells. Data from the absorbance titrations were fitted to the following equation:

$$\left[\frac{A_o}{A_o - A}\right] = \left(\frac{\varepsilon_{BSA}}{\varepsilon_B}\right) + \left(\frac{\varepsilon_{BSA}}{\varepsilon_B . K_{app}}\right) . \left(\frac{1}{C_{compound}}\right)$$

Where A_0 and A are the absorbance values of BSA at 280 nm in the absence and presence of a metal compound, ε_{BSA} and ε_B are the extinction coefficients of BSA and the bound complex (*viz.* adduct of a metal compound and BSA), K_{app} is the apparent association constant and $C_{compound}$ is the concentration of a metal compound. From the equation above, the following double reciprocal plot can be produced and the apparent association constant (K_{app}) is found from the ratio of the intercept to the slope [**24**].

$$\frac{1}{(A_o - A)} \; vs \left(\frac{1}{C_{compound}}\right)$$

- *Fluorescence spectrophotometric titrations*
  Alterations of the BSA emission spectrum were evaluated upon progressive additions of the respective metal compound concentrations. Fluorescence emission spectra were run at 298 K with the width of emission and excitation slits attuned to 5 nm. Data acquisition were done in the wavelength range of 300 – 500 nm at an excitation wavelength of 280 nm. The data obtained was used to calculate the Stern-Volmer quenching constant (K_{SV}) using the Stern-Volmer relationship [**25**]:

$$\frac{I_0}{I} = 1 + K_{SV}\,[complex]$$

Where I_0 and I are the emission intensities in the absence and presence of the metal compounds, respectively. The K_{SV} values were gained from the slope of the plot:

$$\frac{I_0}{I} \; vs \; [complex]$$

The quenching rate constant (K_q) could then be determined from the equation:

$$K_{SV} = K_q \, \tau_0$$

Where τ_0 is the lifetime of the protein (10^{-8} s) without a quencher.

- *Competitive binding studies*

  Competitive binding experiments were performed using two different site markers (competitors), *viz*. warfarin for site I and ibuprofen for site II. Firstly, an equal concentration of the competitor was added to the BSA (each at 5 µM) and changes in the fluorescence spectra were noted. The fluorescence titration was then performed by varying the concentration of the metal compound in this BSA-competitor solution while monitoring the spectral changes [**26**]. The data from the titrations were also fitted to the Stern-Volmer plot and the obtained quenching and rate constants were compared to those in the absence of the competitors [**27**].

2.4.12 In vitro anticancer cell line studies

- The cytotoxicity of selected metal compounds against the HeLa and HCC70 triple negative breast carcinoma cell lines were determined using the MTT assay as previously described [**28**]. In this assay, metabolically active cells convert the MTT dye to a blue formazan product that can be detected spectrophotometrically. Briefly, cells were seeded in a 96 well plate in complete medium, allowed to adhere overnight and incubated with a selective concentration range for the compounds (including a vehicle control and positive controls: 5-Fluorouracil and Paclitaxel in triplicate for 96-hours. Thereafter, the cells were incubated with MTT reagent for 4 hours, the resulting formazan crystals solubilized in SDS solution overnight and the absorbance at 595 nm measured. The IC_{50} values were calculated using non-linear regression in GraphPad Prism 4.0.

2.4.13 Cytotoxicity assays for EC_{50} determination

- HCC70 triple negative breast carcinoma cells (ATCC CRL-2315) were cultured according to ATCC in complete RPMI containing FBS (10 % [*v/v*]), penicillin (100 U/ml), streptomycin (100 µg/ml), amphotericin (12.5 µg/ml) and L-glutamine (2 mM). The sensitivity to selected compounds and the positive controls (5-fluorouracil and paclitaxel) was determined in a resazurin assay. For all replicates, 5×10^3 cells/well were seeded in the appropriate growth medium into the wells of a 96 well plate. The cells were allowed to adhere overnight and were treated in triplicate (100 µM - 0.005 µM). The plate was incubated at 37 °C in an atmosphere of 9 % CO_2 for 96 hours. Resazurin reagent (0.009 mM) was added to each well after the 96-hour incubation. The plate was incubated at 37°C and the fluorescence (Ex 560: Em 590) was read after 4 hours. The half maximum response concentration (EC_{50}) was calculated by non-linear regression using GraphPad Prism version 4.0. All the data had a good fit with R^2 value ranging from 0.8258-0.9959. Compounds lacking significant toxicity in the range tested are reported as an $EC_{50} > 100$ µM.

2.5 References

1. S. Mathew, N. Sajina and K. R. Haridas, *The Chemist*, 2016, **89**, 2-7.

2. A. Tavman and A. Cinarli, *Inorg. Chim. Acta.*, 2014, **421**, 481-488.

3. K. Swarnalatha, P. Rathnamala, A. Babu and N. Bhuvanesh, *J. Struct. Chem.*, 2016, **57**, 1554-1560.

4. M. B. Ismail, I. N. Booysen, M. P. Akerman and C. Grimmer, *J. Organomet. Chem.*, 2017, **833**, 18-27.

5. D. Kovala-Demertzi, P. N. Yadav, J. Wiecek, S. Skoulika, T. Varadinova and M. A. Demertzis, *J. Inorg. Biochem.*, 2006, **100**, 1558-1567.

6. W.-S. Hong, C.-Y. Wu, C.-S. Lee, W.-S. Hwang and M. Y. Chiang, *J. Organomet. Chem.*, 2004, **689**, 277-285.

7. M. B. Ismail, I. N. Booysen and M. P. Akerman, *Inorg. Chem. Com.*, 2017, **78**, 78-81.

8. M. B. Ismail, I. N. Booysen and M. P. Akerman, *Inorg. Chim. Acta.*, 2018, **477**, 257-269.

9. G. Sheldrick, *Acta Crystallogr., Sect. A: Found. Adv.*, 2008, **64**, 112-122.

10. L. Farrugia, *Journal of Applied Crystallography*, 2012, **45**, 849-854.

11. *Journal*, Bruker APEX2, SAINT and SADABS (2010). Bruker AXS Inc. Madison. Wisconsin, USA.

12. Frisch MJ, Trucks GW, Schlegel HB, Scuseria GE, Robb MA, Cheeseman JR, Scalmani G, Barone V, Petersson GA, Nakatsuji H, Li X, Caricato M, Marenich AV, Bloino J, Janesko BG, Gomperts R, Mennucci B, Hratchian HP, Ortiz JV, Izmaylov AF, Sonnenberg JL, Williams, Ding F, Lipparini F, Egidi F, Goings J, Peng B, Petrone A, Henderson T, Ranasinghe D, Zakrzewski VG, Gao J, Rega N, Zheng G, Liang W, Hada M, Ehara M, Toyota K, Fukuda R, Hasegawa J, Ishida M, Nakajima T, Honda Y, Kitao O, Nakai H, Vreven T, Throssell K, Montgomery Jr JA, Peralta JE, Ogliaro F, Bearpark MJ, Heyd JJ, Brothers EN, Kudin KN, Staroverov VN, Keith TA, Kobayashi

R, Normand J, Raghavachari K, Rendell AP, Burant JC, Iyengar SS, Tomasi J, Cossi M, Millam JM, Klene M, Adamo C, Cammi R, Ochterski JW, Martin RL, Morokuma K, Farkas O, Foresman JB, Fox DJ (2009) Gaussian 09 Rev. A.01.

13. I. N. Booysen, S. Maikoo, M. P. Akerman and B. Xulu, *Trans. Met. Chem.*, 2015, **40**, 397-404.

14. P. Krishnamoorthy, P. Sathyadevi, K. Senthilkumar, P. T. Muthiah, R. Ramesh and N. Dharmaraj, *Inorg. Chem. Com.*, 2011, **14**, 1318-1322.

15. R. Ramachandran and P. Viswanathamurthi, *Spectrochim. Acta, Part A.*, 2013, **103**, 53-61.

16. M. Reichmann, S. Rice, C. Thomas and P. Doty, *J. Am. Chem. Soc.*, 1954, **76**, 3047-3053.

17. M. Kaplanis, G. Stamatakis, V. D. Papakonstantinou, M. Paravatou-Petsotas, C. A. Demopoulos and C. A. Mitsopoulou, *J. Inorg. Biochem.*, 2014, **135**, 1-9.

18. G. M. Morris, R. Huey, W. Lindstrom, M. F. Sanner, R. K. Belew, D. S. Goodsell and A. J. Olson, *J. Comput. Chem.*, 2009, **30**, 2785-2791.

19. W.-X. Hong, F. Huang, T. Huan, X. Xu, Q. Han, G. Wang, H. Xu, S. Duan, Y. Duan and X. Long, *J. Inorg. Biochem.*, 2018, **180**, 54-60.

20. E. Krieger and G. Vriend, *Bioinformatics*, 2014, **30**, 2981-2982.

21. D. Duhovny, R. Nussinov and H. J. Wolfson, 2002, Algorithms in Bioinformatics, Springer, 185-200.

22. D. Schneidman-Duhovny, Y. Inbar, R. Nussinov and H. J. Wolfson, *Nucleic Acids Res.*, 2005, **33**, W363-W367.

23. D. H. Atha, U. Manne, W. E. Grizzle, P. D. Wagner, S. Srivastava and V. Reipa, *J. Histochem. Cytochem.*, 2010, **58**, 1005-1014.

24. W. Zhong, Y. Wang, J.-S. Yu, Y. Liang, K. Ni and S. Tu, *J. Pharm. Sci.*, 2004, **93**, 1039-1046.

25. H. Paul, T. Mukherjee, M. Mukherjee, T. K. Mondal, A. Moirangthem, A. Basu, E. Zangrando and P. Chattopadhyay, *J. Coord. Chem.*, 2013, **66**, 2747-2764.

26. M. D. Meti, S. T. Nandibewoor, S. D. Joshi, U. A. More and S. A. Chimatadar, *J. Pharm. Anal.*, 2015, **5**, 249-255.

27. N. Na, D.-Q. Zhao, H. Li, N. Jiang, J.-Y. Wen and H.-Y. Liu, *Molecules*, 2016, **21**, 54-67.

28. J.-A. de la Mare, J. C. Lawson, M. T. Chiwakata, D. R. Beukes, A. L. Edkins and G. L. Blatch, *Invest. New Drug.*, 2012, **30**, 2187-2200.

Chapter 3

Structure-activity correlations of ruthenium compounds with mono- or *bis*-heterocyclic chelates

3.1 Introduction

Ruthenium-based anticancer drugs have demonstrated cytotoxicity against a wide variety of cancer cells accompanied with minimal side effects to healthy cells [**1-3**]. It is hypothesized that the biocompatibility of these potential metallopharmaceuticals culminates from the similar chemistry of ruthenium and the essential metal, iron, as these elements are group congeners [**4**]. In addition, ruthenium can induce cancer cell apoptosis through utilization of its high coordination affinities to nucleotides [**5**]. Alteration of the co-ligands within the coordination sphere of ruthenium have been shown to lead to intriguing structure-activity relationships and diverse mechanisms of action [**6**]. In fact, the leading candidates of ruthenium chemotherapeutic agents, *e.g. trans*-[$RuCl_4$(DMSO)(Im)](ImH)] (ImH = protonated imidazole, NAMI-A), are pro-drugs which are activated upon hydrolysis [**7**]. Furthermore, conjugated aromatic chelating ligands of ruthenium complexes are able to promote DNA interaction through intercalation or groove-binding as the possible mechanism of anticancer activity [**8**].

Current research focuses on designing target-specific ruthenium anticancer drugs and involves encompassing biologically relevant moieties (BAMs) in ligand scaffolds where the meticulously selected BAMs may facilitate defined biodistribution patterns [**9**]. This design approach is exemplified by arene ruthenium(II) compounds with flavone or chromone analogs, where a correlation between the lipophilicity and the *in vitro* screening of melanoma cell lines was found [**10**]. In addition, a fascinating bifunctional ruthenium(II) complex, (ethacrynic acid-

g6-benzylamide)(1,3,5-triaza-7-phosphaadamantane)dichloride (ethaRAPTA) induced death of MCF-7 breast cancer cells, which is regarded as a significant advancement considering that these cells are resistant to cisplatin [**11**]. The dual functionality of this metal complex stems from the inherent cytotoxicity of the RAPTA constituent and the ethacrynic acid-*g6*-benzylamide moiety's glutathione *S*-transferase inhibiting capability which combats drug resistance.

Heterocyclics such as benz(imidazole/othiazole) moieties, see **Figure 3.1**, are common to various organopharmaceuticals and their derivatives have been shown to exhibit *in vivo* therapeutic activities to common human cancers [**12-14**]. Moreover, metal-ligand synergistic correlations have been observed where the metal complexes have shown higher activities than their corresponding benz(imidazole/othiazole)-derived free-ligands. This phenomena is illustrated by the antimicrobial bioassays conducted on the nickel compound, $[Ni_3(abb)_3(H_2O)_3(\mu\text{-ttc})](ClO_4)_3\cdot 3H_2O\cdot EtOH$ and its free-ligand, 1-(1*H*-Benzimidazol-2-yl)-*N*-(1*H*-benzimidazol-2-ylmethyl)methanamine (aab) which showed that the metal compound displayed higher antimicrobial activity than the free-ligand [**15**]. In fact, complementary biological and anticancer activities of metal-based chemotherapeutic drugs can improve their efficacy by negating the common side-effects associated with secondary infections [**16**].

(a) **(b)**

Figure 3.1: *Structures of (a) bezimidazole and (b) benzothiazole.*

In this chapter, we report the synthesis and characterization of new ruthenium(II) compounds bearing *bis*-heterocyclic ligands (see **Figure 3.2**) as well as exploring the structure-activity correlations of the aforementioned metal compounds and ruthenium compounds with mono-heterocyclic chelates which were previously reported in my M.Sc dissertation (the majority thereof published [**17**]), $[RuCl(Hobz)_2(PPh_3)]Cl$ (**3**) and (Hobz = 2-hydroxyphenylbenzimidazole $[Ru^{III}Cl(obs)_2(PPh_3)]$) (**4**) (Hobs = 2-hydroxyphenylbenzothiazole). Two novel diamagnetic ruthenium compounds, *cis*-

[$Ru^{II}Cl_2(PPh_3)_2$(ombb)] (**1**) and *trans*-[$Ru^{II}Cl(PPh_3)_2$(bbb)] (**2**) were isolated from the reactions of *trans*-[$RuCl_2(PPh_3)_3$] with *bis*-benzimidazole ligands, 2,2'-[oxy*bis*(methylene)]-*bis*-(1*H*-benzimidazole) (ombb) and 4,4'-*bis*(1*H*-benzimidazol-2-yl)-2,2'-bipyridine (bbb), respectively. The DNA and BSA interaction, antioxidant capabilities and *in vitro* anticancer activities of the ruthenium compounds **1** – **4** were evaluated.

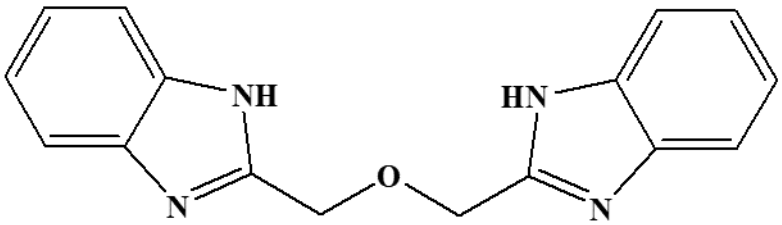

ombb

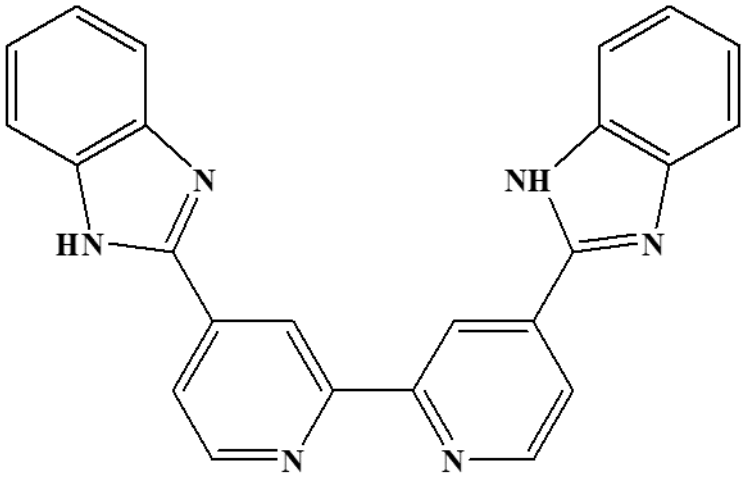

bbb

Figure 3.2: *Structures of the bis-benzimidazoles, ombb and bbb.*

3.2 Experimental

*3.2.1 Synthesis of cis-[$Ru^{II}Cl(PPh_3)_2$(ombb)] (**1**)*

An equimolar reaction between ombb (29.03 mg, 104.3 µmol), *trans*-[$RuCl_2(PPh_3)_3$] (100 mg, 104.3 µmol) and ammonium hexafluorophosphate (17.00 mg, 104.3 µmol) was carried out in 20 cm^3 of methanol. The reaction mixture was heated until reflux for 3 hours. Thereafter, the resulting red solution was allowed to cool to room temperature. Thereafter, red, rectangular crystals were formed over several days *via* slow diffusion of the mother liquor which were suitable for X-ray analysis. Yield: 74%. M.P: 250.5 – 258.3 ºC. IR (ν_{max}/cm^{-1}): *v*(N-H) 3051 (w); *v*(C=N) 1431 (s); *v*(Ru-[PPh_3]$_2$) 690 (vs). ^{1}H NMR (295K/ d^6 – C_2D_6SO/ ppm): 7.80 (q, 14H, *H1, H2, H3, H4*); 7.65 – 7.52 (m, 30H, *2 x PPh$_3$*); 7.50 (q, 4H, *H7, H8, H9, H10*); 5.31 (s, 4H, *H5, H5', H6, H6'*). ^{31}P NMR (295K/ d_6 – C_2D_6SO/ ppm): 38.46. UV-Vis (DCM, ε, M^{-1} cm^{-1}): 266 nm (970); 272 nm (910); 384 nm (220); 431 nm (sh, 180); 588 nm (110).

*3.2.2 Synthesis of trans-[$Ru^{II}Cl_2(PPh_3)_2$ (bbb)] (**2**)*

A hot solution of bbb (0.0376 g) in DMSO (5ml) was added dropwise to a refluxing mixture of *trans*-[$RuCl_2(PPh_3)_3$] (100 mg, 104.3 µmol) in methanol. The resulting mixture was heated for 3 hours and then cooled to room temperature. Brick-red crystals, which were of X-ray quality, were formed over a period of time *via* slow diffusion. Yield: 77 %. M.P: 217.3 – 221.7 º C. IR (ν_{max}/cm^{-1}): *v*(N-H) 3054 (w), *v*(C=N) 1431 (s), *v*(C-O-C) 1088, *v*(Ru-[PPh_3]$_2$) 692. ^{1}H NMR (295 K/ d^6 – C_2D_6SO/ ppm): 9.09 (s, 2H, *H12, H17*); 9.11 (d, 2H, *H10, H14*); 7.83 (d, 2H, *H9, H15*); 7.69 (dd, 4H, *H2, H5, H18, H23*); 7.51 – 7.04 (m, 34H, *H3, H4, H21, H22, 2 x PPh$_3$*). ^{31}P NMR (295K/ d^6 – C_2D_6SO/ ppm): 29.02. UV-Vis (DCM, ε, M^{-1} cm^{-1}): 273 nm (6490); 309 nm (8490); 352 nm (10060); 438 nm (sh, 2600); 512 nm (1370); 712 nm (300).

3.3 X-ray crystallography

The crystallographic data for metal compounds **1** and **2**.C_2H_6OS were acquired on a Bruker Apex Duo equipped with an Oxford Instruments Cryojet functioning at variable temperatures [200(2) K for **1** and 100(2) K for **2**.C_2H_6OS] and an Incoatec microsource operating at 30 W power. Crystal and structure refinement of **2**.C_2H_6OS data are reported in **Table 3.1** while its experimental geometrical parameters are given in **Table 3.2**. A low resolution structure of the metal complex salt **1** stabilized by a PF_6^- ion is shown in **Figure 3.13**. The X-ray beams were generated with MoKα (for **1**) and CuKα (for **2**.C_2H_6OS) with wavelengths of 0.71073 and 1.54178 Å, respectively. Radiation exposures during data collection of both metal compounds were at a crystal-to-detector distance of approximately 50 mm.

Data collection was performed under the following conditions: omega and phi scans with exposures taken at 30 W X-ray power and 0.50º frame widths by means of APEX2 [**18**]. The data were reduced using the program SAINT [**18**], implementing scan speed scaling, outlier rejection as well as standard Lorentz and polarization correction factors. A SADABS semi-empirical multi-scan absorption correction was applied to the data [**19**]. Direct methods, SHELX-2016 [**20**] and WinGX [**21**] were used in the refinement. The difference density map was used to locate all non-hydrogen atoms and anisotropically refined with SHELX-2016 [**20**]. All hydrogen atoms were included as idealised contributors in the least squares process. Their positions were calculated using a standard riding model with C-$H_{aromatic}$ distances of 0.93 Å and U_{iso} = 1.2 U_{eq}, C-$H_{methylene}$ distances of 0.99 Å and U_{iso} = 1.2 U_{eq} and C-H_{methyl} distances of 0.98 Å and U_{iso} = 1.5 U_{eq}.

3.4 Computational details

The Gaussian 09W software package was used to conduct *ab initio* calculations [**22**]. The computational parameters of **1** and **2** employed during their geometry optimizations were harmonized with those previously reported for **3** and **4** whereby the B3LYP functional as well as the LANL2DZ basis set were used [**17**]. Prior to any calculations, the respective counter-anion and the DMSO molecule of crystallization for **1** and **2** were omitted which rendered their starting conformers. Only **molecule I** of ruthenium compound **1** were optimized as its two

crystallographically independent molecules share the same structural features and hence exhibit similar bond lengths and angles, see **Figure 3.15**.

Computational data validation of **1** and **2** was established by the optimized and experimental geometrical parameters being reasonably in accordance. The minor discrepancies are justified by the absence of inter- and intramolecular interactions within the energetically minimized structures. In addition, the simulated IR spectra showed no vibrational bands with negative Eigen values, which corroborates that the optimized structures of **1** and **2** are global minima on their respective potential energy surfaces. Evidently, the Root-Mean-Square-Deviation (RMSD) values between the optimized conformer of **1** and its individual crystallographic interdependent molecules are low, see **Figure 3.16**.

3.5 Results and discussion

*3.5.1 Synthesis and spectral characterization of **1** and **2***

The diamagnetic ruthenium compounds **1** and **2** were isolated in moderate yields by separate equimolar reactions of ombb and bbb with *trans*-[$RuCl_2(PPh_3)_3$] in methanol. The source of the PF_6^- counter-ion of compound **1** emanates from the addition of ammonium hexafluorophosphate in an equivalent molar amount with respect to the metal precursor. For **1**, the *bis*-heterocyclic ligand (ombb) functions as a neutral tridentate chelator whereby coordination occurs through the benzimidazole nitrogen and bridging ether oxygen donor atoms. In the case of **2**, the ligand bbb coordinates *via* its neutral $N_{py}N_{py}$ donor set affording a constrained five-membered chelate ring *trans*-orientated to the *cis*-chloride co-ligands. These diamagnetic metal compounds were found to be stable in air as well as soluble in high boiling point aprotic solvents (*viz.* DMSO and DMF), while they exhibit moderate solubility in chlorinated solvents.

Generally, the signals of **1** and **2** in their ^1H NMR spectra display shifts with respect to analogous signals found in the proton spectra of their free ligands. These spectral differences resemble coordination of organic chelators to transition metal centres, see **Figures 3.3** and **3.4** [**23**]. In particular, the aromatic protons associated with the benzimidazole phenyl rings are shielded upon coordination of the ombb (in **1**) and bbb (in **2**) organic chelators. Common to

both proton spectra of the metal compounds are the presence of the intense multiplets between the regions of 7.65 – 7.04 ppm, which are characteristic of the triphenylphosphine co-ligands [**24**]. Furthermore, the singlet associated with the methylene protons adjacent to the ethereal oxygen (*viz. H5, H5', H6 and H6'*) in **1** displays a noticeable shift from 5.39 to 5.31 ppm, which is attributed to ring current effects of the chelating aromatic benzimidazole, and these proton NMR spectral changes provide tangible evidence of O-coordination [**25, 26**]. A single peak was observed in each decoupled ^{31}P NMR spectra, which confirmed the presence of magnetically equivalent phosphorous atoms within the coordination spheres of the respective metal compounds, see **Figures 3.5** and **3.6**.

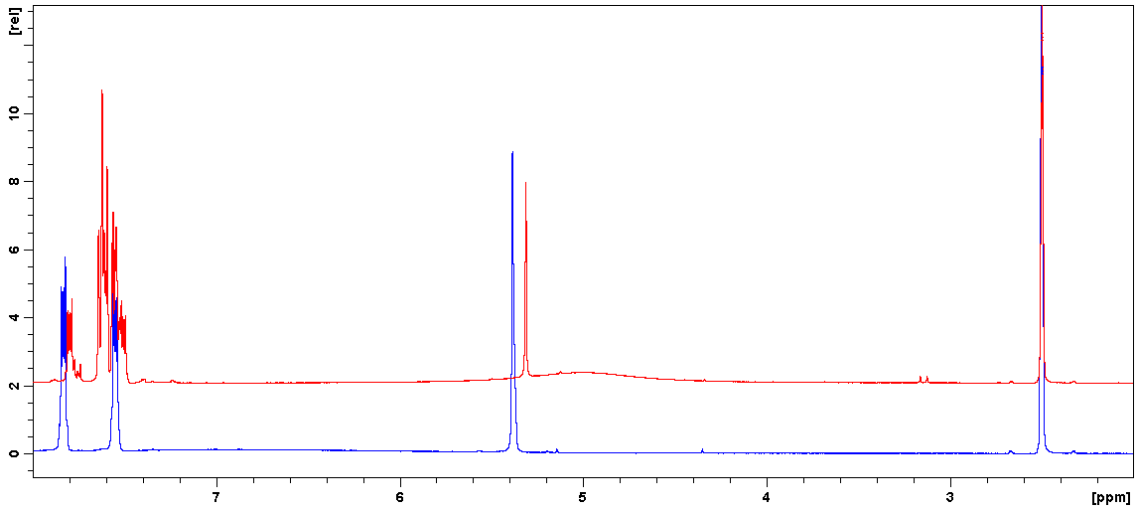

Figure 3.3: *Overlay ^{1}H NMR spectra of ombb (blue) and compound **1** (red).*

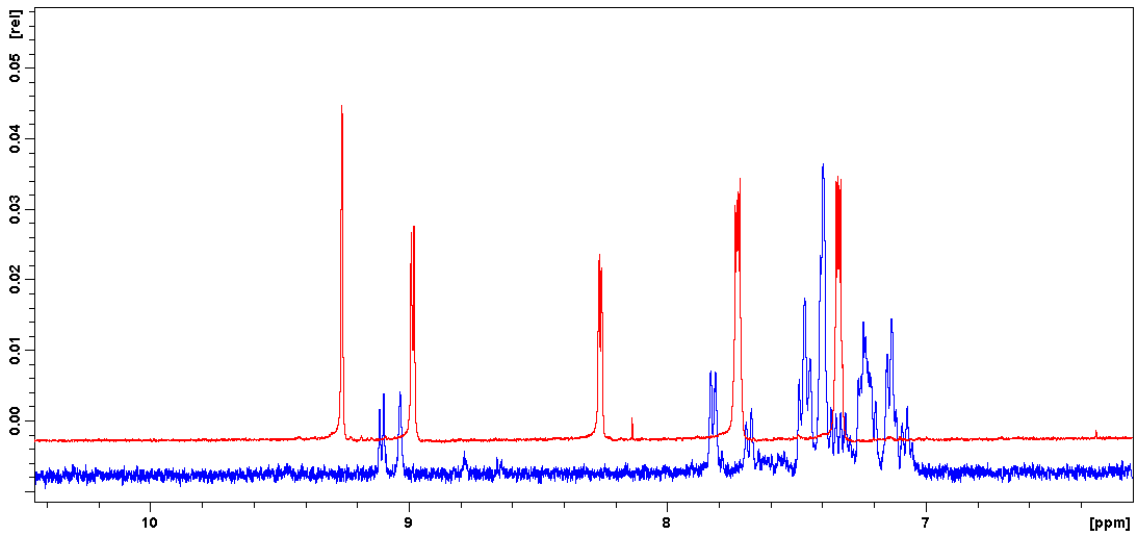

Figure 3.4: *Overlay ^{1}H NMR spectra of bbb (red) and complex **2** (blue).*

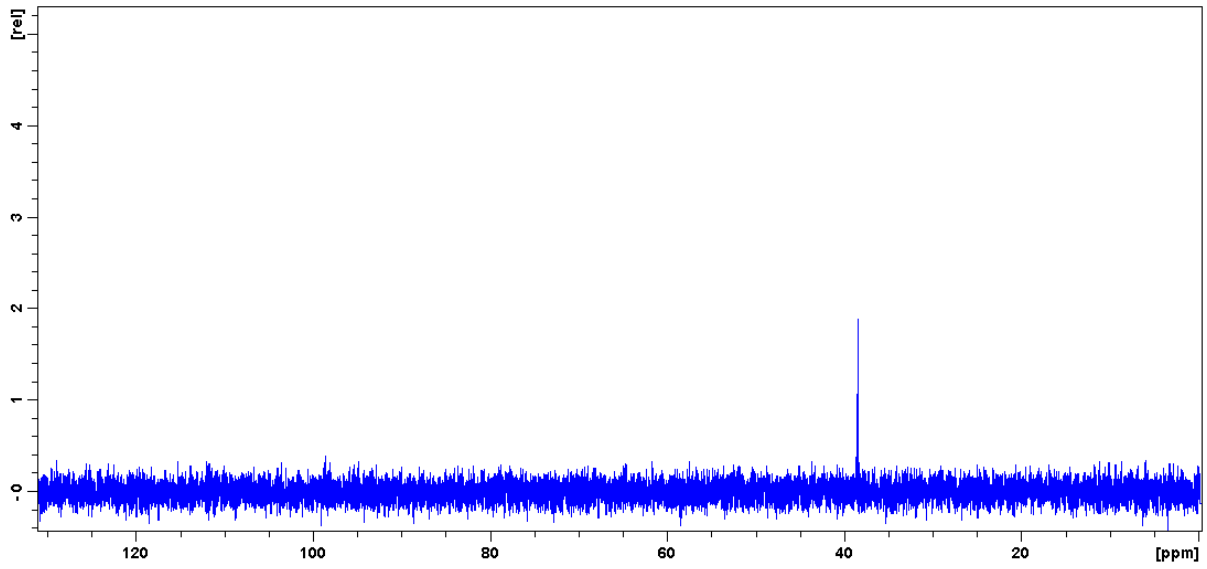

Figure 3.5: *^{31}P NMR spectrum compound **1**.*

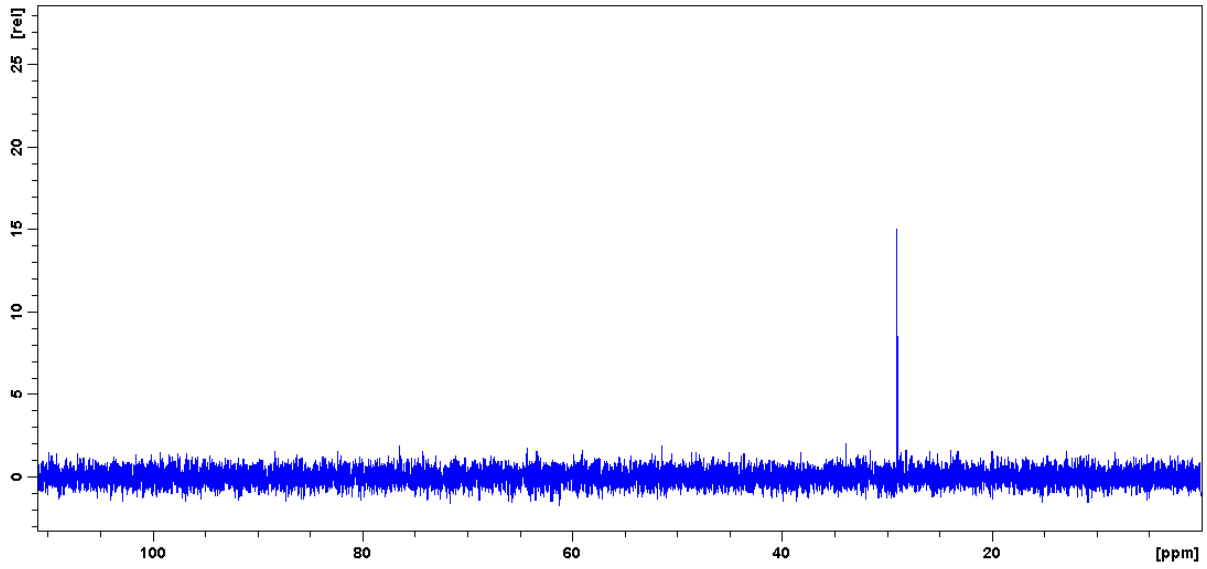

Figure 3.6: *^{31}P NMR spectrum complex **2**.*

The solid-state infrared spectra of **1** and **2** illustrate their intense intracyclic *v*(C=N) [1431 cm^{-1} for **1** and **2**] which are found at lower wavenumbers in comparison to those found in the IR spectra of their free-ligands, ombb (at 1459 cm^{-1}) and bbb (at 1441 cm^{-1}), see **Figures 3.7** and **3.8**. The same trend is observed when comparing the coordinated (at 1088 cm^{-1}) and uncoordinated (at 1142 cm^{-1} for ombb) ether stretches of **1** and its corresponding free-ligand, which is also another influential feature of coordinative bonding. IR Simulations show that the C=N benzimidazole and pyridyl stretches of **1** appear jointly at 1495 cm^{-1}, while the

v(C=N)$_{benzimidazole}$ of **2** is found at 1484 cm^{-1}. Weak IR vibrational bands are found at 3051 and 3054 cm^{-1} in the experimental IR spectrum of **2,** which are accounted to the benzimidazole N-H vibrations. The dominating infrared experimental stretches (at 690 cm^{-1} for **1** and 692 cm^{-1} for **2**) in the respective IR spectra of the metal compounds are typical of v(Ru-P) and are similar to those found in other ruthenium compounds [**27, 28**].

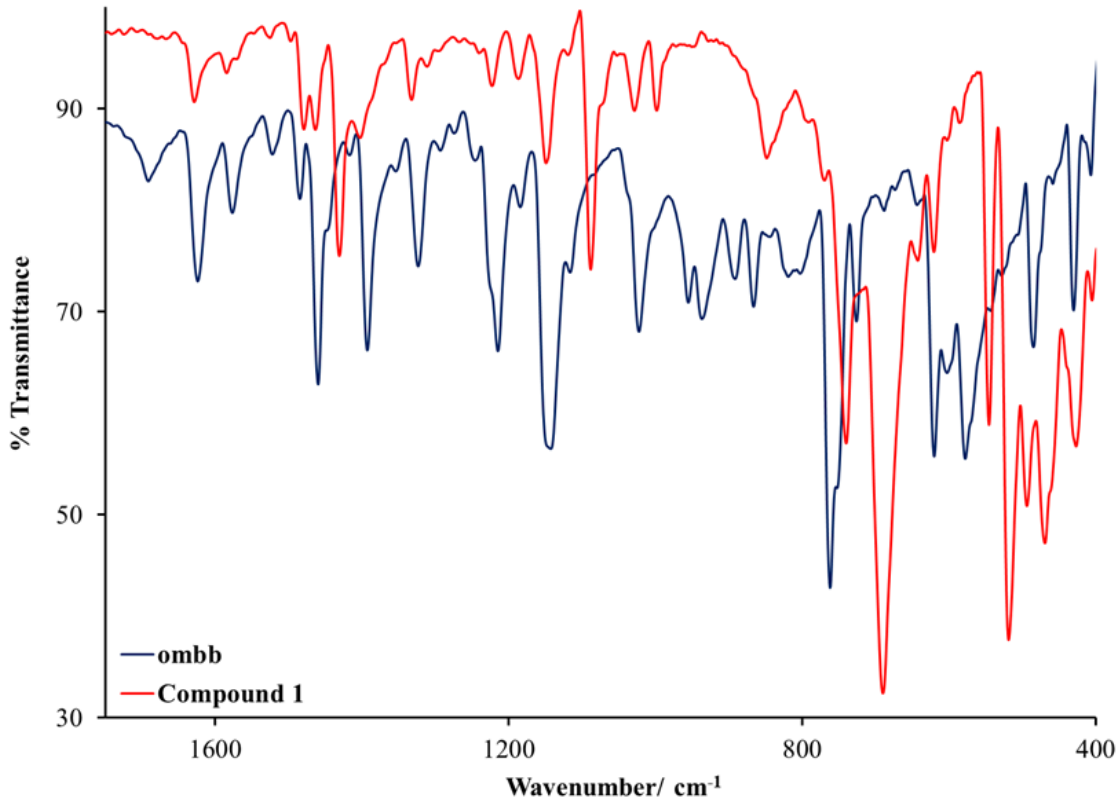

Figure 3.7: *Overlay IR spectra of the free-ligand, ombb and compound **1** between 1750 and 400 cm^{-1}.*

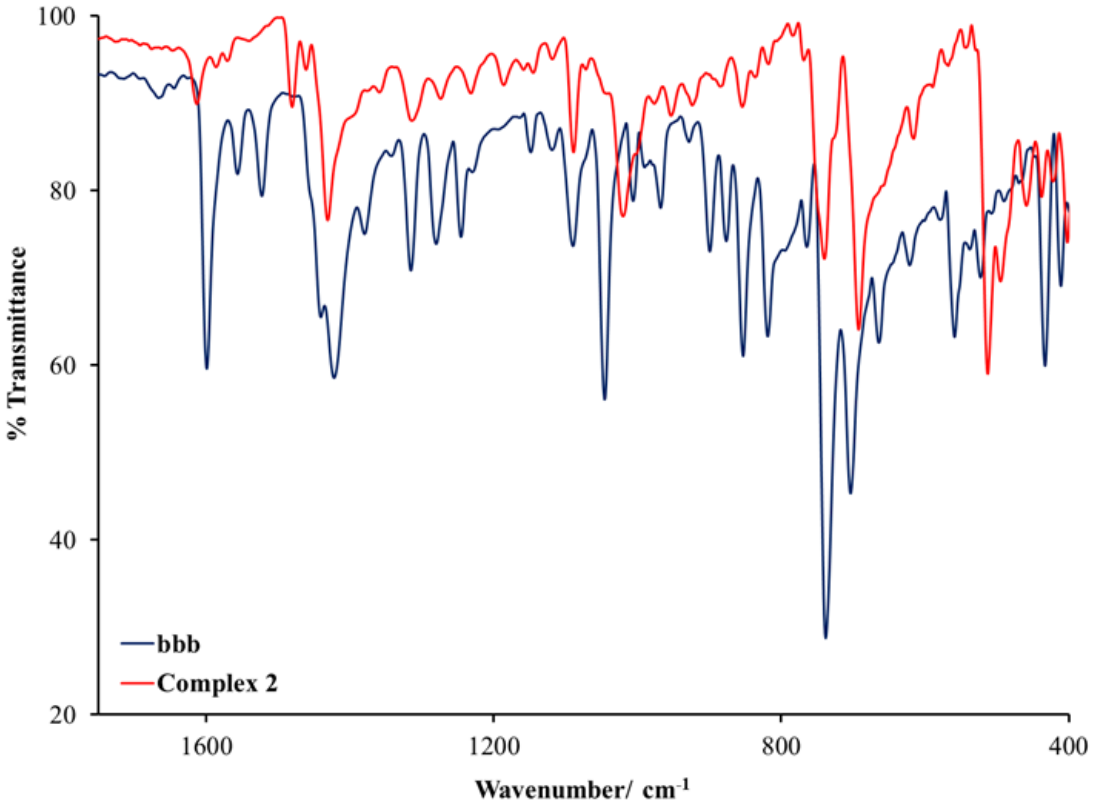

Figure 3.8: *Overlay IR spectra of the free-ligand, bbb and complex **2** between 1750 and 400 cm^{-1}.*

As expected, the UV-visible spectra of the metal compounds show several intense intraligand π-π* transitions below 300 (for **1**) and 400 nm (for **2**), which mostly originate from the *pi*-conjugated moieties of their respective organic chelators, see **Figures 3.9** and **3.10**. At more red-shifted regions between 400 and 600 nm, *p*(Cl) → *d*(Ru), Ligand-to-Metal Charge Transfer (LMCT) bands are found. A distinctive metal-based electronic transition is found in the UV-Vis spectrum of **2** (at 712 nm) converse to the absence of a *d*-*d* electronic transition in the UV-Vis spectrum of **1,** which is largely ascribed to the low spin d^6 electron configuration of its central metal ion [**17**].

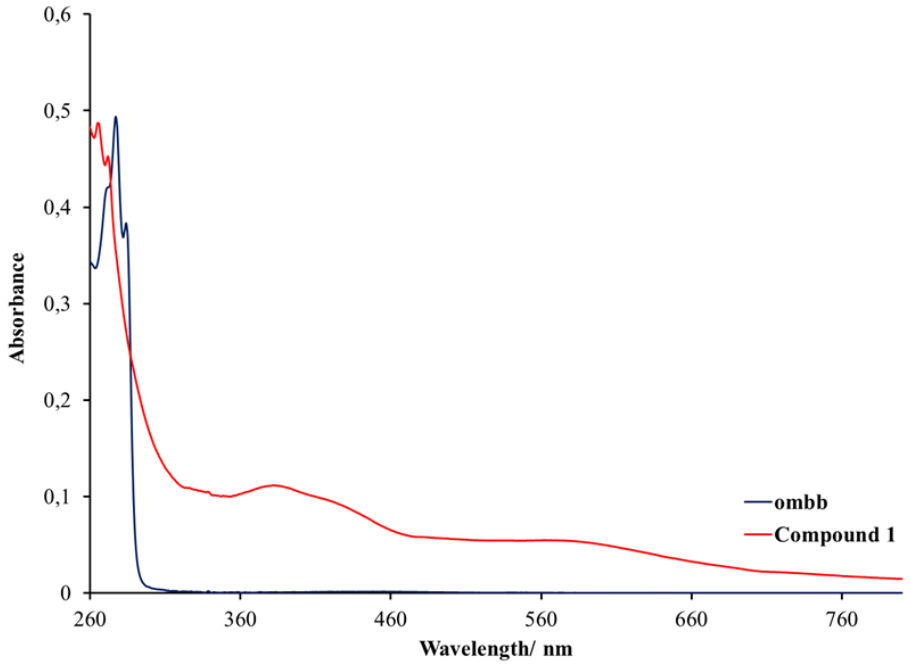

Figure 3.9: *Overlay UV-Vis spectra of complex **1** and its ligand, ombb.*

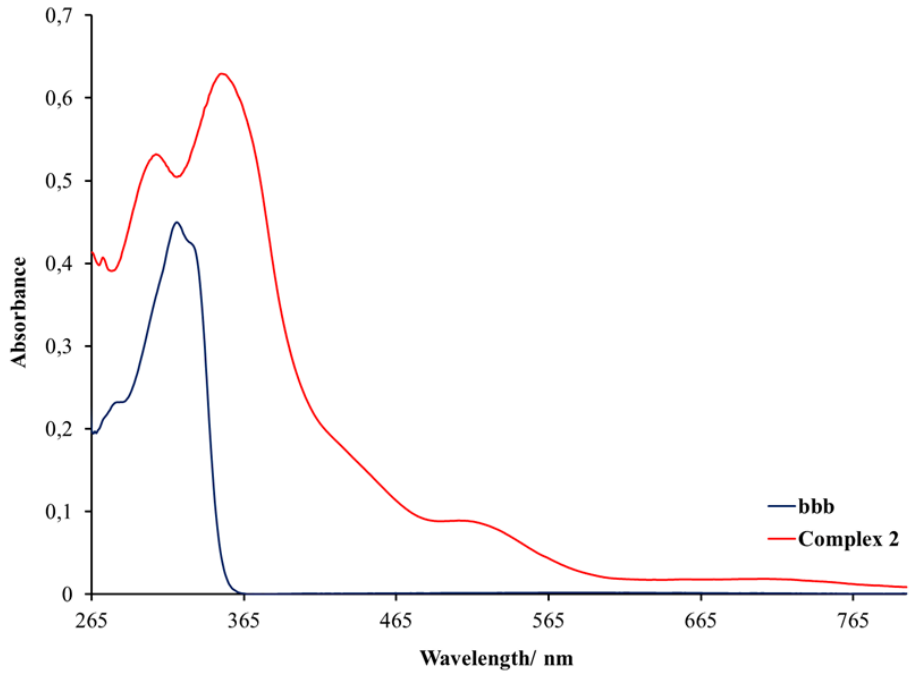

Figure 3.10: *Overlay UV/Vis spectra of complex **2** and its ligand, bbb.*

*3.5.2 Electrochemistry of **1** and **2***

The redox properties of the metal compounds were investigated by means of voltammetric experiments. The cyclic voltammogram (CV) of **1** displays one irreversible redox process (E_{pa} = 1.36 V *vs* Ag | AgCl), which is attributed to the single electron oxidation of the metal centre, while a quasi-reversible redox process [ΔE_p(**2**) = 80 mV and ΔE_p(ferrocene) = 90 mV] is found in the CV of **2** (E_{pa} = 0.42 V and E_{pc} = 0.34 V *vs* Ag| AgCl) which is attributed to the d^5/d^6 system interconversion, see **Figures 3.11** and **3.12**. Diffusion-controlled behaviour at incrementing scan rates was observed for both redox processes and the CVs of the corresponding free-ligands shows no activities within the potential windows of concern. A squarewave voltammogram of **2** exhibited a solitary peak affirming a single redox process and hence no other concealed redox processes are observed within its CV. Literature trends corroborate the assignment of the redox processes, *e.g.* the CVs of ruthenium(II) complex salts, [Ru(η^5-C_5H_5)(PPh_3)$_2$(L)](PF_6) (HL = 5-phenyl-1*H*-tetrazole and imidazole) display one irreversible oxidation process each at E_{pa} = 1.22 V and 1.25 V, respectively [**29**].

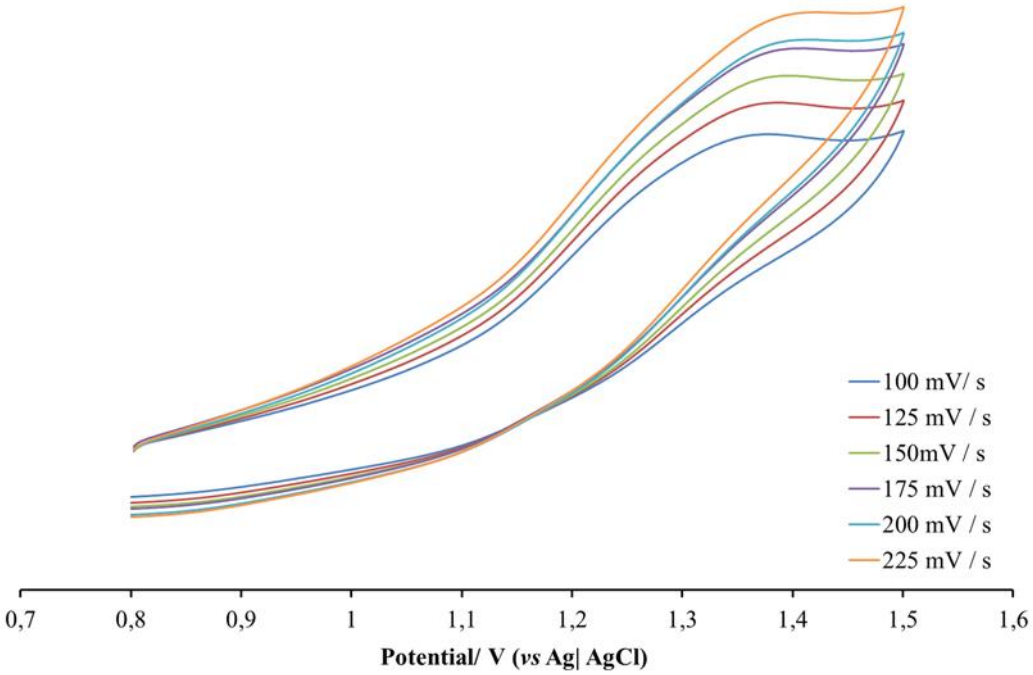

Figure 3.11: *Overlay CVs of compound **1** at incrementing scan rates.*

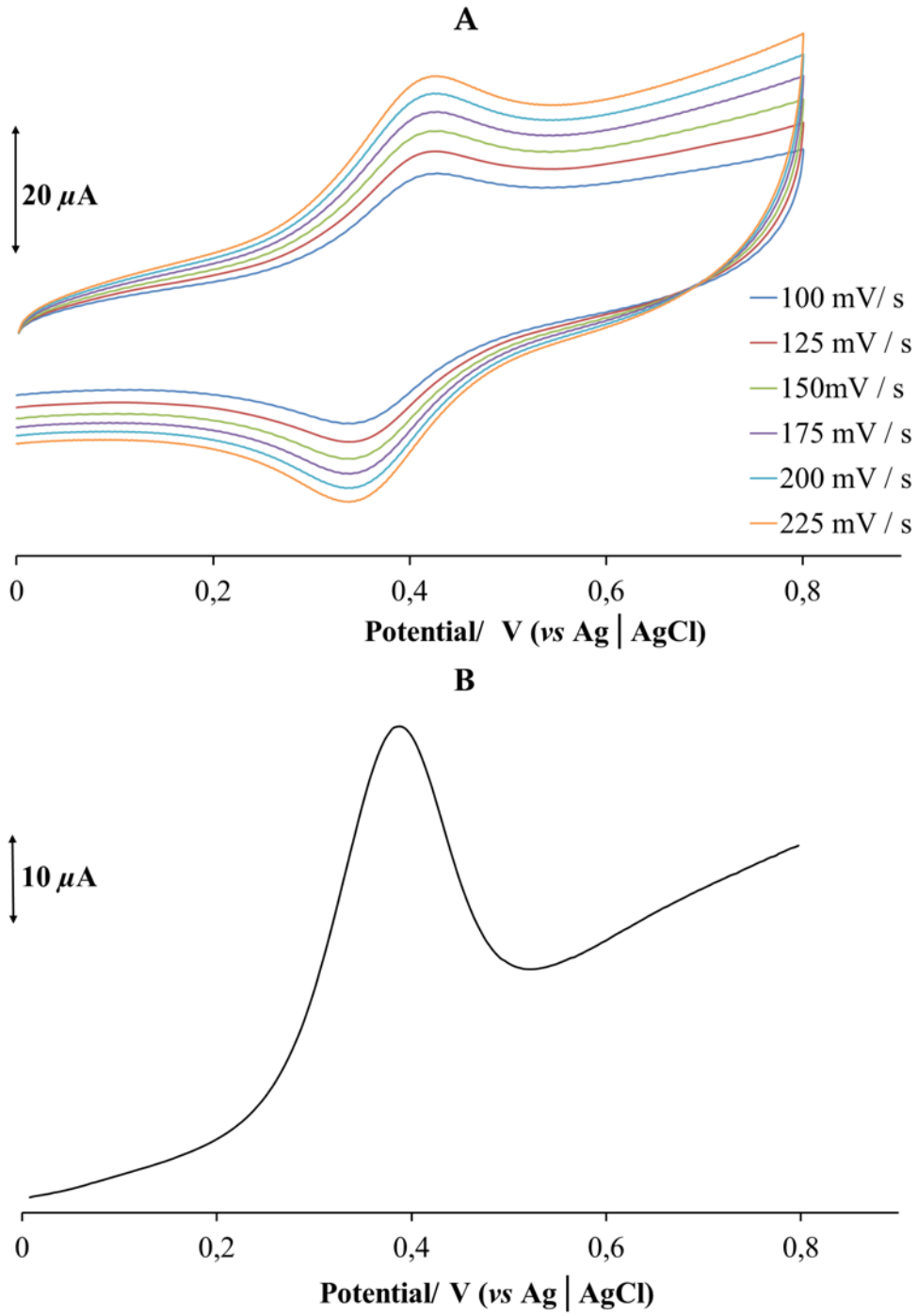

Figure 3.12: *(**A**) – Overlay CVs of **2** at incrementing scan rates and (**B**) – the SWV of **2** at 100 mV/s.*

3.5.3 Crystallographic descriptions

*(a) Crystal structure of **1***

Only a low resolution structure of the metal complex salt **1** stabilized by a PF_6^- ion could be obtained and is shown in **Figure 3.13**.

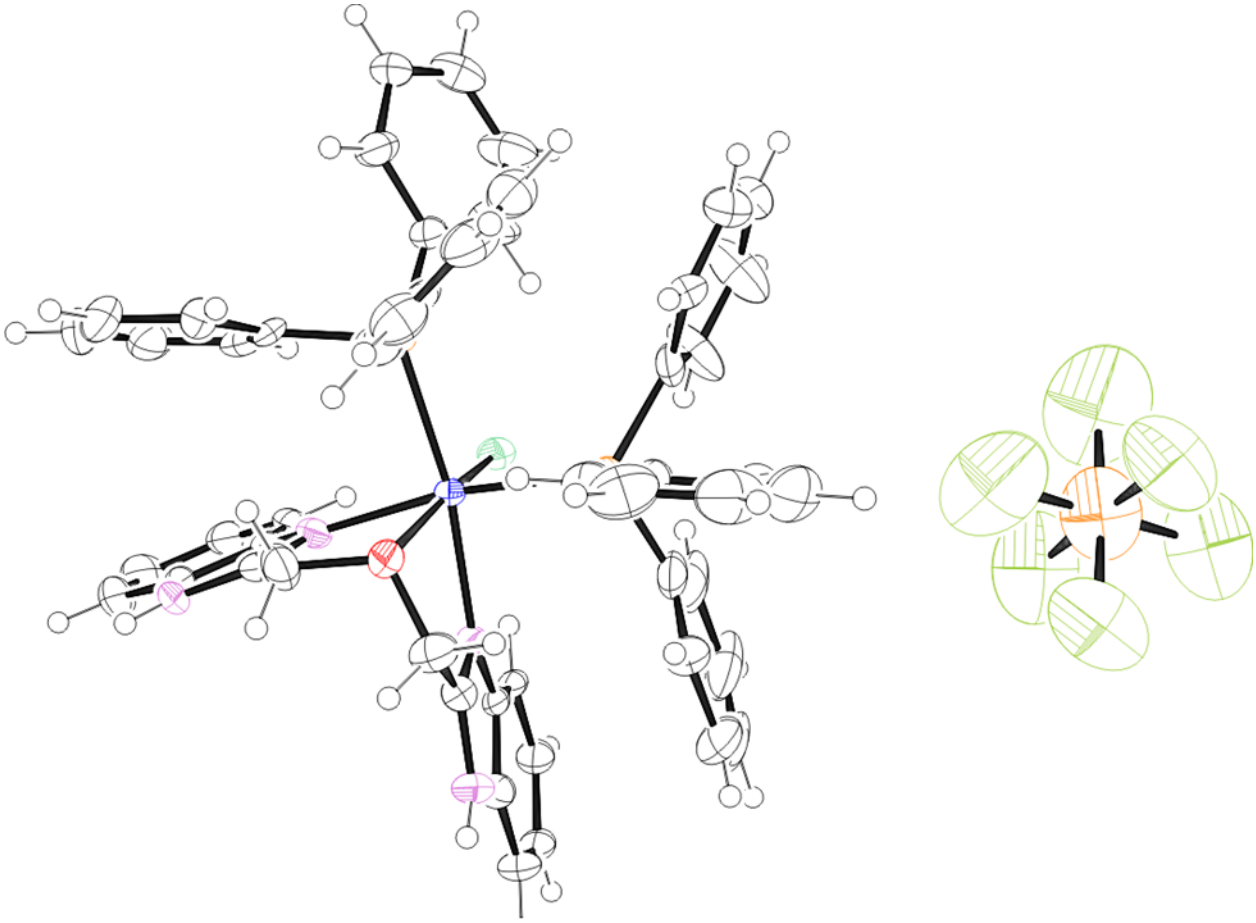

Figure 3.13: *Low resolution structure of **1**.*

*(b) Crystal structure of **2***

Each monoclinic unit cell of **2** is occupied by four molecules of **2** as well as two DMSO molecules of crystallization, which jointly crystallizes out in a $P2_1/c$ space group. Minimal direct interaction is observed between the two crystallographic independent molecules of **2**. However, the bridging solvent molecule of crystallization reinforces the packing arrangement

through non-classical hydrogen bonding interactions. Consequently, the crystal lattice indicates that molecules of **2** pack in variable concentric columns whereby molecule **II** fragments orientate parallel with the [*b*]-axis and molecule **I** fragments are directed in an alternating opposing manner, perpendicular to the [*a*]-axis.

These molecules share the same structural features and hence the geometrical parameters of only **molecule I** will be discussed. Significant octahedral distortion is observed within the Cl1Cl2N3N4 basal plane, which is largely induced by the constrained five membered chelate rings [N3-Ru-N4 = 79.0(1)º], see **Figure 3.14**. In particular, the opposing bond angle [Cl1-Ru-Cl2 = 95.36(3)º] is wider than the expected 90º bond angle. Indicatively, the non-linear P1-Ru-P2 angle of 174.15(4)º shows deviation from octahedral ideality and this culminates into non-equidistant Ru-P bonds [Ru-P1 = 2.4027(9) Å and Ru-P2 = 2.3720(9) Å].

Although, the pyridyl nitrogen donor atoms experienced the same *trans*-influence as imposed on by the chloro co-ligands, the ruthenium to pyridyl nitrogen bonds [Ru-N3 = 2.030(3) Å and Ru-N4 =2.044(3) Å] differ. This crystallographic trend has previously been observed in similar ruthenium(II) bipyridyl (bipy) compounds, namely *trans*-[$RuCl_2$(R^2-bipy)(PPh_3)$_2$], where the derivatized symmetrical bipy bidentate chelators (R^2-bipy) are *N6*, *N6′*-dimethyl-2, 2′-bipyridine-6,6′-diamine, *N4*, *N4′*-dimethylthio-2, 2′-bipyridine and *N4*, *N4′*-di(tertiary-butyl)-2, 2′-bipyridine [**30-32**]. The ruthenium to chloride bond lengths [Ru-Cl1 = 2.4396(8) Å and Ru-Cl2 = 2.450(1) Å] are comparable to analogous bonds found in other ruthenium(II) complexes bearing bipyridine chelates with Ru-Cl bond distances ranging from 2.3248(12) Å to 2.475(2) Å [**30-32**]. Noteworthy, the lack of inter- and intramolecular interactions for the optimized molecular model of **2** causes equal distances for its particular *cis*-orientated ruthenium to pyridyl nitrogen (Ru-N =2.0559 Å) and chloro (Ru-Cl = 2.5441 Å) coordination bonds as well as those comprised with the *trans*-[$Ru(PPh_3)_2$]$^{2+}$ core (Ru-P = 2.5129 Å).

Furthermore, the benzimidazole moieties of the bbb chelators lies out of the mean calculated Cl1Cl2N3N4 basal plane brought about by the freedom of rotation of the adjoining C7-C8 [1.461(5) Å] and C16-C17 [1.462(5) Å] single bonds, which are predictably longer than the pyridyl carbon-to-carbon double bonds [*e.g.* C12-C13 = 1.388(5) Å]. A calculated centroid to centroid distance of 3.548 Å between the C25-C30 phenyl and C8-C13N3 pyridyl rings suggest intramolecular interaction just outside the range of classical *pi*-stacking interactions (≤ 3.5 Å). This intramolecular interaction coupled with the limited degrees of rotation for the C13-C16

[1.463(4) Å] single bond being part of the chelate ring, affords a wider dihedral angle for the C8-C13N3 pyridyl ring (*w.r.t.* the mean calculated Cl1Cl2N3N4 basal plane) than the C14-C7N4 pyridyl ring. Upon evaluating the bond distances within the benzimidazole moieties, it can be clearly shown that the C7-N1 [1.359(4) Å] and C17-N5 [1.331(5) Å] bonds exhibit double bond character when comparing these bonds to other C-N_{cyclic} bonds [*e.g.* C19-N5 = 1.386(6) Å , C6-N1 = 1.387(5) Å , C14-N4 = 1.354(4) Å and C10-N3 = 1.345(4) Å].

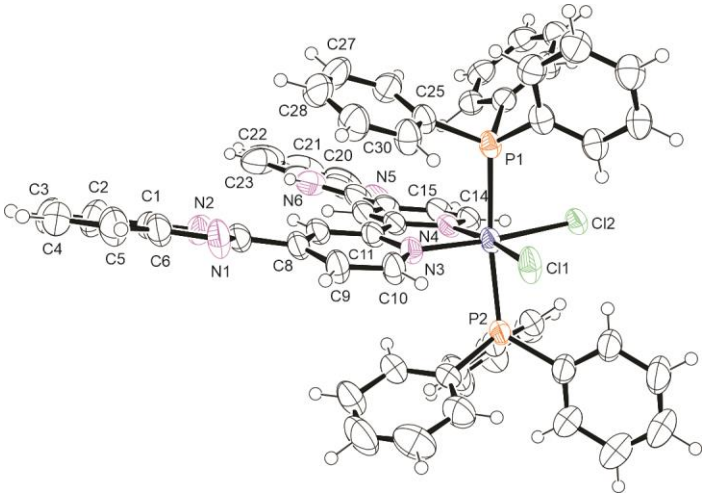

Figure 3.14: *ORTEP view of compound **2** showing 50 % probability displacement ellipsoids and the atom labelling. Molecule of crystallization has been omitted for clarity.*

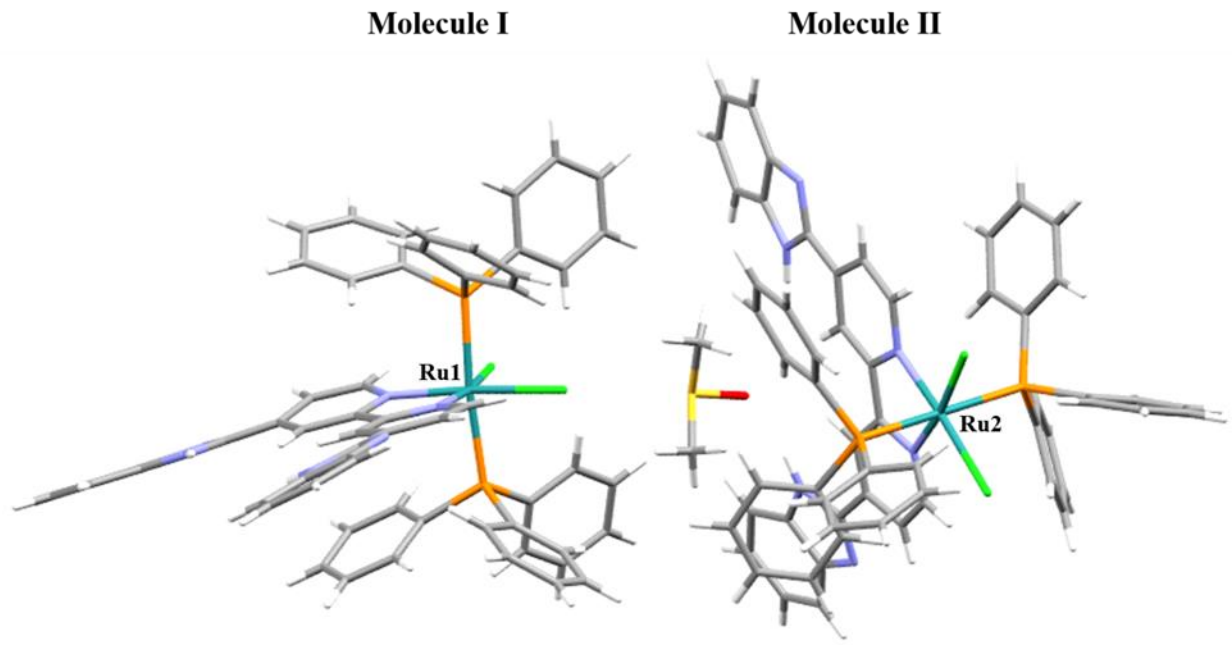

Figure 3.15: *A perspective view of the monoclinic unit cell of **2** being occupied by its two crystallographically independent molecules and a DMSO molecule of crystallization.*

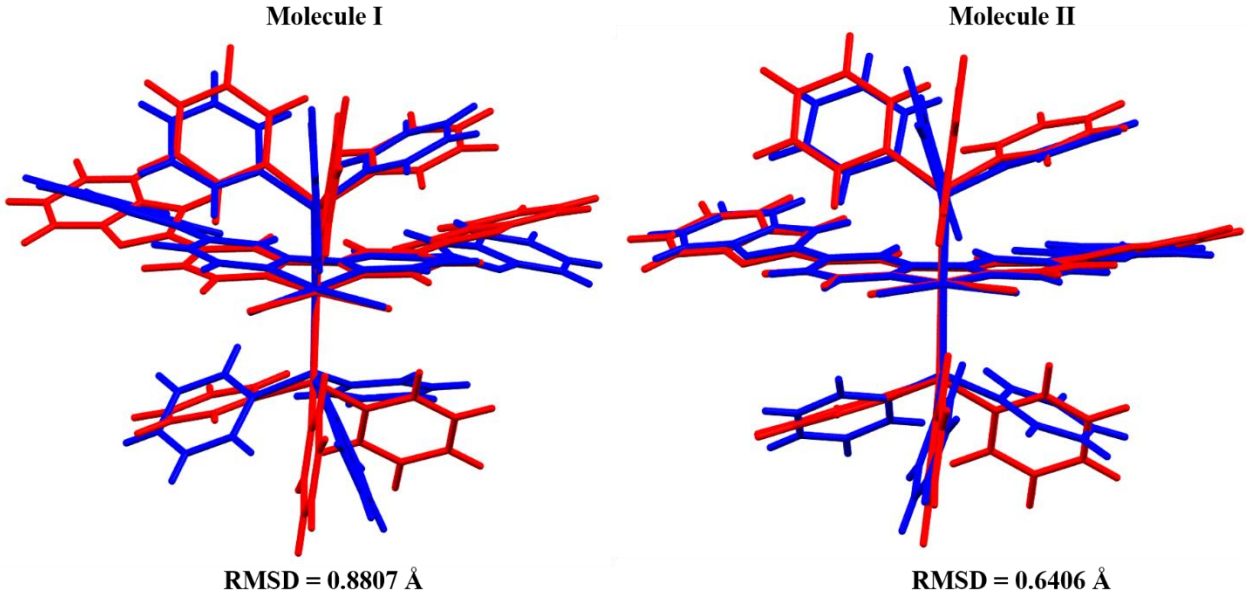

Figure 3.16: *Comparative RMSD values generated from overlay structures of the optimized (red) and respective crystallographically different molecules of **2** (blue).*

Table 3.1: *Crystal and structure refinement data for complex* ***2.***

Chemical formula	$2(C_{60}H_{46}Cl_2N_6P_2Ru).C_2H_6OS$
Formula weight	2248.00
Temperature (K)	100(2)
Crystal system	Monoclinic
Space group	$P2_1/c$
Unit cell dimensions (Å , º)	a = 29.1740(4)
	b = 19.2876(3)
	c = 21.7332(3)
	α = 90
	β = 94.500(1)
	γ = 90
Crystal size (mm)	0.18 x 0.11 x 0.08
V (Å ^{3})	12191.5(3)
Z	4
Density (calc.) (Mg/ m^3)	1.225
Absorption coefficient (mm^{-1})	3.87
F (000)	4616
Θ range for data collection (deg)	2.8º; 66.6º
Index ranges	$-34 \leq h \leq 34$ $-22 \leq k \leq 22$ $-23 \leq l \leq 19$
Reflections measured	128562
Observed reflections ($I > 2\sigma(I)$	20905
Independent reflections	17212
Data/ restraints/ parameters	17212/0/1315
Goodness of fit on F^2	1.02
Observed R; *wR*2	0.038; 1.02
R_{int}	0.052

Table 3.2: *Selected bond lengths [Å] and angles [º] for complex **2**.*

	Experimental	**Optimized**
Ru-P1	2.4027(9)	2.5129
Ru-P2	2.3720(9)	2.5125
Ru-N3	2.030(3)	2.0559
Ru-N4	2.044(3)	2.0559
Ru-Cl1	2.4396(8)	2.5441
Ru-Cl2	2.450(1)	2.5441
C7-C8	1.461(5)	1.4642
C16-C17	1.462(5)	1.4642
C12-C13	1.388(5)	1.4049
C13-C16	1.463(4)	1.4716
C7-N1	1.359(4)	1.3384
C17-N5	1.331(5)	1.3383
C19-N5	1.386(6)	1.4036
C6-N1	1.387(5)	1.4036
C14-N4	1.354(4)	1.3677
C10-N3	1.345(4)	1.3677
N3-Ru-N4	79.0(1)	79.25
Cl1-Ru-Cl2	95.36(3)	95.59
P1-Ru-P2	174.15(4)	171.43

*3.5.4 Antioxidant studies of **1** – **4***

Oxidative stress has been implicated as one of the major causes of DNA mutation and excessive free radical concentrations in the blood stream can escalate cancer progression [**33**]. Natural antioxidants such as Vitamin C are often not potent enough to inhibit the exponential growth of cancerous tumours induced by free radicals. Organoruthenium complexes have been shown to be highly effective scavengers of various free radicals, which largely stems from the redox active metal centre and its organic ligand's capabilities to donate an electron and proton, respectively [**34, 35**]. The radical scavenging activities of the ruthenium compounds **1 – 4** were investigated towards the NO and DPPH radicals, respectively, refer to **Table 3.3**.

The low IC_{50} values (**Table 3.3**) of the ruthenium compounds strongly supports their exceptional antioxidant activities, which are shown to be more potent than the standard antioxidant vitamin C [IC_{50} (DPPH) = 141 µM; IC_{50} = 210 µM]. These favourable IC_{50} values could be ascribed to the attached ligands acting synergistically to enhance the radical scavenging activity of **1** – **4**, as benzimdazole and benzothiazole derivatives are known to possess good antioxidant properties [**36, 37**]. The higher antioxidant activities for the paramagnetic compound **4** can be explained by the unpaired electron in the low spin d^5 orbital, which increases the propensity of the complex cation of **3** to neutralize the DPPH and NO free-radicals more effectively. The acidity of any available protons on the ligands may also be increased due to the electron deficient Ru(III) metal center, which may also positively impact the radical scavenging capability of the compound [**38**]. The obtained IC_{50} values are within the range of those obtained for other documented ruthenium compounds, for example, the IC_{50} values for some ruthenium carbonyl compounds were reported to be within the ranges of 24.0 – 59.7 µM and 6.7 – 11 µM for the DPPH and NO radicals, respectively [**39**].

Table 3.3: *Antioxidant activities of compounds **1** – **4** and Vitamin C against the DPPH and NO radicals.*

Compound	DPPH Radical	NO Radical
	IC_{50} (µM)	**IC_{50} (µM)**
1	45	10
2	47	12
3	29	8
4	40	10
Vitamin C	141	210

**standard deviation is less than 8 % of mean values*

*3.5.5 DNA interaction studies of **1** – **4***

(a) UV-Vis titrations

The potential of transition metal compounds as chemotherapeutic drugs can be readily gauged from their affinities to DNA [**40**]. These metal compounds have illustrated diverse DNA interaction modes; for instance, their metal centres can directly coordinate to donor atoms within the DNA double helix or these metal compounds can facilely form DNA adducts *via* DNA intercalation between the DNA base pairs, resulting in major- or minor DNA groove binding [**5**]. Numerous methods have been utilized to monitor the progressive formation of DNA-metal complex adducts, however one of the most versatile and simplest techniques is UV-Vis spectrophotometry [**41**].

Electronic spectral changes associated with DNA intercalation usually entails the decrementing absorbance of an aromatic chromophore's intra-ligand transition (*viz.* hypochromism) accompanied with a progressive red shift of the corresponding wavelength maximum (*viz.* bathochromism) [**42**]. These UV-Vis spectral alterations are accounted to *pi*-stacking interactions between a *pi*-conjugated chelator and the DNA base pairs [**43**]. The contradictory UV-Vis spectral observations, the hyperchromic effect, can arise from groove-binding as well

as electrostatic attractions between the DNA and metal compound. Hypochromism is known to compromise the structural integrity of DNA by inducing denaturation or cleavage [**44**].

The UV-Vis spectral profiles depicting the DNA binding titrations for **1** and **2** reveal hypochromism (2.15 % at λ_{max} = 347 nm and 21.14 % at λ_{max} = 379 nm) with red shifts of 3 nm and 4 nm, respectively, see **Figure 3.17** and **3.18**. In addition, diffuse isosbestic points are observed at 295, 361 and 511 nm in the UV-Vis spectral profile of **2**, which indicates that the metal compound exhibits a homogenous binding mode towards DNA. Synonymously, the arene ruthenium(II) complex, [(η^6-$C_{12}H_{18}$)RuCl(PFPdpm)] [PFPdpm = 5-(penta-fluoro)phenyldipyrromethene] showed red shifts (of approximately 2 nm) for its intra-ligand and MLCT bands accompanied with gradual decreases in the absorbance values (under 10% hypochromism) during its ct-DNA binding UV-visible spectrophotometric experiment [**45**]. The steric demands of the *trans*-[$Ru(PPh_3)$]$^{2+}$ core affords a significantly lower intrinsic binding constant for **1** (K_b =1.5 *x* 10^5 M^{-1}) [**46**]. Similarly, a ruthenium carbonyl compound, [RuCl(CO)(dppb)(bipy)]PF_6 illustrated hypochromic behaviour, however its sterically crowded *bis*(diphenylphosphine)butane (DPPB) co-ligand impeded DNA intercalation and favoured groove-binding based on its lower K_b (3.78 *x* 10^4 M^{-1}) value in comparison to ethidium bromide with a K_b value of 10^6 M^{-1} as well as other metal-based DNA intercalators [**47-49**]. Comparatively, the larger intrinsic binding constant (K_b) of **2** (1.2 *x* 10^7 M^{-1}) is higher than that obtained for [(η^6-$C_{12}H_{18}$)RuCl(PFPdpm)] (6.5 x 10^4 M^{-1}), which hints at multimodal interactions of **2** with ct-DNA. Thus, the ruthenium compounds **1** and **2** can be regarded as preferential groove-binders.

Diverse spectral alterations were observed in the overlay UV-visible spectra of **3** upon its titration with ct-DNA, attesting to this metal complex's variable DNA interactive modes, see **Figure 3.19**. Individual decreasing (λ_{max} = 294 nm) and increasing (λ_{max} = 329 nm) intraligand transitions are bridged by an isosbestic point appearing at 308 nm, while similarly, a broad shoulder centralized at 390 nm and a very low-intensity *d-d* transition band at 639 nm disappears with the appearance of a low intensity MLCT band at 517 nm. These UV-Vis spectral changes are symbolic of stereoelectronic redistributions with Hobz organic chelators of **3** upon interaction with ct-DNA. Of particular interest is the appearance of the metal-based electronic transition, which is suggestive of the metal centre reducing and, hypothetically, this arises from coordinative bonding of the ruthenium to selected DNA base pairs. Analogous to

the *bis*-heterocyclics (**1** and **2**), hypochromism (18 %) of **3**'s intra-ligand transition (monitored at 331 nm) is observed, see **Figure 3.19**. In addition, a clear appearance of a distinct MLCT band is detected at 416 nm, which again indicates reduction of the metal centre upon coordination with the ct-DNA structure (as in the case of **3**). The calculated intrinsic binding constants (9 *x* 10^4 M^{-1} for **3** and 2 *x* 10^5 M^{-1} for **4**) of the ruthenium mono-heterocyclic compounds are both smaller in magnitude than classical intercalators, which suggest that metal complexes **3** and **4** are predominately DNA groove-binders [**49**].

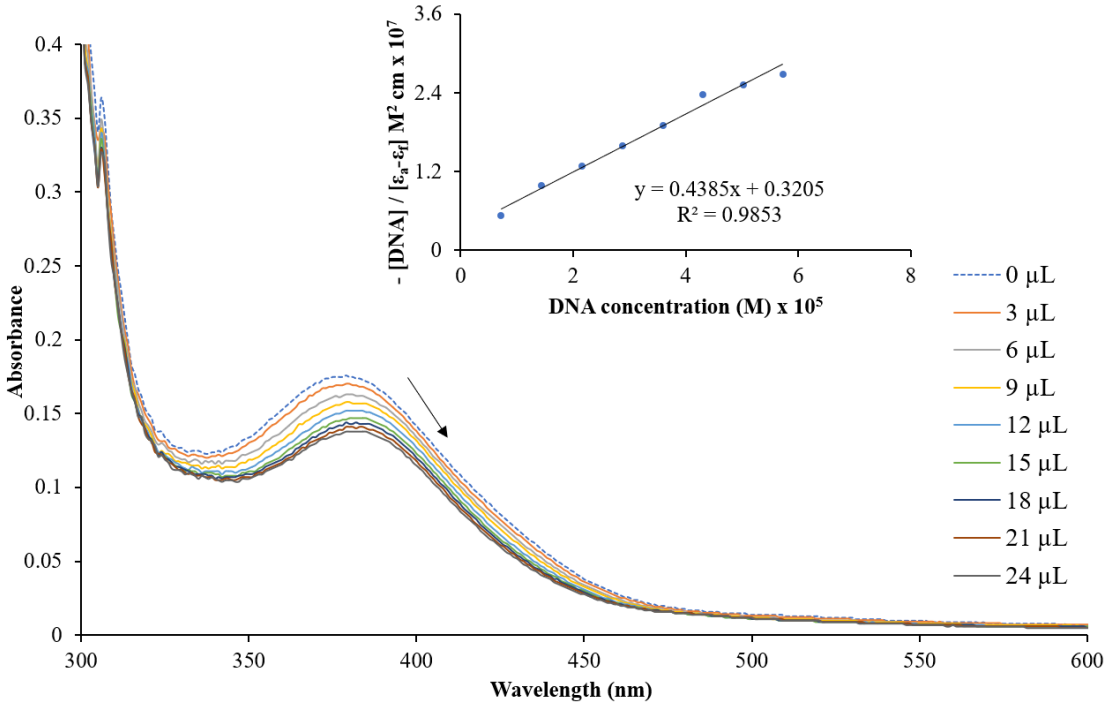

Figure 3.17: *Overlay UV-Vis spectra of compound **1** in the absence and presence of increasing amounts of ct-DNA. A dashed line indicates the initial spectrum. Inset: Plot of* $[DNA]/(\varepsilon_a - \varepsilon_f) \times 10^9$ *vs* $[DNA] \times 10^6$ *and the linear fit for the titration.*

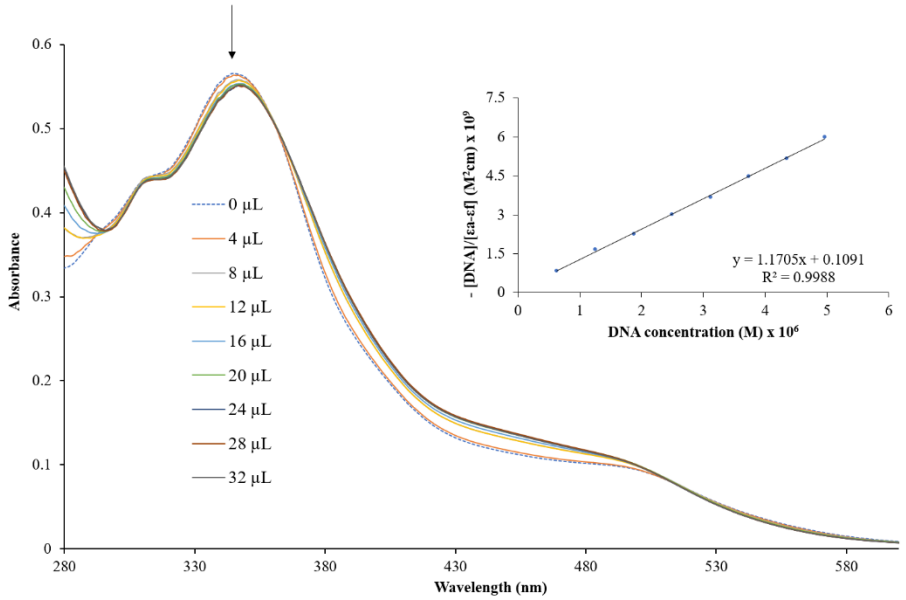

Figure 3.18: *Overlay UV-Vis spectra of compound **2** in the absence and presence of increasing amounts of ct-DNA. A dashed line indicates the initial spectrum. Inset: Plot of [DNA]/(εa - εf) x 10⁶ vs [DNA] x 10⁴ and the linear fit for the titration.*

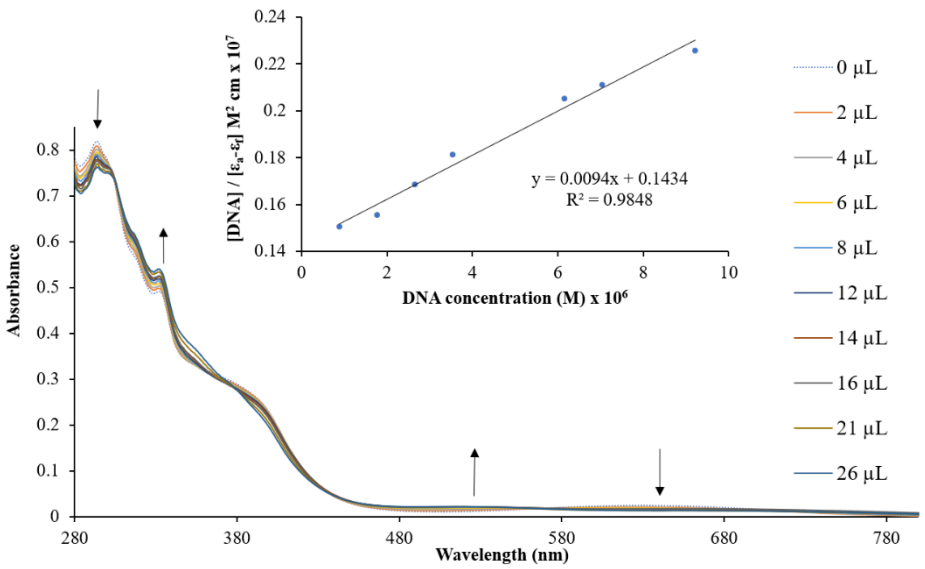

Figure 3.19: *Overlay UV-Vis spectra of compound **3** in the absence and presence of increasing amounts of ct-DNA. A dashed line indicates the initial spectrum. Inset: Plot of [DNA]/(εa - εf) x 10⁶ vs [DNA] x 10⁶ and the linear fit for the titration.*

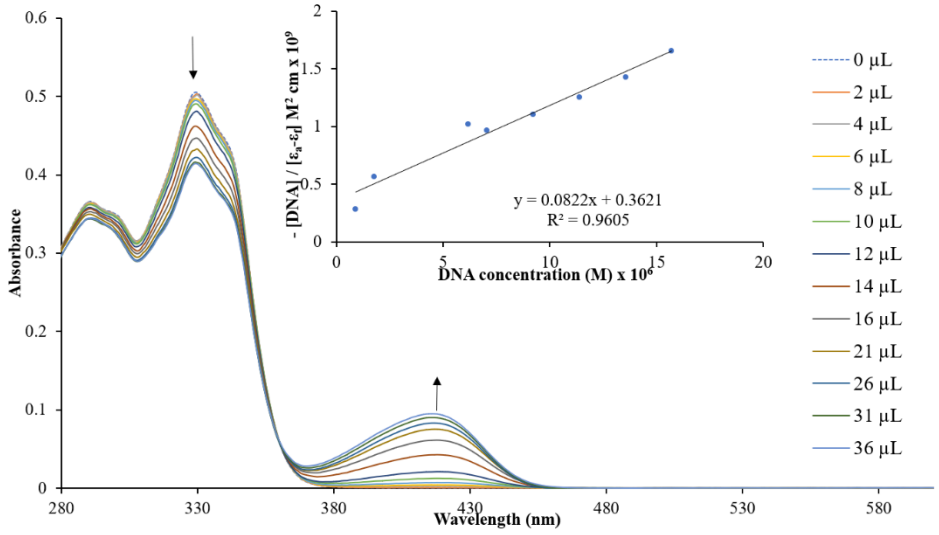

Figure 3.20: *Overlay UV-Vis spectra of compound **4** in the absence and presence of increasing amounts of ct-DNA. A dashed line indicates the initial spectrum. Inset: Plot of [DNA]/(ε_a - ε_f) x 10^7 vs [DNA] x 10^6 and the linear fit for the titration.*

(*b*) *Agarose gel electrophoresis and competitive binding studies*

The UV Agarose gel electrophoresis of human genomic DNA isolated from cancer cell lines demonstrated that each of the ruthenium compounds could interact with DNA and resulted in a reduction in the fluorescence intensity of ethidium bromide (EtBr) staining. Compounds **1** and **2** demonstrated a dose-dependent and significant reduction in fluorescence intensity of EtBr staining (**Figure 3.21**). The extent of the metal compounds' DNA interactive capabilities can be directly correlated to the corresponding apparent DNA binding constants where **1** and **2** have higher intrinsic DNA binding constants and afford substantial reduction in the fluorescence intensity of EtBr. Furthermore, the Hoechst DNA binding competition studies corroborate that the metal compounds **1** – **4** are DNA groove-binders, see **Figures 3.22** and **3.23**. In particular, the concentration-dependent studies affirm that the respective metal compounds exhibit gradually higher DNA binding affinities than the classical DNA groove-binder, Hoechst.

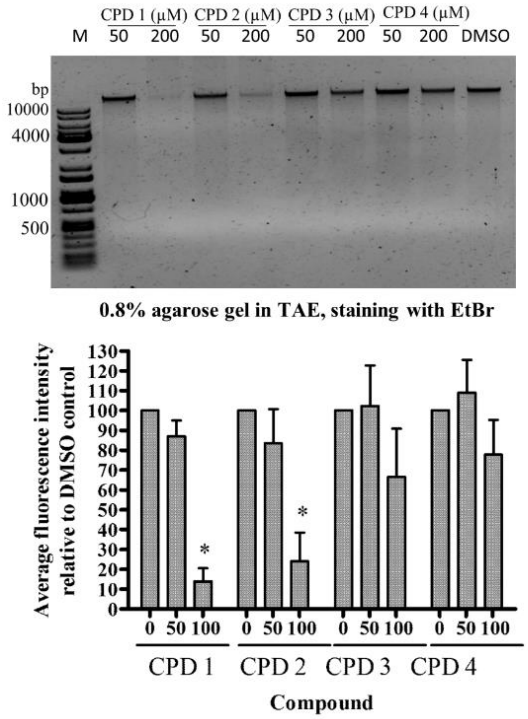

Figure 3.21: *Analysis of interaction of the metal compounds with human genomic DNA by agarose gel electrophoresis. The average fluorescence intensity of the DNA bands was quantified by ImageJ and is shown relative to the intensity of the DMSO control (± SEM, n=3). Statistical significance was assessed by two-way ANOVA with Bonferroni post-tests, where * indicates $p < 0.05$.*

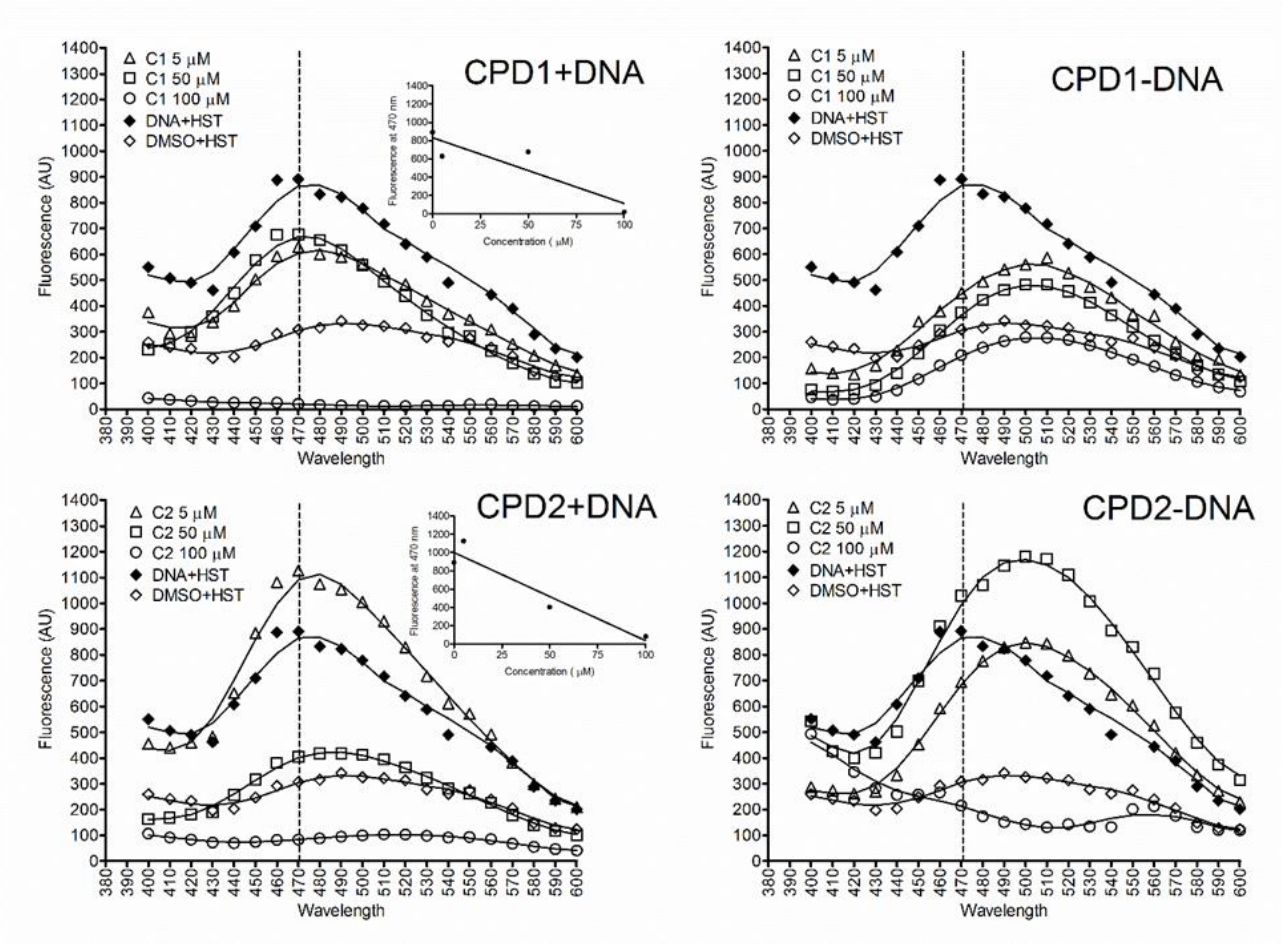

Figure 3.22: *DNA binding assay illustrating that the metal compounds **1** and **2** competes with Hoechst-33342 for binding to the minor groove of DNA. Fluorescence emission spectra for Hoechst-33342 (HST) alone or DNA in the presence or absence of metal compounds **1** and **2** (at concentrations of 5, 50 or 100 μM). DMSO was used as the vehicle control. The panels on the left show the emission spectra for the respective metal compounds in the presence of Hoechst-33342 and DNA, while the panels on the right show the emission spectra of the metal compounds with Hoechst-33342 in the absence of DNA. The dotted line indicates the emission maximum at 470 nm and the inset graphs on the left hand panel show the change in maximum emission at 470 nm as a function of increasing compound concentration (5, 50 and 100 μM).*

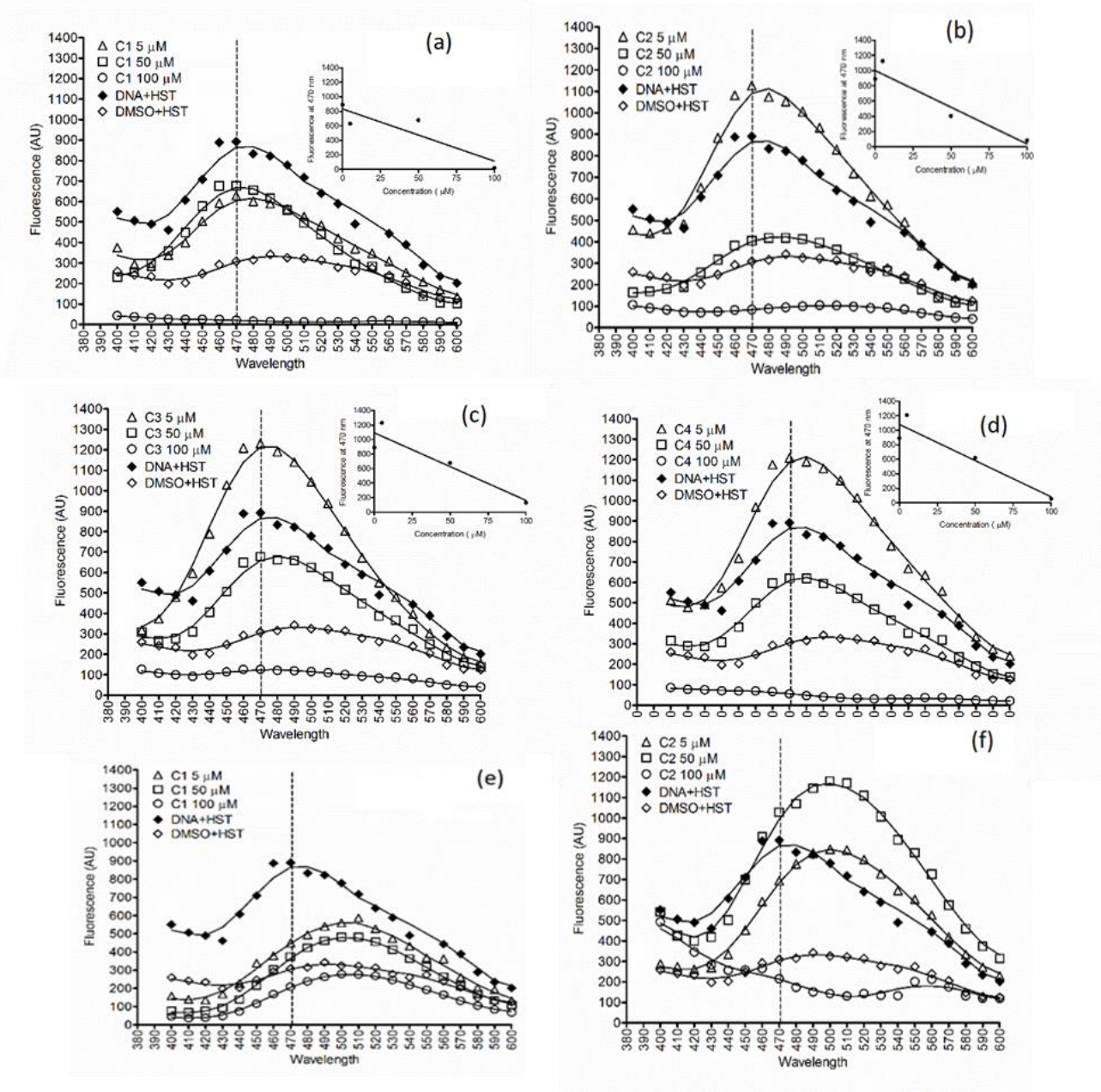

Figure 3.23: *DNA binding assay illustrating that the compounds **3** and **4** competes with Hoechst-33342 for binding to the minor groove of DNA. Fluorescence emission spectra for Hoechst-33342 (HST) in DNA (**a** – **d**) or alone (**e** – **f**). The aforementioned samples were exposed to varying concentrations (of 5, 50 or 100 μM) of the respective metal compounds. DMSO was used as the vehicle control. The dotted line indicates the emission maximum at 470 nm and the inset graphs show the change in maximum emission at 470 nm as a function of increasing compound concentrations.*

*(**c**) Molecular docking*

Molecular docking simulations were conducted to gain more insight into the DNA interactive modes of **1** – **4**, respectively, see **Figures 3.24 – 3.27**. Interestingly, all the metal compounds are predominately minor groove binders, including **2,** even though it has a significantly larger Van der Waals radius of 11.076 Å from its geometric centre than that predicted for the other Zn conformers of **1** (8.326 Å), **3** (8.280 Å) and **4** (8.270 Å). Relatively, the total binding energies (-6.02 kcal/mol for **1**, -7.48 kcal/mol for **2**, -6.4 kcal/ mol for **3** and 7.48 kcal/ mol for **4**) of the DNA-metal compound hybrids are similar, which justifies their mutual DNA binding mode. From the visual inspection of the molecular docking results, it is evident that the presence of the bulky PPh_3 co-ligands and the steric factors of the chelating ligand (in **1**) of the metal compounds inhibit DNA intercalation.

The predicated hybrid of **1** illustrates that the ombb chelator is localized within the minor groove while closely engaging with hydrogen-bonding and non-classical interactions (< 2.6 Å) originating from its respective benzimidazole amino protons and chloro co-ligand to the opposing phosphate backbones. Secondary interactions between the DNA receptor and ombb ligand occur *via* the GCGCAT DNA sequence. For **2**, only one of its benzimidazole moieties and a phenyl group of the PPh_3 co-ligand dock within the minor groove, affording interactions with T-A and G-C DNA base pairs. The **2**-DNA adduct is further stabilized by the other phenyl groups of the PPh_3 co-ligand with their adjacent phosphate chains, while hydrogen-bonding is observed between the outer benzimidazole moiety and the nearest phosphates. The mono-benz(imidazole/othiazole) metal compounds have similar orientations with respect to the DNA structure, with their $[RuCl(PPh_3)]^+$ cores largely positioned within the minor grooves leading to general close contacts with the G-C DNA base pairs and phosphate backbone (for Cl only). These DNA adducts are reinforced by the organic chelating ligands interacting with the closest phosphate chain. Computational justification for the gradual shifts of the respective metal compounds' intra-ligand transitions are deduced from the interactions between optimized conformers and the relevant DNA base pairs.

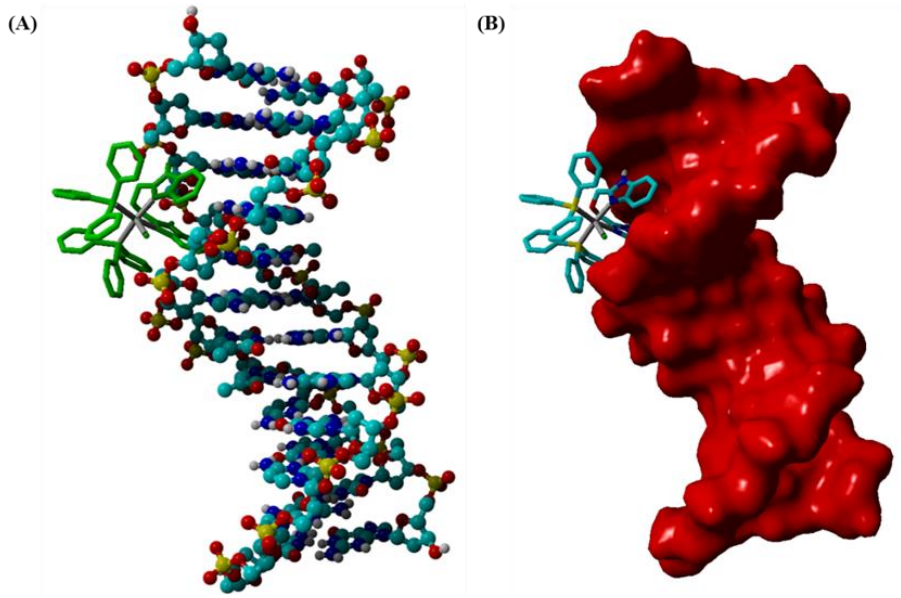

Figure 3.24: *Minor groove binding of compound **1** into the B-DNA structure: (**A**) shows DNA in ball and stick view whereas (**B**) shows the molecular surface view of DNA.*

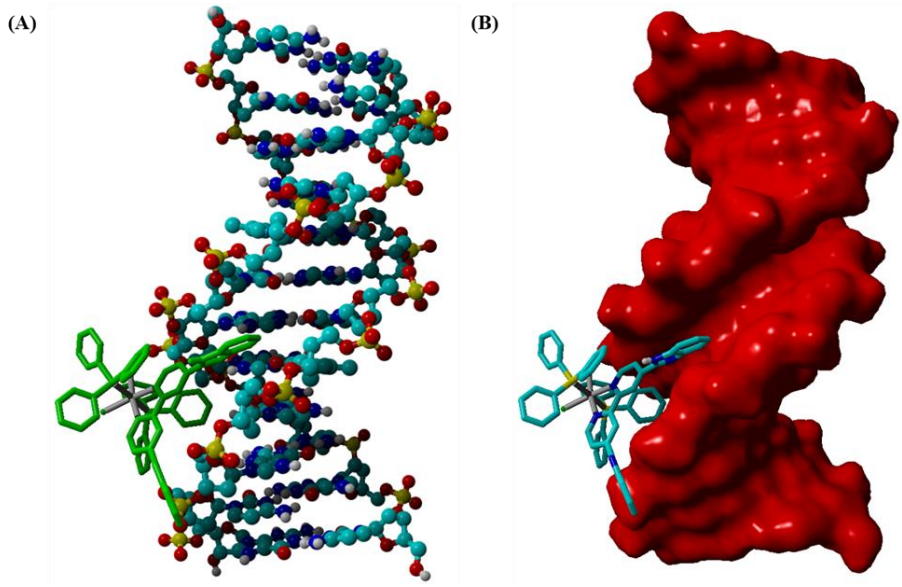

Figure 3.25: *Compound **2** primarily docked into the minor groove of B-DNA: (**A**) shows the molecular surface view of DNA whereas (**B**) shows DNA in ball and stick view.*

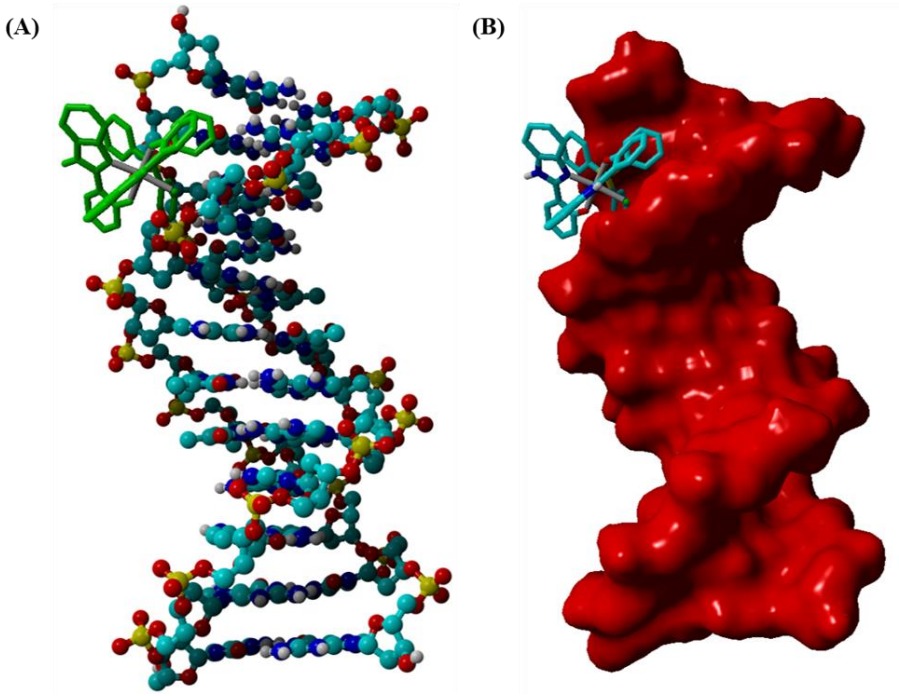

Figure 3.26: *Compound **3** primarily docked into the minor groove of B-DNA: (**A**) shows the molecular surface view of DNA whereas (**B**) shows DNA in ball and stick view.*

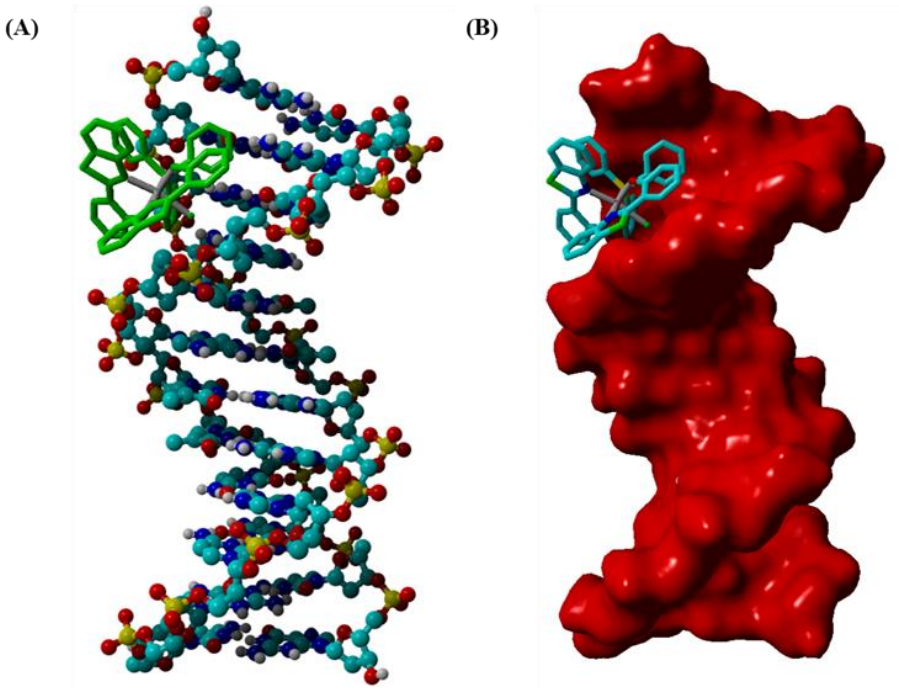

Figure 3.27: *Compound **4** primarily docked into the minor groove of B-DNA: (**A**) shows DNA in ball and stick view whereas (**B**) shows the molecular surface view of DNA.*

3.5.6 BSA interaction studies

Serum albumins are major dissoluble proteins in the circulatory system and serve as primary transport media for numerous pharmaceuticals and physiologically relevant compounds [**50**]. In particular, the affinity of a pharmaceutical to albumin has a significant influence on its pharmacokinetics. Mechanistically, the drug carrier protein can induce the careful reversible uptake and release of pharmaceuticals through altering its flexible structure while retaining its structural integrity. Primarily, inorganic and organic-based medicinal compounds have been shown to bind to BSA domains **IIA** and **IIIA** subdomains [**51**].

Biomolecular titrations between the *in vivo* drug carrier protein, BSA and the respective ruthenium compounds **1** – **4** were monitored using UV-Vis spectrophotometry and fluorescence emission spectroscopy. Gradual variations in intensities are indications of the conformational changes in the BSA structure induced by the additions of the individual metal compounds whilst any shifts in the electronic spectral bands reveals whether a metal compound is bound to the BSA chromophore in its hydrophobic or hydrophilic environments [**52, 53**].

(a) UV-Vis titrations

Data attained from the UV-visible spectrophotometric titrations illustrated distinct hyperchromism accompanied by slight blue-shifts which are observed in the separate UV-Vis spectra of **1**, **2** and **3**, see **Figures 3.28, 3.29** and **3.30**. These spectral observations concur with literature trends which suggest that minor unwinding of the protein strands occur upon reacting with the metal complex, leading to non-exposure of the polar tryptophan residues' microenvironment of BSA, for hydrogen-bonding interactions with water molecules [**54**].

Similarly, the distinguishing absorption band of BSA gradually increased upon interaction with **4**, however a minor red-shift of the peak maxima was noted, see **Figure 3.31**. The aforementioned electronic spectral changes are attributed to the structural BSA integrity being compromised by its interaction with the metal complex. Consequently, the unfolding protein backbone exposes the tryptophan residues to aqueous media rendering increasing polarity and hydrophilicity for the BSA chromophore [**55, 56**]. An explanation for the difference in trends could be explained by the larger number of hydrogen-bonding sites on compounds **1** – **3**, which

results in more stable adduct formations with BSA. As a result, less unfolding of the protein backbone occurs which keeps the tryptophan residues unexposed and well-hidden in the hydrophobic protein cavity [**57, 58**].

From the double reciprocal plots of $1 / (A_0 - A)$ *versus* $1 / C_{complex}$, the apparent association constants (K_{app}) for **1**, **2**, **3** and **4** were calculated to be $1.80 \times 10^5\ M^{-1}$, $7.47 \times 10^6\ M^{-1}$, $4.66 \times 10^4\ M^{-1}$ and $2.00 \times 10^4\ M^{-1}$, respectively. These apparent association constants (K_{app}) are of similar magnitude to those obtained for other ruthenium complexes and moreover, these K_{app} values can also be regarded as ideal binding affinities towards BSA, which are considered to be between $10^4 - 10^6\ M^{-1}$ [**59-61**]. The larger binding constants associated with the *bis*-heterocyclic metal complexes **1** and **2** can be attributed to their larger sizes which allows more favourable hydrophobic interaction with the BSA interfacial surface. The presence of the chloride co-ligands also promotes higher reactivities as the halides are known to undergo *in vivo* ligand substitution to form aqua adducts that generate active coordination centres [**62**].

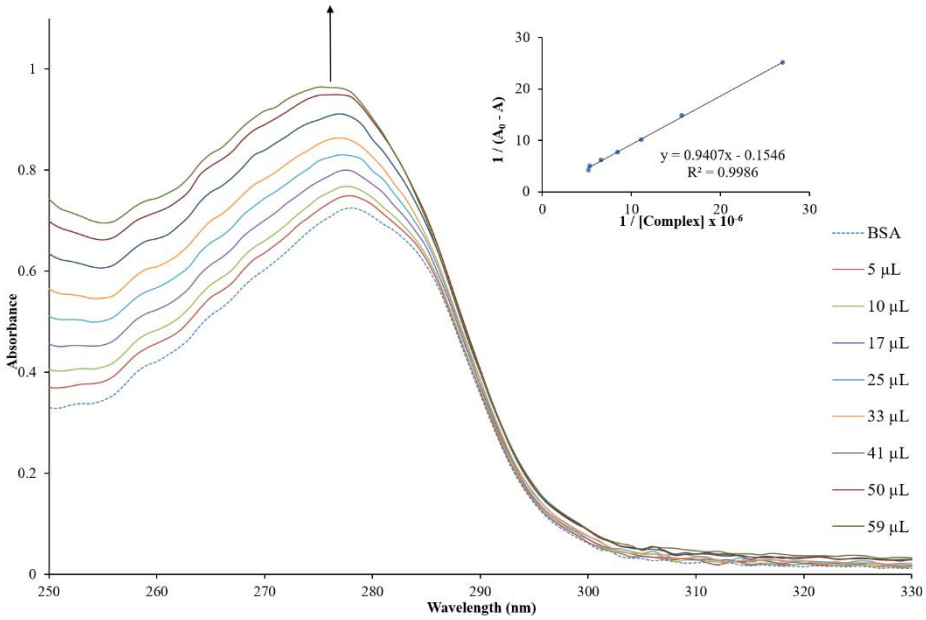

Figure 3.28: *UV-Vis spectral profile depicting the titration between compound **1** and BSA. The inset is the double reciprocal plots of $1 / (A_0 - A)$ versus $1 / C_{complex}$.*

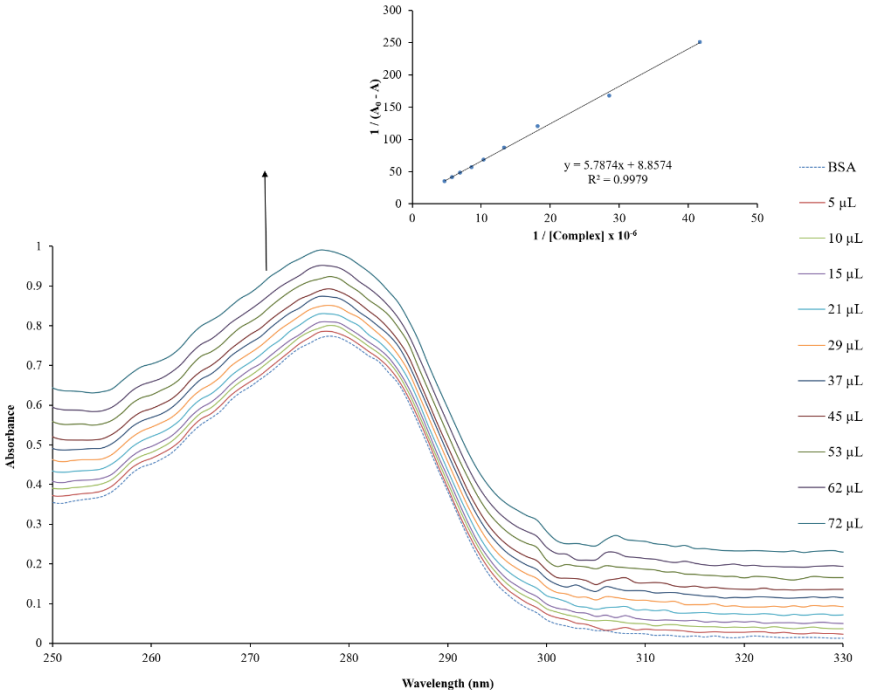

Figure 3.29: *UV-Vis spectral profile depicting the titration between compound **2** and BSA. The inset is the double reciprocal plot of 1 / (A_0 – A) versus 1 / $C_{complex}$.*

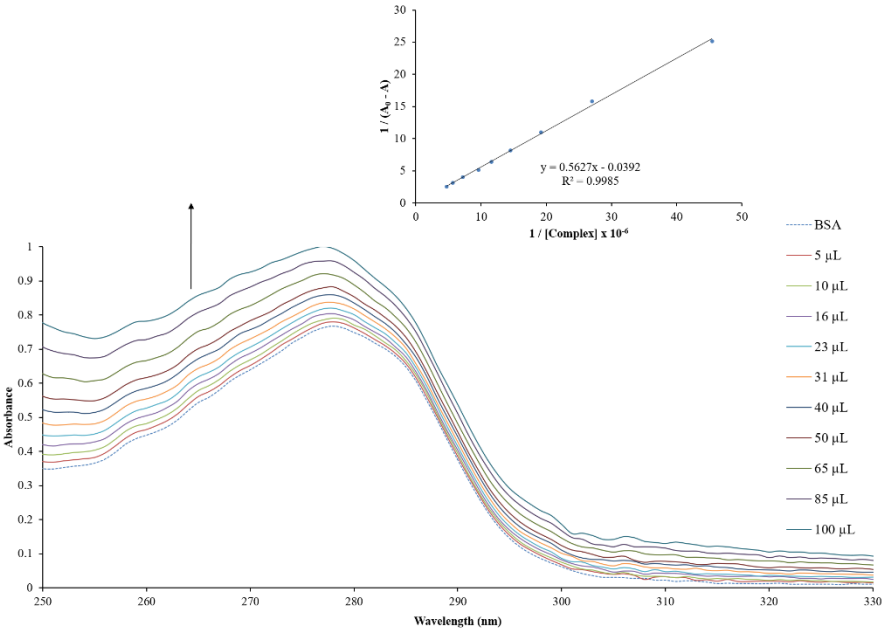

Figure 3.30: *UV-Vis spectral profile depicting the titration between compound **3** and BSA. The inset is the double reciprocal plot of 1 / (A_0 – A) versus 1 / $C_{complex}$.*

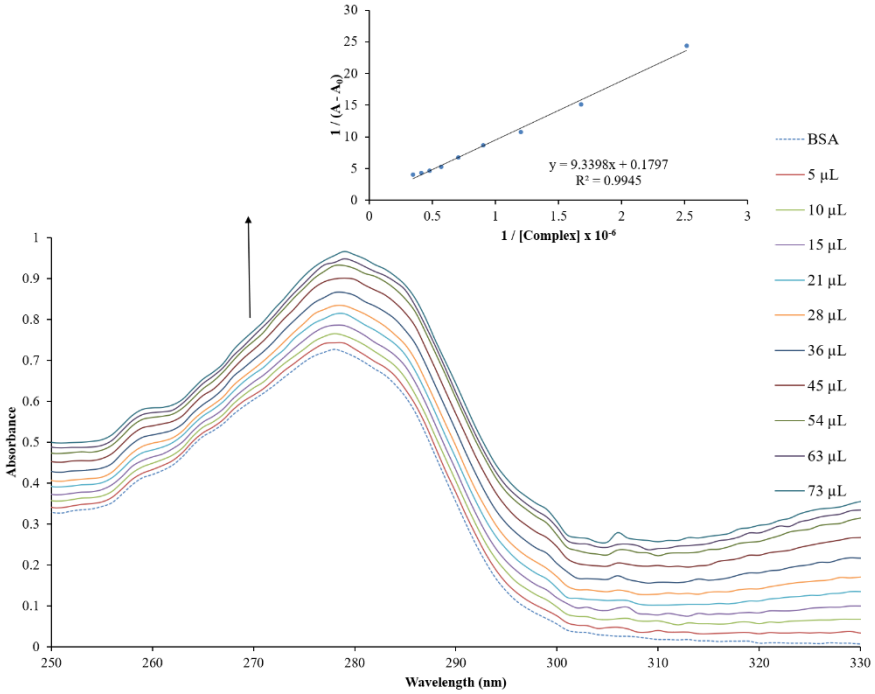

Figure 3.31: *UV-Vis spectral profile depicting the titration between compound **4** and BSA. The inset is the double reciprocal plot of 1 / (A_0 – A) versus 1 / $C_{complex}$.*

(b) *Fluorescence titrations*

BSA readily undergoes fluorescence quenching if one or more of its accessible domains are occupied by a quencher, which leads to increasing concentrations of the non-fluorescent active BSA-quencher. Similarly to the UV-Vis spectrophotometry titration analysis, any changes in the conformation or environment of BSA due to interactions with a metal compound can result in quenching, with shifts in the characteristic BSA emission peak [**63**]. Steady-state fluorescence quenching of BSA peak maximum occurs in the presence of all metal compounds, which affirms the formation of the BSA-metal compound aggregates, see **Figures 3.32** – **3.35**.

Blue-shifts in the BSA peak maxima occurs upon interaction with **1**, **2** and **3**, whereas a red-shift is observed when the protein is titrated against **4**. These findings are consistent with those found in the molecular absorption spectrophotometric titrations, whereby compounds **1** – **3** induces less unfolding of the protein thus keeping the BSA chromophore in a more

hydrophobic environment, while compound **4** bares the BSA chromophore to an enhanced hydrophilic environment by increasing protein unfolding [**64**]. The quenching (K_{SV}) and quenching rate (K_q) constants were derived from the Stern-Volmer relationship and are shown in **Table 3.4**.

The obtained K_q values indicate that the fluorescence decay is a process of static quenching since these values are of a larger magnitude than that of quenchers involved in a dynamic equilibrium process (2 x 10^{10} M^{-1} s^{-1}) [**63, 65**]. Since K_{SV} is the binding constant for static quenching, it can be used to determine the binding affinities of the respective ruthenium compounds towards BSA. The results conclude that the *bis*-heterocyclic ruthenium compounds (**1** and **2**) exhibit higher binding affinities for BSA than the *mono*-heterocyclic ruthenium compounds (**3** and **4**), which is consistent with the findings presented in the UV-Vis spectrophotometric analysis. Quenching constants of similar magnitude were documented for other ruthenium compounds, for example, *cis*-[Ru(quin)(dppm)$_2$]PF_6 [quin = quinaldate; dppm = *bis*(diphenylphosphino)methane] display K_{SV} and K_q values of 0.77 x 10^5 M^{-1} and 1.10 x 10^{13} M^{-1} s^{-1}, respectively [**66**].

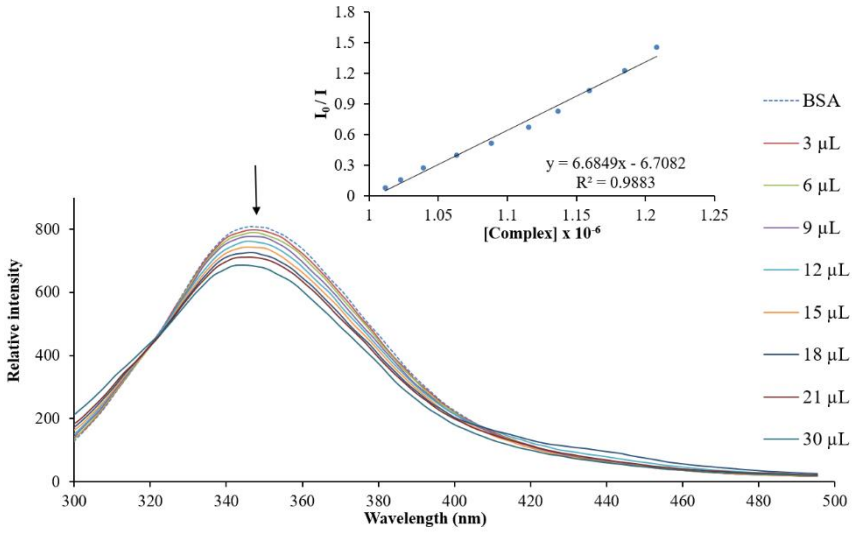

Figure 3.32: *Fluorescence emission spectral profile depicting the titration between compound **1** and BSA. The inset is the Stern-Volmer plot.*

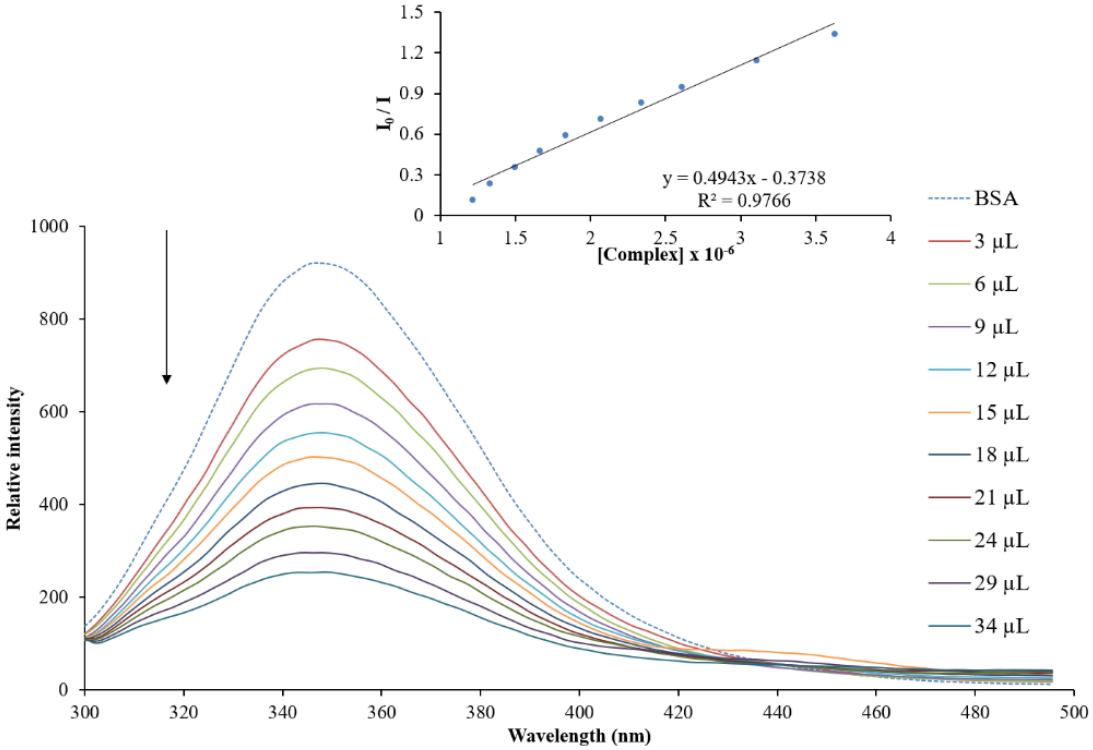

Figure 3.33: *Fluorescence emission spectral profile depicting the titration between compound **2** and BSA. The inset is the Stern-Volmer plot.*

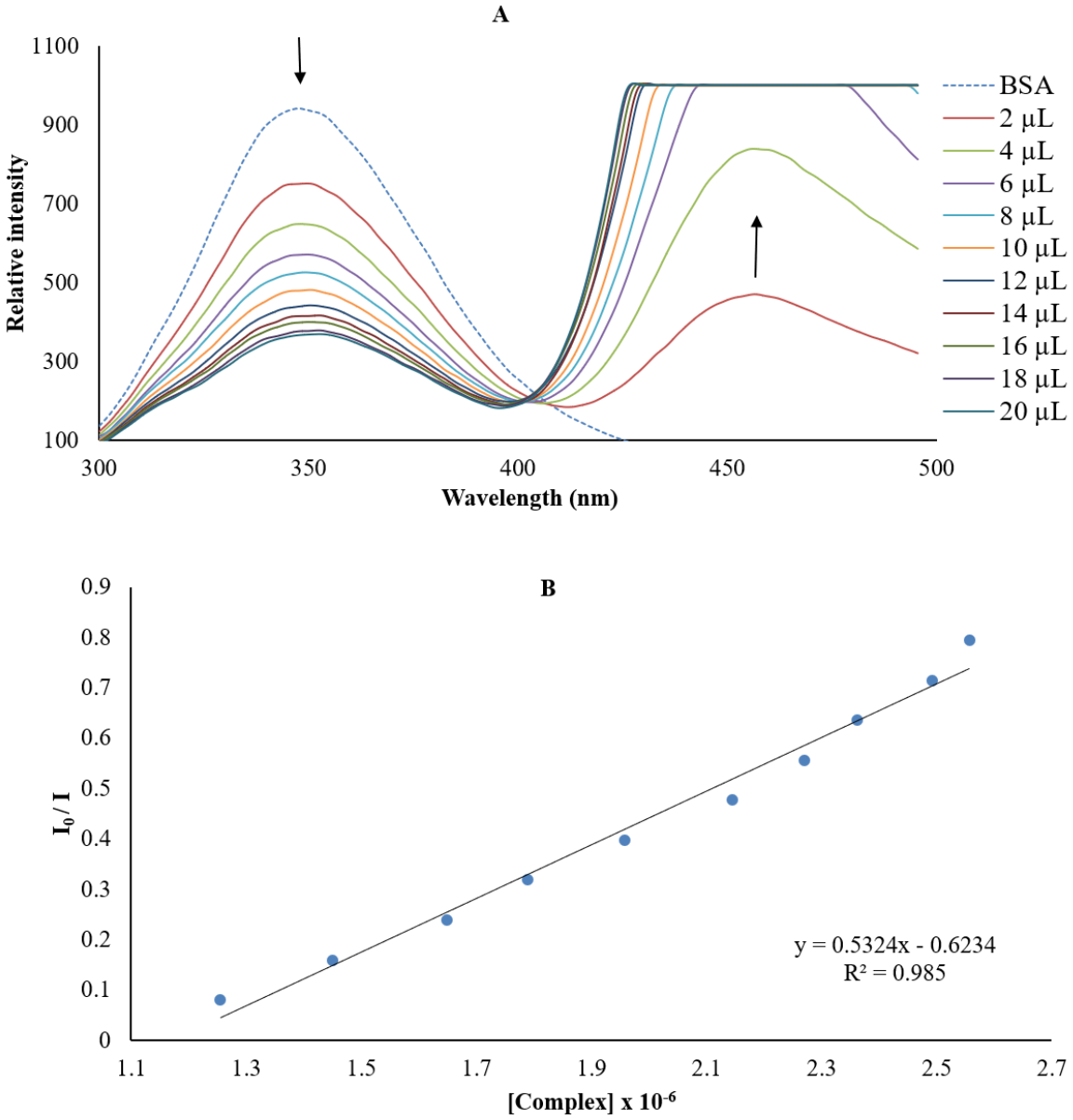

Figure 3.34: (**A**) *Fluorescence emission spectral profile depicting the titration between compound **3** and BSA.* (**B**) *The Stern-Volmer plot. The **M** symbol corresponds to the increasing emission peak associated with the metal complex.*

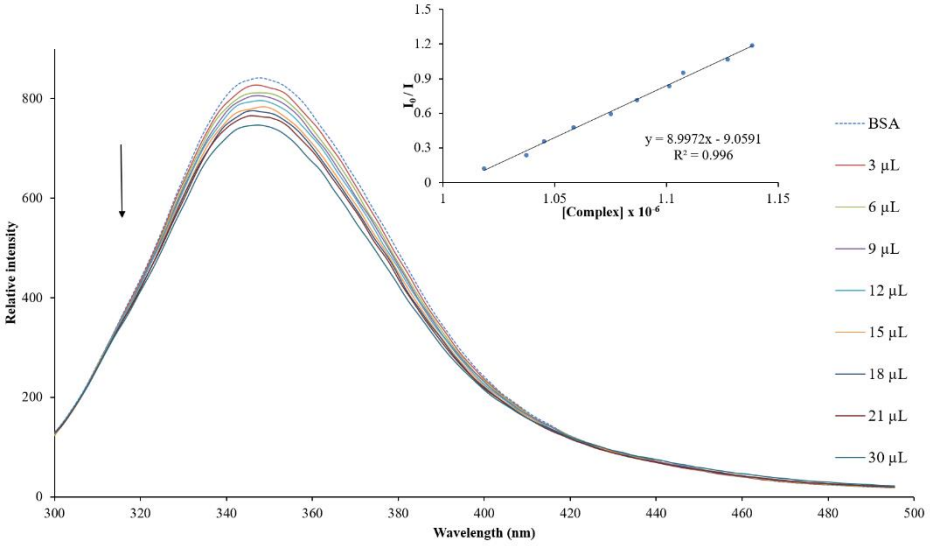

Figure 3.35: *Fluorescence emission spectral profile depicting the titration between compound **4** and BSA. The inset is the Stern-Volmer plot.*

Table 3.4: Quenching parameters obtained of the composites comprised of BSA and the corresponding metal compounds.

Compound	K_{SV} (M^{-1})	K_q (M^{-1} s^{-1})
1	1.47×10^5	1.47×10^{13}
2	1.98×10^5	1.98×10^{13}
3	1.85×10^5	1.85×10^{13}
4	1.11×10^4	1.11×10^{12}

(c) *Molecular docking*

BSA molecular docking simulations illustrate the respective metal compounds exhibit two classical docking patterns, see **Figures 3.36** – **3.39**. Partial docking of compound **1** within the cavity of the BSA subdomain **IIIA** (consistent with site **II**) leads to a higher total binding energy (-5.65 kcal/mol) for **1** than that of compound **2** (-10.28 kcal/mol**)** which docks well within the BSA **IIA** subdomain (consistent with site **I**). As a result, the BSA hybrid of **1** are

stabilized by weak interactions with fewer amino acid residues (*viz.* PRO415, GLN416, LYS499, VAL468 and LYS533) than the extensive network of close-proximity interactions observed within the hybrid of **2** and BSA. Indicative to the common DNA binding pattern of **3** and **4**, these structural analogues have nearly identical modes of interactions with BSA, whereby **4** has a lower total binding energy (-8.98 kcal/mol) than **3** (-7.93 kcal/mol), which is a result of the amido protons (N-H) of **3** interacting with BSA *via* classical hydrogen-bonding with GLU291 (at 2.896 Å) and VAL292 (at 2.411 Å) residues.

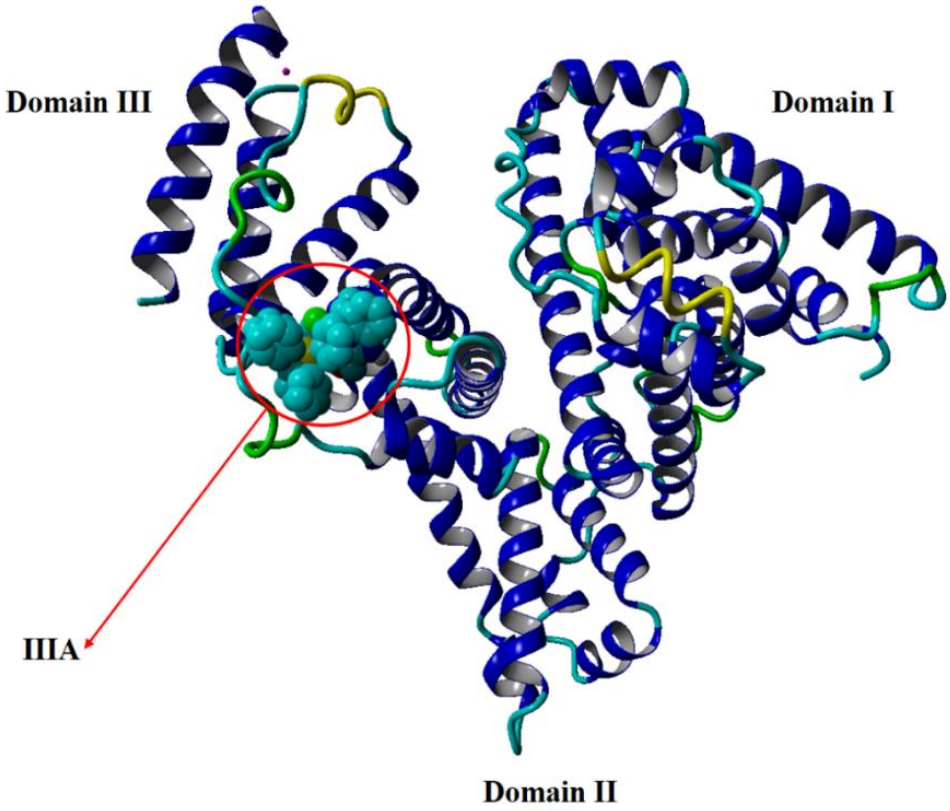

Figure 3.36: *Compound **1** binding in the site **IIIA** of BSA.*

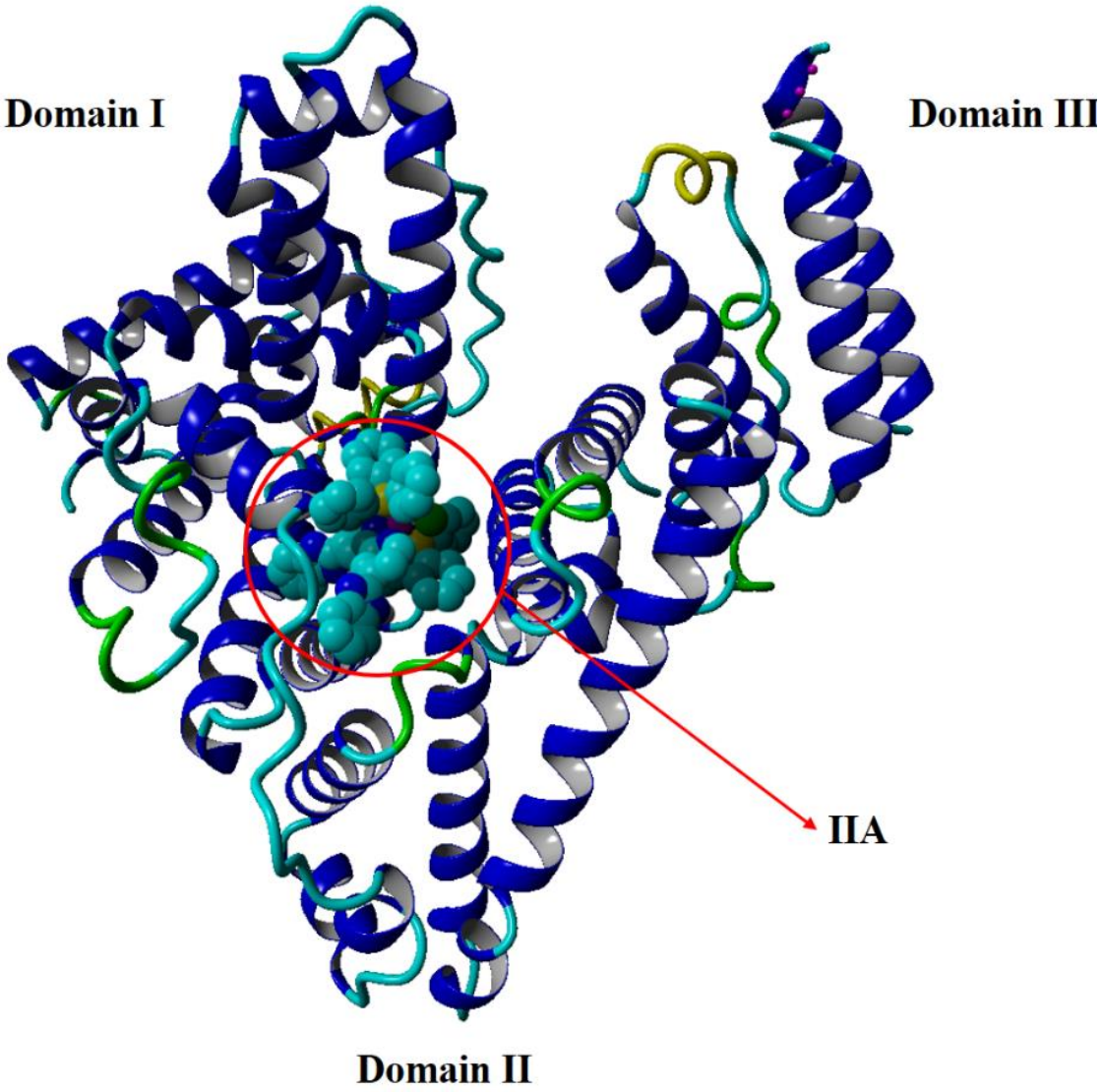

Figure 3.37: *Compound **2** binding in the site **IIA** of BSA.*

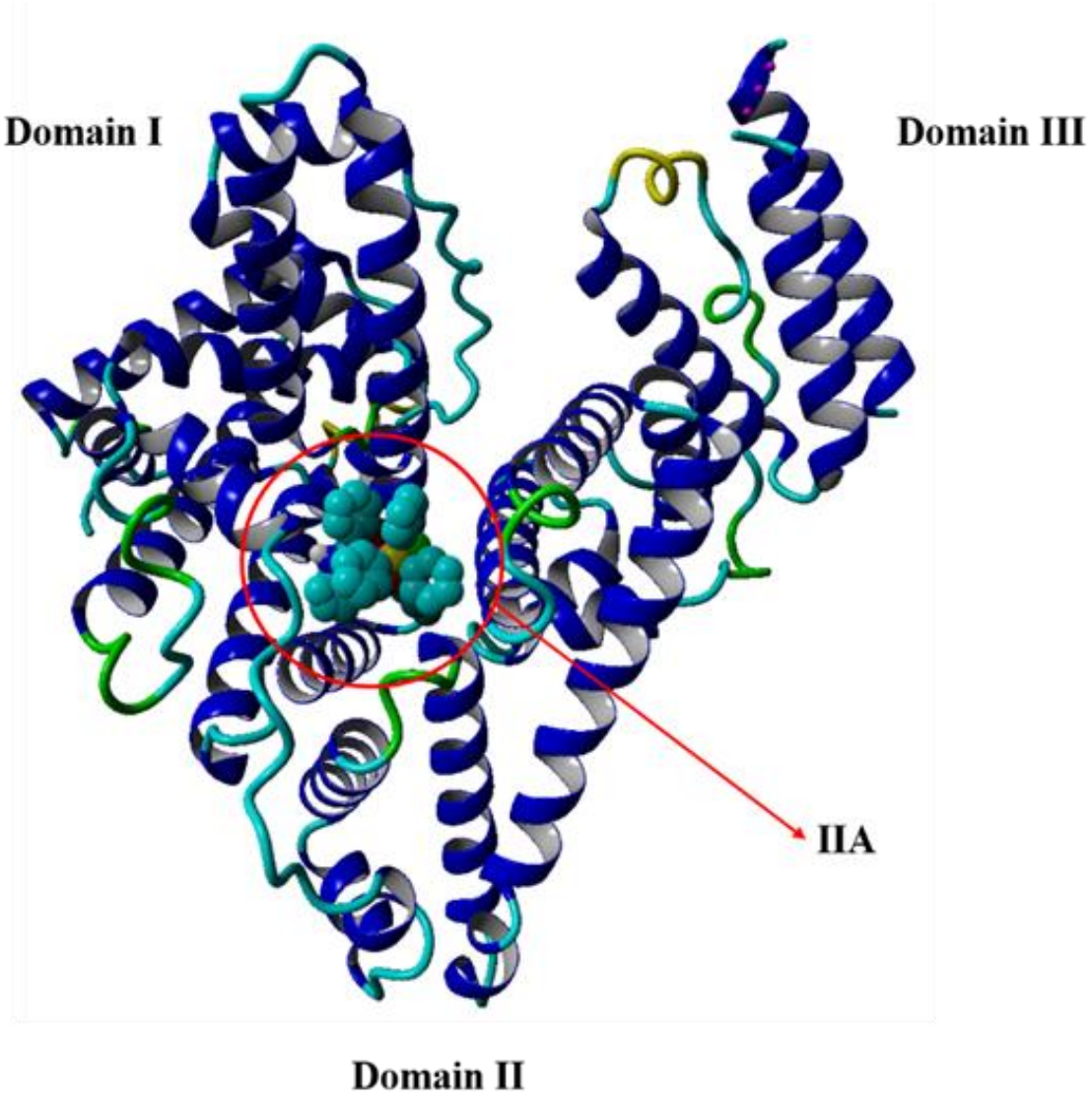

Figure 3.38: *Compound **3** binding in the **IIA** site of BSA.*

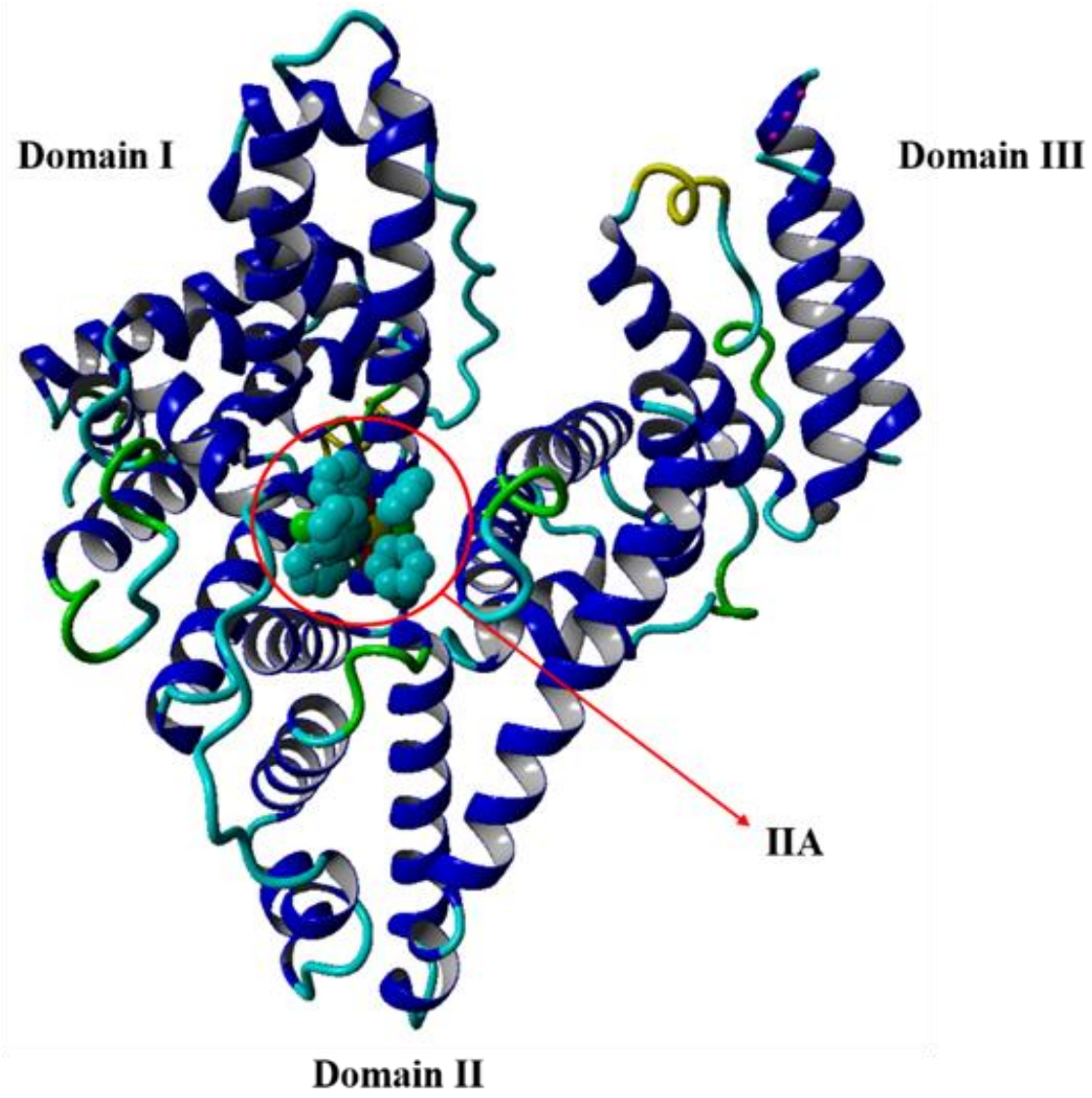

Figure 3.39: *Compound **4** binding in the **IIA** site of BSA.*

3.5.7 *In vitro anti-cancer activity*

The cytotoxicity of the ruthenium compounds **1** – **4** against the two cancer cell lines were assessed using an MTT assay and the results are shown in **Table 3.5**. The commonly used chemotherapeutic agent 5-FU was included as one of the positive controls and displayed modest cytotoxicity against HCC70 cells, with an IC_{50} of 127.07 (± 8.61) µM. The ruthenium compounds showed greater cytotoxicity than 5-FU with IC_{50} values of 88.20 (± 1.10), 44.07 (± 1.12) and 39.37 (± 1.15) µM, respectively. On the other hand, compound **2** was non-toxic to

HCC70 and HeLa cells. The non-toxicity of **2** could be due to its lower cell membrane permeability despite it having comparable DNA interactive capabilities to the other metal compounds [**67**]. In addition, the ruthenium compounds **1 - 4** exhibited significantly lower anti-cancer cellular activities than that of the antineoplastic drug, paclitaxel.

Table 3.5*: Cytotoxicity analysis of the ruthenium compounds against the different cancer cells.*

Compounds	IC_{50} **values against HCC70 cells**	**IC_{50} values against HeLa cells**
1	88.20 ± 1.10 µM (R^2 = 0.9656)	17.42 ± 1.14 µM (R^2 = 0.9491)
2	Non-toxic	Non-toxic
3	44.07 ± 1.12 µM (R^2 = 0.9702)	16.59 ± 1.16 µM (R^2 = 0.9328)
4	39.37 ± 1.15 µM (R^2 = 0.9593)	26.13 ± 1.16 µM (R^2 = 0.9215)
5-FU	127.07 ± 8.61 µM (R^2 = 0.8667)	-
Paclitaxel	3.06 ± 1.11 nM (R^2 = 0.9595)	-

3.6 References

1. T. Lazarević, A. Rilak and Ž. D. Bugarčić, *Eur. J. Med. Chem.*, 2017, **142**, 8-31.

2. P. Zhang and P. J. Sadler, *J. Organomet. Chem.*, 2017, **839**, 5-14.

3. S. Thota, D. A. Rodrigues, D. C. Crans and E. J. Barreiro, *J. Med. Chem.*, 2018, **61**, 5805-5821.

4. A. Merlino, *Coord. Chem. Rev.*, 2016, **326**, 111-134.

5. B. J. Pages, D. L. Ang, E. P. Wright and J. R. Aldrich-Wright, *Dalton Trans.*, 2015, **44**, 3505-3526.

6. L. Zeng, P. Gupta, Y. Chen, E. Wang, L. Ji, H. Chao and Z.-S. Chen, *Chem. Soc. Rev.*, 2017, **46**, 5771-5804.

7. B. G. Dwyer, E. Johnson, E. Cazares, K. L. M. Holman and S. R. Kirk, *J. Inorg. Biochem.*, 2018, **182**, 177-183.

8. A. Levina, A. Mitra and P. A. Lay, *Metallomics*, 2009, **1**, 458-470.

9. F. Caruso, R. Pettinari, M. Rossi, E. Monti, M. B. Gariboldi, F. Marchetti, C. Pettinari, A. Caruso, M. V. Ramani and G. V. Subbaraju, *J. Inorg. Biochem.*, 2016, **162**, 44-51.

10. A. Pastuszko, K. Majchrzak, M. Czyz, B. Kupcewicz and E. Budzisz, *J. Inorg. Biochem.*, 2016, **159**, 133-141.

11. S. Chatterjee, I. Biondi, P. J. Dyson and A. Bhattacharyya, *J. Inorg. Biochem.*, 2011, **16**, 715-724.

12. G. Yamin and D. B. Teplow, *J. Neurochem.*, 2017, **140**, 210-215.

13. G. Yadav and S. Ganguly, *Eur. J. Med. Chem.*, 2015, **97**, 419-443.

14. M. Taha, N. H. Ismail, S. Imran, M. Selvaraj, H. Rashwan, F. U. Farhanah, F. Rahim, K. S. Kesavanarayanan and M. Ali, *Bioorg. Chem.*, 2015, **61**, 36-44.

15. P. Kopel, D. Wawrzak, V. Langer, K. Cihalova, D. Chudobova, R. Vesely, V. Adam and R. Kizek, *Molecules (Basel, Switzerland)*, 2015, **20**, 10360-10376.

16. N. S. Ng, M. J. Wu and J. R. Aldrich-Wright, *J. Inorg. Biochem.*, 2018, **180**, 61-68.

17. I. N. Booysen, S. Maikoo, M. P. Akerman and B. Xulu, *Trans. Met. chem.*, 2015, **40**, 397-404.

18. *Journal*, Bruker APEX2, SAINT and SADABS (2010). Bruker AXS Inc. Madison. Wisconsin, USA.

19. R. H. Blessing, *Acta Crystallogr., Sect. A: Found. Adv.*, 1995, **51 (Pt 1)**, 33-38.

20. G. Sheldrick, *Acta Crystallogr., Sect. A: Found. Adv.*, 2008, **64**, 112-122.

21. L. Farrugia, *J. Appl. Crystallogr.*, 2012, **45**, 849-854.

22. Frisch MJ, Trucks GW, Schlegel HB, Scuseria GE, Robb MA, Cheeseman JR, Scalmani G, Barone V, Petersson GA, Nakatsuji H, Li X, Caricato M, Marenich AV, Bloino J, Janesko BG, Gomperts R, Mennucci B, Hratchian HP, Ortiz JV, Izmaylov AF, Sonnenberg JL, Williams, Ding F, Lipparini F, Egidi F, Goings J, Peng B, Petrone A, Henderson T, Ranasinghe D, Zakrzewski VG, Gao J, Rega N, Zheng G, Liang W, Hada M, Ehara M, Toyota K, Fukuda R, Hasegawa J, Ishida M, Nakajima T, Honda Y, Kitao O, Nakai H, Vreven T, Throssell K, Montgomery Jr JA, Peralta JE, Ogliaro F, Bearpark MJ, Heyd JJ, Brothers EN, Kudin KN, Staroverov VN, Keith TA, Kobayashi R, Normand J, Raghavachari K, Rendell AP, Burant JC, Iyengar SS, Tomasi J, Cossi M, Millam JM, Klene M, Adamo C, Cammi R, Ochterski JW, Martin RL, Morokuma K, Farkas O, Foresman JB, Fox DJ (2009) Gaussian 09 Rev. A.01.

23. R. Haddad, E. Yousif and A. Ahmed, *SpringerPlus*, 2013, **2**, 510-515.

24. T. Satyanarayana and K. V. Reddy, *J. Chem. Sci.*, 1987, **99**, 237-242.

25. G. Stojcevic and M. C. Baird, *Dalton Trans.*, 2009, DOI: 10.1039/B908726E, 8864-8877.

26. Y. Mikata, T. Fujimoto, T. Fujiwara and S.-i. Kondo, *Inorg. Chim. Acta.*, 2011, **370**, 420-426.

27. I. N. Booysen, A. Adebisi, M. P. Akerman, O. Q. Munro and B. Xulu, *J. Coord. Chem*, 2016, **69**, 1641-1652.

28. I. N. Booysen, S. Maikoo, M. Piers Akerman, B. Xulu and O. Munro, *J. Coord. Chem.*, 2013, **66**, 3673-3685.

29. V. Moreno, J. Lorenzo, F. X. Aviles, M. H. Garcia, J. P. Ribeiro, T. S. Morais, P. Florindo and M. P. Robalo, *Bioinorg. Chem. Appl.*, 2010, **2010**, 936834.

30. M. O. Santiago, A. A. Batista, M. P. de Araújo , C. L. Donnici , I. d. S. Moreira, E. E. Castellano, J. Ellena, S. d. Santos and S. L. Queiroz, *Trans. Met. Chem.*, 2005, **30**, 170-175.

31. Y. W. Song, Z. Yu and Q. F. Zhang, *Acta Crystallogr., Sect. E: Crystallogr. Commun.*, 2006, **62**, m520-m522.

32. B. C. Roy, S. Debnath, K. Chakrabarti, B. Paul, M. Maji and S. Kundu, *Org. Chem. Front.*, 2018, **5**, 1008-1018.

33. G. Pizzino, N. Irrera, M. Cucinotta, G. Pallio, F. Mannino, V. Arcoraci, F. Squadrito, D. Altavilla and A. Bitto, *Oxid. Med. Cell. Longev.*, 2017, **2017**, 1-13.

34. T. Sathiya Kamatchi, N. Chitrapriya, S. K. Kim, F. R. Fronczek and K. Natarajan, *Eur. J. Med. Chem.*, 2013, **59**, 253-264.

35. T. Bal-Demirci, M. Şahin, E. Kondakçı, M. Özyürek, B. Ülküseven and R. Apak, *Spectrochim. Acta. A.*, 2015, **138**, 866-872.

36. G. Ayhan-Kilcigİl, C. Kuş, T. Çoban, B. Can-Eke, S. Özbey and M. Iscan, *J. Enzyme Inhib. Med. Chem.*, 2005, **20**, 503-514.

37. C. Prouillac, P. Vicendo, J.-C. Garrigues, R. Poteau and G. Rima, *Free. Radic. Biol. Med.* , 2009, **46**, 1139-1148.

38. G. Prakash, R. Manikandan, P. Viswanathamurthi, K. Velmurugan and R. Nandhakumar, *J. Photochem. Photobiol. B.*, 2014, **138**, 63-74.

39. D. H. Atha, U. Manne, W. E. Grizzle, P. D. Wagner, S. Srivastava and V. Reipa, *J. Histochem. Cytochem.*, 2010, **58**, 1005-1014.

40. J. C. García-Ramos, R. Galindo-Murillo, F. Cortés-Guzmán and L. Ruiz-Azuara, *J. Mex. Chem. Soc.*, 2013, **57**, 245-259.

41. R. Hajian and T. Guan Huat, *J. Spectrosc.*, 2013, **2013**, 8.

42. S. Bhattacharya and S. S. Mandal, *Biochim. Biophys. Acta.*, 1997, **1323**, 29-44.

43. N. Shahabadi, S. Mohammadi and R. Alizadeh, *Bioinorg. Chem. Appl.*, 2011, **2011**, 429241.

44. M. Sirajuddin, S. Ali and A. Badshah, *J. Photochem. Photobiol. B.*, 2013, **124**, 1-19.

45. R. P. Paitandi, R. S. Singh, S. Mukhopadhyay, G. Sharma, B. Koch, P. Vishnoi and D. S. Pandey, *Inorg. Chim. Acta.*, 2017, **454**, 117-127.

46. W. M. Motswainyana and P. A. Ajibade, *Advances in Chemistry*, 2015, **2015**, 21.

47. A. P. Carnizello, M. I. Barbosa, M. Martins, N. H. Ferreira, P. F. Oliveira, G. M. Magalhaes, A. A. Batista and D. C. Tavares, *J. Inorg. Biochem.*, 2016, **164**, 42-48.

48. M. Cory, D. D. McKee, J. Kagan, D. W. Henry and J. A. Miller, *J. Am. Chem. Soc.*, 1985, **107**, 2528-2536.

49. F. Gao, H. Chao, F. Zhou, X. Chen, Y.-F. Wei and L.-N. Ji, *J. Inorg. Biochem.*, 2008, **102**, 1050-1059.

50. M. M. Milutinovic, A. Rilak, I. Bratsos, O. Klisuric, M. Vranes, N. Gligorijevic, S. Radulovic and Z. D. Bugarcic, *J. Inorg. Biochem.*, 2017, **169**, 1-12.

51. K. Karami, M. Alinaghi, Z. Amirghofran and J. Lipkowski, *Inorg. Chim. Acta.*, 2018, **471**, 797-807.

52. W. Zhong, Y. Wang, J.-S. Yu, Y. Liang, K. Ni and S. Tu, *J. Pharm. Sci.*, 2004, **93**, 1039-1046.

53. H. Paul, T. Mukherjee, M. Mukherjee, T. K. Mondal, A. Moirangthem, A. Basu, E. Zangrando and P. Chattopadhyay, *J. Coord. Chem.*, 2013, **66**, 2747-2764.

54. Z. Cheng and R. Liu, *Spectrochim. Acta. A.*, 2013, **115**, 92-105.

55. V. D. Suryawanshi, L. S. Walekar, A. H. Gore, P. V. Anbhule and G. B. Kolekar, *J. Pharm. Anal.*, 2016, **6**, 56-63.

56. A.-Z. Wu, C.-Z. Lin, Y.-J. Zhai, J.-L. Zhuo and C.-C. Zhu, *J. Pharm. Anal.*, 2013, **3**, 61-65.

57. A. Mishra, A. Malakar, H. T. Biswal, M. K. Barman and G. Krishnamoorthy, *J. Mol. Recognit.*, 2015, **28**, 299-305.

58. T. T. Herskovits, B. Gadegbeku and H. Jaillet, *J. Biol. Chem.*, 1970, **245**, 2588-2598.

59. V. Ravi Kumar, P. Nagababu, G. Srinivas, M. Rajender Reddy, M. Vinoda Rani, M. Ravi and S. Satyanarayana, *J. Coord. Chem.*, 2017, **70**, 3790-3809.

60. C.-Y. Wong, L.-H. Chung, S. Lin, D. S.-H. Chan, C.-H. Leung and D.-L. Ma, *Sci. Rep.*, 2014, **4**, 7136.

61. T. Topală, A. Bodoki, L. Oprean and R. Oprean, *Clujul medical*, 2014, **87**, 215-219.

62. L. Messori, P. Orioli, D. Vullo, E. Alessio and E. Iengo, *Eur. J. Biochem.*, 2000, **267**, 1206-1213.

63. A. Varlan and M. Hillebrand, *Molecules (Basel, Switzerland)*, 2010, **15**, 3905-3919.

64. B. Ojha and G. Das, *Chem. Phys. Lipids.*, 2011, **164**, 144-150.

65. R. Ramachandran and P. Viswanathamurthi, *Spectrochim. Acta. A.*, 2013, **103**, 53-61.

66. E. N. da Silva, P. A. da Silva, A. E. Graminha, P. F. de Oliveira, J. L. Damasceno, D. C. Tavares, A. A. Batista and G. Von Poelhsitz, *Bioinorg. Chem. Appl.*, 2017, **2017**, 2562780.

67. M. S. Refat, T. Sharshar, K. M. Elsabawy, M. Y. El-Sayed and A. M. A. Adam, *J. Mol. Liq.*, 2016, **222**, 334-349.

Chapter 4

Synthesis, characterization and cytotoxic studies of ruthenium complexes with Schiff bases encompassing biologically relevant moieties

4.1 Introduction

Current widespread interests in the bioinorganic chemistry of ruthenium stems largely from its diverse coordination chemistry and the fact that selected ruthenium complexes have afforded fewer side effects than established platinum-based chemotherapeutic agents [**1**]. The optimal activities of the ruthenium anticancer agents have been ascribed to their capabilities to mimic the biodistribution patterns of iron-containing biomolecules [**2**]. For instance, mechanistic studies have revealed that many ruthenium complexes have high affinity for transferrin receptors on malignant growths [**3**].

Recent progress to enhance drug efficacies of metallopharmaceuticals embrace the hypothesis of designing them with biologically active chaperones [**4**]. The versatility of this drug design approach is elaborated by the wide range of potential ligands that can function as variable site-specific chaperones while improving the pharmacodynamics and pharmacokinetics of the resultant ruthenium complexes [**5**]. For example, metal complex cations of ruthenium coordinated to the biologically active components, ibuprofen or diclofenac, displayed generally improved or comparable cytotoxicity than Cisplatin [**6**].

Herein, we consider carbohydrazide Schiff bases incorporating benzothiazole and uracil moieties, as stabilizing scaffolds for the *trans*-[$Ru^{III}(PPh_3)_2$] core. Moreover, uracil and benzothiazole derivatives are essential pharmacophores in various antitumour agents [**7-9**]. The latter is illustrated in the organic compounds, *N*-formyl-2-(5-nitrothiophen-2-yl)benzothiazole-6-carbohydrazide and 1-(2,3-dihydro-5*H*-1,4-benzodioxepin-3-yl)uracil which presented anticancer effects towards MCF7 breast cancer cells where the mechanism of activities are largely facilitated by inhibition of various enzymatic pathways [**10, 11**]. In addition, synergistic effects between ruthenium complexes with benzothiazole or uracil [**Figure 4.1**] chelating polypyridyl ligands have shown to result in optimal structure-activity relationships [**12, 13**]. For instance, the diamagnetic ruthenium complex salts, *cis*-$[Ru(bpy)_2(uip)]^{2+}$ (bpy = 2,2'-bipyridyl, uip is 2-(5-uracil)-1*H*-imidazo[4,5-*f*][1,10]phenanthroline) and *cis*-$[Ru(bpy)_2(5\text{-}bbtb)]^{2+}$ (bbtb = *bis*(benzothiazol-2-yl)-2,2'-bipyridine) illustrated high DNA intercalating capabilities which culminated into *in vitro* anticancer activities against a wide range of human cancer cells [**12, 13**].

(a) **(b)**

Figure 4.1: *Molecular structures of (a) uracil and (b) benzothiazole.*

In this chapter, we report the formation and characterization of paramagnetic novel ruthenium complexes, *cis-Cl, trans-P*-$[RuCl_2(PPh_3)_2(L)]$ (L = bpc for **1**, ttc for **2** and tpc for **3**) with carbohydrazide Schiff bases containing the benzothiazole (Hbpc, *N*-[1,3-benzothiazole-2-ylmethylidene]pyridine-2-carbohydrazide), uracil moieties (Httc, *N*-((uracil-5-yl)methylene)thiophene-2-carbohydrazide and Htpc, *N*-[(uracil-5-yl)methylidene]pyridine-2-carbohydrazide), see **Figure 4.2**. Biomolecular interactive studies with DNA and BSA and the antioxidant abilities of the above-mentioned metal compounds, as well as two previously isolated ruthenium(II) complexes bearing uracil moieties (*viz. trans*-$[RuCl(PPh_3)_2(Htdp)]$ (Htdp = 5-((thiophen-3-yl)methyleneamino)-6-amino-1,3-dimethyluracil) (**4**) and $[RuCl(PPh_3)(H_3ucp)]$ (H_4ucp = 2,6-*bis*-((6-amino-1,3-

dimethyluracilimino)methylene)pyridine) (**5**)), were explored. Previous studies have shown that compound **5** is benign in the presence of skeletal muscle cells and subsequently illustrated promising insulin-mimetic activities in streptozotocin-induced diabetic rats [**14, 15**]. This provides additional impetus to explore the aforementioned ruthenium complex's *in vitro* activities as a target-specific anticancer metal-based drug.

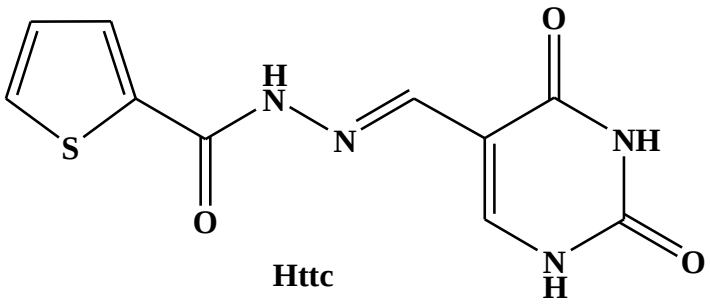

Httc

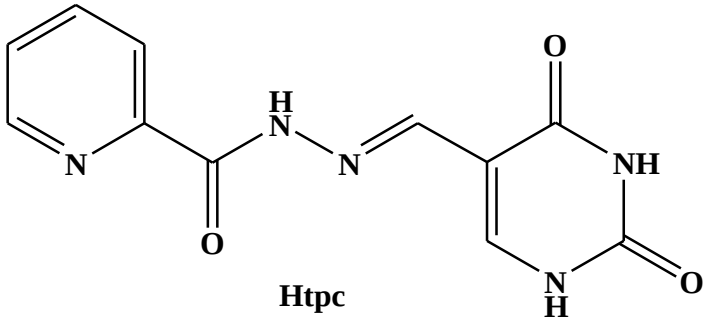

Htpc

Figure 4.2: *Structures of the Httc and Htpc hydrazide Schiff bases.*

4.2 Experimental

4.2.1 *Synthesis of cis-Cl, trans-P-[RuCl$_2$(PPh$_3$)$_2$(bpc)] (1)*

A one-pot reaction consisting of pyridine-2-carbohydrazide (0.0143 g, 104 mmol), benzothiazole-2-carboxaldehyde (0.0170 g, 104 mmol) and *trans*-[RuCl$_2$(PPh$_3$)$_3$] (0.100 g, 0.104 mmol) was carried out in absolute ethanol (30 cm^3). The reaction mixture was heated at reflux for 5 hours. Thereafter, the red solution was cooled and filtered at room temperature. Over a course of several days, red rectangular crystals were formed in the mother liquor which were appropriate for X-ray analysis. Yield: 54 %. M.P: 143.2 – 144.1 ºC. Molar conductivity (DCM, 10^{-3} M): 44.7 ohm^{-1} cm^{-2} mol^{-1}. IR (ν_{max}/cm^{-1}): υ(C=N) 1666 (br, w); *υ*(C=N)$_{benzothiazole}$ 1430 (s); υ(C-N) 1090 (s); υ(Ru-[PPh$_3$]$_2$) 742 (vs), 691 (s). UV-Vis (DCM, ε, M^{-1} cm^{-1}): 278

nm (8950); 339 nm (3810); 352 nm (3820); 392 nm (sh, 3060); 541 nm (2550); 648 nm (sh, 140).

4.2.2 Synthesis of cis-Cl, trans-P-[$RuCl_2(PPh_3)_2$(ttc)] (2)

Equimolar amounts of Httc (0.0276 g, 0.104 mmol) and *trans*-[$RuCl_2(PPh_3)_3$] (0.100 g, 0.104 mmol) were measured out in 20 cm^3 of methanol and heated at reflux for 3 hours. The resulting green solution was cooled, filtered and allowed to cool to room temperature. X-ray quality green crystals were formed in the mother liquor *via* slow evaporation. Yield: 73 %. M.P: 226.9 – 228.2 ºC. Molar conductivity (DCM, 10^{-3} M): 49.7 ohm^{-1} cm^{-2} mol^{-1}. IR (ν_{max}/cm^{-1}): ν(N-H)$_{uracil}$ 3649 (br, m); ν(C=O)$_{uracil}$ 1716 (s), 1675 (m); ν(C=N) 1597 (br, m); ν(thiophene) 1424 (s), 1228, 1180 (m); (C-N) 1090 (m) ν(Ru-[PPh_3]$_2$) 744 (m), 691 (vs). UV-Vis (DCM, ε, M^{-1} cm^{-1}): 275 nm (6170); 298 nm (4580); 400 nm (1850); 670 nm (15).

4.2.3 Synthesis of cis-Cl, trans-P-[$RuCl_2(PPh_3)_2$(tpc)] (3)

A reaction mixture of Htpc (0.0252 g, 104 mmol) and *trans*-[$RuCl_2(PPh_3)_3$] (0.100 g, 0.104 mmol) in methanol (20 cm^3) was heated under reflux for 3 hours. The subsequent brown-green solution was cooled and filtered. After a week of slow diffusion, green cubic crystals formed in the mother liquor which were submitted for X-ray analysis. Yield: 77 %. M.P: 229.9 – 232.2 ºC. Molar conductivity (DCM, 10^{-3} M): 42.4 ohm^{-1} cm^{-2} mol^{-1}. IR (ν_{max}/cm^{-1}): ν(N-H)$_{uracil}$ 3627 (w); ν(C=O)$_{uracil}$ 1715 (m), 1670 (s); ν(C=N)$_{imino}$ 1571 (br, m); (C-N) 1090 (m); ν(Ru-[PPh_3]$_2$) 742 (s), 691 (vs). UV-Vis (DCM, ε, M^{-1} cm^{-1}): 281 nm (3200); 303 nm (3060); 410 nm (970); 687 nm (10).

4.3 X-ray crystallography

Crystallographic data for **1** – **3** were attained using a Bruker Apex Duo equipped with an Oxford Instruments Cryojet operating at temperature of 100(2) K and an Incoatec microsource

functioning at 30 W power. Crystal and structure refinement information are summarized in **Table 4.4** while their experimental and geometrical parameters are given in **Tables 4.5 – 4.7**. The X-ray beams were generated with MoKα using radiation exposures during data collection at a crystal-to-detector distance of approximately 50 mm.

Data accumulation were done under the following conditions: phi and omega scans with exposures taken at 30 W X-ray power and 0.50º frame widths with APEX2 [**12**]. Data reduction was executed with the aid of the SAINT program [**12**]. In particular, scan speed scaling, standard Lorentz and polarization correction factors as well as outlier rejection were applied to the acquired data. Furthermore, the reduced data was further refined with SADABS semi-empirical multi-scan absorption correction [**16**]. In addition, WinGX [**17**] and SHELX-2016 [**18**] programs were utilized as direct methods to solve the crystal structures. All non-hydrogen atoms were located using the difference density map and anisotropically refined with SHELX-2016 [**18**]. All hydrogen atoms were included as idealized contributors in the least squares process. Their positions were calculated by a standard riding model with C-$H_{methylene}$ distances of 0.99 Å and U_{iso} = 1.2 U_{eq}, C-$H_{aromatic}$ distances of 0.93 Å and U_{iso} = 1.2 U_{eq}, and C-H_{methyl} distances of 0.98 Å and U_{iso} = 1.5 U_{eq}.

4.4 Computational details

Ab initio calculations were conducted using the Gaussian 09W software package [**19**]. The geometry optimizations of the individual metal complexes were performed using DFT calculations by employing the LANL2DZ basis set in conjunction with the B3LYP exchange-correlation functional [**20**]. The starting conformers were generated by deleting the solvent molecules of crystallization while one of the independent molecules of **1** was omitted. In particular, molecule **I** was considered for the DFT calculations as the metal centres in both the independent molecules have identical coordination environments, see **Figure 4.19**. Computational algorithms utilized during the optimisations of the respective metal complexes were validated by the good comparison between their corresponding actual and computed bond angles and distances. The minute differences in the simulated and experimental geometrical parameters are attributed to the lack of short contacts occurring with the gas-phase optimized conformers. Method validation was supported by the frequency calculations which showed that

the vibrational bands of the metal complexes all have positive Eigen values. The good comparison between the optimized and calculated conformers are emphasized by the reasonably low Root-Mean-Square-Deviation (RMSD) values, see **Figures 4.28** – **4.30**.

4.5 Results and discussion

4.5.1 *Synthesis and spectral characterization of **1**, **2** and **3***

The paramagnetic ruthenium compounds were produced in moderate to good conversion yields from equimolar reactions of *trans*-[$RuCl_2(PPh_3)_3$] with *N*-[1,3-benzothiazole-2-ylmethylidene]pyridine-2-carbohydrazide (Hbpc) and *N*-[(uracil-5-yl)methylidene]pyridine-2-carbohydrazide (Htpc),and *via* a one pot synthesis with *N*-((uracil-5-yl)methylene)thiophene-2-carbohydrazide (Httc) and *trans*-[$RuCl_2(PPh_3)_3$]. All the Schiff base ligands function as monoanionic bidentate chelators coordinating *via* the N_{imino} and O_{enol} donor atoms, which are characteristic of the preferential coordination modes of other hydrazide Schiff base chelating-ligands [**21-23**]. The ruthenium(III) compounds **1-3** displayed high solubility in most aprotic and chlorinated solvents (*e.g.* DMSO and DCM) as well as moderate solubility in alcoholic media as well as were found to be non-electrolytic in DCM [**24**].

Frequency simulations assisted with the assignments of the experimental vibrational bands observed in the solid-state FTIR spectra of **1** – **3**, see **Figures 4.3 – 4.8**. For instance, the vibrations of the imino bonds are simulated at 1514 cm^{-1} (for **1**), 1478 cm^{-1} (for **2**) and 1527 cm^{-1} (for **3**) while the corresponding real infrared stretches were observed at 1666, 1597 and 1571 cm^{-1} as medium-intensity and broad vibrational bands [**25, 26**]. Evidence of coordination *via* the imino nitrogen atoms in **2** and **3** manifest from the shifting of the frequencies of their imino bonds to higher wavenumbers, from 1567 and 1543 cm^{-1} for Httc and Htpc, respectively [**27**]. Vibrations of the ruthenium-to-phosphorus bonds of **1** – **3** were calculated at 538 cm^{-1} whereas the analogous bonds require higher energies to experimentally vibrate at 691 (for **1** - **3**), 742 (for **1** and **3**) and 744 (for **2** only) cm^{-1}. Moreover, the latter experimental metal-to-ligand vibrations are quite comparable with other metal complexes with the *trans*-$[Ru(PPh_3)_2]^{2+}$ core [**28**]. Furthermore, the actual high-intensity ketonic uracil [1716 and 1675 cm^{-1} for **2** and 1715 and 1670 cm^{-1} for **3**] vibrations are in accordance with those computed

[1725 and 1690 cm^{-1} for **2** and 1724 and 1688 cm^{-1} for **3**]. Interestingly, the aliphatic free ligand-based vibrational bands emanating from the $C{=}O_{amide}$ (at 1625 cm^{-1} for Httc and 1666 cm^{-1} for Htpc) and $N\text{-}H_{amide}$ (at 2963 cm^{-1} for Httc and 2900 cm^{-1} for Htpc) bonds are absent in the experimental IR spectra of their metal complexes which are representative of the loss of the carbonyl group and N-H proton due to enolization, see **Figure 4.9** [**29, 30**]. In addition, the enolic forms of the chelated Schiff bases show no *ν(*OH) signals in the experimental IR spectra of **2** and **3** which affirms that successive coordination of the Schiff bases resulted in the deprotonation of the enol hydrogens of the respective chelators. The IR spectra of gas-phase models of **1** and **2** show that their uracil amido bonds occur at highest energies (3641 and 3609 cm^{-1} for **2** and 3640 and 3610 cm^{-1} for **3**) while the analogous bonds appears as medium-intensity stretches at 3649 and 3627 cm^{-1} in their experimental IR spectra, respectively. Readily distinguishable vibrational bands observed in the FTIR spectra of **1** – **3**, appear mutually at 1090 cm^{-1} which are assigned to the vibrations of their aliphatic N-N bridge. Similarly, the *ν*(thiophene) [1180, 1228, 1424 cm^{-1} for **2** and 1151, 1228, 1415 cm^{-1} for Httc] and $\nu(C{=}N)_{benzothiazole}$ [1430 cm^{-1} for **1**] signals occur in similar regions compared to other compounds, *e.g. trans*-$[RuCl(PPh_3)_2(Htdp)]$ (H_2tdp = 5-((thiophen-3-yl)methyleneamino)-6-amino-1,3-dimethyluracil) and $(\mu\text{-Htba,Cl})_2[RuCl(PPh_3)]_2$ (Htba = *N*-(thiophene)methyl-benzoxazole-2-amine) [**31, 32**].

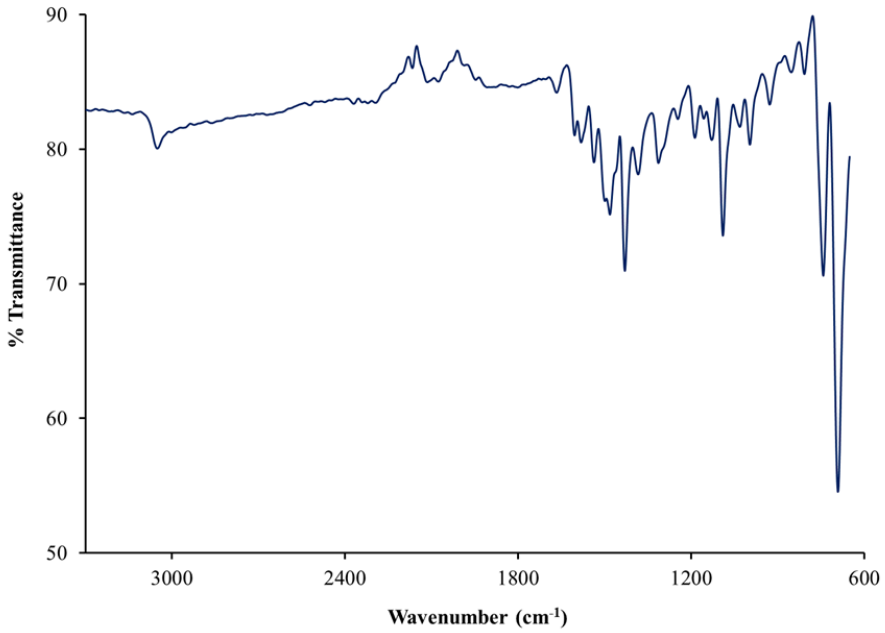

Figure 4.3: *IR spectrum of **1** between 3300 and 600 cm^{-1}.*

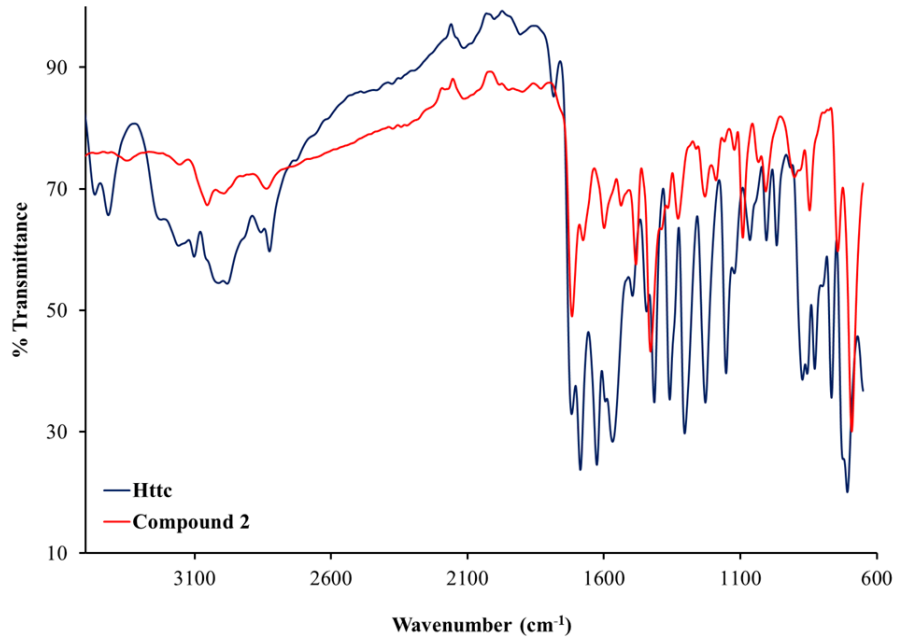

Figure 4.4: *Overlay IR spectra of the free-ligand, Httc and its metal complex, **2** between 3500 and 600 cm^{-1}.*

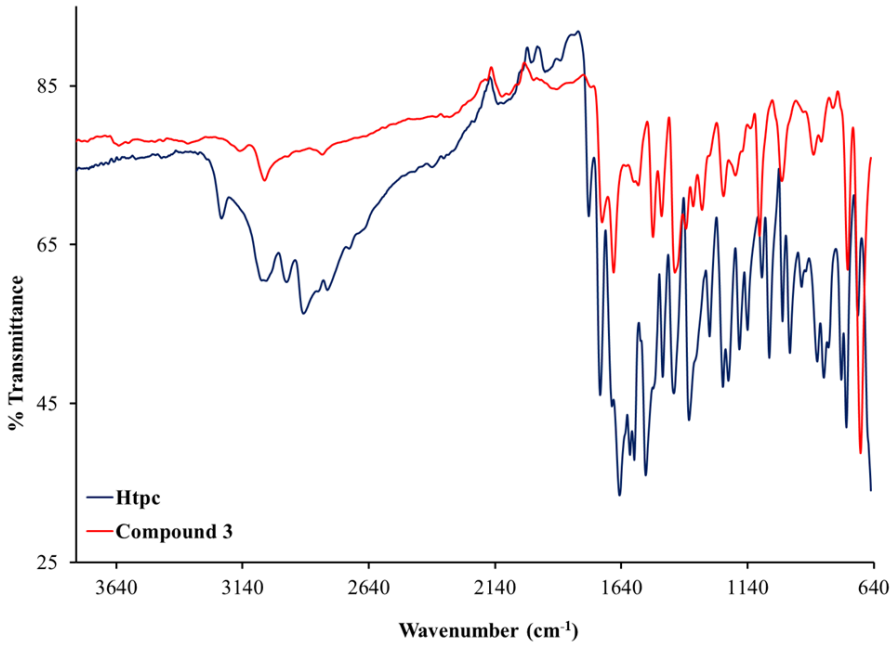

Figure 4.5: *Overlay IR spectra of the free-ligand, Htpc and its metal complex,* ***3*** *between 3800 and 640 cm^{-1}.*

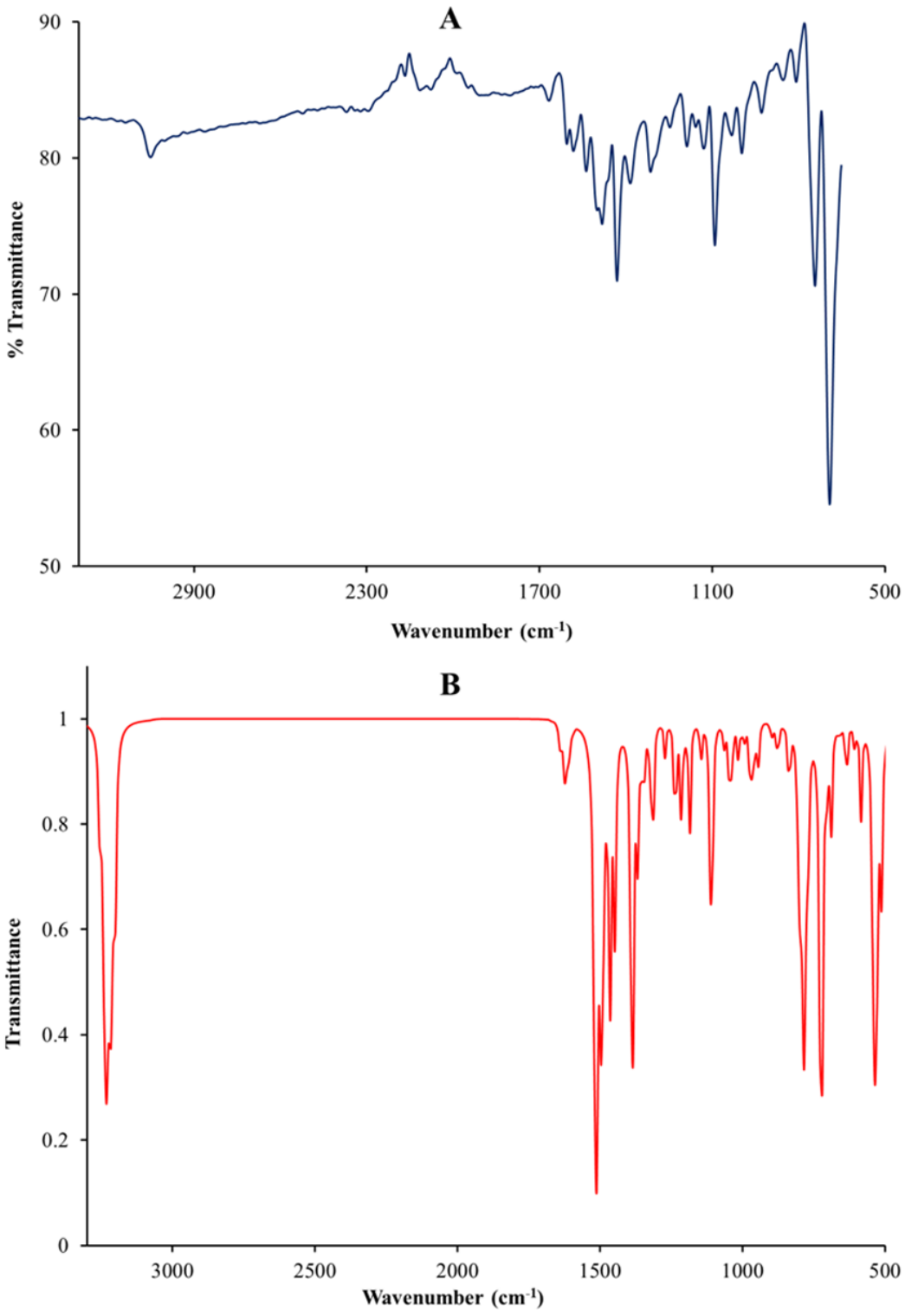

Figure 4.6: *Experimental (**A**) and simulated (**B**) IR spectra of **1**.*

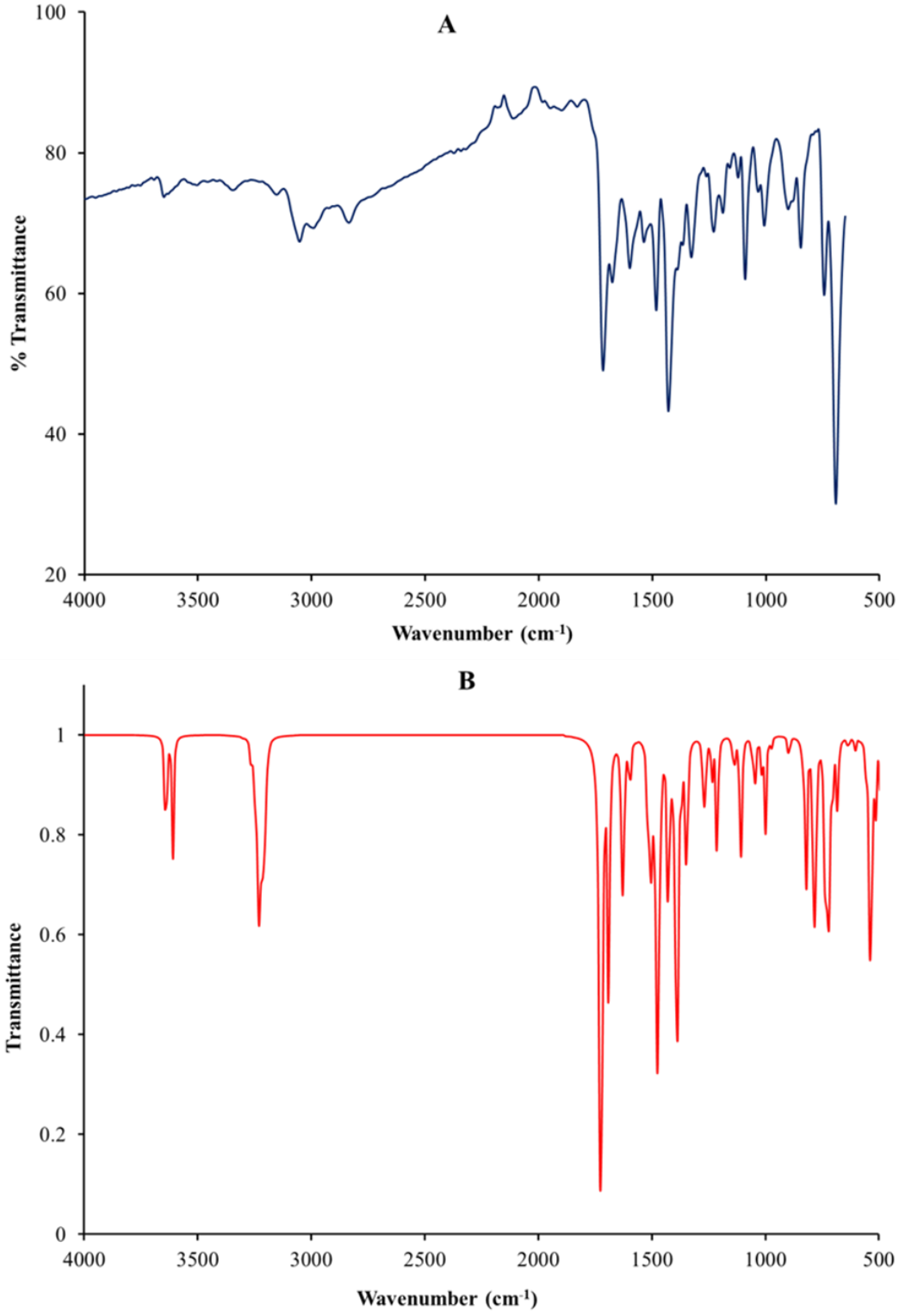

Figure 4.7: *Experimental (**A**) and simulated (**B**) IR spectra of **2**.*

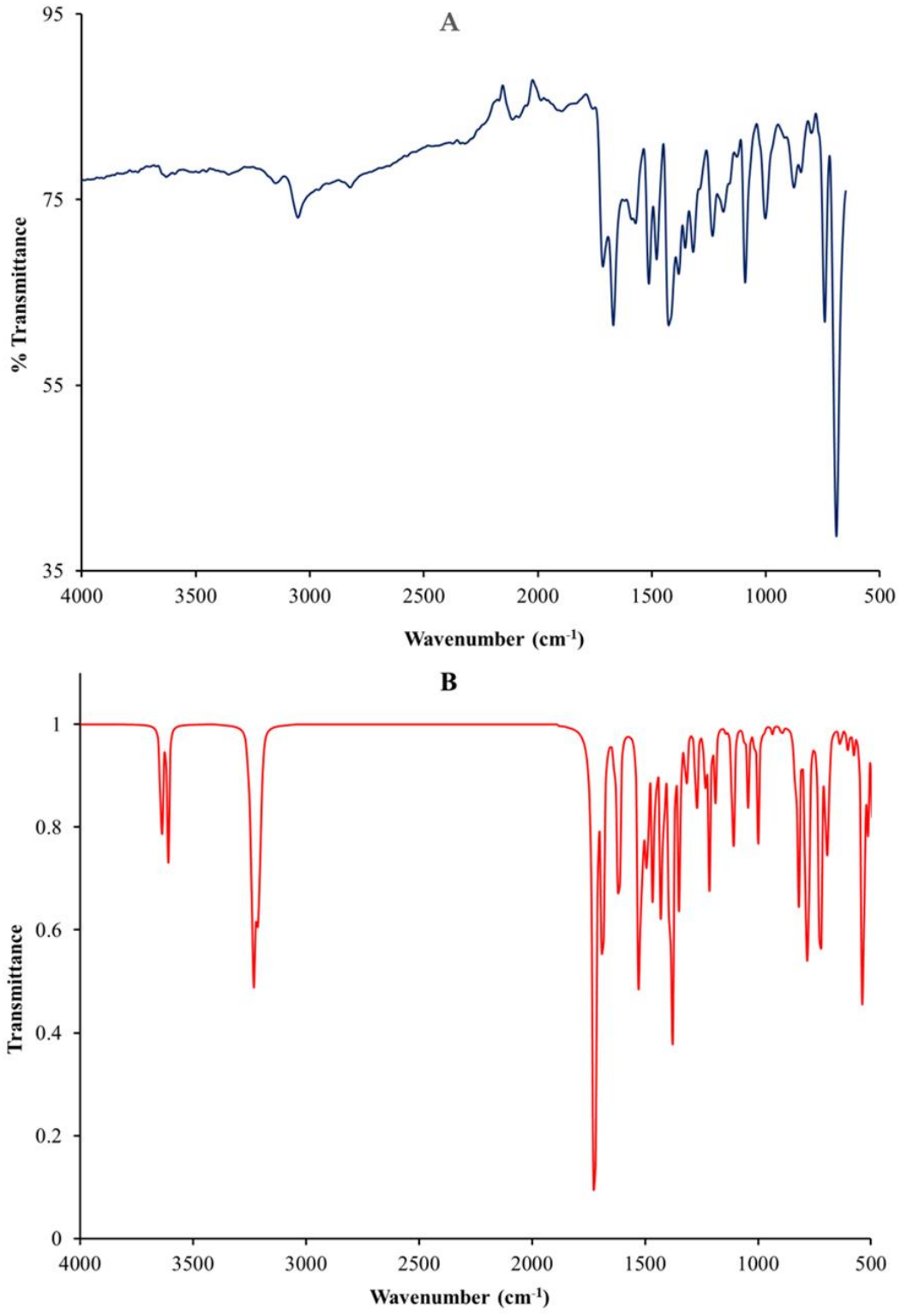

Figure 4.8: *Experimental (**A**) and simulated (**B**) IR spectra of **3**.*

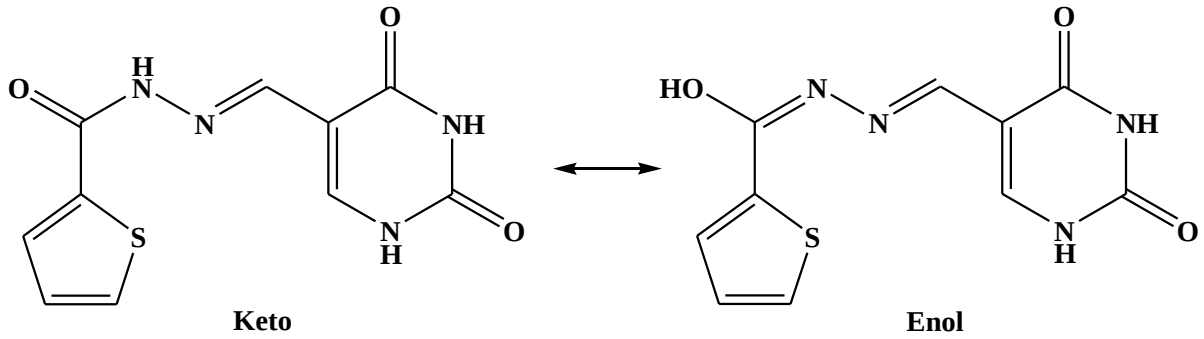

Figure 4.9: *An example of the keto-enol tautomerization occurring for the Httc free-ligand.*

A sequence of intra-ligand transitions ($\pi - \pi^*$) below 400 nm were observed in the electronic spectra of the metal complexes whilst ligand-to-metal charge transfer ($L_\pi - T_{2g}$) (LMCT) bands were noticeable within the range of 400 – 600 nm, obscuring weaker bands, see **Figures 4.10 – 4.12**. Metal-based electronic transitions with low extinction coefficients were observed between 648 – 687 nm and these electronic transitions can be readily assigned to the $^2T_{2g}$ - $^2A_{2g}$ excitation which is typical for ruthenium(III) complexes [**33, 34**]. In fact, the experimental electronic transitions of the respective metal complexes resemble the orbital-contributions within their corresponding simulated frontier orbitals. In particular, their Highest-Occupied-Molecular-Orbital (HOMO) configurations mutually show substantial contributions from the d_{xz} and $p\pi$(Cl) orbitals as well as the *pi*-orbitals originating from the respective Schiff base chelators, refer to **Table 4.1**. The latter rationalizes the occurrence of the intra-ligand transitions, LMCT bands and metal-based electronic transitions observed in their individual UV-Vis spectra. In addition, the presence of the d_{x2-y2} orbitals in the LUMO configurations of each metal complex suggests that the experimental metal-based absorption bands are attributed to electronic transitions occurring from the ground state, d_{x2-y2} to the excited state, d_{xz} orbitals.

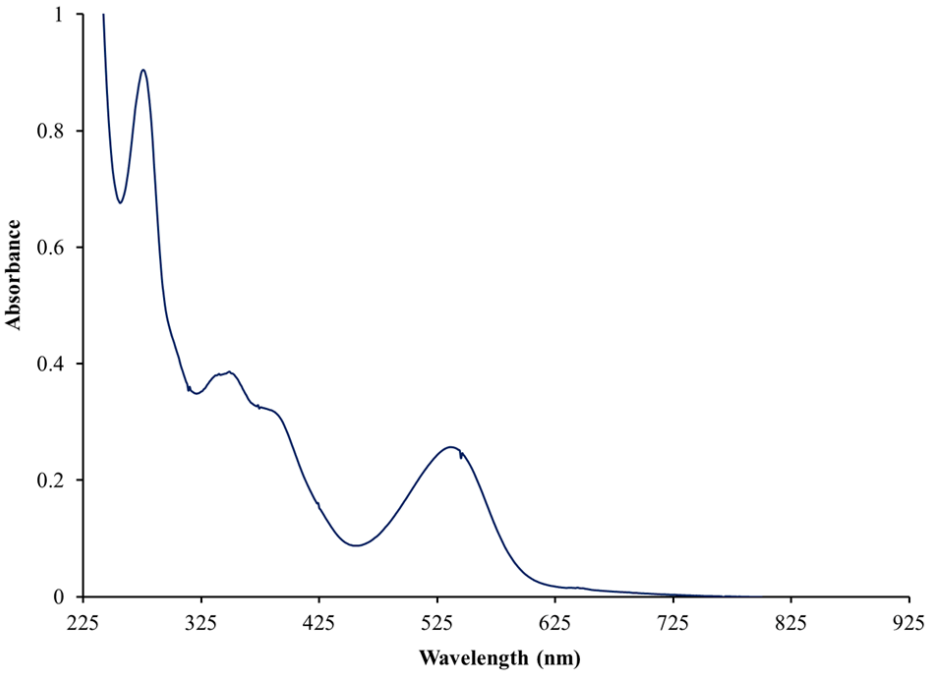

Figure 4.10: *UV-Vis spectrum of **1**.*

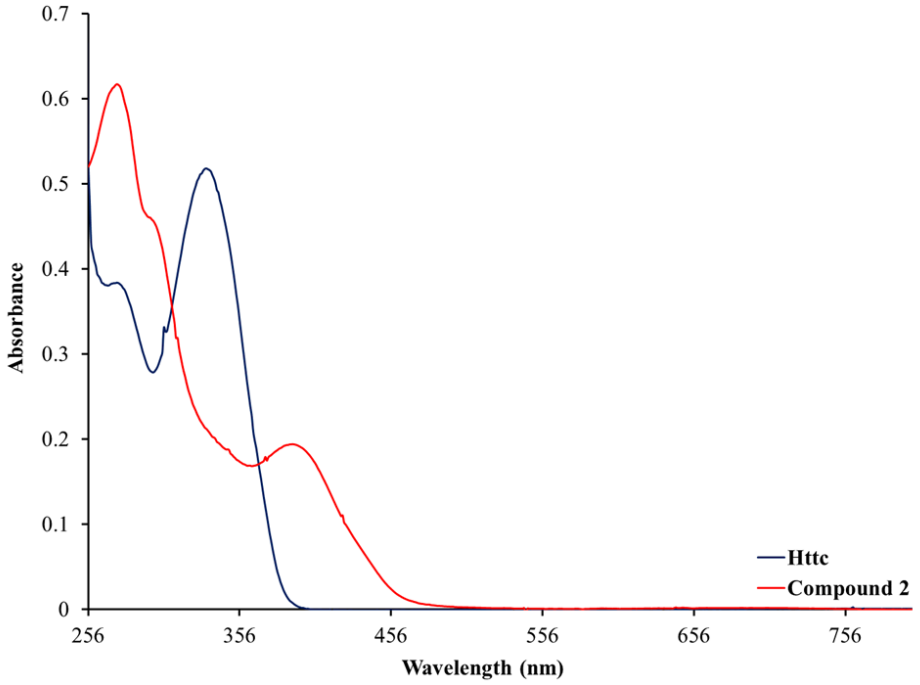

Figure 4.11: *Overlay UV-Vis spectra of metal complex **2** and its free-ligand, Httc.*

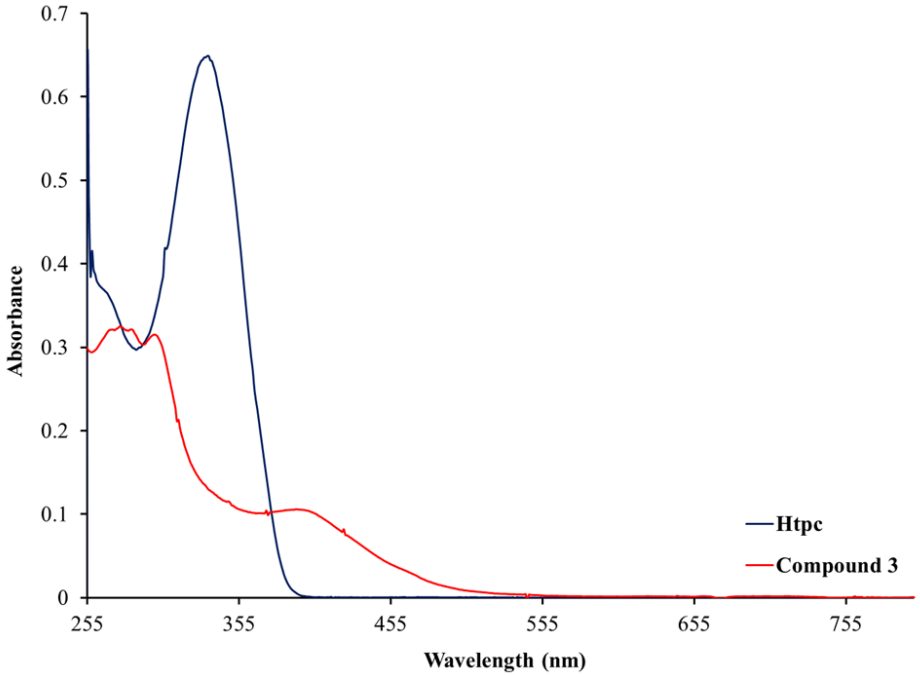

Figure 4.12: *Overlay UV-Vis spectra of metal complex **3** and its ligand, Htpc.*

Table 4.1: *Selected frontier orbitals of metal complexes **1** – **3**.*

HOMO	LUMO
1	
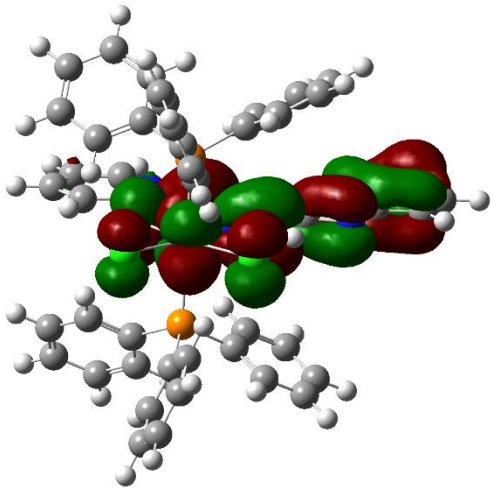	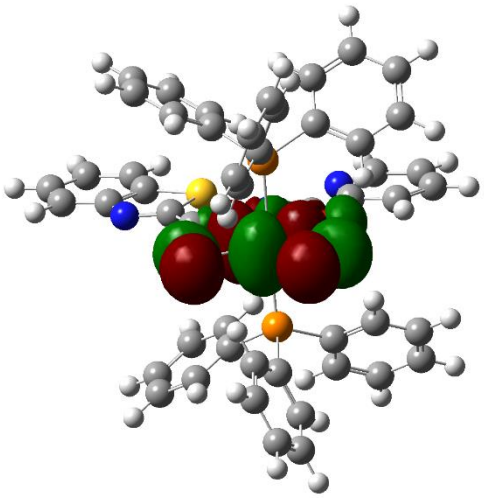
2	

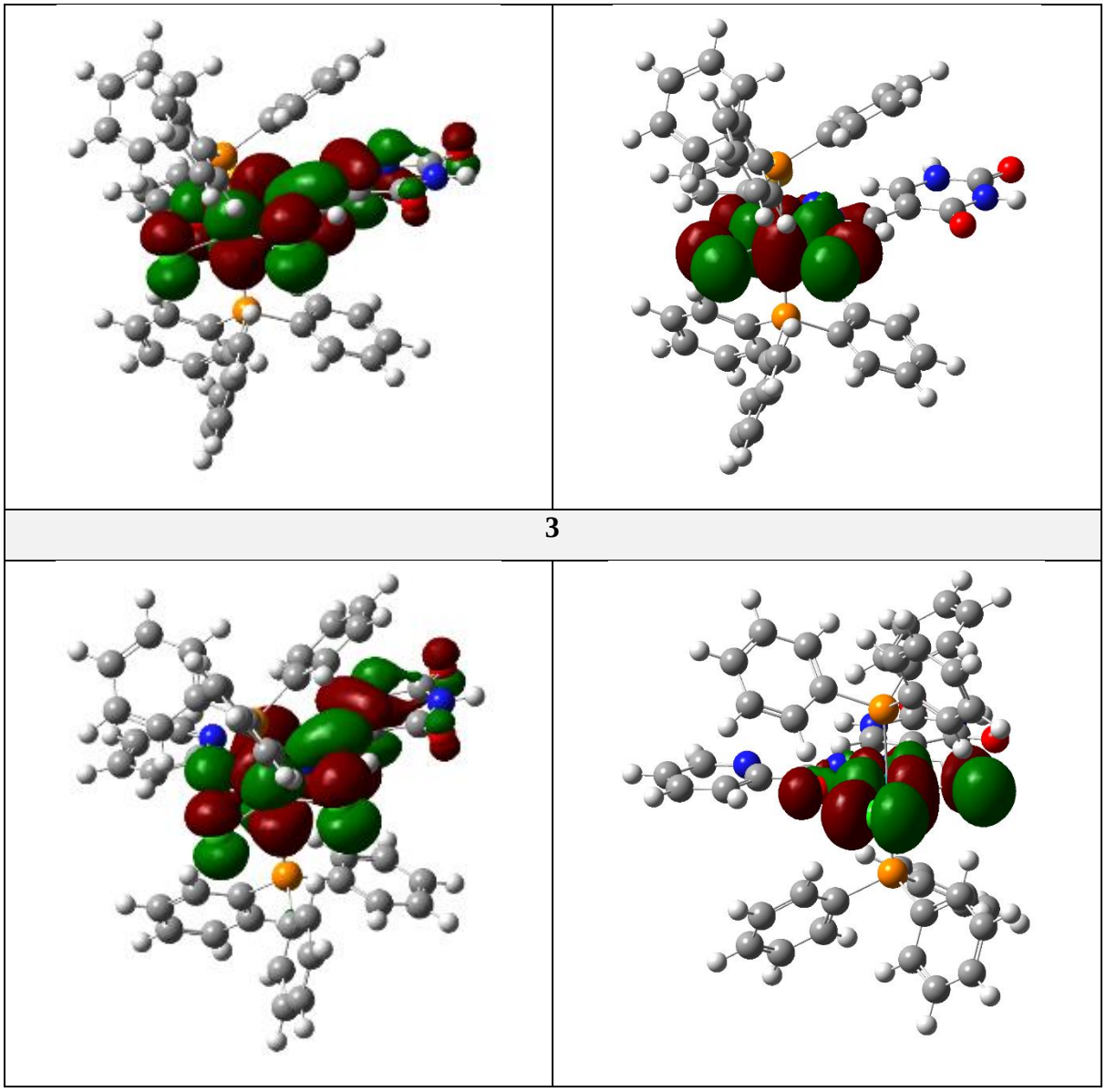

3

ESR spectra were obtained in the solid state at room temperature and in dichloromethane at low temperature, see **Figures 4.13 – 4.15**. Classical isotropic singlets were obtained for each metal complex in the solid state (at 298 K) which gave rise to *g*-values (see **Table 4.2**) comparable to other low spin d^5 ruthenium compounds with $S = ½$ [**35, 36**]. Deviations in the ESR spectra from the typical rhombic ESR signal pattern is reflective of the distortion within the octahedral geometries of **1** – **3** [**37, 38**]. Low temperature (at 77 K) liquid-state ESR spectroscopy of **1** also reveals an almost identical isotropic singlet (*g*-value = 2.33) to that of the solid-state ESR while **2** and **3** shows three distinct signals which suggest longer spin-relaxation lifetimes [**39**]. The ESR parameters of complex **2** and **3** are indicative to those

attained for another paramagnetic ruthenium(III) compound, *trans*-[$Ru(PPh_3)_2(L^1)Cl_2$] (where L^1 = 2-hydroxyacetophenone) at 77 K in a 1:1 dichloromethane: toluene solvent mixture [**40**].

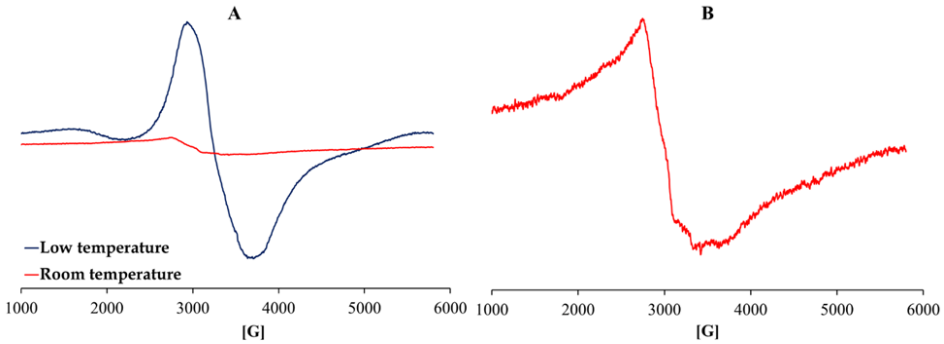

Figure 4.13: *Overlay ESR spectra of **1** at low and room temperatures in the liquid and solid states, respectively.* (**B**): *ESR spectrum of **1** in the solid state at room temperature.*

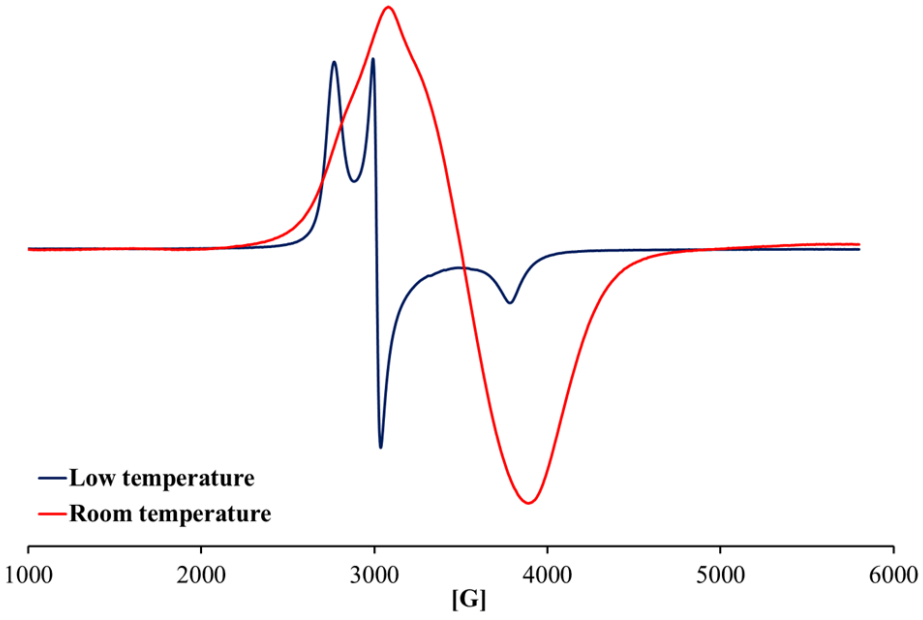

Figure 4.14: *Overlay ESR spectra of **2** at low and room temperatures in the liquid and solid states, respectively.*

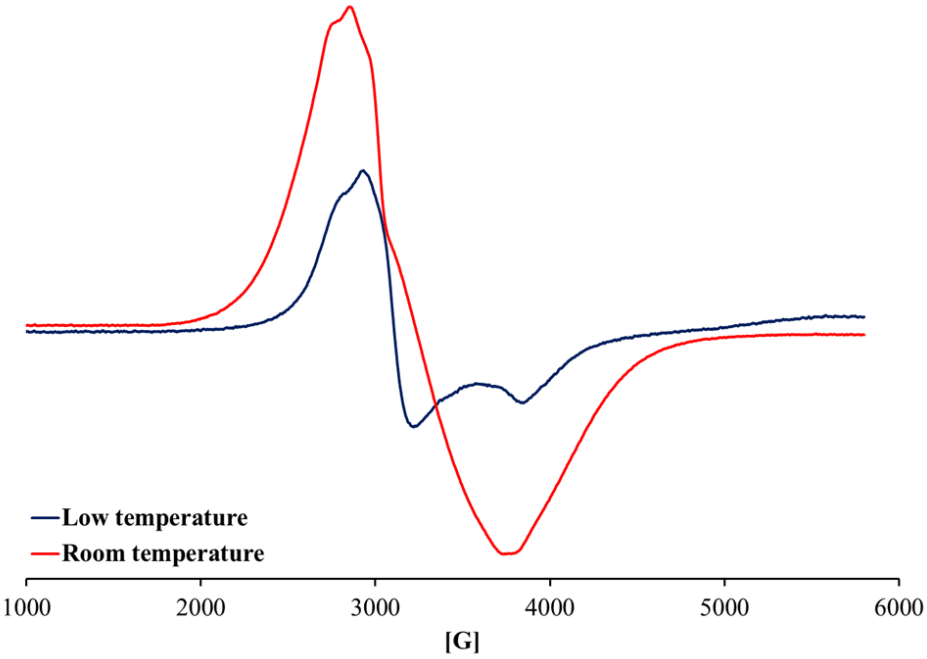

Figure 4.15: *Overlay ESR spectra of **3** at low and room temperatures in the liquid and solid states, respectively.*

Table 4.2: *ESR spectral analysis of metal complexes **1** - **3** at room and low temperatures.*

Sample	State	Temperature	g_x	g_y	g_z	g_{iso}
1	Solid	298 K	-	-	-	2.15
	Liquid	77 K	-	-	-	2.33
2	Solid	298 K	-	-	-	1.99
	Liquid	77 K	1.84	2.32	2.52	-
3	Solid	298 K	-	-	-	2.17
	Liquid	77 K	1.82	2.18	2.39	-

*4.5.2 Electrochemistry of **1** – **3***

The cyclic voltammograms (CVs) for **1** (E_{pa} = 0.39 V *vs* Ag | AgCl), **2** (E_{pa} = 0.47 V *vs* Ag | AgCl) and **3** (E_{pa} = 0.73 V *vs* Ag | AgCl) each exhibit a single redox process which are ascribed to the Ru(III)/ Ru(II) (for **1** and **2**) and the Ru(IV)/ Ru(III) (for **3**) redox couples, respectively, see **Figures 4.16** – **4.18** [**41-43**]. Mutually, the peak current ratios (I_{pa}/I_{pc}) are close to one for the redox processes of the individual metal complexes. In addition, the redox couples for **1** and **3** [ΔE_p(**1**) = ΔE_p(**3**) = 90 mV] are classified as reversible as their peak-to-peak potential separations (see **Table 4.3**) are equivalent to that of the standard, ferrocene (ΔE_p = 90 mV). However, the wider E_p value of 160 mV for **2** illustrate slow electron transfer kinetics occurring during its quasi-reversible redox process. Squarewave voltammetry afforded a solitary peak within the voltammograms of each metal complexes and thus confirmed the presence of a single redox interconversion.

The Randels-Sevcik equation was used to establish diffusion-controlled behaviour for the individual redox processes occurring in all metal complexes:

$$I_{pa} = 0.4463nFA(nF/RT)^{1/2} D^{1/2} v^{½} C_{complex}$$

Where I_{pa} refers to the cathodic peak current, electrode area (A), the number of electrons transferred (n), complex concentration ($C_{complex}$), the scan rate (v) and the diffusion coefficient (D). The plots of I_{pa} *vs* $v^{½}$ displays linear relationships which shows each redox process to be diffusion-controlled.

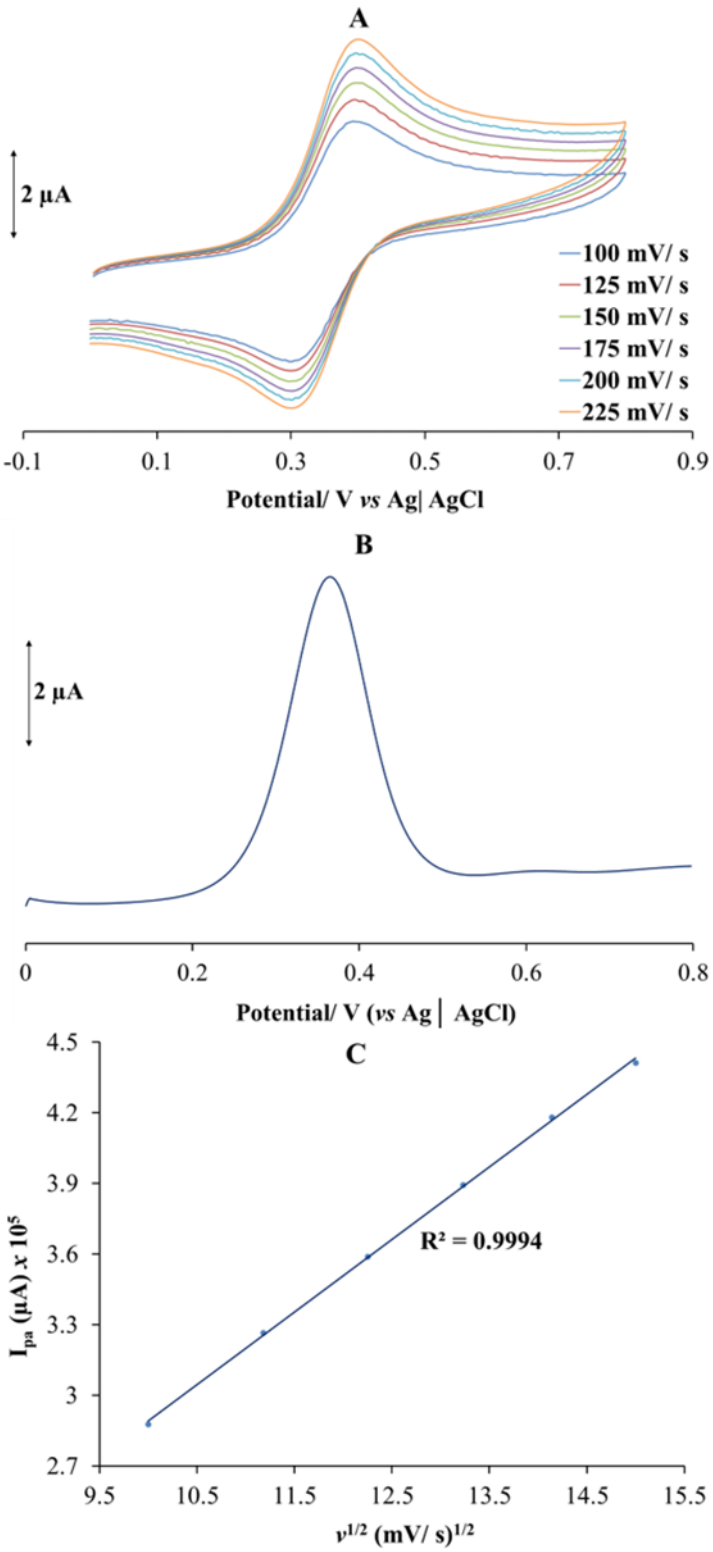

Figure 4.16: *(**A**): Overlay CVs of **1** at variable scan rates. (**B**): Square-wave voltammogram of **1** at 100 mV/s. (**C**): The relationship between the square root of scan rate ($v^{1/2}$) and anodic peak potential (I_{pa}) as per the overlay CV profile.*

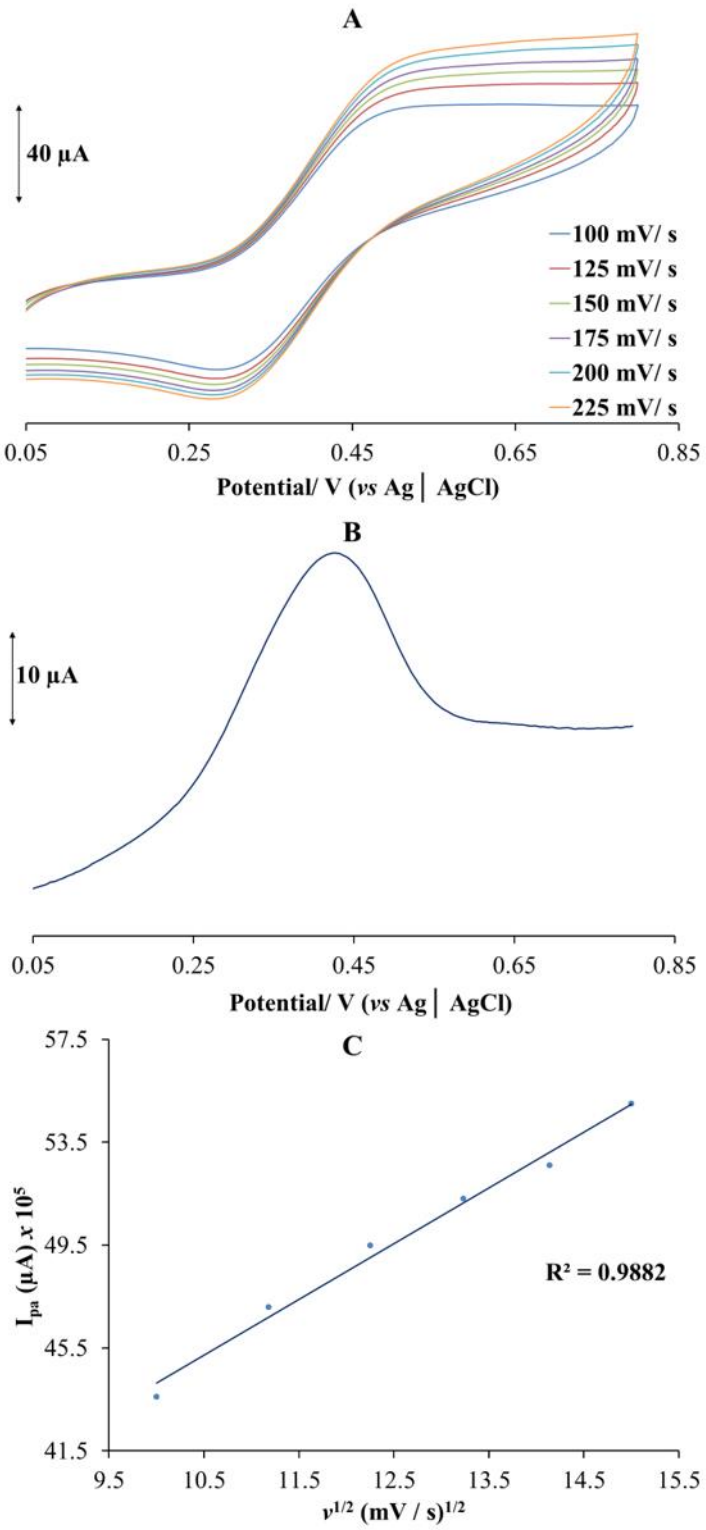

Figure 4.17: *(**A**): Overlay CVs of **2** at variable scan rates. (**B**): Square-wave voltammogram of **2** at 100 mV/s. (**C**): The relationship between the square root of scan rate ($v^{1/2}$) and anodic peak potential (I_{pa}) as per the overlay CV profile.*

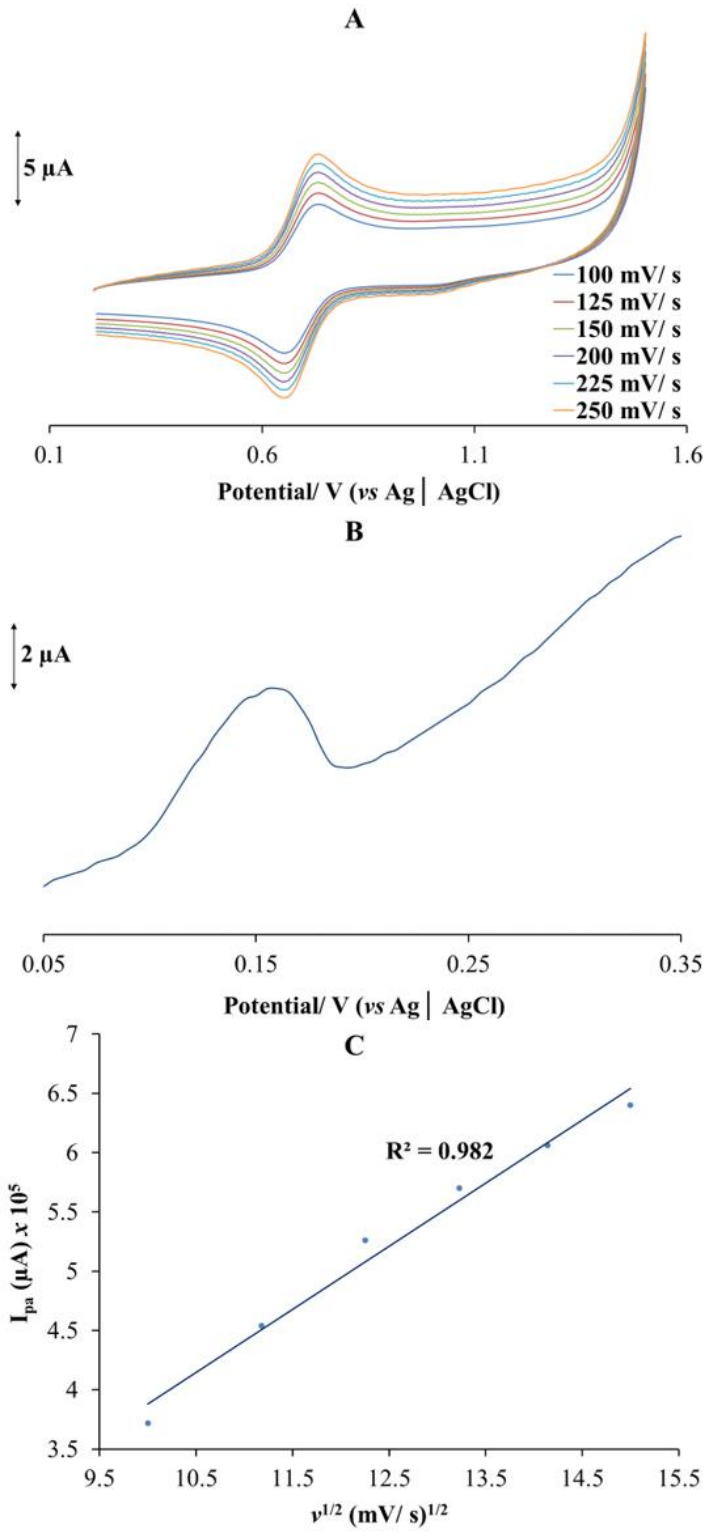

Figure 4.18: *(**A**): Overlay CVs of **3** at variable scan rates. (**B**): Square-wave voltammogram of **3** at 100 mV/s. (**C**): The relationship between the square root of scan rate ($v^{1/2}$) and anodic peak potential (I_{pa}) as per the overlay CV profile.*

Table 4.3: *Selected electrochemical potentials (versus Ag|AgCl) of **1** - **3** at 100 mV/s.*

Compound	E_{pa} (V)	E_{pc} (V)	ΔE_p (V)	$E_{½}$ (V)
1	0.39	0.30	0.09	0.045
2	0.47	0.31	0.16	0.080
3	0.73	0.64	0.09	0.045

*4.5.3 Crystallographic descriptions of **1**, **2** and **3***

Each metal complex possesses a triclinic crystal system and crystallizes in a $P\bar{1}$ space group, see **Table 4.4**. The triclinic unit cell of **1** is occupied by two crystallographically independent molecules whereby each is adjacent to three ethanol molecules of crystallization, see **Figure 4.19**. The crystal lattice is largely stabilized by classical hydrogen-bonding between the benzothiazole nitrogen atoms of molecules **II** and the polar hydrogen atoms of adjacent ethanol molecules of crystallization [(**A**) O-H···N1 = 2.071 Å], see **Figure 4.21**. The aforementioned intermolecular hydrogen-bonds affords an extended network [**B** = 1.903 Å and **C** = 1.923 Å] with two additional ethanol molecules. In addition, the four ethanol molecules positioned next to molecule **I** affords a 6-membered ring with hydrogen bonds ranging from 1.941 to 1.989 Å. Mutually, these networks of hydrogen-bonding interactions allow the molecules of **1** to align with [*a*]-axis.

Hydrogen-bonded dimers of **2** are formed by intramolecular interactions [O3···H'-N3'/ O3'···H-N3= 1.973 Å] between uracil moieties of neighbouring molecules, see **Figure 4.22**. These dimers are cross-linked by methanol molecules of crystallization at N4-H···$O_{methanol}$ = 1.983 Å, (O-H)$_{methanol}$···$O_{methanol}$ = 1.965 Å and (O-H)$_{methanol}$···Cl2 = 2.3371 Å, see **Figure 4.23**. Consequently, the molecules of **2** are orientated co-planar with the [*a*]-axis and perpendicular to the [*c*]-axis. Similarly, molecules of **3** run co-planar with the [*a*]- and [*b*]-axes which is facilitated by the same hydrogen-bonding pattern as observed, *viz.* uracil to uracil hydrogen-bonding interactions [O4···H'-N3'/ O4'···H-N3= 1.961 Å], see **Figure 4.24**. In addition, the crystal lattice of **3** are enforced by the bridging of methanol molecules of crystallization with a series of hydrogen-bonding interactions [N5-H···$O_{methanol\text{-}1}$ = 1.929 Å, (O-H)$_{methanol\text{-}1}$ ···Cl2 = 2.0809 Å, (O-H)$_{methanol\text{-}1}$ ···$O_{methanol\text{-}2}$ = 2.143 Å and (O-H)$_{methanol\text{-}2}$···N1 = 2.3371 Å].

As the structural features of both molecules of complex **1** are nearly identical, only the geometrical parameters of molecule **I** will be discussed. Solid-state structures of the metal complexes show that each ruthenium atom is at the centre of distorted octahedrons where the basal plane are made up of the $N_{imino}O_{amide}$ donor set of the individual chelators and the corresponding chloride co-ligands, see **Figures 4.25** – **4.27**. The basal plane is reinforced by the bulky *trans*-[$Ru(PPh_3)_2$] unit where each metal complex has non-equidistant Ru-P bonds for **1** [Ru-P1= 2.410(1) Å and Ru-P2 = 2.434(1) Å], **2** [Ru-P1= 2.4273(6) Å and Ru-P2 = 2.4020(6) Å] and **3** [Ru-P1= 2.4236(5) Å and Ru-P2 = 2.4082(5) Å] while their *trans-axial* P-Ru-P backbones essentially affords linear bond angles of 179.55(5)º, 177.67(2)º and 177.47(2)º, respectively. Computationally, the respective Ru-P bonds [Ru-P1 = 2.5188 Å, Ru-P2 =2.5186 Å for **1**, Ru-P1 = 2.5172 Å, Ru-P =2.5172 Å for **2** and Ru-P1 = 2.5163 Å for **3**] of each metal complex are essentially equal, which is typified by the optimized conformers computed in the gas phase [**44**]. As expected, the experimental Ru-P bonds of **1** – **3** are longer than that of other ruthenium(II) compounds, *e.g.* [$RuH(CO)(SCN)(PPh_3)_3$], due to the lower acidic character of the metal centre [**45**].

The *trans*-influences imposed on the chloro co-ligands by their opposing $N_{imino}O_{enol}$ donor sets are clearly visible in the optimized [Ru-Cl1 = 2.4292 Å and Ru-Cl2 = 2.4420 Å for **1,** Ru-Cl1 = 2.4366 Å and Ru-Cl2 = 2.4289 Å for **2**, Ru-Cl1 = 2.4321 Å and Ru-Cl2 = 2.4358 Å for **3**] and solid-state structures [Ru-Cl1 = 2.338(1) Å and Ru-Cl2 = 2.329(1) Å for **1,** Ru-Cl1 = 2.3398(7) Å and Ru-Cl2 = 2.3323(6) Å for **2**, Ru-Cl1 = 2.3492(7) Å and Ru-Cl2 = 2.3214(5) Å for **3**] where their corresponding Ru-Cl bonds differ for each metal complex. These ruthenium coordination bonds related well with analogous bonds found within other paramagnetic ruthenium(III) complexes [**46**].

Indicatively, the ruthenium-enol oxygen bonds of **1** – **3**]ranging from 2.017(3) to 2.020(3) Å] are close to the lower limit found for Ru-O_{enol} bonds [2.029(1) – 2.099(2) Å] of other ruthenium hydrazide complexes [**47, 48**]. Therefore, the comparative analysis of these coordination bonds provide sufficient evidence that enolisation occurred in each ligand, followed by the deprotonation of the enol-form prior to coordination [**48**]. Disparity found in the Ru-N_{imino} bonds between the experimental [2.079(5) Å for **1**, 2.076(2) Å for **2** and 2.085(2) Å for **3**] and calculated [2.1084 Å for **1**, 2.1260 Å for **2** and 2.1179 Å for **3** Å] structures emphasizes the

influence of the intermolecular interactions' stabilizing effects for the individual solid-state structures.

Deviations from octahedral ideality (*i.e.* 90º) are observed by the markedly smaller equatorial bite angles [N3-Ru-O1 = 76.50(1)º for **1**, N2-Ru-O1 = 76.71(1)º for **2** and N3-Ru-O1 = 76.80(6)º for **3**]. Furthermore, the *cis*-chloride co-ligands [Cl1-Ru-Cl2 = 100.29(5)º for **1**, 99.90(2)° for **2** and 98.70(2)° for **3**] are forced further apart. Also, the expected linear angles [Cl1-Ru-N3 = 166.6(1)º and Cl2-Ru-O1 = 169.6(1)º for **1**, Cl1-Ru-O1 = 173.55(5)º and Cl2-Ru-N2 = 163.22(6)º for **2** as well as Cl1-Ru-N3 = 164.68(5)º and Cl2-Ru-O2 = 173.38(4)º for **3**] which constitute their corresponding equatorial planes deviate from linearity. The enolic form of the respective carboim chelators are clearly established by comparing the uracil ketonic bonds of **2** [C10-O2 = 1.212(3) Å and C9-O3 = 1.226(4) Å] and **3** [C9-O2 = 1.218(3) Å and C10-O3 = 1.223(3) Å] with the C-O aliphatic bonds [1.277(6) Å for **1**, 1.264(3) Å for **2** and 1.274(3) Å for **3**]. The latter is supported by the fact that aliphatic C-N bonds [1.321(6) Å for **1**, 1.318(4) Å for **2** and 1.315(3) Å for **3**] are comparable to the imino bonds [1.286(7) Å for **1**, 1.295(3) Å for **2** and 1.285(3) Å for **3**] and the localized benzothiazole C=N bond [1.313(7) Å] of **1**. These comparative trends observed within the crystal structures concur with those observed in the optimized structures. Furthermore, there have been other studies which reported the identical coordination modes of hydrazide-derived ligands towards ruthenium. For instance, the ligand, benzoyl pyridine furoic acid hydrazine undergoes enolisation before coordinating to the ruthenium centre through the imino-nitrogen and deprotonated enol oxygen atoms [**49**].

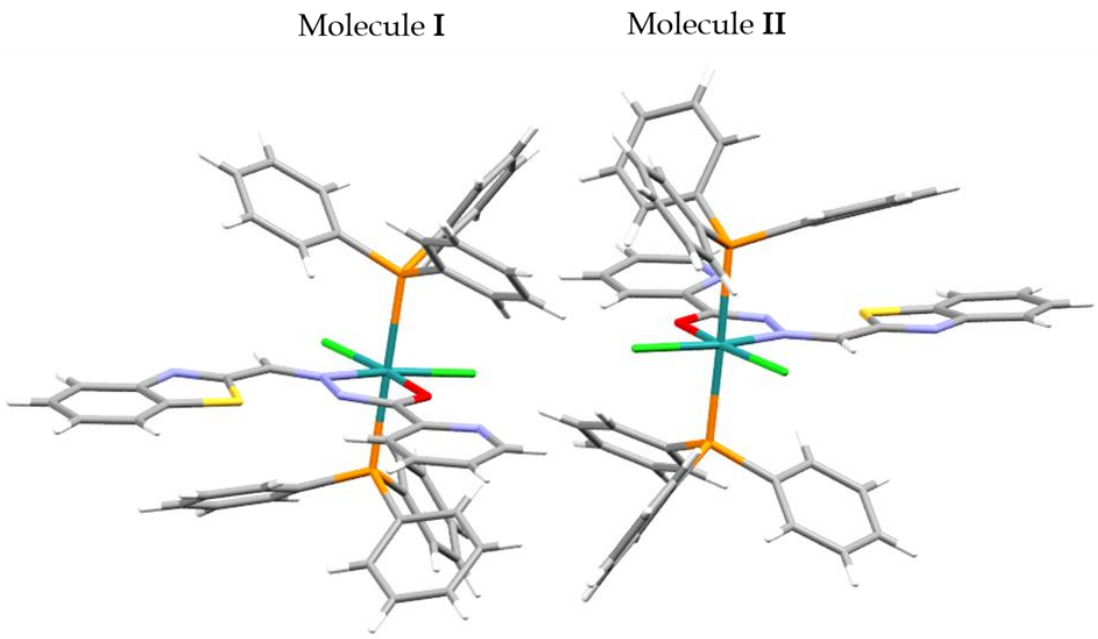

Figure 4.19: *The two independent molecules of **1**.*

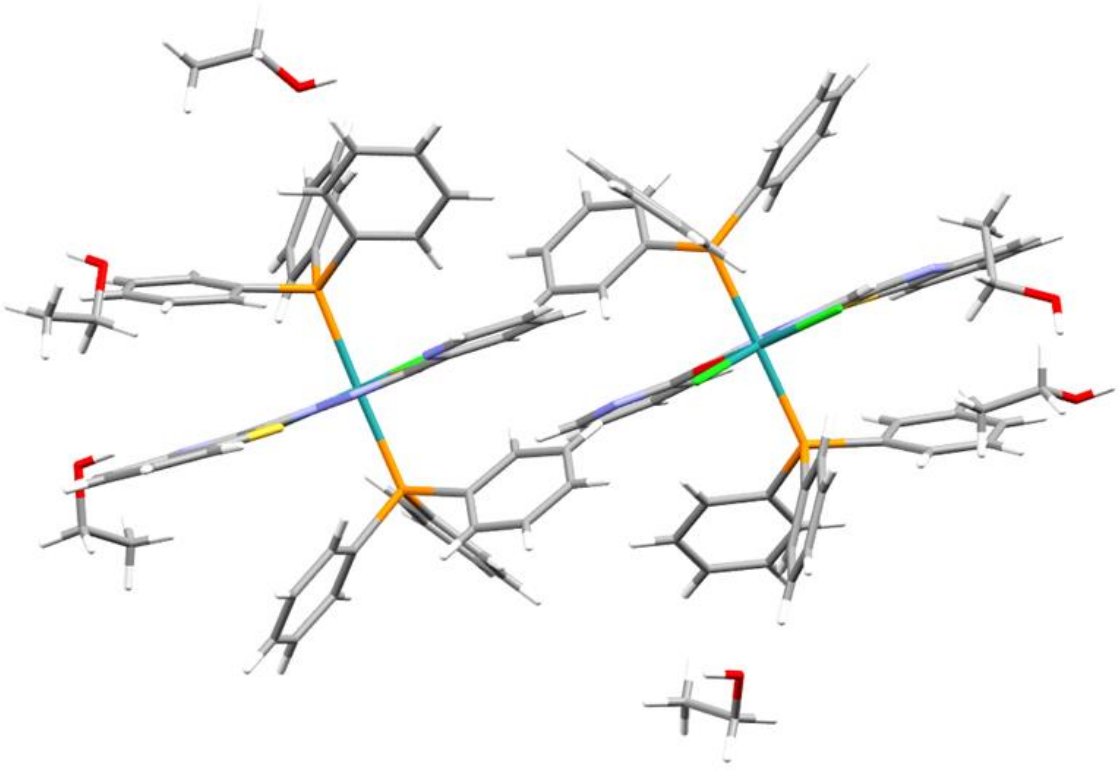

Figure 4.20: *A perspective view of the triclinic unit cell for **1**.*

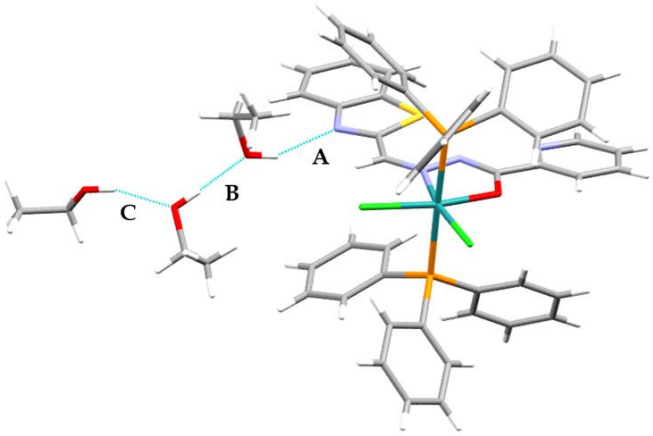

Figure 4.21: *A perspective view depicting classical hydrogen-bonding between the benzothiazole nitrogen atom of molecule **II** (of **1**) and the polar hydrogen atom of the adjacent ethanol molecule of crystallization [(**A**) O-H···N1 = 2.071 Å]. The aforementioned intermolecular hydrogen-bonds affords an extended network [**B** = 1.903 Å and **C** = 1.923 Å] with two additional ethanol molecules.*

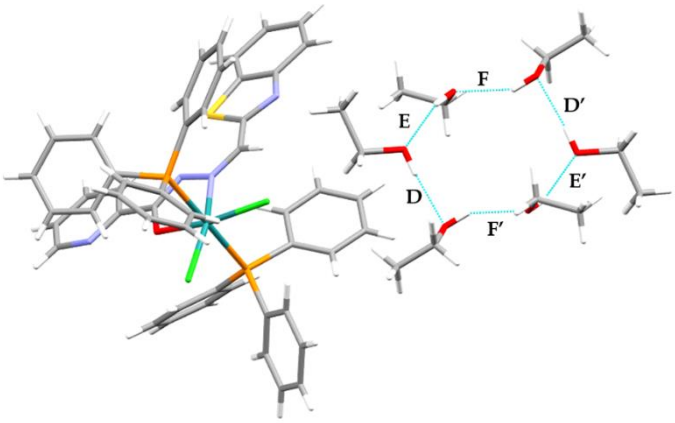

Figure 4.22: *A perspective view of four ethanol molecules positioned next to molecule **I** (of **2**), which affords a 6-membered hydrogen-bonded ring: **E**, **E'** = 1.941 Å; **D**, **D'** = 1.989 Å and **F**, **F'** = 1.970 Å.*

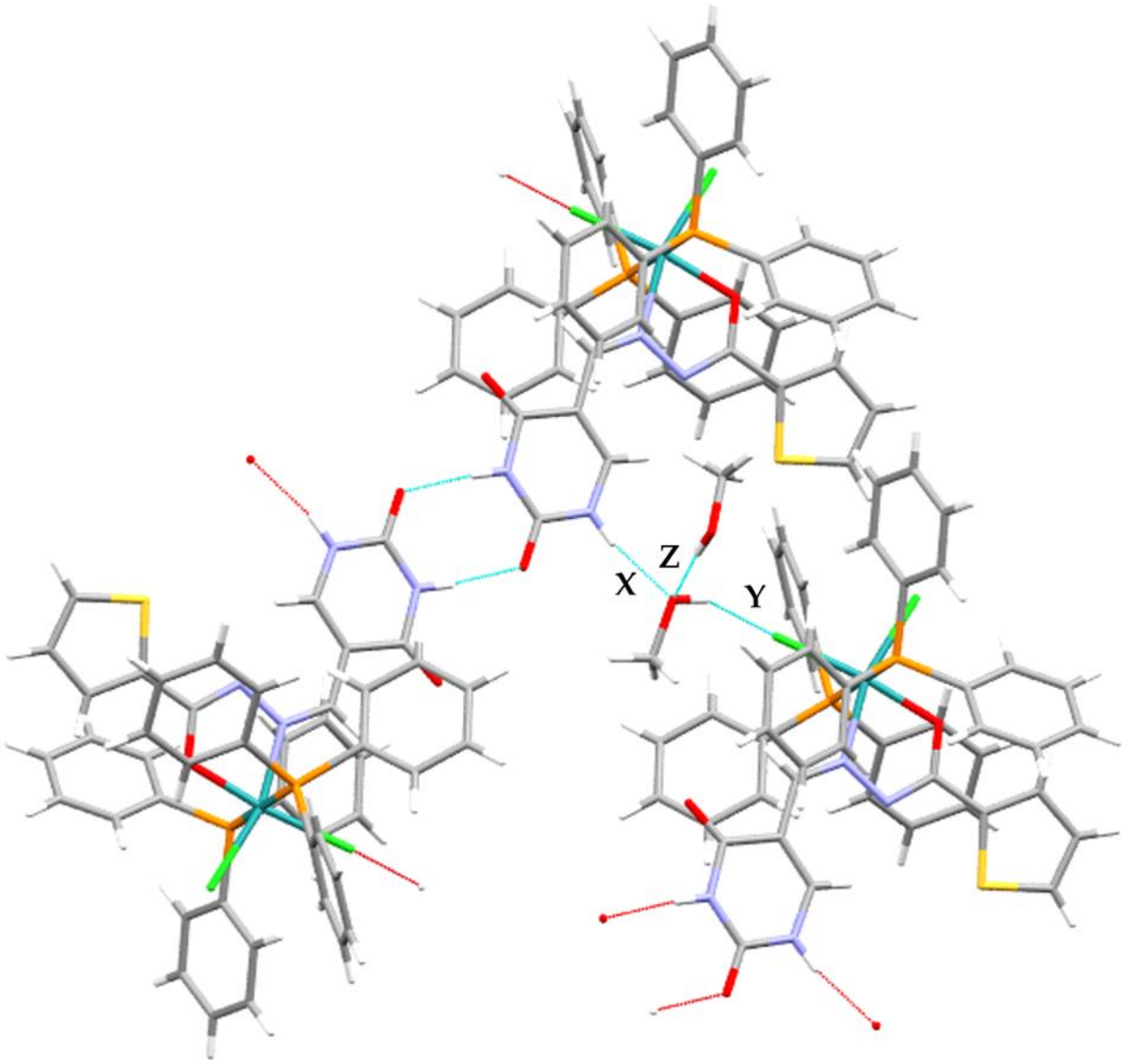

Figure 4.23: *A perspective view of the hydrogen-bonding network occurring within the crystal lattice of* ***2****: O3···H'-N3'/ O3'···H-N3= 1.973 Å (Hydrogen-bonded dimerization); N4-H···$O_{ethanol}$ = 1.983 Å (**X**), (O-H)$_{ethanol}$···$O_{ethanol}$ = 1.965 Å (**Z**) and (O-H)$_{ethanol}$···Cl2 = 2.3371 Å (**Y**).*

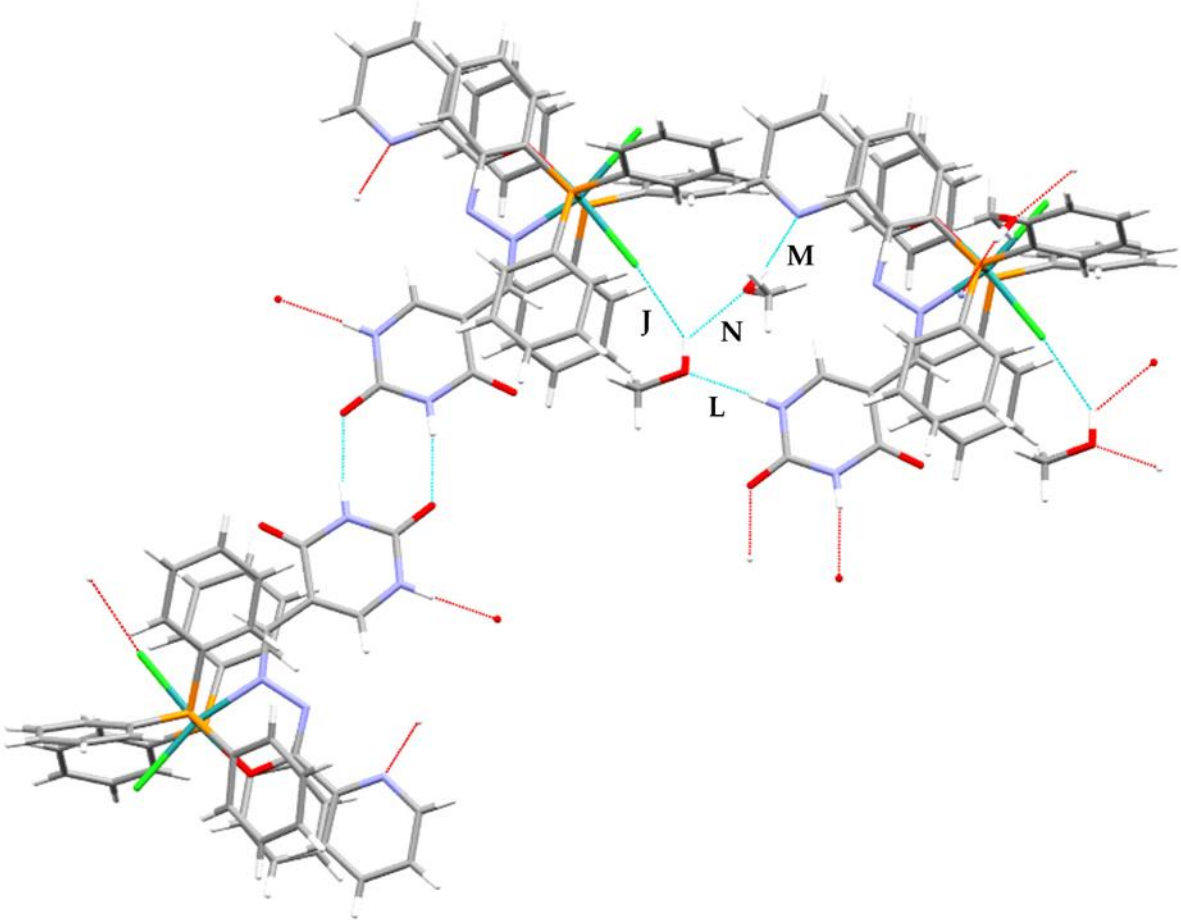

Figure 4.24: *A perspective view of the hydrogen-bonding network occurring within the crystal lattice of **3**: O4···H'-N3'/ O4'···H-N3= 1.961 Å; N5-H···O$_{methanol-1}$ = 1.929 Å (**L**), (O-H)$_{methanol-1}$ ···Cl2 = 2.0809 Å (**J**), (O-H)$_{methanol-1}$ ···O$_{methanol-2}$ = 2.143 Å (**L**) and (O-H)$_{methanol-2}$···N1 = 2.3371 Å (**M**).*

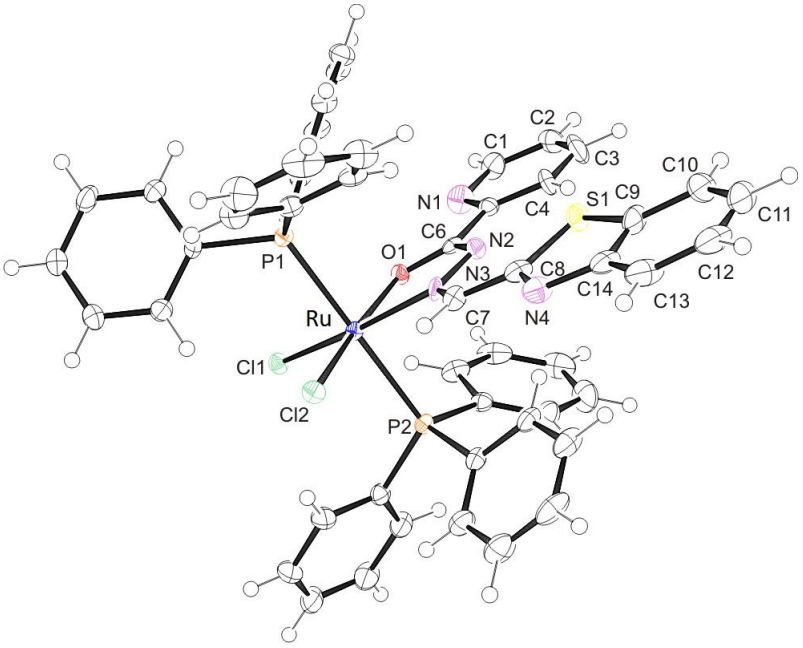

Figure 4.25: *ORTEP view of compound **1** showing 50 % probability displacement ellipsoids and the atom labelling. The solvent molecules of crystallization and the second crystallographically identical molecule of **1** have been omitted.*

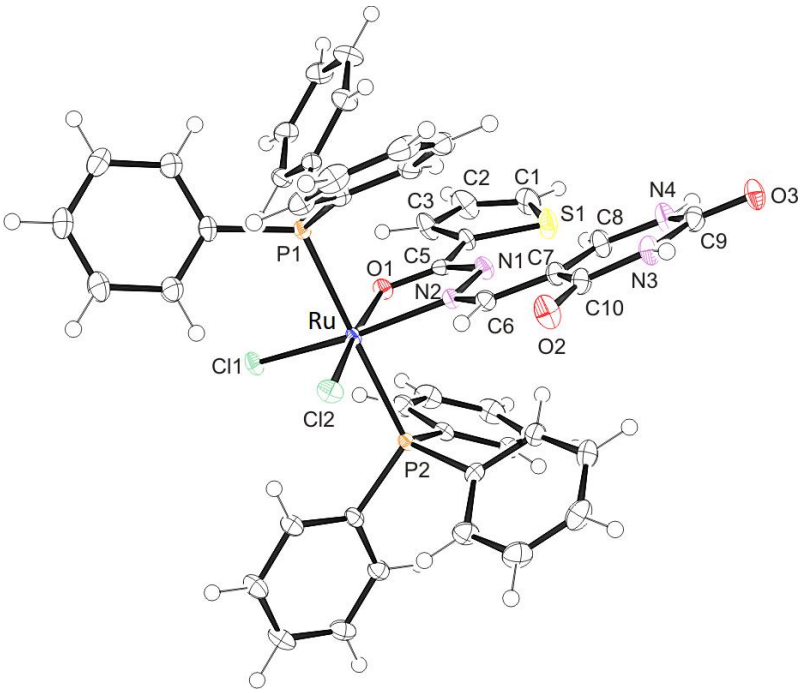

Figure 4.26: *ORTEP view of compound **2** showing 50 % probability displacement ellipsoids and the atom labelling. The solvent molecules of crystallization have been omitted.*

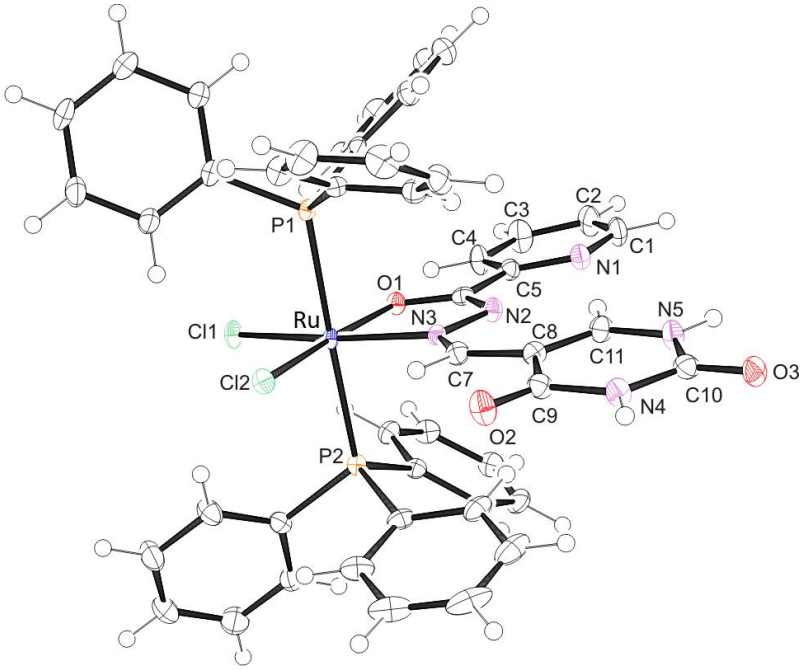

Figure 4.27: *ORTEP view of compound **3** showing 50 % probability displacement ellipsoids and the atom labelling. The solvent molecules of crystallization have been omitted.*

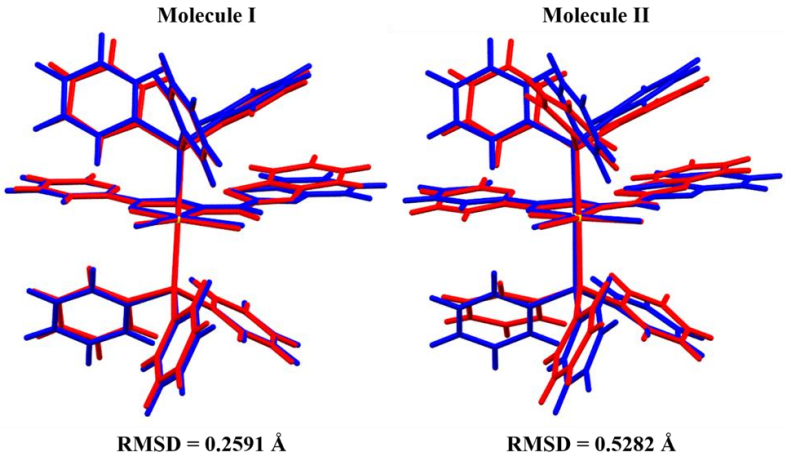

Figure 4.28: *Comparative RMSD values generated from the overlay structure of the optimized (blue) and respective independent crystallographic molecules of **1** (red).*

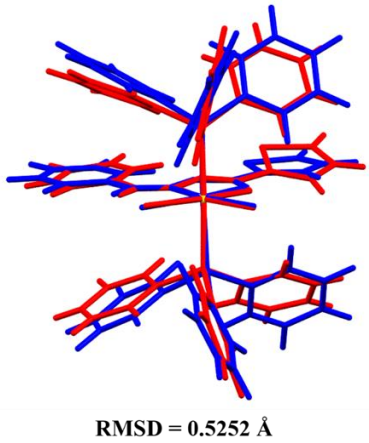

Figure 4.29: *RMSD value generated from the overlay structure of the optimized (blue) and the solid-state structure of **2** (red).*

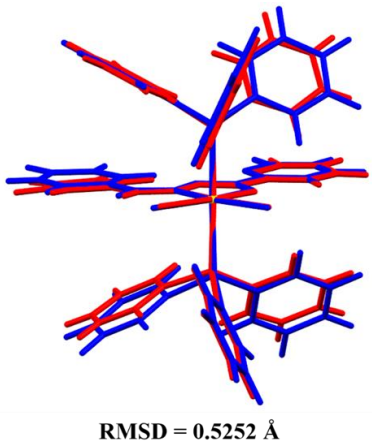

Figure 4.30: *RMSD value generated from the overlay structure of the optimized (blue) and the solid-state structure of **3** (red).*

Table 4.4: *Crystal and structure refinement data for metal compounds **1** – **3**.*

Compound	**1**	**2**	**3**
Chemical formula	$C_{112}H_{114}Cl_4N_8O_8P_4Ru_2S_2$	$C_{46}H_{37}Cl_2N_4O_3P_2RuS \cdot 2(CH_4O)$	$C_{47}H_{38}Cl_2N_5O_3P_2Ru \cdot 2(CH_4O)$
Formula weight	2232.05	1023.85	1018.82
Temperature (K)	100(2)	100(2)	100(2)
Crystal system	Triclinic	Triclinic	Triclinic
Space group	$P\bar{1}$	$P\bar{1}$	$P\bar{1}$
Unit cell dimensions (Å, º)	a = 11.530(2)	a = 10.9806(5)	a = 11.0426(7)
	b = 14.408(2)	b = 11.9045(6)	b = 12.0643(8)
	c = 32.435(5)	c = 18.2231(8)	c = 17.9028(12)
	α = 78.966(5)	α = 76.561(2)	α = 75.140(2)
	β = 85.429(5)	β = 80.146(5)	β = 80.779(3)
	γ = 84.917(4)	γ = 84.136(7)	γ = 83.867(2)
Crystal size (mm)	0.16 × 0.12 × 0.08	0.14 × 0.11 × 0.08	0.14 × 0.11 × 0.09
V (Å^3)	5257.0(15)	2277.85(19)	2270.1(3)
Z	2	2	2
Density (calc.) (mg/ m^3)	1.410	1.493	1.491
Absorption coefficient (mm^{-1})	0.55	0.63	0.59
F(000)	2308	1050	1046
Θ range for data collection (deg., º)	2.5°; 26.7°	1.8°; 27.1°	1.2°; 27.1°
Index ranges	$-11 \leq h \leq 14$ $-18 \leq k \leq 18$ $-40 \leq l \leq 40$	$-14 \leq h \leq 14$ $-15 \leq k \leq 15$ $-23 \leq l \leq 23$	$-14 \leq h \leq 14$ $-15 \leq k \leq 15$ $-22 \leq l \leq 22$
Reflections measured	86933	59583	36780
Observed reflections ($I > 2\sigma > I$)	16594	8869	8667
Independent reflections	21936	9983	9836
Data/ restraints/ parameters	21936/ 0/ 1267	9983/ 1/ 572	9836/ 0/ 581
Goodness of fit on F^2	1.10	1.07	1.06
Observed R; wR^2	0.064; 1.76	0.033; 0.088	0.030; 0.069
R_{int}	0.040	0.025	0.026

Table 4.5: *Selected bond lengths [Å] and angles [º] for **1**.*

	Experimental	**Optimized**
Ru-P1	2.410(1)	2.5188
Ru-P2	2.434(1)	2.5186
Ru-Cl1	2.338(1)	2.4292
Ru-Cl2	2.329(1)	2.4420
Ru-O1	2.017(3)	2.0611
Ru-N3	2.079(5)	2.1084
C6-O1	1.277(6)	1.3263
C6-N2	1.321(6)	1.3333
C7-N3	1.286(7)	1.3147
C8-N4	1.313(7)	1.3230
N3-Ru-O1	76.50(1)	75.54
Cl1-Ru-Cl2	100.29(5)	100.27
P1-Ru-P2	179.55(5)	176.67
Cl1-Ru-N3	166.6(1)	167.56
Cl2-Ru-O1	169.6(1)	167.71

Table 4.6: *Selected bond lengths [Å] and angles [º] for complex **2**.*

	Experimental	**Optimized**
Ru-P1	2.4273(6)	2.5172
Ru-P2	2.4020(6)	2.5172
Ru-Cl1	2.3398(7)	2.4366
Ru-Cl2	2.3323(6)	2.4289
Ru-O1	2.019(1)	2.0661
Ru-N2	2.076(2)	2.1260
C5-O1	1.264(3)	1.3228
C5-N1	1.318(4)	1.3400
C6-N2	1.295(3)	1.3170
C10-O2	1.212(3)	1.2499
C9-O3	1.226(4)	1.2492
N2-Ru-O1	76.71(7)	75.96
Cl1-Ru-Cl2	99.90(2)	100.13
P1-Ru-P2	177.67(2)	176.19
Cl2-Ru-N2	163.22(6)	167.31
Cl1-Ru-O1	173.55(5)	168.52

Table 4.7: *Selected bond lengths [Å] and angles [°] for complex **3**.*

	Experimental	**Optimized**
Ru-P1	2.4236(5)	2.5163
Ru-P2	2.4082(5)	2.5163
Ru-Cl1	2.3492(7)	2.4321
Ru-Cl2	2.3214(5)	2.4358
Ru-O1	2.020(1)	2.0701
Ru-N3	2.085(2)	2.1179
C6-O1	1.274(3)	1.3247
C6-N2	1.315(3)	1.3292
C7-N3	1.285(3)	1.3173
C9-O2	1.218(3)	1.2506
C10-O3	1.223(3)	1.2494
N3-Ru-O1	76.80(6)	75.98
Cl1-Ru-Cl2	98.70(2)	100.52
P1-Ru-P2	177.47(2)	176.36
Cl1-Ru-N3	164.68(5)	167.36
Cl2-Ru-O1	173.38(4)	168.09

*4.5.4 Antioxidant studies of **1** – **5***

Free radicals are extremely unstable species and they readily induce cellular damage by reacting with bio-entities at the *in vivo* level. In fact, reactive oxygen species (ROS) such as hydroxyl and nitric oxide radicals are known to be initiators of DNA damage and mutations [**50, 51**]. Our bodies' natural defence mechanism is to use natural antioxidants including vitamin C, to stem the harmful effects of these cancer-inducing ROS. However, excess ROS concentrations requires more potent radical scavengers which can also act as effective chemotherapeutic agents. Ruthenium compounds can meet the aforementioned requirements due to their optimal redox properties which can facilitate the neutralization of ROS and therefore, meticulously designed ruthenium compounds can serve as metal-based anticancer agents with high efficacies [**23, 50, 52**].

The radical scavenging capabilities of the ruthenium compounds **1** – **5** were investigated towards the neutralization of the DPPH and NO radicals. The experiments concretely support that the metal compounds possess good antioxidant activities which are better than those found for the natural antioxidant, Vitamin C, as seen by their lower IC_{50} values, refer to **Table 4.8**. The higher antioxidant activities of the ruthenium(III) compounds **1** – **3** are promoted by an unpaired electron within the low spin d^5 electronic configurations, which increases the tendencies of the paramagnetic complexes to stabilize these unpaired electrons and thereby scavenging the free radicals [**50**]. These research findings are in agreement with other ruthenium(II) and -(III) compounds documented in literature [**53, 54**].

Table 4.8: *Antioxidant activities of compounds **1** – **5** and Vitamin C against the DPPH and NO radicals.*

Compound	**DPPH Radical**	**NO Radical**
	IC_{50} (µM)[a]	**IC_{50} (µM)[a]**
1	40	19
2	58	18
3	77	16
4	95	56
5	85	60
Vitamin C	141	210

[a] *standard deviation is less than 8 % of mean values*

*4.5.5 DNA interaction studies of **1** – **5***

*(**a**) UV-Vis titrations*

Studying the DNA affinities of metal-based drugs as well as their interactive modes are of pivotal importance to discover new target-specific anticancer drugs. In particular, the diverse DNA interactive patterns of ruthenium complexes include direct covalent interactions with nucleobases, non-covalent interactions such as intercalation, major and minor groove binding as well as electrostatic interactions with the phosphate backbone of DNA [**55**]. Multiple physicochemical techniques have been utilized to probe the DNA binding capabilities including UV-Vis spectrophotometric titrations which are the most commonly utilized technique. Research trends illustrate that UV-Vis spectral alterations provide insight into the DNA binding modes of the metallo-drugs [**56**]. More specifically, progressive decreases in absorbance readings (*viz.* hypochromism) of organometallic chromophores' intra-ligand electronic transitions with an accompanying red shift are associated with DNA intercalation. Hyperchromism are attributed to electrostatic interactions between the metal complex and the DNA double or DNA groove binding of the metal compound. The strength of the DNA interaction is typically consistent with the degree of hypo- or hyperchromic effects and are quantified by intrinsic binding constants, K_b [**56, 57**].

UV-Vis spectral changes were monitored at maximum wavelengths 507, 405 and 395 nm for **1**, **2** and **3**, respectively. Upon controlled additions of ct-DNA to standardized solutions of the respective metal complexes, notable "hyperchromic" effects are observed (3.54 % for **1**, 4.35 % for **2** and 25.23 % for **3**) accompanied by moderate red shifts [around 3 – 5 nm] for **1** and **2**, see **Figures 4.31** – **4.33**. In contrast, no bathochromic shift was seen in the UV-Vis spectral profile of **3**. Consequently, the electronic spectral changes propose that the metal complexes induces breakage of the secondary structure of ct-DNA by undergoing electrostatic binding to the phosphate backbone or binding to the major or minor DNA grooves [**58**].

Moreover, one isosbestic point was observed in the overlay electronic spectra of **1** at 380 nm (**Figure 4.31**) while three diffuse isosbestic points where noticed in the UV-Vis spectral profile for **2**. These observations concur with literature evidence that more species are formed during the ct-DNA-metal complex interactions and show that these metal complexes exhibit one DNA binding mode. Contrastingly, no isosbestic points were seen in the electronic spectral profile

of **3** which is indicative of heterogeneous binding with DNA [**59-61**]. In fact, the structurally similar ruthenium(III) Schiff base compound, $[Ru(pa)(AsPh_3)_2(Cl)]$ (H_2pa = 4-hydroxypyridine-2,6-dicarboxylic acid) exhibited hyperchromic effects without an isosbestic point while $[Ru(hpa)(PPh_3)_2(Cl)]$ displayed clear isosbestic points hinting at its homogeneous DNA binding mode [**61**]. As seen in **Table 4.9**, the intrinsic binding constants (K_b) obtained for **1** – **3** are of the order 10^5 M^{-1}, which is lower than that of known classical intercalators in literature (10^6 M^{-1}), but these diamagnetic ruthenium complexes can still be classified as moderate to strong binders [**62, 63**]. Hence, it is inferred that the interaction between metal complexes **1** – **3** and DNA are indeed non-intercalative and are most probably groove-binders.

Various electronic spectral changes were observed in the UV-Vis spectrum of **4** during its titration with ct-DNA, see **Figure 4.34**. Distinct increasing and decreasing maximum absorption bands (λ_{max} = 266, 272 and 506 nm) that are bridged by four clear isosbestic points (at 268, 288, 480 and 540 nm) were observed, suggesting a homogeneous binding mode of **4** [**61**]. Particularly, the MLCT band at 506 nm shows a significant hypochromic effect (12.64 %) coupled with a blue shift of 7 nm as the concentration of ct-DNA was increased. However, hypochromism with red shifts are usually associated with intercalation and this is not the case. Intercalation of these types of complexes with ct-DNA is highly unlikely due to steric hindrance from the bulky *trans*-$[Ru(PPh_3)]^{2+}$ core. In the case of the biomolecular titrations conducted with **5**, hyperchromism (29.97 % at λ_{max} = 362) and a minor red shift (2 nm) is observed in the UV-Vis spectral profile of **5**, see **Figure 4.35**. Additionally, two isosbestic points are seen at 385 and 505 nm, indicating the formation of new species [**64**]. The K_b values (see **Table 4.9**) for **4** and **5** were found to be 1.9 *x* 10^5 and 4.0 *x* 10^5 M^{-1}, respectively. These are much lower than known intercalators such as ethidium bromide ($K_b = 10^6$ M^{-1}) and partial intercalators ($K_b > 10^6$ M^{-1}). Thus for **4** and **5**, the mode of interaction towards ct-DNA are accounted to groove-binding. Other ruthenium(II) complexes have displayed comparable K_b values, *e.g.*, DNA titrations of $[RuCl_2(PPh_3)]_2(bshctfc)_2$ (bshctfc = *N*-(1,3-benzothiazol-2-yl)hydrazinecarbothioamide-ferrocenyl) revealed hyperchromic effects and red shifts in its UV-Vis spectrum which yielded a K_b value of 1.0 *x* 10^4 M^{-1} [**65**].

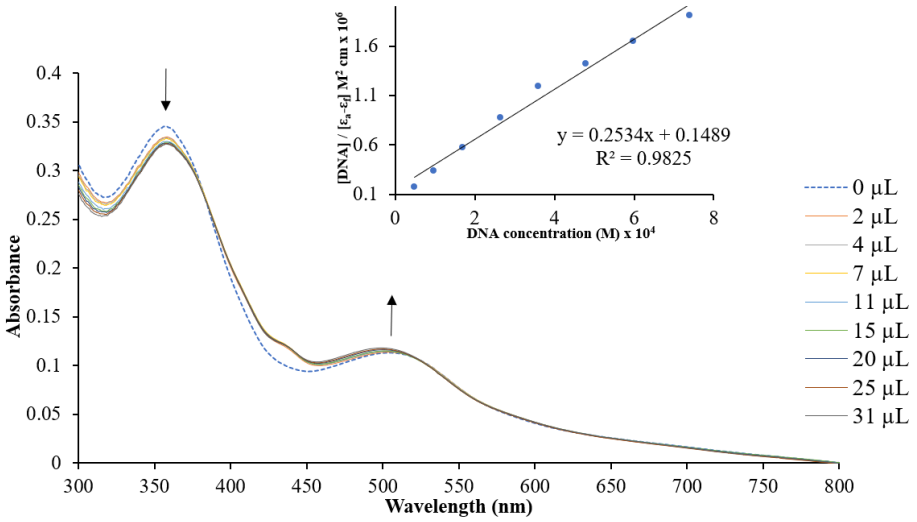

Figure 4.31: *Overlay UV-Vis spectra of compound **1** in the absence and presence of increasing amounts of ct-DNA. A dashed line indicates the initial spectrum.* ***Inset****: Plot of [DNA]/(εa - εf) x 10⁶ vs [DNA] x 10⁴ and the linear fit for the titration.*

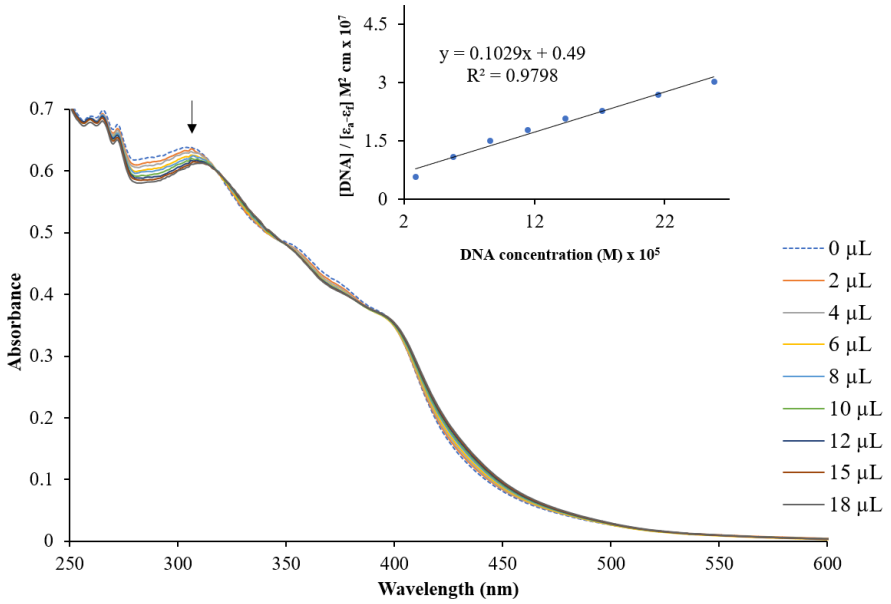

Figure 4.32: *Overlay UV-Vis spectra of compound **2** in the absence and presence of increasing amounts of ct-DNA. A dashed line indicates the initial spectrum.* ***Inset****: Plot of [DNA]/(εa - εf) x 10⁷ vs [DNA] x 10⁵ and the linear fit for the titration.*

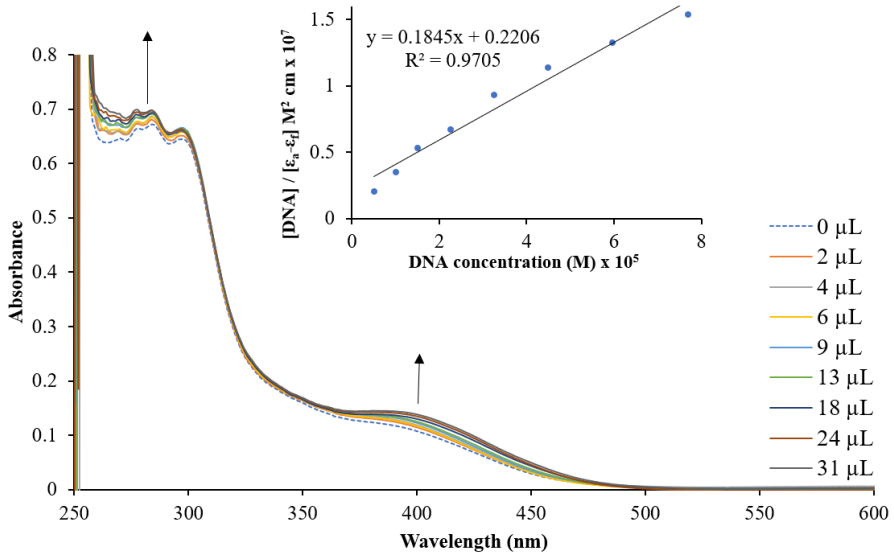

Figure 4.33: *Overlay UV-Vis spectra of compound **3** in the absence and presence of increasing amounts of ct-DNA. A dashed line indicates the initial spectrum.* ***Inset****: Plot of [DNA]/(εa - εf) x 10⁷ vs [DNA] x 10⁵ and the linear fit for the titration.*

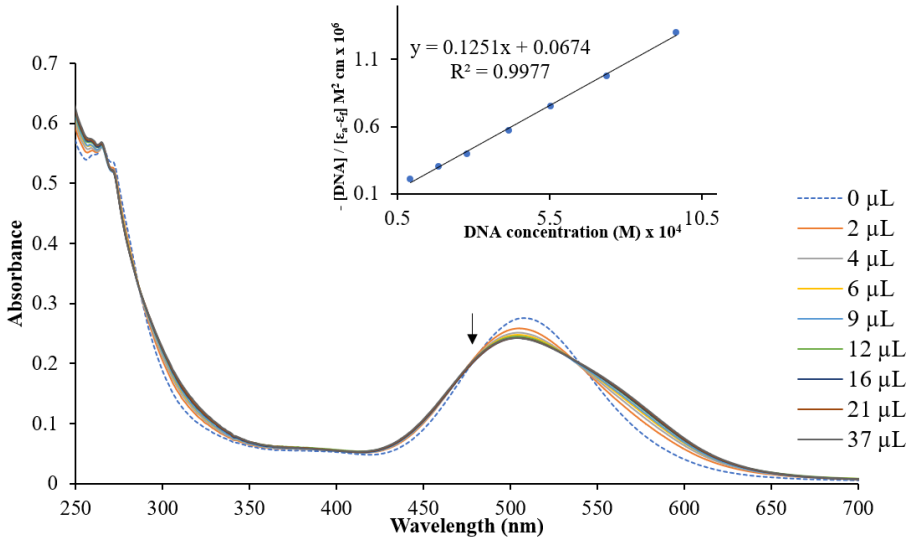

Figure 4.34: *Overlay UV-Vis spectra of compound **4** in the absence and presence of increasing amounts of ct-DNA. A dashed line indicates the initial spectrum.* ***Inset****: Plot of [DNA]/(εa - εf) x 10⁶ vs [DNA] x 10⁴ and the linear fit for the titration.*

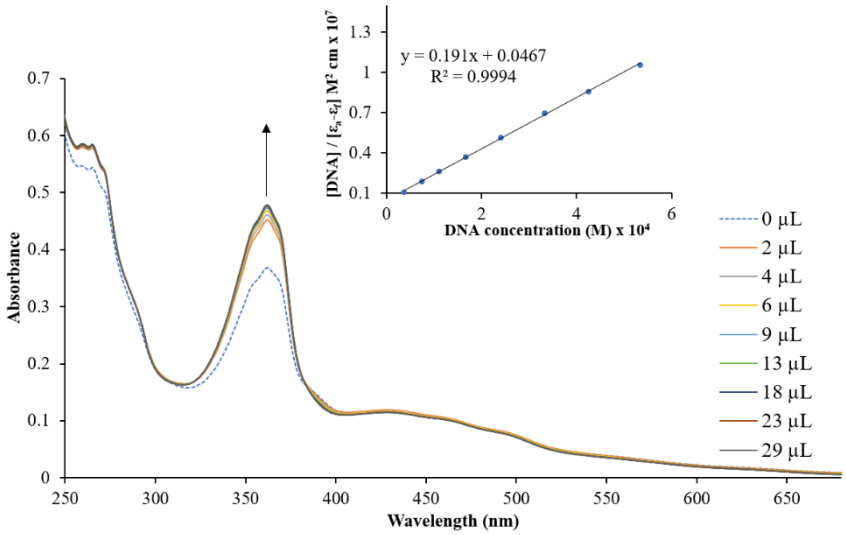

Figure 4.35: *Overlay UV-Vis spectra of compound **5** in the absence and presence of increasing amounts of ct-DNA. A dashed line indicates the initial spectrum. Inset: Plot of [DNA]/(ε_a - ε_f) x 10^6 vs [DNA] x 10^4 and the linear fit for the titration.*

Table 4.9: *Binding constants obtained for **1** – **5** from titration data.*

Compound	K_b (M^{-1})
1	2.5 *x* 10^5
2	2.0 *x* 10^5
3	9.0 *x* 10^5
4	1.9 *x* 10^5
5	4.0 *x* 10^5

(b) *ESR experiments*

ESR experiments conducted in the liquid state were carried out at ambient temperature using the paramagnetic ruthenium complexes **1** – **3** in the absence or presence of ct-DNA [**66**]. These experiments aided in ascertaining whether the interactions of the metal compounds with ct-DNA had any influences on their +III oxidation states, see **Figures 4.36** – **4.38**. After

incubation with ct-DNA, all ruthenium complexes exhibit essentially complete ESR silent behaviour. This spectroscopic data provides additional conclusive evidence of the paramagnetic ruthenium species capabilities to bind to ct-DNA.

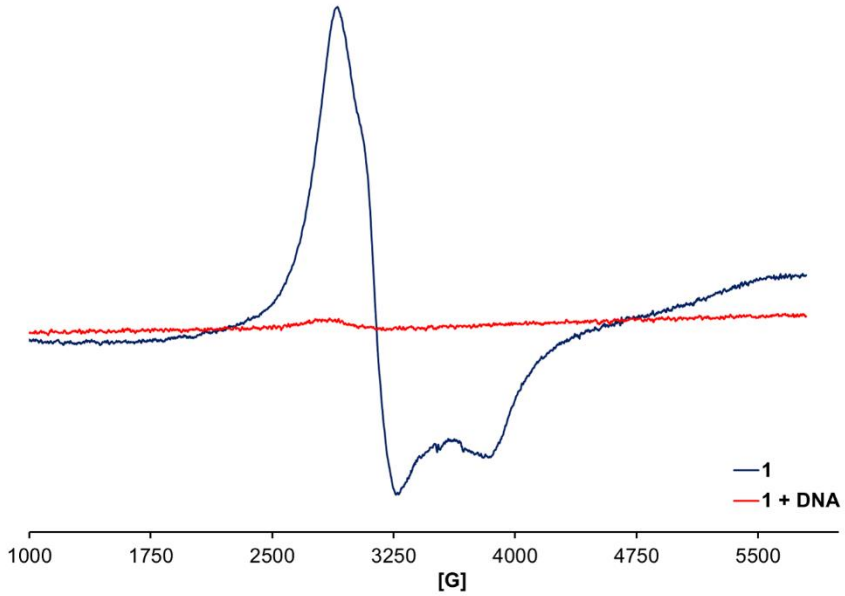

Figure 4.36: *Overlay ESR spectra of **1** (at 1 mM) incubated with ct-DNA and its original sample without ct-DNA. The volume-to-volume ratio of complex **1**: 200 uM ct-DNA is 1.93 cm^3: 0.07 cm^3).*

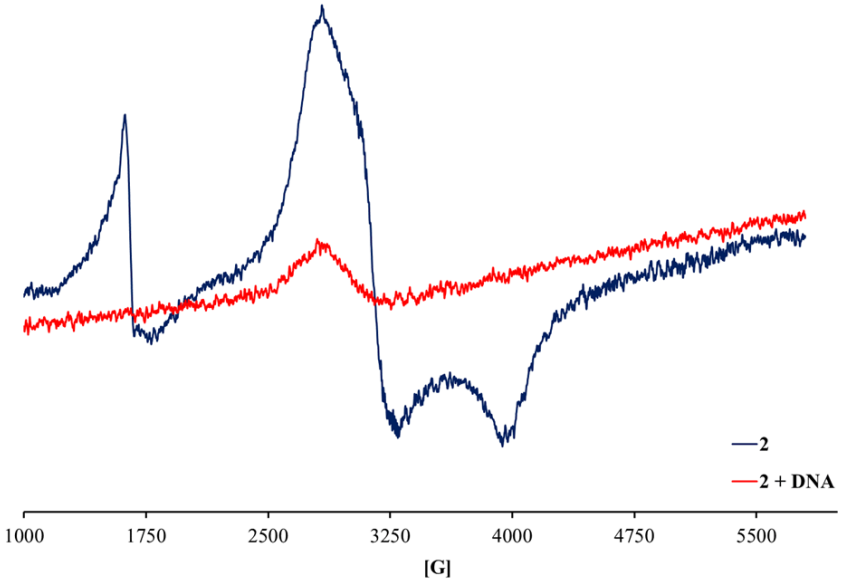

Figure 4.37: *Overlay ESR spectra of **2** (at 1 mM) incubated with ct-DNA and its original sample without ct-DNA. The volume-to-volume ratio of complex **2**: 200 uM ct-DNA is (1.93 cm^3: 0.07 cm^3).*

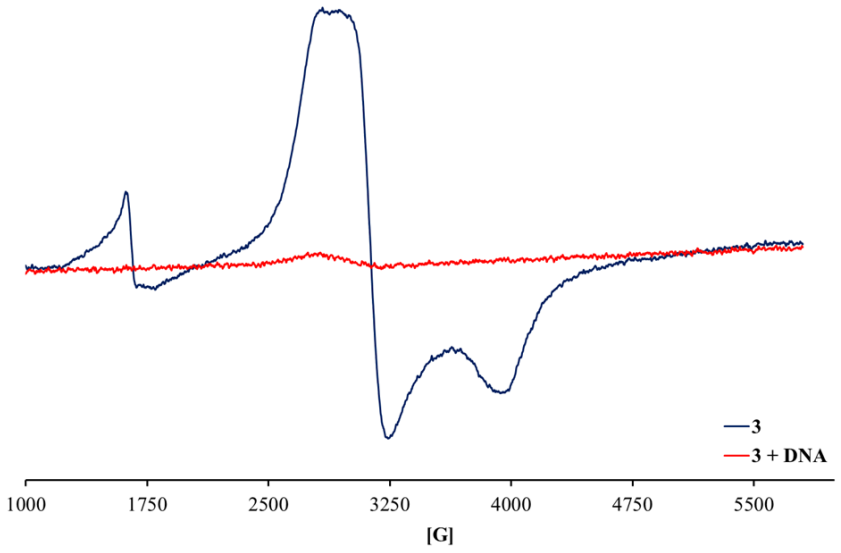

Figure 4.38: *Overlay ESR spectra of **3** (at 1 mM) incubated with ct-DNA and its original sample without ct-DNA. The volume-to-volume ratio of complex **3**: 200 uM ct-DNA is (1.93 cm^3: 0.07 cm^3).*

(c) Agarose gel electrophoresis

The ability of the compounds to interact with ct-DNA was assessed using agarose gel electrophoresis (AGE) (**Figure 4.39**). The intensity of the DNA signal under UV light with and without compounds was quantified in ImageJ and the value calculated relative to the untreated DMSO control is shown under the respective lanes. With the exception of compound **3**, there was a dose-dependent decrease in DNA fluorescence with increasing concentration of the compounds.

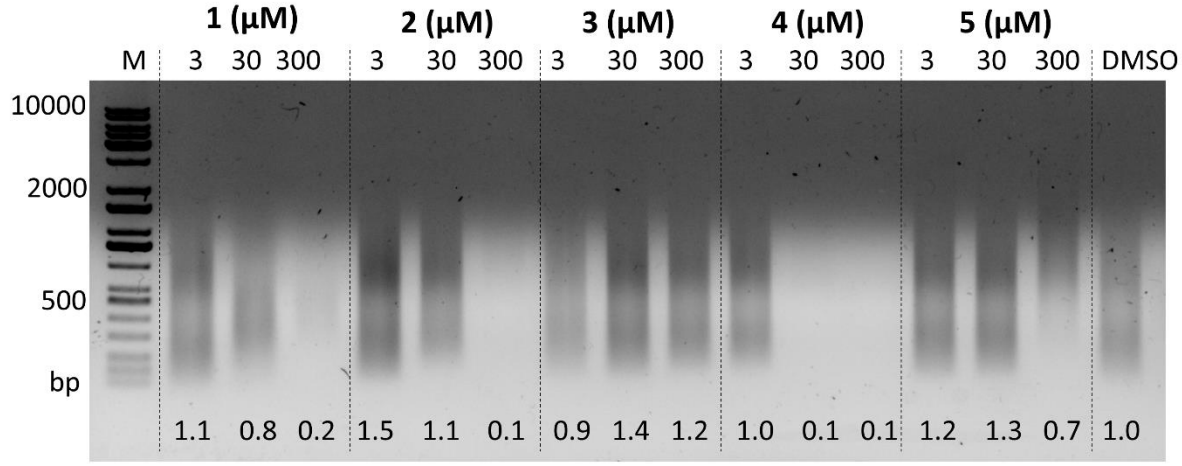

Figure 4.39: *Interaction of the compounds with DNA by agarose gel electrophoresis. Numbers under lanes indicate the DNA fluorescence intensity relative to the DMSO control (which is taken as 1).*

(d) Molecular docking

Molecular docking is a vital computational tool which is widely used to corroborate the DNA binding modes of metal-based drugs [**67**]. The lowest global energy states of **1** – **5** are exothermic terms ranging from -40.52 and -48.88 kJ mol^{-1} which are close to those of other molecules docked to the B-DNA structure [**68, 69**]. Visualizations of the metal compound-DNA adducts clearly illustrate that each metal compound act as DNA groove binders which,

as highlighted before, is the favourable DNA binding mode opposed to DNA intercalation which are inhibited by their bulky PPh_3 co-ligands.

Metal compounds **1**, **3** and **4** are predominantly minor DNA groove-binders whilst **2** and **5** are shown to be primarily major DNA groove-binders, see **Figures 4.40** – **4.44**. The preferential docking mode of **2** and **5** are aided by their corresponding carboim chelating ligands interacting through various intermolecular interactions. In particular, the uracil and thiophene moieties of **2** affords close contacts (< 2.4 Å) with a thymine and an adenine, respectively. These van der Waals interactions are supported by the non-polar intermolecular bonding occurring between a phenyl group (for each PPh_3 co-ligand) and individual thymine as well as ribose moieties. As per the visual inspection, **5** docks particularly well within the major groove and has substantially more interactions with DNA due to having only one bulky PPh_3 co-ligand which provides a plausible justification for its higher K_b value. Moreover, its chloride co-ligand affords two classical hydrogen-bonding interactions with adenine (at 2.571 Å) and thymine (at 2.590 Å) groups while its H_3ucp chelator stabilized the DNA adduct through weak interactions between separate uracil moieties and adjacent guanines as well as a ribose.

In silico DNA interactions of **1**, **3** and **4** illustrate that the chelating carboim ligands have negligible influences on the stabilization of the corresponding B-DNA-metal complex adducts. For **1**, one of its chloride co-ligands renders a close contact with a ribose moiety while selected phenyl groups of the opposing PPh_3 co-ligands interact with the phosphate backbone and a C-G DNA base pair. In fact, **3** and **4** essentially mimics the same DNA interacting patterns as **1** whereby their chloride and PPh_3 co-ligands interact with the DNA backbones while for **3**, a solitary interaction with the C-G DNA base pair is found.

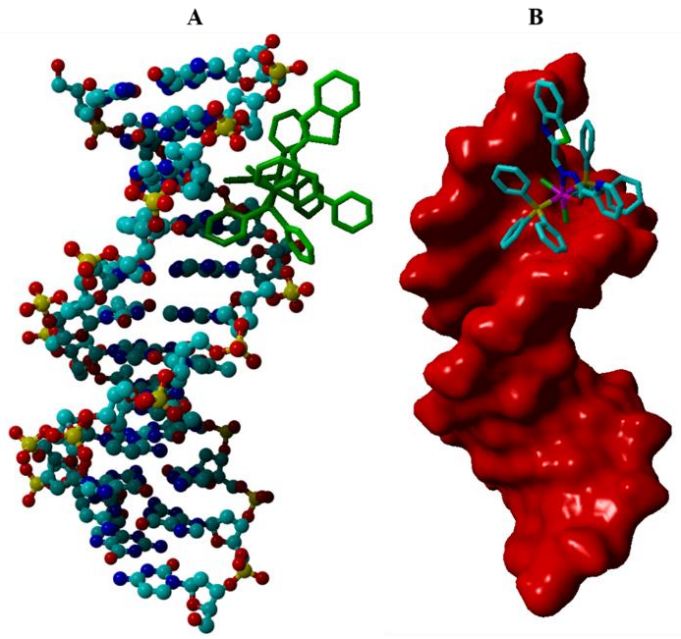

Figure 4.40: *Compound **1** primarily docked into the minor groove of B-DNA: (**A**) shows DNA in ball and stick view whereas (**B**) shows the molecular surface view of DNA. Global energy = - 43.95 kJ.mol^{-1}.*

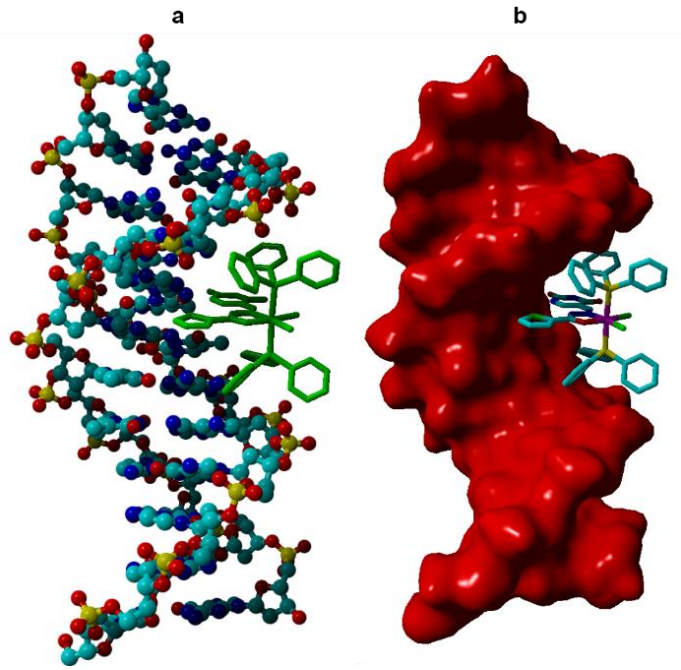

Figure 4.41: *Compound **2** primarily docked into the major groove of B-DNA: (**a**) shows DNA in ball and stick view whereas (**b**) shows the molecular surface view of DNA. Global energy = - 47.88 kJ.mol^{-1}.*

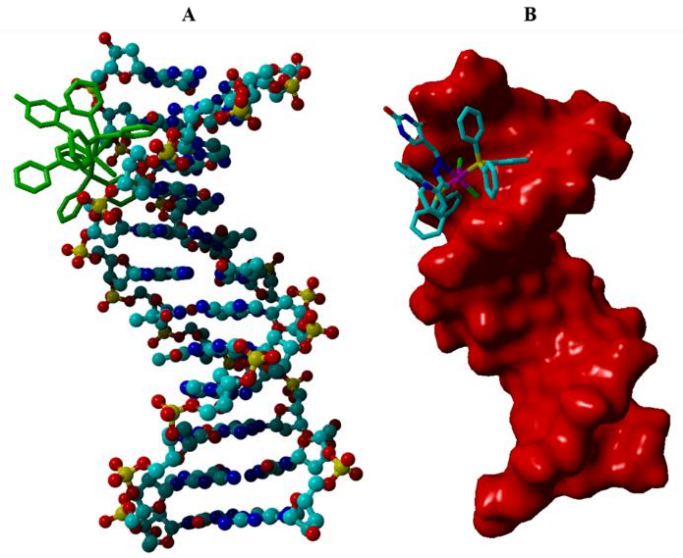

Figure 4.42: *Compound **3** primarily docked into the minor groove of B-DNA: (**A**) shows DNA in ball and stick view whereas (**B**) shows the molecular surface view of DNA. Global energy = - 44.86 kJ.mol^{-1}.*

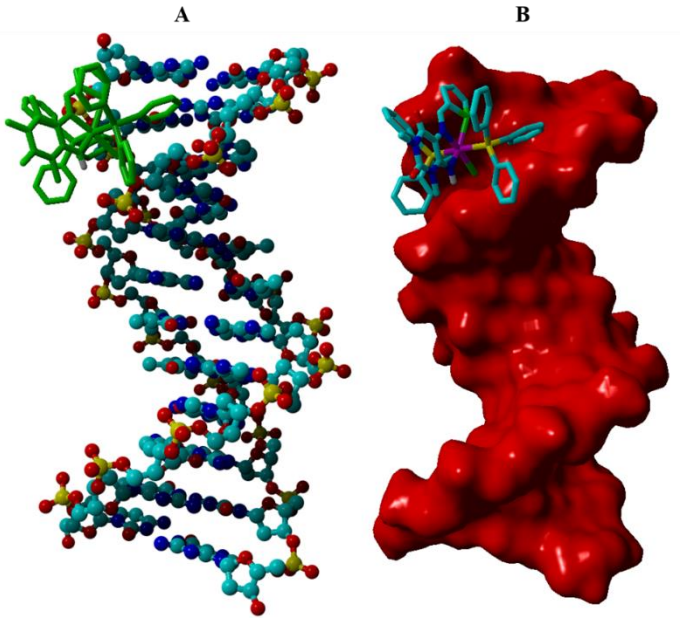

Figure 4.43: *Compound **4** primarily docked into the minor groove of B-DNA: (**A**) shows DNA in ball and stick view whereas (**B**) shows the molecular surface view of DNA. Global energy = - 40.52 kJ.mol^{-1}.*

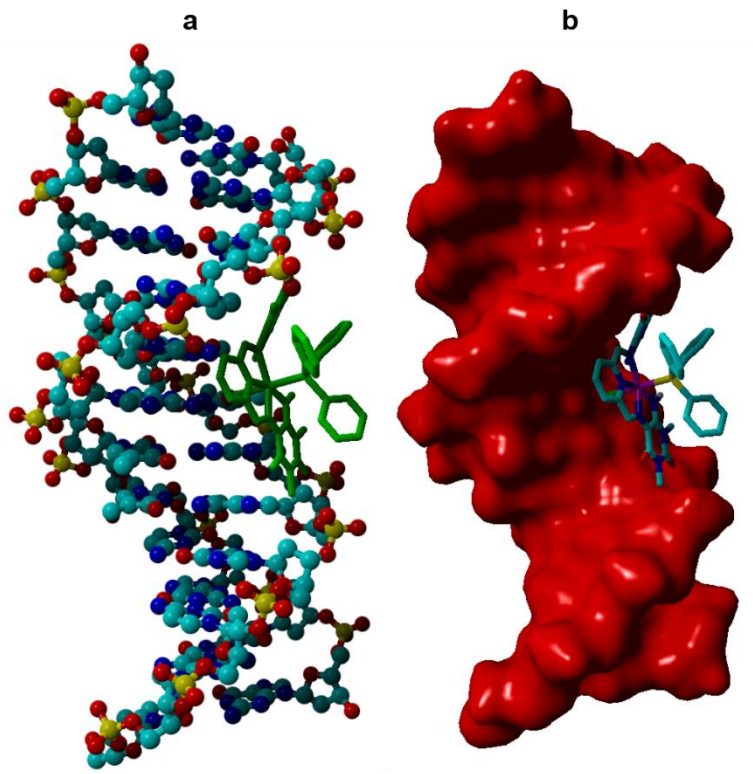

Figure 4.44: *Compound **5** primarily docked into the major groove of B-DNA: (**a**) shows DNA in ball and stick view whereas (**b**) shows the molecular surface view of DNA. Global energy = -48.88 kJ.mol^{-1}.*

4.5.6 BSA interaction studies

Biodistribution, pharmacokinetics and efficacies of pharmaceuticals are largely dependent on their affinities to the drug-carrying proteins in the blood stream. Serum albumins are the most abundant proteins found in a large variety of organisms and have the ability to act as a transporting medium by reversibly binding to various natural-occurring or synthetic bioactive molecules. Bovine serum albumin (BSA) is well suited to investigate the carrier capabilities of metallopharmaceuticals as BSA is a structural analogue to Human serum albumin (HSA) [**70, 71**]. Moreover, chemotherapeutic drug-delivery proteins should have high affinities towards the drug which culminate in stable conjugates of the metal complex and the protein. Ultimately, the latter result in organometal complex-DNA adducts with good structural integrity under physiological conditions but facile drug release must occur once the anticancer drugs have reached different cancerous sites. Characteristic to BSA are their three domains (*viz.* **I**, **II**, **III**) which are further divided into two more subdomains each (*viz.* **A** and **B**). Domains **I** and **II** resides on a mutual framework interface but binding of a moiety to domain **III** have shown to compromise the structural integrity of the protein [**72**].

(a) UV-Vis titrations

The generation of the UV-visible spectra for BSA is a result of its tryptophan residues which are very sensitive to changes around the microenvironment of these chromophores. Any changes in the intensity is an indication that an interaction exists between a metal complex and BSA whilst changes in wavelength shifts are valuable in evaluating the hydrophobicity around the tryptophan residues and thus the extent of unfolding of the protein [**71, 73, 74**]. The UV-Vis spectra of BSA (see **Figures 4.45 – 4.49**) illustrated slight blue shifts and decreases in the absorbance intensities of their BSA peak maxima upon increasing concentrations of **1**, **2** and **3**, respectively. Evidentially, these results reveal that the hydrophobicity around the tryptophan chromophores is increased. Consequently, it is proposed that the metal complexes either cause minor extension or promote increased folding of the BSA strand, therefore keeping the tryptophan in its hydrophobic pocket. These observations suggest that binding of **1** – **5** occur in the hydrophobic subdomain **IIA** [**72, 73, 75**]. The apparent association constants (K_{app}) were calculated to be 4.44 x 10^3, 5.77 x 10^6, 1.11 x 10^6, 5.74 x 10^4 and 1.10 x 10^6 M^{-1} for **1** – **5**,

respectively (**Table 4.10**). In fact, these K_{app} values are similar to those reported in literature for other ruthenium compounds [**76, 77**]. Comparatively, the K_{app} values obtained of **2** – **5** are considered to be strong binders towards BSA as the magnitude of "ideal" binders is known to be between $10^4 – 10^6\ M^{-1}$ [**78**]. The smaller apparent association constant obtained for **1** can be rationalized by its lack of complementary hydrogen-bonding acceptor/ donor sites. Unlike **1**, metal complexes **2** – **4** contains the uracil moieties which possess free N-H and C=O groups that can form strong intermolecular hydrogen bonds with the analogous groups within the BSA structure, rendering in the process stable adducts. This promotes stabilization of the BSA-metal complex system by folding of the BSA strand, thereby keeping the tryptophan concealed within its hydrophobic pocket [**72**].

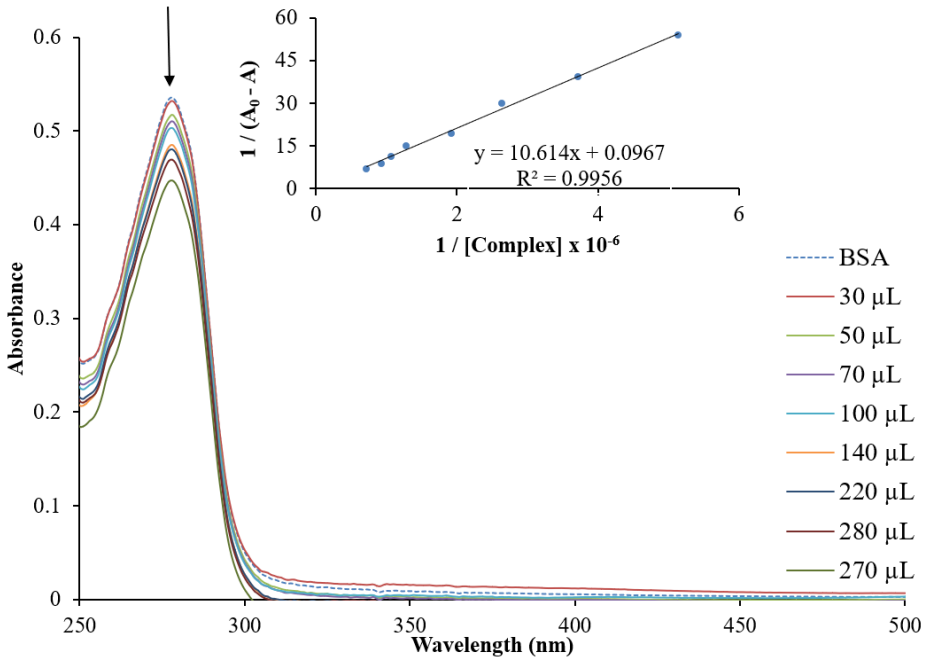

Figure 4.45: *UV-Vis spectral profile depicting the titration between compound **1** and BSA. The inset is the double reciprocal plot of $1 / (A_0 – A)$ versus $1 / C_{complex} \times 10^{-6}$.*

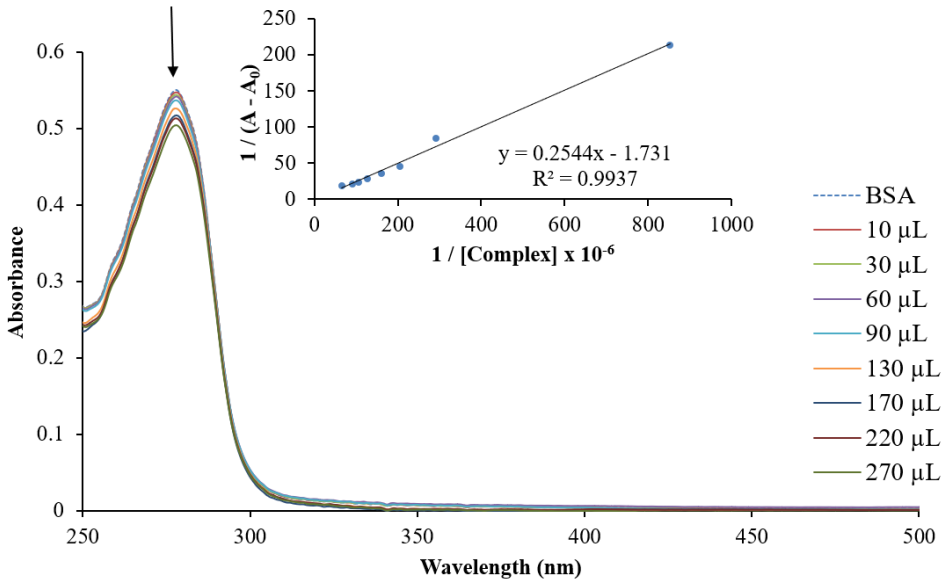

Figure 4.46: *UV-Vis spectral profile depicting the titration between compound **2** and BSA. The inset is the double reciprocal plot of 1 / (A_0 – A) versus 1 / $C_{complex}$ x 10^{-6}.*

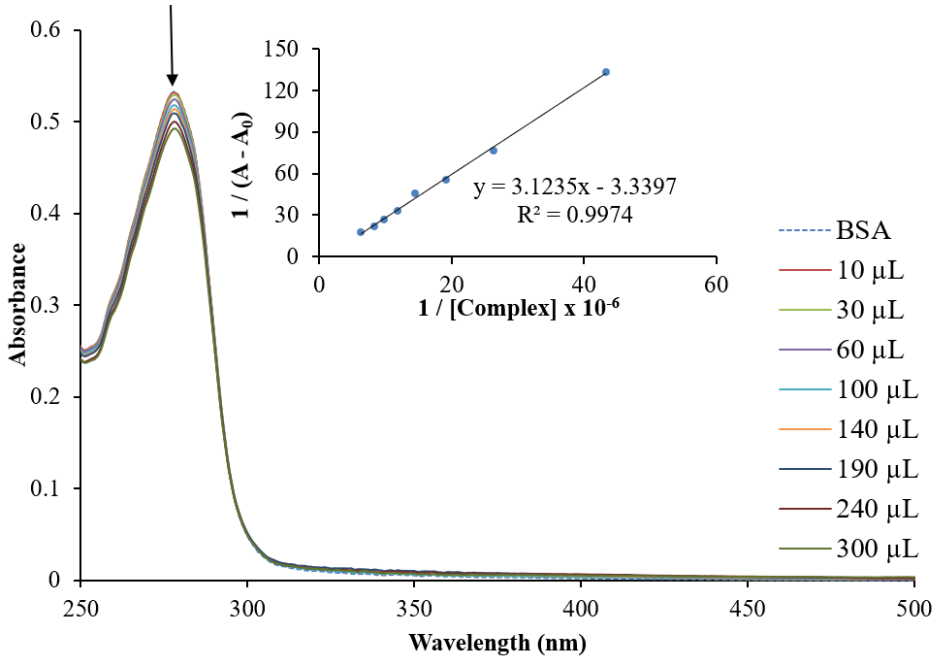

Figure 4.47: *UV-Vis spectral profile depicting the titration between compound **3** and BSA. The inset is the double reciprocal plots of 1 / (A_0 – A) versus 1 / $C_{complex}$ x 10^{-6}.*

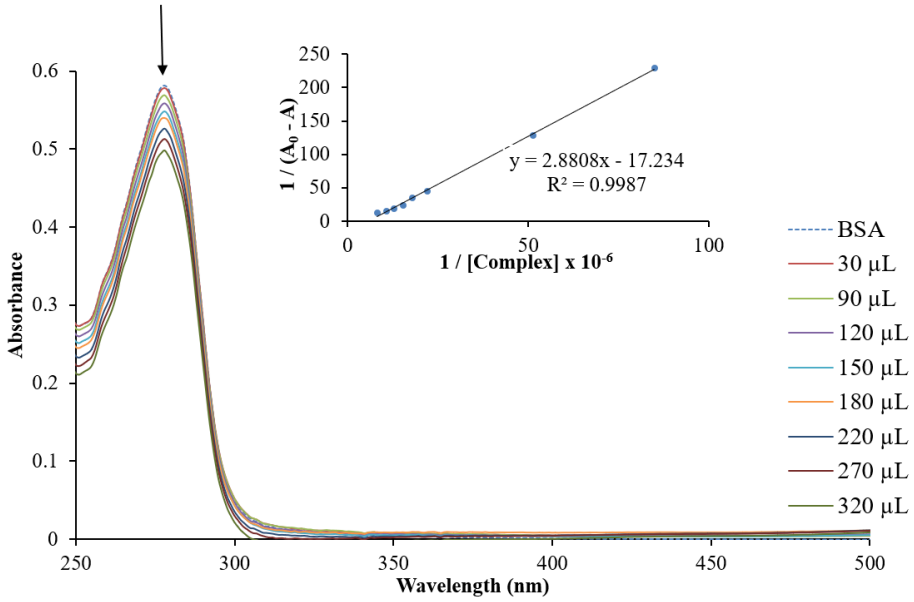

Figure 4.48: *UV-Vis spectral profile depicting the titration between compound **4** and BSA. The inset is the double reciprocal plot of 1 / (A_0 – A) versus 1 / $C_{complex}$ x 10^{-6}.*

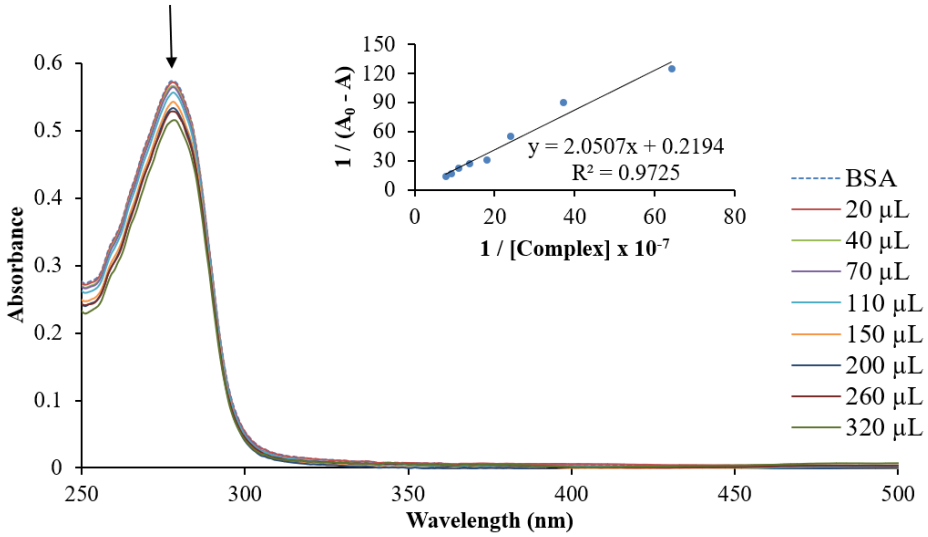

Figure 4.49: *UV-Vis spectral profile depicting the titration between compound **5** and BSA. The inset is the double reciprocal plot of 1 / (A_0 – A) versus 1 / $C_{complex}$ x 10^{-6}.*

Table 4.10: *Apparent association constants (K_{app}) obtained via UV-Vis spectrophotometry for the metal complexes.*

Compound	K_{app} (M^{-1})
1	4.44×10^3
2	5.77×10^6
3	1.11×10^6
4	5.74×10^4
5	1.10×10^6

(b) *Fluorescence titrations*

Fluorescence quenching of BSA upon interaction with the metal complexes were carried out to validate the findings in the UV-Vis spectral study, see **Figures 4.50 – 4.54**. As with UV-Vis spectrophotometry, the fluorescence behaviour of BSA discloses information about its structural dynamics, i.e. the extent of folding and the microenvironment of its tryptophan unit [**79**]. The BSA fluorescence intensities decrease as incrementing amounts of metal complexes **1 – 5** were titrated, indicating that the metal complexes have a sturdy interaction with BSA. Slight blue shifts were observed which, as in the case of the UV-Vis spectrophotometric titration, denotes that the tryptophan molecule of BSA is buried in the hydrophobic pocket because of increased folding (or slight unwinding) of the protein. This also indicates the presence of hydrogen bonding or Van der Waals contacts between the metal complexes and BSA [**80, 81**]. The fluorescence quenching of BSA by each of the metal complexes showed a linear relationship with its concentration (known as the Stern-Volmer relationship) and gave rise to the Stern-Volmer quenching constants (K_{SV}) and the quenching rate constants (K_q) as seen in **Table 4.11**.

The K*q* values (**Table 4.11**) found are all larger than that known for dynamic quenchers (2×10^{10} M^{-1} s^{-1}) therefore the mechanisms for the ruthenium compounds **1 – 5** are considered to be static quenching [**82**]. Additionally, static quenching was confirmed by the overlay BSA UV-visible spectroscopic profiles. Controlled additions of the relative metal complexes produced changes in the absorption bands (*i.e.* dynamic quenching would result in no changes

in the absorption spectra) [**80**]. The K_{SV} (obtained for static quenching) values may be used to confirm the binding affinities of the mononuclear metal complexes with BSA. The results indicate that **2** – **4** display higher binding affinities towards BSA which are consistent with the findings in the titrations study monitored by UV-Vis spectrophotometry. Quenching constants of similar magnitude were observed for other reported ruthenium compounds, *e.g.* [(*p*-cymene)RuClL^2] (L^2 = (*Z*)- *N′*- ((1,3- diphenyl- 1*H*- pyrazol- 4- yl)methylene)) gave rise to a K_{SV} value of 9.52 *x* 10^4 M^{-1} [**83**].

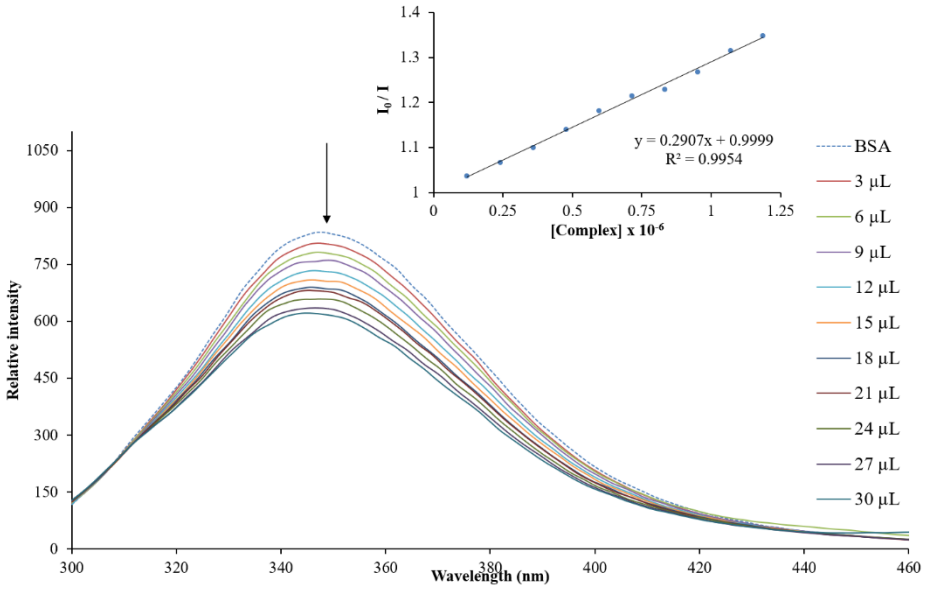

Figure 4.50: *Fluorescence emission spectral profile depicting the titration between compound **1** and BSA. The inset is the Stern-Volmer plot.*

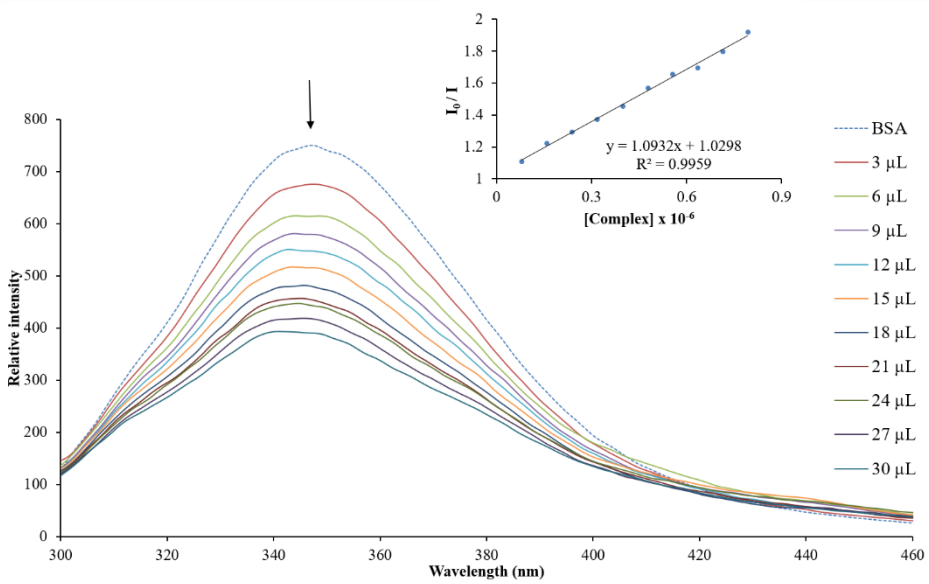

Figure 4.51: *Fluorescence emission spectral profile depicting the titration between compound **2** and BSA. The inset is the Stern-Volmer plot.*

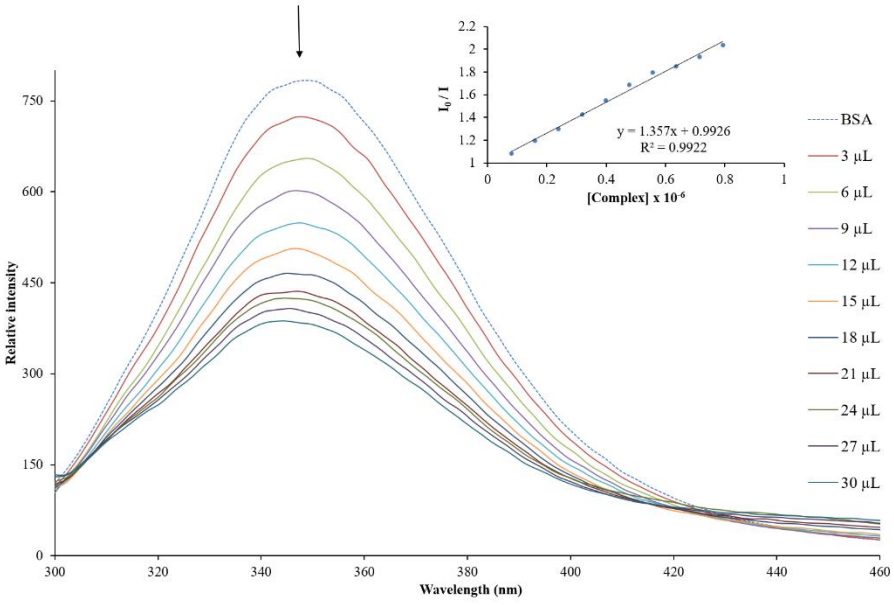

Figure 4.52: *Fluorescence emission spectral profile depicting the titration between compound **3** and BSA. The inset is the Stern-Volmer plot.*

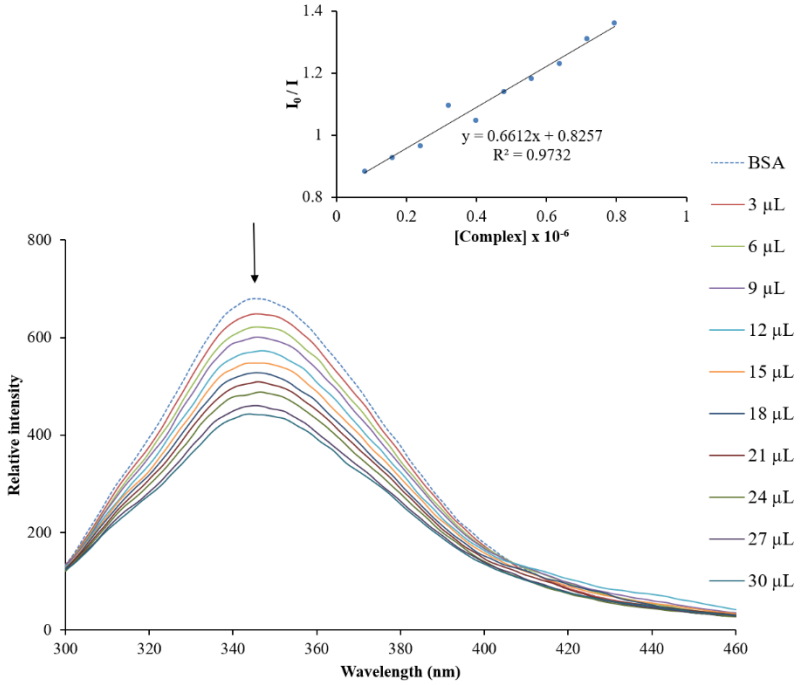

Figure 4.53: *Fluorescence emission spectral profile depicting the titration between compound **4** and BSA. The inset is the Stern-Volmer plot.*

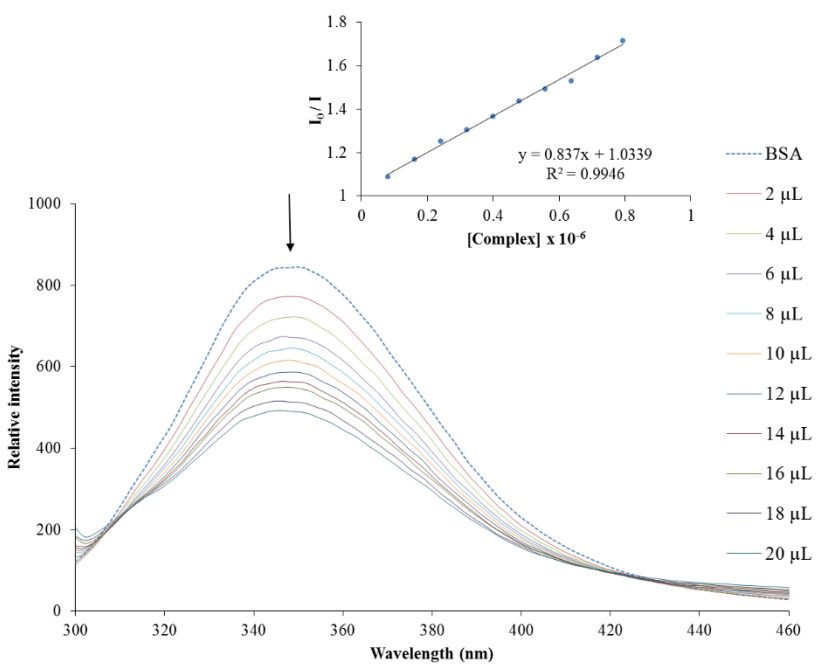

Figure 4.54: *Fluorescence emission spectral profile depicting the titration between compound **5** and BSA. The inset is the Stern-Volmer plot.*

(c) Competitive binding

To determine the preferred binding site of a specific metal complex in BSA, competitive binding experiments were carried out by monitoring the fluorescence quenching of BSA induced by a metal complex in the presence of each site marker: warfarin or ibuprofen, see **Figures 4.55 – 4.59** [**84**]. Furthermore, warfarin has been shown to bind specifically to site **I** whilst ibuprofen has a known affinity for site **II**. Progressive decreases in the fluorescence intensities of BSA occurred when the separate site markers were introduced which denotes the formation of the relating BSA-site marker hybrids. Static quenching ($K_q > 10^{11}$ M^{-1} s^{-1}) were also observed upon introduction of each metal complex to the relevant BSA-site marker hybrids. Of particular importance is that the metal complexes illustrated no specificity towards a BSA binding sites. The latter is based on the comparable Stern-Volmer quenching constants which is in the same order of 10^4 M^{-1} s^{-1} for the data collected in the presence of each site marker.

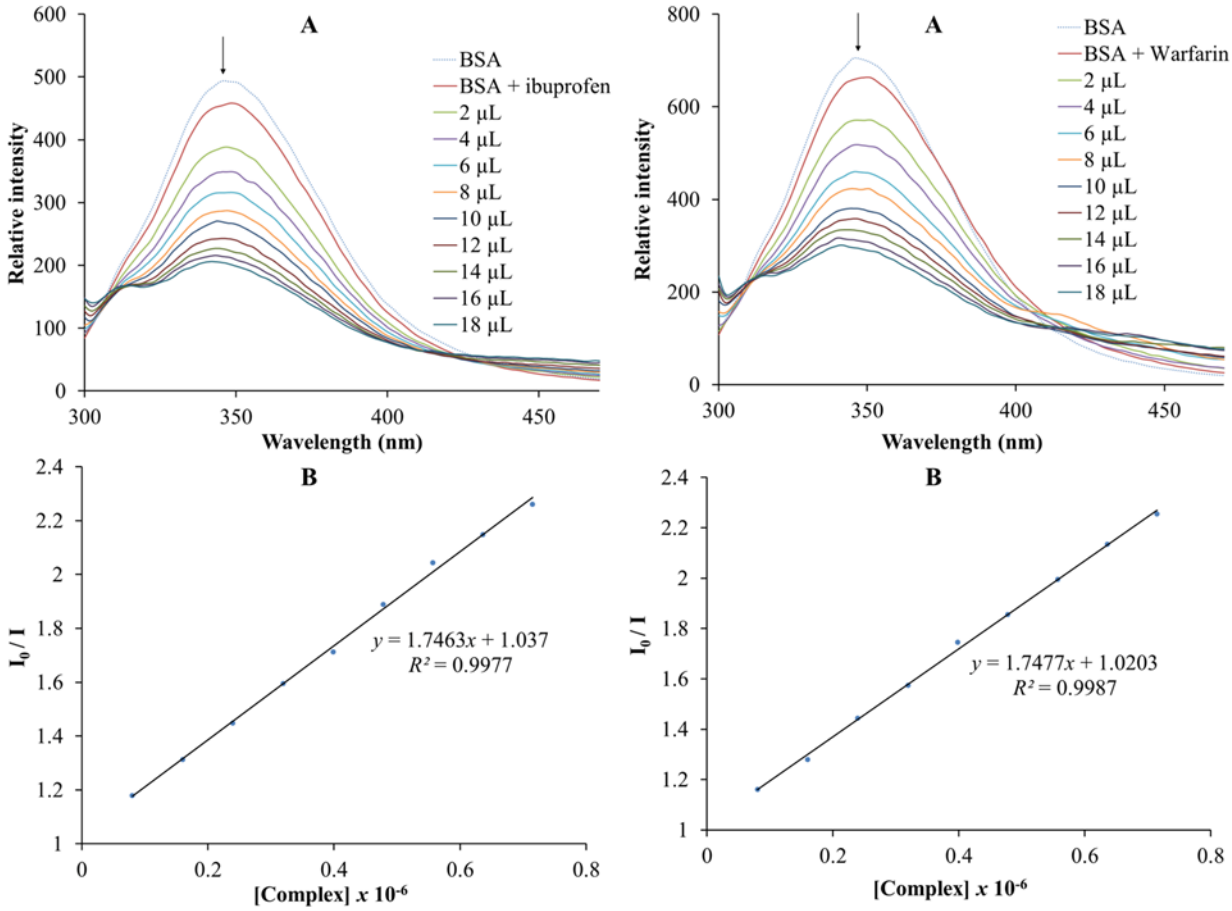

Figure 4.55: *BSA competitive binding between complex **1** and the respective site markers: ibuprofen and warfarin. (**A**): Fluorescence emission spectral profiles of BSA in the absence or presence of a specific site marker. Subsequent sequential additions of the standardized metal complex were added to the individual BSA-site marker samples. (**B**) is the corresponding Stern-Volmer plots.*

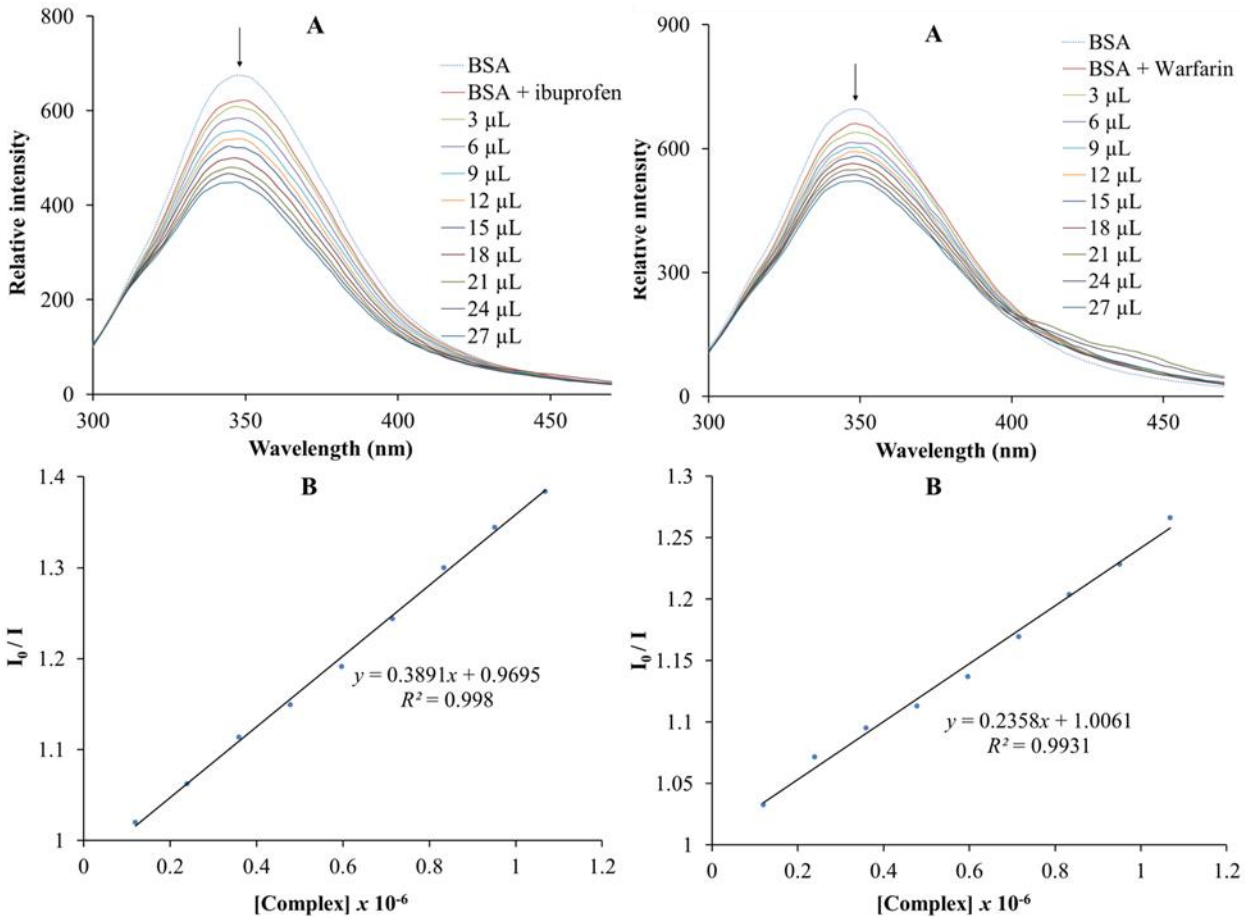

Figure 4.56: *BSA competitive binding between complex **2** and the respective site markers: ibuprofen and warfarin. (**A**): Fluorescence emission spectral profiles of BSA in the absence or presence of a specific site marker. Subsequent sequential additions of the standardized metal complex were added to the individual BSA-site marker samples. (**B**) is the corresponding Stern-Volmer plots.*

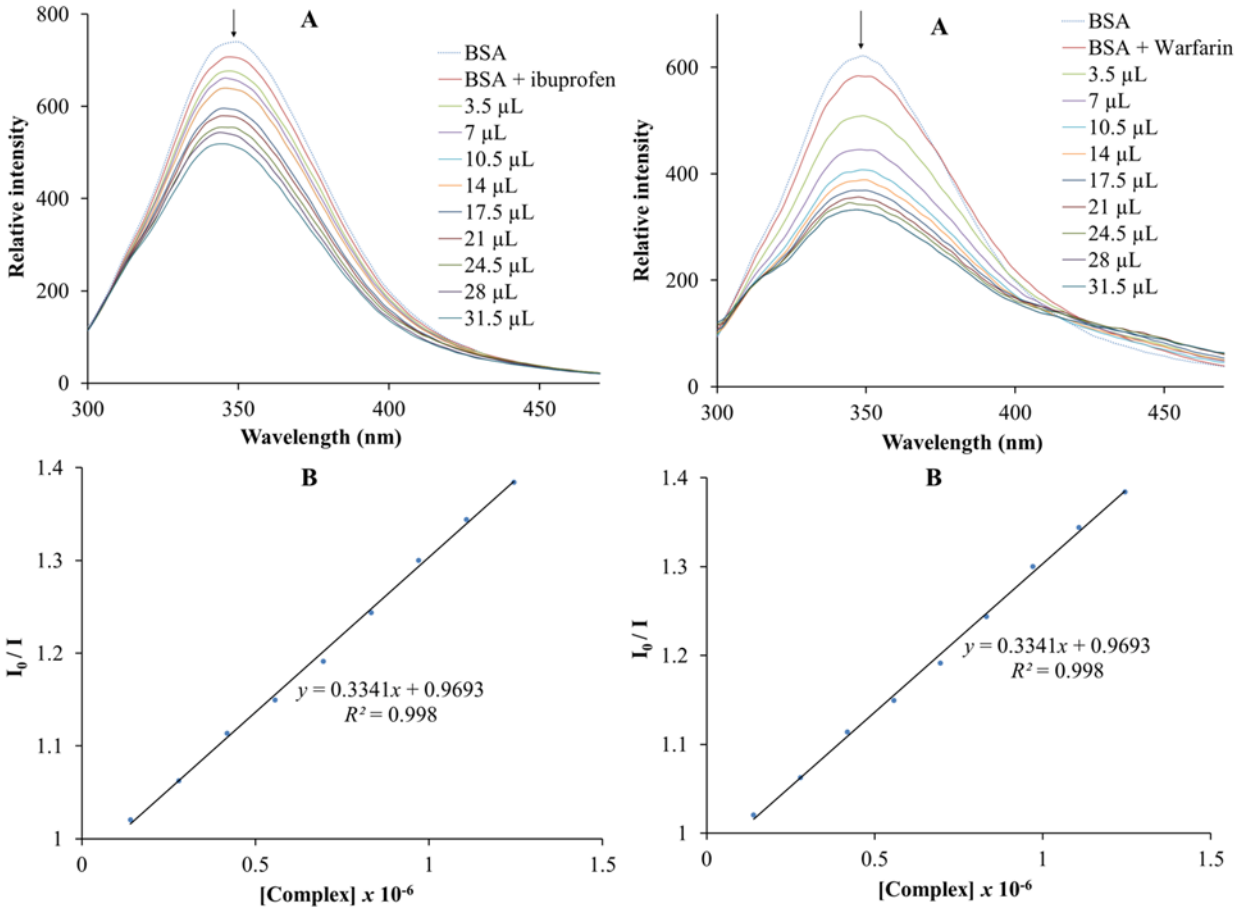

Figure 4.57: *BSA competitive binding between complex **3** and the respective site markers: ibuprofen and warfarin. (**A**): Fluorescence emission spectral profiles of BSA in the absence or presence of a specific site marker. Subsequent sequential additions of the standardized metal complex were added to the individual BSA-site marker samples. (**B**) is the corresponding Stern-Volmer plots.*

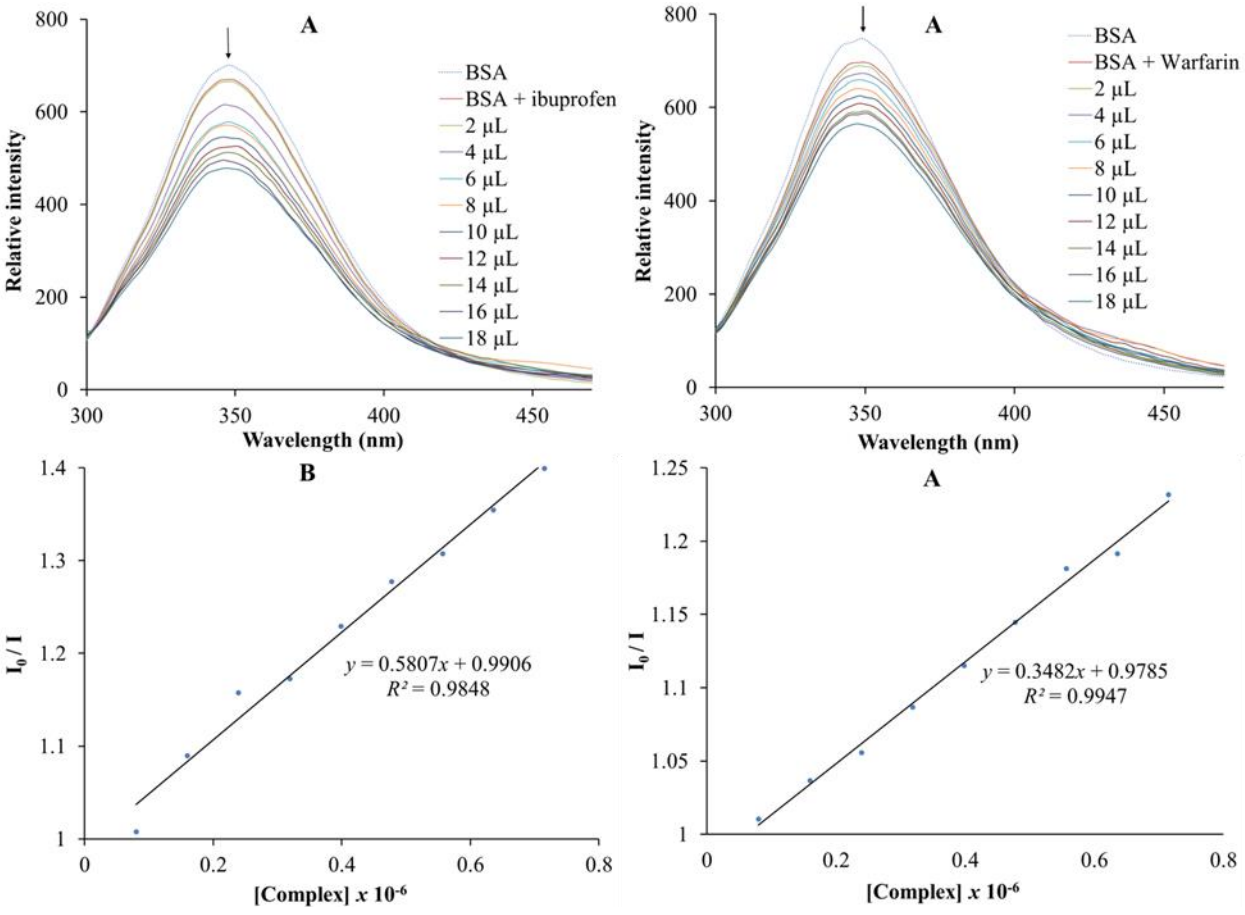

Figure 4.58: *BSA competitive binding between complex **4** and the respective site markers: ibuprofen and warfarin. (**A**): Fluorescence emission spectral profiles of BSA in the absence or presence of a specific site marker. Subsequent sequential additions of the standardized metal complex were added to the individual BSA-site marker samples. (**B**) is the corresponding Stern-Volmer plots.*

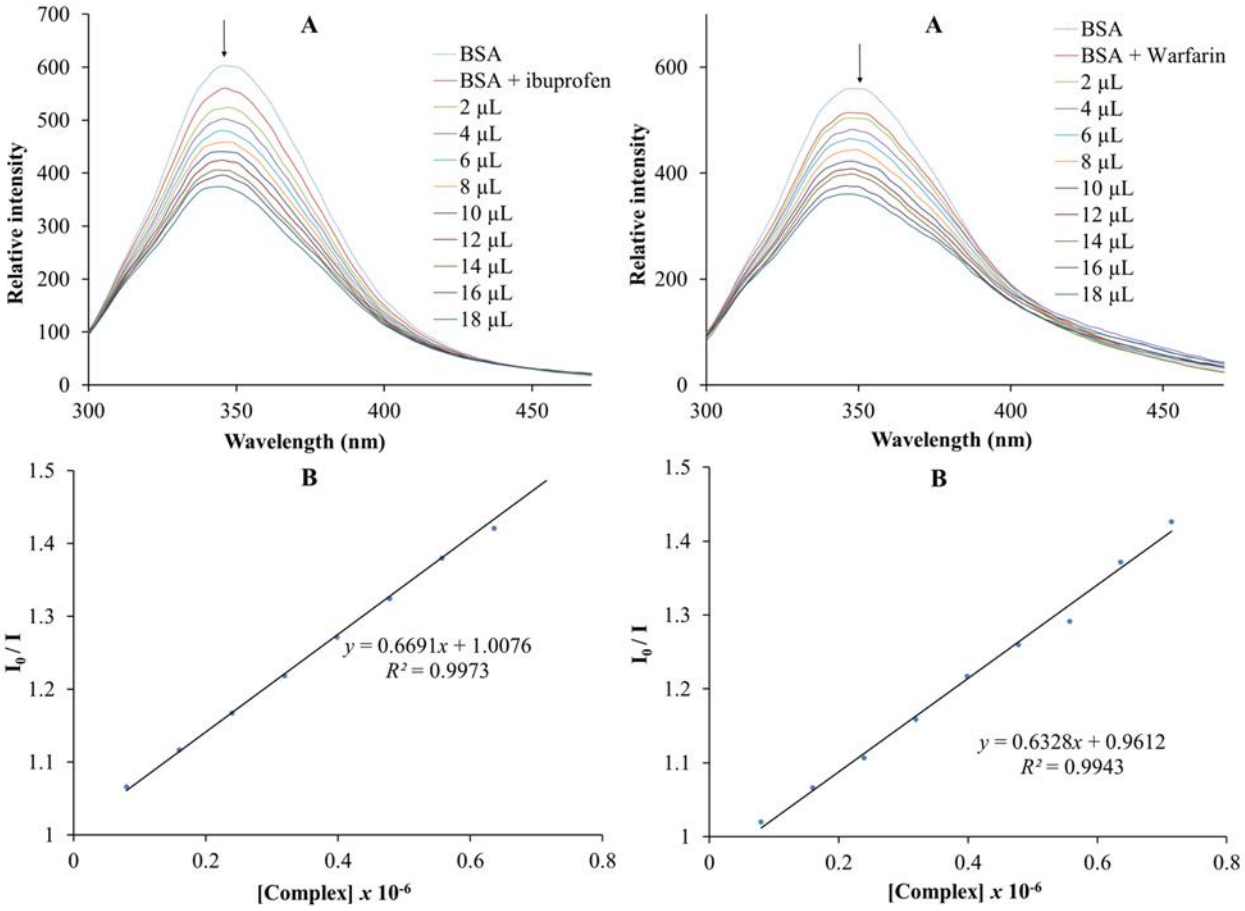

Figure 4.59: *BSA competitive binding between complex **5** and the respective site markers: ibuprofen and warfarin. (**A**): Fluorescence emission spectral profiles of BSA in the absence or presence of a specific site marker. Subsequent sequential additions of the standardized metal complex were added to the individual BSA-site marker samples. (**B**) is the corresponding Stern-Volmer plots.*

Table 4.11: Binding parameters of **1** – **5** attained from BSA competitive binding experiments.

Compound	No Site marker		Ibuprofen		Warfarin	
	K_{SV} (M^{-1})	K_q (M^{-1} s^{-1})	K_{SV} (M^{-1})	K_q (M^{-1} s^{-1})	K_{SV} (M^{-1})	K_q (M^{-1} s^{-1})
1	2.91×10^4	2.91×10^{11}	2.01×10^4	2.01×10^{11}	1.87×10^4	1.87×10^{11}
2	1.09×10^5	1.09×10^{12}	3.89×10^4	3.89×10^{11}	2.36×10^4	2.36×10^{11}
3	1.36×10^5	1.32×10^{12}	2.96×10^4	2.96×10^{11}	3.34×10^4	3.34×10^{11}
4	6.61×10^4	6.61×10^{11}	5.81×10^4	5.81×10^{11}	3.48×10^4	3.48×10^{11}
5	8.37×10^4	8.37×10^{11}	6.69×10^4	6.69×10^{11}	6.33×10^4	6.33×10^{11}

(d) Molecular docking

A rigid docking algorithm was employed to simulate the most energetically favourable binding site of each optimized metal conformer within the BSA crystal structure. These docking simulations illustrate that the ruthenium compounds exhibit two modes of docking whereby **1** – **3** are found in the IIA BSA cavity and the other metal complexes resides within the IB BSA cavity, see **Figures 4.60** – **4.64**. Although, conformer **2** is stabilized by solitary hydrogen-bond (at 2.370 Å) between its closest chloride co-ligand and ARG 194 amino acid residue, it affords the lowest global energy of -53.43 kJ/mol compared to that of the other BSA adducts: -46.96 kJ/mol with **1**, -51.04 kJ/mol with **3**, -48.96 kJ/mol with **4** and -40.98 kJ/mol with **5**. BSA adducts of **1** and **3** are stabilized by non-polar intramolecular interactions with GLU 293, LYS 294 (for **1**) and ALA 294, TRP 213 moieties (for **3**) while **4** and **5** forms close contacts with the GLU 424, PRO 110 (for **4**) and lysine moieties 107 (*viz.* LYS 114 and LYS 431) on either side of **5**.

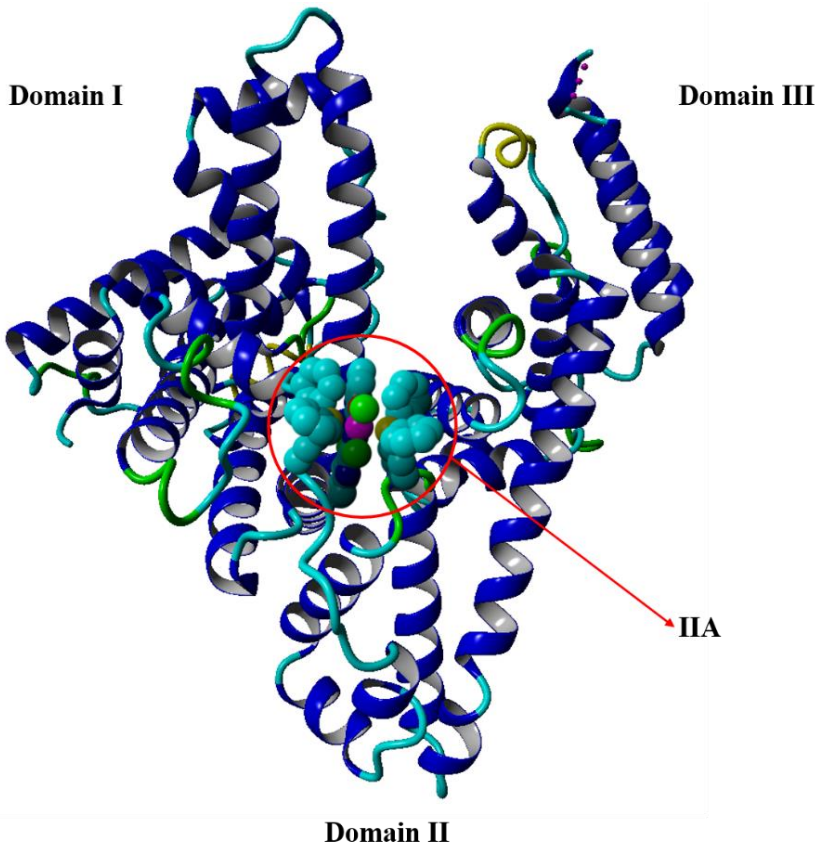

Figure 4.60: *The computed minimum energy adducts of BSA and **1** illustrating the metal complex docking with the **IIA** site of BSA.*

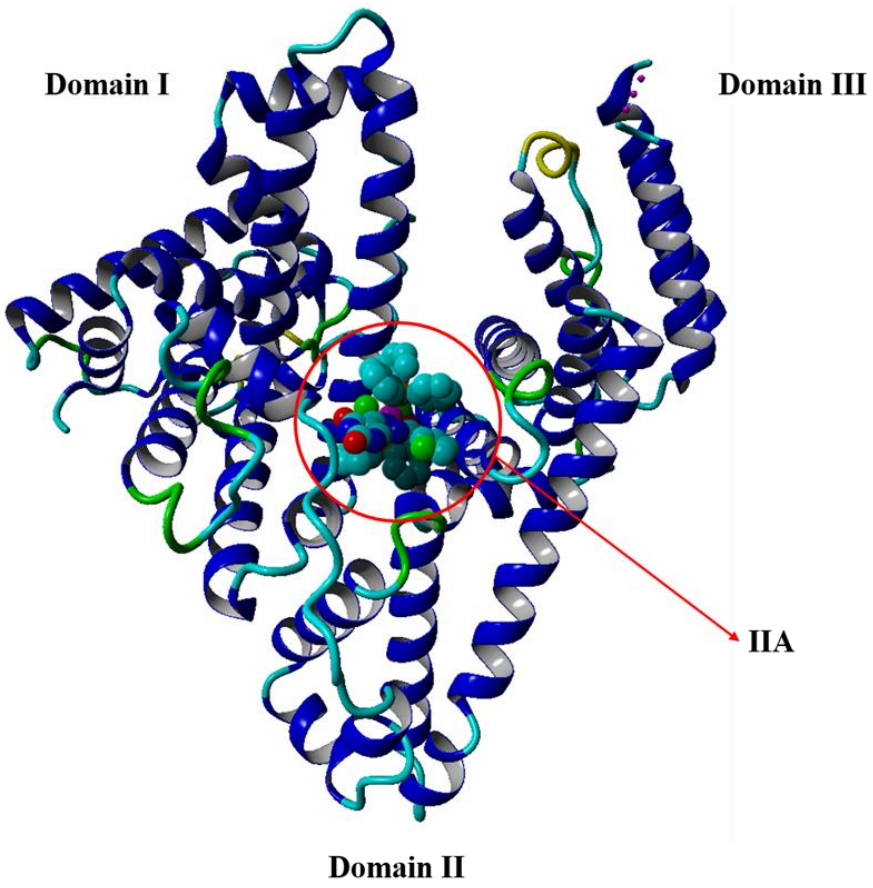

Figure 4.61: *The computed minimum energy adducts of BSA and **2** illustrating the metal complex docking with the **IIA** site of BSA.*

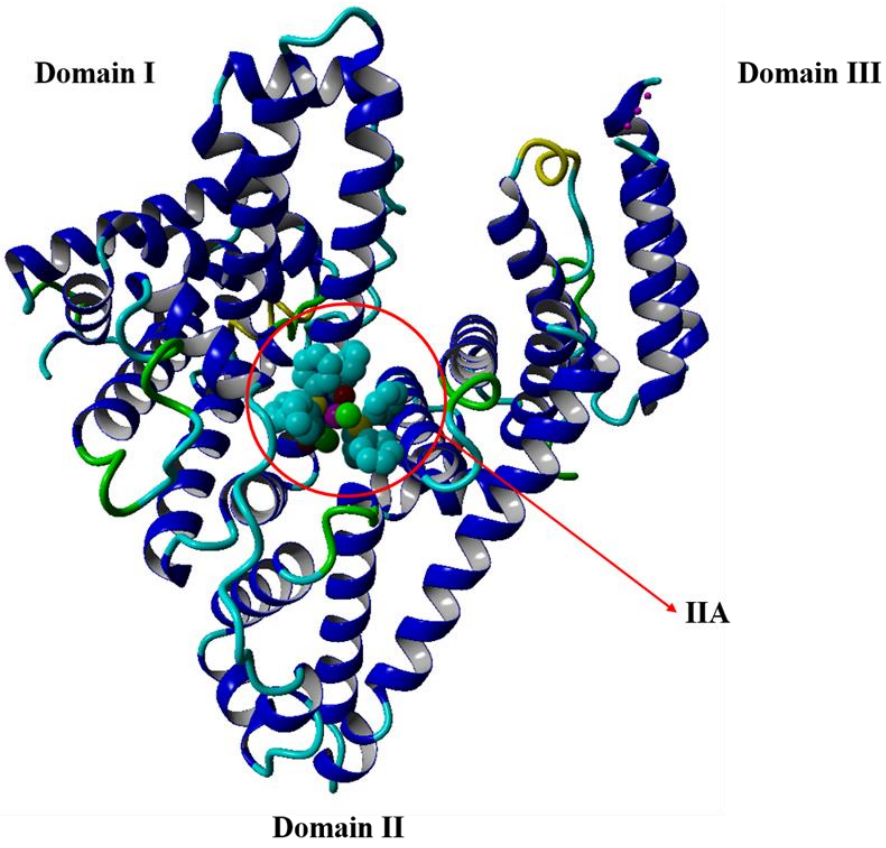

Figure 4.62: *The computed minimum energy adducts of BSA and **3** illustrating the metal complex docking with the **IIA** site of BSA.*

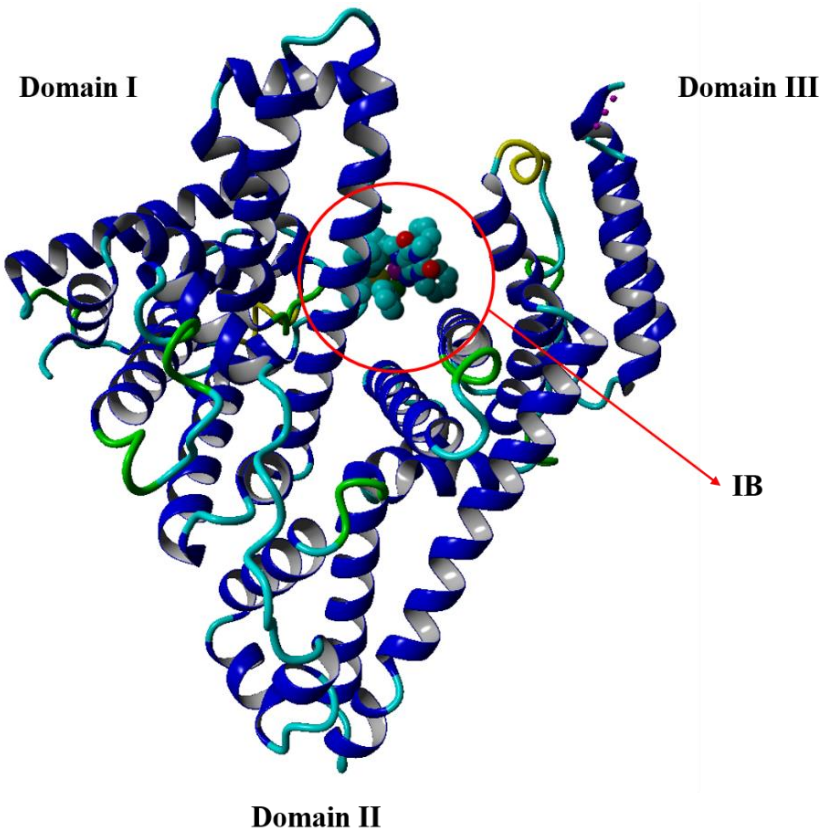

Figure 4.63: *Metal complex **4** occupying the BSA **IB** site.*

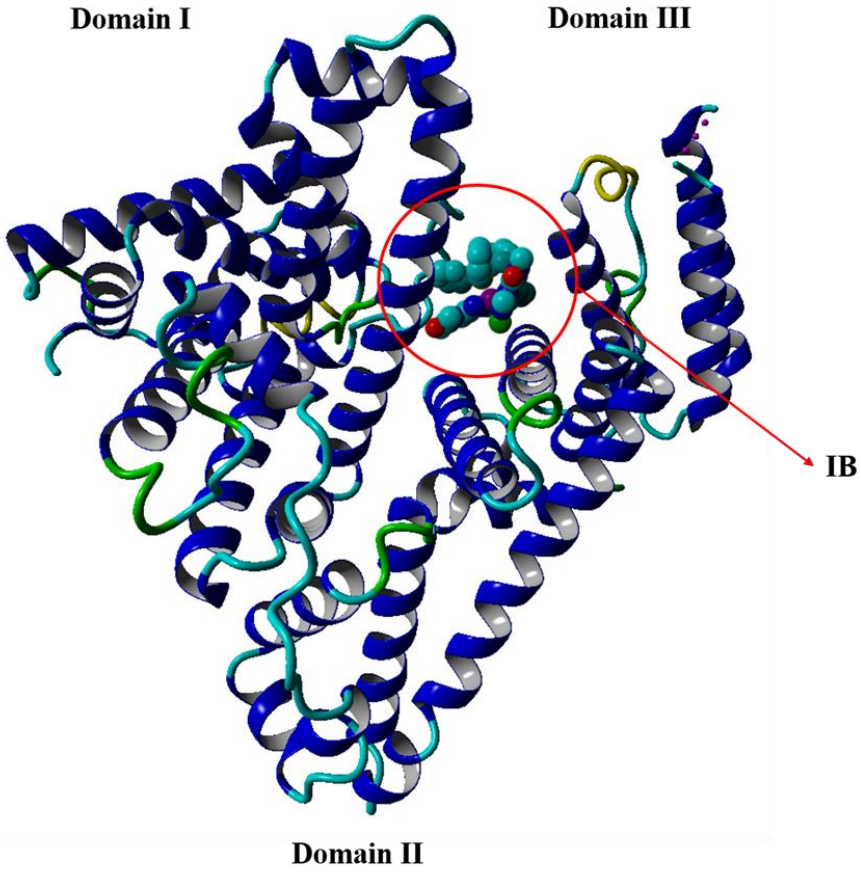

Figure 4.64: *The computed minimum energy adducts of BSA and **5** illustrating the metal complex docking with the **IB** site of BSA.*

4.5.7 In vitro anti-cancer activity

The compounds were assessed for anti-cancer activity in the aggressive HCC70 triple negative breast cancer cell line. Compounds **1** and **2** were not toxic below 100 μM, while compound **4** was the most toxic with an EC_{50} of 3.393 μM. Compounds **3** and **4** had similar EC_{50} values of 29.5 μM and 36.88 μM, respectively (**Table 4.12**).

Table 4.12: EC_{50} values against HCC 70 cells.

Compound	EC_{50}	R^2
1	>100 μM	N/A
2	>100 μM	N/A
3	29.5 μM	0.8905
4	3.4 μM	0.9959
5	36.9 μM	0.9713
5-fluorouracil	86.4 μM	0.8258
Tegafur	487.5 μM	0.9525
Paclitaxel	5.2 nM	0.9810

4.6 References

1. M. Pal, U. Nandi and D. Mukherjee, *Eur. J. Med. Chem.*, 2018, **150**, 419-445.

2. T. Lazarević, A. Rilak and Ž. D. Bugarčić, *Eur. J. Med. Chem.*, 2017, **142**, 8-31.

3. A. R. Timerbaev, *Trends Anal. Chem.*, 2016, **80**, 547-554.

4. J. Zhao, N. Liu, S. Sun, S. Gou, X. Wang, Z. Wang, X. Li and W. Zhang, *J. Inorg. Biochem.*, 2019, **196**, 110684.

5. A. K. Renfrew, *Metallomics*, 2014, **6**, 1324-1335.

6. J. Lopes, J. L. Damasceno, P. F. Oliveira, A. P. Guedes, D. C. Tavares, V. M. Deflon, N. P. Lopes, M. Pivatto, A. A. Batista and P. I. Maia, *J. Braz. Chem. Soc.*, 2015, **26**, 1838-1847.

7. D. B. Longley, D. P. Harkin and P. G. Johnston, *Nat. Rev. Cancer.*, 2003, **3**, 330-338.

8. G. S. Khan, A. Shah, R. Zia ur and D. Barker, *J. Photochem. Photobiol., B.*, 2012, **115**, 105-118.

9. S. Tzanopoulou, M. Sagnou, M. Paravatou-Petsotas, E. Gourni, G. Loudos, S. Xanthopoulos, D. Lafkas, H. Kiaris, A. Varvarigou and I. C. Pirmettis, *J. Med. Chem.*, 2010, **53**, 4633-4641.

10. J. R. Rodrigues, J. Charris, J. Camacho, A. Barazarte, N. Gamboa and F. Antunes, *Anticancer Res.*, 2012, **32**, 2721-2726.

11. J. A. Marchal, M. C. Núñez, I. Suárez, M. Díaz-Gavilán, J. A. Gómez-Vidal, H. Boulaiz, F. Rodríguez-Serrano, M. A. Gallo, A. Espinosa and A. Aránega, *Breast Cancer Res. Treat.*, 2007, **105**, 237-246.

12. F. Gao, H. Chao, J.-Q. Wang, Y.-X. Yuan, B. Sun, Y.-F. Wei, B. Peng and L.-N. Ji, *J. Biol. Inorg. Chem.*, 2007, **12**, 1015-1027.

13. C. B. Spillane, N. C. Fletcher, S. M. Rountree, H. van den Berg, S. Chanduloy, J. L. Morgan and F. R. Keene, *J. Biol. Inorg. Chem.*, 2007, **12**, 797-807.

14. L. Mabuza, M. Gamede, S. Maikoo, I. Booysen, P. Ngubane and A. Khathi, *Molecules*, 2018, **23**, 1721-1731.

15. L. P. Mabuza, M. W. Gamede, S. Maikoo, I. N. Booysen, P. S. Ngubane and A. Khathi, *Diabet. Metab. synd. Ob.*, 2019, **12**, 217-223.

16. R. H. Blessing, *Acta Crystallogr., Sect. A: Found. Adv.*, 1995, **51 (Pt 1)**, 33-38.

17. L. Farrugia, *J. Appl. Crystallogr.*, 2012, **45**, 849-854.

18. G. Sheldrick, *Acta Crystallogr., Sect. A: Found. Adv.*, 2008, **64**, 112-122.

19. Frisch MJ, Trucks GW, Schlegel HB, Scuseria GE, Robb MA, Cheeseman JR, Scalmani G, Barone V, Petersson GA, Nakatsuji H, Li X, Caricato M, Marenich AV, Bloino J, Janesko BG, Gomperts R, Mennucci B, Hratchian HP, Ortiz JV, Izmaylov AF, Sonnenberg JL, Williams, Ding F, Lipparini F, Egidi F, Goings J, Peng B, Petrone A, Henderson T, Ranasinghe D, Zakrzewski VG, Gao J, Rega N, Zheng G, Liang W, Hada M, Ehara M, Toyota K, Fukuda R, Hasegawa J, Ishida M, Nakajima T, Honda Y, Kitao O, Nakai H, Vreven T, Throssell K, Montgomery Jr JA, Peralta JE, Ogliaro F,

Bearpark MJ, Heyd JJ, Brothers EN, Kudin KN, Staroverov VN, Keith TA, Kobayashi R, Normand J, Raghavachari K, Rendell AP, Burant JC, Iyengar SS, Tomasi J, Cossi M, Millam JM, Klene M, Adamo C, Cammi R, Ochterski JW, Martin RL, Morokuma K, Farkas O, Foresman JB, Fox DJ (2009) Gaussian 09 Rev. A.01.

20. L. Gramni, N. Vukea, A. Chakraborty, W. J. Samson, L. M. K. Dingle, B. Xulu, J.-A. de la Mare, A. L. Edkins and I. N. Booysen, *Inorg. Chim. Acta.*, 2019, **492**, 98-107.

21. R. Raveendran and S. Pal, *J. Organomet. Chem.*, 2007, **692**, 824-830.

22. M. Mohanraj, G. Ayyannan, G. Raja and C. Jayabalakrishnan, *Mat. Sci. Eng. C. Mater.*, 2016, **69**, 1297-1306.

23. M. Mohanraj, G. Ayyannan, G. Raja and C. Jayabalakrishnan, *J. Photochem. Photobiol., B.*, 2016, **158**, 164-173.

24. C. Rodrigues, A. A. Batista, J. Ellena, E. E. Castellano, D. Benítez, H. Cerecetto, M. González, L. R. Teixeira and H. Beraldo, *Eur. J. Med. Chem.*, 2010, **45**, 2847-2853.

25. M. B. Ismail, I. N. Booysen, M. P. Akerman and C. Grimmer, *J. Organomet. Chem.*, 2017, **833**, 18-27.

26. M. B. Ismail, I. N. Booysen and M. P. Akerman, *Trans. Met. Chem.*, 2017, **42**, 405-412.

27. A. Ourari, M. Khelafi, D. Aggoun, G. Bouet and M. A. Khan, *Adv. Phys. Chem.*, 2011, **2011**.

28. I. N. Booysen, A. Adebisi, M. P. Akerman, O. Q. Munro and B. Xulu, *J. Coord. Chem.*, 2016, **69**, 1641-1652.

29. C. Jayabalakrishnan, R. Karvembu and K. Natarajan, *Synth. React. Inorg. Chem.*, 2003, **33**, 1535-1553.

30. B. Garga, P. Singh and J. Sharma, *Synth. React. Inorg. Chem.*, 2000, **30**, 803-813.

31. I. N. Booysen, S. Maikoo, M. Piers Akerman, B. Xulu and O. Munro, *J. Coord. Chem.*, 2013, **66**, 3673-3685.

32. I. N. Booysen, A. Adebisi and M. P. Akerman, *Inorg. Chim. Acta.*, 2015, **433**, 13-20.

33. N. Ljubijankić, A. Zahirović, E. Turkušić and E. Kahrović, *Croat. Chem. Acta.*, 2013, **86**, 215-222.

34. I. P. Ejidike and P. A. Ajibade, *Bioinorg. Chem. Appl.*, 2016, **2016**.

35. T. Risse, D. Hollmann and A. Brückner, *In situ electron paramagnetic resonance (EPR)–a unique tool for analysing structure and reaction behaviour of paramagnetic sites in model and real catalysts*, The Royal Society of Chemistry London, 2015.

36. Q. A. d. Paula, A. A. Batista, O. R. Nascimento, A. J. d. Costa-Filho, M. S. Schultz, M. R. Bonfadini and G. Oliva, *J. Braz. Chem. Soc.*, 2000, **11**, 530-536.

37. I. N. Booysen, A. Adebisi, O. Q. Munro and B. Xulu, *Polyhedron*, 2014, **73**, 1-11.

38. C. P. Matos, A. Valente, F. Marques, P. Adão, M. P. Robalo, R. F. de Almeida, J. C. Pessoa, I. Santos, M. H. Garcia and A. I. Tomaz, *Inorg. Chim. Acta.*, 2013, **394**, 616-626.

39. V. Atsarkin, G. Vasneva, V. Demidov, M. Gutmann and G. Böttger, *J. Exp. Theor. Phys.*, 1999, **69**, 610-615.

40. F. Basuli, A. K. Das, G. Mostafa, S.-M. Peng and S. Bhattacharya, *Polyhedron*, 2000, **19**, 1663-1672.

41. Z. Shirin and R. Mukherjee, *Polyhedron*, 1992, **11**, 2625-2630.

42. D. Bhattacharyya, S. Chakraborty, P. Munshi and G. K. Lahiri, *Polyhedron*, 1999, **18**, 2951-2959.

43. R. Ramesh, D. Nallasamy, R. Karvembu and K. Natarajan, *Indian J. Chem., Sect. A: Inorg., Bio-inorg., Phys., Theor. Anal. Chem.*, 2000, **39**, 1079-1082.

44. L.-H. Tang, X. Chen, A.-Q. Jia, Z. Xin and Q.-F. Zhang, *Inorg. Chim. Acta.*, 2018, **480**, 108-112.

45. J. Małecki, *Polyhedron*, 2010, **29**, 2489-2497.

46. J. Gu, L.-M. Shi, X.-F. Ma, A.-Q. Jia and Q.-F. Zhang, *Inorg. Chim. Acta.*, 2017, **466**, 382-388.

47. R. Ramachandran, G. Prakash, P. Viswanathamurthi and J. Malecki, *Inorg. Chim. Acta.*, 2018, **477**, 122-129.

48. E. Jayanthi, S. Kalaiselvi, V. V. Padma, N. S. Bhuvanesh and N. Dharmaraj, *Dalton Trans.*, 2016, **45**, 1693-1707.

49. M. Alagesan, N. S. Bhuvanesh and N. Dharmaraj, *Dalton Trans.*, 2014, **43**, 6087-6099.

50. G. Prakash, R. Manikandan, P. Viswanathamurthi, K. Velmurugan and R. Nandhakumar, *J. Photochem. Photobiol., B.*, 2014, **138**, 63-74.

51. M. S. Hatwalne, *Indian. J. Anaesth.*, 2012, **56**, 227-233.

52. P. Srivastava, R. Mishra, M. Verma, S. Sivakumar and A. K. Patra, *Polyhedron*, 2019, DOI: https://doi.org/10.1016/j.poly.2019.04.009, 132-140.

53. R. Ramachandran and P. Viswanathamurthi, *Spectrochim. Acta, Part A.*, 2013, **103**, 53-61.

54. K. Sampath and C. Jayabalakrishnan, *DJ J. Eng. Chem. Fuel.*, 2016, **1**, 40-53.

55. V. Brabec and J. Kasparkova, *Coord. Chem. Rev.*, 2018, **376**, 75-94.

56. T. Topala, A. Bodoki, L. Oprean and R. Oprean, *Farmacia*, 2014, **62**, 1049-1061.

57. M. Sirajuddin, S. Ali and A. Badshah, *J. Photochem. Photobiol., B.*, 2013, **124**, 1-19.

58. S. Sathiyaraj, G. Ayyannan and C. Jayabalakrishnan, *J. Serb. Chem. Soc.*, 2014, **79**, 151-165.

59. R. Hajian and F. Panahi, *Indian J. Chem., Sect. A: Inorg., Bio-inorg., Phys., Theor. Anal. Chem.*, 2013, **52**, 1251-1256.

60. K. W. Kohn, M. J. Waring, D. Glaubiger and C. A. Friedman, *Cancer Res.*, 1975, **35**, 71-76.

61. T. S. Kamatchi, N. Chitrapriya, H. Lee, C. F. Fronczek, F. R. Fronczek and K. Natarajan, *Dalton Trans.*, 2012, **41**, 2066-2077.

62. A. P. Carnizello, M. I. Barbosa, M. Martins, N. H. Ferreira, P. F. Oliveira, G. M. Magalhães, A. A. Batista and D. C. Tavares, *J. Inorg. Biochem.*, 2016, **164**, 42-48.

63. F. A. Beckford, A. Stott, P. C. Mbarushimana, M.-A. LeBlanc, K. Hall, S. Smith, J. L. Bullock, D. J. Houghton, A. A. Holder and N. Gerasimchuk, *Interdiscip. J. Chem.*, 2016, **1**, 1-15.

64. D. Lazić, A. Arsenijević, R. Puchta, Ž. D. Bugarčić and A. Rilak, *Dalton Trans.*, 2016, **45**, 4633-4646.

65. K. Sampath, S. Sathiyaraj and C. Jayabalakrishnan, *Med. Chem. Res.*, 2014, **23**, 958-968.

66. D. Abdullin, N. Florin, G. Hagelueken and O. Schiemann, *Angew. Chem. Int. Ed.* , 2015, **54**, 1827-1831.

67. S. Tabassum, M. Zaki, M. Afzal and F. Arjmand, *Eur. J. Med. Chem.*, 2014, **74**, 509-523.

68. G. Balakrishnan, T. Rajendran, K. S. Murugan, M. S. Kumar, V. K. Sivasubramanian, M. Ganesan, A. Mahesh, T. Thirunalasundari and S. Rajagopal, *Inorg. Chim. Acta.*, 2015, **434**, 51-59.

69. S. Ghosh, P. Kundu, B. K. Paul and N. Chattopadhyay, *RSC. Adv.*, 2014, **4**, 63549-63558.

70. P. Naik, S. Chimatadar and S. Nandibewoor, *Spectrochim. Acta, Part A.*, 2009, **73**, 841-845.

71. X. Kong, Y. Liu and Y. Chen, *J. Polym. Sci. Eng.*, 2018, **1**, 30-42.

72. K. Malarkani, I. Sarkar and S. Selvam, *J. Pharm. Anal.*, 2018, **8**, 27-36.

73. A. Varlan and M. Hillebrand, *Molecules*, 2010, **15**, 3905-3919.

74. R. Kumaran and P. Ramamurthy, *J. Fluoresc.*, 2011, **21**, 1499-1508.

75. M. Rajabi, M. A. Khalilzadeh, F. Tavakolinia, P. Signorelli, R. Ghidoni and E. Santaniello, *DNA Cell Biol.*, 2012, **31**, 783-789.

76. V. Ravi Kumar, P. Nagababu, G. Srinivas, M. Rajender Reddy, M. Vinoda Rani, M. Ravi and S. Satyanarayana, *J. Coord. Chem.*, 2017, **70**, 3790-3809.

77. L. Luzuriaga and M. F. Cerdá, *Adv. Biol. Chem.*, 2012, **2**, 262-267.

78. M. Nešić, I. Popović, A. Leskovac and M. Petković, *BioMetals*, 2016, **29**, 921-933.

79. P. Vijayan, P. Viswanathamurthi, P. Sugumar, M. N. Ponnuswamy, M. D. Balakumaran, P. T. Kalaichelvan, K. Velmurugan, R. Nandhakumar and R. J. Butcher, *Inorg. Chem. Front.*, 2015, **2**, 620-639.

80. Y. Sun, B. Su, Q. Xu and R. Liu, *Appl. Spectrosc.*, 2012, **66**, 791-797.

81. Z. Tavsan, P. K. Yaman, E. Subasi and H. A. Kayali, *J. Biol. Inorg. Chem.*, 2018, **23**, 425-435.

82. V. Arumugam, R. Rajamanikandan, M. Ilanchelian, K. G. Moodley and G. G. Redhi, *Spectrochim. Acta. A.*, 2019, **210**, 299-307.

83. N. Sankar, J. Eswaran, T. Murugan, B. Nattamai S.P, M. A. Neelakantan and K. M. Velusamy, *Organoruthenium (II) complexes featuring pyrazole-linked Schiff base ligands: Crystal structure, DNA/BSA interactions, cytotoxicity and molecular docking: Half-sandwiched ruthenium complexes Pyrazole schiff base ligand*, 2019.

84. X. Zhang, L. Li, Z. Xu, Z. Liang, J. Su, J. Huang and B. Li, *PLoS One*, 2013, **8**, e59106.

Chapter 5

Formation, characterization and biomolecular interactions of new ruthenium compounds with thiosemicarbazone or benzothiazole Schiff base chelates

5.1 Introduction

Among the key design attributes for the next-generation of metal-based chemotherapeutic drugs is target specificity which defines the capability of a drug to kill cancerous cells while being benign to healthy tissue [**1**]. In particular, *N*-heterocyclic coordination compounds of ruthenium have sparked interest in the design of novel anti-cancer agents as these metal complexes could be potential substitute drugs for current established chemotherapeutic drugs with undefined biodistribution patterns [**2**]. In comparison to platinum-based anticancer pharmaceuticals, these leading ruthenium-containing chemotherapeutics exhibit comparable cytotoxicity but are physiologically more compatible owing to ruthenium's similar properties to the essential metal, iron [**3**].

A topical design strategy in organoruthenium drugs comprises the use of biologically active chelators that can tailor the biodistribution patterns towards specific cancers [**4**]. This design approach has resulted in promising multi-targeted drugs which display good target specificity which is induced by synergetic effects of the metal centre and its bio-active chelating ligands [**5-7**]. Herein, we consider two prominent bio-active moieties (*viz.* benzothiazole and

thiosemicarbazide) [**Figure 5.1**] as potential pharmacophores which were incorporated into multidentate Schiff bases.

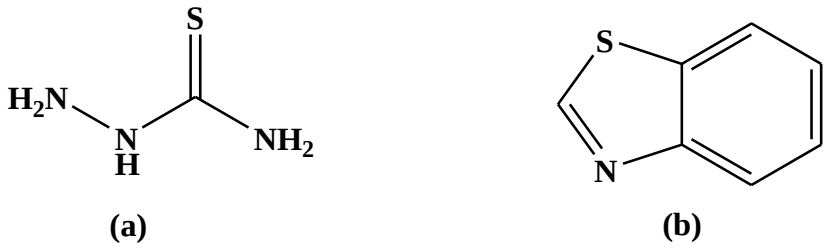

(a) **(b)**

Figure 5.1: *Structures of (a) thiosemicarbazide and (b) benzothiazole.*

Our selections are motivated by the fact that the benzothiazole group is a common synthon for numerous organic pharmaceuticals whilst the derivatives of thiosemicarbazide are of considerable interest since they display a broad spectrum of biological activities [**8-10**]. Moreover, ruthenium compounds with *N*-donor ligands encompassing either of these biological active moieties, have shown more enhanced *in vitro* anticancer activities than their free ligands [**11, 12**]. In addition, the anticancer activities of this class of metal-based drugs can be readily modulated by their structures, *e.g.* the ruthenium(II) complex salt, *cis*-$[Ru(bipy)_2(4,5'\text{-bbtb})]^{2+}$ (bbtb = *bis*-(benzothiazol-2-yl)-2,2'-bipyridine) interacts with ct-DNA *via* groove-binding due to the steric demands of its *N*-donor chelating [**13**].

In this chapter, we report the formation and characterization of ruthenium(II) and -(III) compounds with Schiff bases with benzothiazole or thiosemicarbazone moieties. These ruthenium compounds: *trans-P*-$[RuCl(PPh_3)_2(pmt)]Cl$ (**1**), *trans-P*-$[RuCl(PPh_3)_2(tmc)]Cl$ (**2**) and *cis-Cl, trans-P*-$[RuCl_2(PPh_3)_2(btm)]$ (**3**) were isolated from the coordination reactions of *trans*-$[RuCl_2(PPh_3)_3]$ with the Schiff bases 1-((pyridin-2-yl)methylene)thiosemicarbazide (Hpmt), 1-((thiophen-2-yl)methylene)thiosemicarbazide (Htmc) and 2-((5-hydroxypentylimino)methyl)benzothiazole (btm), respectively [see **Figure 5.2**]. We have also probed the interaction of the metal compounds with calf thymus (CT)-DNA and BSA as well as studied their radical scavenging abilities.

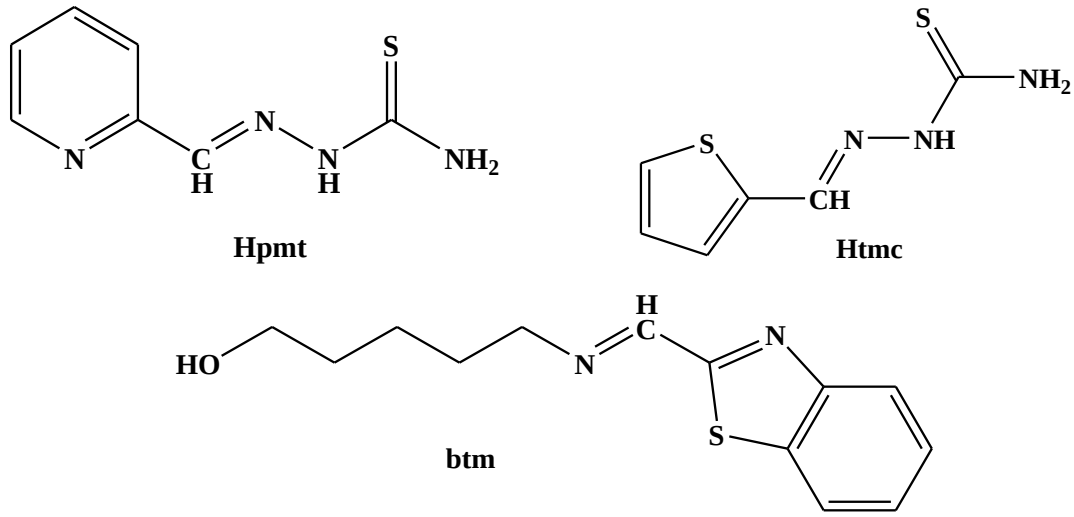

Figure 5.2: *Structures of Schiff bases Hpmt, Htmc and btm.*

5.2 Experimental

*5.2.1 Synthesis of trans-P-[RuCl(PPh$_3$)$_2$(pmt)]Cl (**1**)*

A 1:1 molar reaction of Hpmt (0.0188 g, 0.104 mmol) and *trans*-[$RuCl_2(PPh_3)_3$] (0.100 g, 0.104 mmol) was heated until reflux for 3 hours in ethanol (20 cm^3). The brick-red solution was cooled to room temperature and a shiny brown precipitate filtered. The brown precipitate was dissolved in dichloromethane and placed in a diffusion chamber with hexane in the adjacent chamber. After several days, rectangular XRD quality crystals were afforded. Yield: 51 %, m.p: 203.4 – 205.0 ºC. IR (ν_{max}/cm^{-1}): ν(N-H) 3468 (w), 3049 (br, m); ν(C=N)$_{thiolate}$ 1586 (w); ν(C=N)$_{imino}$ 1552 (m); ν(C-N)$_{thiolate}$ 1431 (s); ν(N-N)$_{thiolate}$ 1088 (s); ν(Ru-[PPh_3]$_2$) 691 (s), 742 (vs). UV-Vis (DCM, ε, M^{-1} cm^{-1}): 282 nm (1730); 311 nm (1350); 368 nm (830); 481 nm (620); 680 nm (sh, 70).

*5.2.2 Synthesis of trans-P-[RuCl(PPh$_3$)$_2$(tmc)]Cl (**2**)*

A mixture of Htmc (0.0193 g, 0.104 mmol) and *trans*-[$RuCl_2(PPh_3)_3$] (0.100 g, 0.104 mmol) in ethanol (20 cm^3) was heated until reflux for 3 hours. The resulting brown precipitate was filtered by gravity, dissolved in dichloromethane and placed in a diffusion chamber with hexane. After a few days, brown rectangular crystals which were suitable for X-ray analysis, were obtained. Yield: 47 %. m.p: 222 – 226 ºC. IR (ν_{max}/cm^{-1}): ν(N-H) 3353 (br, m), 3048 (w);

ν(C=N)*thiolate* 1608 (m); ν(C=N)*imino* 1579 (s); ν(C-N)*thiolate* 1431 (s); ν(C=N)*thiolate* 1090 (s); ν(Ru-[PPh_3]$_2$) 694 (s), 742 (vs). UV-Vis (DCM, ε, M^{-1} cm^{-1}): 266 nm (3660); 329 nm (1070); 359 nm (1100); 447 (410); 589 nm (sh, 60).

*5.2.3 Synthesis of cis-Cl, trans-P-[$RuCl_2(PPh_3)_2$(btm)] (**3**)*

The title compound was formed from the equimolar reaction between btm (0.0259 g, 0.104 mmol) and *trans*-[$RuCl_2(PPh_3)_3$] (0.100 g, 0.104 mmol) after 3 hours of heating at reflux temperature in 20 cm^3 methanol. The resulting maroon solution was filtered, cooled to room temperature and allowed to stand at STP. X-ray quality cubic-shaped crystals were grown from the slow evaporation of the mother liquor. Yield: 33 %, m.p: 280.7 – 284.0 ºC. IR (ν_{max}/cm^{-1}): ν(O-H) 3461 (br, m); ν(C=N)*imino* 1534 (m); ν(C=N)*benzothiazole* 1479 (m); ν(C-N)*benzothiazole* 1429 (s); ν(Ru-[PPh_3]$_2$) 691 (s), 739 (vs). ^{1}H NMR (295 K/ d^6 - CD_6SO/ ppm): 8.19 (1H, d, *H5*); 8.04 (1H, d, *H2*); 7.50 - 7.10 (33H, m, *2 x PPh3, H3, H4, H8*); 4.35 (1H, s, *OH*); 1.50 - 1.43 (2H, m, *H13, H13', H12, H12'*); 1.50 – 1.05 (6H, m, *H11, H11'*, *H10, H10'*, *H9, H9'*). ^{31}P NMR (295K/ d_6 - CD_6SO/ ppm): 26.39. UV-Vis (DCM, ε, M^{-1} cm^{-1}): 282 nm (4340); 344 nm (sh, 740); 390 nm (sh, 160); 531 nm (840).

5.3 X-ray crystallography

X-ray crystallographic data of the respective metal complexes was collected using a Bruker Apex Duo equipped with an Oxford Instruments Cryojet which were operated at variable temperatures [293(2) K for **2**.2(CH_2Cl_2), 100(2) K for **1**.CH_2Cl_2 and **3**.CH_3OH] and an Incoatec microsource running at 30 W power. The details of the crystal structure refinement are summarized in **Table 5.4** while the experimental and optimized geometrical parameters are given in **Tables 5.5** – **5.7**. X-ray radiation were induced with MoKα with a wavelength of 0.71073 Å. A mutual crystal-to-detector distance of approximately 50 mm during radiation exposure.

Other instrumental conditions includes phi and omega scans with exposures taken at 30 W X-ray power and 0.50º frame widths with APEX2 [**14**]. The data processing was conducted by firstly using the SAINT program [**14**] to reduce the data set by implementing standard Lorentz and polarization correction factors, scan speed scaling as well as outlier rejection. Afterwards,

SADABS semi-empirical multi-scan absorption correction [**15**] was applied which served as correction of the data. The structures were solved by making use of direct methods, WinGX [**16**] and SHELX-2016 [**17**]. Subsequently, the non-hydrogen atoms were found by means of the difference density map and anisotropically refined with SHELX-2016 [**17**]. All hydrogen atoms were defined as idealized contributors in the least squares process. A standard riding model was used to determine the hydrogen positions where the following parameters were used with C-H_{methyl} distances of 0.98 Å, U_{iso} = 1.5 U_{eq}, C-$H_{methylene}$ distances of 0.99 Å, U_{iso} = 1.2 U_{eq}, C-$H_{aromatic}$ distances of 0.93 Å and U_{iso} = 1.2 U_{eq}.

5.4 Computational details

Gaussian 09W software package was used to conduct *ab initio* calculations [**18**]. The geometric optimizations for **1 - 3** were done using DFT calculations using the LANL2DZ basis set. Individual starting conformers were directly derived from the respective crystal structures whereby all solvent molecules of crystallization and counter-ions were deleted. The employed computational algorithms were validated by reasonably good agreements found between the optimized and experimental geometrical parameters as well as the computed infrared spectra show no simulated vibrations with negative Eigen values [**19**]. Consequently, the latter implies that the optimized conformers are true global minima within their individual potential energy surfaces.

5.5 Results and discussion

5.5.1 Synthesis and spectral characterization

The novel ruthenium compounds **1** and **2** were isolated in moderate yields from respective equimolar coordination reactions of *trans*-[$RuCl_2(PPh_3)_3$] with Hpmt and Htmc whilst a 1:1 molar reaction with btm resulted in the isolation of metal complex **3** in low yield. In the case of **1** and **2**, both their Schiff base chelators coordinate as monoanionic tridentate chelators *via* their $S_{thiolate}N_{imino}N_{pyridine}$ (in **1**) $S_{thiolate}N_{imino}S_{thiophene}$ (in **2**) donor sets. Numerous ruthenium complexes with thiosemicarbazone Schiff bases have shown preferential coordination modes through their imino nitrogen and thiolate sulphur donor atoms, *e.g.* [$Ru(CO)Cl(PPh_3)_2(TSC^{N-}$

^{S})] (TSC^{N-S} = 1-((thiophen-2-yl)methylene)thiosemicarbazide) [**20**]. In fact, thiosemicarbazone ligands can exist in different tautomeric forms; as a thione tautomer or in the thiol forms, refer to **Scheme 5.1**. Therefore as per literature trends, thiosemicarbazone ligands can function as neutral tridentate chelators in the thione form or anionic chelators in the thiolate forms [**20-22**].

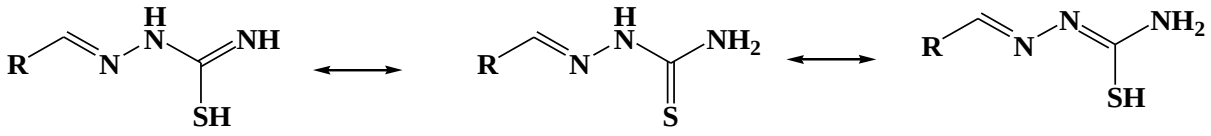

(b) **(a)** **(c)**

Scheme 5.1: *Tautomers of thiosemicarbazone: (**a**) thione, (**b**) thiol form 1 and (**c**) thiol form 2.*

Comprehensive literature searches conducted using the Cambridge Crystallographic Database (CCDC) and Scifinder reveals that several ruthenium compounds with Hpmt and Htmc as well as their closely related derivatives, have been isolated. In the solid-state structures, *cis*-[Ru(pmt)$_2$(dppb)]·H$_2$O (dppb = 1, 4-*bis*(diphenylphosphino)butane) and *cis*-[Ru(tmc)$_2$(P(pTol)$_3$)$_2$] (pTol = *tri*-*p*-tolylphosphine)), it is illustrated that the pmt and tmc chelators are in the thiol form 2 while the Htmc analogue, 2-acetyl-5-methyl-thiophene thiosemicarbazone (TSC^2) coordinated as S$_{thioketone}$ monodentate neutral chelators towards the ruthenium(II) arene core of [(η^6-*p*-cymene)Ru(S-TSC^2)Cl$_2$] [**23, 24**]. Scifinder searches where Hpmt and Htmc were used as individual sub-structures, coordinated to ruthenium afforded results which portray the diverse coordination behaviours of these ligands. In particular, Htmc and their derivatives predominately coordinate through their neutral imino nitrogen and thioketone sulphur donor sets (*e.g. cis*-[RuCl$_2$(Hmtc)$_2$]Cl) while deprotonation of Htmc's aliphatic amido nitrogen can also occur which renders constrained four-membered chelate rings, *e.g. trans*-[Ru(mtc)$_2$(PPh$_3$)$_2$] [**25, 26**]. Also, tridentate S$_{thiophene}$N$_{imino}$S$_{thioketone}$ stabilizations of the *cis*-[RuCl$_2$]$^+$ core have been reported, *e.g. cis*-[RuCl$_2$(Hmtcpy)]Cl (Hmtcpy = *N*-(α-pyridyl)thiophene-2-aldehyde thiosemicarbazone) [**27**]. Metal chelation of Htmc tautomers in the thiol form (**c**) are known to occur (*e.g trans*-[RuCl$_2$(PPh$_3$)$_2$(η^2-N,S-5-Cl-mtc) (5-Cl-Hmtc = 1-((5-chlorothiophen-2-yl)methylene)thiosemicarbazide) [**28**]. Similarly, Hpmt and its analogues have coordination susceptibilities towards ruthenium, occurring *via* bidentate and tridentate chelation which are quite prevalent [**29, 30**]. In fact, octahedral saturation by this class of thiosemicarbazone have occurred in the form of "3+3" and "3+2" (*e.g.*

$[Ru(acpmt)_2].3Cl$, acpmt = 2-acetylpyridine-(2-methylthiosemicarbazone)) ruthenium complex salts [**31**]. With the exception of **1** and **2**, the heteronuclear compound, (μ-2-((2-(oxy)-1-naphthyl)methylene)hydrazinecarbimidothioato)-carbonyl-chloro-tris(triphenylphosphine)-nickel-ruthenium is the only example where a thiosemicarbazide-derived Schiff base is in the thiol (b) tautomeric form, when coordinated to ruthenium [**32**].

In **3**, btm functions as a neutral bidentate chelator *via* the $N_{imino}N_{benzothiazole}$ donor set which corresponds well with trends found within literature. In particular, ruthenium compounds with benzothiazole moieties have shown tendencies in coordination affinity, whereby the $N_{benzothiazole}$ donor atom bonds to soft acceptor metal centres such as ruthenium(II). An example of this phenomenon is the diamagnetic ruthenium compound, $[Ru(pybs)(PPh_3)(CH_3CN)_2Cl]Cl$ (pybs = 2-(2-pyridyl)benzothiazole) [**33**]. Furthermore, the metal compounds **1** – **3** are stable in air, soluble in chloroform, dichloromethane, dimethyl sulfoxide and tetrahydrofuran as well as partially soluble in alcoholic media and acetonitrile.

The ^{1}H NMR spectrum of the diamagnetic metal complex **3** is dominated by a multiplet within the region 7.50 - 7.10 ppm which is partly owing to the triphenylphosphine co-ligands [**34**], see **Figure 5.3**. Evidence of coordination through the imino nitrogen arises from a significant shift of its singlet (8.64 ppm in the proton spectrum of the free ligand) which now forms part of the multiplet region (7.50 - 7.10 ppm) [**35**]. Clearly evident, are signals for the protons of the benzothiazole moiety (*viz. H2, H3, H4, H5)* which show noteworthy changes upon coordination. More specifically, a multiplet between 8.21 – 8.11 ppm (for *H2* and *H5*) within the free-ligand's proton spectrum splits into two individual doublets (at 8.19 and 8.04 ppm) in the proton spectrum of **3** while the remaining benzothiazole protons which originally formed part of the intense multiplet between 7.60 – 7.50 ppm (for *H8* and *H9*) coalesce into the multiplet region between 7.50 – 7.10 ppm as observed in the ^{1}H NMR spectrum of **3**. This is indicative of the change in the environment around the benzothiazole moiety post coordination. Similarly, the aliphatic protons coalesce into two broad poorly resolved signals. Magnetic equivalence of the *trans*-axial phosphorous atoms were confirmed by the presence of a single peak in the ^{31}P NMR spectrum [**36**], see **Figure 5.4**.

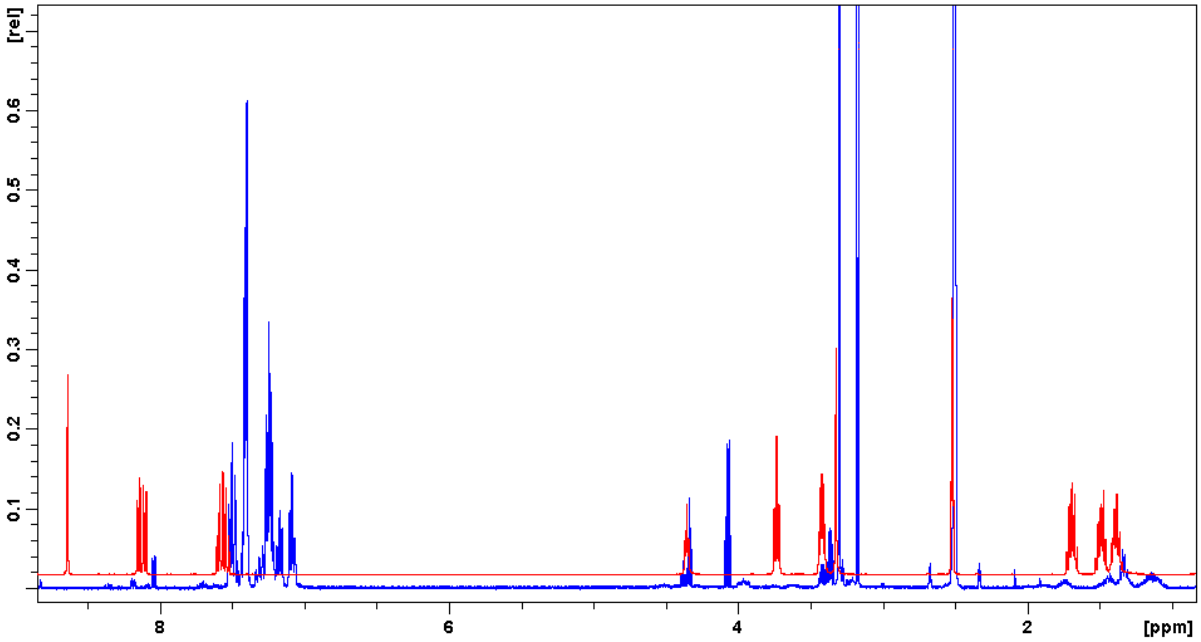

Figure 5.3: *Overlay ^{1}H NMR spectra of btm (red) and compound **3** (blue).*

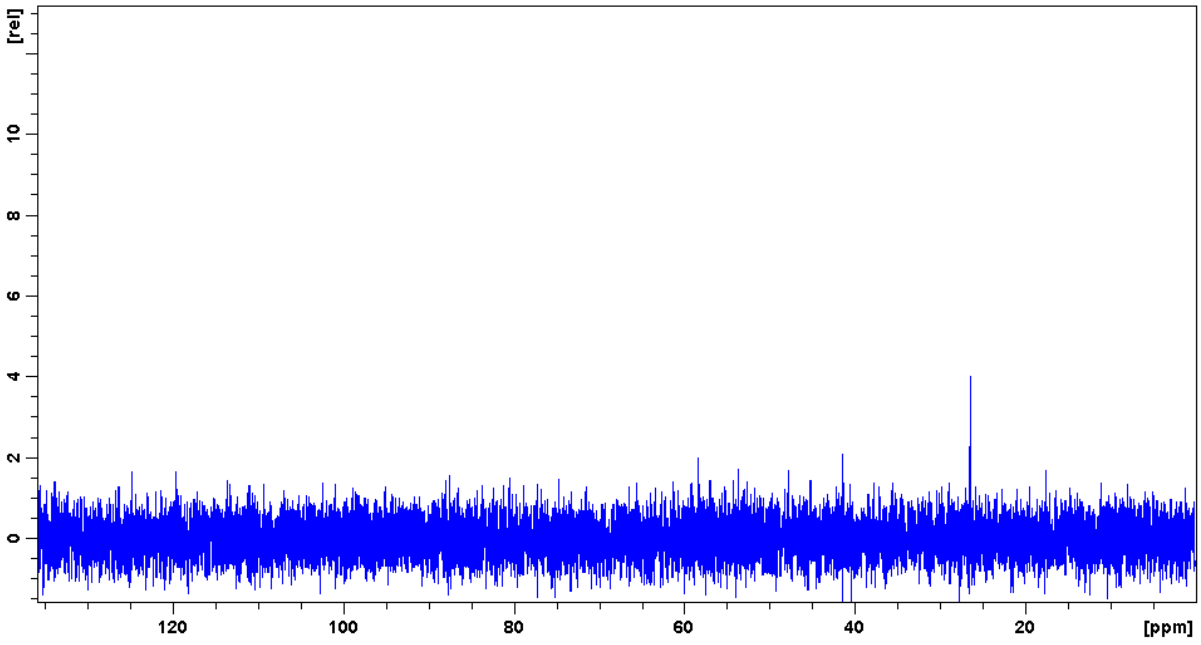

Figure 5.4: *^{31}P NMR spectrum compound **3**.*

Frequency simulations were executed to aid in the interpretation of the experimental infrared spectra of **1** – **3**, see **Figures 5.5** – **5.10**. Indicatively, to their NMR spectra, the ruthenium-to-phosphorous infrared stretches distinctively appear between 691 and 742 cm^{-1} which occur in the same wavenumber region [746 – 522 cm^{-1}] as other ruthenium Schiff bases stabilized by *trans*-$[Ru(PPh_3)_2]^+$ cores [**37, 38**]. The related computed vibrations associated with the *trans*-

$[Ru(PPh_3)_2]^+$ cores occur at lower wavenumbers in the simulated IR spectra of **1** (at 536 cm^{-1}), **2** (at 534 cm^{-1}) and **3** (at 536 cm^{-1}). The characteristic Schiff base functionalities of **1** – **3** resonate at variable positions [1542 cm^{-1} for **1**, 1610 cm^{-1} for **2** and 1566 cm^{-1} for **3**] in their calculated infrared spectra which emphasizes the variable stereo-electronic properties of their individual chelating ligands. Consequently, the corresponding imino experimental vibrational bands occur at 1552, 1579 and 1534 cm^{-1}, respectively [**39, 40**]. Solid-state IR spectra of the free thiosemicarbarzone ligands (Hpmt and Htmc) exhibit medium to strong vibrational bands at 1603 cm^{-1} (for Hpmt), 1595 cm^{-1} (for Htmc) and 1636 cm^{-1} (for btm); due to the stretches of the imine bonds. Typically, upon coordination of Schiff bases, the imino stretches appear at lower wavenumbers with respect to the free Schiff bases and are associated with coordination *via* the imino nitrogen donor atoms [**41**].

As mentioned before, thiosemicarbazone ligands can exist in different tautomeric forms; a thione or thiol form. Therefore, as per literature trends, thiosemicarbazone ligands can function as neutral tridentate chelators in the thione form or anionic tridentate chelators in the thiolate forms [**20, 41**]. The experimental IR bands appearing at 1229 and 1274 cm^{-1} within the spectra of the free ligands, Hpmt and Htmc are ascribed to the vibrations of the C=S bonds. However, these vibrational bands are not present in the solid-state IR spectra of **1** and **2**, while new IR stretches at 1586 (for **1**) and 1608 cm^{-1} (for **2**) ascribed to the $\nu(C{=}N)_{thiolate}$ bonds are evident. Consequently, the latter provides evidence of the conversion of Hpmt and Htmc to their respective thiolate forms prior to coordination. The analogous simulated bonds of **1** and **2** vibrates at 1607 and 1622 cm^{-1}, respectively.

The signals of the ν(N-H) are calculated at 3578, 3503 cm^{-1} for **1** and 3580, 3507 cm^{-1} for **2** while that of the ν(N-H) of **3** occurs at 3678 cm^{-1}. Experimentally, the amido bonds are found as weak intensity bands at 3468, 3049 cm^{-1} for **1** and 3353, 3048 cm^{-1} for **2** while the medium-intensity band of **3** at 3461 cm^{-1} is accounted to the alcohol vibration. In addition, distinctive common real vibrations found in the experimental spectra of **1** and **2** which are accounted to the aliphatic ν(C-N) [1431 cm^{-1} for **1** and **2**] and ν(N-N) [1088 cm^{-1} for **1** and 1090 cm^{-1} for **2**] signals while the intracyclic ν(C-N) signal of **3** [1429 cm^{-1}] occurs at a similar position as those of **1** and **2**. Interestingly, the simulated IR spectra of **1** and **2** shows that it requires higher energies to induce the vibrations of their bridging N-N bonds [1217 cm^{-1} for **1** and 1194 cm^{-1} for **2**] oppose to their C-N bonds [1065 cm^{-1} for **1** and 1072 cm^{-1} for **2**]. Furthermore, the $\nu(C{=}N)_{imino}$ and $\nu(C{=}N)_{benzothiazole}$ signals of **3** appear at 1566 and 1484 cm^{-1} in its simulated IR

spectrum whereas two medium-intensity vibrational bands at 1534 and 1480 cm^{-1} are assigned to the conforming signals in the experimental infrared spectrum.

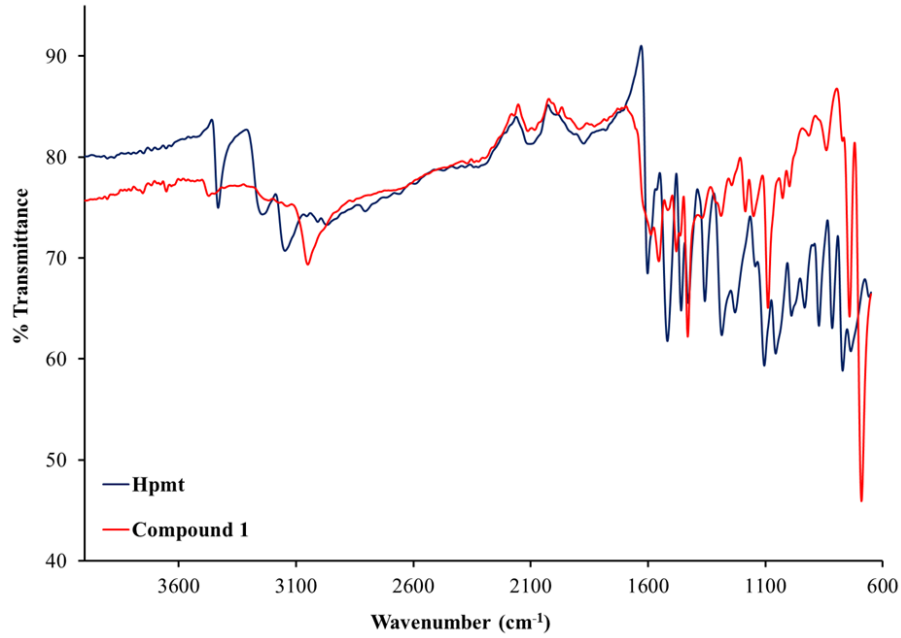

Figure 5.5: *Overlay IR spectra of the free-ligand, Hpmt and complex **1** between 4000 and 600 cm^{-1}*

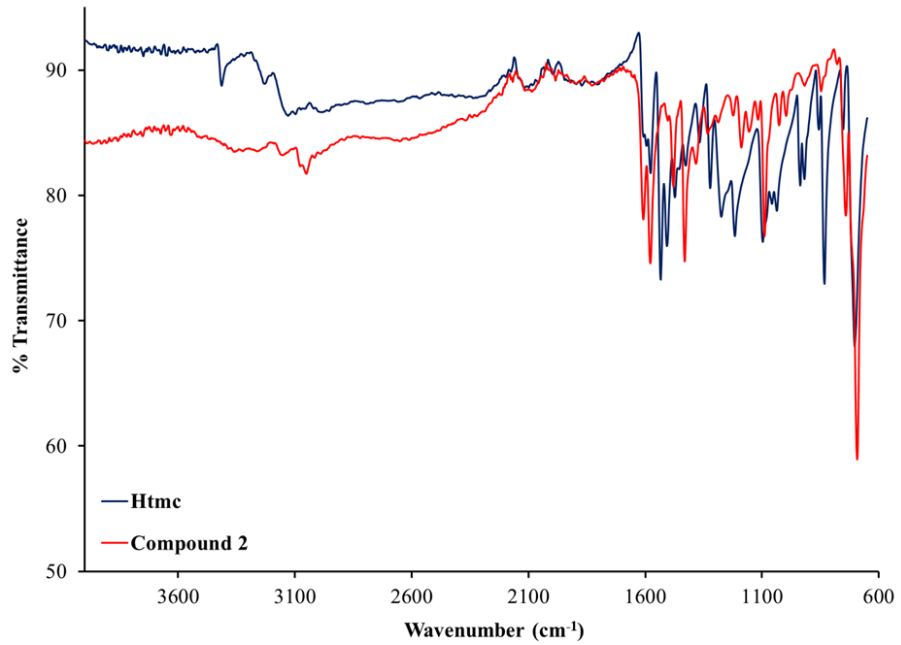

Figure 5.6: *Overlay IR spectra of the free-ligand, Htmc and complex **2** between 4000 and 600 cm^{-1}.*

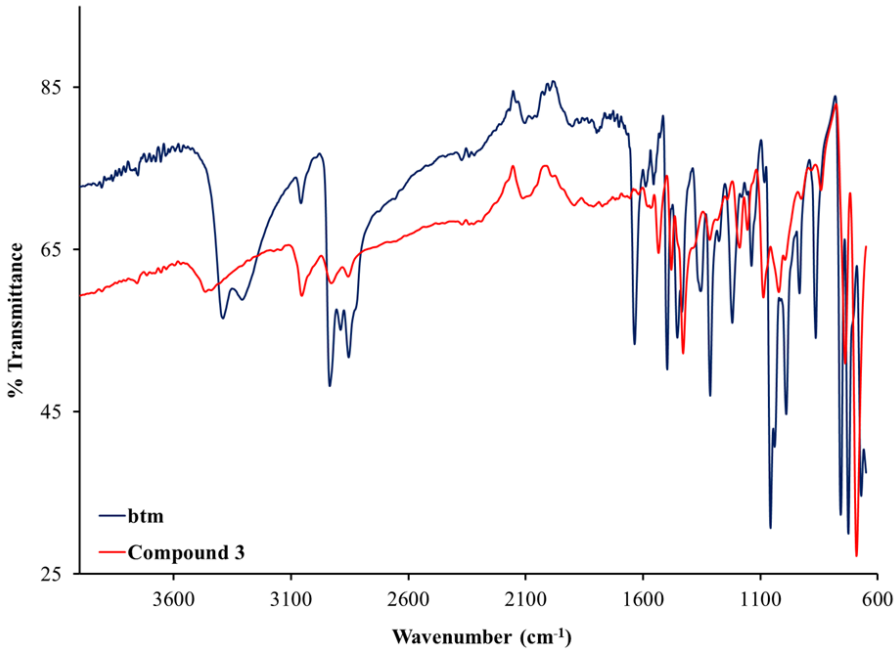

Figure 5.7: *Overlay IR spectra of the free-ligand, bmt and complex **3** between 4000 and 600 cm^{-1}.*

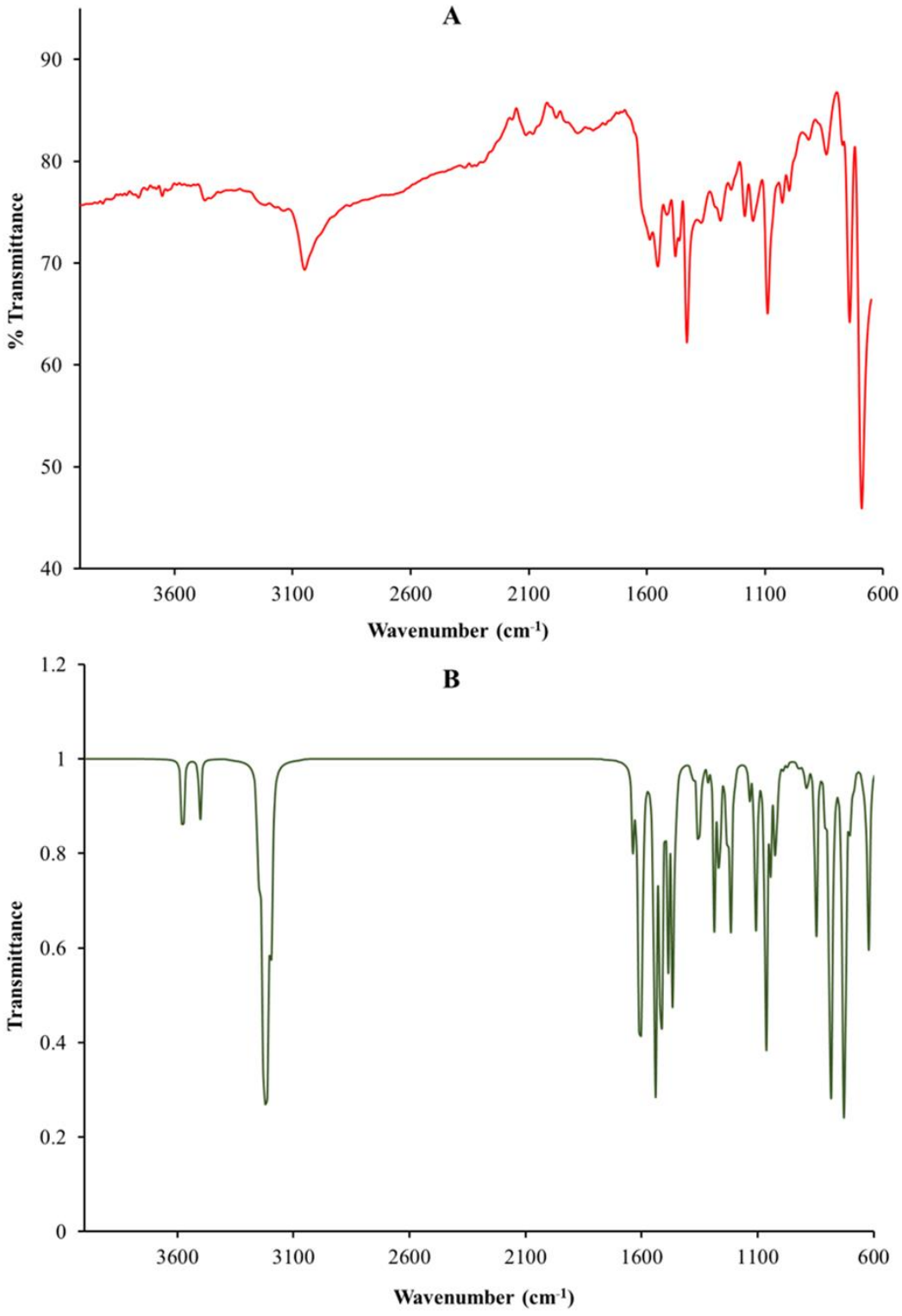

Figure 5.8: *IR spectra of the experimental (**A**) and optimized (**B**) structures of **1**.*

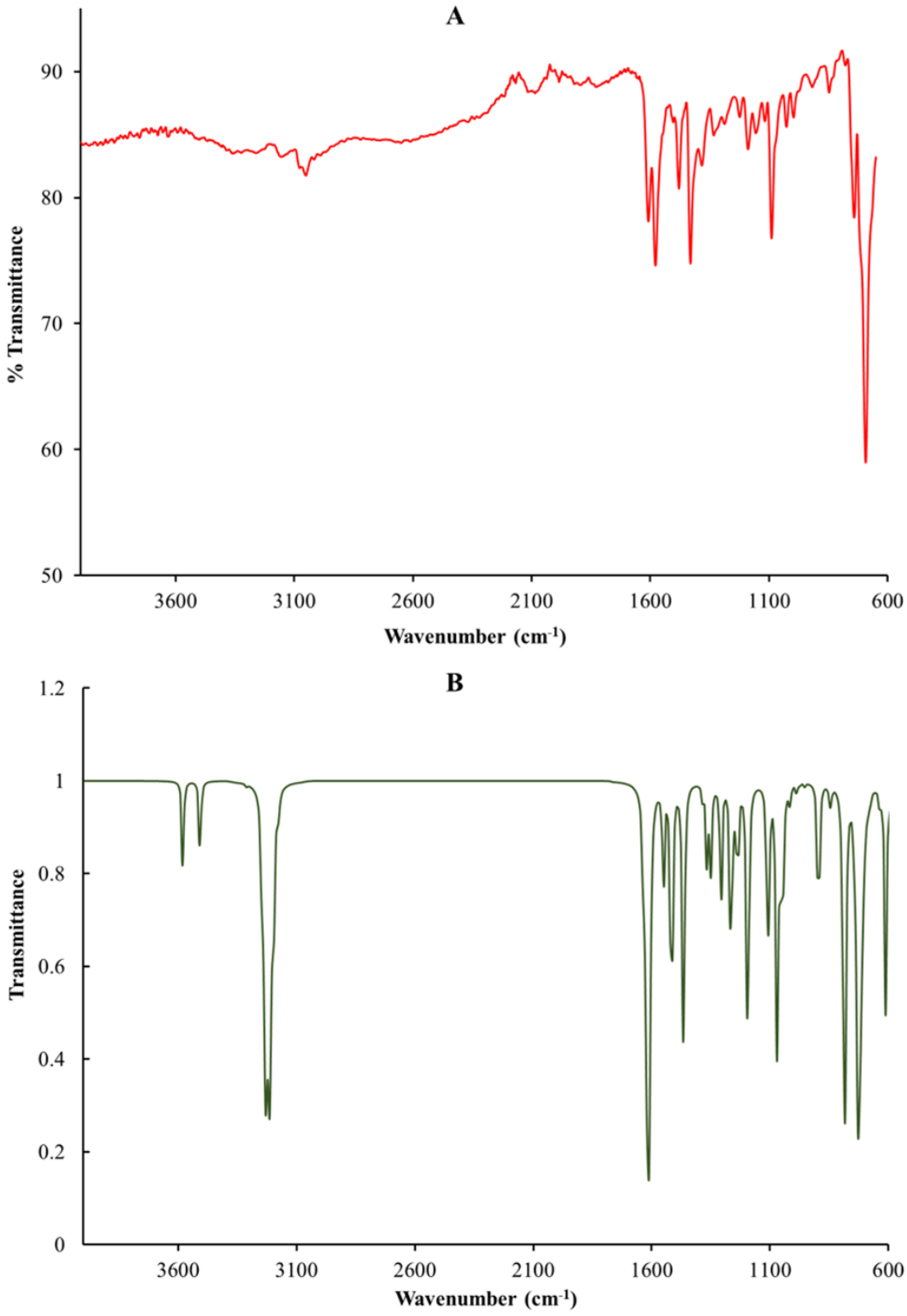

Figure 5.9: *IR spectra of the experimental (**A**) and optimized (**B**) structures of **2**.*

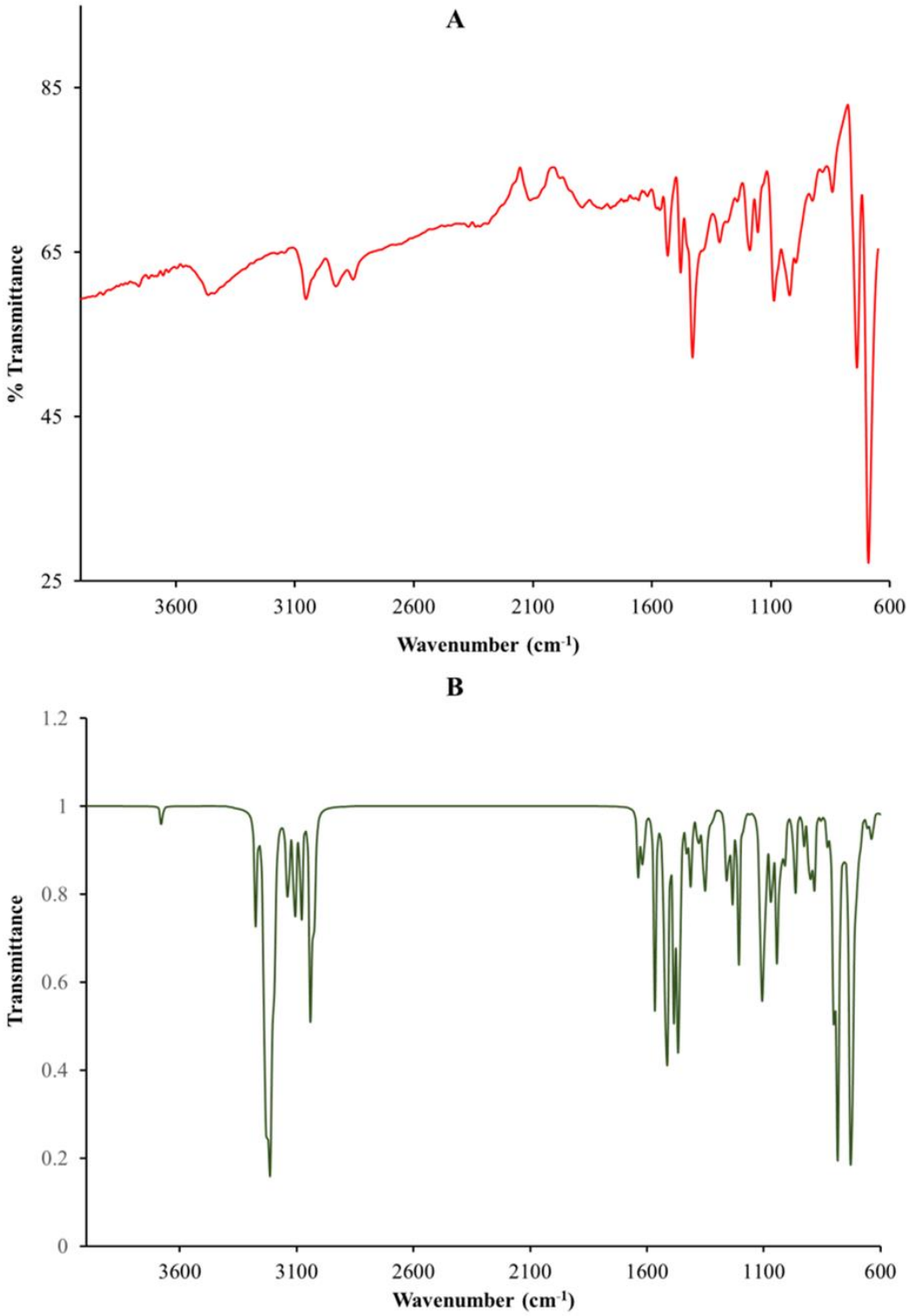

Figure 5.10: *IR spectra of the experimental (**A**) and optimized (**B**) structures of **3**.*

UV-visible spectra of the metal compounds were recorded in the non-coordinative solvent, dichloromethane at room temperature, see **Figures 5.11** – **5.13**. All the metal compounds exhibited intense $\pi - \pi^*$ intraligand transitions below 300 nm while charge electronic transitions observed in the region 308 – 533 nm are attributed to charge-transfer (CT) bands [**42**]. The nature of these CT bands were investigated by evaluating the surfaces of the computed Highest Occupied- (HOMO) and Lowest Unoccupied Molecular Orbitals (LUMO) for the respective metal compounds, see **Table 5.1**. Noticeably, the HOMO surfaces of **1** – **3** show contributions originating from their relevant chloro co-ligands but these donations are absent in their corresponding LUMO surfaces which suggests that the CT-bands could be predominately ascribed to Cl(p_π) → Ru($d\pi$) Ligand-to-Metal CT bands. Electronic density rearrangements within the individual Schiff base chelators of **1** – **3** are observed between the corresponding HOMOs and LUMOs which justify the experimental intraligand electronic transitions observed within their UV-visible spectra. At more red-shifted wavelengths, metal-based electronic transitions with relatively low molar extinction coefficients are observed for the paramagnetic ruthenium compounds **1** (680 nm) and **2** (589 nm). Parity can also be found between the occurrence of these experimental metal-based transitions and the relating frontier molecular orbitals surfaces where d_{xy}-orbital contributions are observed in their respective HOMO surfaces while the LUMO surfaces contains contributions from the $d_{x2\text{-}y2}$ (for **1**) and d_{z2} (for **2**) orbitals.

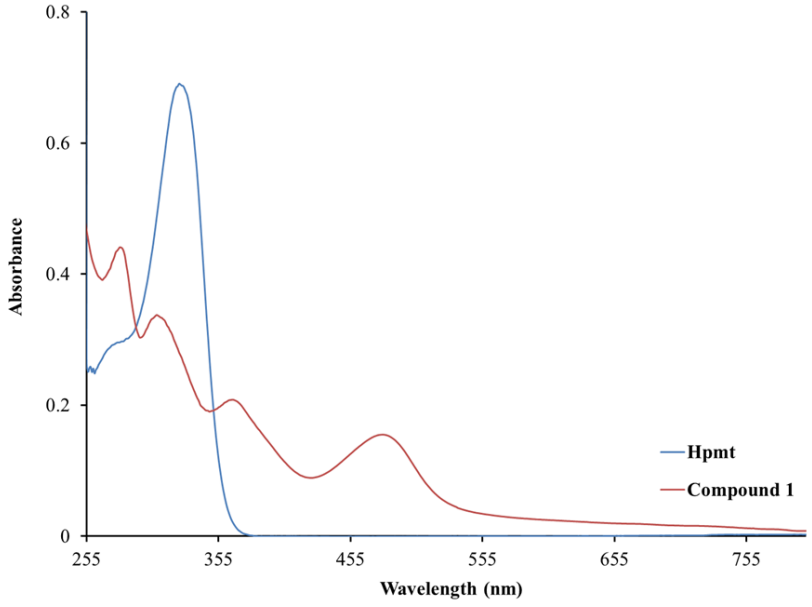

Figure 5.11: *Overlay UV-Vis spectra of **1** and its free-ligand, Hpmt.*

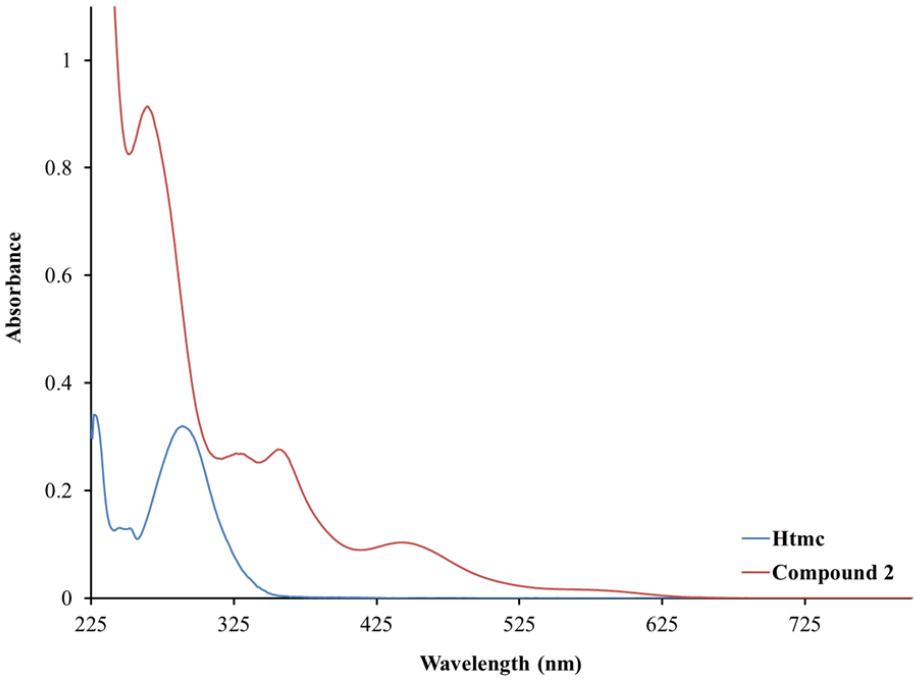

Figure 5.12: *Overlay UV-Vis spectra of **2** and its free-ligand, Htmc.*

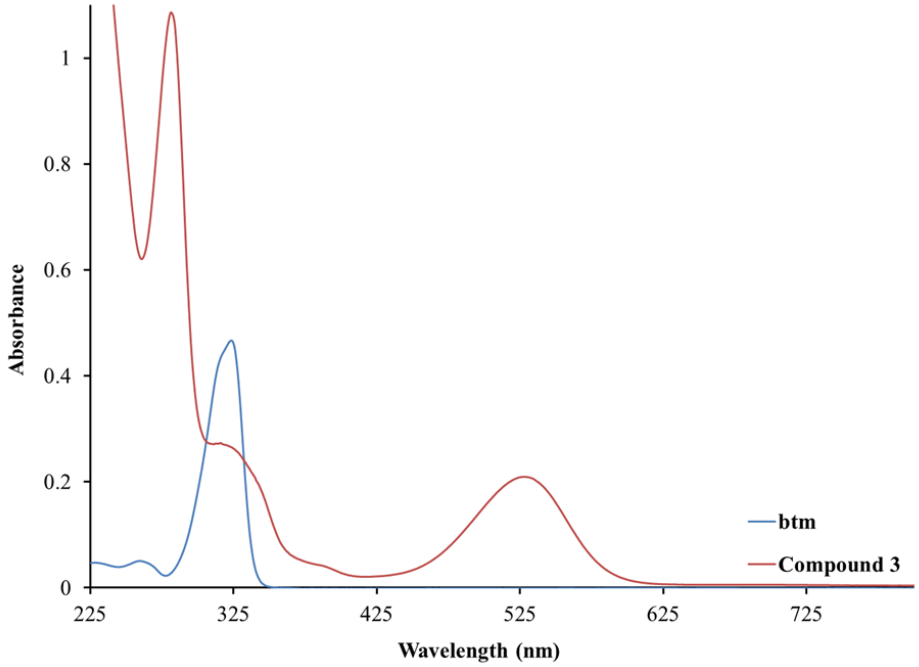

Figure 5.13: *Overlay UV-Vis spectra of **3** and its free-ligand, btm.*

Table 5.1: *Computed HOMO and LUMO frontier orbitals of* ***1 – 3****.*

HOMO	LUMO
1	
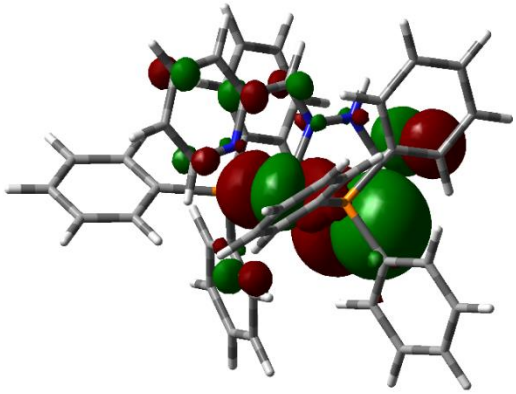	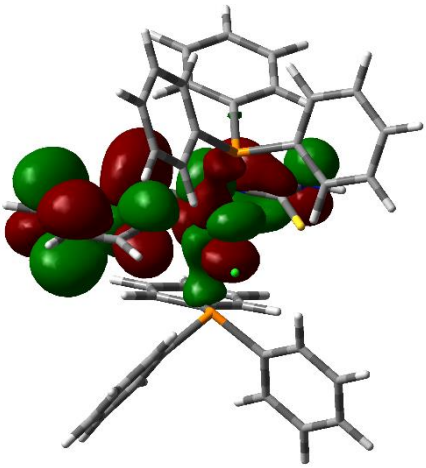
2	
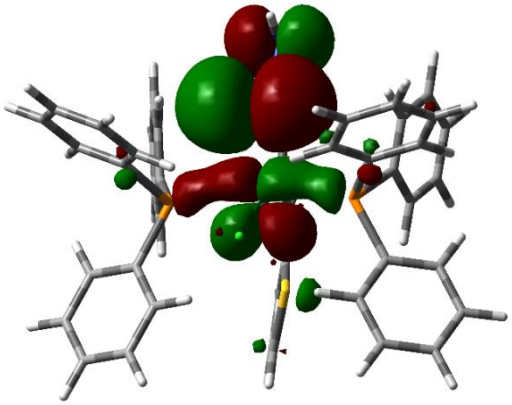	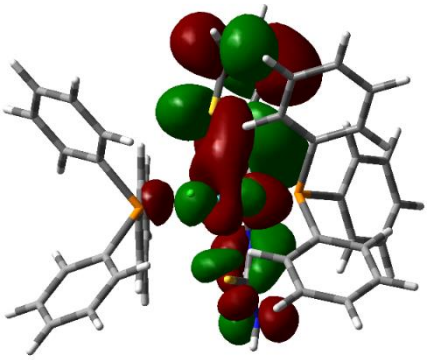
3	
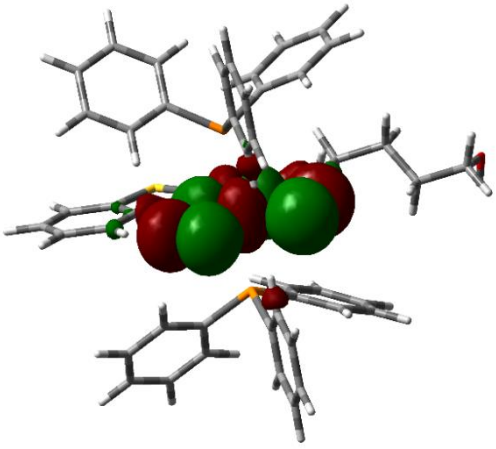	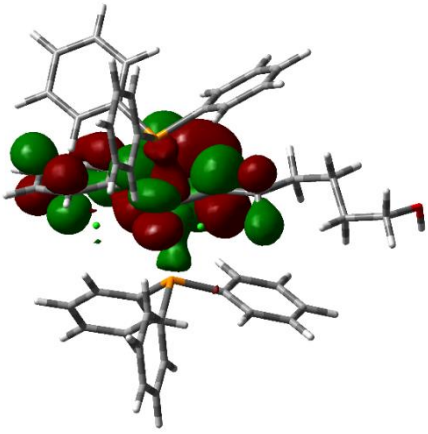

Solid and liquid samples were used during EPR analysis which were collected at room and low temperatures for **1** and **2**, refer to **Figures 5.14** and **5.15**. The solid state EPR spectra of both metal compounds show three distinctive signals with different *g*-values (*viz.* $g_x \neq g_y \neq g_z$), signifying the presence of magnetic anisotropy and rhombic distortion of their octahedral geometries [**43**], refer to **Table 5.2**. In the case of the liquid samples of **1** and **2**, single isotropic signals were attained due to faster relaxation life times. Collectively, the *g*-values obtained were comparable to other low-spin d^5 ruthenium compounds with distorted octahedral geometries. For example, *g*-values were attained in ESR spectra of the ruthenium complexes, *trans*-[$RuCl_4(H_2mtpO)(dmso)$]·$4H_2O$ (HmtpO = 5-methyl-1,2,4-triazolo[1,5-*a*]pyrimidin-7(4*H*)-one) (g_{iso} = 2.3) and [$(CH_3)_2NH_2$]*trans*-[$RuCl_4(HmtpO)_2$] with g*x*, g*y* and g*z* values of 3.20, 2.75 and 1.75, respectively [**44**].

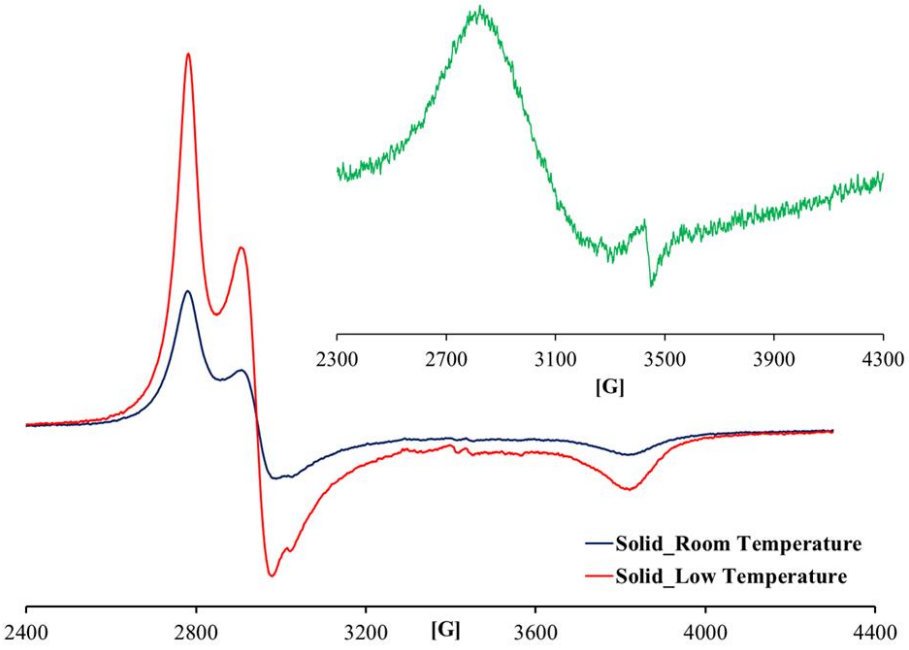

Figure 5.14: *ESR spectra of **1** collected in the solid state at room (at 298 K) and low (at 77 K) temperatures.* ***Inset****: An identical ESR spectrum attained for the liquid samples collected at the two different temperatures.*

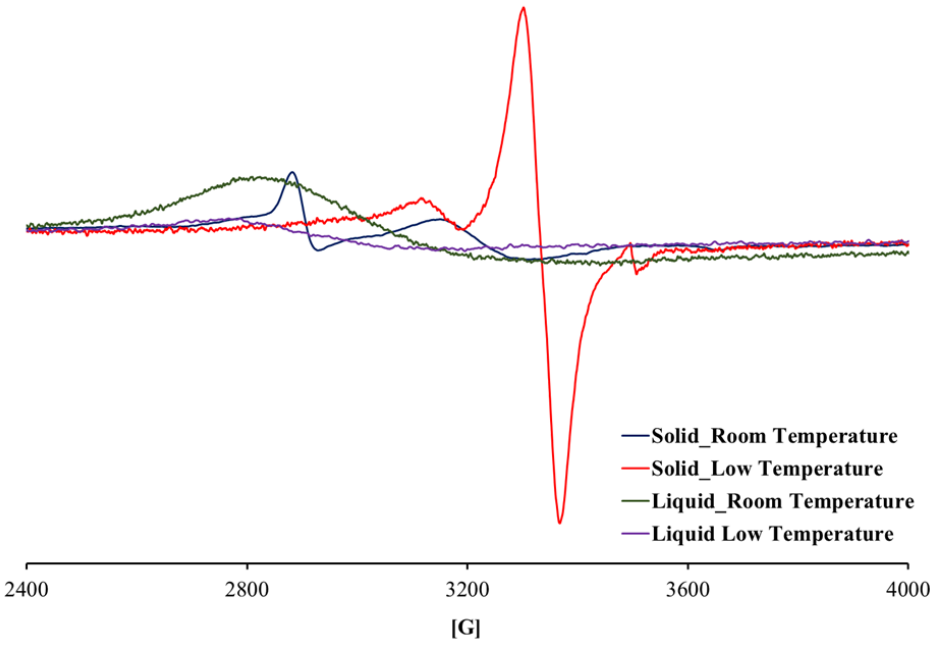

Figure 5.15: *ESR spectra of **2** collected at room (at 298 K) and low (at 77 K) temperatures.*

Table 5.2: *Selected ESR spectral data of **1** and **2** at room and low temperatures.*

Sample	State	Temperature	*gx*	g_y	*gz*	*giso*
1	Solid	77 K	2.52	2.38	1.83	-
		298 K	2.53	2.38	1.83	-
	Liquid	77 K	-	-	-	2.28
		298 K	-	-	-	2.27
2	Solid	77 K	2.24	2.10	1.98	-
		298 K	2.43	2.18	1.91	-
	Liquid	77 K	-	-	-	2.27
		298 K	-	-	-	2.38

5.5.2 Electrochemistry

The cyclic voltammogram (CV) of **1** showed two redox couples labelled **A** ($E_{½}$ = 0.60 V *vs* Ag| AgCl) and **B** ($E_{½}$= 0.88 V *vs* Ag | AgCl), which are ascribed to metal-based redox processes

as the CV of the free-ligand (Hpmt) did not show any redox activity within the same potential window, see **Figure 5.16**. Redox processes for **1** can be assigned to the Ru(III)/ Ru(IV) redox couple for **A** and the Ru(II)/ Ru(III) redox couple for **B** whereas the CVs of **2** and **3** each containing a single quasi-reversible redox wave are assigned to the Ru(III)/ Ru(IV) redox couple for **2** ($E_{½}$ = 0.60 V *vs* Ag| AgCl) and a halfwave potential of 0.32 V *vs* Ag| AgCl for the d^5-d^6 interconversion of **3**, see **Figures 5.17** and **5.18**. These diffusion-controlled redox processes afforded, as expected, singular (for **2** and **3**) and dual (for **1**) symmetrical peaks within the SWV. The aforementioned redox assignments are made based on its comparative redox potentials to other cyclometallated monomeric compounds. More specifically, voltammetry analysis of the cyclopentadienyl diamagnetic ruthenium complexes, [Ru(η^5-C_5H_5)(PPh_3)L_x] (where HL_x denotes the 5-nitrofuryls with varying thiosemicarbazones) illustrated halfwave potentials ranging from 0.40 to 0.45 V (*vs* Ag| AgCl) within the coordinative solvent, dimethylsulphoxide and these redox potentials were accounted to the Ru(II)/ Ru(III) redox couple [**45**]. As per literature trends, **1** showed a potential difference of 1.48 V between its metal-based redox couple which are comparable to the paramagnetic ruthenium compound, [Ru^{III}(Sal-etsc)(H-Sal-etsc)(PPh_3)] (H-Sal-etsc = salicylaldehyde-4(*N*)-ethylthiosemicarbazone) where its Ru(III)/Ru(IV) and Ru(III)/Ru(II) redox couples appear at 0.602 V and -0.609 V (*vs* Ag| AgCl), respectively [**46**]. In addition, a series of sulfoxide metal complex salts, [Ru$(bpy)_2$(OSOBnR)](PF_6) (bpy = 2, 2'–bipyridine, OSOBnR = 4-substituted benzylsulfinylbenzoate and R =NO_2, F, Cl, H, CH_3, CF_3 or OCH_3) illustrated two quasi-reversible redox couples in the proximities of 0.89 to 0.94 V (*vs* Ag | $AgPF_6$) as well as 0.53 and 0.54 V(*vs* Ag | $AgPF_6$) which were assigned to their photo-induced S- and O-bonded isomers of their metal complex cations [**47**].

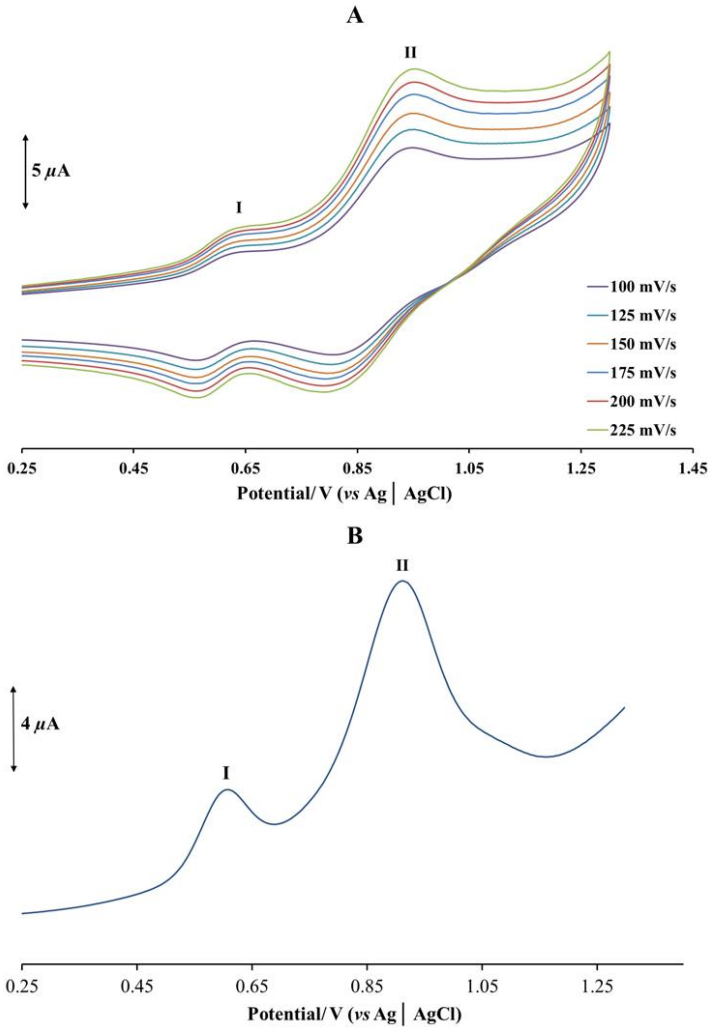

Figure 5.16: *(**A**) Overlay CVs of **1** at variable scan rates. (**B**) SWV of **1** at 100 mV/ s.*

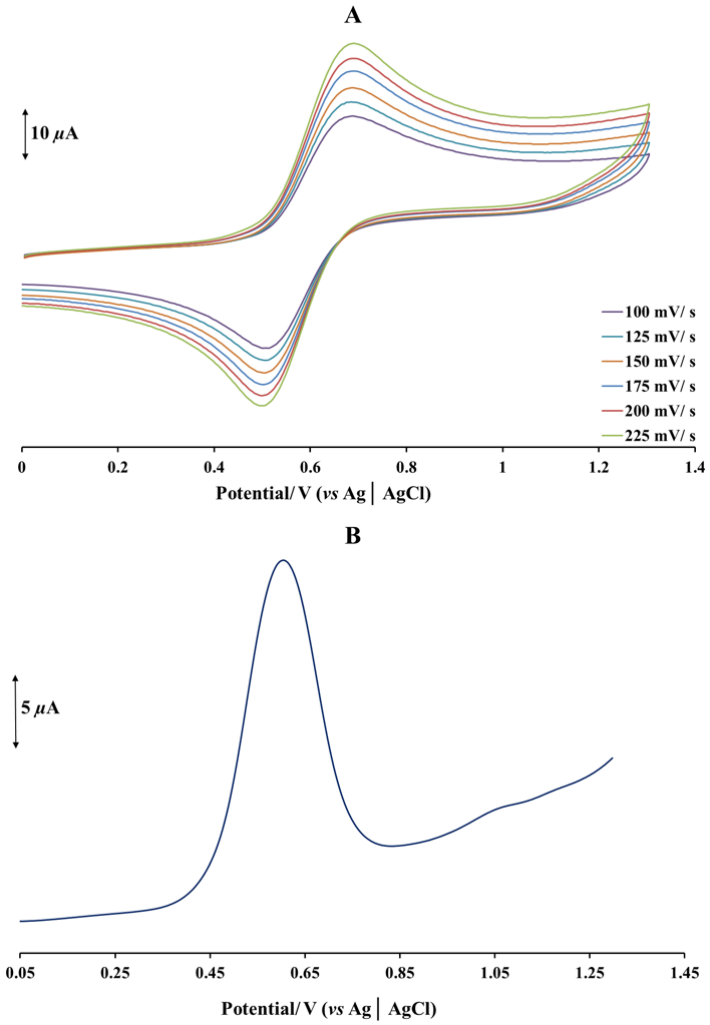

Figure 5.17: *(**A**) Overlay CVs of **2** at variable scan rates. (**B**) SWV of **2** at 100 mV/ s.*

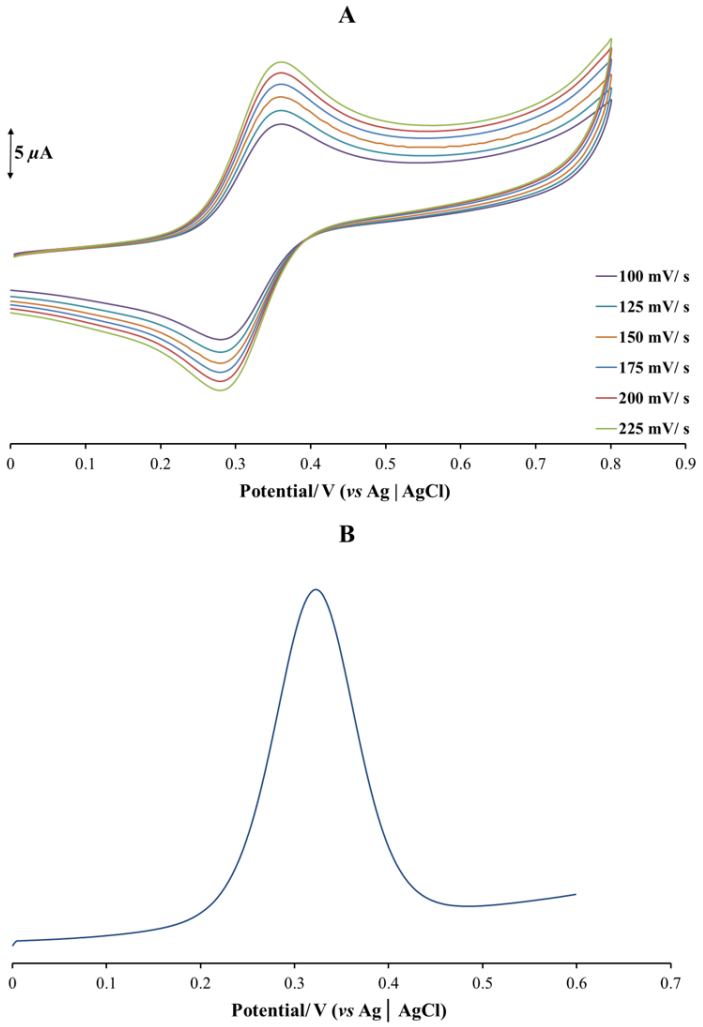

Figure 5.18: *(**A**) Overlay CVs of **3** at variable scan rates. (**B**) SWV of **3** at 100 mV/ s.*

Table 5.3: *Selected CV parameters of **1** - **3** recorded in DCM at 100 mV.*

Compound	**1**		**2**	**3**
	A	**B**		
E_{pa} (V)	0.64	0.94	0.69	0.36
E_{pc} (V)	0.56	0.81	0.51	0.28
ΔE_p (mV)	80	130	180	80
$E_{½}$ (V)	0.60	0.88	0.60	0.32

5.5.3 Crystallographic descriptions

Solid-state structures of the metal compounds possess orthorhombic (for **1**) and monoclinic crystal systems (for **2** and **3**) where their respective unit cells occupy two (for **3**) or four molecules (for **1** and **2**). Molecules of the metal compounds co-crystallize with dichloromethane or ethanol molecules of crystallization (*viz.* two dichloromethane molecules or one ethanol molecule) within in the *Ima2* (for **1**), and *Cc* (for **2**) and $P2_1$ (for **3**) space groups. Interestingly, each molecule of **2** and **3** affords analogous hydrogen-bonded chains facilitated by classical intermolecular hydrogen bonding with the chloride cations and the amido (*i.e.* N-H) groups of adjacent molecules, see **Figures 5.19** and **5.20**. The aforementioned hydrogen-bonding network is also reinforced by hydrogen-bonding that occurs between the amido bonds of the metal compounds and their co-crystallized solvent molecules see **Figures 5.21** and **5.22**. Consequently, the molecules and ions of **1** and **2** are aligned with the [*c*]-axis. Indicatively, the molecules of **3** runs in columns which are co-planar to the [*b*]-axis and this arrangement is supported by the bridging methanol molecules which affords hydrogen-bonding interactions with neighbouring molecules of **3**, see **Figure 5.23**.

Coordination behaviours of the individual Schiff bases chelators induce the formation of constrained 5-membered rings within the corresponding basal planes of **1** – **3** which renders octahedral distortion given by their individual bite angles [N2-Ru-N1 = 77.74(15)°, N2-Ru-S = 83.19(2)° for **1**, N1-Ru-S2 = 78.7(1)°, N1-Ru-S1 = 82.2(1)° for **2** and N1-Ru-N2 = 78.2(3)° for **3**] all deviating from the ideal equatorial bond angle of 90º, see **Figures 5.24** – **5.26**. In turn, the respective constrained bite angles of **1** and **2** rationalizes the N1-Ru-Cl1 [178.42(12)°], N1-Ru-S [160.93(10)°] for **1** and S1-Ru-S2 [160.01(4)°], N1-Ru-Cl1 [177.8(1)°] for **2** are non-linear while the opposing bond angle [Cl1-Ru-Cl2 = 90.17(7)º] (*w.r.t.* the bite angle of **3**) are essentially equal to 90º but the neighbouring bond angles [Cl1-Ru-N1 = 100.2(2)° and Cl2-Ru-N2 = 91.5(2)°] differ from the aforementioned idealized bond angle.

Gas-phase conformers of **1** – **3** mimic the same trends in the aforementioned bond angle discrepancies between the solid-state and computed conformers and are largely attributed to the absence of the hydrogen-bonding interactions within the latter, refer to **Tables 5.5** – **5.7**. Reasonable parity is also found with the calculated [P1-Ru-P2 = 173.129° for **1**, 175.198° for **2** and 170.184º for **3**] and experimental [P1-Ru-P2 = 173.26(4)° for **1**, 175.46(4)° for **2** and 177.05(8)º for **3**] bond angles of the *trans*-[$Ru(PPh_3)_2$] cores of the respective metal compounds

but their Ru-P bond lengths differ which suggest varying polarizability for analogous phosphorous donor atoms across the optimized [Ru-P1/P2 = 2.5113 Å for **1**, Ru-P1 = 2.5175 Å, Ru-P2 = 2.5135 Å for **2** and Ru-P1 = 2.5255 Å, Ru-P1 = 2.5289 Å for **3**] and experimental [Ru-P1/P2 = 2.3788(7) Å for **1**, Ru-P1 = 2.399(1) Å, Ru-P2 = 2.393(1) Å for **2** and Ru-P1 = 2.402(2) Å, Ru-P1 = 2.402(2) Å for **3**] structures. Similarly, disparity is also observed for the other ruthenium to soft donors (*viz.* Cl and S) experimental and calculated bond lengths, refer to **Tables 5.5** – **5.7**. Despite the aforementioned anomalies, fairly low RMSD values are attained for the overlay structures for the computed conformers and related crystal structures, see **Figure 5.27**.

Experimental coordination bonds of **1** – **3** compare well with those found in literature. In particular, the Ru-P bonds are comparable to other ruthenium(II) and –(III) Schiff base complexes with *trans-axial* triphenylphosphine co-ligands [**48-50**]. In addition, the actual ruthenium-to-halide bonds of **1** [Ru-Cl1 = 2.4289(11) Å] and **2** [Ru-Cl1 = 2.421(1) Å] are shorter than those of **3** [Ru-Cl1 = 2.435(2) Å and Ru-Cl2 = 2.448(2) Å] which emphasizes the higher Lewis acidic characters of the paramagnetic metal centres of **1** and **2**. Variable *trans*-influence is imposed on the chloride co-ligands of **3** by its imino and benzimidazole nitrogens which results in differing Ru-Cl distances that differs. The Ru-$S_{thiolate}$ bond lengths of 2.3812(12) for **1** and 2.345(1) Å for **2** are similar to those of other ruthenium thiosemicarbazones where coordination occurs *via* the chelating ligands' neutral imino nitrogens and deprotonated thiolate sulfurs. For instance, the dimeric ruthenium(III) compound, $(\mu\text{-S})_2[(H_2nptsc)_2]$ (H_2nptsc = 1-((2-hydroxynaphthalen-3-yl)methylene)thiosemicarbazide) had respective Ru-S distances of 2.250(5) and 2.262(6) Å while the analogous bonds of the diamagnetic ruthenium(II) compounds, [Ru(H-Sal-tsc)(CO)Cl-$(PPh_3)_2$] (H-Sal-tsc = salicylaldehydethiosemicarbazone) and [Ru(Sal-tsc)(CO)$(PPh_3)_2$] are 2.4012(7) and 2.344(2) Å, respectively [**51, 52**]. Similarly, the ruthenium(III) to imino nitrogen bonds of **1** [Ru-N2 = 1.970(4) Å] and **2** [Ru-N1 = 2.039(4) Å] compares well with those [1.962(15) and 2.062(15) Å] of the aforementioned paramagnetic ruthenium compound. Metal coordination to the sp^2-benzothiazole nitrogen donor of **3** affords bonds [Ru-N1 = 2.089(6)] which is essentially equal to the Ru-$N_{benzothiazole}$ bond [2.079(2) Å] of [RuCl$(obs)_2(PPh_3)$] (Hobs = 2-hydroxyphenylbenzothiazole) while its Ru-N_{imino} bond of **2** and the Ru-$N_{pyridyl}$ bonds are in accordance to bond distances of ruthenium(II) compounds with 2-((pyridin-2-yl)methyleneamino) moieties [**53-55**].

The mutual tautomeric forms of the pmt and tmc chelators can be unequivocally established when comparing their thiolate bonds [C7-S = 1.703(5) Å for **1** and C4-S2 = 1.721(5) Å for **2**] with that of the intracyclic C-S bonds [C7-S = 1.726(8) Å and C1-S = 1.724(9) Å] of **3**. In addition, the shorter C7-N4 [1.331(6) Å] than C7-N3 [1.357(6) Å] of **1** suggest double bond character for the former. This double bond is similar to the intracyclic C=N pyridine [C5-N1 = 1.337(6) Å and C1-N1 = 1.338(6) Å] bonds. However, the C6-N3 bond was found to be longer than the C6-N2 bond which implies that *pi*-delocalization occur throughout the N3C6N2N1 aliphatic moiety. Evidently, the intraligand N-N bonds of **1** [1.368(6) Å] and **2** [1.380(6) Å] differ. The localized imino bonds are also comparable [C6-N2 = 1.305(6) Å for **1**, C5-N1 = 1.298(7) Å for **2** and C8-N2 = 1.30(1) Å for **3**].

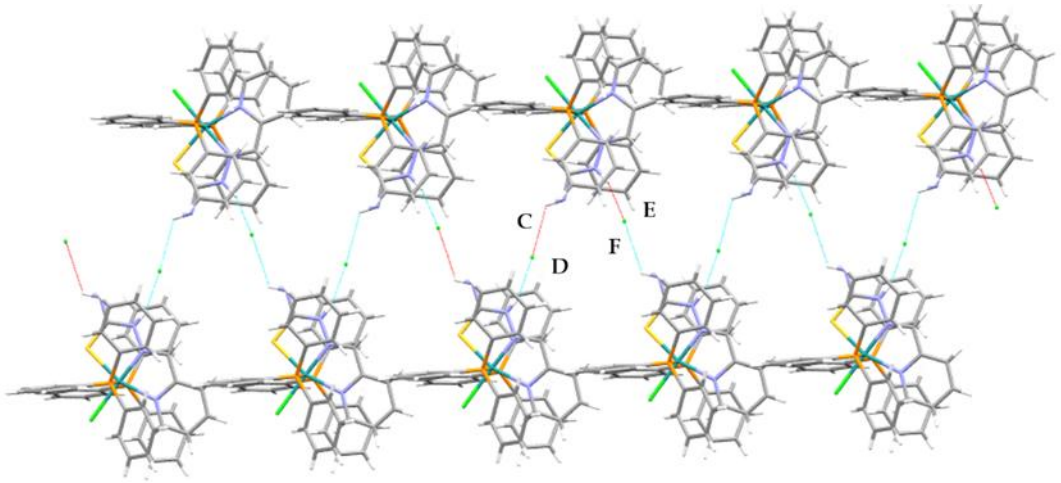

Figure 5.19: *A perspective view of the crystal lattice of **1** illustrating the intermolecular hydrogen-bonding interactions between chloride cations and neighbouring molecules of **1**: **C**, N4-H···Cl2A = 2.78 Å, **D**, Cl2A··· HA-N3A= 2.175 Å, **E**, N3-H···Cl2 = 2.175 Å and **F**, Cl2···N4C-HC··· = 2.78 Å.*

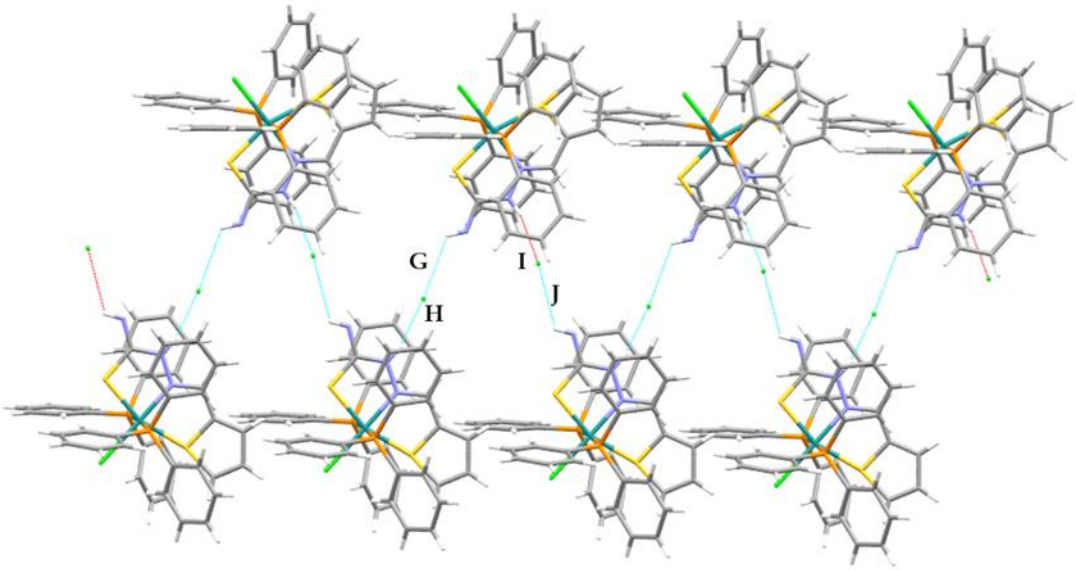

Figure 5.20: *A perspective view of the crystal lattice of **2** illustrating the intermolecular hydrogen-bonding interactions between chloride cations and neighbouring molecules of **2**: **G**, N4-H···Cl2A = 2.88(6) Å, **H**, Cl2A··· HA-N3A= 2.248 Å, **I**, N3-H···Cl2 = 2.248 Å and **J**, Cl2···N4C-HC··· = 2.248 Å.*

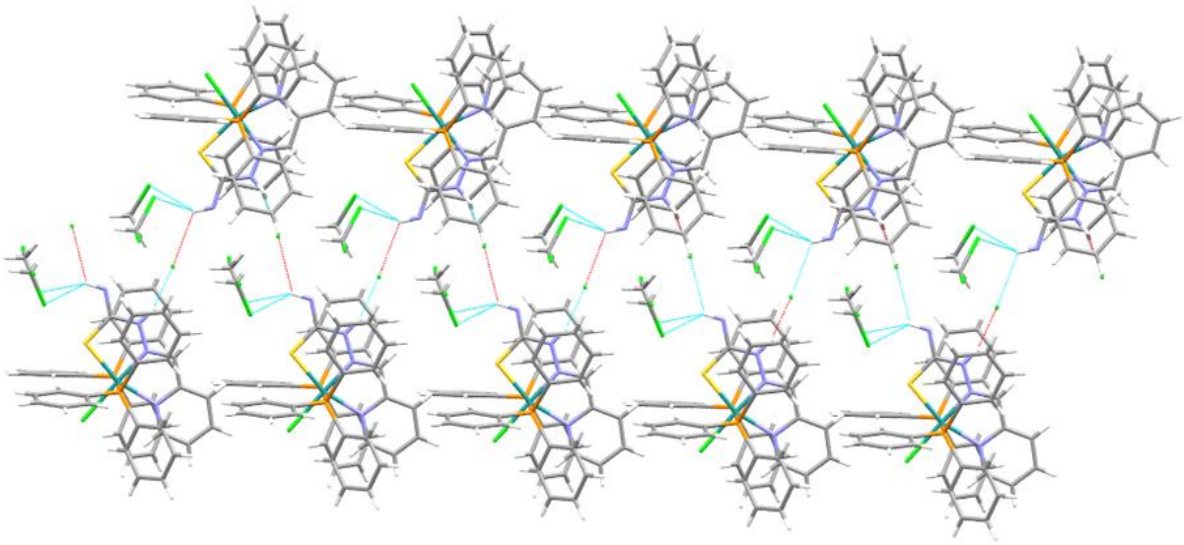

Figure 5.21: *An extended hydrogen-bonding pattern of **1** where the solvent molecules of crystallization have been included. A mutual distance of 2.89 Å is measured between respective chloro atoms and the N4-H groups of neighbouring molecules.*

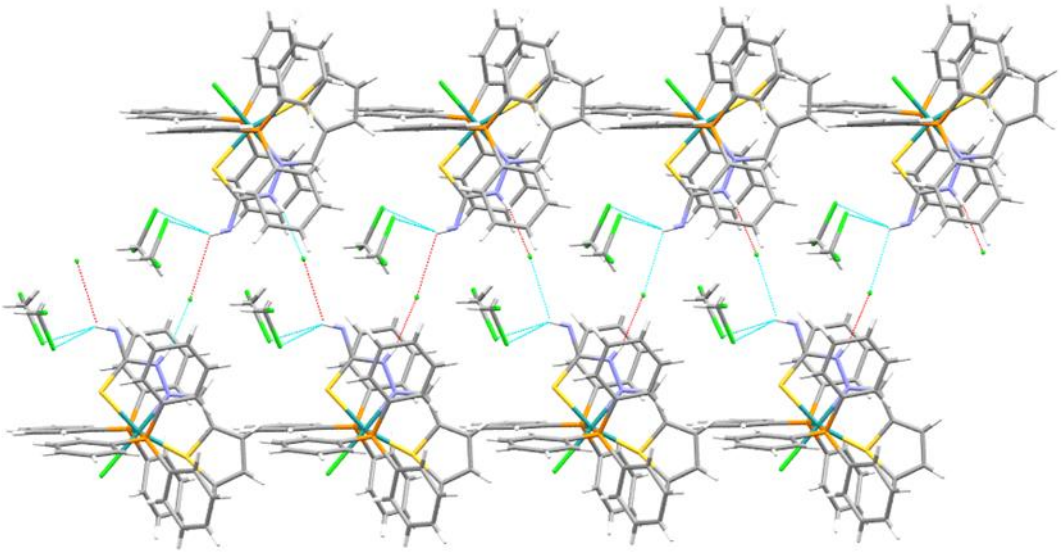

Figure 5.22: *An extended hydrogen-bonding pattern of **2** where the solvent molecules of crystallization have been included. A mutual distance of 2.847 Å is measured between respective chloro atoms and the N4-H groups of neighbouring molecules.*

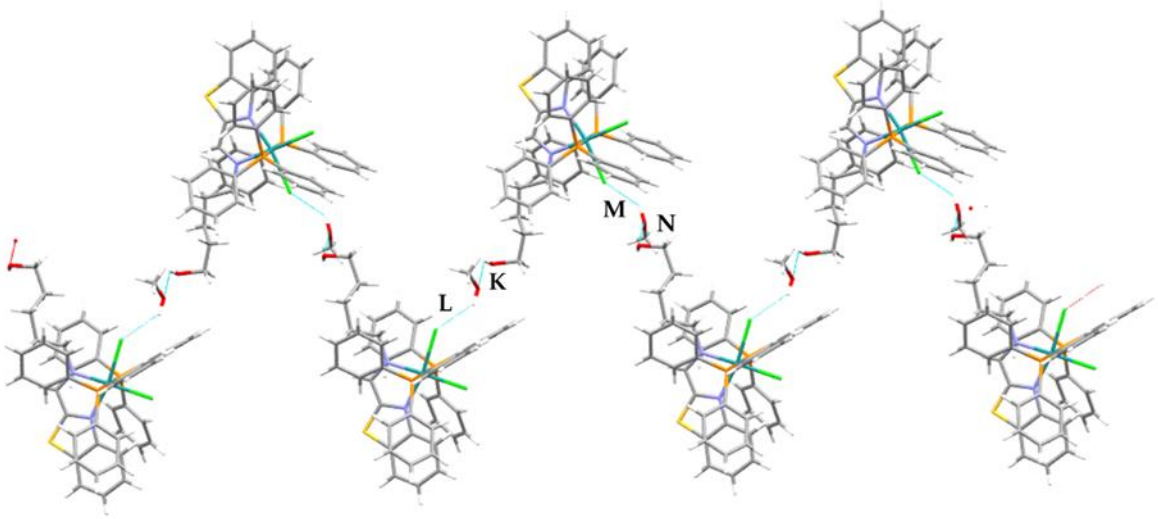

Figure 5.23: *A perspective view of the hydrogen-bonding occurring within the crystal lattice of **3** along its [b]-axis: **K**, O1-H14···O2 = 2.20 Å, **L**, O2-H40···Cl2A = 2.444 Å, **M**, Cl2···O2B-H40B = 2.444 Å and **N**, O2B···H14B-O1B = 2.20 Å.*

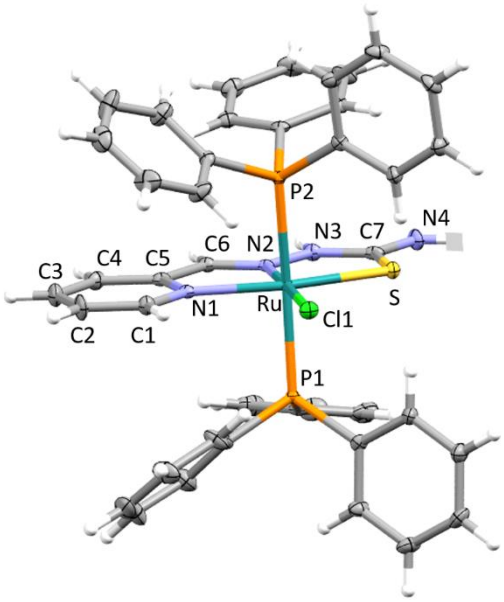

Figure 5.24: *ORTEP view of compound **1** showing 50 % probability displacement ellipsoids and the atom labelling. The solvent molecule of crystallization and the second counterion have been omitted.*

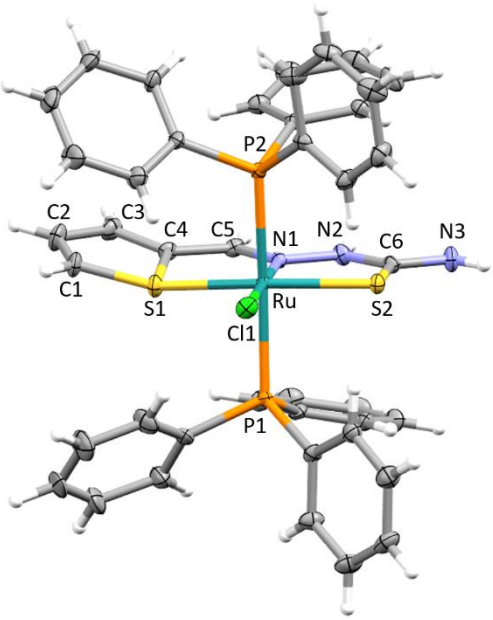

Figure 5.25: *ORTEP view of compound **2** showing 50 % probability displacement ellipsoids and the atom labelling. The solvent molecules of crystallization and the counterion have been omitted.*

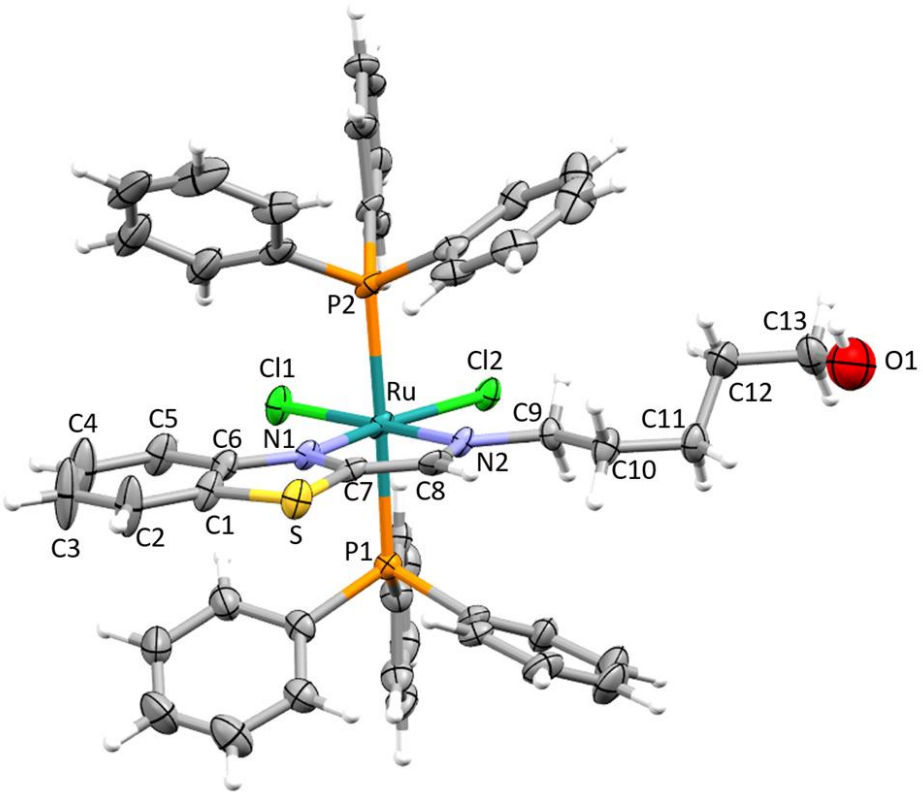

Figure 5.26: *ORTEP view of compound 3 showing 50 % probability displacement ellipsoids and the atom labelling. The solvent molecules of crystallization have been omitted.*

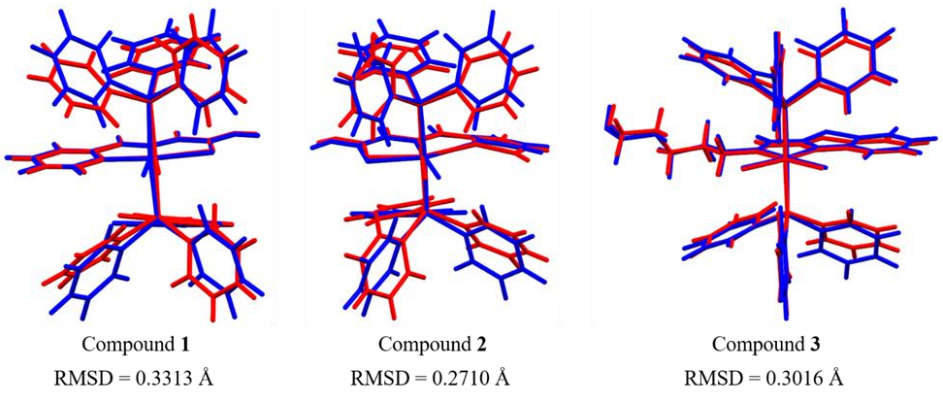

Figure 5.27: *Overlay structures of the optimized (blue) and crystal structures (red) for the metal complex cations of **1** and **2** as well as metal complex **3**.*

Table 5.4: *Crystal and structure refinement data for metal compounds **1** – **3**.*

Compound	**1**·2(CH_2Cl_2)	**2**·2(CH_2Cl_2)	**3**·CH_4O
Chemical formula	$C_{43}H_{38}ClN_4P_2RuS$·2(CH_2Cl_2)·Cl	$C_{42}H_{36}ClN_3P_2RuS_2$·2($CH_2Cl_2$)·Cl	$C_{49}H_{46}Cl_2N_2OP_2RuS$·$CH_4O$
Formula weight	1046.59	1050.62	976.89
Temperature (K)	100(2)	293(2)	100(2)
Crystal system	Orthorhombic	Monoclinic	Monoclinic
Space group	*Ima2*	*Cc*	*P2₁*
Unit cell dimensions (Å, º)	*a* = 22.7541(18)	*a* = 24.665(5)	*a* = 11.6529(6)
	b = 20.8853(15)	*b* = 20.590(2)	*b* = 11.1307(8)
	c = 9.6321(7)	*c* = 9.6333(10)	*c* = 12.4983(6)
	α = 90	*α* = 90	*α* = 90
	β = 90	*β* = 111.074(4)	*β* = 113.447(2)
	γ = 90	*γ* = 90	*γ* = 90
Crystal size (mm)	0.24 × 0.15 × 0.09	0.33 × 0.19 × 0.11	0.14 × 0.11 × 0.09
V (Å^3)	4577.4(6)	4565.1(8)	2288.9(2)
Z	4	4	2
Density (calc.) (Mg/ m^3)	1.517	1.529	1.417
Absorption coefficient (mm^{-1})	0.85	0.89	0.62
F (000)	2124	2136	1008
Θ range for data collection (deg)	2.65°; 28.10°	2.65°; 28.23°	2.97°; 27.22°
Index ranges	-30 ≤ *h* ≤ 30 -27 ≤ *k* ≤ 27 -12 ≤ *l* ≤ 12	-32 ≤ *h* ≤ 32 -27 ≤ *k* ≤ 27 -12 ≤ *l* ≤ 12	-14 ≤ *h* ≤ 14 -18 ≤ *k* ≤ 21 -15 ≤ *l* ≤ 15
Reflections measured	11493	11323	17785
Observed reflections ($I > 2\sigma(I)$)	5800	5668	8335
Independent reflections	3973	5512	6880
Data/ restraints/ parameters	4075/ 1/ 295	4951/ 2/ 527	8335/ 56/ 563
Goodness of fit on F^2	1.13	1.07	1.05
Observed R; wR^2	0.023; 0.062	0.033; 0.107	0.49; 0.124
R_{int}	0.022	0.033	0.046

Table 5.5: *Selected bond lengths [Å] and angles [º] for **1**.*

	Experimental	**Optimized**
Ru-Cl1	2.4289(11)	2.5481
Ru-P1	2.3788(7)	2.5113
Ru-P2	2.3788(7)	2.5113
Ru-S	2.3812(12)	2.5177
Ru-N1	2.101(4)	2.1052
Ru-N2	1.970(4)	2.0022
N1-C1	1.337(6)	1.3588
N1-C5	1.338(6)	1.3895
C6-N2	1.305(6)	1.3307
N2-N3	1.368(6)	1.3592
C7-N3	1.357(6)	1.4167
C7-N4	1.331(6)	1.3018
C7-S	1.703(5)	1.8216
P1-Ru-P2	173.26(4)	173.129
N2-Ru-S	83.19(12)	83.078
N2-Ru-N1	77.74(15)	79.254
N2-Ru-Cl1	178.42(12)	174.003
N1-Ru-S	160.93(10)	162.332

Table 5.6: *Selected bond lengths [Å] and angles [º] for complex **2**.*

	Experimental	**Optimized**
Ru-P1	2.399(1)	2.5175
Ru-P2	2.393(1)	2.1528
Ru-Cl1	2.421(1)	2.5135
Ru-S1	2.383(1)	2.6918
Ru-S2	2.345(1)	2.4290
Ru-N1	2.039(4)	2.0731
C6-S2	1.705(5)	1.8213
C1-S1	1.714(5)	1.8070
C4-S2	1.721(5)	1.8097
C5-N1	1.298(7)	1.3270
N1-N2	1.380(6)	1.3783
C6-N2	1.325(7)	1.4021
C6-N3	1.345(6)	1.3018
S1-Ru-S2	160.01(4)	161.450
N1-Ru-Cl1	177.8(1)	177.431
N1-Ru-S2	78.7(1)	78.548
N1-Ru-S1	82.2(1)	83.623
P1-Ru-P2	175.46(4)	175.198

Table 5.7: *Selected bond lengths [Å] and angles [º] for **3**.*

	Experimental	**Optimized**
Ru-Cl1	2.435(2)	2.5525
Ru-Cl2	2.448(2)	2.5245
Ru-N1	2.089(6)	2.1286
Ru-N2	2.010(7)	2.0446
Ru-P1	2.402(2)	2.5255
Ru-P2	2.387(3)	2.5289
C7-N1	1.333(9)	1.3444
C6-N1	1.40(1)	1.4182
C8-N2	1.30(1)	1.3243
C7-S	1.726(8)	1.8089
C1-S	1.724(9)	1.8156
P1-Ru-P2	177.05(8)	170.184
Cl1-Ru-Cl2	90.17(7)	92.172
Cl1-Ru-N1	100.2(2)	98.182
Cl2-Ru-N2	91.59(2)	90.960
N1-Ru-N2	78.2(3)	78.690

5.5.4 Antioxidant studies

Abnormal oxidative stress is a substantial contributor to the onset of numerous non-communicable diseases (*e.g.* cancer) [**56**]. Hence, complementary synthetic drugs with high efficacies are required to supplement the body's natural defence mechanisms (*e.g*. vitamin C) for scavenging of elevated concentrations reactive oxygen species (ROS) within the blood stream [**57**]. Organoruthenium species have sparked interest as metal-based antioxidants whereby their mechanism of activities to retard oxidative damage is hypothesized to be co-dependent on the metal's redox properties and the ligands propensity to quench the radical by proton donation or gets involved in combination reactions with the ROS [**58, 59**].

The radical scavenging capabilities of **1** – **3**, against the DPPH and NO radicals were studied and compared to the *in vitro* antioxidant activities with the standard, vitamin C. The 50%

inhibitory concentration (IC_{50}) values of the metal compounds (**Table 5.8**) varies from 44 to 85 µM against the DPPH radical and from 27 to 64 µM against the NO radical. It can be concluded that the ruthenium complexes displayed significantly higher antioxidant activities in comparison to the natural antioxidant, vitamin C. As expected, the paramagnetic complexes (**1** and **2**) showed higher antioxidant activities due to the unpaired electrons which scavenges free radicals in an effort to stabilize the d^5 configurations [**60, 61**].

Table 5.8: *Antioxidant activities of compounds **1** – **3** and vitamin C against the DPPH and NO radicals.*

Compound	DPPH Radical	NO Radical
	IC_{50} (µM)	**IC_{50} (µM)**
1	57	34
2	44	27
3	85	64
Vitamin C	141	210

Standard deviation is less than 8 % of mean values

5.5.5 DNA interaction studies

(a) UV-Vis titrations

UV-visible spectroscopy is the most predominate technique used to evaluate the interactions between metal complexes and calf-thymus (CT) DNA [**61**]. Using this investigative tool, the interactive strength between the metal complex and the biomolecule can be assessed while the nature of the UV-Vis spectral changes provide structural indicators regarding the metal complex-DNA adducts [**62**]. In general, hyperchromism and hypochromism are characteristic UV-Vis spectral features that are closely associated when the double helix structure of DNA interacts with metal complexes. In particular, the occurrence of hyperchromism is reflective of the comprised DNA structural integrity due to binding of the metal complex *via* the minor or major grooves of DNA or through electrostatic binding. Conversely, the observation of

hypochromism can be accounted to the intercalative DNA binding mode of metal complexes which are typically facilitated by their *pi*-conjugated chelators and selected DNA base pairs [**63**].

UV-visible spectral titrations between the metal compounds and ct-DNA were done by monitoring their individual MLCT bands (at 473 nm for **1**, at 448 nm for **2** and at 526 nm for **3**), see **Figures 5.28 – 5.30**. Upon progressive increments of ct-DNA to **1**, hypochromism (6.60 %) and a red shift of 2 nm were observed in the UV-Vis spectral profile of **1**. A distinctive isosbestic point appears at 485 nm which indicates the formation of a new specie in solution and is indicative for single mode DNA binding interaction [**64**]. These experimental observations are usually suggestive of an intercalative mode of binding towards ct-DNA. However, metal compound **1** is structurally unfavourable for DNA intercalation due to its bulky *trans*-[$Ru(PPh_3)_2$] core. This is further supported by the obtained K_b value of 7.95 *x* 10^5 M^{-1} which is lower in magnitude than other classical intercalators and partial intercalators whose K_b values have a magnitude of 10^6 M^{-1} and higher [**64, 65**]. It is therefore inferred that the DNA binding mode of **1** is non-intercalative and that the metal compound most probably interacts with the secondary structure of DNA *via* electrostatic interactions or groove-binding.

Titrimetric research data show that with increasing standardized amounts of ct-DNA, overall hyperchromisms of 3 % and 1.44 % are observed in the UV-Vis spectral profiles of **2** and **3**, respectively. This is accompanied by a red shift for **2** (7 nm) and a blue shift for **3** (5 nm) as well as diffuse isosbestic points which are present in the individual overlay UV-visible spectra of these metal compounds (at 590 nm, 358 nm, 330 nm for **2** and at 526 nm, 324 nm for **3**). The aforementioned electronic spectroscopic changes are illustrative of homogeneous interconversion from the species of the free metal compounds to their corresponding ct-DNA adducts. Based on these research findings, it is concluded that the metal compounds cause partial uncoiling of the DNA (*viz.* damage to the secondary structure) due to external contacts with the DNA through electrostatic interactions or *via* groove-binding [**65, 66**]. Furthermore, the MLCT peak maxima shifts of **1** and **2** are characteristic of metal centres coordinating towards the N7-DNA base pairs, whereas the lack of a red shift in **3** could be due to electrostatic interactions of the metal complex towards the DNA phosphate backbones [**67**]. The obtained K_b values for **2** and **3** were found to be 4.00 *x* 10^5 M^{-1} and 2.20 *x* 10^5 M^{-1} respectively which, as in the case of **1**, is lower than that of known DNA intercalators. These K_b values obtained are comparable to that of the complex salt, $[Ru(dmb)_2(pdtp)](ClO_4)_2$ (where dmb = 4,4'-dimethyl-

2,2'-bipyridine and pdtp = 3-(pyridine-2-yl)-as-triazino[5,6-*f*]phenanthrene) with a K_b value of 8.30 *x* 10^5 M^{-1} [**68**].

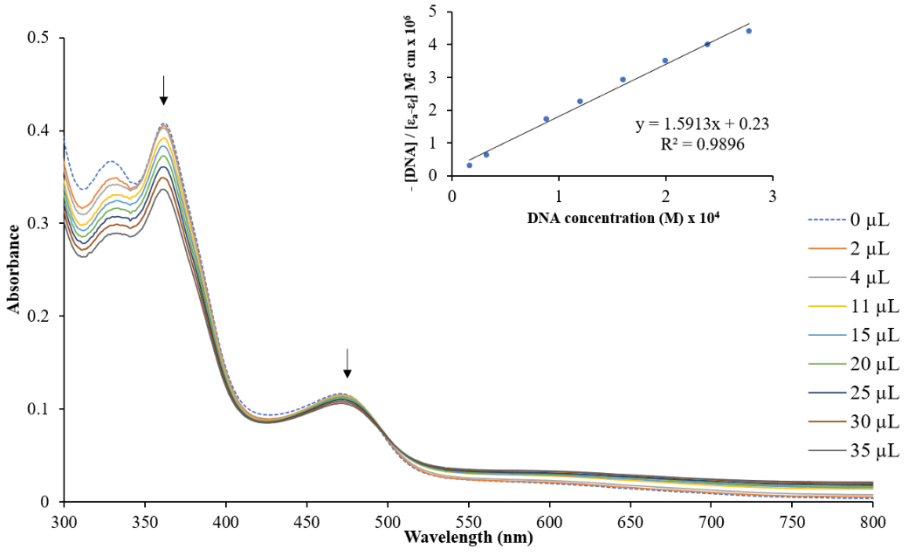

Figure 5.28: *Overlay UV-Vis spectra of compound **1** in the absence and presence of increasing amounts of ct-DNA. A dashed line indicates the initial spectrum.* ***Inset:*** *Plot of [DNA]/(εa - εf) x 10^7 vs [DNA] x 10^5 and the linear fit for the titration.*

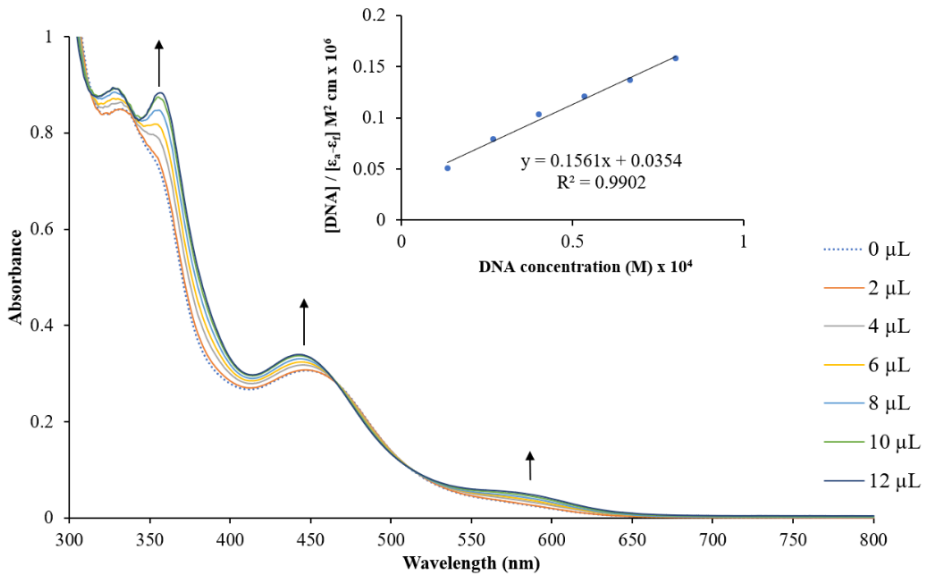

Figure 5.29: *Overlay UV-Vis spectra of compound **2** in the absence and presence of increasing amounts of ct-DNA. A dashed line indicates the initial spectrum.* ***Inset:*** *Plot of [DNA]/(εa - εf) x 10^9 vs [DNA] x 10^6 and the linear fit for the titration.*

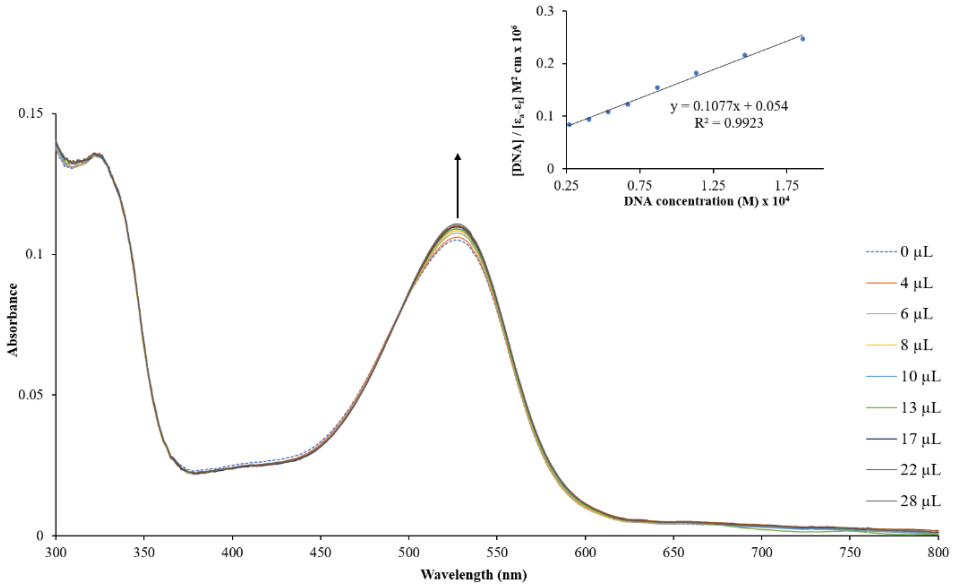

Figure 5.30: *Overlay UV-Vis spectra of compound **3** in the absence and presence of increasing amounts of ct-DNA. A dashed line indicates the initial spectrum.* ***Inset:*** *Plot of* $[DNA]/(\varepsilon_a - \varepsilon_f) \times 10^7$ *vs* $[DNA] \times 10^5$ *and the linear fit for the titration.*

*(**b**) Molecular docking*

Molecular docking can contribute to rational drug design and aid in elucidating the mechanisms of activities for prospective metallopharmaceuticals [**69**]. To explore the most feasible binding site, docking studies have been carried out using the optimized conformers of the respective metal compounds as ligands while the B-DNA crystal structure was used as a target. The lowest global energy states were calculated to be -47.89, -43.62 and -46.57 kJ mol^{-1} for the B-DNA hybrids of metal compounds **1**, **2** and **3**, respectively. These global energies are close to that of other small molecules that have been docked favourably to the B-DNA structure [**70, 71**]. Metal compound **1** dock partially within the DNA major groove of the DNA whilst **2** and **3** are partial DNA minor groove binders, see **Figures 5.31** – **5.33**.

The partial interaction of the metal compounds towards B-DNA can be accounted to their steric demands which is evident when comparing the DNA minor groove width of approximately 12 Å and the Van der Waals (VdW) radii of **1** (8.381 Å), **2** (8.488 Å) and **3** (9.851 Å) (*w.r.t.* their corresponding geometric centres). Noticeably, the preferential DNA interactive modes of the metal compounds occur, even though metal compound **1** has a lower VdW radius than that of

2 and **3**. This implies that the DNA binding modes of the metal compounds are largely dictated by intramolecular interactions between their optimized conformers and the B-DNA structure. The N4 atom and chloro co-ligand of compound **1** shows close-contacts with a thymine moiety and complex **3** interacts to G-C DNA base pair while no intermolecular interactions are observed between compound **2** and the DNA base pairs. Mutually, the triphenylphosphine co-ligands of the respective metal compounds anchors it to the phosphate backbones with close contacts occurring at distances between 2.474 and 2.755 Å.

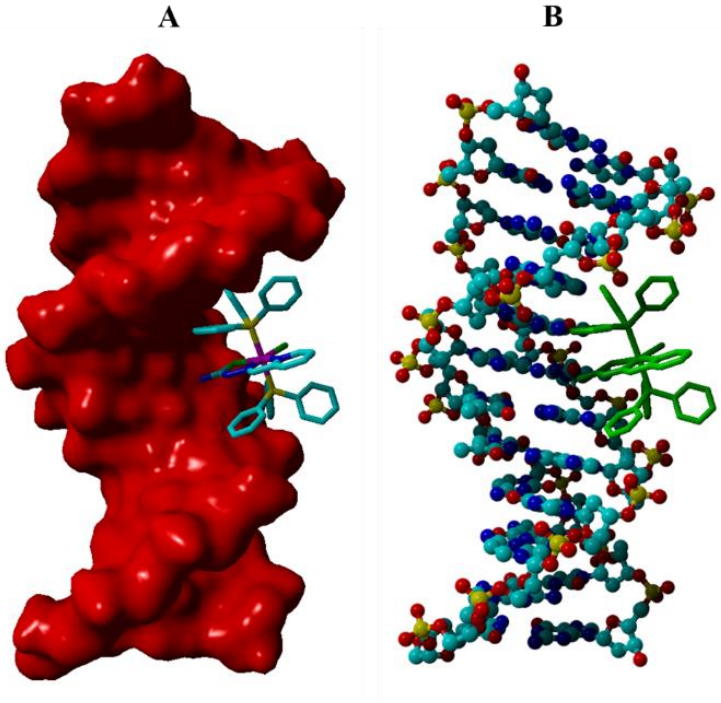

Figure 5.31: *Compound **1** primarily docked into the major groove of B-DNA: (**A**) shows the molecular surface view of DNA whereas (**B**) shows DNA in ball and stick view.*

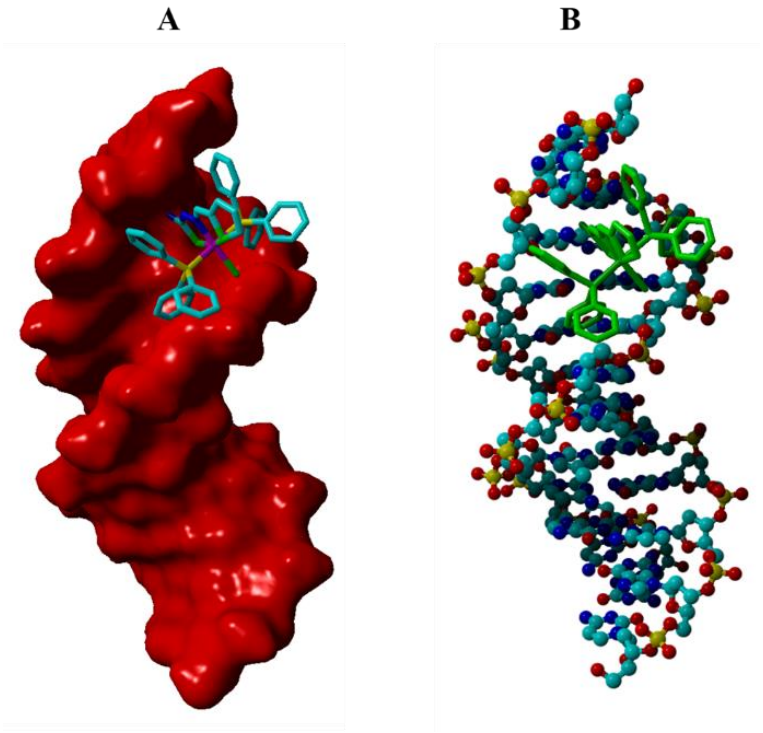

Figure 5.32: *Compound **2** primarily docked into the minor groove of B-DNA: (**A**) shows the molecular surface view of DNA whereas (**B**) shows DNA in ball and stick view.*

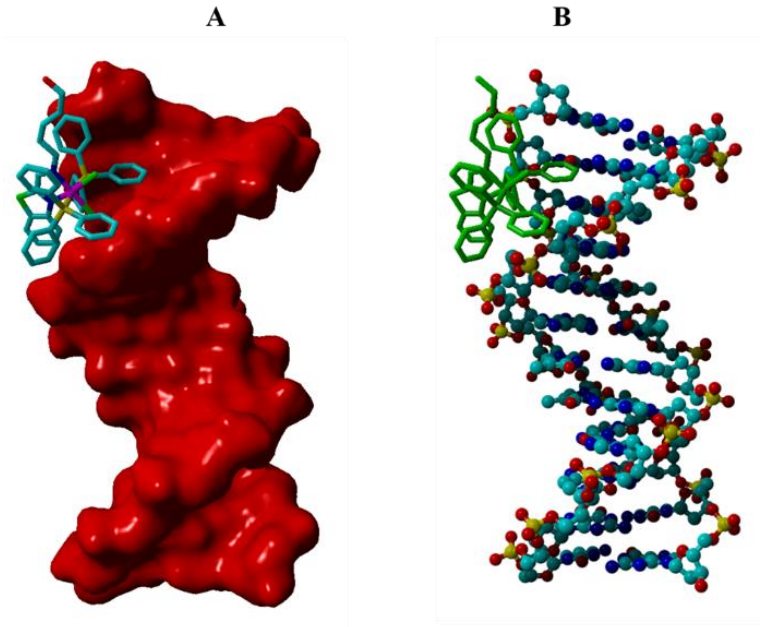

Figure 5.33: *Compound **3** primarily docked into the minor groove of B-DNA: (**A**) shows the molecular surface view of DNA whereas (**B**) shows DNA in ball and stick view.*

5.5.6 BSA interaction studies

Serum albumin is the leading protein in blood plasma which plays an important role in the *in vivo* transport of pharmaceuticals. Consequently, the study of the binding properties of potential medicinal drugs towards serum albumin is of great importance in drug discovery. In this regard, the binding properties of bovine serum albumin has been broadly studied due to its structural homology with human serum albumin [**72**]. Preferably, to function as an ideal transporter, a protein should maintain its structural features as much as possible upon binding with a drug. In its native state (folded), BSA consists of three globular domains (**I**, **II** and **III**) which are subdivided into two smaller subdomains (**A** and **B**). Known binding sites for metal-based and organic compounds are typically the subdomains **IIA** and **IIIA** (known as sites **I** and **II**) [**73-75**]. Well-defined electronic transitions in the UV-Visible absorption and fluorescence spectra of BSA are due to its tryptophan residues and any structural fluctuations of BSA can result in variations of these spectroscopic fingerprint signals [**76**].

(a) UV-Vis titrations

From the analysis of the BSA UV-Vis absorption spectra, it can be generally seen that with an increase in the concentration of a metal compound, slight blue shifts and distinct hypochromism are observed, see **Figures 5.34 – 5.36**. These UV-Vis spectral changes are indicative of conformational changes of the BSA structure and changes in the polarity around the tryptophan residue. The aforementioned observations suggest that the metal compounds stabilize the BSA structure upon binding which promotes folding of the BSA strand, thereby masking the tryptophan residue within its hydrophobic pocket [**76-79**]. The apparent association constants (K_{app}) were calculated to be 2.21×10^4 M^{-1}, 2.00×10^4 M^{-1} and 1.80×10^4 M^{-1}, respectively. The binding affinity towards BSA must be strong enough to carry out transportation but also low enough to ensure that the metal compound is eventually released to the pharmacological targets. These metal compounds are therefore considered to be strong binders towards BSA as they fall within range of other "ideal" binders ($10^4 – 10^6$ M^{-1}) [**80**].

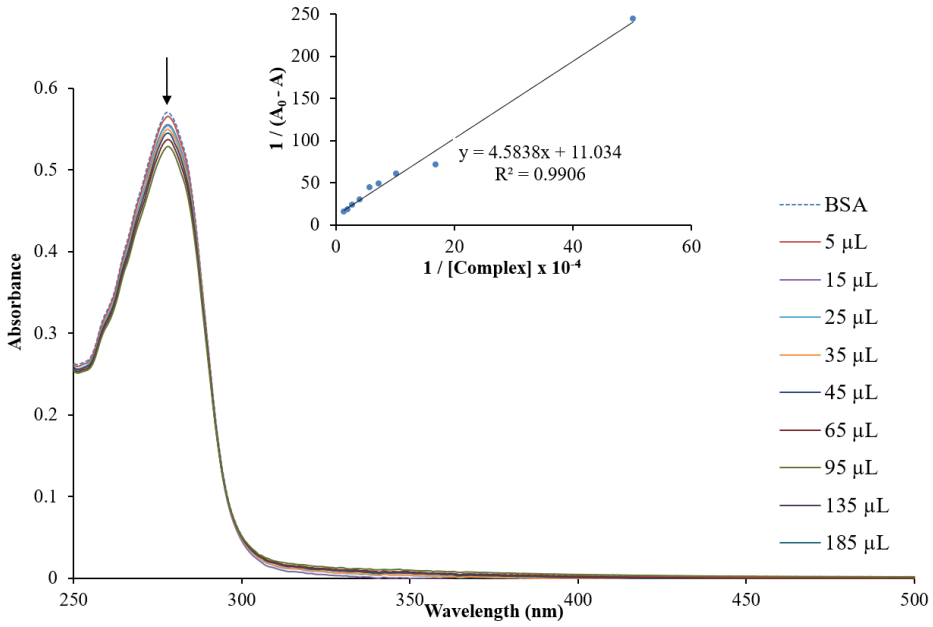

Figure 5.34: *UV-Vis spectral profile depicting the titration between compound **1** and BSA. The inset is the double reciprocal plots of 1 / (A_0 – A) versus 1 / $C_{complex}$ x 10^{-4}.*

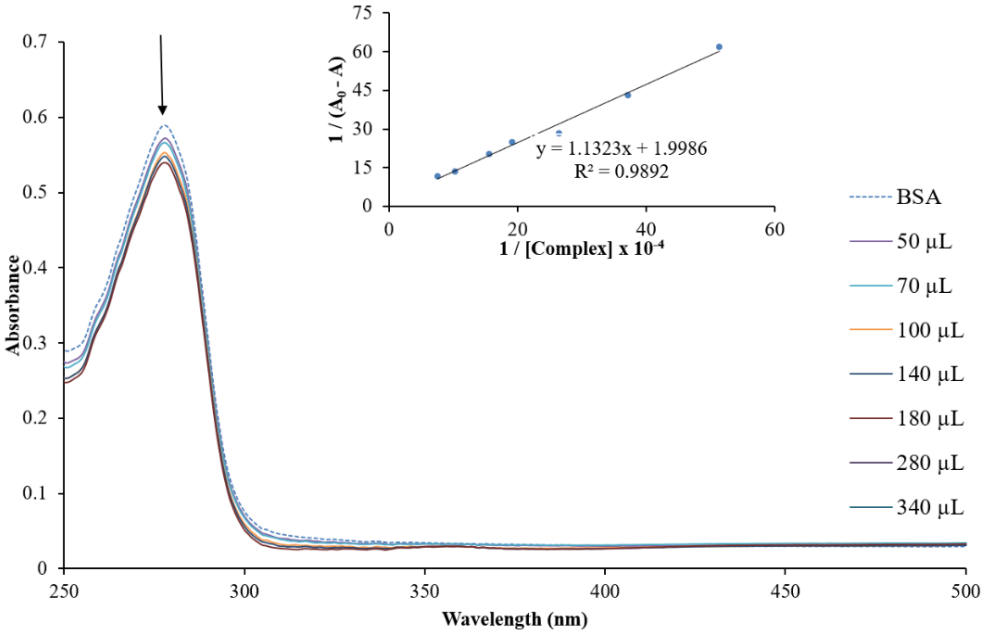

Figure 5.35: *UV-Vis spectral profile depicting the titration between compound **2** and BSA. The inset is the double reciprocal plots of 1 / (A_0 – A) versus 1 / $C_{complex}$ x 10^{-4}.*

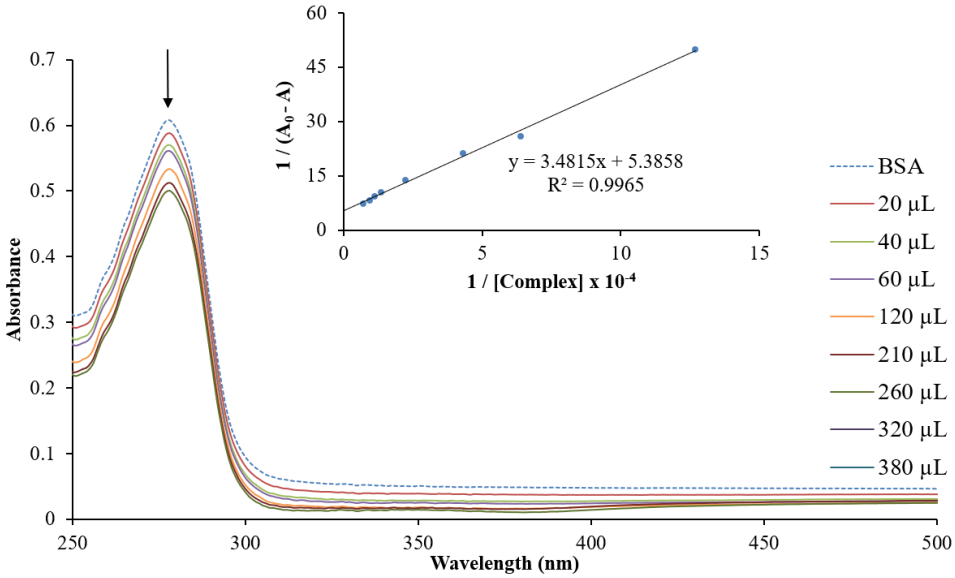

Figure 5.36: *UV-Vis spectral profile depicting the titration between compound **3** and BSA. The inset is the double reciprocal plots of 1 / (A_0 – A) versus 1 / $C_{complex}$ x 10^{-4}.*

(b) *Fluorescence titrations*

To corroborate the research findings of the UV-visible spectrophotometric study, fluorescence quenching of BSA, incurred by each of the metal compounds were monitored. Indicatively, alterations in the fluorescence profile of BSA can be directly correlated to conformational changes in the BSA structure by detecting changes in the microenvironment of the tryptophan chromophore [**81**]. **Figures 5.37 – 5.39** illustrate the emission spectral effects of subsequent additions of standardized aliquots of the individual metal compounds to BSA. It is clearly seen that the characteristic emission band of BSA (due to the tryptophan residue) decreases progressively during each titration, which supports the formation of the metal compound-BSA adducts. In addition, a minor blue shift accompanied the later within the BSA fluorescence spectra, which is synonymous of the tryptophan residues being enclosed in a hydrophobic pocket due to increased folding of the BSA strand (consistent with the results in the UV-Vis study)[**73, 82, 83**].

This research data substantiates the increased BSA folding as a result of hydrogen bonding or Van der Waals contact during the interaction of the metal compounds with BSA within its

hydrophobic subdomain **IIA** [**28, 84**]. From their Stern-Volmer plots, the Stern-Volmer constants (K_{SV}) and quenching rate constants (K_q) were calculated (see **Table 5.9**). Static quenching of BSA as induced by the metal complexes was confirmed by the obtained K_q values (**Table 5.9**) which were significantly higher than the maximum scatter collision constant for dynamic quenching (2×10^{10} M^{-1} s^{-1}). The latter is also supported by the characteristic UV-Vis spectral changes in the UV-Vis profile of BSA upon addition of the individual metal compounds [**75, 82, 85**]. Other ruthenium compounds in literature have reported similar K_{SV} and K_q values, *e.g.* the ruthenium(II) compounds, $[Ru(bpy)_2smp](PF_6)$ (bpy = 2,2'-bipyridine, smp = sulfamethoxypyridazine) and [Ru(η^6-*p*-cymene)(diclo)Cl] (Hdiclo = 2-[(2,6-dichlorophenyl)amino]benzeneacetic acid) possessed K_{SV} values of 1.02×10^5 M^{-1} and 6.45×10^4 M^{-1}, respectively [**80, 86**].

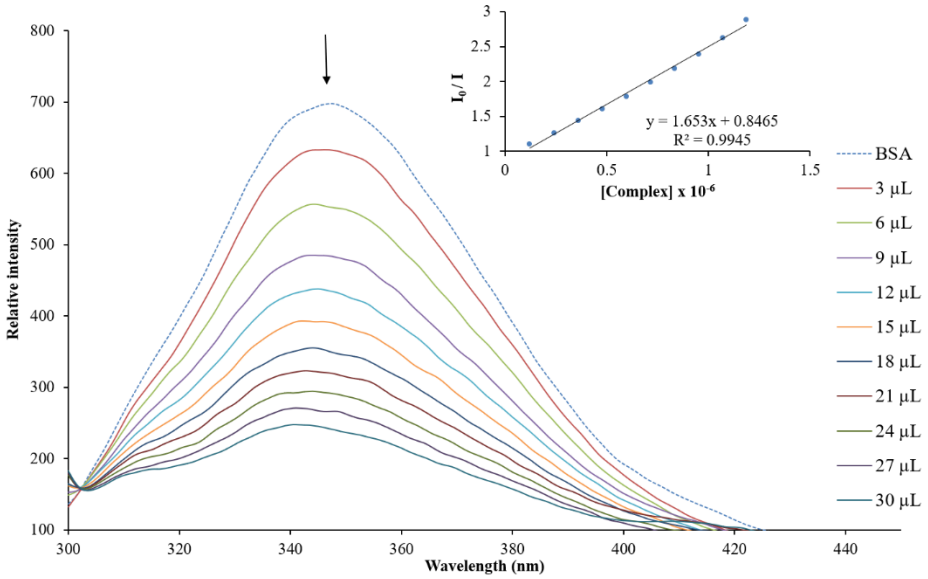

Figure 5.37: *Fluorescence emission spectral profile depicting the titration between compound **1** and BSA. The inset is the Stern-Volmer plot.*

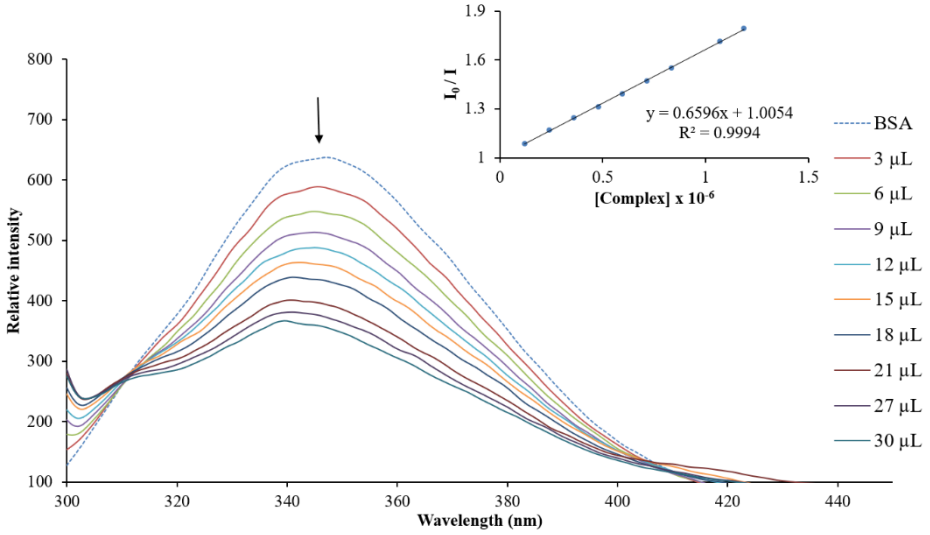

Figure 5.38: *Fluorescence emission spectral profile depicting the titration between compound **2** and BSA. The inset is the Stern-Volmer plot.*

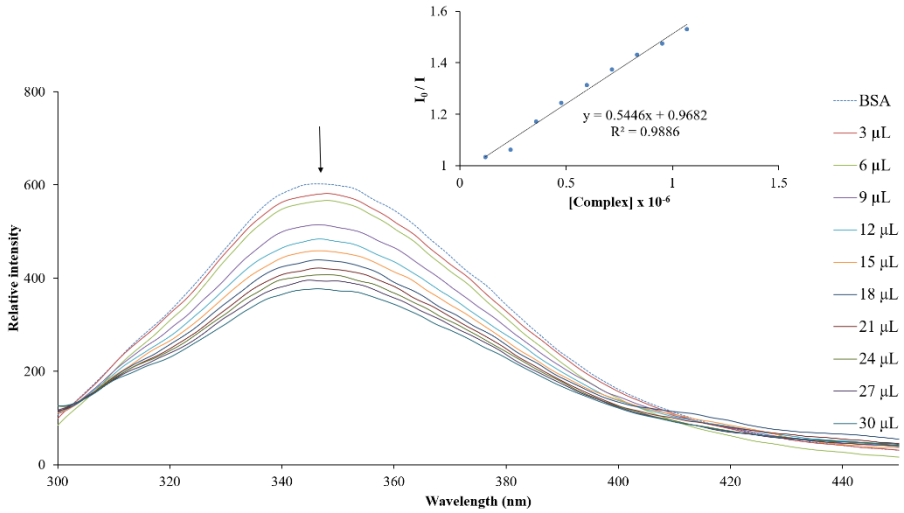

Figure 5.39: *Fluorescence emission spectral profile depicting the titration between compound **3** and BSA. The inset is the Stern-Volmer plot.*

(c) Competitive binding

The principal binding sites for serum albumin are sites **I** and **II** which are situated in subdomain **IIA** and **IIIA**, respectively. Fluorescence spectroscopy is a useful tool in the method of site marker fluorescence probes to investigate the nature of binding sites and their affinities for

different compounds [**87**]. Warfarin and Ibuprofen were utilized as site markers for sited **I** and **II,** respectively. The quenching of BSA by the metal compounds in the presence of each site marker was followed and the K_{SV} values determined as well as compared to the K_{SV} value obtained in the absence of the site markers, see **Figures 5.40** – **5.42**. **Table 5.9** shows the K_{SV} values of the metal compounds in the presence of the different site markers. A significant quenching of the BSA-containing systems with both site markers, by each of the metal complexes is observed and the K_{SV} values of both systems decrease, relative to the systems in the absence of the site markers. These observations relate to the fact that the metal compounds displace both site markers and therefore can bind to both sites **I** and **II** within BSA. However, since a larger decrease of K_{SV} values were observed for the BSA-Warfarin, site **I** (located in subdomain **IIA**) in BSA is considered the main binding site for all compounds [**87**].

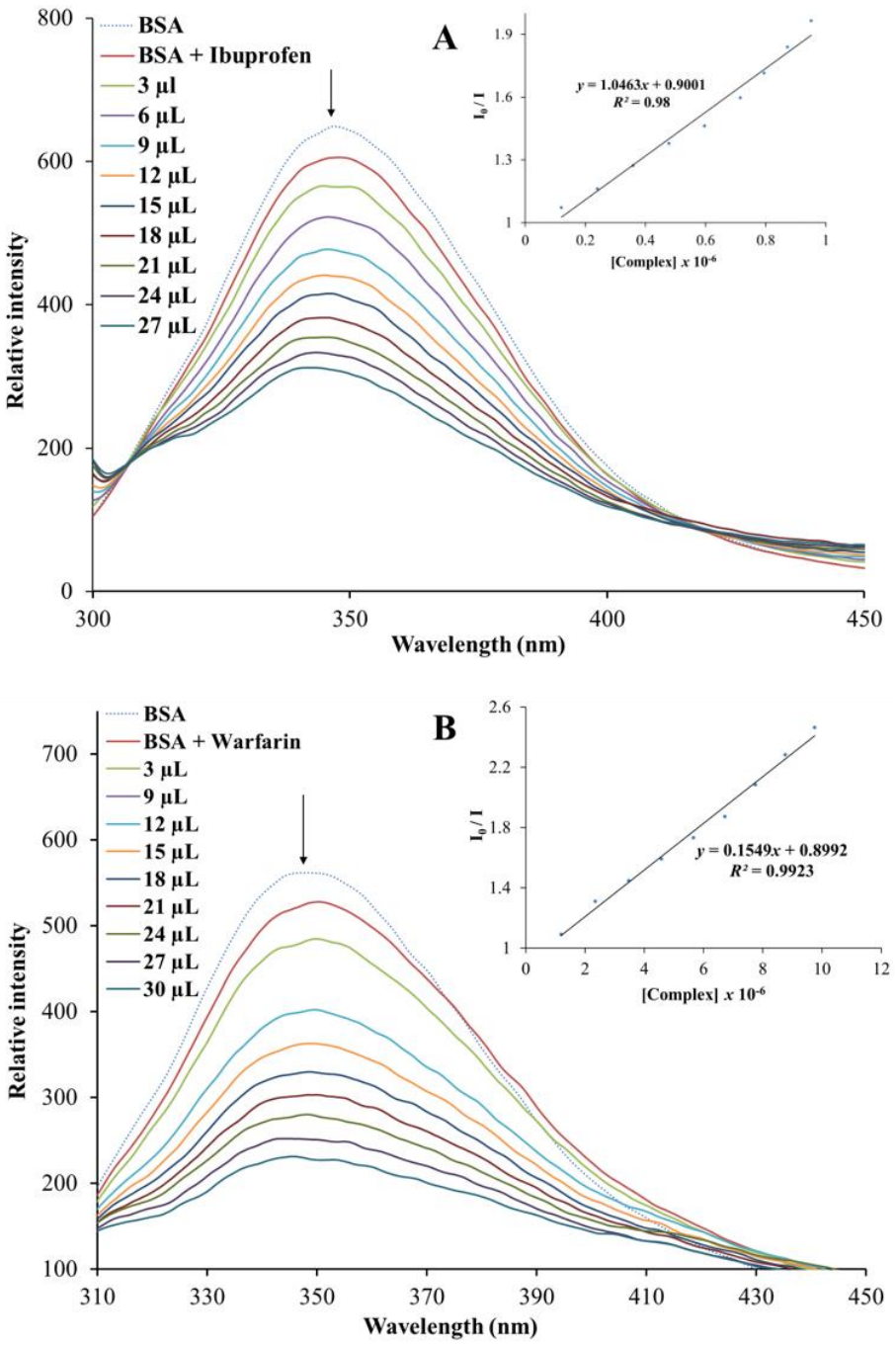

Figure 5.40: *Fluorescence emission spectral profiles of BSA with equimolar amounts of (**A**) Warfarin and (**B**) Ibuprofen upon the addition of **1**.*

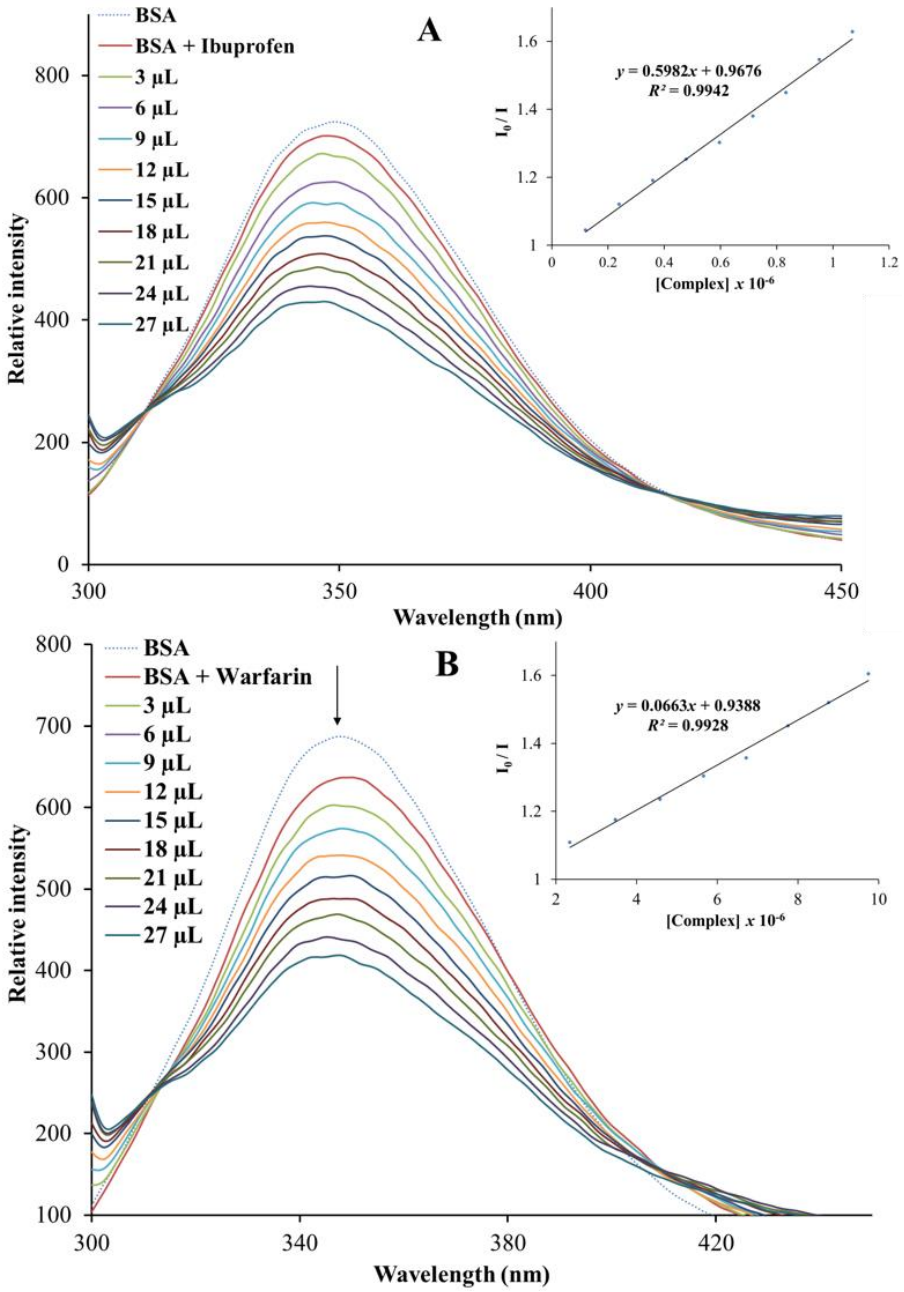

Figure 5.41: *Fluorescence emission spectral profile of BSA with equimolar amounts of (**A**) Warfarin and (**B**) Ibuprofen upon the addition of **2**.*

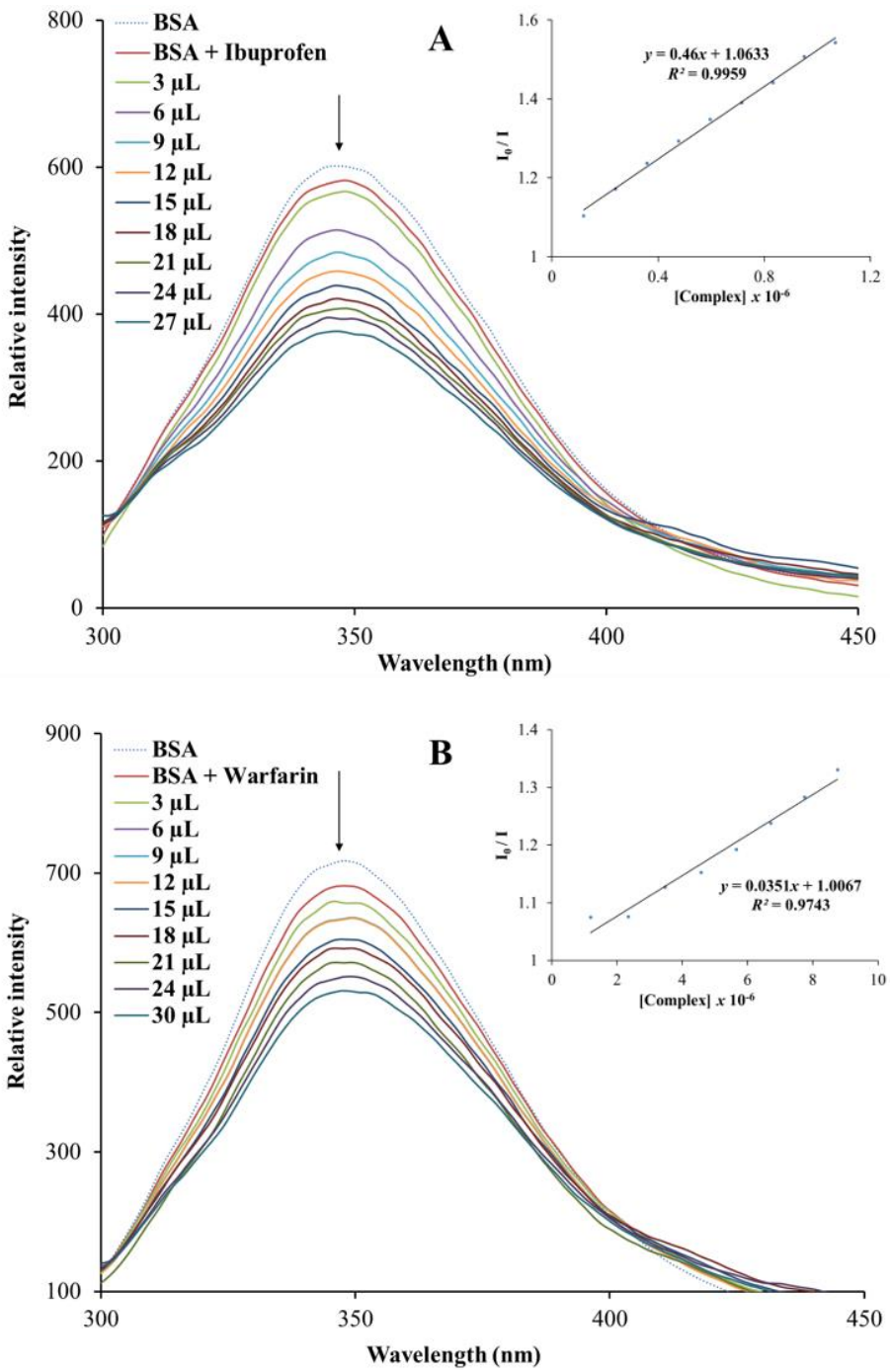

Figure 5.42: *Fluorescence emission spectral profile of BSA with equimolar amounts of (**A**) Warfarin and (**B**) Ibuprofen upon the addition of **3**.*

Table 5.9: *Binding parameters of **1** – **3** from BSA fluorescence experiments.*

Compound	No Site marker		Ibuprofen		Warfarin	
1	**K_{SV} (M^{-1})**	**K_q (M^{-1} s^{-1})**	**K_{SV} (M^{-1})**	**K_q (M^{-1} s^{-1})**	**K_{SV} (M^{-1})**	**K_q (M^{-1} s^{-1})**
	1.65×10^5	1.65×10^{13}	1.05×10^5	2.01×10^{13}	1.55×10^4	1.87×10^{12}
2	6.60×10^4	6.60×10^{12}	5.98×10^4	3.89×10^{12}	6.63×10^3	2.36×10^{11}
3	5.14×10^4	5.14×10^{12}	4.60×10^4	5.37×10^{12}	3.34×10^3	3.34×10^{11}

(d) *Molecular docking*

The favoured orientations of all metal compounds with respect to BSA were predicted using molecular docking studies. The results show that the complexes interact with the BSA molecule in the hydrophobic subdomains **IB** and **IIA**, see **Figures 5.43** – **5.45**. Compound **1** binds with the surface of subdomain **IB** through non-polar intermolecular interactions between its PPh_3 co-ligand and amino acid residue ASP 37. Compound **2** exhibits the best binding mode, as reflected by the lowest global energy (- 50.65 kJ mol^{-1}) and is seen to dock well within the **IIA** subdomain *via* adducts formed through interactions between the thiol sulfur with ARG 194 and the PPh_3 co-ligand with TRP 213. The metal-BSA adducts of **3** are stabilized within the **IB** subdomain by non-polar interactions between the phenyl ring of the benzothiazole moiety and the PPh_3 co-ligand with the amino acid residues LYS 114 and ARG 144 of the BSA molecule.

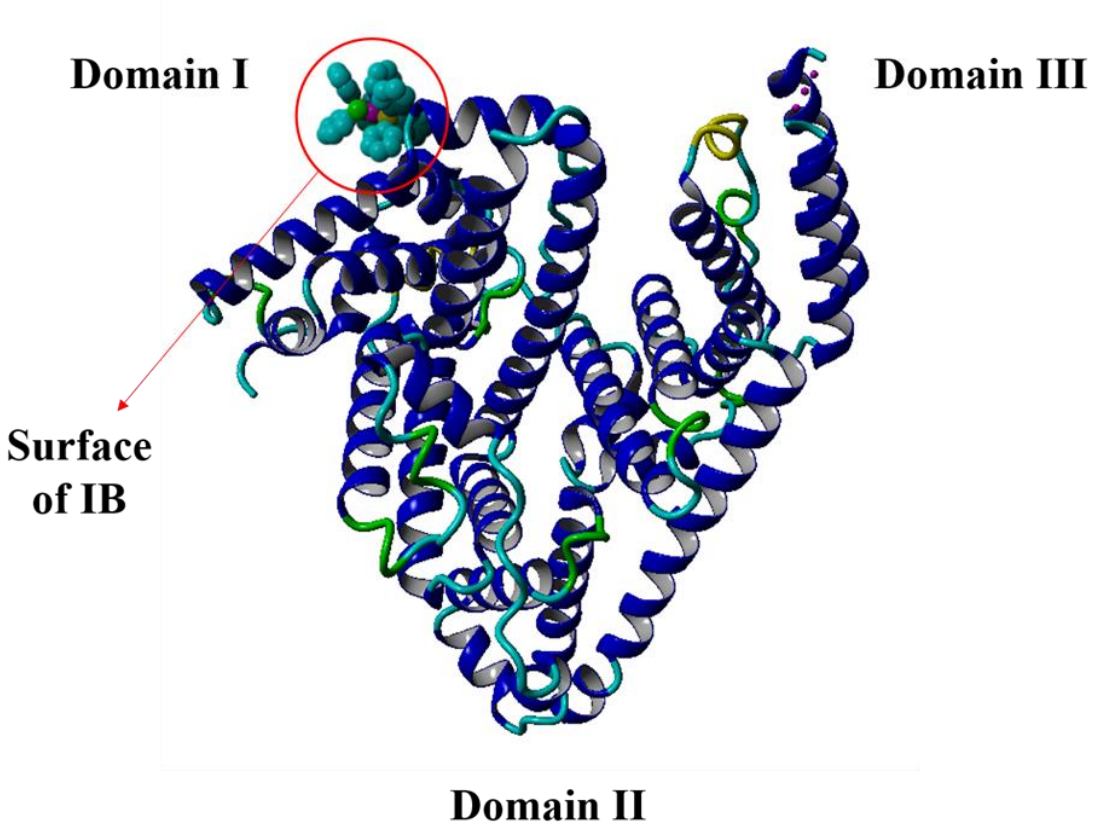

Figure 5.43: *The computed minimum energy adducts of BSA and **1** illustrating that the metal complex docking at the surface of the **IB** site of BSA.*

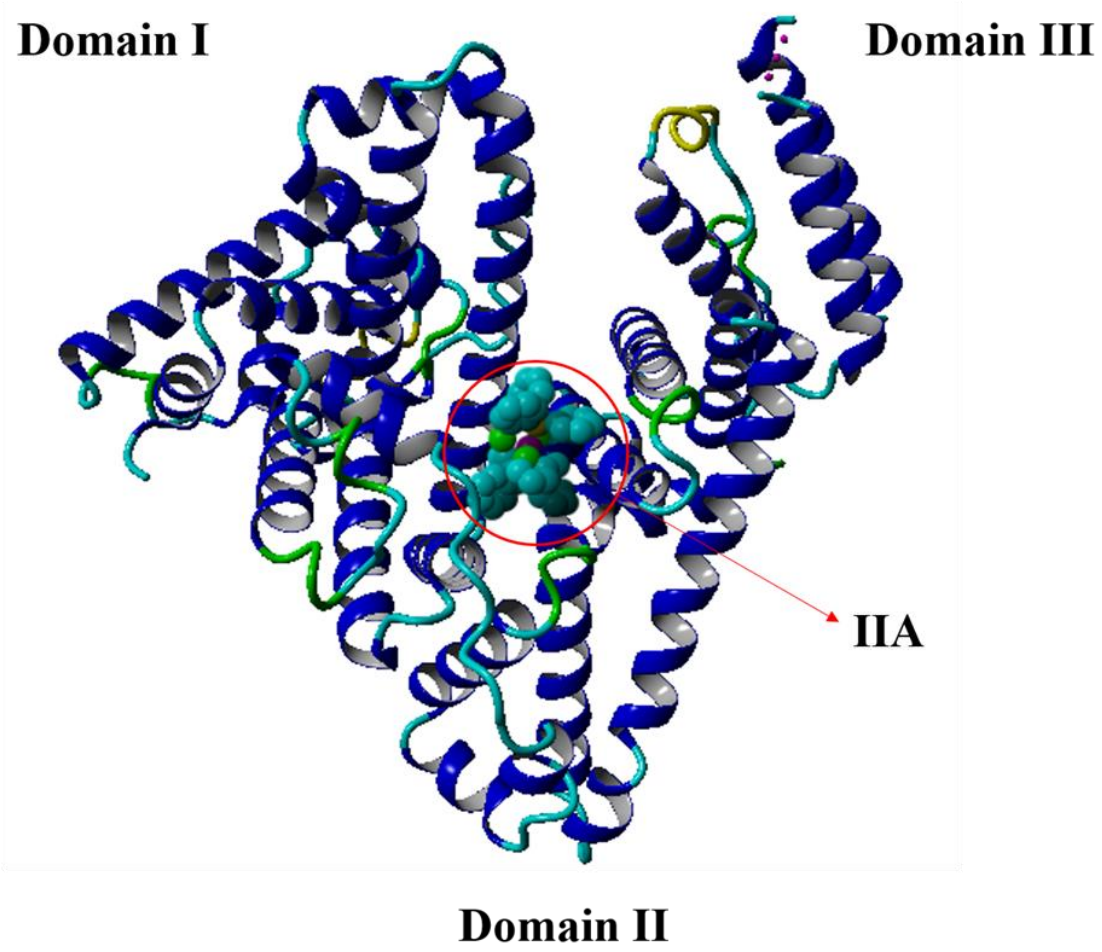

Figure 5.44: *The computed minimum energy adducts of BSA and **2** illustrating that the metal complex docking with the **IIA** site of BSA.*

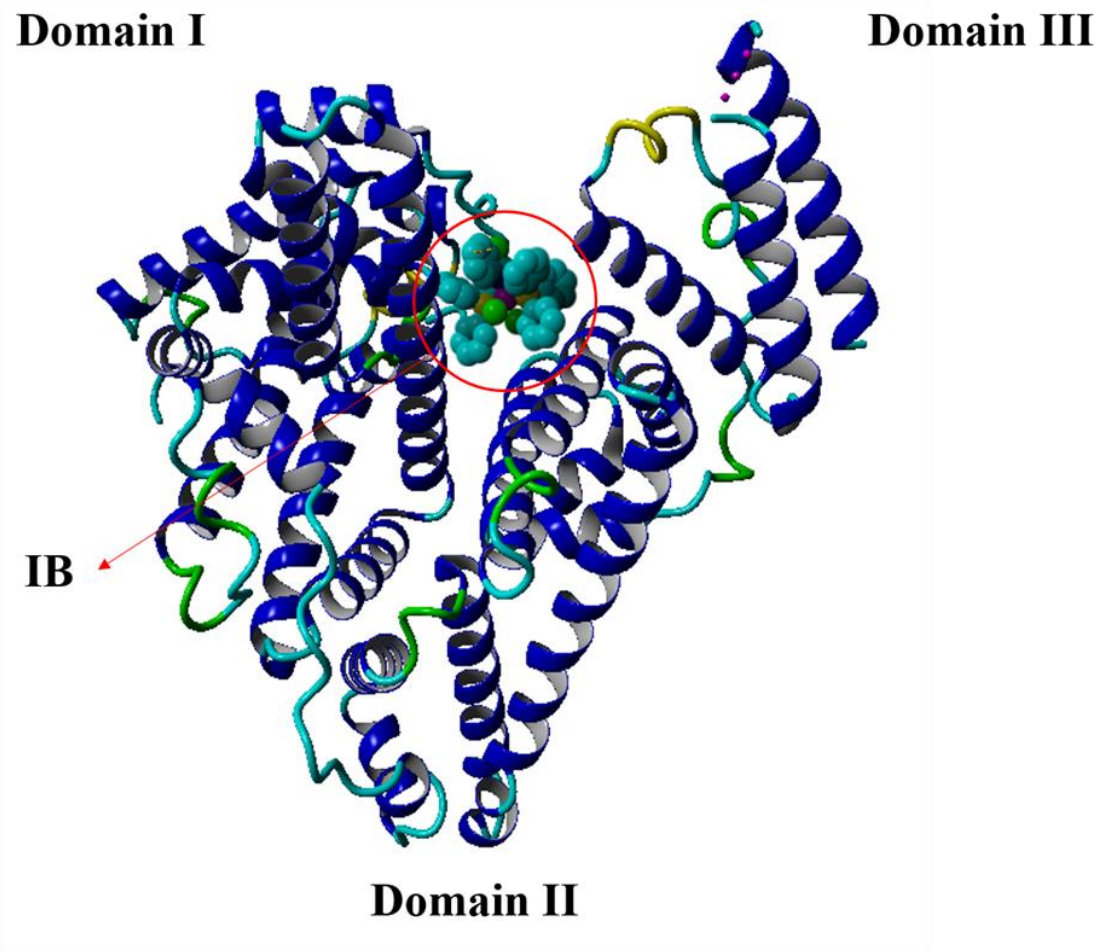

Figure 5.45: *The computed minimum energy adducts of BSA and **3** illustrating that the metal complex docking with the **IB** site of BSA.*

5.6 References

1. U. Ndagi, N. Mhlongo and M. E. Soliman, *Drug Des. Devel. Ther.*, 2017, **11**, 599-616.

2. A. Notaro and G. Gasser, *Chem. Soc. Rev.*, 2017, **46**, 7317-7337.

3. L. Zeng, P. Gupta, Y. Chen, E. Wang, L. Ji, H. Chao and Z.-S. Chen, *Chem. Soc. Rev.*, 2017, **46**, 5771-5804.

4. P. Kumar, S. Swagatika, S. Dasari, R. S. Tomar and A. K. Patra, *J. Inorg. Biochem.*, 2019, **199**, 110769.

5. M. M. Kasprzak, L. Szmigiero, E. Zyner and J. Ochocki, *J. Inorg. Biochem.*, 2011, **105**, 518-524.

6. M. Kubanik, W. Kandioller, K. Kim, R. F. Anderson, E. Klapproth, M. A. Jakupec, A. Roller, T. Söhnel, B. K. Keppler and C. G. Hartinger, *Dalton Trans.*, 2016, **45**, 13091-13103.

7. Z. Wang, H. Qian, S.-M. Yiu, J. Sun and G. Zhu, *J. Inorg. Biochem.*, 2014, **131**, 47-55.

8. A. Rouf and C. Tanyeli, *Eur. J. Med. Chem.*, 2015, **97**, 911-927.

9. S. Sardari, S. Feizi, A. H. Rezayan, P. Azerang, S. Mohammad Shahcheragh, G. Ghavami and A. Habibi, *Iran. J. Pharm. Res.*, 2017, **16**, 1128-1140.

10. S. Singhal, S. Arora, S. Agarwal, R. Sharma and N. Singhal, *World. J. Pharm. and Pharm. Sci.*, 2013, **2**, 4661-4681.

11. M. Richert, M. Walczyk, M. Cieslak, J. Kazmierczak-Baranska, K. Krolewska, G. Wrzeszcz, T. Muzioł and S. Biniak, *Dalton Trans.*, 2019, **48**, 10689-10702.

12. K. Sampath, S. Sathiyaraj and C. Jayabalakrishnan, *Spectrochim. Acta, Part A.*, 2013, **105**, 582-592.

13. C. B. Spillane, N. C. Fletcher, S. M. Rountree, H. van den Berg, S. Chanduloy, J. L. Morgan and F. R. Keene, *J. Biol. Inorg. Chem.*, 2007, **12**, 797-807.

14. *Journal*, Bruker APEX2, SAINT and SADABS (2010). Bruker AXS Inc. Madison. Wisconsin, USA.

15. R. H. Blessing, *Acta Crystallogr., Sect. A: Found. Adv.*, 1995, **51 (Pt 1)**, 33-38.

16. L. Farrugia, *J. Appl. Crystallogr.*, 2012, **45**, 849-854.

17. G. Sheldrick, *Acta Crystallogr., Sect. A: Found. Adv.*, 2008, **64**, 112-122.

18. Frisch MJ, Trucks GW, Schlegel HB, Scuseria GE, Robb MA, Cheeseman JR, Scalmani G, Barone V, Petersson GA, Nakatsuji H, Li X, Caricato M, Marenich AV, Bloino J, Janesko BG, Gomperts R, Mennucci B, Hratchian HP, Ortiz JV, Izmaylov

AF, Sonnenberg JL, Williams, Ding F, Lipparini F, Egidi F, Goings J, Peng B, Petrone A, Henderson T, Ranasinghe D, Zakrzewski VG, Gao J, Rega N, Zheng G, Liang W, Hada M, Ehara M, Toyota K, Fukuda R, Hasegawa J, Ishida M, Nakajima T, Honda Y, Kitao O, Nakai H, Vreven T, Throssell K, Montgomery Jr JA, Peralta JE, Ogliaro F, Bearpark MJ, Heyd JJ, Brothers EN, Kudin KN, Staroverov VN, Keith TA, Kobayashi R, Normand J, Raghavachari K, Rendell AP, Burant JC, Iyengar SS, Tomasi J, Cossi M, Millam JM, Klene M, Adamo C, Cammi R, Ochterski JW, Martin RL, Morokuma K, Farkas O, Foresman JB, Fox DJ (2009) Gaussian 09 Rev. A.01.

19. L. Gramni, N. Vukea, A. Chakraborty, W. J. Samson, L. M. K. Dingle, B. Xulu, J.-A. de la Mare, A. L. Edkins and I. N. Booysen, *Inorg. Chim. Acta.*, 2019, **492**, 98-107.

20. H. Yildirim, E. Guler, M. Yavuz, N. Ozturk, P. K. Yaman, E. Subasi, E. Sahin and S. Timur, *Mater. Sci. Eng. C.*, 2014, **44**, 1-8.

21. P. Mishra, M. Jha, R. C, C. Kumar, *Orient. J. Chem.*, 2013, **29**, 1651-1656.

22. P. Novak, K. Pičuljan, T. Biljan, T. Hrenar, M. Cindrić, M. Rubčić and Z. Meić, *Croat. Chem. Acta.*, 2007, **80**, 575-581.

23. T. S. Lobana, G. Bawa, R. J. Butcher, B.-J. Liaw and C. W. Liu, *Polyhedron*, 2006, **25**, 2897-2903.

24. W.-S. Hong, C.-Y. Wu, C.-S. Lee, W.-S. Hwang and M. Y. Chiang, *J. Organomet. Chem.*, 2004, **689**, 277-285.

25. D. Agarwal, D. Khan and D. Ahmad, *J. Chem. Pharm. Res.*, 2013, **5**, 240-245.

26. T. S. Lobana, G. Bawa, A. Castineiras, R. J. Butcher and M. Zeller, *Organometallics*, 2007, **27**, 175-180.

27. C. Jain, P. Mundley and R. Bajaj, *J. Indian Chem. Soc.*, 1992, **69**, 777-779.

28. Z. Tavsan, P. K. Yaman, E. Subasi and H. A. Kayali, *J. Biol. Inorg. Chem.*, 2018, **23**, 425-435.

29. N. Bharti, M. R. Maurya, F. Naqvi and A. Azam, *Bioorg. Med. Chem. Lett.*, 2000, **10**, 2243-2245.

30. S. K. Chattopadhyay and S. Ghosh, *Inorg. Chim. Acta.*, 1989, **163**, 245-253.

31. O. E. Offiong and S. Martelli, *Trans. Met. Chem.*, 1997, **22**, 263-269.

32. P. Kalaivani, R. Prabhakaran, F. Dallemer and K. Natarajan, *RSC Adv.*, 2014, **4**, 51850-51864.

33. M. Maji, P. Sengupta, S. K. Chattopadhyay, G. Mostafa, C. Schwalbe and S. Ghosh, *J. Coord. Chem.*, 2001, **54**, 13-24.

34. T. Satyanarayana and K. V. Reddy, *J. Chem. Sci.*, 1987, **99**, 237-242.

35. H. L. Singh, J. Singh and A. Mukherjee, *Bioinorg. Chem. Appl.*, 2013, **2013**, 425832.

36. K. Balasubramanian, R. Karvembu, R. Prabhakaran, V. Chinnusamy and K. Natarajan, *Spectrochim. Acta, Part A.*, 2007, **68**, 50-54.

37. R. Kumar, S. Kumar, M. Bala, A. Ratnam, U. Singh and K. Ghosh, *J. Organomet. Chem.*, 2018, **863**, 77-83.

38. G. Kalaiarasi, S. R. J. Rajkumar, S. Dharani, F. R. Fronczek and R. Prabhakaran, *J. Organomet. Chem.*, 2018, **866**, 223-242.

39. M. Al-Noaimi, F. F. Awwadi, B. Atallah, D. Taher, A. Hammoudeh, H. Lang and T. Rüffer, *Polyhedron*, 2017, **123**, 47-55.

40. I. N. Booysen, A. Adebisi, M. P. Akerman, O. Q. Munro and B. Xulu, *J. Coord. Chem.*, 2016, **69**, 1641-1652.

41. S. Singh, F. Athar, M. R. Maurya and A. Azam, *Eur. J. Med. Chem.*, 2006, **41**, 592-598.

42. R. R. Kumar, R. Ramesh and J. G. Małecki, *J. Photochem. Photobiol., B.*, 2016, **165**, 310-327.

43. R. Prabhakaran, V. Krishnan, K. Pasumpon, D. Sukanya, E. Wendel, C. Jayabalakrishnan, H. Bertagnolli and K. Natarajan, *Preparation, spectral characterization, electrochemistry, EXAFS, antibacterial and catalytic activity of new ruthenium(III) complexes containing ONS donor ligands with triphenylphosphine/arsine*, 2006.

44. M. Fandzloch, A. Wojtczak, J. Sitkowski and I. Łakomska, *Polyhedron*, 2014, **67**, 410-415.

45. M. Fernández, E. R. Arce, C. Sarniguet, T. S. Morais, A. I. Tomaz, C. O. Azar, R. Figueroa, J. D. Maya, A. Medeiros and M. Comini, *J. Inorg. Biochem.*, 2015, **153**, 306-314.

46. R. Prabhakaran, P. Kalaivani, R. Jayakumar, M. Zeller, A. Hunter, S. Renukadevi, E. Ramachandran and K. Natarajan, *Metallomics*, 2011, **3**, 42-48.

47. B. L. Porter, B. A. McClure, E. R. Abrams, J. T. Engle, C. J. Ziegler and J. J. Rack, *J. Photochem. Photobiol., A.*, 2011, **217**, 341-346.

48. L.-H. Tang, X. Chen, A.-Q. Jia, Z. Xin and Q.-F. Zhang, *Inorg. Chim. Acta.*, 2018, **480**, 108-112.

49. L.-H. Tang, F. Wu, H. Lin, A.-Q. Jia and Q.-F. Zhang, *Inorg. Chim. Acta.*, 2018, **477**, 212-218.

50. J. Ji, X. Chen, H. Lin, A.-Q. Jia and Q.-F. Zhang, *Inorg. Chim. Acta.*, 2019, **494**, 105-111.

51. P. Kalaivani, R. Prabhakaran, P. Poornima, F. Dallemer, K. Vijayalakshmi, V. V. Padma and K. Natarajan, *Organometallics*, 2012, **31**, 8323-8332.

52. S. Datta, M. Drew and S. Bhattacharya, *Indian J. Chem., Sect. A: Inorg., Bio-inorg., Phys., Theor. Anal. Chem.*, 2011, **50A**, 1403-1409.

53. A. Garza-Ortiz, P. U. Maheswari, M. Siegler, A. L. Spek and J. Reedijk, *New J. Chem*, 2013, **37**, 3450-3460.

54. I. N. Booysen, S. Maikoo, M. P. Akerman and B. Xulu, *Trans. Met. Chem.*, 2015, **40**, 397-404.

55. L. C. Matsinha, P. Malatji, A. T. Hutton, G. A. Venter, S. F. Mapolie and G. S. Smith, *Eur. J. Inorg. Chem.*, 2013, **2013**, 4318-4328.

56. Y. Lin, M. Jiang, W. Chen, T. Zhao and Y. Wei, *Biomed. Pharmacother.*, 2019, **118**, 109249.

57. K. Neha, M. R. Haider, A. Pathak and M. S. Yar, *Eur. J. Med. Chem.*, 2019, **178**, 687-704.

58. P. Srivastava, R. Mishra, M. Verma, S. Sivakumar and A. K. Patra, *Polyhedron*, 2019, DOI: https://doi.org/10.1016/j.poly.2019.04.009.

59. M. M. da Silva Paula, C. T. Pich, F. Petronilho, L. B. Drei, M. Rudnicki, M. R. de Oliveira, J. C. F. Moreira, J. A. P. Henriques, C. V. Franco and F. Dal Pizzol, *Redox Rep.*, 2005, **10**, 139-143.

60. G. Prakash, R. Manikandan, P. Viswanathamurthi, K. Velmurugan and R. Nandhakumar, *J. Photochem. Photobiol., B.*, 2014, **138**, 63-74.

61. M. Sirajuddin, S. Ali and A. Badshah, *J. Photochem. Photobiol., B.*, 2013, **124**, 1-19.

62. S. U. Rehman, T. Sarwar, M. A. Husain, H. M. Ishqi and M. Tabish, *Arch. Biochem. Biophys.*, 2015, **576**, 49-60.

63. S. Sathiyaraj, G. Ayyannan and C. Jayabalakrishnan, *J. Serb. Chem. Soc.*, 2014, **79**, 151-165.

64. S. Arunachalam, N. P. Priya, C. Jayabalakrishnan and V. Chinnusamy, *Int. J. App. Biol. Pharm.*, 2011, **2**, 110-122.

65. S. Sathiyaraj, K. Sampath and C. Jayabalakrishnan, *Synth. React. Inorg., Met.-Org., Nano-Met. Chem.*, 2014, **44**, 1261-1271.

66. N. Shahabadi and S. Mohammadi, *Bioinorg. Chem. Appl.*, 2012, **2012**, 571913.

67. G. Raja and C. Jayabalakrishnan, *Cent. Eur. J. Chem.*, 2013, **11**, 1010-1018.

68. X.-L. Hong, Z.-H. Liang and M.-H. Zeng, *J. Coord. Chem.*, 2011, **64**, 3792-3807.

69. A. de Almeida, B. L. Oliveira, J. D. Correia, G. Soveral and A. Casini, *Coord. Chem. Rev.*, 2013, **257**, 2689-2704.

70. G. Balakrishnan, T. Rajendran, K. Senthil Murugan, M. Sathish Kumar, V. K. Sivasubramanian, M. Ganesan, A. Mahesh, T. Thirunalasundari and S. Rajagopal, *Inorg. Chim. Acta.*, 2015, **434**, 51-59.

71. S. Ghosh, P. Kundu, B. K. Paul and N. Chattopadhyay, *RSC Adv.*, 2014, **4**, 63549-63558.

72. A. R. Simović, R. Masnikosa, I. Bratsos and E. Alessio, *Coord. Chem. Rev.*, 2019, **398**, 113011.

73. Q. Zhang and Y. Ni, *RSC Adv.*, 2017, **7**, 39833-39841.

74. M. Dieaconu, A. Ioanid, S. Iftimie and S. Antohe, *Dig. J. Nanomater. Bios.*, 2012, **7**, 1125-1138.

75. V. D. Suryawanshi, L. S. Walekar, A. H. Gore, P. V. Anbhule and G. B. Kolekar, *J. Pharm. Anal.*, 2016, **6**, 56-63.

76. Z. Chi, B. Hong, X. Ren, K. Cheng, Y. Lu and X. Liu, *Spectrosc. Lett.*, 2018, **51**, 279-286.

77. L. Xu, Y. N. Liu, W. J. Mei, X. M. Huang, T. F. Chen, J. Liu and W. J. Zheng, *Chem. Res. Chin. Univ.*, 2010, **26**, 693-698.

78. M. Rajabi, M. Khalilzadeh, F. Tavakolinia, P. Signorelli, R. Ghidoni and E. Santaniello, *DNA Cell Biol.*, 2011, **31**, 783-789.

79. R. Kumaran and P. Ramamurthy, *J. Fluoresc*, 2011, **21**, 1499-1508.

80. A. Melo, J. Santana, K. Nunes, B. Rodrigues, N. Castilho, P. Gabriel, A. Moraes, M. Marques, G. de Oliveira, Í. Souza, H. Terenzi and E. Pereira-Maia, *Molecules*, 2019, **24**, 2154.

81. S. R. Hsieh, P. M. Reddy, C. J. Chang, A. Kumar, W. C. Wu and H. Y. Lin, *Polymers*, 2016, **8**, 238.

82. Y. Sun, B. Su, Q. Xu and R. Liu, *Appl. Spectrosc.*, 2012, **66**, 791-797.

83. S. T. Li, Z. Y. Ma, X. Liu, J. L. Tian and S. P. Yan, *Appl. Organomet. Chem.*, 2017, **31**, e3802.

84. K. Malarkani, I. Sarkar and S. Selvam, *J. Pharm. Anal.*, 2018, **8**, 27-36.

85. N. Sankar, J. Eswaran, T. Murugan, M. A. Neelakantan and K. Velusamy, *App. Organomet. Chem.*, 2019, **33**, e4751.

86. P. Mandal, B. K. Kundu, K. Vyas, V. Sabu, A. Helen, S. S. Dhankhar, C. M. Nagaraja, D. Bhattacherjee, K. P. Bhabak and S. Mukhopadhyay, *Dalton Trans.*, 2018, **47**, 517-527.

87. T. Wybranowski, B. Ziomkowska, A. Cwynar and S. Kruszewski, *Opt. Appl.*, 2014, **44**, 357-364.

Chapter 6

Stabilization of the ruthenium(II) and -(III) centres by chelating *N*-donor ligands: Synthesis, Characterization, Biomolecular affinities and Computational studies

6.1 Introduction

Innovative metal-based anticancer drugs are essential to evolve the efficacy of chemotherapy from the current non-target specificity and prevalent cancer resistant development of established platinum-based drugs [**1**]. In particular, ruthenium shares similar electronic and redox properties to its physiologically-relevant group congener, iron and these commonalities have accounted to lower toxicity to non-cancerous cells of the ruthenium-anticancer compounds than platinum chemotherapeutic drugs. In addition, non-sterically hindered ruthenium anticancer drugs can be regarded as pro-drugs as their substitution kinetics towards biological nucleophiles and bimolecular modes of interactions mimics that of Cisplatin [**1**].

However, the next generation of ruthenium anticancer drugs should have tailored biodistribution patterns and hence current design strategies entails the inclusion of bio-active moieties into multidentate ligands, which can facilitate bioavailability, target-specificity and cytotoxicity. This design strategy is illustrated in the diamagnetic arene ruthenium(II) compound, $Ru(\eta^5\text{-}Cp)(PPh_3)(2,2'\text{-}bipy\text{-}4,4'\text{-}R)]^+$ (R = dibiotin ester) which contains

biotinylated groups anchored *via* a bipyridine chelator [**2**]. The aforementioned metal complex salt showed markedly higher anticancer activities than cisplatin in selected breast cancer cell lines. In our present research study, we have utilized chromone-, antipyrine-encompassing imines and cinnamaldehyde, cuminaldehyde-derived Schiff bases as potential biomarkers for cancerous cells [**Figure 6.1**].

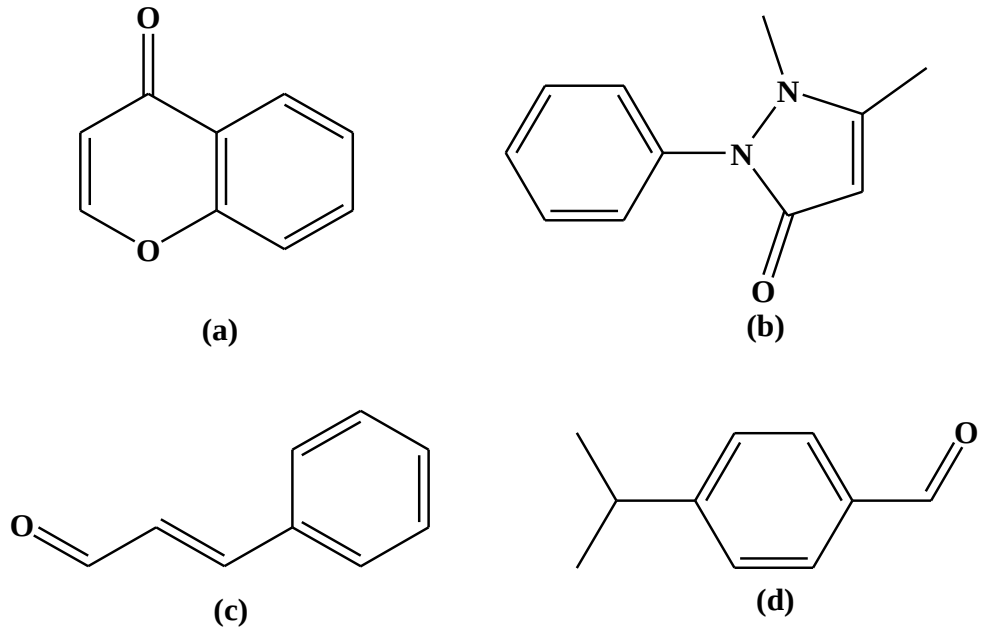

Figure 6.1: *Structures of (a) chromone, (b) antipyrine, (c) cinnamaldehye and (d) cuminaldehyde.*

The secondary metabolite, chromone has been incorporated as a pharmacophore in various medicinal drugs while those derived from the essential oils, cinnamaldehyde and cuminaldehyde portrays a wide variety of their inherent antioxidant and antimicrobial activities as well as new bio-activities [**3, 4**]. Particularly, Schiff bases of the essential oils when coordinated to M(II) centres afforded metallo-drugs, $[Ni(tcum)_2]$ (Htcum = cuminaldehyde thiosemicarbazone) and $[Cu(tcin)(H_2O)Cl]$ (Htcin = *trans*-cinnamaldehyde thiosemicarbazone), which exhibited proliferation against the U937 human cell lines [**5**]. Also, organic derivatives of antipyrine have displayed a broad range of anticancer activities which has been improved for ruthenium complexes containing antipyrine analogous [**6**]. Ruthenium Schiff base complexes with chromone and antipyrine groups have also shown considerable biological activities, *e.g.* [Ru(η^6-*p*-cymene)-(chromone)Cl] and $[RuCl(CO)(PPh_3)L]$ (HL = 4-(2-(2-hydroxyphenyl)ethylideneamino)-1,2-dihydro-2,3-dimethyl-1-phenylpyrazol-5-one)

produced good cytotoxic effects when screened against the human cervical cancer cell line, HeLa [**7, 8**].

In this chapter, three novel ruthenium(III) compounds were isolated from equimolar reactions of the metal precursor, *trans*-[$RuCl_2(PPh_3)_3$] with each of the Schiff bases, cumbh (*N'*-(4-isopropylbenzylidene)benzohydrazide), cumap (1,5-dimethyl-2-phenyl-4-10-1,2-dihydro-3*H*-pyrazol-3-one) and cinap (1,5-dimethyl-2-phenyl-4-10-1,2-dihydro-3*H*-pyrazol-3-one) [**Figure 6.2**]. These coordination reactions which resulted in the formation of the paramagnetic metal compounds *fac*-[$RuCl_3(PPh_3)$(ap)] (**1**), *trans*-P-[$Ru(PPh_3)_2$(cinap)$_2$] (**2**) and *cis*-Cl, *trans*-P-[$RuCl_2(PPh_3)_2$(cumbh)] (**3**). Structural elucidations were established using single X-Ray diffraction and supplemented with spectroscopic characterization. Interestingly for **1**, the solid state structure showed that cumap underwent hydrolysis and consequently, only the ap moiety coordinated to the *trans*-[$RuCl_2(PPh_3)_3$] unit, as opposed to **2** and **3** where the Schiff bases remained intact upon coordination. Furthermore, the antioxidant abilities and biological interactive studies with DNA and BSA of the above mentioned compounds, as well as two previously synthesised compounds containing the chromone and 4-aminoantipyrine moieties (*trans*-P, *cis*-Cl-[Ru(pch)$Cl_2(PPh_3)_2$] (**4**) (pch = 4-((pyridine-2ylimino)methylene)-chromone) and *cis*-[$RuCl_2$(bpap)(PPh_3)] (**5**) (bpap = 2,6-*bis*-((antipyrine-imino)methylene)pyridine)) were investigated [**9**].

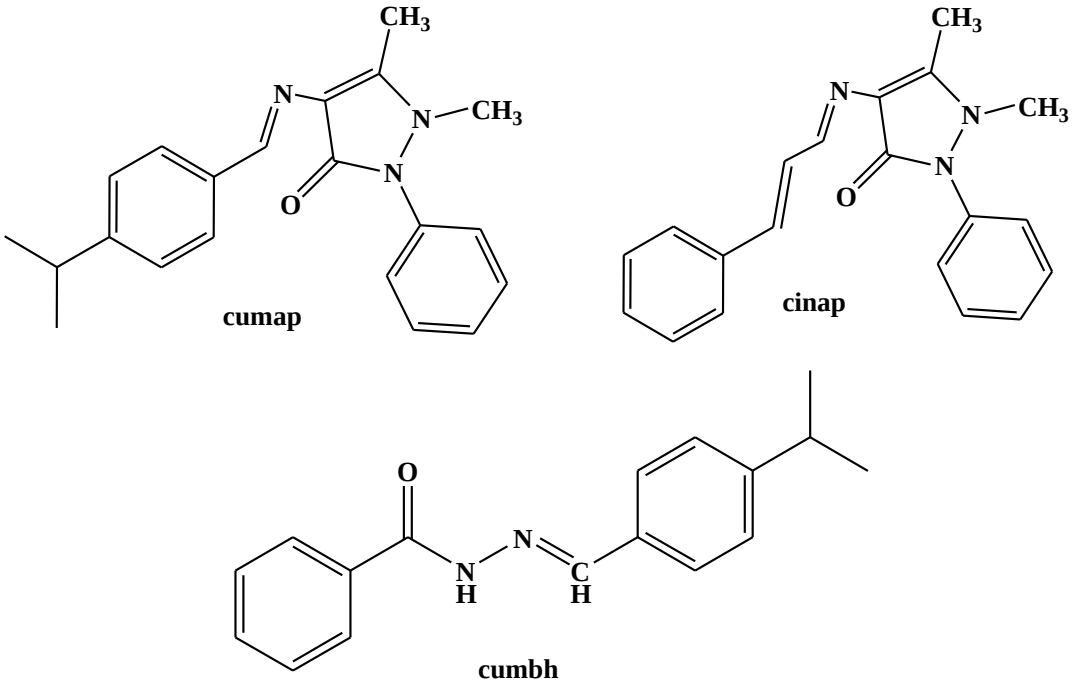

Figure 6.2: *Structures of Schiff bases utilized.*

6.2 Experimental

6.2.1 Synthesis of [RuCl$_3$(PPh$_3$)(ap)] (1)

A 1:1 molar reaction between cumap (0.0348 g, 0.104 mmol) and *trans*-[RuCl$_2$(PPh$_3$)$_3$] (0.100 g, 0.104 mmol) was carried out at elevated temperature until reflux in toluene (30 cm^3). The dark red solution was cooled to room temperature, filtered and stored at STP conditions. After several days, rectangular-shaped, red crystals were formed in the mother liquor which were appropriate for X-ray analysis. Yield: 46 %. M.P: 271.6 – 274 ºC. Molar conductivity (DCM, 10^{-3} M): 14.3 ohm^{-1} cm^{-2} mol^{-1}. IR (ν_{max}/cm^{-1}): ν(N-H) 3050 (m); ν(C=O) 1565 (s); ν(Ru-[PPh$_3$]) 692 (vs). UV-Vis (DCM, ε, M^{-1} cm^{-1}): 290 nm (20540); 339 nm (18310); 461 nm (3360).

6.2.2 Synthesis of trans-P-[Ru(PPh$_3$)$_2$(cinap)$_2$](PF$_6$) (2)

A mixture of cinap (0.0331 g, 0.104 mmol), *trans*-[RuCl$_2$(PPh$_3$)$_3$] (0.100 g, 0.104 mmol) and ammonium hexafluorophosphate (17.00 mg, 0.104 mmol) in methanol (20 cm^3) was heated until reflux for 3 hours. The green solution was then cooled to room temperature and filtered. Green square-shaped crystals formed in the mother liquor after a few days. Yield: 32 %. M.P: 216.4 – 220.0 ºC. Molar conductivity (DCM, 10^{-3} M): 32.9 ohm^{-1} cm^{-2} mol^{-1}. IR (ν_{max}/cm^{-1}): ν(C=N)$_{imine}$ 1486 (s); ν(N-C-O)$_{enolic}$ 1184 (m); ν(Ru-[PPh$_3$]$_2$) 693, 746 (vs). UV-Vis (DCM, ε, M^{-1} cm^{-1}): 359 nm (19480); 418 nm (sh, 9590); 629 nm (2470).

6.2.3 Synthesis of cis-Cl, trans-P-[RuCl$_2$(PPh$_3$)$_2$(cumbh)] (3)

Equimolar amounts of cumbh (0.0278 g, 0.104 mmol) and *trans*-[RuCl$_2$(PPh$_3$)$_3$] (0.100 g, 0.104 mmol) were heated until reflux in ethanol (20 cm^3) for 4 hours. The resulting green solution was cooled to room temperature and filtered. Green rectangular crystals formed in the mother liquor over several days at STP. Yield: 27 %. M.P: 259.5 – 265.0 ºC. Molar conductivity (DCM, 10^{-3} M): 26.7 ohm^{-1} cm^{-2} mol^{-1}. IR (ν_{max}/cm^{-1}): ν(C=N)$_{imine}$ 1479 (s); ν(N-C-O)$_{enolic}$

1186 (m); ν(Ru-[PPh_3]$_2$) 689, 742 (vs). UV-Vis (DCM, ε, M^{-1} cm^{-1}): 260 nm (sh, 18360); 265 nm (sh, 17870); 271 nm (sh, 14330); 325 nm (5420); 389 nm (sh, 3260); 624 nm (1200).

6.3 X-ray crystallography

Crystallographic data for the mononuclear compounds was collected on a Bruker Apex Duo furnished with an Oxford Instruments Cryojet. The diffractometer was operated at a low temperature of 100(2) K and an Incoatec microsource was tuned at 30 W power. Their crystal and structure refinement are summarized in **Table 6.2** while the experimental geometrical parameters are shown in **Tables 6.3** – **6.5**. An X-ray beam was generated with MoKα radiation source with a wavelength of 0.71073 Å and radiation exposures were at a common crystal-to-detector distance of approximately 50 mm. In addition, data collection were achieved *via* omega and phi scans at 0.50º frame widths, using APEX2 [**10**]. Data reduction were implemented with the aid of the SAINT program [**10**], whereby scan speed scaling, standard Lorentz and polarization correction factors and also outlier rejection were applied. A semi-empirical multi-scan absorption correction algorithm, SADABS was used for data correction [**11**]. Direct methods, WinGX [**12**] and SHELX-2016 [**13**] were applied to the solid-state structures. The *x, y, z* coordinates of the non-hydrogen atoms were established using the difference density map and anisotropically refined with SHELX-2016 [**13**]. Furthermore, three-dimensional orientations of the hydrogens were incorporated as idealized contributors in the least squares process and their positions were computed using a standard riding model with C-$H_{methylene}$ distances of 0.99 Å, U_{iso} = 1.2 U_{eq}, C-H_{methyl} distances of 0.98 Å, U_{iso} = 1.5 U_{eq}, C-$H_{aromatic}$ distances of 0.93 Å and U_{iso} = 1.2 U_{eq}.

6.4 Computational details

Gaussian 09W software package was employed to conduct the *ab initio* calculations [**14**]. Geometric optimizations of **1** – **3** were done using DFT calculations by engaging the LANL2DZ basis set and B3LYP functional [**15**]. The toluene molecule of crystallization of **1** and the counter-anion of **2** were omitted before any calculations. Validation of the computational data for the respective metal compounds was established by the good

comparison between the optimized and experimental geometrical parameters. The lack of influential close contacts in the optimized conformers accounts for their minor discrepancies when compared to their corresponding solid-state structures. Moreover, the non-negative Eigen vibrational bands attained in the calculated IR spectra of **1** – **3** affirmed the globalized energy-minimizations of the computed structures. Consequently, relatively low Root-Mean-Square-Deviation (RMSD) values between the optimized conformer and the solid-state structures were generated, see **Figure 6.17**.

6.5 Results and discussion

*6.5.1 Synthesis, spectral characterization and redox properties of **1**, **2** and **3***

The paramagnetic complexes, $[RuCl_3(PPh_3)ap]$ (**1**), *trans*-P-$[Ru(PPh_3)_2(cinap)_2]$ (**2**) and *cis*-Cl, *trans*-P-$[RuCl_2(PPh_3)_2(cumbh)]$ (**3**) were isolated in low to moderate yields from equimolar coordination reactions between *trans*-$[RuCl_2(PPh_3)_3]$ and the Schiff bases: cumap (1,5-dimethyl-2-phenyl-4--1,2-dihydro-3*H*-pyrazol-3-one), cinap (1,5-dimethyl-2-phenyl-4-([3-phenylprop-2-en-1-ylidene]amino)-1,2-dihydro-3*H*-pyrazol-3-one) and cumbh (*N'*-(4-isopropylbenzylidene)benzohydrazide), respectively. It is clearly evident from the spectroscopic data of **1** that the cumap Schiff base hydrolyzed upon coordination which afforded the neutral bidentate $N_{amino}O_{ketonic}$ coordination mode of the ap (4-aminoantipyrine) moiety whilst the cinap and cumbh Schiff bases remained intact in their corresponding metal compounds, **2** and **3**. The cinap ligand (for **2**) coordinated in a '2 + 2' manner through its monoanionic donor sets ($N_{imine}O_{enol}$) while the remaining octahedral coordination sites are occupied by triphenylphosphine co-ligands. In contrast to **2**, only a single unit of the cumbh ligand functioned as a monoanionic chelator ($N_{imine}O_{enol}$) for **3** leading to the stabilization of the diamagnetic metal centre by the *cis*-orientated chloride and *trans*-positioned triphenylphosphonine co-ligands. In our recent study, we have computationally illustrated that the Schiff base functionality of cumap is weaker compared to that of cinap. Consequently, this rationalized the formation of **1** and **2**.

Low molar conductivity values for **1** – **3** (14.3 – 26.7 ohm^{-1} cm^{-2} mol^{-1}) measured in a non-coordinative solvent confirms that these metal compounds are neutral molecules [**16**]. In addition, these compounds display mid to high solubility in polar aprotic solvents and moderate

solubility in alcoholic media. The IR spectrum of **1** show medium-to-strong bands (3050 and 1565 cm^{-1}) ascribed to the vibrations of the amino and ketonic bonds while an intense vibrational band at 692 cm^{-1} is ascribed to (Ru-[PPh_3]), see **Figures 6.3** – **6.5** [**17**]. The *trans*-[$Ru(PPh_3)_2$] of **2** and **3** unit appears as dual finger print bands between 689 – 746 cm^{-1}. The hydrolysis of the cumap is confirmed by the absence of its imino signal (at 1595 cm^{-1}) in the IR spectrum of **1** while a shift of the ketonic vibrational band to a lower frequency, is suggestive of coordinative bonding between the ketonic oxygen and the metal centre. Furthermore, shifts are also observed when comparing the IR spectra of **2** and **3** with their corresponding free-ligands' IR spectra whereby the $\nu(C=N)_{imino}$ signals occur at lower frequencies in those of the metal complexes than those of their related free-ligands. In the IR spectrum of **2**, the signals associated with the ketonic C=O bond (originally observed at 1637 cm^{-1} in the IR spectrum of the free-ligand) disappears which is a distinctive feature of the enol form of the chelator coordinating [**18**]. The overlay IR spectra of **3** and its uncoordinated ligand, indicates the loss of the N-H amide group which is represented by the disappearance of the infrared stretch at 3236 cm^{-1} and a new infrared stretch (appearing at 1186 cm^{-1}) emanating from the formation of the C-O enolic signal. Hence, the latter IR spectral changes support the conversion of cumbh to its enol form, and its subsequent deprotonation upon coordination to the metal centre [**19, 20**].

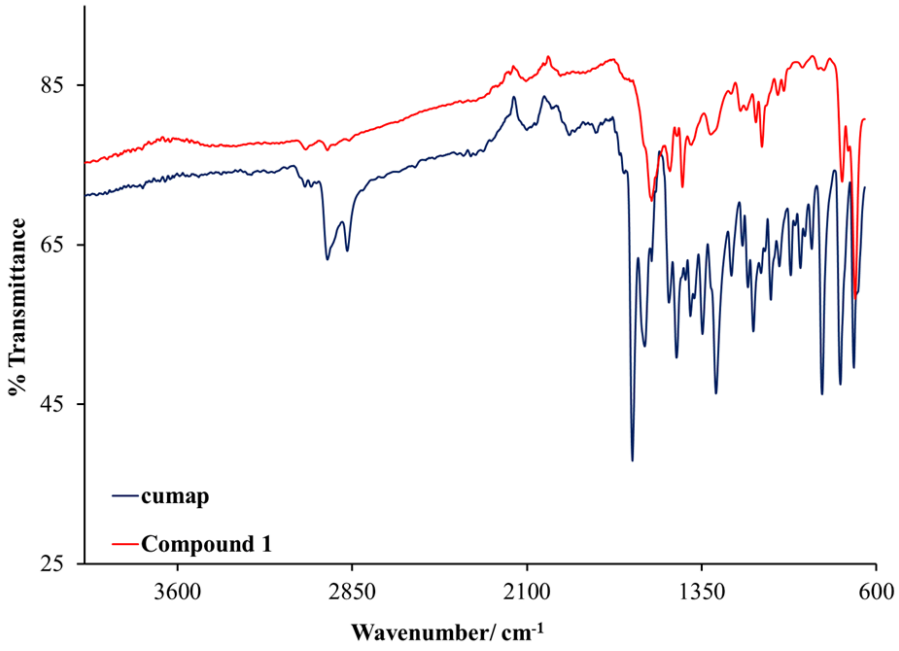

Figure 6.3: *Overlay IR spectra of the free-ligand, cumap and metal complex **1** between 4000 and 600 cm^{-1}.*

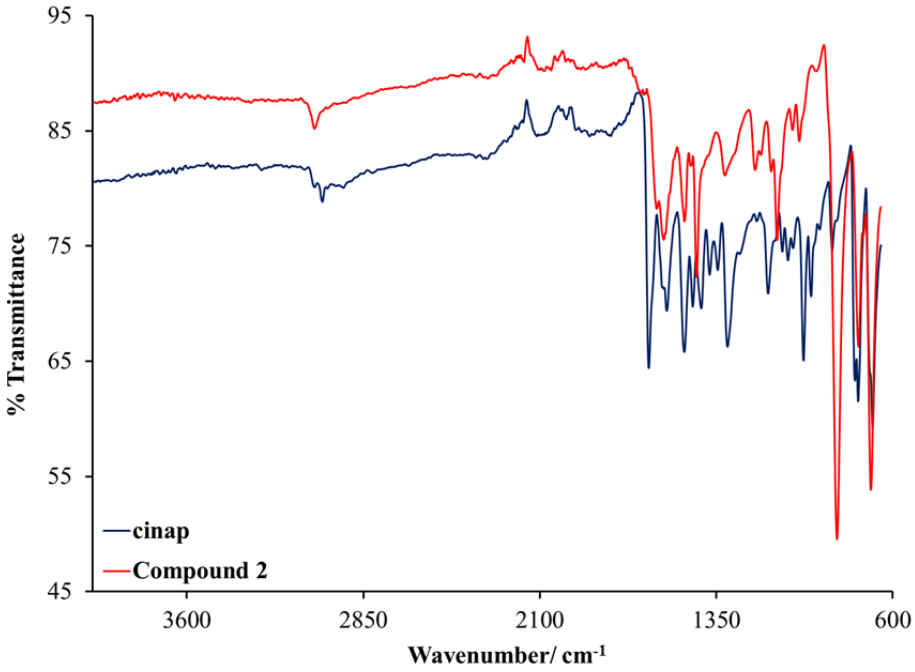

Figure 6.4: *Overlay IR spectra of the free-ligand, cinap and metal complex **2** between 4000 and 600 cm^{-1}.*

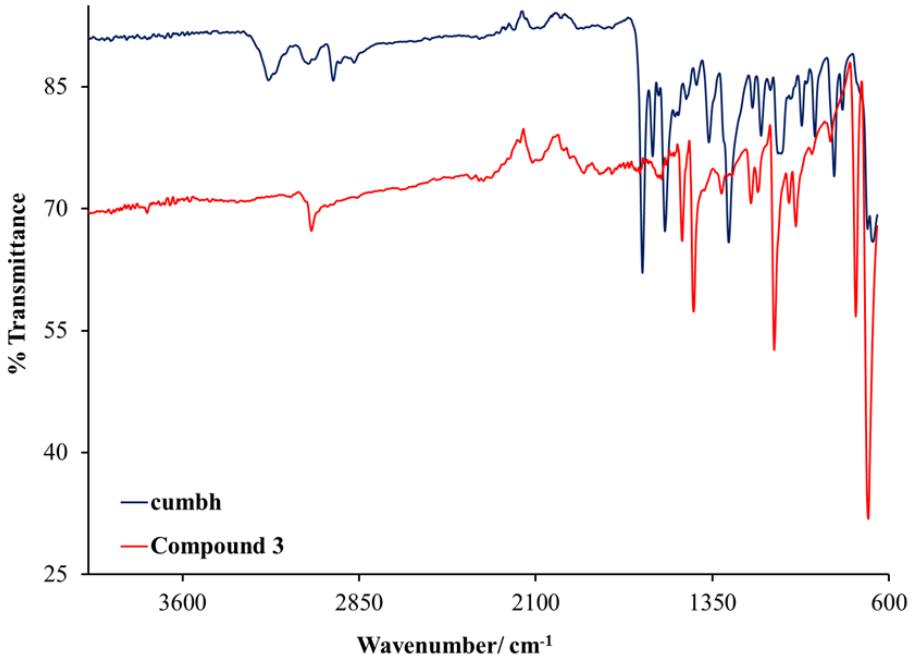

Figure 6.5: *Overlay IR spectra of the free-ligand, cumbh and metal complex **3** between 4000 and 600 cm^{-1}.*

UV-visible spectra of **1** – **3** display several absorption bands in the UV region below 400 nm, which are readily assigned to ligand-centred $\pi - \pi^*$ and $n - \pi^*$ transitions occurring within the

Schiff base chelates [**21, 22**], **Figures 6.6 – 6.8**. Broad absorption bands appearing in the visible region in the spectra of **1** and **2**, between 418 – 461 nm, are mainly attributed to Ligand-to-Metal Charge Transfer (LMCT) bands. Truncated intensity *d – d* transitions are observed for **2** and **3** at 629 and 624 nm respectively, due to their low-spin d^5 electronic configurations. However, no metal-based electronic transition was observed for **1** which hints at the ap moiety acting as a strong-field ligand that culminates into a larger crystal-field splitting energy [**21, 23**].

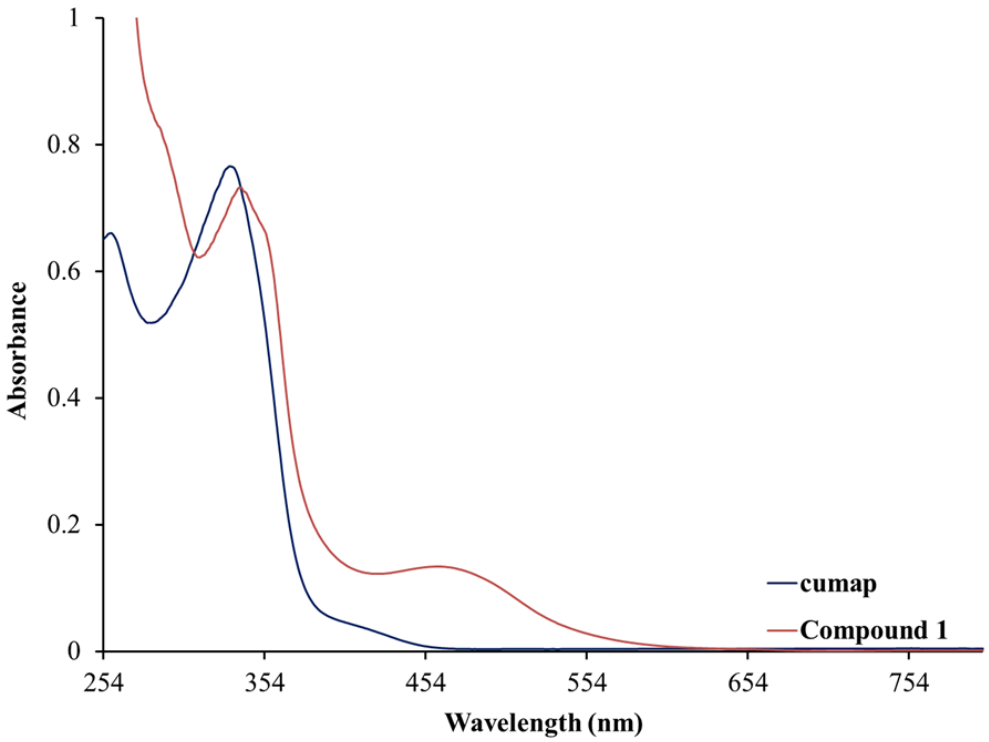

Figure 6.6: *Overlay UV-Vis spectra of complex **1** and its ligand, cumap.*

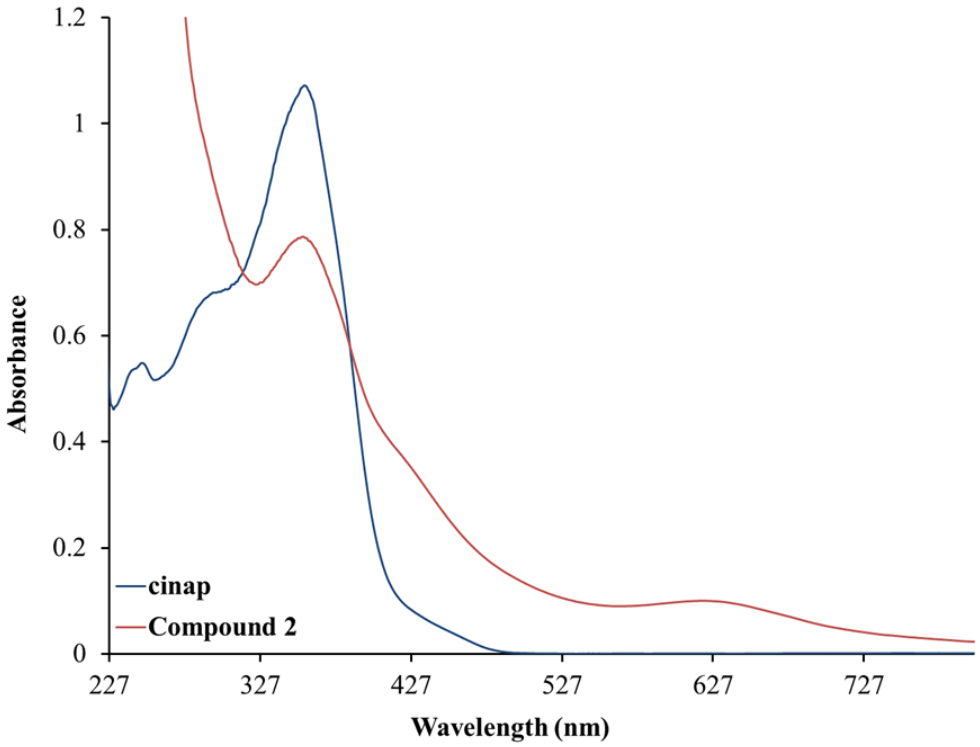

Figure 6.7: *Overlay UV-Vis spectra of complex **2** and its ligand, cinap.*

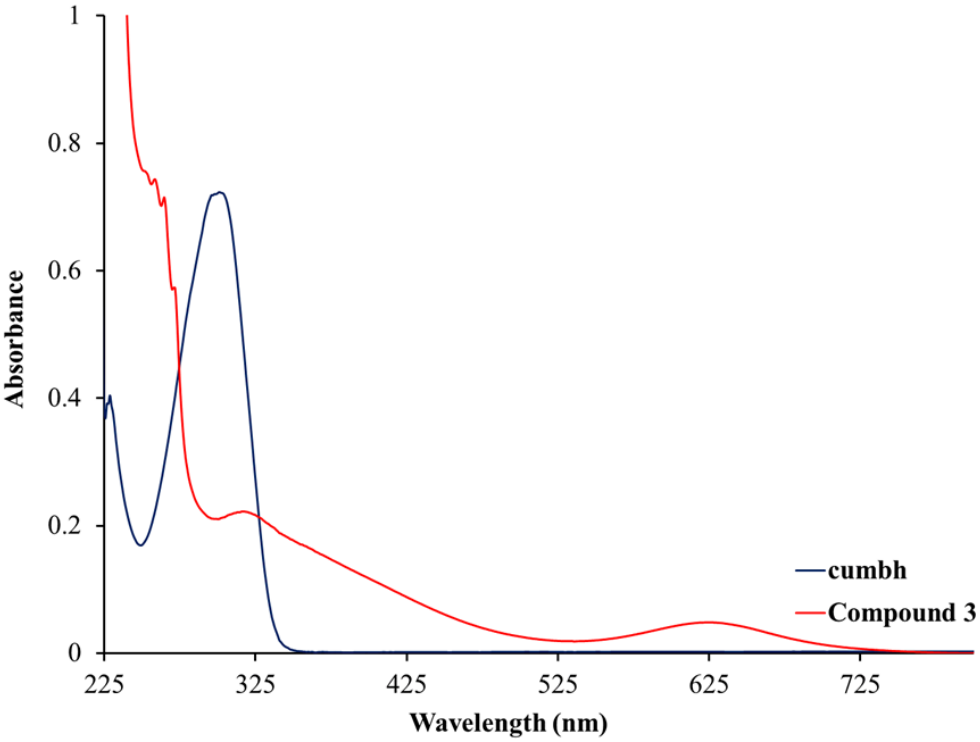

Figure 6.8: *Overlay UV-Vis spectra of complex **3** and its ligand, cumbh.*

The paramagnetic nature of the metal centres for the respective metal compounds were determined by ambient ESR spectroscopy, see **Figure 6.9**. Asymmetry within the octahedrons of **1** and **3** is clearly evident which culminates into poor resolved rhombic patterns (g_x = 2.27 for **1** and 2.26 for **3**) [**24**]. In contrast, the symmetrical orientation of the co-ligands occupying coordination sphere of **2** renders three signals, *viz.* g_x = 2.42, g_y = 2.00 and g_z = 1.78. Overall, the nature of the ESR spectra and *g*-values obtained are characteristic of octahedral organoruthenium(III) complexes. Typical examples in literature include the paramagnetic ruthenium compounds *trans*-[RuCl*(*AsPh$_3$*)*$_2$(Nap-Nmtsc)] (Nmtsc = napthaldehyde-*N*-methylthiosemicarbazide) and *trans*-[RuCl$_2$(AsPh$_3$)$_2$(L$_2$)] (HL$_2$ = 4-methoxy-2-hydroxybenzophenone) which exhibit respective isotropic and rhombic ESR spectra with *g*-values ranging from 1.84 to 2.36 [**24, 25**].

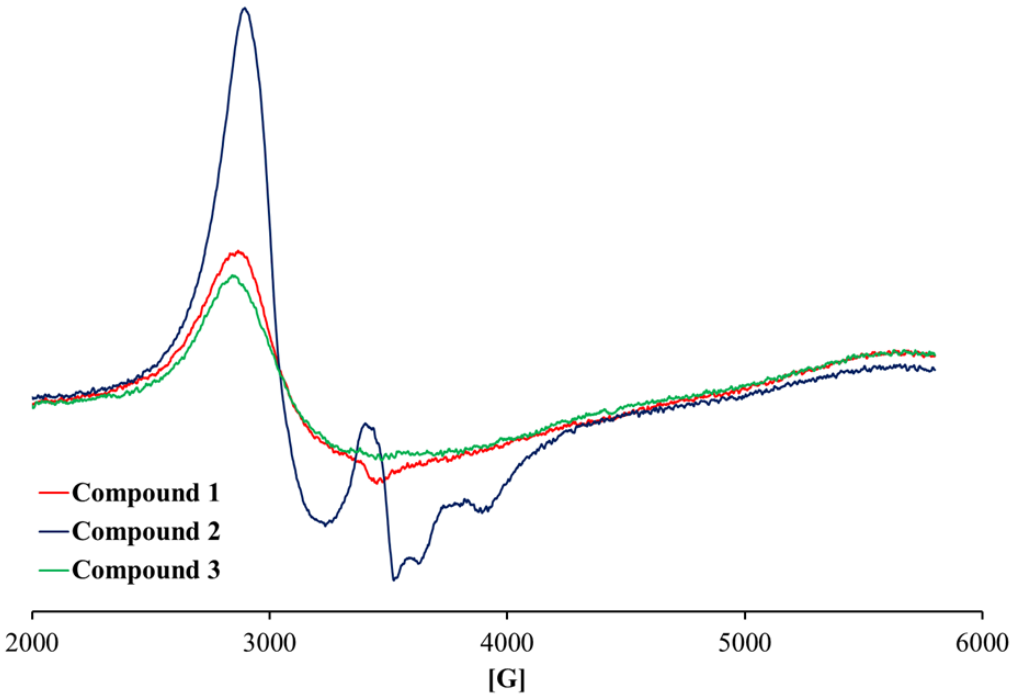

Figure 6.9: *Overlay solution ESR spectra of the respective metal compounds.*

*6.5.2 Electrochemistry of **1** – **3***

Electron-transfer properties of **1** – **3** were probed in dichloromethane *via* cyclic voltammetry (CV) and squarewave voltammetry (SWV), see **Figures 6.10** – **6.12**. The CVs of the metal compounds show single redox waves which are all considered as quasi-reversible as their peak-to-peak separations differ from the standard ferrocene (ΔE_p = 90 mV *vs* Ag| AgCl), refer to **Table 6.1**. Notably, sharp peaks are observed within CV of **1** which are typical of adsorption on a working electrode surface [**26**]. The propensity of **1** to induce electrode modification is tentatively ascribed to its smaller size which allows its molecules to immobilize as a thin film on the GCE. The redox couples of **1** ($E_{½}$ = 0 V *vs* Ag | AgCl) and **2** ($E_{½}$ = 1.11 V *vs* Ag | AgCl) can be readily ascribed to respective Ru(II)/Ru(III) and Ru(III)/Ru(IV) couples whereas the redox couple of **3** ($E_{½}$ = -1.05 V *vs* Ag | AgCl) is assigned to the d^5/ d^6 interconversions [**27-29**]. These assignments are based on the similarity of their half-wave potentials with that of other ruthenium(III) species, *e.g.* *mer*-$[Ru^{III}(bpy)(CH_3OH)Cl_3]$ (bpy = bipyridine) display redox couples of -0.33 and +1.32 V (*vs* Ag| Ag^+) [**27-29**].

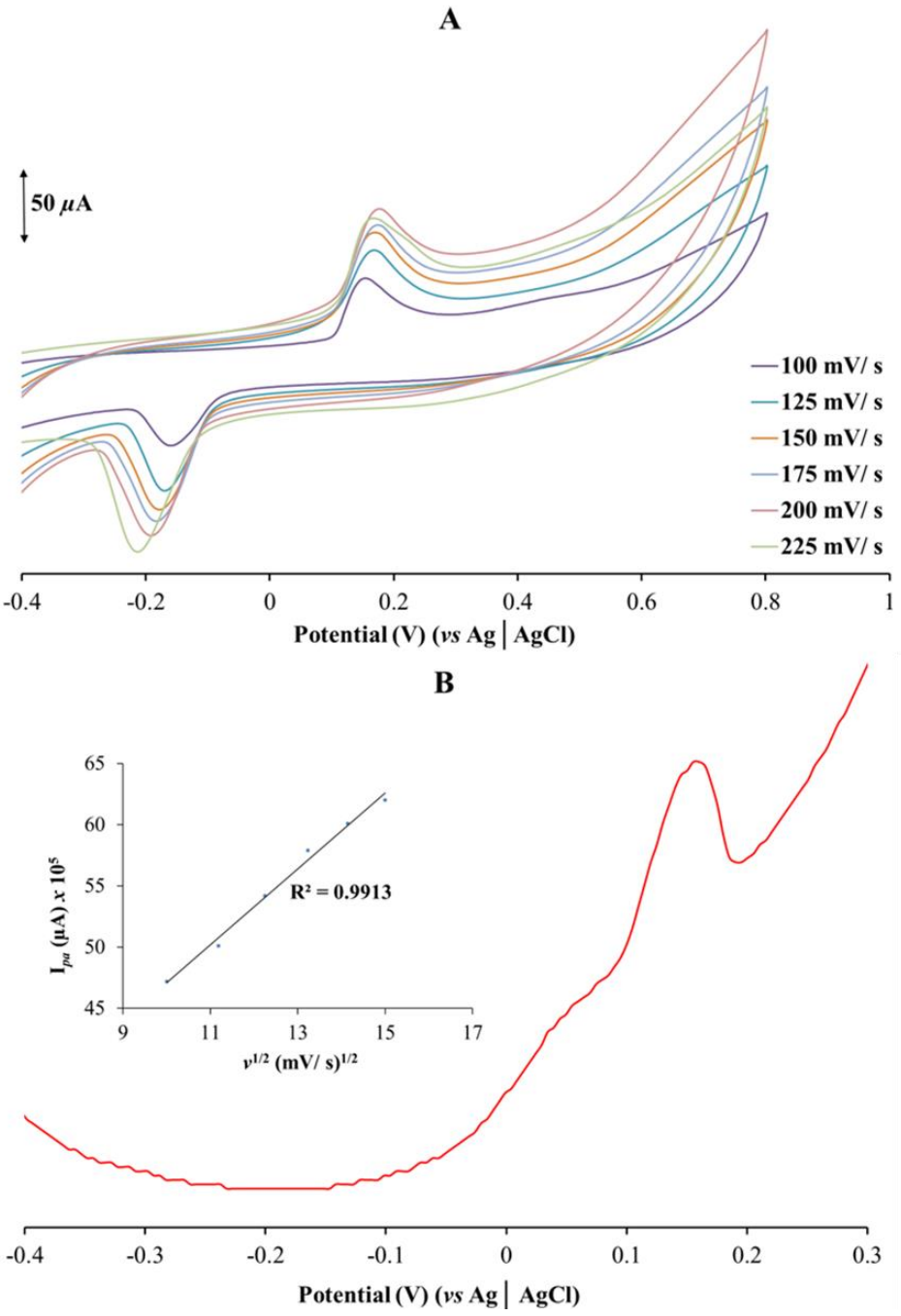

Figure 6.10: *(**A**) Overlay CVs of **1** at variable scan rates. (**B**) SWV of **1** at 100 mV/ s. Inset is the Randles-Svcek plot.*

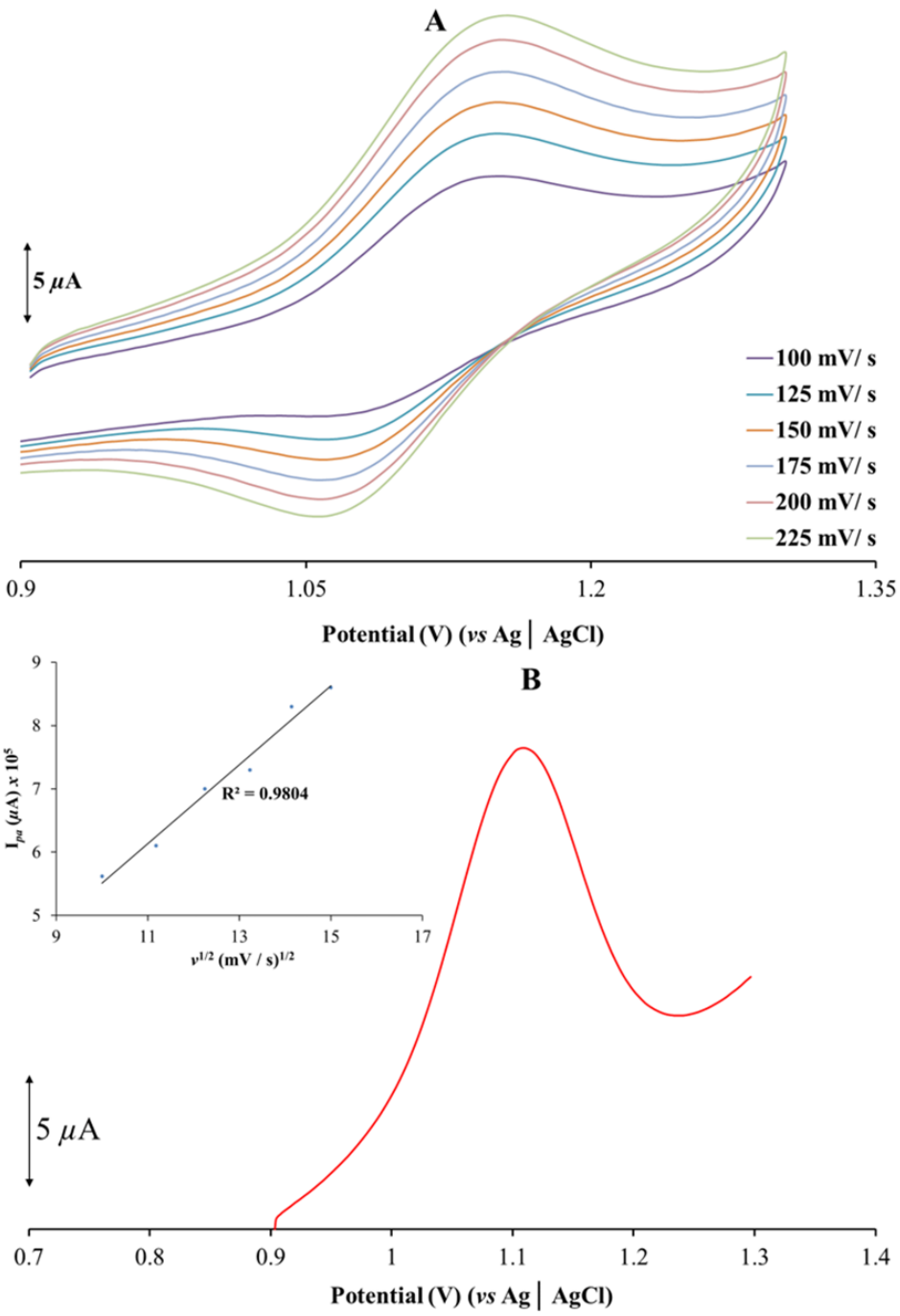

Figure 6.11: *(**A**) Overlay CVs of **2** at variable scan rates. (**B**) SWV of **2** at 100 mV/ s. Inset is the Randles-Svcek plot.*

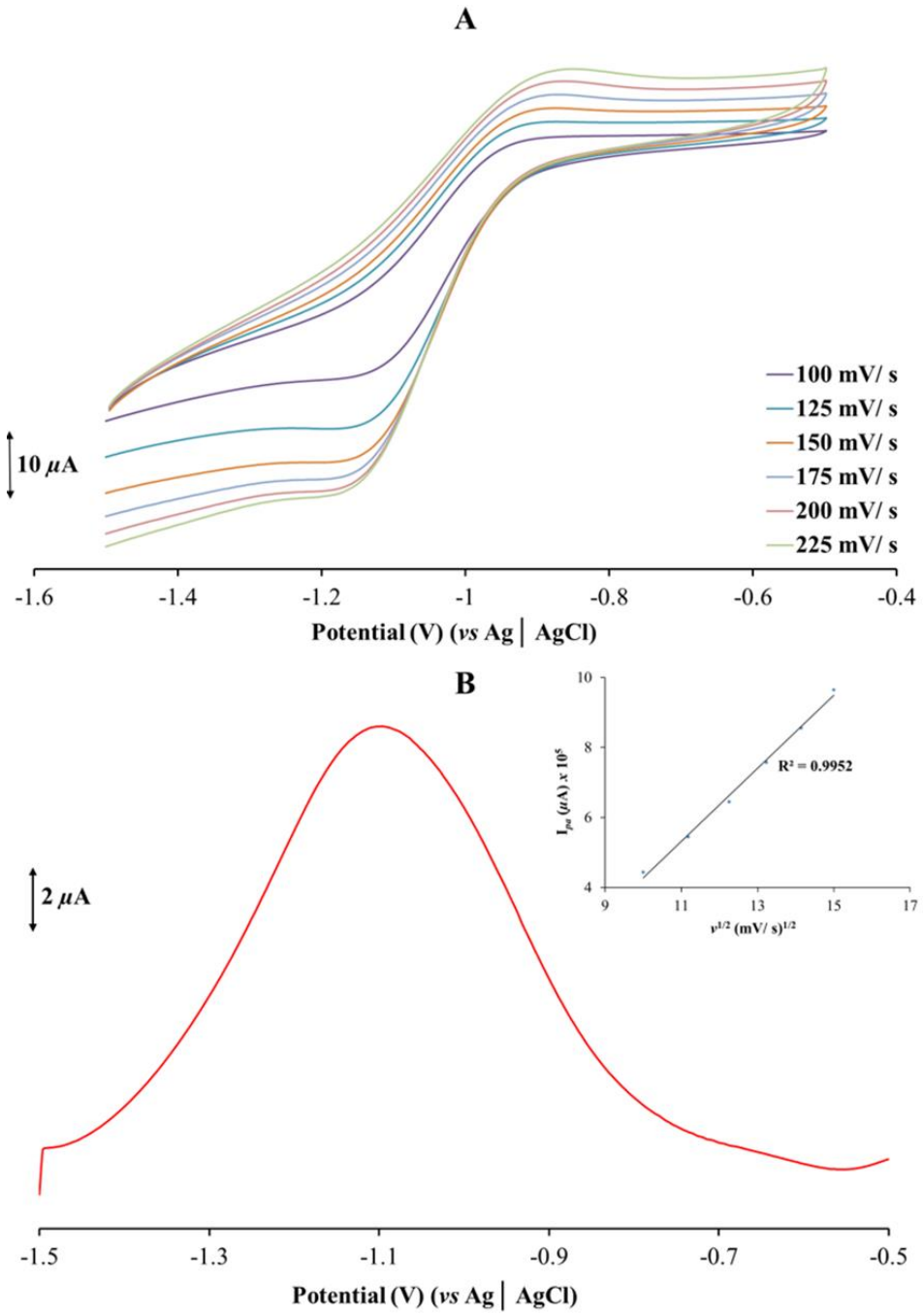

Figure 6.12: *(**A**) Overlay CVs of **3** at variable scan rates. (**B**) SWV of **3** at 100 mV/ s. Inset is the Randles-Svcek plot.*

Table 6.1: *Selected CV parameters recorded in DCM at 100 mV/ s.*

Compound	**1**	**2**	**3**
E_{pa} (V)	0.16	1.15	-0.95
E_{pc} (V)	-0.16	1.07	-1.14
ΔE_p (V)	0.32	0.08	0.19
$E_{½}$ (V)	0	1.11	-1.05

*6.5.3 Crystallographic descriptions of **1** – **3***

The mononuclear compounds **2** and **3** both exhibit a monoclinic crystal system with **2** co-crystallizing with a PF_6 counter-ion in a $P2_1/n$ space group while **3** crystallizing as a single molecule in a $P2_1/c$ space group, see **Figures 6.13** – **6.15**. Hydrogen-bonded dimers of **1** crystallizes along with toluene molecules of crystallization, see **Figure 6.16**. Non-classical close contacts between the hexafluorophosphate counter-ions and their adjacent molecules of **2** allow these molecules to pack in columns aligned with the [*b*]- and [*c*]-axes. Similarly, non-polar interactions between neighbouring molecules of **3** orientate co-planar with respect to the [*b*] and [*c*]-axes.

Constrained five-membered chelate rings [O-Ru-N3 = 83.3(1)°, O1-Ru-N1/ O2-Ru-N4= 82.63(14)° and O1-Ru-N1 = 76.33(6)°] within the respective ruthenium compounds induce octahedral distortion. In particular, the opposing donor atoms of **1** afford non-linear bond angles [Cl1-Ru-Cl3 = 169.42(4)°, P-Ru-N3 = 178.61(8)° and 173.20(7)°. Furthermore, the N1-Ru-O1 [82.63(14)°], N4-Ru-O2 [82.63(14)°], N1-Ru-O2 [97.37(14)°] and N4-Ru-O1 [97.37(14)°] bond angles of **2** that constitute the O2N4O1N1 basal plane differ from the idealized value of 90° but the P1-Ru-P2, O1-Ru-O2 and N1-Ru-N4 are linear. Contrastingly, the *trans*-$[Ru(PPh_3)_2]^{3+}$ [176.51(2)°] of **3** is non-linear and it has a wide Cl1-Ru-Cl2 [99.67(2)°] bond angle.

As expected, the Ru-$O_{ketonic}$ bond of **1** [2.101(2) Å] is shorter than the Ru-O_{enol} bond of **2** [Ru-O1/O2 = 2.153(3) Å] but **3** [2.029(2) Å] has a longer Ru-O_{enol} bond than **2** which is due to variable *trans*-influence by their respective enolic O-donor atoms. Though, the analogous bonds [1.984(1) and 2.003(1) Å] of the paramagnetic ruthenium compound,

[$RuCl(obs)_2(PPh_3)_2$] (Hobs = 2-hydroxyphenylbenzothiazole) were comparable to those of **3** [**30**]. Indicatively, the hybridization of the nitrogen donor atoms can be discriminated based on the respective Ru-N_{amino} [2.201(3) Å for **1**] and Ru-N_{imino} [2.112(4) Å for **2** and 2.201(3) Å for **3**] bond lengths. As per literature trends, the higher Lewis acidic character of **2** and **3** affords elongated ruthenium-to-nitrogen bonds than the '3+3' ruthenium(II) Schiff base complex, [$Ru(tpsal)_2$] (Htpsal = 3,5-*di*-*tert*-butyl-*N*-(2-(methylsulfanyl)phenyl)-salicylaldimine) with Ru-N_{imino} bond distances of 2.051(5) and 2.053(5) Å. However, the Ru^{III}-N_{amino} bonds are especially rare where predominately shorter Ru^{II}-N_{amino} bonds of monomeric diamagnetic ruthenium complexes were found in the Cambridge Crystallographic Database Centre (CCDC) [**31**-**33**]. *Trans*-axial orientations of the triphenylphosphine co-ligands in **2** [Ru-P1 = 2.4066(14) Å and Ru-P2 = 2.4065(14) Å] and **3** [Ru-P1 = 2.39365(5) Å and Ru-P2 = 2.4074(6) Å] affords similar Ru-P bonds whereas in **1** [Ru-P = 2.304(1) Å], the amino nitrogen imposes a stronger *trans*-effect on the phosphorus donor atom. These ruthenium-to-phosphorous distances and the chloro coordination [Ru-Cl1 = 2.355(1) Å, Ru-Cl2 = 2.318(1) Å for **1** and Ru-Cl1 – 2.3449(7) Å, Ru-Cl2 = 2.3360(6) Å for **2**] bonds are comparable to other ruthenium(III) complexes found within literature [**34**-**37**].

The comparison between the ketonic bond of **1** [C1-O = 1.274(4) Å] and the enol bonds of the other metal compounds [C30-O2 = 1.275(6) Å for **2** and C30-O2 = 1.281(2) Å for **3**] unequivocally show that the former exhibit double bond character. Indicatively, the C1-N1 [1.374(4) Å], C2-N3 [1.438(4) Å] and C3-N2 [1.366(5) Å] single bonds of **1** are elongated when compared to the imino bonds of **2** [C9-N1/ C26-N4 = 1.276(7) Å] and **3** [C10-N1 = 1.374(4) Å]. Interestingly, the characteristic N-N intracyclic antipyrine bonds of **1** [N2-N3 = 1.401(4) Å] and **2** [N2-N2/ N5-N6 = 1.390(7) Å] compares well with the corresponding aliphatic bond of **3** [N1-N2 = 1.404(2) Å]. Consequently, the neighbouring C11-N2 [C11-N2 = 1.314(3) Å] bond is a localized *pi*-bond whereas those of the C-N antipyrine moieties of **1** and **2** [N2-C11/ N5-C28 = 1.352(7) Å and N3-C13/ N5-C30 = 1.359(7) Å] are sigma bonds.

Equivalent bonding patterns were observed within the optimized conformers when examining the computed geometrical parameters. Besides the absence of influential intra- and intermolecular close contacts in the optimized structures, discrepancies between the experimental and calculated Ru-Cl/ P bond lengths are noted. These anomalies are suggested by the variable degree polarizabilities of chlorine and phosphorous. Accordingly, higher

octahedral distortion is observed in the optimized structure of **1** based on the following simulated bond angles: Cl1-Ru-Cl3 = 161.61°, P-Ru-N3 = 172.11° and O-Ru-Cl2 = 167.36.

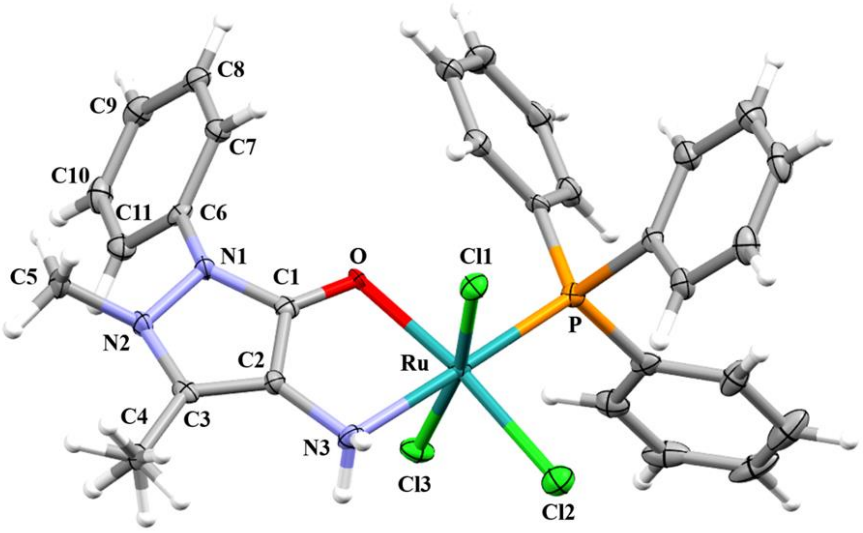

Figure 6.13: *ORTEP view of metal complex **1** showing 50 % probability displacement ellipsoids and the atom labelling. The solvent molecule of crystallization has been omitted for the sake of clarity.*

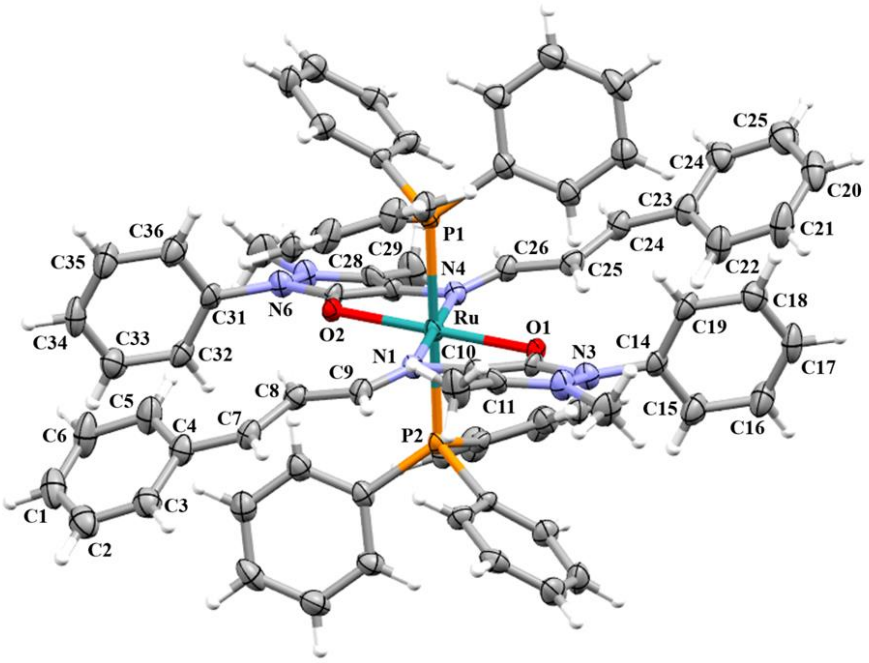

Figure 6.14: *ORTEP view of compound **2** showing 50 % probability displacement ellipsoids and the atom labelling. The counterion has been omitted.*

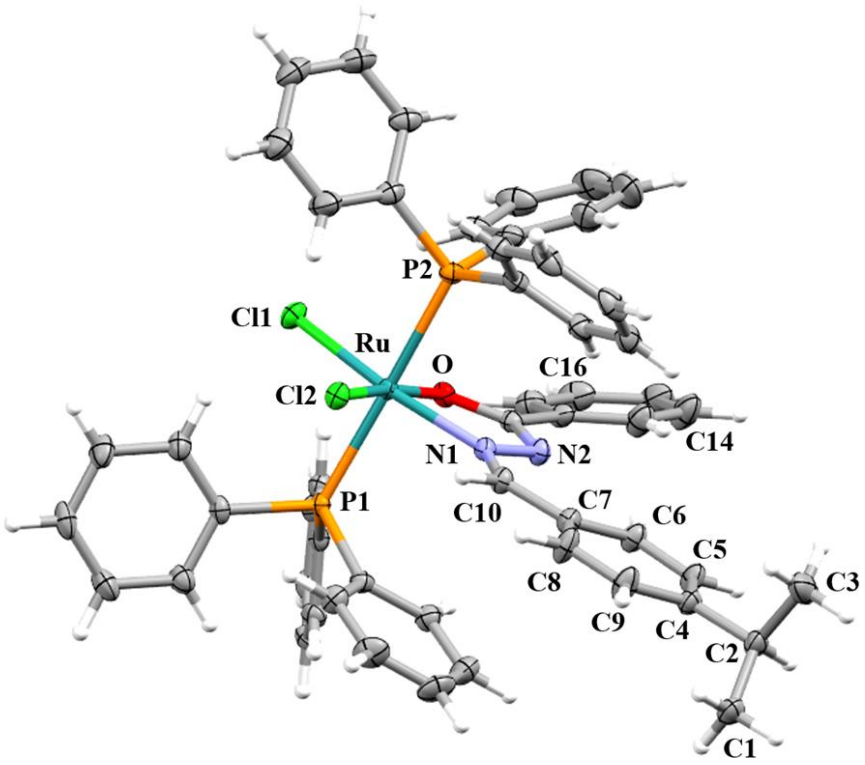

Figure 6.15: *ORTEP view of metal complex **3** showing 50 % probability displacement ellipsoids and the atom labelling.*

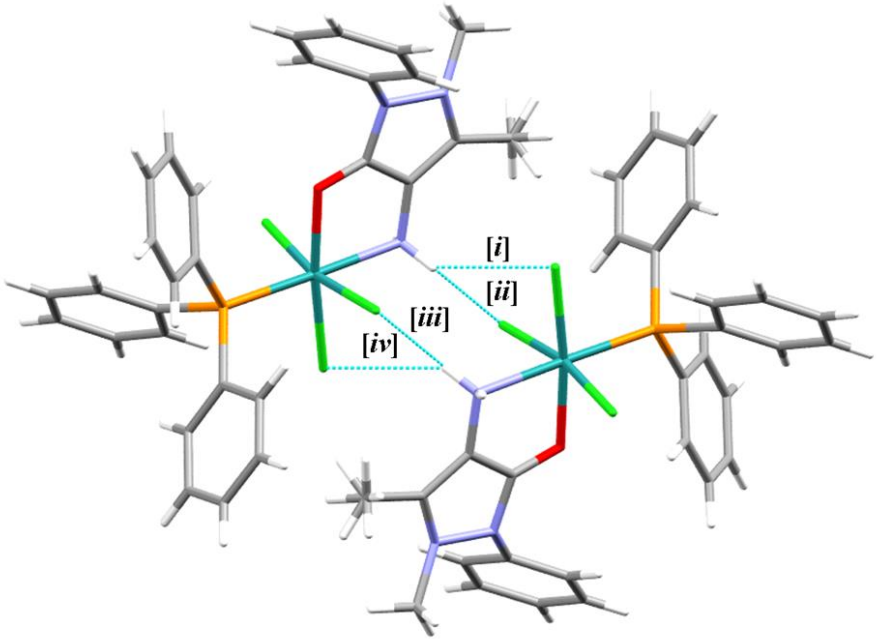

Figure 6.16: *A perspective view of **1** illustrating the reinforcing interactions occurring within a hydrogen-bonded dimer: [**i**] = 2.919 Å, [**ii**] = 2.580 Å, [**iii**] = 2.919 Å and [**iv**] = 2.580 Å.*

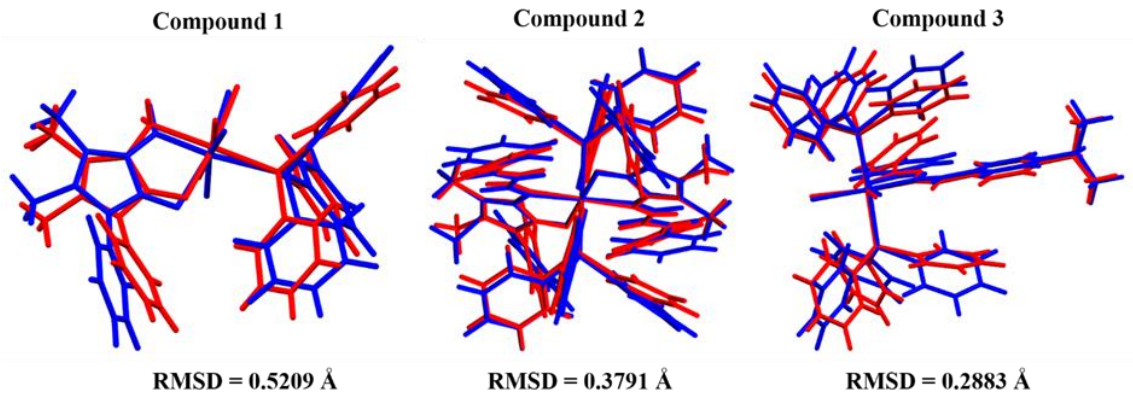

Figure 6.17: *Comparative RMSD values generated from the overlay structures of the optimized structures (blue) and their corresponding solid-state structures (red).*

Table 6.2: *Crystal data and structure refinement data for metal compounds **1** – **3**.*

Compound	**1**· C_7H_8	**2**·2(PF_6)	**3**
Chemical formula	$C_{29}H_{28}Cl_3N_3OPRu$· C_7H_8	$C_{76}H_{68}N_6O_2P_2Ru$·2(PF_6)	$C_{53}H_{47}Cl_2N_2OP_2Ru$
Formula weight	765.07	1550.31	961.83
Temperature (K)	100(2)	100(2)	100(2)
Crystal system	Monoclinic	Monoclinic	Monoclinic
Space group	*P2₁/c*	*P2₁/n*	*P2₁/c*
Unit cell dimensions (Å, º)	*a* = 17.1746(14)	*a* = 13.8422(13)	*a* = 22.6852(19)
	b = 10.2679 (9)	*b* = 14.9830(12)	*b* = 10.6935(9)
	c = 19.9184(15)	*c* = 16.8327(15)	*c* = 20.1473(15)
	α = 90	α = 90	α = 90
	β = 103.950(3)	β = 104.312(4)	β = 109.933 (3)°
	γ = 90	γ = 90	γ = 90
Crystal size (mm)	0.31 × 0.18 × 0.12	0.21 × 0.14 × 0.09	0.24 × 0.19 × 0.11
V (Å^3)	3409.0(5)	3382.7(5)	4594.6 (6)
Z	4	2	4
Density (calc.) (Mg/ m^3)	1.491	1.522	1.390
Absorption coefficient (mm^{-1})	0.78	0.41	0.57
F (000)	1564	1588	1980
Θ range for data collection (deg)	2.7°; 26.3°	2.5°; 26.5°	2.7°; 28.3°
Index ranges	-21 ≤ *h* ≤ 20 -8 ≤ *k* ≤ 12 -23 ≤ *l* ≤ 24	-16 ≤ *h* ≤ 17 -18 ≤ *k* ≤ 13 -21 ≤ *l* ≤ 20	-30 ≤ *h* ≤ 30 -14 ≤ *k* ≤ 14 -26 ≤ *l* ≤ 22
Reflections measured	21296	24263	44634
Observed reflections (*I* > 2σ (*I*)	6965	6825	11302
Independent reflections	5034	4729	9305
Data/ restraints/ parameters	6965/ 2/ 406	6825/ 0/ 459	11302 / 0/ 522
Goodness of fit on F^2	1.02	1.10	1.01
Observed R; wR^2	0.043; 0.091	0.072; 0.150	0.034; 0.077
R_{int}	0.053	0.044	0.046

Table 6.3: *Selected bond lengths [Å] and angles [º] for* ***1****.*

	Experimental	**Optimized**
Ru-Cl1	2.355(1)	2.3971
Ru-Cl2	2.318(1)	2.4355
Ru-Cl3	2.342(1)	2.4315
Ru-P	2.304(1)	2.6139
Ru-O	2.101(2)	2.2961
Ru-N3	2.201(3)	1.9101
N2-N3	1.401(4)	1.4322
C1-O	1.274(4)	1.2758
C2-N3	1.438(4)	1.3710
C1-N1	1.374(4)	1.3848
C3-N2	1.366(5)	1.3923
O-Ru-N3	83.3(1)	80.33
P-Ru-Cl2	90.26(4)	88.26
Cl1-Ru-Cl3	169.42(4)	161.61
P-Ru-N3	178.61(8)	172.11
O-Ru-Cl2	173.20(7)	167.36

Table 6.4: *Selected bond lengths [Å] and angles [º] for complex **2**.*

	Experimental	**Optimized**
Ru-O1	2.153(3)	2.1959
Ru-O2	2.153(3)	2.1959
Ru-N1	2.112(4)	2.1372
Ru-N2	2.112(4)	2.1372
Ru-P1	2.4066(14)	2.5923
Ru-P2	2.4065(14)	2.5923
C9-N1	1.276(7)	1.3657
C26-N4	1.276(7)	1.3657
N2-N3	1.390(7)	1.4387
N5-N6	1.390(7)	1.4387
N2-C11	1.352(7)	1.4377
N3-C13	1.359(7)	1.3778
N5-C28	1.352(7)	1.3778
N5-C30	1.359(7)	1.4377
C30-O2	1.275(6)	1.2977
C13-O1	1.275(6)	1.2977
P1-Ru-P2	180	180
O1-Ru-O2	180	180
N1-Ru-N4	180	180
N1-Ru-O1	82.63(14)	80.60
N4-Ru-O2	82.63(14)	80.60
N1-Ru-O2	97.37(14)	99.40
N4-Ru-O1	97.37(14)	99.400

Table 6.5: *Selected bond lengths [Å] and angles [°] for **3**.*

	Experimental	**Optimized**
Ru-Cl1	2.3449(7)	2.4199
Ru-Cl2	2.3360(6)	2.4467
Ru-O	2.029(2)	2.0539
Ru-N1	2.065(2)	2.1206
Ru-P1	2.39365(5)	2.4873
Ru-P2	2.4074(6)	2.4872
C10-N1	1.289(3)	1.3048
N1-N2	1.404(2)	1.4400
C11-N2	1.314(3)	1.3256
C11-O2	1.281(2)	1.3206
O1-Ru-N1	76.33(6)	75.88
Cl1-Ru-Cl2	99.67(2)	99.11
P1-Ru-P2	176.51(2)	175.99

*6.5.4 Antioxidant studies of **1** – **5***

Regulation of reactive oxygen species (ROS) within biological media since normal cellular operation is dependent on the latter [**38**]. An increase in ROS can cause oxidative damage to vital biomolecules or tissue which may contribute to numerous diseases, such as cancer, hypertension and Parkinson's disease [**39, 40**]. Antioxidants derivatized from metal coordination have recently gained attention in safeguarding biological systems from the negative effects of ROS and the Schiff base complexes of ruthenium are among these [**23**]. The radical scavenging capabilities of **1** – **5** were assessed against the DPPH and NO radicals and compared to the natural antioxidant, Vitamin C (the standard). The formulated ruthenium compounds are seen to possess higher DPPH (IC_{50} = 12 – 61 µM) and NO (IC_{50} = 21 – 54 µM) radical scavenging activities than the standard (Vitamin C) and are within range if the activities seen for other ruthenium compounds [**40, 41**]. Due to the desire to stabilize the unpaired electron in the d^5 orbital, higher activities are observed for the paramagnetic metal compounds **1** – **4** (as seen by their lower IC_{50} values) [**42, 43**].

Table 6.6: *Antioxidant activities of **1** – **5** and Vitamin C against the DPPH and NO radicals.*

Compound	DPPH Radical	NO Radical
	IC_{50} (µM)	**IC_{50} (µM)**
1	30	44
2	48	45
3	12	21
4	42	28
5	61	54
Vitamin C	141	210

Standard deviation is less than 8 % of mean values

6.5.5 DNA interaction studies

(a) UV-Vis titrations

DNA is a critical target for anticancer transition metal complexes and thus their modes of interactions and affinities towards the ct-DNA is of high importance. Electronic spectroscopy is a technique that is universally employed to assess the binding interactions between metal compounds and DNA. Generally, this is achieved by monitoring changes in the UV-Vis spectral profile of a metal compound when exposed to standardized volumes of Calf Thymus DNA (ct-DNA). Electrostatic or non-intercalative modes of binding may result in hyperchromic- or hypochromic effects with no significant wavelength shifts. However, an intercalative mode of binding results in a hyperchromic effect with a significant red shift owing to the robust $\pi - \pi^*$ stacking interaction between the aromatic chromophore of a chelator and the base pairs of DNA [**44, 45**].

Absorbance spectra of the metal compounds were distinctively changed upon the progressive additions of ct-DNA, see **Figures 6.18** – **6.22**. Numerous clear isosbestic points are noted in the individual UV-visible spectral profiles of **1** – **5** which reveal the presence of more than one spectroscopically distinct chromophore in solution (*viz.* free and bound) and is suggestive of a

single binding mode of the respective metal complexes with DNA [**46**]. With the introduction of ct-DNA, hypochromicity along with a slight red shift of the absorption band at 461 nm is detected. Despite the fact that the intrinsic binding constant (K_b) of **1**, 2.67 x 10^6 M^{-1}, is of the same magnitude as known traditional intercalators (10^6 M^{-1}) [**47, 48**], it is anticipated that **1** is a DNA groove-binder. This is largely due to the presence of the bulky triphenylphosphine co-ligand which impedes the DNA intercalation of **1**.

Diminishing metal-based electronic transitions for **2** (at 620 nm) and **3** (at 625 nm) accompanied with no batchochromic shifts suggest coordinative bonding between the respective metal compounds and the phosphate group on the backbone or with the DNA base pairs within the major or minor grooves of DNA [**49-51**]. In addition, an appearance of a charge transfer band at 425 nm in the UV-visible spectra of **2** is indicative of a new specie forming in solution due to the binding of the metal complex to DNA. A similar trend is seen by a disappearance of an absorption band at 317 nm with a simultaneous appearance of a shoulder at 382 nm in the overlay UV-visible spectra of **3**. Hypochromism was also observed in the UV-visible spectral profile of **5** at 383 nm; whilst that of **4** indicates overall hyperchromism.

The intrinsic binding constants (K_b) were found to be between 2.75 – 7.00 x 10^5 M^{-1} for **2** – **5**, which further corroborates the fact that their DNA binding mode is indeed non-intercalative since the K_b values are smaller than for known intercalators or partial intercalators like ethidium bromide (1.80 x 10^6 M^{-1}) or $[Ru(phen)_2(dppz)]^{2+}$ (> 10^6 M^{-1}), which is most likely due to the steric hindrance of the bulky PPh_3 co-ligands [**46, 52**]. Furthermore, groove-binding ruthenium complexes $[Ru(dmp)_2PMIP]^{2+}$ (dmp = 2,9-dimethyl-1,10-phenanthroline and PMIP = 2-(4-methylphenyl)imidazo[4,5-*f*]1,10-phenanthroline) and $[Ru(SPF)(PPh_3)_2Cl_2]$ (SPF = sparfloxacin) have alike K_b values of 2.70 x 10^5 M^{-1} and 8.41 x 10^6 M^{-1}, respectively [**53, 54**].

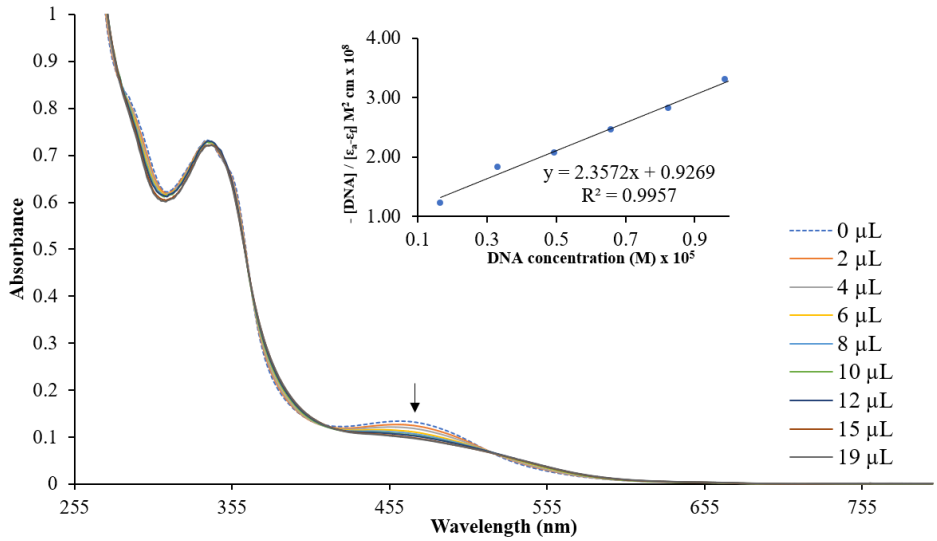

Figure 6.18: *Overlay UV-Vis spectra of compound **1** in the absence and presence of increasing amounts of ct-DNA. A dashed line indicates the initial spectrum. **Inset**: Plot of [DNA]/(εa - εf) x 10⁸ vs [DNA] x 10⁵ and the linear fit for the titration.*

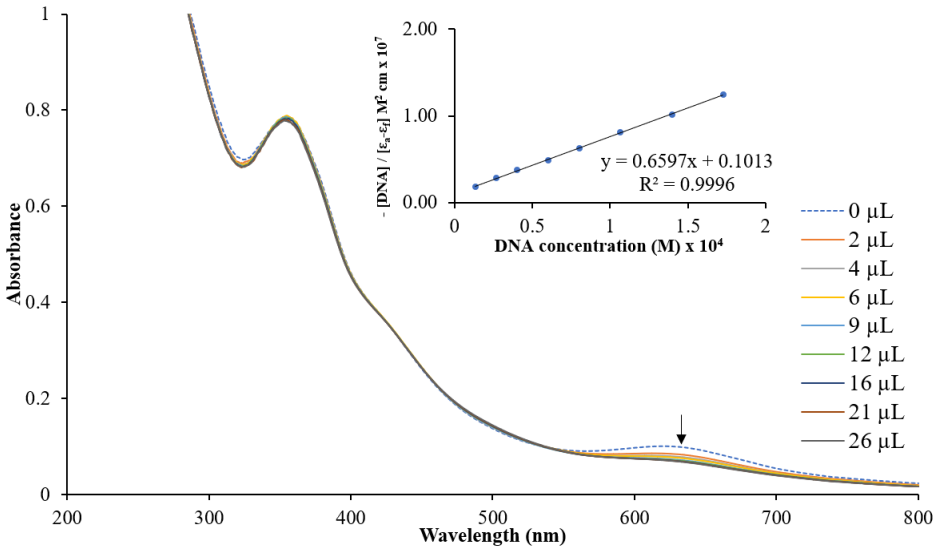

Figure 6.19: *Overlay UV-Vis spectra of compound **2** in the absence and presence of increasing amounts of ct-DNA. A dashed line indicates the initial spectrum. **Inset**: Plot of [DNA]/(εa - εf) x 10⁷ vs [DNA] x 10⁴ and the linear fit for the titration.*

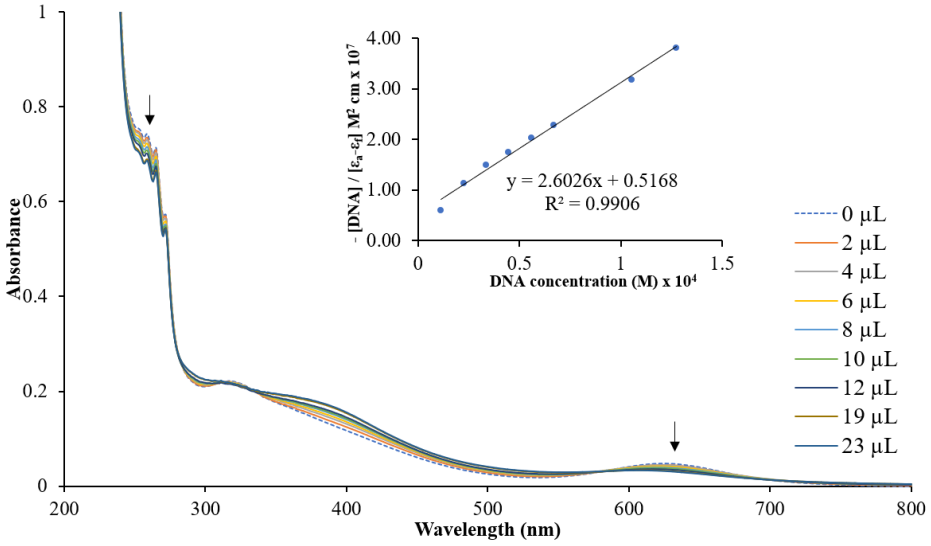

Figure 6.20: *Overlay UV-Vis spectra of compound **3** in the absence and presence of increasing amounts of ct-DNA. A dashed line indicates the initial spectrum. **Inset**: Plot of [DNA]/(εa - εf) x 10⁷ vs [DNA] x 10⁴ and the linear fit for the titration.*

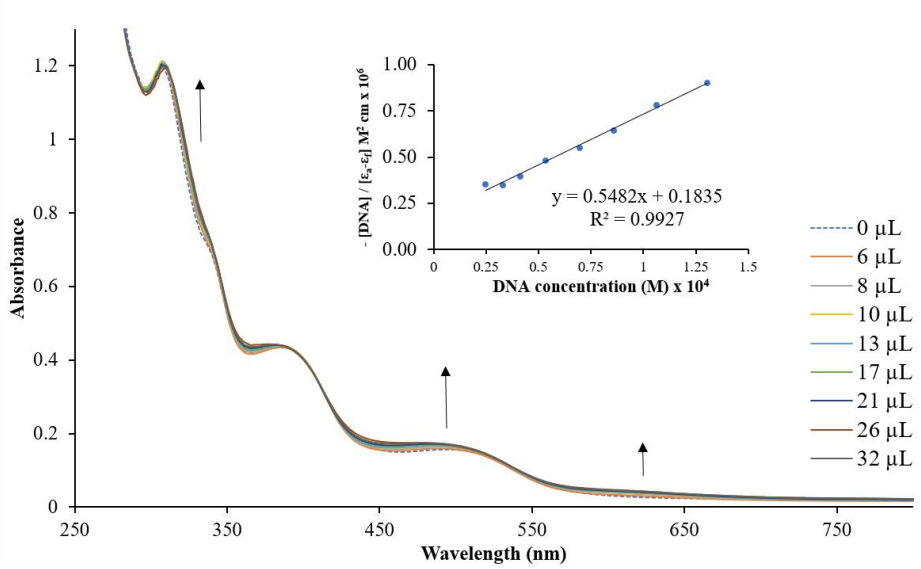

Figure 6.21: *Overlay UV-Vis spectra of compound **4** in the absence and presence of increasing amounts of ct-DNA. A dashed line indicates the initial spectrum. **Inset**: Plot of [DNA]/(εa - εf) x 10⁶ vs [DNA] x 10⁴ and the linear fit for the titration.*

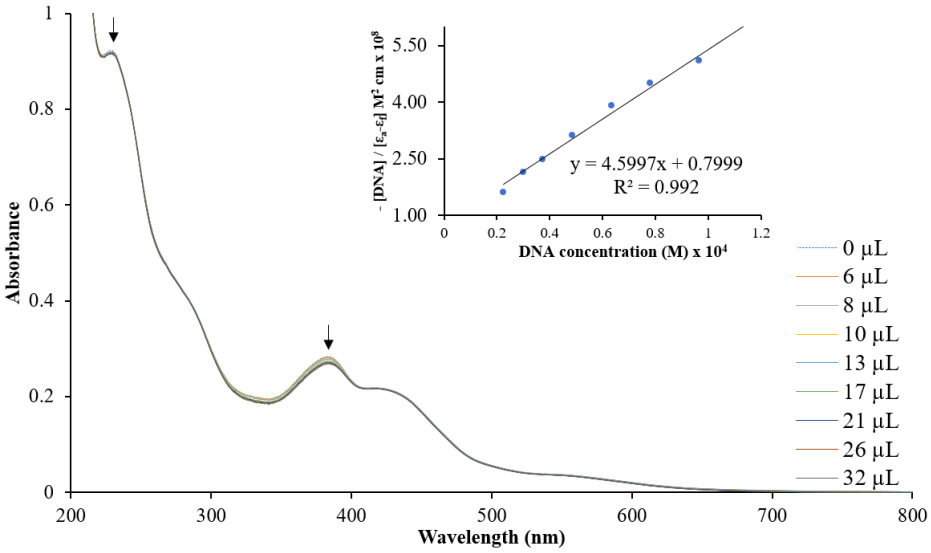

Figure 6.22: *Overlay UV-Vis spectra of compound **5** in the absence and presence of increasing amounts of ct-DNA. A dashed line indicates the initial spectrum.* ***Inset****: Plot of [DNA]/(*ε_a *-* ε_f*) x* 10^8 *vs [DNA] x* 10^4 *and the linear fit for the titration.*

Table 6.7: *Intrinsic DNA binding constants obtained for **1** – **5** from DNA titration data.*

Compound	K_b (M^{-1})
1	2.67 *x* 10^6
2	7.00 *x* 10^5
3	5.20 *x* 10^5
4	2.75 *x* 10^5
5	5.00 *x* 10^5

*(**b**) Molecular docking*

Molecular docking simulations were performed using the individual optimized conformers of **1** – **5** and the B-DNA crystal structure, see **Figures 6.23** – **6.27**. The minimum energy adducts confirms that all the metal compounds are DNA groove-binders with global energies ranging from -45.29 to 53.88 kJ/mol [**55, 56**]. More specifically, computations illustrated that **2** and **3** dock within the major groove with base pair interactions (below 2.63 Å) of A-T, T-A for **2** and

A-T; A-T; T-A for **3** while secondary supporting close contacts occur between the triphenylphosphine co-ligands and the phosphate backbones. Compounds **4** and **5** dock in close proximity of the B-DNA minor groove whereby predominately interactions (below 2.70 Å) with ribose and phosphate moieties of the B-DNA structure occur whilst a single non-polar close contact is observed with a guanine group at 2.744 Å.

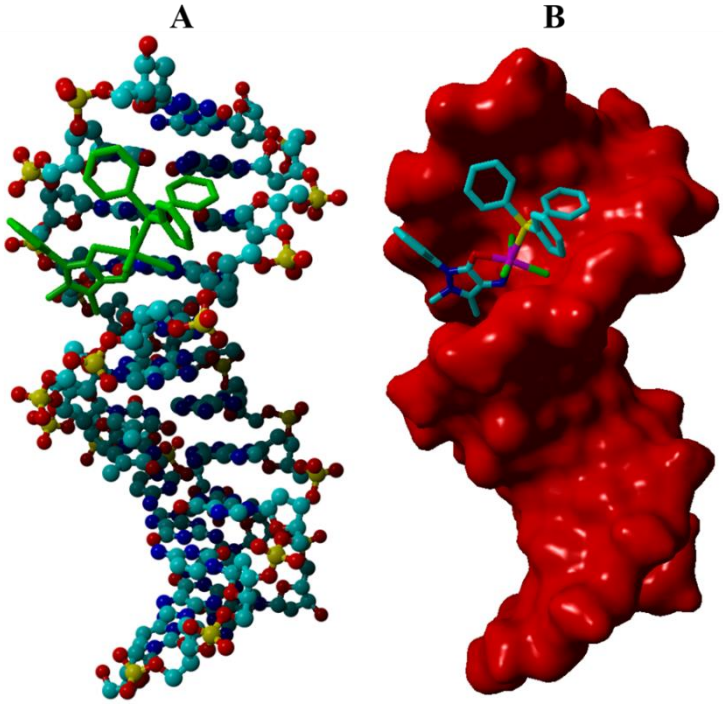

Figure 6.23: *Compound **1** primarily docked into the major groove of B-DNA: (**A**) shows DNA in ball and stick view whereas (**B**) shows the molecular surface view of DNA. Global energy = - 45.29 kJ.mol^{-1}.*

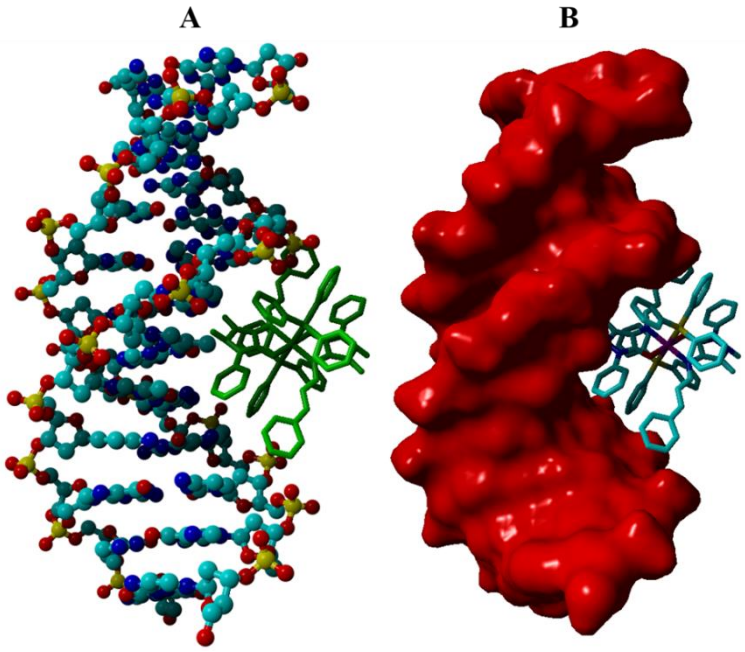

Figure 6.24: *Compound **2** primarily docked into the major groove of B-DNA: (**A**) shows DNA in ball and stick view whereas (**B**) shows the molecular surface view of DNA. Global energy = - 52.34 kJ.mol^{-1}.*

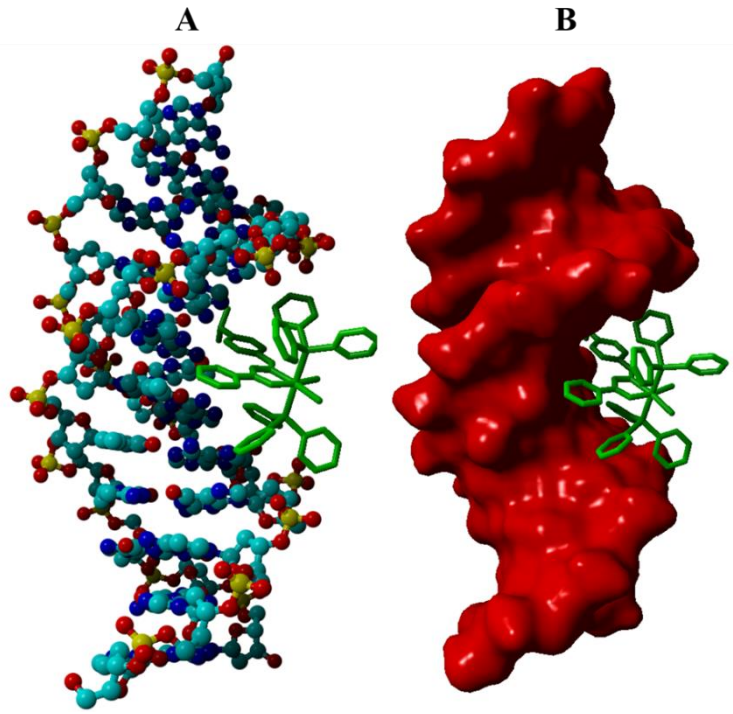

Figure 6.25: *Compound **3** primarily docked into the major groove of B-DNA: (**A**) shows DNA in ball and stick view whereas (**B**) shows the molecular surface view of DNA. Global energy = - 52.77 kJ.mol^{-1}.*

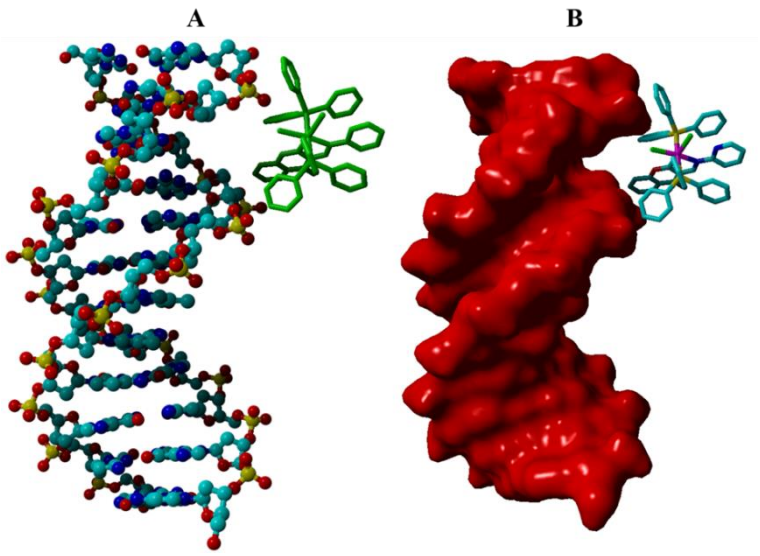

Figure 6.26: *Compound **4** primarily docked into the minor groove of B-DNA: (**A**) shows DNA in ball and stick view whereas (**B**) shows the molecular surface view of DNA. Global energy = - 48.12 kJ.mol^{-1}.*

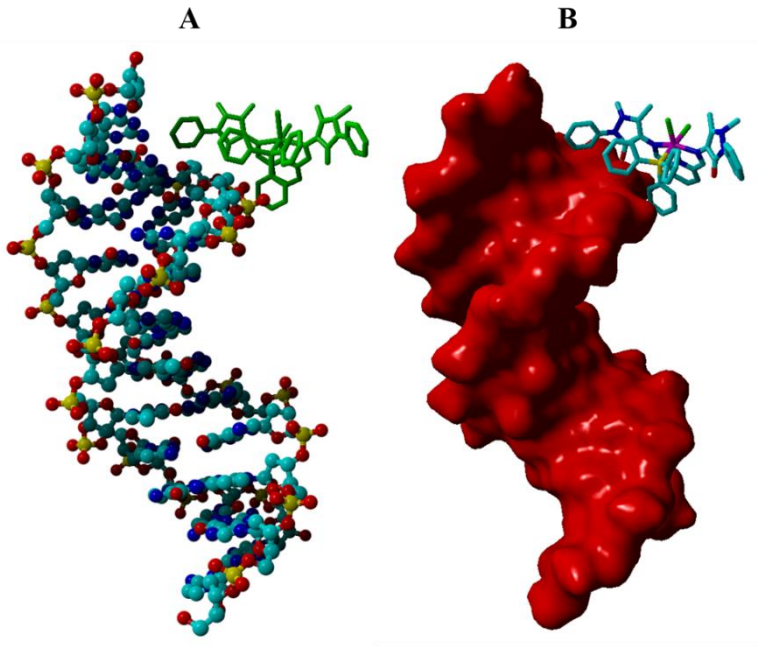

Figure 6.27: *Compound **5** primarily docked into the minor groove of B-DNA: (**A**) shows DNA in ball and stick view whereas (**B**) shows the molecular surface view of DNA. Global energy = - 53.88 kJ.mol^{-1}.*

*6.5.6 BSA interaction studies of **1** – **5***

Serum albumins play important roles in metabolism and have the ability to reversibly bind and hence transport many endo- and exogenous substances in the mammalian system. Consequently, the binding properties of serum albumin with organometallic species are often conducted to study the mechanism of interaction between them, which helps contribute to the development of physiologically compatible agents. Bovine serum albumin (BSA) is widely used as the selected protein model due to its structural similarity with human serum albumin (HSA) [**57**]. In order to evaluate the ability of BSA to function as an appropriate transporter of the selected complexes, the extent of folding (or unfolding) of the BSA strand upon binding with each of the metal compounds was studied by means of UV-Vis and fluorescence spectroscopy. The distinct peaks in the spectra of the protein are due to tryptophan residues within a BSA hydrophobic pocket and therefore, any changes in the spectra reflects conformational changes of the BSA strand. Preferably, the protein should be able retain its native state (folded) as much as possible in order to function as an ideal transporter [**58**].

(a) UV-Vis titrations

Upon analysing the UV-Vis spectra of BSA [**Figures 6.28 – 6.32**], in the presence of incrementing concentrations of **1 – 5**, decreases in the absorbance intensities are observed which indicates that interactions between BSA and the respective metal compounds occurred [**59, 60**]. Moreover, slight blue shifts are seen in the absorption maxima in the UV-visible spectral profiles of **1**, **2**, **3** and **5** which are characteristic of increased polarity around the tryptophan residue in BSA. Consequently, these metal compounds promote folding of the protein and stabilizing it upon binding by concealing it within the BSA's hydrophobic pocket [**61-64**]. Contrarily, a red shift was observed in the UV BSA titration profile of **4** which is suggestive of slight unwinding of the BSA strand by the metal complex which exposes the tryptophan residue to a more hydrophilic environment in aqueous media [**65, 66**]. This could be due to a fewer number of hydrogen bonding sites on **4**, which results in fewer stable adducts formed with the BSA and does not encourage folding of the protein [**67, 68**].

The apparent association constants (K_{app}) were calculated graphically from the double reciprocal plots of $1 / (A_0 - A)$ Versus $1 / C_{complex}$ and are shown in **Table 6.8**. The metal

compounds are considered as "ideal" binders towards BSA since their association constants are within the range of $10^4 – 10^6$ M^{-1} of other strong ruthenium-based binders [**69-71**]. Based on the K_{app} values obtained, metal compounds **1**, **2** and **5** are seen to have higher binding affinities towards BSA. The higher BSA affinities of **2** and **5** are attributed to their larger sizes of their organic chelators which encourages increased interactions at BSA's hydrophobic surface while the chloride co-ligands of **1** promotes hydrogen-bonding interactions within the hydrophilic BSA cavity.

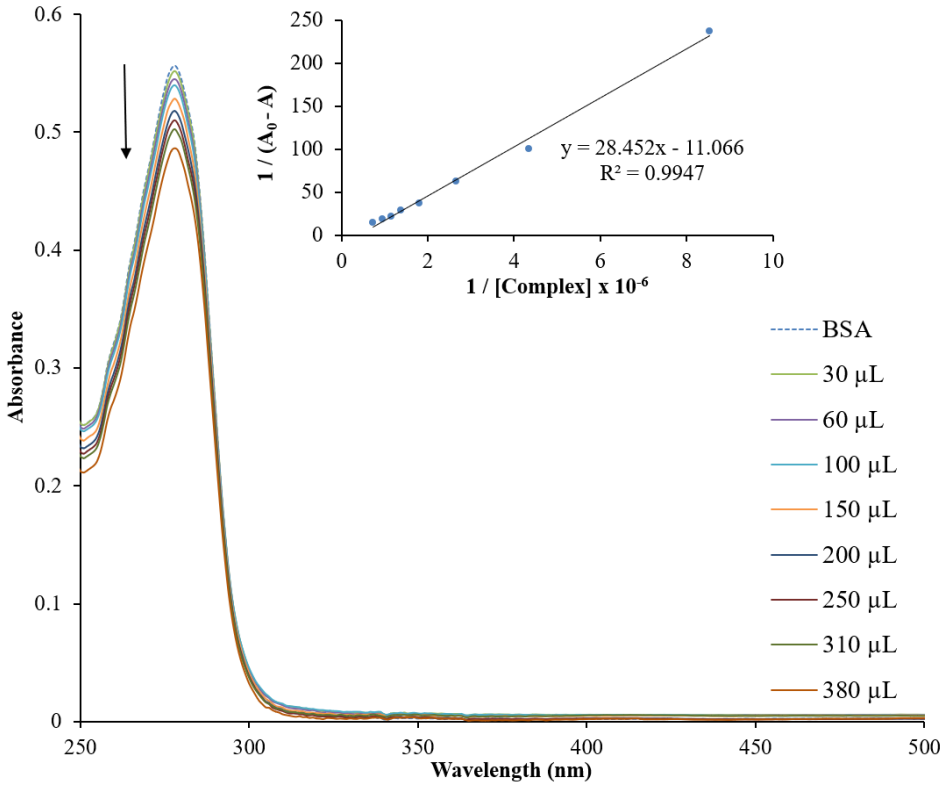

Figure 6.28: *UV-Vis spectral profile depicting the titration between compound **1** and BSA. The inset is the double reciprocal plots of $1 / (A_0 – A)$ versus $1 / C_{compound} \times 10^{-6}$.*

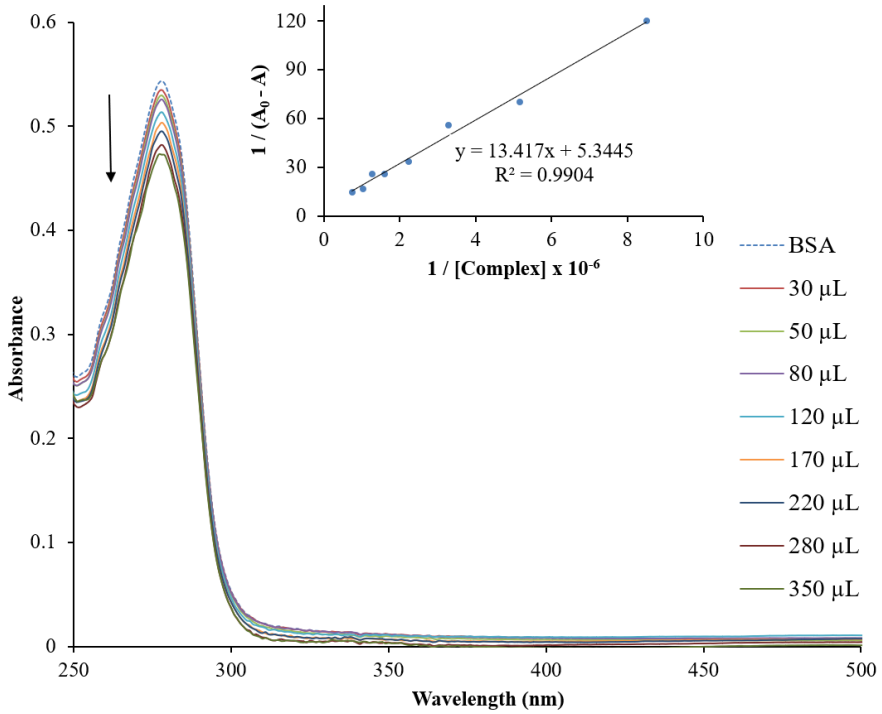

Figure 6.29: *UV-Vis spectral profile depicting the titration between compound **2** and BSA. The inset is the double reciprocal plots of 1 / (A_0 – A) versus 1 / $C_{compound}$ x 10^{-6}.*

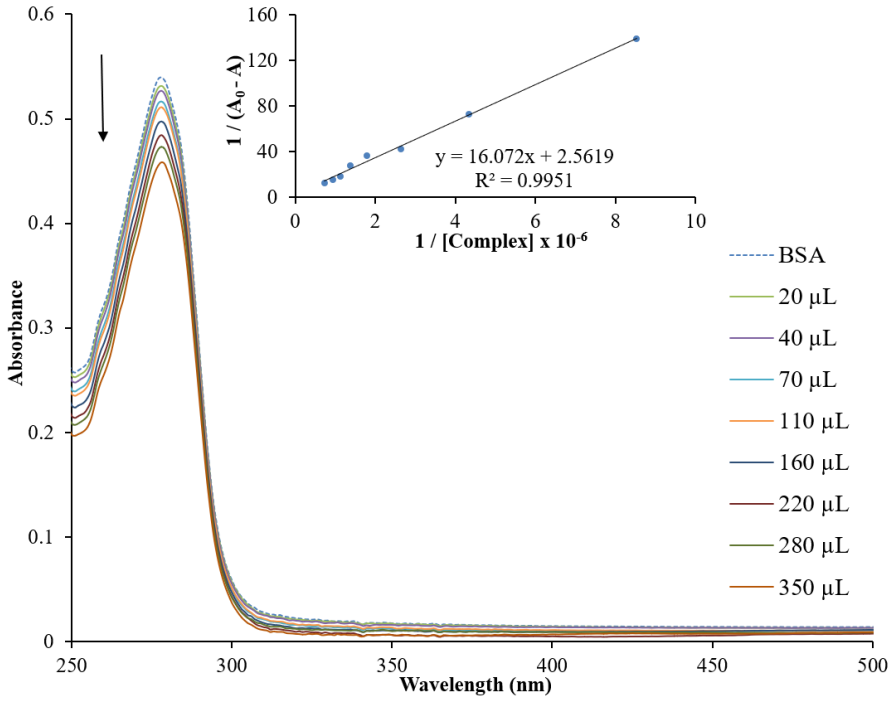

Figure 6.30: *UV-Vis spectral profile depicting the titration between compound **3** and BSA. The inset is the double reciprocal plots of 1 / (A_0 – A) versus 1 / $C_{compound}$ x 10^{-6}.*

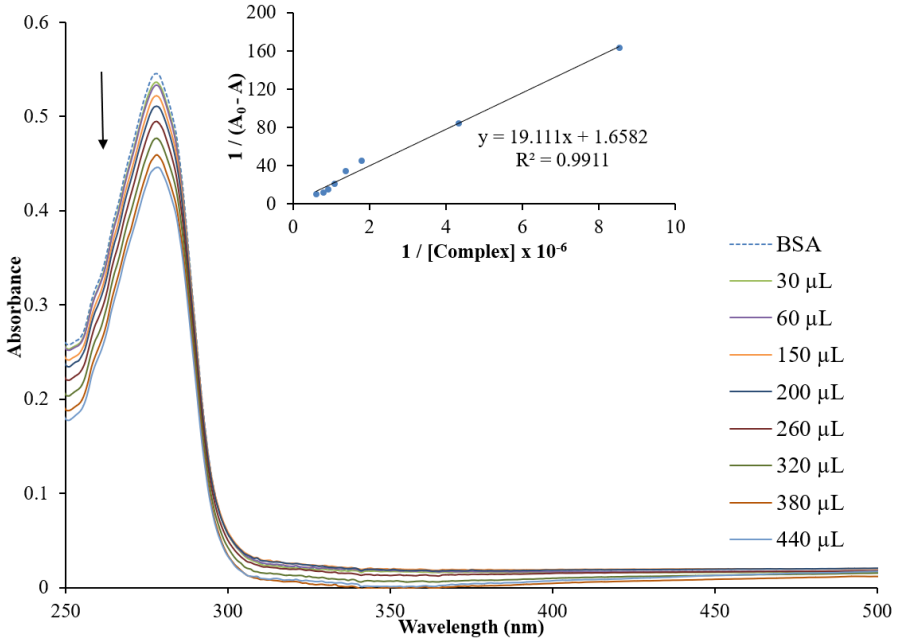

Figure 6.31: *UV-Vis spectral profile depicting the titration between compound **4** and BSA. The inset is the double reciprocal plots of 1 / (A_0 – A) versus 1 / $C_{compound}$ x 10^{-6}.*

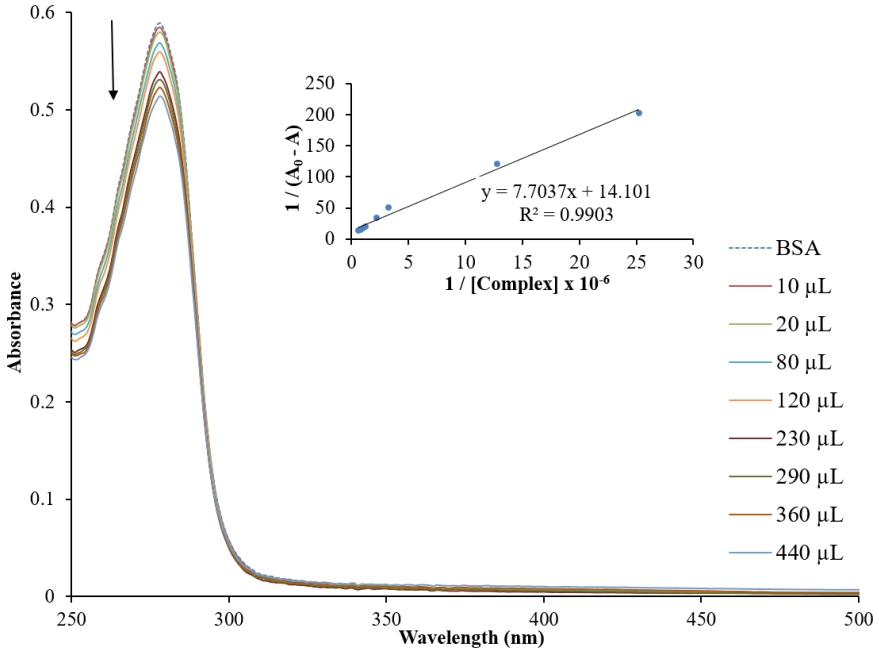

Figure 6.32: *UV-Vis spectral profile depicting the titration between compound **5** and BSA. The inset is the double reciprocal plots of 1 / (A_0 – A) versus 1 / $C_{compound}$ x 10^{-6}.*

Table 6.8: *Apparent association constants (K_{app}) obtained via UV-Vis spectrometry for **1** – **5**.*

Compound	K_{app} (M^{-1})
1	3.69×10^5
2	5.34×10^5
3	1.28×10^5
4	8.29×10^4
5	1.76×10^6

(b) *Fluorescence titrations*

The fluorescence quenching of BSA was investigated in the presence of increasing amounts of each metal compound. A decrease in the fluorescence intensities of BSA is noticed upon the addition of the respective organometallic compounds which is indicative of an interaction between the latter and former. Moreover, blue shifts of the emission maxima are seen for **1**, **2**, **3** and **5**, whilst a red shift is observed for **4**. This validates the UV-Vis study as it suggests that **1**, **2**, **3** and **5** promotes folding of the BSA strand due to Van der Waals or hydrogen interactions (*i.e.* tryptophan residues moved more into hydrophobic pocket) whilst **4** promotes slight unwinding (*i.e.* tryptophan group moved towards the hydrophilic surface) [**72, 73**].

The Stern-Volmer quenching constants (K_{SV}) and quenching rate constants (K_q) were obtained from the linear Stern-Volmer plots, refer to **Table 6.9**. The K_{SV} values may be used to assess the binding affinities of the metal compounds towards BSA and the results are consistent with the findings in the UV-Vis study, in that **1**, **2** and **5** have higher affinities for BSA. A static quenching mechanism for the ruthenium compounds was confirmed by considerable changes in spectra of the UV-Vis study as well as the fact that the K_q values found are greater than the maximum scatter collision constant responsible for dynamic quenching (2×10^{10} M^{-1} s^{-1}) [**69, 72**].

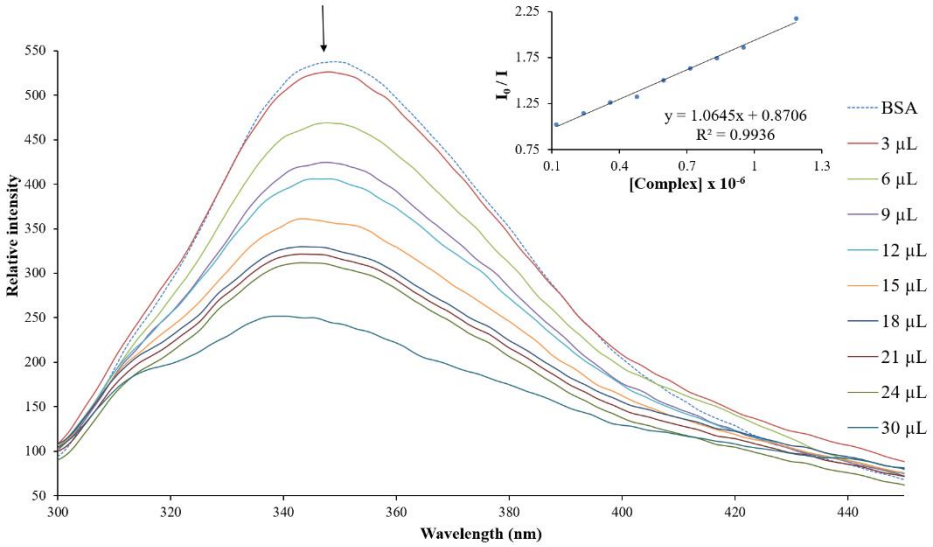

Figure 6.33: *Fluorescence emission spectral profile depicting the titration between compound **1** and BSA. The inset is the Stern-Volmer plot.*

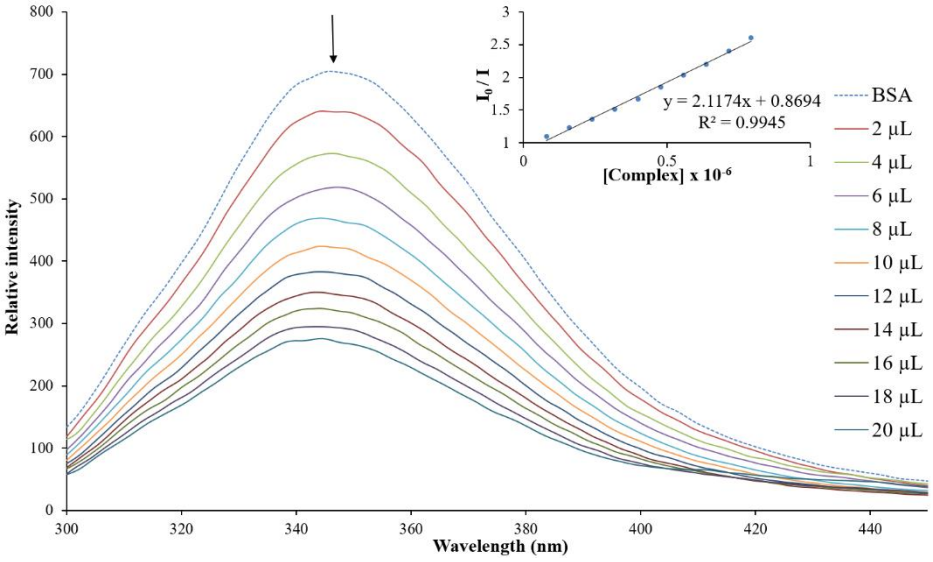

Figure 6.34: *Fluorescence emission spectral profile depicting the titration between compound **2** and BSA. The inset is the Stern-Volmer plot.*

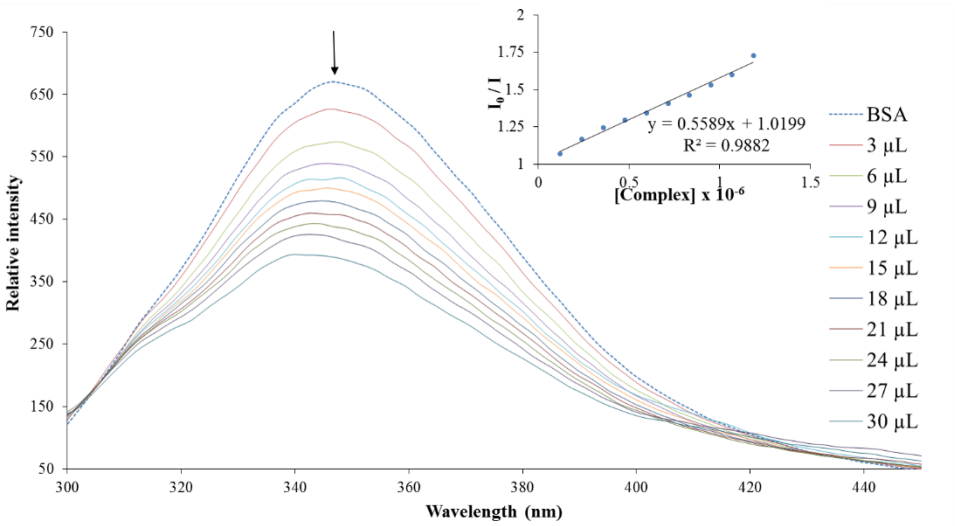

Figure 6.35: *Fluorescence emission spectral profile depicting the titration between compound **3** and BSA. The inset is the Stern-Volmer plot.*

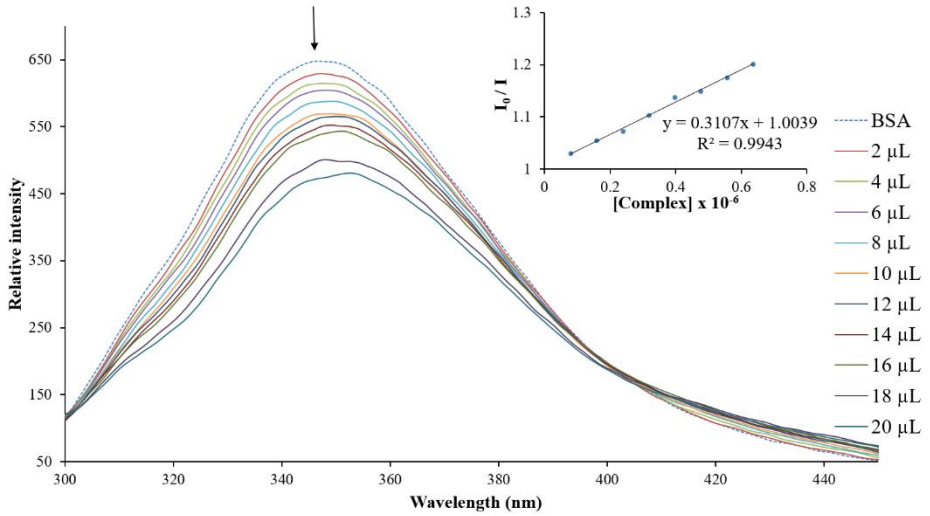

Figure 6.36: *Fluorescence emission spectral profile depicting the titration between compound **4** and BSA. The inset is the Stern-Volmer plot.*

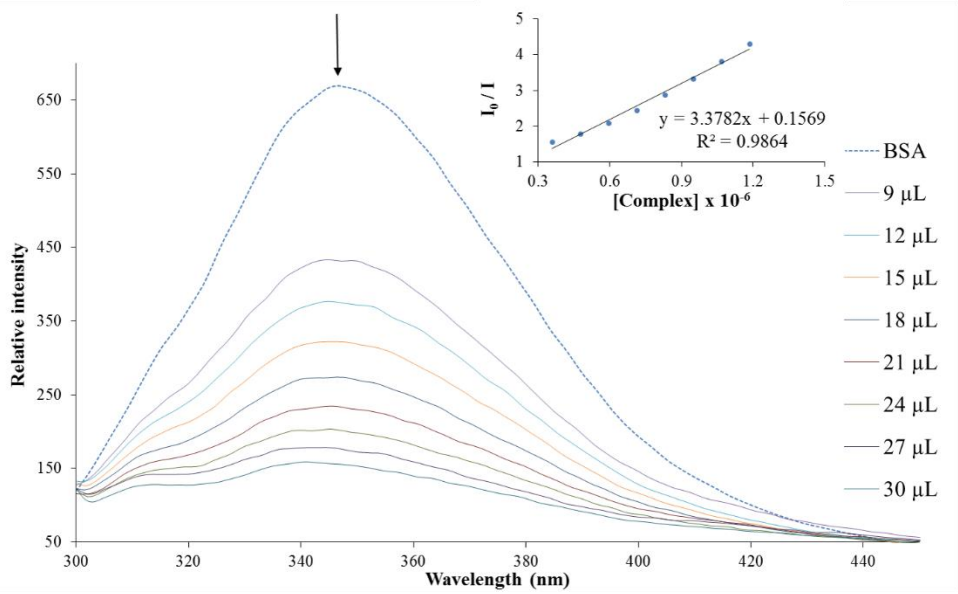

Figure 6.37: *Fluorescence emission spectral profile depicting the titration between compound **5** and BSA. The inset is the Stern-Volmer plot.*

(c) Competitive binding

BSA shows distinct binding sites with various specificities, the most significant ones being referred to as sites **I** and **II** which are located in hydrophobic subdomains **IIA** and **IIIA**, respectively. Competitive binding experiments were conducted by observing the fluorescence quenching capabilities of BSA of each metal compound in the presence of a site marker in order to ascertain their preferred binding site within the BSA structure. Site markers are small molecules that have precise binding locations within the BSA structure [**74**]. In particular, Warfarin was used as a site marker for site **I** whilst Ibuprofen was used for site **II**. As the concentration of each metal compound was increased, the emission maxima of BSA were decreased expressively in the presence of both site markers. The Stern-Volmer plots were then used to determine the K_{SV} values for the respective BSA-Warfarin and BSA-Ibuprofen systems. The preferred binding sites of each metal compound was determined by their ability to displace each site marker, this was done by comparing the K_{SV} values in the absence and presence of each site marker. It is seen that the K_{SV} values of the BSA-Ibuprofen systems are not significantly different in magnitude relative to the K_{SV} values in the absence of any site markers, however, a pronounced decrease is seen with the K_{SV} values of the BSA-Warfarin systems. These experimental trends propose that the ruthenium compounds are able to displace Warfarin

from its binding site in BSA and therefore assume site **I** (situated in subdomain **IIA**) as the preferred binding site [**75**].

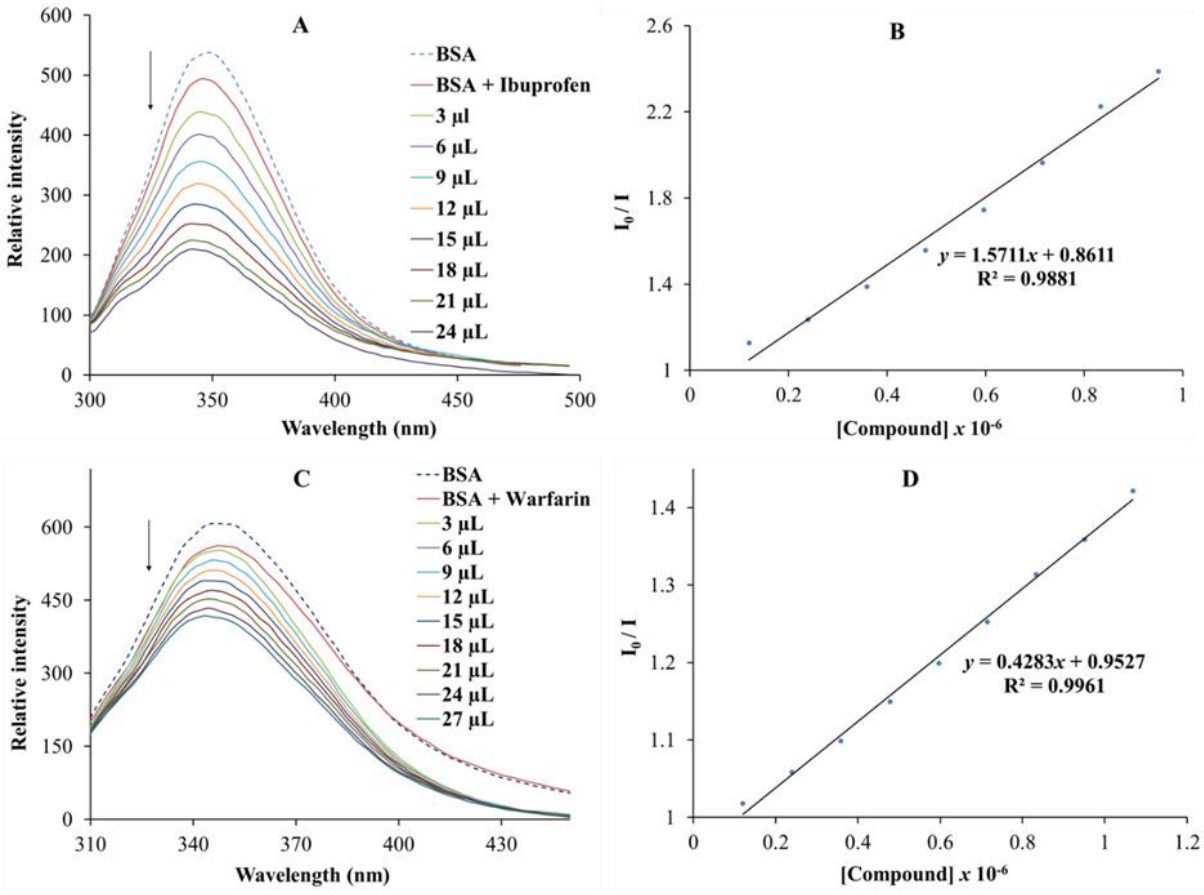

Figure 6.38: *Fluorescence emission spectral profiles of BSA upon the addition of standardized volumes of **1** in the presence of equimolar amounts of (**A**) Warfarin or (**C**) Ibuprofen. **B** and **D** are the respective Stern-Volmer plots.*

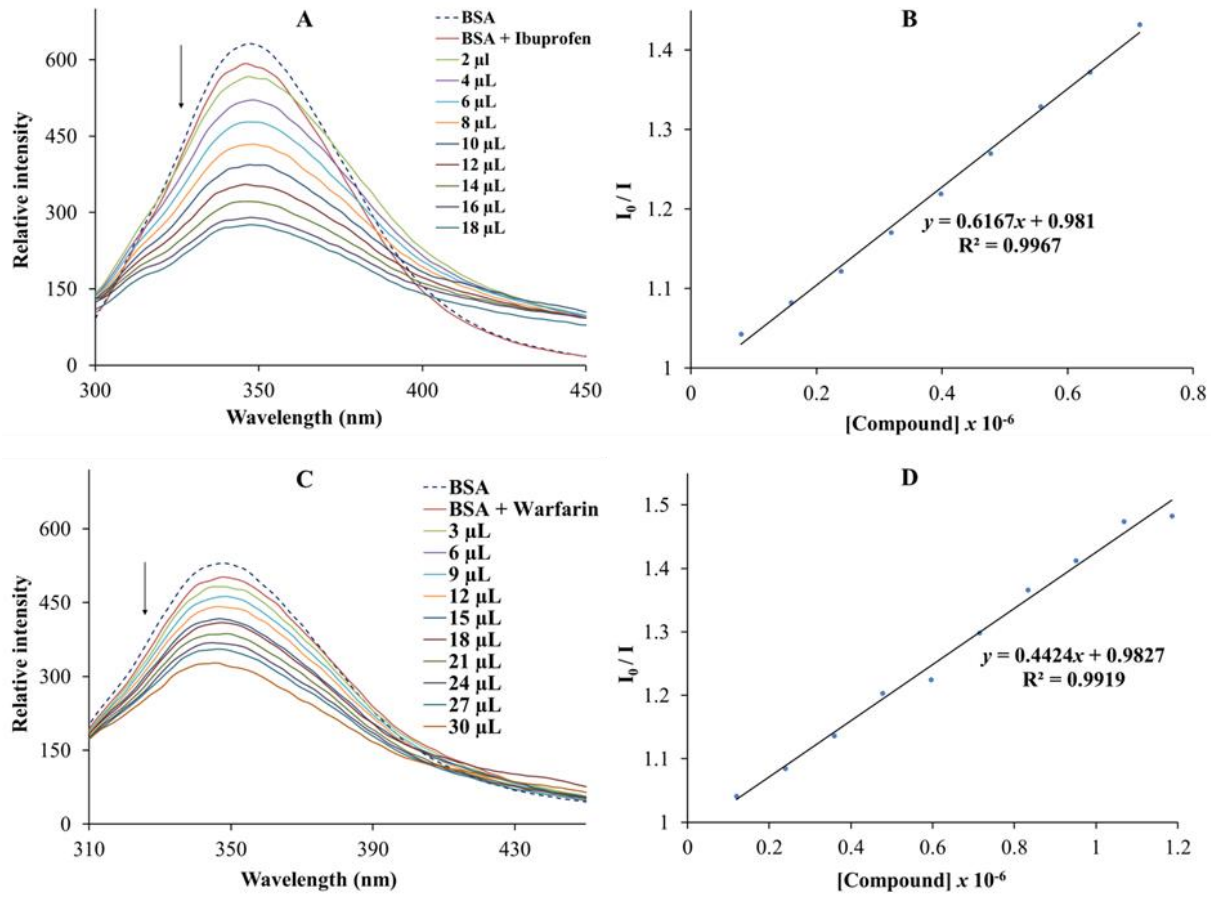

Figure 6.39: *Fluorescence emission spectral profiles of BSA upon the addition of standardized volumes of **2** in the presence of equimolar amounts of (**A**) Warfarin or (**C**) Ibuprofen. **B** and **D** are the respective Stern-Volmer plots.*

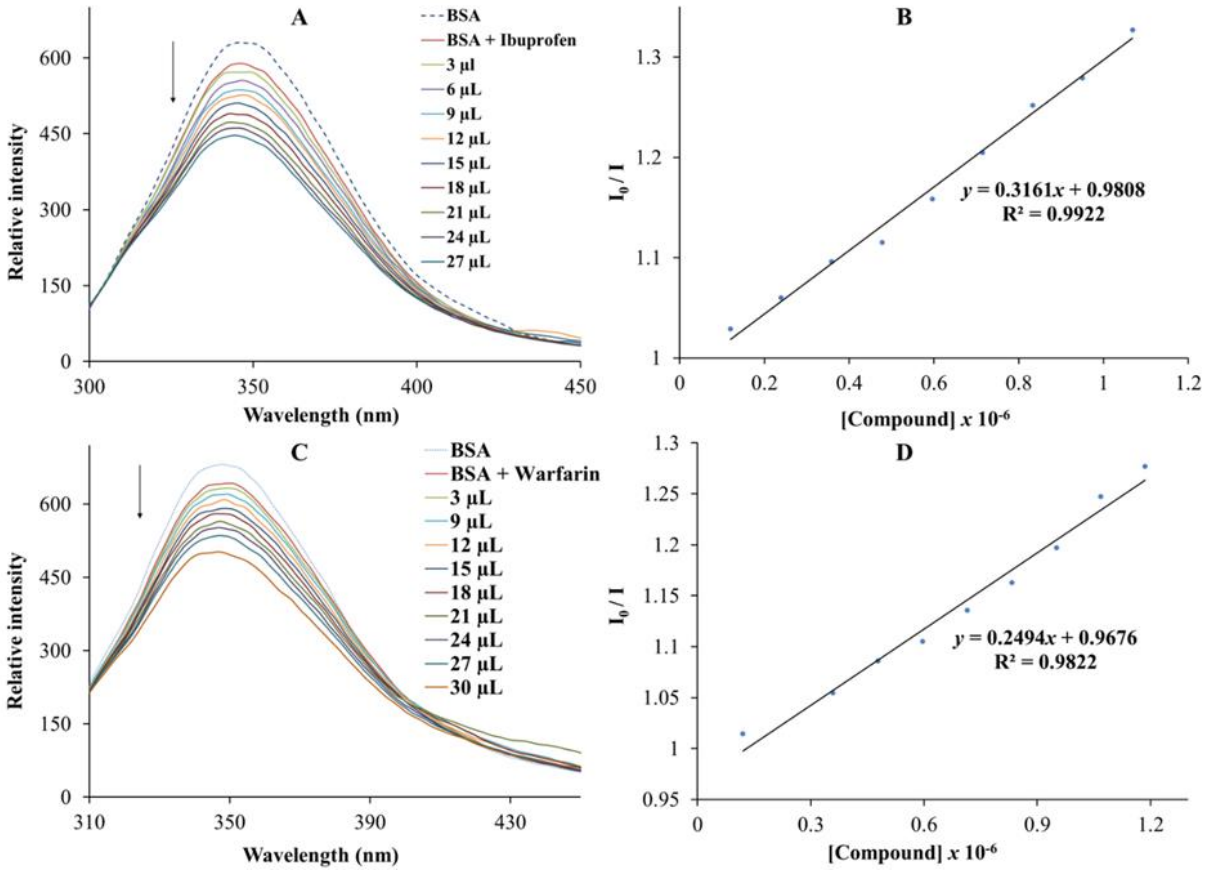

Figure 6.40: *Fluorescence emission spectral profiles of BSA upon the addition of standardized volumes of **3** in the presence of equimolar amounts of (**A**) Warfarin or (**C**) Ibuprofen. **B** and **D** are the respective Stern-Volmer plots.*

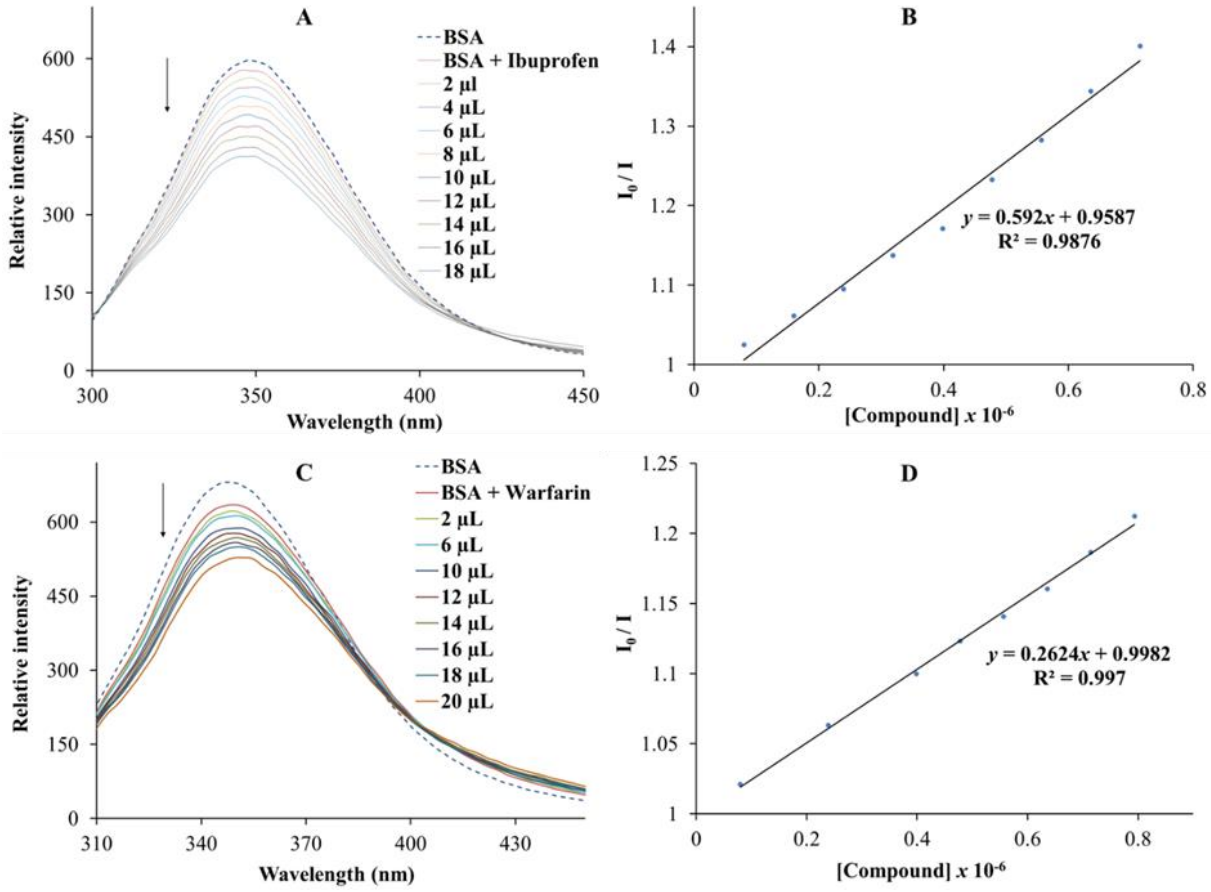

Figure 6.41: *Fluorescence emission spectral profiles of BSA upon the addition of standardized volumes of **4** in the presence of equimolar amounts of (**A**) Warfarin or (**C**) Ibuprofen. **B** and **D** are the respective Stern-Volmer plots.*

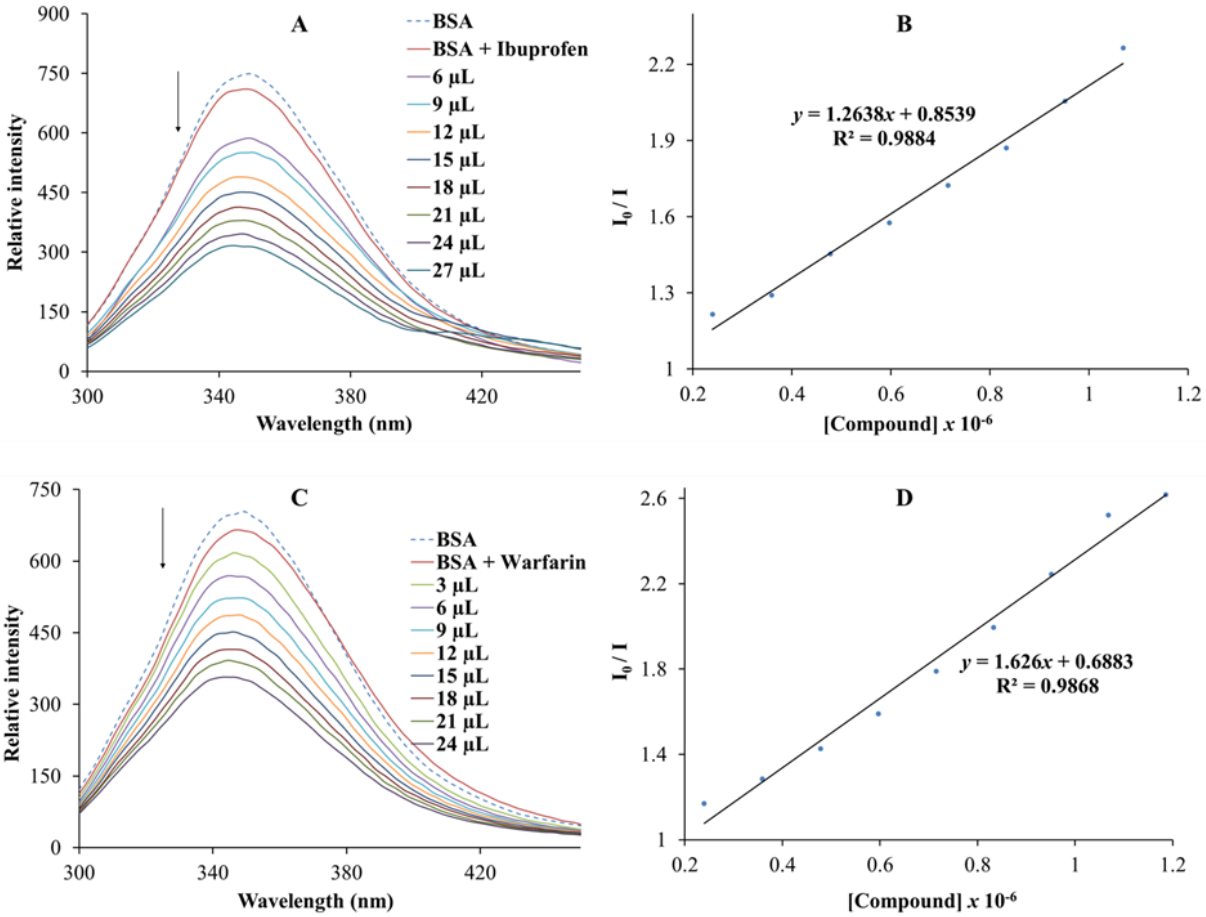

Figure 6.42: *Fluorescence emission spectral profiles of BSA upon the addition of standardized volumes of **5** in the presence of equimolar amounts of (**A**) Warfarin or (**C**) Ibuprofen. **B** and **D** are the respective Stern-Volmer plots.*

Table 6.9: *Binding parameters of **1** – **5** from BSA fluorescence experiments.*

Compound	No Site marker		Ibuprofen		Warfarin	
1	K_{SV} (M^{-1})	K_q (M^{-1} s^{-1})	K_{SV} (M^{-1})	K_q (M^{-1} s^{-1})	K_{SV} (M^{-1})	K_q (M^{-1} s^{-1})
	1.06×10^5	1.06×10^{13}	1.57×10^5	1.57×10^{13}	4.28×10^4	4.28×10^{12}
2	2.12×10^5	2.12×10^{13}	2.11×10^5	2.11×10^{13}	4.42×10^4	4.42×10^{12}
3	5.59×10^4	5.59×10^{12}	3.16×10^4	3.16×10^{12}	2.79×10^3	2.79×10^{11}
4	3.11×10^4	3.11×10^{12}	5.92×10^4	5.92×10^{12}	3.21×10^3	3.21×10^{11}
5	3.38×10^5	3.38×10^{13}	1.26×10^5	1.26×10^{13}	9.38×10^4	9.38×10^{12}

6.6 References

1. A. R. Simović, R. Masnikosa, I. Bratsos and E. Alessio, *Coord. Chem. Rev.*, 2019, **398**, 113011-113036.

2. L. Côrte-Real, B. Karas, P. Gírio, A. Moreno, F. Avecilla, F. Marques, B. T. Buckley, K. R. Cooper, C. Doherty and P. Falson, *Eur. J. Med. Chem.*, 2019, **163**, 853-863.

3. F. A. Al-Bayati and M. J. Mohammed, *Pharm. Biol.*, 2009, **47**, 61-66.

4. N. Wongkattiya, P. Sanguansermsri, I. H. Fraser and D. Sanguansermsri, *J. Complement. Integr. Med.*, 2019, doi: 10.1515/jcim-2018-0195.

5. F. Bisceglie, S. Pinelli, R. Alinovi, M. Goldoni, A. Mutti, A. Camerini, L. Piola, P. Tarasconi and G. Pelosi, *J. Inorg. Biochem.*, 2014, **140**, 111-125.

6. P. Deshmukh, P. K. Soni, A. Kankoriya, A. K. Halve and R. Dixit, *Int. J. Pharm. Sci. Rev. Res.*, 2015, **34**, 162-170.

7. G. Raja, R. J. Butcher and C. Jayabalakrishnan, *Spectrochim. Acta, Part A.*, 2012, **94**, 210-215.

8. I. Yousuf, F. Arjmand, S. Tabassum and M. Ahmad, *New J. Chem.*, 2019, **43**, 5475-5487.

9. I. N. Booysen, S. Maikoo, M. P. Akerman and B. Xulu, *Polyhedron*, 2014, **79**, 250-257.

10. *Journal*, Bruker APEX2, SAINT and SADABS (2010). Bruker AXS Inc. Madison. Wisconsin, USA.

11. R. H. Blessing, *Acta Crystallogr., Sect. A: Found. Adv.*, 1995, **51 (Pt 1)**, 33-38.

12. L. Farrugia, *J. Appl. Crystallogr.*, 2012, **45**, 849-854.

13. G. Sheldrick, *Acta Crystallogr., Sect. A: Found. Adv.*, 2008, **64**, 112-122.

14. Frisch MJ, Trucks GW, Schlegel HB, Scuseria GE, Robb MA, Cheeseman JR, Scalmani G, Barone V, Petersson GA, Nakatsuji H, Li X, Caricato M, Marenich AV, Bloino J, Janesko BG, Gomperts R, Mennucci B, Hratchian HP, Ortiz JV, Izmaylov AF, Sonnenberg JL, Williams, Ding F, Lipparini F, Egidi F, Goings J, Peng B, Petrone A, Henderson T, Ranasinghe D, Zakrzewski VG, Gao J, Rega N, Zheng G, Liang W, Hada M, Ehara M, Toyota K, Fukuda R, Hasegawa J, Ishida M, Nakajima T, Honda Y, Kitao O, Nakai H, Vreven T, Throssell K, Montgomery Jr JA, Peralta JE, Ogliaro F, Bearpark MJ, Heyd JJ, Brothers EN, Kudin KN, Staroverov VN, Keith TA, Kobayashi R, Normand J, Raghavachari K, Rendell AP, Burant JC, Iyengar SS, Tomasi J, Cossi M, Millam JM, Klene M, Adamo C, Cammi R, Ochterski JW, Martin RL, Morokuma K, Farkas O, Foresman JB, Fox DJ (2009) Gaussian 09 Rev. A.01.

15. L. Gramni, N. Vukea, A. Chakraborty, W. J. Samson, L. M. K. Dingle, B. Xulu, J.-A. de la Mare, A. L. Edkins and I. N. Booysen, *Inorg. Chim. Acta*, 2019, **492**, 98-107.

16. C. Rodrigues, A. A. Batista, J. Ellena, E. E. Castellano, D. Benítez, H. Cerecetto, M. González, L. R. Teixeira and H. Beraldo, *Eur. J. Med. Chem.*, 2010, **45**, 2847-2853.

17. J. D. Wilton-Ely, M. Wang, S. J. Honarkhah and D. A. Tocher, *Inorg. Chim. Acta*, 2005, **358**, 3218-3226.

18. R. Maurya, A. Pandey, J. Chaurasia and H. Martin, *J. Mol. Struct.*, 2006, **798**, 89-101.

19. B. Garga, P. Singh and J. Sharma, *Synth. React. Inorg. M.*, 2000, **30**, 803-813.

20. C. Jayabalakrishnan, R. Karvembu and K. Natarajan, *Synth. React. Inorg. M.*, 2003, **33**, 1535-1553.

21. A. Garza-Ortiz, P. U. Maheswari, M. Lutz, M. A. Siegler and J. Reedijk, *J. Biol. Inorg. Chem.*, 2014, **19**, 675-689.

22. R. R. Kumar, R. Ramesh and J. G. Małecki, *J. Photochem. Photobiol., B.*, 2016, **165**, 310-327.

23. I. Ejidike and P. Ajibade, *Int. J. Mol. Sci.*, 2016, **17**, 60.

24. R. Prabhakaran, V. Krishnan, K. Pasumpon, D. Sukanya, E. Wendel, C. Jayabalakrishnan, H. Bertagnolli and K. Natarajan, *App. Organomet. Chem.*, 2006, **20**, 203-213.

25. N. Raja, R. Ramesh and Y. Liu, *Polyhedron*, 2012, **31**, 196-201.

26. A. D. Mülazımoğlu, E. Yılmaz and İ. E. Mülazımoğlu, *Sensors*, 2012, **12**, 3916-3928.

27. E. Eskelinen, P. Da Costa and M. Haukka, *J. Electroanal. Chem.*, 2005, **579**, 257-265.

28. F. Basuli, A. K. Das, G. Mostafa, S.-M. Peng and S. Bhattacharya, *Polyhedron*, 2000, **19**, 1663-1672.

29. R. Ramesh and K. Natarajan, *Indian J. Chem., Sect. A: Inorg., Bio-inorg., Phys., Theor. Anal. Chem.*, 1995, **34**, 535-539.

30. I. N. Booysen, S. Maikoo, M. P. Akerman and B. Xulu, *Tran. Met. Chem.*, 2015, **40**, 397-404.

31. M. Loza and A. Z. Slawin, *Dalton Trans.*, 1999, 2917-2921.

32. P. Govindaswamy and M. R. Kollipara, *J. Coord. Chem.*, 2006, **59**, 131-136.

33. J.-m. Manoli, A. P. Gaughan Jr and J. A. Ibers, *J. Organomet. Chem.*, 1974, **72**, 247-259.

34. L. R. Dinelli, G. Von Poelhsitz, E. E. Castellano, J. Ellena, S. E. Galembeck and A. A. Batista, *Inorg. Chem.*, 2009, **48**, 4692-4700.

35. S. Q. Wu, Y. Miyazaki, M. Nakano, S. Q. Su, Z. S. Yao, H. Z. Kou and O. Sato, *Chem.: Eur. J.*, 2017, **23**, 10028-10033.

36. P. Braunstein, D. Matt, D. Nobel, S.-E. Bouaoud, B. Carluer, D. Grandjean and P. Lemoine, *Dalton Trans.*, 1986, 415-419.

37. J. V. McArdle, A. J. Schultz, B. J. Corden and R. Eisenberg, *Inorg. Chem.*, 1973, **12**, 1676-1681.

38. G.-J. Cao, X. Jiang, H. Zhang, J. Zheng, T. R. Croley and J.-J. Yin, *J. Environ. Sci. Health C.*, 2017, **35**, 223-238.

39. T. S. Kamatchi, P. Kalaivani, F. R. Fronczek, K. Natarajan and R. Prabhakaran, *RSC Adv.*, 2016, **6**, 46531-46547.

40. M. Mohanraj, G. Ayyannan, G. Raja and C. Jayabalakrishnan, *App. Organomet. Chem.*, 2016, **30**, 550-560.

41. M. Mohanraj, G. Ayyannan, G. Raja and C. Jayabalakrishnan, *J. Photochem. Photobiol., B.*, 2016, **158**, 164-173.

42. I. N. Booysen, A. Adebisi and M. P. Akerman, *Inorg. Chim. Acta*, 2015, **433**, 13-20.

43. G. Prakash, R. Manikandan, P. Viswanathamurthi, K. Velmurugan and R. Nandhakumar, *J. Photochem. Photobiol., B.*, 2014, **138**, 63-74.

44. B. J. Pages, D. L. Ang, E. P. Wright and J. R. Aldrich-Wright, *Dalton Trans.*, 2015, **44**, 3505-3526.

45. P. Jayaseelan, S. Prasad, S. Vedanayaki and R. Rajavel, *Arab. J. chem.*, 2016, **9**, S668-S677.

46. T. S. Kamatchi, N. Chitrapriya, H. Lee, C. F. Fronczek, F. R. Fronczek and K. Natarajan, *Dalton Trans.*, 2012, **41**, 2066-2077.

47. A. P. Carnizello, M. I. Barbosa, M. Martins, N. H. Ferreira, P. F. Oliveira, G. M. Magalhães, A. A. Batista and D. C. Tavares, *J. Inorg. Biochem.*, 2016, **164**, 42-48.

48. F. A. Beckford, A. Stott, P. C. Mbarushimana, M.-A. LeBlanc, K. Hall, S. Smith, J. L. Bullock, D. J. Houghton, A. A. Holder and N. Gerasimchuk, *Interdiscip. J. Chem.*, 2016, **1**, 1-15.

49. S. Sathiyaraj, K. Sampath and C. Jayabalakrishnan, *Synth. React. Inorg., Met.-Org., Nano-Met. Chem.*, 2014, **44**, 1261-1271.

50. N. Shahabadi and S. Moradi Fili, *J. Coord. Chem.*, 2018, **71**, 2843-2855.

51. G. Raja and C. Jayabalakrishnan, *Cent. Eur. J. Chem.*, 2013, **11**, 1010-1018.

52. W. M. Motswainyana and P. A. Ajibade, *Advances in Chemistry*, 2015, **2015**, 859730.

53. P. Zhang, J. Chen and Y. Liang, *Acta. Biochim. Biophys. Sin.*, 2010, **42**, 440-449.

54. M. N. Patel, H. N. Joshi and C. R. Patel, *J. Chem. Sci.*, 2014, **126**, 739-749.

55. G. Balakrishnan, T. Rajendran, K. S. Murugan, M. S. Kumar, V. K. Sivasubramanian, M. Ganesan, A. Mahesh, T. Thirunalasundari and S. Rajagopal, *Inorg. Chim. Acta*, 2015, **434**, 51-59.

56. S. Ghosh, P. Kundu, B. K. Paul and N. Chattopadhyay, *RSC Adv.*, 2014, **4**, 63549-63558.

57. J. A. Zhao, S. Zhi, H. Yu, J. Zhang, J. Zhang and J. Hu, *J. Coord. Chem.*, 2017, **70**, 3110-3131.

58. Q. Zhang and Y. Ni, *RSC Adv.*, 2017, **7**, 39833-39841.

59. W. Zhong, Y. Wang, J.-S. Yu, Y. Liang, K. Ni and S. Tu, *J. Pharm. Sci.*, 2004, **93**, 1039-1046.

60. H. Paul, T. Mukherjee, M. Mukherjee, T. K. Mondal, A. Moirangthem, A. Basu, E. Zangrando and P. Chattopadhyay, *J. Coord. Chem.*, 2013, **66**, 2747-2764.

61. X. Lei, L. Ya-nan, M. Wen-jie, H. Xiao-mei, C. Tian-feng, L. Jie and Z. Wen-jie, *Chem. Res. Chin. Univ.*, 2010, **26**, 693-698.

62. Z. Chi, B. Hong, X. Ren, K. Cheng, Y. Lu and X. Liu, *Spectrosc. Lett.*, 2018, **51**, 279-286.

63. R. Kumaran and P. Ramamurthy, *J. Fluoresc.*, 2011, **21**, 1499-1508.

64. M. Rajabi, M. A. Khalilzadeh, F. Tavakolinia, P. Signorelli, R. Ghidoni and E. Santaniello, *DNA Cell Biol.*, 2012, **31**, 783-789.

65. V. D. Suryawanshi, L. S. Walekar, A. H. Gore, P. V. Anbhule and G. B. Kolekar, *J. Pharm. Anal.*, 2016, **6**, 56-63.

66. A.-Z. Wu, C.-Z. Lin, Y.-J. Zhai, J.-L. Zhuo and C.-C. Zhu, *J. Pharm. Anal.*, 2013, **3**, 61-65.

67. T. T. Herskovits, B. Gadegbeku and H. Jaillet, *J. Biol. Chem.*, 1970, **245**, 2588-2598.

68. A. Mishra, A. Malakar, H. T. Biswal, M. K. Barman and G. Krishnamoorthy, *J. Mol. Recognit.*, 2015, **28**, 299-305.

69. T. Topală, A. Bodoki, L. Oprean and R. Oprean, *Clujul Med.*, 2014, **87**, 215-219.

70. A. C. de Melo, J. M. Santana, K. J. Nunes, B. L. Rodrigues, N. Castilho, P. Gabriel, A. H. Moraes, M. d. A. Marques, G. A. de Oliveira and Í. P. de Souza, *Molecules*, 2019, **24**, 2154.

71. V. Ravi Kumar, P. Nagababu, G. Srinivas, M. Rajender Reddy, M. Vinoda Rani, M. Ravi and S. Satyanarayana, *J. Coord. Chem.*, 2017, **70**, 3790-3809.

72. A. Varlan and M. Hillebrand, *Molecules*, 2010, **15**, 3905-3919.

73. B. Ojha and G. Das, *Chem. Phys. Lipids.*, 2011, **164**, 144-150.

74. X. Zhang, L. Li, Z. Xu, Z. Liang, J. Su, J. Huang and B. Li, *PLoS One*, 2013, **8**, e59106.

75. F. Zsila, *Mol. Pharmaceutics.*, 2013, **10**, 1668-1682.

Conclusion and future work

7.1 Conclusions

The foremost aims of this research project were fulfilled:

- The design, synthesis and characterization of new and known biologically relevant multidentate heterocyclic compounds and Schiff bases.
- Investigation of the coordination modes for the aforementioned ligand systems towards ruthenium(II) and –(III) centres.
- Structural elucidations of the resultant metal compounds with the aid of various physicochemical techniques.
- Probing the redox properties and radical scavenging activities of the formulated metal compounds using voltammetric and spectrophotometric methods, respectively.
- Computational and experimental biomolecular interaction studies formed an integral part of this research project while *in vitro* anticancer studies of selected ruthenium compounds were conducted.

In chapter 3, novel ruthenium compounds with *bis*-heterocyclic ligands were formed (**1** and **2**) and characterized by spectroscopic techniques and single crystal X-ray analysis. Variable metal-based redox potentials were attained for **1** and **2**, which can be attributed to the nature of the coordination environments surrounding their individual ruthenium(II) centres. The biological interaction studies of these and previously reported ruthenium complexes (**3** and **4**) were probed. The paramagnetic complex cation of **3** showed the highest radical scavenging activities, which was ascribed to its d^5 metal centre enhancing its propensity to neutralize NO and DPPH radicals. The diverse structural features among the ruthenium compounds **1** – **4** also had implications on their DNA interaction capabilities, with intrinsic binding constants ranging from the magnitude of 10^4 – 10^7 M^{-1}.

However, molecular docking simulations corroborated that the Zn analogues of **1** – **4** are preferential groove-binders. All the metal compounds exhibited optimal affinities towards the drug delivery protein, BSA, whereby their proposed mechanisms of interactions were dictated by the stereoelectronic properties of the corresponding chelators. With the exception of the non-toxic compound **2**, the ruthenium compounds were more cytotoxic to breast cancer cells *in vitro* than the chemotherapy drug 5-FU.

Chapter 4 describes the solid-state structures of **1** – **3** which portray the distinctive $N_{imino}O_{enol}$ coordination mode of ruthenium compounds containing carbohydrazide Schiff bases. Vibrational and electronic spectra of these novel metal complexes were discerned using their corresponding simulated data which were supported by literature trends. The redox potentials for their metal-based interconversions were comparable to those obtained for other paramagnetic ruthenium(III) complexes. Antioxidant studies of the aforementioned ruthenium(III) complexes as well as a candidate anti-diabetic metal-based drug, $[RuCl(PPh_3)(H_3ucp)]$ (**5**) and its mono-imine derivative, *trans*-$[RuCl(PPh_3)_2(Htdp)]$ (**4**), revealed substantially lower IC_{50} values than the standard, Vitamin C. Experimental DNA interaction studies aided by *in silico* calculations showed that **1** – **5** are groove-binders where the stereo-electronic properties of the carboim chelators were a major contributive factor in the stabilization of the corresponding calculated DNA-ruthenium complex adducts. DNA incubated samples of the different metal complexes showed predominately ESR silent behaviours which provide irrefutable evidence of interaction between the individual metal complex and the helical biomolecule. The influence of the carboim chelating ligands were again evident when probing the BSA affinities of the respective ruthenium complexes where apparent association constants (K_{app}) were found to be in the order of $10^3 – 10^6$ M^{-1}, which is indicative of moderate to strong binders. High Stern-Volmer quenching constants (K_{SV}) substantiated the optimal BSA binding capabilities of **1** – **5.** Competitive BSA binding studies illustrate that the metal complexes indiscriminately bind to the BSA **IIA** or **IB** cavities. Compound **4** was the most effective at interaction with DNA as measured by AGE and this correlated with the lowest EC_{50} value in HCC70 cells.

Chapter 5 demonstrates the stabilization of *trans*-$[Ru(PPh_3)_2]^{3+/2+}$ core by tridentate thiosemicarbazones and bidentate benzothiazole imines. The crystal structures of **1** and **2** depicted a rare tautomeric form of the chelating ligands which is unique to monomeric ruthenium compounds while the neutral btm moiety in **3**, coordinates *via* its N_{imino} $N_{benzothiazole}$ donor set. Physicochemical characterization data such as UV-Vis and IR spectra were computationally rationalised. Voltammograms of the metal compounds were dominated by metal-based redox transformations and the paramagnetic ruthenium compounds exhibit superior radical scavenging activities. The individual metal compounds showed relatively high intrinsic DNA binding constants ($K_b > 10^5$ M^{-1}) and in conjunction with the characteristic electronic spectral alterations, were accounted to groove-binding. The preferential *in silico* groove-binding modes of the respective metal compounds were primarily dominated by nature of the close contacts as opposed to steric factors. BSA interactions monitored by fluorescence and UV-Vis spectrophotometric titrations, showed that the metal compounds interact non-discriminately within the protein's hydrophobic cavities. Molecular docking simulations show that metal compounds interact mainly with BSA in its hydrophobic subdomains **IB** and **IIA**.

Chapter 6 includes paramagnetic ruthenium(III) compounds: *fac*-$[RuCl_3(PPh_3)(ap)]$ (**1**) (ap = 4-aminoantipyren), *trans*-P-$[Ru(PPh_3)_2(cinap)_2](PF_6)$ (**2**) (cinap = 1, 5-dimethyl-2-phenyl-4-1,2-dihydro-3*H*-pyrazol-3-one) and *cis*-Cl, *trans*-P-$[RuCl_2(PPh_3)_2(cumbh)]$ (**3**) (cumap = 1,5-dimethyl-2-phenyl-4-1,2-dihydro-3*H*-pyrazol-3-one) which were synthesized and characterized by various physicochemical techniques. Voltammograms of the respective metal compounds showed quasi-reversible redox processes which were attributed to metal-based interconversion. The biological properties of these and formerly reported ruthenium compounds (**4** and **5**) were studied. Paramagnetism of selected metal compounds promoted higher radical scavenging capabilities. All the metal compounds exhibited groove-binding capabilities as per electronic spectrophotometric and molecular docking studies. Fluorescence and UV-Vis spectrophotometric titrations of each metal compound against BSA revealed these behave as dynamic quenchers with strong binding affinities towards site **I**.

7.2 Future work

The work performed on heterocyclic chelators can be expanded to include polyfunctional heterocyclic ligands such as *tris*-/ *tetrakis*-benzimidazoles or –benzothiazoles [**Figure 7.1**]. This will produce an interesting structure activity relationship (SAR) study between the coordination modes of *mono*-, *bis*-, *tris*- and *tetrakis*-heterocyclic ruthenium compounds and their corresponding anticancer activities. In fact, these types of ligands are capable of forming multicomponent compounds or coordination polymeric networks which have unique structural features [**1**]. In addition, the free ligands and their metal complexes have displayed strong binding affinities towards DNA [**1-3**].

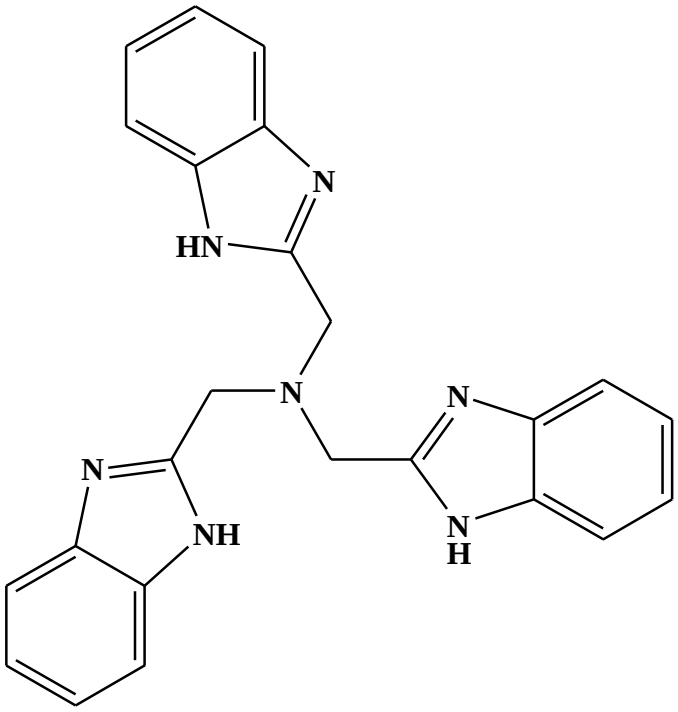

Figure 7.1: *An example of a polyfunctional heterocyclic ligand, tris(2-benzimidazylmethyl)amine.*

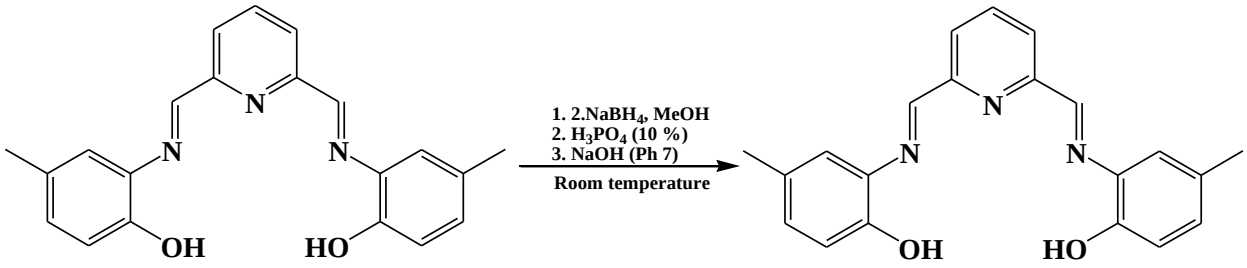

Figure 7.2: *Synthetic route of the reduction of the Schiff base, bis-2,6-bis[(2-hydroxy-5-methylphenyl)-iminomethyl]pyridine to its corresponding amine, bis-2,6-bis[(2-hydroxy-5-methylphenyl)-aminomethyl]pyridine.*

Reduction of Schiff bases to their corresponding amines could be viable option to circumvent the reversible hydrolysis of imines. This can be easily achieved using the reducing agent sodium borohydride, followed by a dissolution in phosphoric acid and then a basification with sodium hydroxide [**4**]. Furthermore, as illustrated in this research study, the presence of the bulky PPh_3 co-ligands, prevent intercalation of the ruthenium complexes between the DNA base pairs. This setback can be overcome by the use of a less sterically hindered ruthenium precursor. An ideal candidate would be a ruthenium arene precursor as these metal precursors afford metal complexes that exhibit strong dual intercalative and groove-binding coordinative DNA binding modes [**5**]. Plausible candidates as metal precursors include the (benzene)ruthenium(II) chloride or dichloro(*p*-cymene)ruthenium(II) dimers, see **Figure 7.3** [**6**].

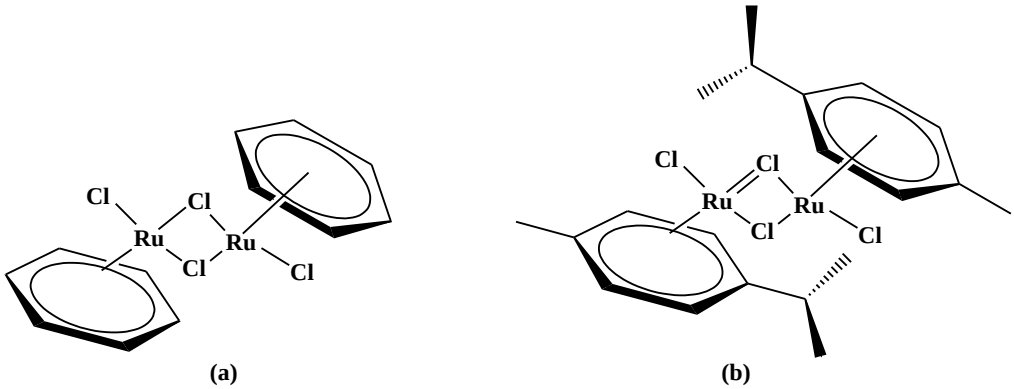

Figure 7.3: *Structures of the (**a**) (benzene)ruthenium(II) chloride (**b**) the dichloro(p-cymene)ruthenium(II) dimers.*

Ruthenium drugs are known to utilized two transport proteins within the physiological system, *viz.* serum albumin and transferrin. Therefore the protein binding studies can be expanded to include the interaction of the ruthenium complexes with transferrin. This can be achieved using spectroscopic methods such as fluorescence spectroscopy [**7, 8**].

7.3 Research outputs

The research findings of this study will be published in international, peer-reviewed journals (as mentioned in the declaration).

Manuscript submitted and comments being attended to:

- Maikoo, S.; Chakraborty, A.; Vukea, N.; Dingle, L.M.K.; Samson, W.J.; de la Mare, J.; Edkins, A.L.; Booysen, I.N. "Structure-activity correlations of ruthenium compounds with *mono*- or *bis*-heterocyclic chelates". *Polyhedron,* 2019.

Manuscripts to be submitted:

- Maikoo, S.; Dingle, L.M.K.; Chakraborty, A.; Xulu, B.; Edkins, A.L.; Booysen, I.N. "Synthetic, characterization and cytotoxic studies of ruthenium complexes with Schiff bases encompassing biologically relevant moieties', 2019.
- Maikoo, S.; Booysen, I.N.; Xulu, B. "Formation, characterization and biomolecular interactions of new ruthenium compounds with thiosemicarbazone or benzothiazole Schiff base chelates". 2019.
- Maikoo, S.; Booysen, I.N.; Xulu, B. "Stabilization of the ruthenium(II) and -(III) centres by chelating N-donor ligands: Synthesis, Characterization, Biomolecular affinities and Computational studies". 2019.

7.4 References

1. H. Wu, Y. Bai, J. Yuan, H. Wang, G. Pan, J. Kong, *Synth. React. Inorg. M.*, 2013, **43**, 237-242.

2. Y.-H. Ji, D. Bur, W. Häsler, V. R. Schmitt, A. Dorn, C. Bailly, M. J. Waring, R. Hochstrasser and W. Leupin, *Bioorg. Med. Chem.*, 2001, **9**, 2905-2919.

3. N. Chandrashekhar, V. Gayathri and N. Nanje Gowda, *Magn. Reson. Chem.*, 2009, **47**, 666-673.

4. M. Fondo, J. Corredoira-Vázquez, A. M. GarcíaDeibe and J. Sanmartín-Matalobos, *Proceedings*, 2019, **9**, 2-6.

5. V. Brabec and J. Kasparkova, *Coord. Chem. Rev.*, 2018, **376**, 75-94.

6. G. Balamurugan, S. Balaji, R. Ramesh and N. S. Bhuvanesh, *Appl. Organometal. Chem.*, 2019, **33**, e4696.

7. M. Pongratz, P. Schluga, M. A. Jakupec, V. B. Arion, C. G. Hartinger, G. Allmaier and B. K. Keppler, *J. Anal. Atom. Spectrom.*, 2004, **19**, 46-51.

8. J. G. Estrada and R. A. Sánchez-Delgado, *J. Mex. Chem. Soc.*, 2013, **57**, 169-174.